Epoxy vitrimer materials based on disulfide exchange chemistry : experimental study and modeling of the stress relaxation - application to composites reinforced by nanofibrillated cellulose

Isis Castro Cabrera

UNIVERSITÉ DE TOULON

LABORATOIRE MAPIEM

ÉCOLE DOCTORALE 548 – MER & SCIENCES

LABORATOIRE MATERIAUX POLYMERES INTERFACES ENVIRONNEMENT MARIN (MAPIEM)

THÈSE présentée par :

Isis CASTRO CABRERA

Soutenue le 13 Septembre 2021

Pour obtenir le grade de Docteur en Chimie

Discipline : chimie et physico-chimie des polymères

Epoxy vitrimer materials based on disulfide exchange chemistry: experimental study and modeling of the stress relaxation - application to composites reinforced by nanofibrillated cellulose

Sous la direction de : Pascal CARRIERE
Co-encadrée par : Sophie BERLIOZ et Armand FAHS

JURY:

M^me^ Edith PEUVREL-DISDIER	CR CNRS HDR, CEMEF, Mines ParisTech, Sophia Antipolis	**Rapporteure**
M. Renaud NICOLAŸ	Professeur/ESPCI Paris	**Rapporteur**
M. Maurice BROGLY	Professeur, Université de Haute-Alsace, Laboratoire de photochimie et Ingénierie Macromoléculaire	**Examinateur**
M. Hugues BRISSET	Professeur, Université de Toulon, Laboratoire MAPIEM	**Examinateur**
M. Jean-Pierre HABAS	Professeur, Institut Charles Gerhardt Montpellier	**Examinateur**
M^me^ Sophie BERLIOZ	Maître de conférences, Université de Toulon	**Co-encadrante**
M. Armand FAHS	Ingénieur de Recherche, Université de Toulon	**Co-encadrant**
M. Pascal CARRIERE	Maître de conférences, HDR Université de Toulon	**Directeur de thèse**

Remerciements

Tout d'abord, je tiens à remercier Jean-François CHAILAN, directeur du laboratoire MAPIEM pour m'avoir permis d'effectuer mon travail de thèse au sein du laboratoire. Je remercie aussi le CONACYT pour m'avoir accordé la bourse 471702 qui m'a permis de réaliser mon travail de thèse et au « comité de becarios CONACYT Carlos Pellicer Cámara » pour leur soutien.

Je remercie les membres du jury Dr. Edith PEUVREL-DISDIER et Pr. Renaud NICOLAŸ, rapporteurs de cette thèse, ainsi que le Pr. Jean-Pierre HABAS, le Pr. Maurice BROGLY, et le Pr. Hugues BRISSET examinateurs de ce travail. Je les remercie pour leur intérêt et leur enthousiasme pour l'évaluation de ce travail de thèse.

Je remercie également mon directeur de thèse, le Dr. Pascal CARRIERE, et mes co-encadrants, le Dr. Sophie BERLIOZ et le Dr. Armand FAHS, qui m'ont accompagné avec rigueur tout au long de la réalisation de ce projet. Merci aussi pour votre patience à mon égard.

Sophie, merci bien pour tout ton soutien, toutes les agréables discussions et conseils tout au long de ma thèse.

Au sein du laboratoire, je remercie l'ensemble du personnel du SIM, Jean-Michel, Edwige, Mélanie, Edmond et Céline, pour leur soutien et leurs conseils sur l'utilisation des équipements. Lenaïk, merci pour toute ton aide et tes nombreuses explications sur DMA. Bruno, merci pour ton soutien avec la RMN. Marlène, tout extrême gratitude pour ta vigilance liée à ma sécurité au laboratoire et de ton aide dans les moments difficiles. Guy Louarn, merci bien pour toutes les explications de l'XPS. Un remerciement au Dr. Gerhard Althoff-Ospelt, chez Bruker BioSpin pour leur aide dans les analyses du RMN.

Merci Hugues, André, et Christine pour votre disponibilité lors de l'organisation de mes enseignements.

Tout au long de mon séjour au laboratoire MAPIEM, j'ai eu l'occasion de partager de bons moments au laboratoire, au bureau et à la plage. Commençons par ceux que j'ai vu partir vers d'autres horizons : Vytalys, Clém, Manu "le président", Cocleto, William, Alain, Anthony, Ouassim, Nadja et Amonda, merci beaucoup pour toute cette bonne humeur.

Passons maintenant aux doctorants pour qui je souhaite voir franchir la ligne d'arrivée : Aurélie merci beaucoup de t'être souciée de moi, Nathan, Elora, Yacoub, Alexandre, Nacer, Linh, Alex et (sûrement) Stéphane, merci pour toute votre bonne humeur.

Elisa + Lua et Gabriela, *muito obrigado* pour m'avoir écouté et m'avoir prêté une épaule sur laquelle m'appuyer pour pouvoir continuer. Lucile et Raph, merci beaucoup pour vos bons encouragements et tous vos conseils.

Au fond du laboratoire, dans ce que j'appelle "ma grotte" ou "salle d'analyse mécanique" pour les gens normaux, comment oublier deux personnes aussi incroyables que Sigrid et Manar. Les filles, merci d'avoir été avec moi pendant des heures et des heures, pour vos bonnes discussions et vos bons souhaits. Vous êtes toutes les deux incroyables.

A l'entrée de notre bâtiment, les gardiens du Bât. X, les doctorants de MIO-LIS, Caro, Mélanie, Anthony, Kubeb, Baptiste, Marion, Ahmed, Maxence, Paul, William (le pou !) et Guillaume merci beaucoup d'avoir rendu ce chapitre de ma vie appelé thèse si agréable.

Pendant mon séjour en France, je remercie les filles CANOVAS-ZEA, Sandra, Adriana et Virginia, qui m'ont aidée à m'installer dans le Sud depuis octobre 2016 et avec qui j'ai parcouru plusieurs kilomètres ici et là. De même, mes plus sincères remerciements à une famille attachante qui m'a soutenue inconditionnellement, les PAIX-PICARD-LEROY. Merci beaucoup, Odile, Jean-François, Guillaume, Amber, Marie-Anne, Benoit et la petite Blanche pour leur soutien inconditionnel. C'est grâce à vous tous que j'ai pu me sentir chez moi, si loin de la mienne.

Maintenant, sans oublier d'où je viens, le Mexique, je veux remercier mes amis "QFOS" Ger et Less, qui m'ont toujours fait confiance pendant tant d'années. Helen, merci de m'avoir aidé à trouver le courage de continuer si loin de chez moi. Aux désormais docteurs et chercheurs Leonardo Moreno et Ruben Adame, qui m'ont convaincue que la rhéologie est belle, de m'aventurer au-delà de chez moi et qui ont continués à me conseiller de si loin. Merci beaucoup les gars.

De si loin aussi, je veux remercier ma famille, maman, Ramses et Vita, merci d'avoir cru en moi. Tout au long de mes études, vous m'avez toujours montrée votre amour et patience, m'aidant à trouver le courage de continuer. Malgré la distance, vous étiez toujours inquiets pour moi. A mon père je remercie de m'avoir encouragé dans ces moments compliqués. *Con gran amor, y admiración para mamá y Vita quienes siempre han estado ahí, me han guiado y siempre me han animado a seguir adelante, seguir mis sueños.*

Enfin, je voudrais dire un grand merci à Benoît. Chaque fois que je voulais sauter du bateau, tu étais toujours là pour m'encourager à continuer, m'aidant à trouver mon chemin avec amour et patience.

Abbreviation and Variables

AFM: Atomic Force Microscopy

AIE: Aggregation-induced emission

4-APD: 4-aminophenyl disulfide

BER: Bond Exchange Reaction

CNC: Cellulose Nano Crystal

CP-MAS: Cross Polarization, magic angle spinning

DSC: Dynamic Scanning Calorimetry

DDM: 4,4'- diaminodiphenylmethane

DGEBA: Diglycidyl ether of bisphenol A

DMA: Dynamic Mechanical Analysis

DMF: *N, N*-dimethylformamide

EDX: Energy-Dispersive X-ray spectroscopy

EMP: Ethyl 2-mercaptopropionate

EtOH: Ethanol

FTIR: Fourier transform infrared

GPS: 3-glyxidoxypropyltrimethoxysilane

GMPES: 3-glycidoxypropyldimethylethoxysilane

KWW: Kohlrausch-Williams-Watts model

MFC: Micro Fibrillated Cellulose

NFC: Nano Fibrillated Cellulose

NMR: Nuclear Magnetic Resonance

R: Universal gas constant

SEM: Scanning Electron Microscopy

Tan δ: Damping factor

*T*α: α-relaxation temperature

*T*g: Glass transition temperature

TGA: Thermogravimetric Analysis

THF: Tetrahydrofurane

*T*v: Topology freezing temperature

*T*m: Melting transition temperature

TTSP: Time-Temperature-Superposition Principle

XPS: X-ray Photoelectron Spectroscopy

WLF: Williams, Landel and Ferry empirical model

a_T: Horizontal shifting factor

C_1: Model parameter of the WLF model

C_2: Model parameter of the WLF model

E_i: Prefactor parameter of the adapted model

Ea: Activation energy (kJ/mol)

G': Storage modulus (GPa) (shear)

E': Storage modulus (GPa) (elongation or bending)

R: Universal gas constant (8.314 $J*mol^{-1}*K^{-1}$)

rpm: Rounds per minute

T: Temperature (°C/K)

β_i: Stretched exponent decay

λ: Relaxation time (min)

η: Viscosity (Pa*s)

ρ: Crosslink density (mol/m^3)

ω: Angular frequency

Index

General introduction

General introduction

Epoxy resins have drawn the attention of many industries due to their versatility in numerous domains, from adhesives to polymer matrices for composite materials. Hence, they have become objects of numerous researches. Despite their versatility, day by day, the markets need new lightweight and high-performance materials to deal not only with industry requirements but also to reduce the growing production of waste materials. In this context, the covalent adaptable networks (CANs) and the incorporation of nanofillers are two advantageous options for solving some of the most limiting problems of thermosetting materials, such as the ***re-processability and the durability***. ***CANs*** are dynamic crosslinked materials ***displaying self-healing properties and re-processability***, two desirable attributes to extend the lifetime of products, and the thermosets' recyclability. Thus, these dynamic networks have retained the attention of several works. ***Vitrimer*** materials ***are*** an example of these interesting ***CANs***.

Vitrimer materials were introduced by Leibler and co-workers in a first pioneering work based on reversible transesterification chemistry. The interesting transesterification exchange mechanism was studied several decades ago, like the one performed by Matějka and Dušek (1984). The vitrimers are characterized for behaving like a glassy solid at temperatures below their, like an elastomer above their *T*g, and like a viscoelastic liquid at temperatures where the exchange reaction occurs (topology freezing temperature or *T*v). At temperatures superior to their topology freezing temperature *T*v, the material can flow (if *T*v>*T*g), undergoing topological changes through speed molecular rearrangements while preserving its crosslink density. Contrary to polymers, vitrimers' viscosity displays a progressive variation with temperature, like vitreous silica or strong liquids. Hence, the dynamic reversible covalent bond of vitrimers gives them re-processability despite a permanent crosslink density.

Since the first promising work of Leibler *et al*. (2011), the list of crosslink networks with reversible exchange mechanisms with vitrimer properties grow day by day. One of them is the disulfide exchange mechanism. Odriozola *et al.* re-worked (2016) the challenging reversible crosslink of diglycidy ether of bisphenol A (DGEBA) and 4-aminophenyl disulfide (4-APDS), classifying it as a vitrimer material. Their results evidenced the ***re-processability of the DGEBA–4-APDS system*** reinforced by glass fibers in the presence of a reactive solvent for further applications. The reversibility of this system was evidenced 30 years ago by Tesoro and co-workers (1990), showing good thermo-mechanical properties strongly linked to the aromatic structures present in both the prepolymer epoxy and the dynamic hardener. Nonetheless, ***the characterization*** as a vitrimer

material ***of DGEBA–4-APDS system was not fully evidenced***.

The objective of this thesis is to study in detail this vitrimer system and then the evolution of these properties with the addition of natural fibers to obtain a composite material. Finally, the perspective is engaged to improve the ultimate properties of the composite by functionalizing the natural fibers' reinforcement.

In the first results Chapter (Chapter III), the first objective proposed in this work is to evidence if the system DGEBA–4-APDS is a truly vitrimer material displaying all the characteristics that define it such as:

- a constant crosslink density at all temperatures
- it can flow and fully relax
- the presence of a new transition temperature different from the *T*g or *T*m: The *T*v
- its viscosity that follows an Arrhenius-type behavior.

The ***vitrimer*** relaxation behavior is usually firstly ***described by the Maxwell*** equation. This relation is the easiest constitutive equation used to describe an ideal viscoelastic material that manifests viscous and elastic characteristics together. The vitrimer networks are real materials that do not precisely follow the Maxwell relaxation model, so the vitrimer relaxation description must be consider with caution.

Moreover, the relaxation behavior of vitrimers is usually evaluated at temperatures well above the *T*g, where the exchange reactions are operating. ***For the DGEBA–4-APDS system***, it is not possible to perform the analysis in the same way because both transition temperatures are in a short temperature range. This fact suggests that the fast exchange reactions are partially restricted because the reversible bonds are slightly embedded into the rigid network. So that, two ***relaxation behaviors may be overlapped,*** displaying a staggering relaxation which is ***impossible to describe by*** only using the ***Maxwell model***. Therefore, ***the second objective address in the Chapter III is to provide an adapted relaxation model to describe the relaxation behavior of this vitrimer system more accurately***. The model proposes an analysis of the system in a more integrated way, analyzing the relaxation of the bond exchange reaction without neglecting the segmental chain relaxation of polymer networks. Different stoichiometries are explored to understand the relaxation phenomena linked to the concentration of covalent adaptable bonds and the variation of the glass transition temperature. The stoichiometry variation allows a clearer understanding of the parameters employed in the model to describe the relaxation behavior of the DGEBA–4-APDS system.

Incorporation of nanofillers, such as ***Nano Fibrillated Cellulose*** (NFC) into DGEBA–4-APDS resin might allow manufacturing ***a sustainable lightweight composite*** material with enhanced mechanical properties. This is a promising way to solve the most limiting problem of thermosetting composite materials as sustainability. ***The third objective of this work, developed in the Chapter IV, the production of a vitrimer-based composite (DGEBA–4-APDS-NFC)***, was inspired in the challenging impregnation method developed by Berglund *et al.* (2014). This interesting technique leads to an advantageous distribution of epoxy resin inside the cellulosic matrix. The mechanical properties of the composite must be enhanced while maintaining its thermal resistance and all vitrimers' properties. The study of the stress relaxation of the composite allowed ***to verify the robustness of the stress relaxation model applied to vitrimer composite material***. The Chapter IV addresses issues concerning the parameters' evolution of the stress relaxation model due to the NFC presence.

The NFC has proved to be a sustainable lightweight filler able to enhance the mechanical properties of composite materials. Nonetheless, it displays inconvenience such as the self-agglomeration or a high hygroscopic level. These drawbacks limit the NFC incorporation into an epoxy matrix and reduce the durability of the composite. Then, the ***NFC surface modification*** has proved to be a good strategy to ***overcome self-agglomeration and durability*** issues, promising results such as:

- better interfacial adhesion and covalent bonds between the modified cellulose fibers and epoxy-resins,
- an easier diffusion of the epoxy resin into the fibrils,
- improvement of the resistance to water of natural fibrils to prevent accelerated aging.

These advantageous changes might allow to produce a composite with not only enhanced mechanical properties but also a higher durability. Given the beneficial changes introduced by the cellulose surface modification, ***the fourth objective, discussed in the Chapter V, is to modify the surface of the NFC with a deep understanding of the grafted structure.***

The explored surface modification uses silane coupling agents. The complex siloxane network formed around the fibrils is analyzed in detail in Chapter V. The chemical and physical adsorption network is also studied since this surface plays a crucial role in obtaining an enhanced composite.

Chapter I : Previous works

1. Previous works

1.1 Epoxy resins

Epoxy resins, which belong to the thermosetting family, are important polymeric materials that are increasingly in demand. They are used in various applications such as coatings, electronic materials, adhesives, automobile, construction, and matrices for fiber-reinforced composites due to their combination of strength, chemical inertness, and thermal performance. The value of the current worldwide market is approximately 20 billion USD (**Figure I-1**). [1, 2]

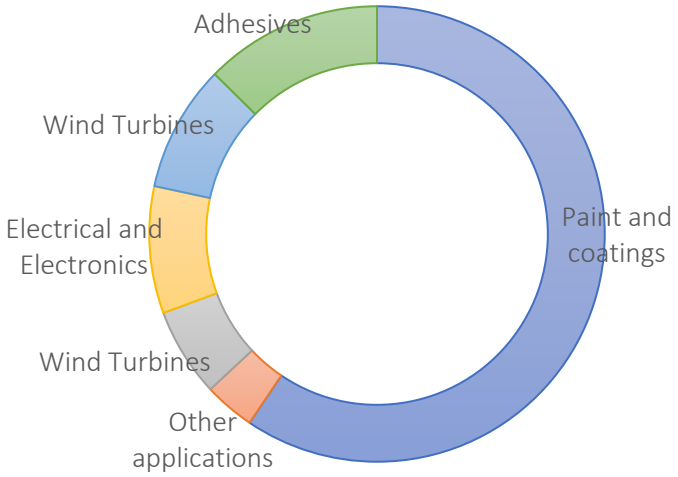

Figure I-1. Comparison of the world market for epoxy resins by value[1].

Their versatility has been the main reason for the steady growth rate of applications since their first synthesis in 1891 and the two-independent works in late 1940 by Pierre Castan in Switzerland and Sylvan Greenlee in the United States[3].

The name epoxy resin is usually given to the prepolymer or epoxy monomer and the cured resin. The prepolymer possesses two or more epoxy groups (epoxide or oxirane), usually on terminal positions. The prepolymer epoxy can react and produce crosslinked structures with several hardener systems. Secondary amines and acid anhydrides are the most commonly used hardeners.

1.1.1 Curing of glycidyl ether resins

The epoxide group can react with several substance classes. In the crosslinking process, curing agents can be categorized as following [3, 4, 5].

1) Alkaline curing agents, such as:
   - Primary and secondary aliphatic amines. The formed hydroxyls are highly reactive. The most commons are diethylene triamine (DETA) and tetraethylene pentaamine (TEPA).
   - Aromatic amines. The cured systems with these amines offer a higher thermal and chemical resistance than the systems cured with aliphatic species. The most commons are *m*-phenylenediamine (MPDA), 4,4-diamino diphenyl sulfone (DADS), and 4,4'-diaminodiphenyl methane (DDM).
   - Cyclic amines. When used as crosslinkers, they provide thermosets with intermediate properties between those obtained with the aliphatic and the aromatic amines. These specific properties are appreciated in some applications like adhesive coatings. The most commons are piperidine, *N*-(2-aminoethyl)piperazine (AEP), menthanediamine, and *m*-xylylene diamine (*m*-XDA).
2) Acid curing agents, like:
   - Phenols. The properties of cured systems with bisphenol-A epoxy are especially used in coating applications for corrosion-resistant pipes. The mechanism involves poly-addition to epoxy resins and is activated by acids such as p-toluenesulphonic acid.
   - Organic acid. Dicarboxylic acids are commonly used. The reaction mechanism involves the addition of the carboxy group and the esterification. Anhydrides are also used as curing agents; they follow the same reaction mechanism after a ring-opening in the presence of water. Tertiary amines are commonly used to catalyze the reaction.
   - Polysulfides. The mercaptan groups are sufficiently acid to react with epoxy resins. The polymercaptans can cure at temperatures as low as -40°C. Therefore, they are useful on adhesive formulation where a rapid cure is required.

1.1.2 Curing reactions of epoxy resins with amines

The crosslinking mechanism of epoxy-amine systems is summarized in **Figure I-2**. The mechanism was originally proposed by Smith *et al.* (1961) and Horie *et al.* (1970). The opening of the epoxy rings generates complexes based on hydrogen bonds (**Figure I-2 a, c,** and **e**). The hydroxyl-epoxy complex formation confers the network an autocatalytic effect during the crosslinking reaction (**Figure I-2b, d, and f**). The esterification reaction may occur at high temperatures. The reaction is catalyzed by the tertiary amines generated during the reaction (Mezzega *et al.,* 2000). It is important to remark that in the case of the aromatic amines, the tertiary amines formed throughout the curing do not catalyze

the homopolymerization at temperatures below 150 °C (Rozenber *et al.* 1986) [6].

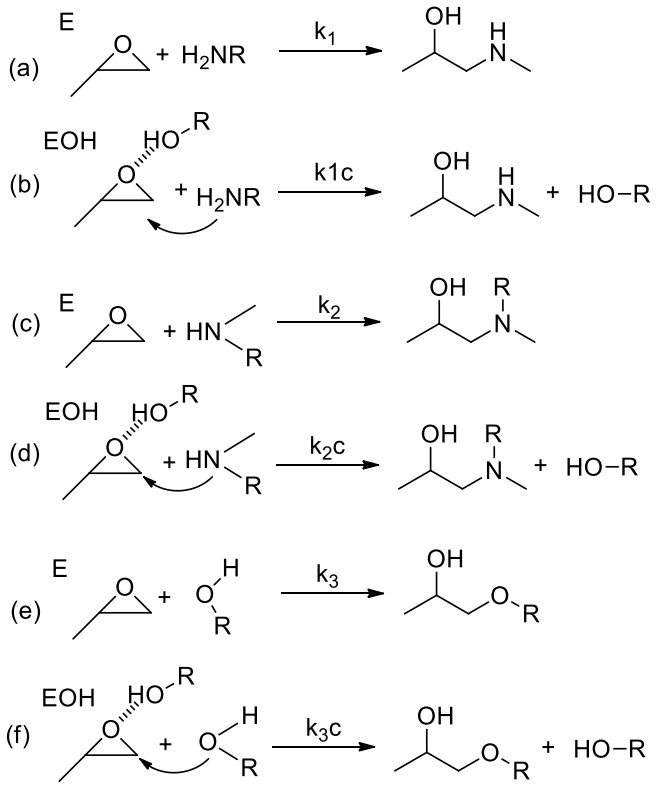

Figure I-2. Opening of epoxy cycles by primary amines a) with catalyst and b) without catalyst. The epoxy cycle opening by secondary amines, and c) with catalyst, and d) without catalyst. Homopolymerization process e) with catalyst and f) without catalyst.

Throughout the curing process, the epoxy-amine blend presents physical and structural changes due to an increment of the molecular weight and viscosity. Two main phenomena can be distinguished: gelation and vitrification.

- In the gelation process (**Figure I-3**), an increment of the molecular weight M_w is observed. It is in line with the formation of a network structure and hence, an increase of the viscosity, which tends to infinity. This point is called the gel point. During this stage, the shear viscosity η_o diverges to infinity, the loss and storage modulus (G" and G') are identical, and the loss factor (*tan δ*) is the same for different frequencies.

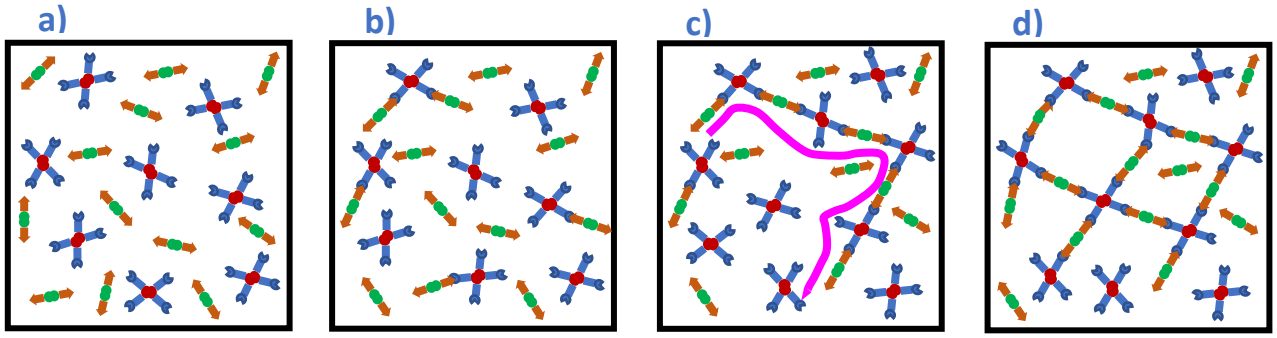

Figure I-3. Chemical structure evolution during crosslinking of a reactive system: a) resin and hardener, b) linear/branched oligomers, c) sol/gel transition, d) 3D network[6].

- In the vitrification, the material undergoes a transition from rubber to a glassy state. At this point, the crosslinking reaction decelerates because of the decrease in the molecular chains' mobility in the glassy state and the decrease of amines diffusion in the network. The conversion is still possible but far slower.

Previous works, such as Ochi *et al.* (1981; 1991), have shown the importance of the curing process temperature. A curing cycle with different steps allows gelation at low temperatures, and then the temperature is gradually increased for the vitrification process. Finally, the use of a post-curing temperature superior to the maximal *T*g promotes to obtain as much as possible the maximal crosslink density of the network. Moreover, following this process allows reducing the internal stresses which could appear during curing[7, 8].

1.1.3 Glass transition temperature (*T*g)

The glass transition temperature, also called *T*g, is the temperature range at which the amorphous regions experiment a transition from a rigid state to a more flexible state. It is more practically defined as the temperature where the molecular structure is transformed from a brittle solid to a ductile or rubber solid[9]. Generally, below the glass transition temperature range, the molecular movements are frozen with fewer changes in properties. Still, when the *T*g is surpassed, abrupt molecular movements occur, resulting in a decrease in elastic modulus and a change in physical properties such as specific heat capacity (Cp), coefficient of thermal expansion, or dielectric constant. From a kinetic point of view, the glass transition temperature and the resulting non-equilibrium character of the glassy state are responsible for phenomena of structural relaxation, glass transition hysteresis, and physical aging[10].

Figure I-4 schematizes the enthalpy (or specific volume) during a cooling rate. The curve departs from the equilibrium (from point A to B), where the structural relaxation times become sufficiently long that the system cannot equilibrate completely. Then, the curve goes to a non-equilibrium state (from point B to C). The temperature of the transition between equilibrium and non-equilibrum stat is the glass transition region[11, 12]. The transition temperature shows a dependence on cooling rate, so it can also be explained in terms of a relaxation time function (λ), which considers the cooperative nature of the molecular relaxation. So that, the molecular relaxation on temperature and of the instantaneous structure $G(t)$, a product of a cooling rate from a liquid-like state to a glassy state, i.e., $\lambda = \frac{\eta}{G}$. $\eta = \eta_0 \exp\left(\frac{Ea}{RT}\right)$.

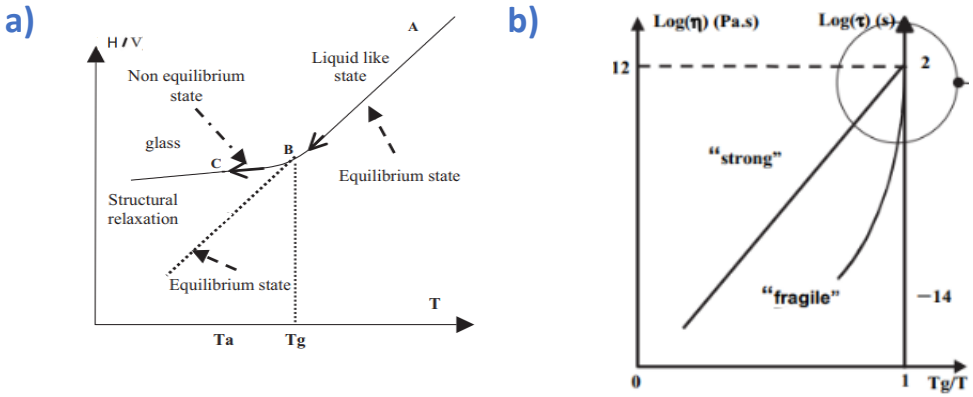

Figure I-4. a) Evolution of the enthalpy/free volume as a function of the cooling rate, b) classification of glass-forming liquids based on viscosity variations with the normalized reduced *T*g/T proposed by Angell[11].

In epoxy resins, the stoichiometric ratio is defined as r=[A]/[E], where [A] and [E] are the number of the chemical function of amine and the epoxy monomers. When r<1, it means an excess of epoxy, r=1 determines the stoichiometric formulation, and r>1 implies an amine excess. The variation of this ratio might impact its architecture, resulting in changes in free volume or cross-link density. In turns, this change modifies the mechanical and thermal properties[13].

An interesting research performed by Williams *et al.* (1991) and Montserrat *et al.* (2001) showed how stoichiometry takes an important role in the *T*g. The work also showed how the maximal *T*g value of an epoxy resin is obtained using a functionality ratio equal to 1 (**Figure I-5**)[14, 15].

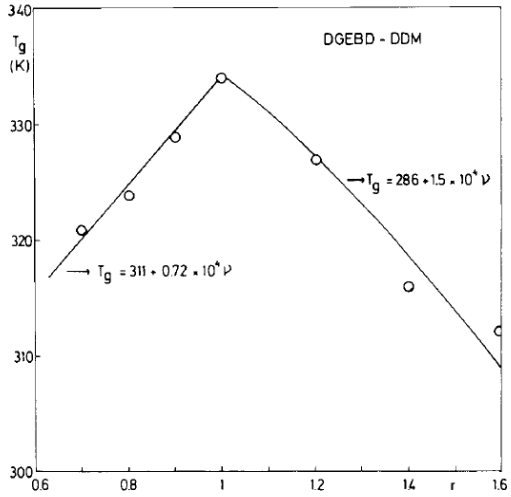

Figure I-5. Glass transition temperature vs. stoichiometric ratio for the DGEBD-DDM system[15].

The resins prepared with an excess of epoxy (r<1) give the network some bulky groups situated at the end of the epoxy chain. This excess of terminal groups increases the free volume and, consequently, decreases the resin's glass transition[14]. The other possible case, when an excess of amine is added (r>1), the free volume also increases, and therefore, the network presents a lower glass transition[14]. Morgan *et al.* (1984) postulate that off-stoichiometry epoxy resins tend to give branched structures and they react partially [16].

1.1.4 Epoxy resin composites

Throughout human history, composite materials have been used to enhance a special material's performance, from pottery in prehistory to airplane fuselage today.

The good performance and epoxy resin's reactivity enable them to be the perfect candidate to produce a composite material. Their chemistry facilitates their bonding with different kinds of fillers like glass, carbon, or aramid fibers. Another interesting approach to produce epoxy resin composites is surface functionalization. The nano-fillers with the appropriate groups at their surface may promote physical and chemical bonds between the nanomaterial and the resin. Under appropriate conditions, nano-additives can increase polymers' strength by adding only 1% weight of filler[1].

Nowadays, epoxy composites represent approximately 10% of the value of the epoxy resin market. A remarkable use for these epoxy composites is producing new lighter materials, a growing sector all the time. For instance, the Glace Laminate Aluminum Reinforced Epoxy (GLARE) is employed in the fuselage of the Airbus A380 [17]. For the Airbus A350 or Boeing 787, approximately 50% of their mass comes from composite materials[18, 19, 20] (**Figure I-6**).

Composite materials can also be found in numerous industries such as electronic (electronic circuit plaque, recovering), medical (prosthesis, implants), nautical (vessels), sport (skies, bicycles), luxury automobile (chassis), among others.

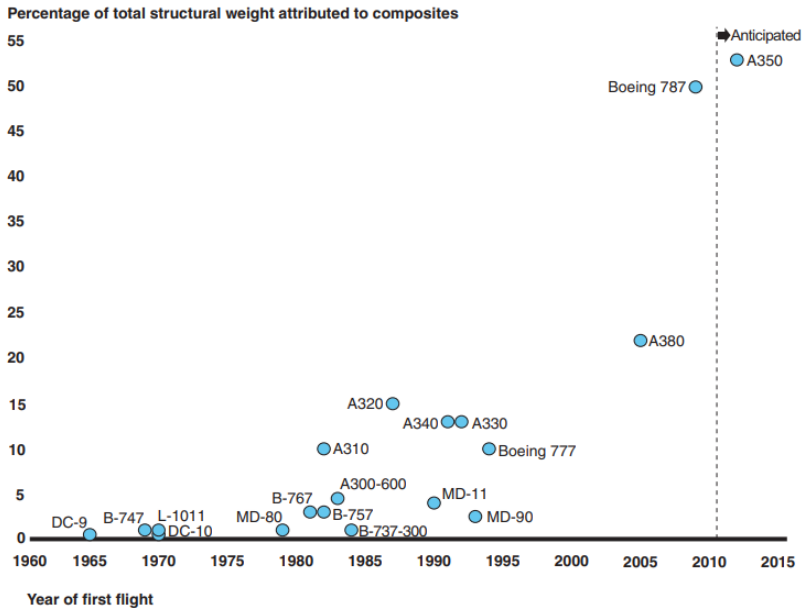

Figure I-6. Commercial airplane models over time by the percentage of composites[18].

1.1.4.1 Epoxy resin reinforced with natural fibers.

Throughout the 20th century, many research groups have shown a particular interest in adding nanofillers to the polymer matrix to enhance its properties [21]. Such is the case of Chanzy and Cavaillé (1995), who achieved a high-performance skeletal bio-composite[22]. The material consisted of a poly(styrene-*co*-butyl acrylate) latex reinforced with cellulose nanowhiskers isolated from tunicates. The network presented a significant improvement of the mechanical properties in the rubbery state. This phenomenon was associated with the formation of a percolated whisker network into the polymer matrix, linked together by hydrogen bonds. The good mechanical enhancement obtained as the stiffness rose triggered many researches incorporating cellulose whiskers in polymeric matrices. In the epoxy thermoset field, we can find notable works of incorporating cellulose whiskers in different and original methods such as water emulsion[23], impregnation[24, 25], suspension in solvents[26], among others. The results were composites that demonstrate a significant improvement of the storage modulus even with a low quantity of cellulose whiskers (the experiments were carry out with 5 to 30% w/w).

Another interesting pathway to incorporate cellulose into an epoxy matrix consists of modifying chemically the surface of fibrils. The modified surface could enhance the fibril cellulose dispersion,

the compatibility with matrices and introduce an extra functionality that could provide the desired property in an afterward application, such as silane grafting[27], hyperbranched aromatic polyamide[28], acetylation[29] , or poly ethylenimine grafting[30].

Silane grafting has drawn attention due to the large variety of silanes with diverse functionalities that could be easily added using no-hazardous solvents (section 1.1.9.7). For instance, in a first promising work using modified cellulose into epoxy resin, Drzal *et al.* (2008) elaborated an epoxy resin system containing microfibrillated cellulose with silanes. They concluded that the presence of silanes onto fibrils surface enhances the dispersion of filler. Again, they reported a stronger adhesion between microfibrils and matrix, and thus a rise of mechanical properties of the composite[27]. Zhou *et al.* (2013) presented similar results to Drzal and coworkers, elaborating an epoxy resin with silylated bamboo fibers. Both works were performed by using 3-glycidyloxypropyltriethoxysilane as the silylated agent. This increment is ascribed to the formation of chemical bonds between the cellulose and the epoxy thanks to the coupling agent[31]. Nevertheless, in both cases, the interface structure is not clear. Since the silane chemistry is complex and the reagents employed tend to form silica networks, physical adsorption, and chemical reactions are involved[32, 33, 34].

1.1.5 Self-healing epoxy resins

The self-healing behavior was inspired by biological systems that can repair themselves after suffering damage. The interest in developing this kind of material grows day by day due to the large potential for solving some of the most limiting problems of thermoset materials, such as safety, durability, and re-processability.

Thanks to their high versatility, epoxy resins are the object of numerous studies whose purpose is to develop a manner to acquire the self-healing property by chemical engineering. An interesting gap to fill with these promising materials is the heal of microcracks. The microcracks are the precursor of structural failures. Self-healing could extend the lifetime of products, reduces maintenance costs, and diminishes polymer waste.

1.1.5.1 Epoxy self-healing resins made of healing microcapsules

A strategy to repair the damage in epoxy resins was developed by White *et al.* (2001), who incorporated microencapsulated healing agents. The microencapsulated agentsreact via ring-opening metathesis polymerization (ROMP) with Grubbs catalyst previously introduced into the epoxy matrix. After damage, the crack propagation takes place (**Figure I-7a**), entering in contact with the healing agent and the catalyst into the matrix (**Figure I-7b**), and finally, the polymerization (**Figure I-7c**).

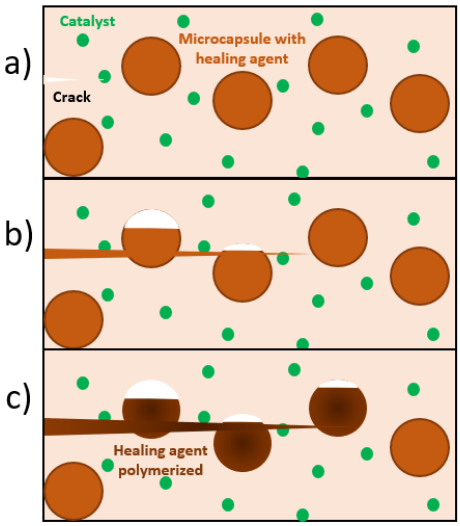

Figure I-7. Autonomic healing concept. a) cracks form in the matrix wherever damage occurs, b) the crack ruptures the microcapsules, releasing the healing agent into the crack plane through capillary action, c) the healing agent contacts the catalyst, triggering polymerization that bonds the crack faces closed[35].

When the polymer was healed, the mechanical properties were restored at 60% from the virgin composite[35, 36].This strategy provides autonomous self-healing because it is unnecessary to have any exterior intervention to start the self-healing mechanism. However, after several tests, the polymer loses its healing performance[37].

Caruso *et al.* (2007) established a mono-capsule self-healing system using solvent-filled microcapsules[38] into an epoxy resin. Chlorobenzene was the first encapsulated solvent to exhibit autonomic self-healing of epoxy resins with a healing efficiency of 82% at 20% capsule loading [38]. This method presents the advantage of avoiding metal catalysts, but the chlorobenzene's high toxicity has encouraged the research to find less toxic solvents. The healing efficiency achieved using less toxic solvents like phenylacetate (PA) and ethyl phenylacetate (EPA) has been superior to 100%, exhibiting multiple healing events over time. The behavior is explained due to a reaction of residuals amines in the matrix. The damaged polymer surfaces are wetted and swelled, conferring “accessibility” to the residuals amines and further crosslinking with the residual epoxy functions, allowing a recovering of virgin mechanical properties and healing the crack [39, 40].

Lately, Yuan *et al.* (2008) developed a dual-capsule self-healing material by introducing diglycidyl tetrahydro-o-phthalate (DTHP) and mercaptan/tertiary amine in two types of microcapsules. When the fracture occurs, the microcapsules open, and both the DTHP and the hardener go together into the damage sites and then polymerize to repair the cracks. The healing efficiency reported was slightly more than 100%, so the healed portions present a higher cracking resistance than the matrix.

The healing agent is quite stable and durable, preventing the composites' healing capability from deterioration during storage [41].

Zhang *et al.* (2009) employed healing agents based on cationic chain polymerization of boron trifluoride diethyl etherate ($(C_2H_5)_2O{\cdot}BF_3$) into an epoxy system of EPON 828 and triethylenetetraamine (TETA). The results showed that cracks could be quickly re-bonded with a satisfied healing efficiency around 80%. Long terms tests indicated that self-healing remained unchanged within five months[42].

1.1.5.2 Self-healing epoxy resins made with reversible covalent bonds.

The incorporation of reversible covalent bonds such as those obtained with Diels-Alder (DA) reaction[43, 44], disulfide chemistry, alkoxyamine moieties, and transesterification reactions, etc., into epoxy networks is another promising strategy to heal and recycle thermosets. Some of these innovative networks are presented below.

1.1.5.2.1 Diels Alders

Diels-Alder reaction (DA) is a [4+2] cycloaddition involving a diene and a dienophile. DA reaction is a thermo-reversible reaction. The group formed by DA reaction (DA adduct) is thermally unstable and can experiment a reverse reaction (rDA). At high temperatures (even above 200 °C), the diene and dienophile are generated, and at low temperatures, the adduct is reformed. The chemical equilibrium is highly sensible to the temperature (**Figure I-8**) [45].

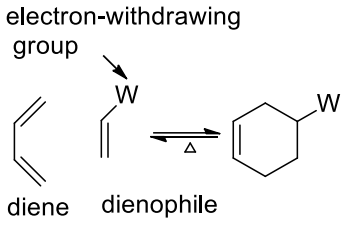

Figure I-8. Schema of thermoreversible Diels-Alders reaction.

Wudl *et al.* (2002) presented an interesting network based on DA and rDA reactions. The material presents similar mechanical properties to a commercial epoxy resin at room temperature. They registered that the linkage disconnection occurs at temperatures above 120°C and that the linkage reconnection takes place after cooling. It was possible to appreciate macroscopically the mending (**Figure I-9b** and **c**). Besides, this process does not require any catalysts or special surface treatments.

The reaction is triggered by thermal stress. The healing efficiency achieved at 150°C was 50% (**Figure I-9a**). This process was described as fully reversible. This study ushered in numerous researches using thermo-reversible reactions[46].

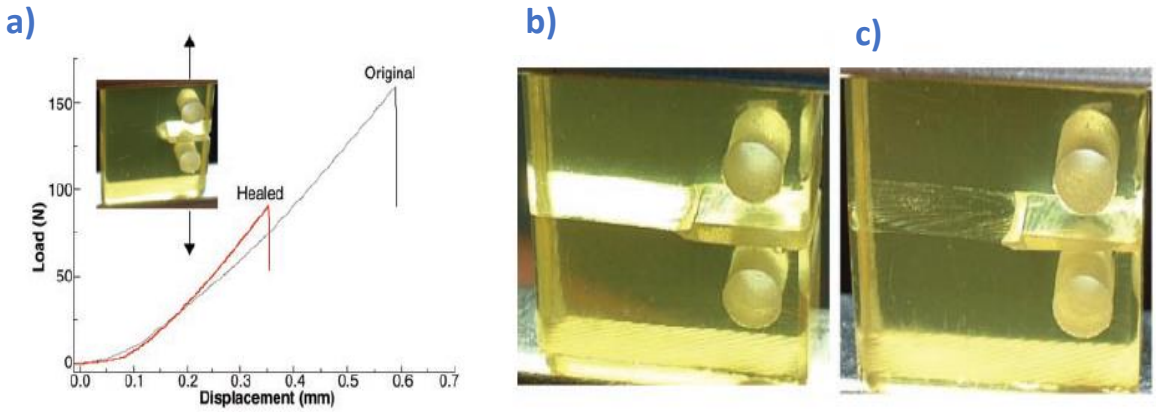

Figure I-9. Mending efficiency of polymer-based on DA and rDA reaction, a) mending efficiency obtained by fracture toughness testing of compact tension test specimens, b) broken specimen before thermal treatment, and c) specimen after thermal treatment[46].

Lately, Wang *et al.* (2015) developed an epoxy-resin from a diamine DA adduct cross-linker. The network behaves like a typical thermoset at room conditions, but it can be reprocessed at elevated temperatures (**Figure I-10**). The thermal analysis revealed a reversible cross-linking behavior of DA adducts and a series of complex reactions, such as epoxies-amines reaction, Michael's addition by maleimide, and amine homopolymerization by maleimide moieties. Solubility tests were carried out in DMF at room temperature, revealing only a swelling of epoxy. Still, when the sample was heated at 130 °C, the crosslinked polymer was fully soluble after 30 min. This phenomenon suggests that the high temperatures promote decross-linking reactions. The shear strength achieved after the healing process shows a performance of 170% compared to cured samples[47].

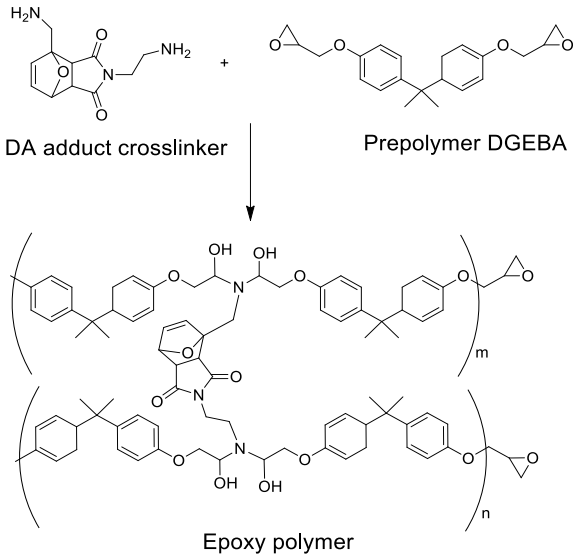

Figure I-10. Curing reaction between diamine DA adduct cross-linker and DGEBA prepolymer[47].

Another innovative method to manufacture a thermo-reversible crosslinking system based on DA reaction was proposed by Turkenburg *et al.* (2015). Their approach consists of two steps: 1) a bulk pre-polymerization of the epoxy amine system with furfuryl, being careful that the molar mass was low enough to maintain its viscosity, 2) the bismaleimide (BMI) addition, via batch extrusion to minimize the exposure time of BMI at a high temperature (**Figure I-11**). This procedure prevents Michael's addition between the amine and the maleimide. Also, the BMI crosslinked agent's ratio variation was explored: the highest crosslink density was found at 0.95. At this ratio, the network is less susceptible to swell[48].

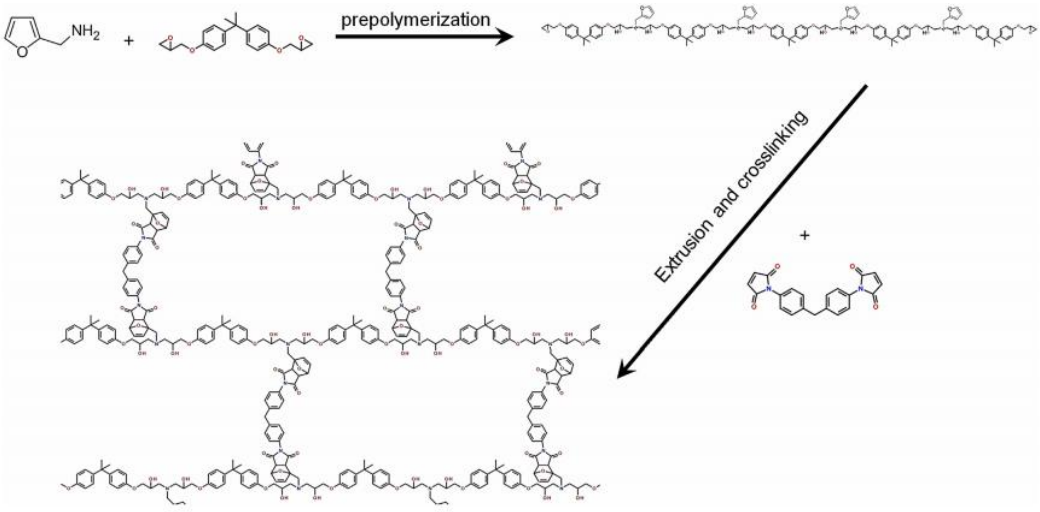

Figure I-11. The schematic reaction between furfuryl amine and DGEBA bulk pre-polymerization, followed by network formation using BMI as thermo-reversible cross-linker by extrusion and Michael addition of furfuryl amine[48].

1.1.5.2.2 Transesterification

Transesterification is a process where an ester is transformed into another through an interchange of the alkoxy moiety. The transformation occurs essentially by simply mixing the two components since the reaction is an equilibrium process (**Figure I-12**)[49].

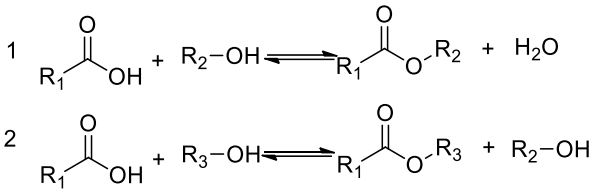

Figure I-12. Transesterification schematization, 1) condensation reaction (esterification), 2) exchange of ester function (transesterification). Both reactions are in equilibrium.

Transesterification is a classic organic chemistry reaction that numerous researchers have studied due to its potential industrial applications. Early research probed the reaction under acid or basic catalyst conditions. Still, the need for a highly efficient and selective process promoted the research of new catalysts such as amine, Lewis acid, metal alkoxide, titanium tetraalkoxide, and organotin catalysts[50].

The notable work of Matějka *et al.* (1984) in the field of epoxy resins from epoxy-acid chemistry drew the attention of this chemistry in the field of reversible networks. Their work showed how transesterification of poly (hydroxy esters) leads to gelation and formation of crosslinked structures from Azelaic acid (AA), phenyl glycidyl ether (PGE), and diglycidyl ether of bisphenol A (DGEBA). Tertiary amines catalyze this reaction[51]. They also varied the stoichiometric ratio between the epoxy and carboxylic acid, which allowed them to observe more precisely all reactions. In the transesterification, the obtained hydroxy ester was transformed into a diester and 1,2-diol. It is a reversible reaction.

Williams *et al.* (2005) worked on a system based on diglycidyl ether of bisphenol A (DGEBA) and palmitic acid (PA) in the presence of benzyl dimethylamine (BDMA) at the different stoichiometric ratios. When the ratio DGEBA/PA is superior to 1, the transesterification is significant. This work perfectly exemplifies the reaction's reversibility from a solid to a liquid by heating the compound above PA's melting temperature[52].

More recently, Williams *et al.* (2013) described a self-healing bio-polymer network based on epoxidized soybean oil (ESO) and citric acid (CA) without a catalyst. The self-healing performance of the system was demonstrated after heating fractured samples at 160°C for 1 and 2h. The welded samples showed a very similar performance to the cured sample (**Figure I-13**)[53].

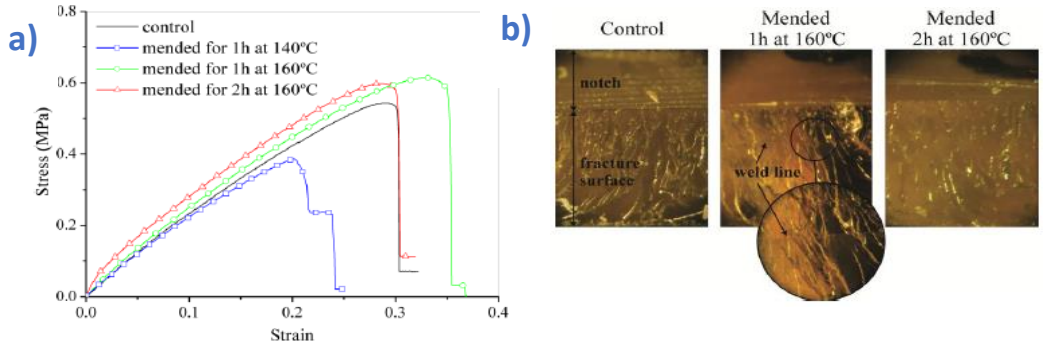

Figure I-13. Healing response of ESO-CA networks, 1) Stress-strain curve for lap shear test of mended samples and control, and 2) images of fracture surfaces of mended samples and control[53].

Within the extensive research of transesterification, Leibler *et al.* (2012) explored transesterification's catalytic control, enabling to heal crosslinked polymers from networks based on diglycidyl ether bisphenol A, dicarboxylic and tricarboxylic fatty acid with and without a catalyst. The catalyst used in the first approach was zinc acetate. The importance of the catalyst concentration on the control of the transesterification reaction and the welded efficiency was evidenced. It was shown that the transesterification reaction time was 15h at 150°C for the networks synthesized without catalyst, while this time was reduced to 2h using 5 mol % of catalyst at the same temperature (**Figure I-14a**). The study showed the importance of the amount of catalyst present in the network (**Figure I-14b**). It revealed the effects of the time and the temperature on the healing process to reach high mechanical properties (**Figure I-14**c)[54].

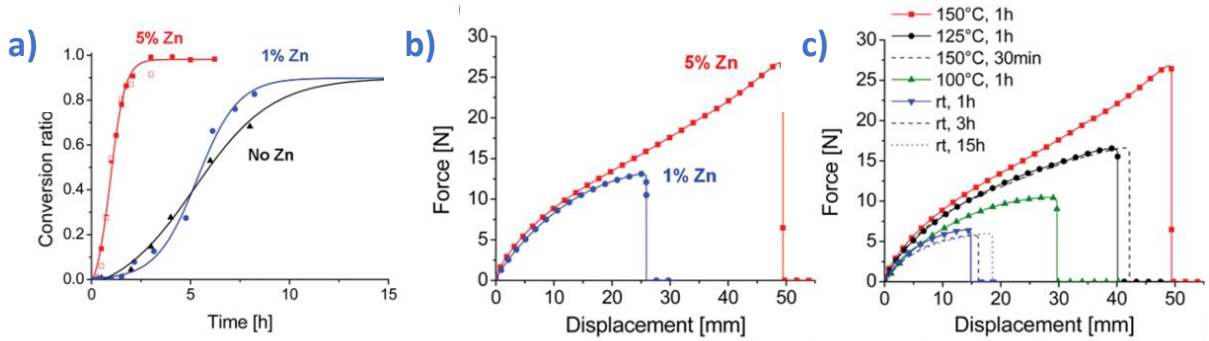

Figure I-14. Effect of the metal catalyst in transesterification exchange reaction, 1) transesterification kinetics without and with different percentage of catalyst, 2) samples loaded with different catalyst concentration and welded for 1h/150°C, and c) samples loaded with 5 mol % $Zn(OAC)_2$ and welded under different conditions[54].

Ji *et al.* (2014) presented an epoxy system with carbon nanotubes dispersed in the matrix, manipulating the transesterification reaction. The network was welded by light in a few seconds or

minutes. This behavior is linked to the presence of carbon nanotubes, which absorb the light energy of almost all wavelengths, transforming it into heat and repairing the inflicted damage. Furthermore, carbon nanotubes can convert electric or magnetic energy into heat, an important attribute for futures applications. This approach suppresses the long heating exposition to weld them, preventing possible oxidations phenomena and concentrating the energy just in the damaged area[55].

1.2.5.2.3 Disulfide exchange

Organosulfur compounds are abundant in nature, and they are essential for life. In the field of polymers, the sulfur atoms are present in the polymer backbone or are introduced as thiol groups into the polymer chain. The thiol functions can be converted into disulfide groups upon oxidation, and they can undergo nucleophilic substitution, S_N2 with free thiol groups, resulting in a thiol-disulfide exchange. This last reaction is very important in biological systems since it is responsible for the enzymatic formation and opening of protein structures[56].

In the area of epoxy resins, Tesoro *et al.* (1990) reported an epoxy resin made of reversible bonds, i.e., it can be cleaved and reformed without a significant sacrifice in the resin properties. The dynamic epoxy resin was based on crosslinking agents containing disulfide, giving it a dynamic character. Their systems were performed by employing EPON 828 prepolymer, the dynamic hardener 4-aminophenyl disulfide (4-APDS). The results were compared with the reference hardener 4,4'-diaminodiphenyl methane (DDM). Both networks performed with different hardeners under the same stoichiometric conditions displayed similar thermomechanical properties. Epoxy systems by using DDM as hardener have been widely studied and present excellent properties for several applications [57, 58, 59]. Consequently, the use of 4-APDS as a hardener seems to be an interesting alternative while providing a dynamic behavior.

Tesoro and coworkers' studies also look at the importance of varying the stoichiometric ratios of epoxy/amine. Their work evaluated the reduction under Bu_3P/diglyme of resins cured with 4-APDS for then, re-cure the reduced resins by following an oxidation process, and by reacting the thiol groups formed after the reduction with bifunctional groups as bismaleimide (**Figure I-15**).

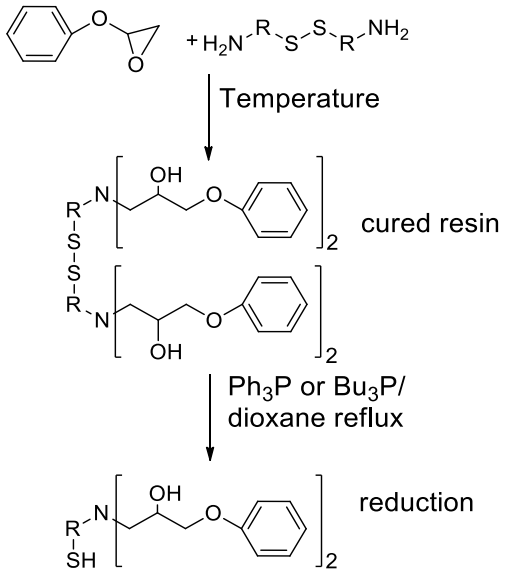

Figure I-15. The schematic reaction of cured and reduced disulfide compounds[57].

Almost two decades later, Klumperman *et al.* (2011) presented another thermoset system based on a disulfide epoxy resin with a tetrafunctional thiol. They showed the possibility to heal a "damage" made to the sample at moderated temperatures (60 °C) thanks to the disulfide exchange reaction. The solubility test evidenced the selective scission of disulfide groups in solvents such as DMF and 1,6-hexane dithiol. The healing efficiency was studied by tensile mechanical tests. If the fractured surfaces of the sample were joined as close as possible after the break and then heated at a moderated temperature, the mechanical properties were fully restored in 1h (**Figure I-16a**). The material was healed several times, displaying mechanical properties fully restored (**Figure I-16b**). The influence of disulfide concentration was also explored, showing that the self-healing efficiency was almost 100% with a high concentration of disulfide groups (20% wt) (**Figure I-16c**). It is interesting to remark that the material's rheological properties showed an elastic modulus independent of the frequency, event at elevated temperatures. It suggests that the quantity of bonds is permanent (**Figure I-16d**)[60].

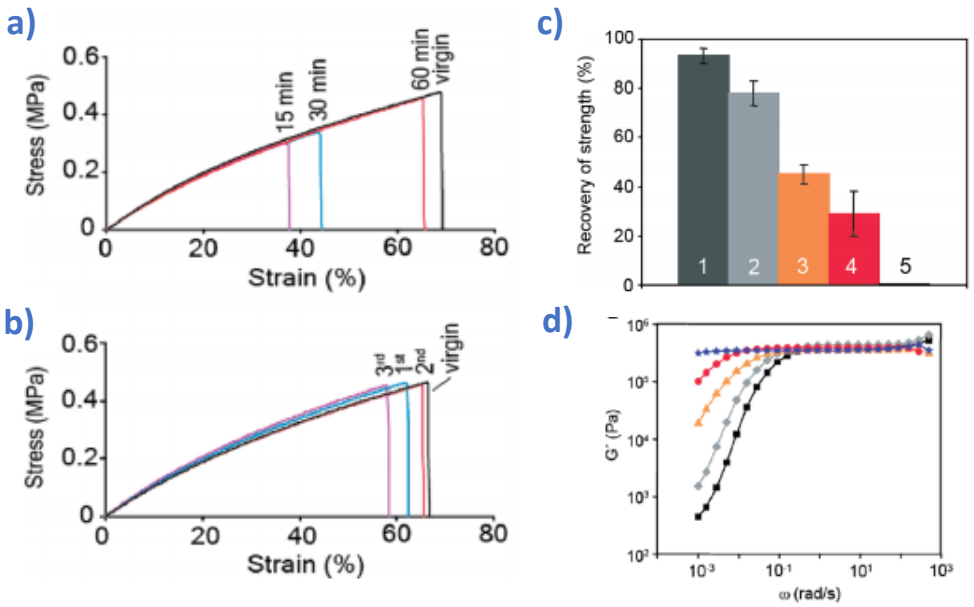

Figure I-16. Healing efficiency of network based on disulfide bond, a) stress-strain curves as a function of the healing time at 60°C, b) stress-strain curves after repetitive healing experiments, c) recovery of strength of healed samples with different concentration of disulfide groups (1:20 wt%, 2:15 wt%, 3:10 wt%, 4:5 wt%, 5:0 wt%), d) frequency dependence of storage modulus of the material[60].

To go further, Klumperman *et al.* (2013) implemented self-healing networks based on thiol-disulfide bond exchange. In this case, the performed healing efficiency was up to 99% depending on the raw materials and the healing time. During the curing, some free thiol groups are left; thus the material loses its rearranging ability (**Figure I-17**). This phenomenon increases over time, especially during the healing process, because the cracked surfaces are more susceptible to react with oxygen. Multiple stress relaxation mechanisms were observed and attributed to the disappearance of thiol-groups by oxidation and to the deterioration of the dynamic properties over time. The ability to fully relax before oxidation of this disulfide-thiol system demonstrates that the thermoset network can rearrange through an exchange reaction[61]. This mechanism has also been observed in the crosslinked materials based on methacrylate[62] and poly(disulfides)[63].

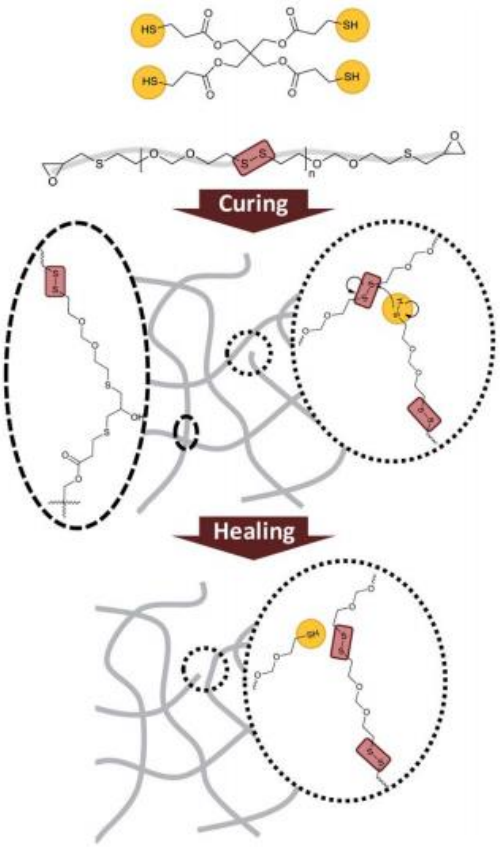

Figure I-17. The schematization of curing reaction and the subsequent healing ability of a network to rearrangement[60].

The epoxy resin disintegration has drawn attention because it opens the possibility of reprocessing. Otsuka *et al.* (2016), inspired by Tesoro and their coworker's effort, designed a new network with structural rigidity and facile degradability. The resins contained disulfide bonds in diamine moieties and/or epoxy moieties (**Figure I-18**). The tensile test revealed mechanical properties quite similar to the resin without dynamic bonds. The degradation of resins was achieved easily in almost all the systems, and like Tesoro, the sample with functionality ratio 1:1, 4-APDS: DGEBA, presented swelling and achieved degradation of only 20% [64, 65].

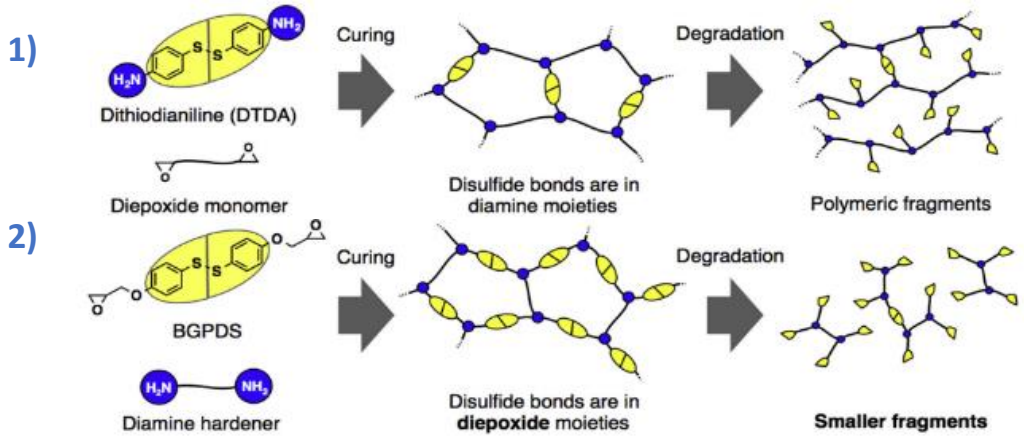

Figure I-18. The schematization of 1) Tesoro work by using disulfide bonds in one moiety, and 2) Otsuka work by employing in both moieties the disulfide bond[64].

A re-processable and recyclable network was also explored by Odriozola *et al.* (2016). They developed a fiber-reinforced polymer composite off-stoichiometry amine: epoxy, showing a good mechanical performance that could be reshaped and healed under adequate temperature/pressure. Like Tesoro and Otsuka, the network performed by Odriozola and co-workers dissolves it, most likely due to the excess of dynamic hardener (or disulfide bonds). This method allows changing the fibers broken after mechanical stress if they suffer important damages and re-use the epoxy resin[66].

1.1.6 Covalent Adaptable Networks

Bowman *et al.* (2010) defined covalent adaptable networks (CANs) as networks that contain a sufficient number and topology of reversible covalent bonds to enable the crosslinked network structure to respond chemically to an applied stimulus. The behavior of these networks after an external stimulus (such as light or temperature) is classified into two main groups depending on their exchange mechanism[67, 68, 69, 70].

- **Dissociative**. This mechanism is also described as a reversible addition or condensation crosslinking rearrangement. The crosslink exchange mechanism occurs when a chemical bond is broken and then reformed at another place, i.e., it follows a bond-breaking, bond-forming reaction sequence (**Figure I-19**). The connectivity is lost and reformed subsequently. Some examples are the crosslink networks based on thermo-reversible reactions as Diels-Alders[46, 48], isocyanate and imidazole[71, 72], esterification's and hydrolysis of boronic esters[73, 74], or carbene dimerization reactions.

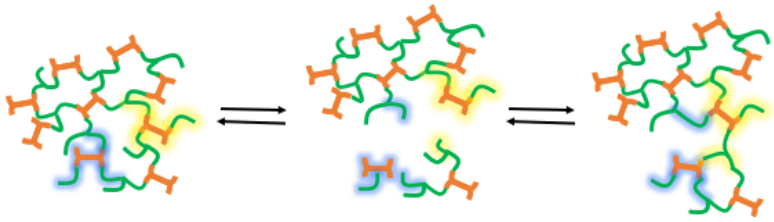

Figure I-19. Dissociative Exchange reaction.

- **Associative**. The mechanism is described as reversible exchange rearrangement. The crosslink arrangement occurs when an active species undergoes an exchange reaction that results in a bond exchange producing a new active species, i.e., it follows a bond-forming, bond-breaking sequence (**Figure I-20**). The connectivity is never lost. Some examples are transesterification[75], transamination[76], siloxane silanol exchange[77]. The networks exhibiting this mechanism have been named **vitrimers**.

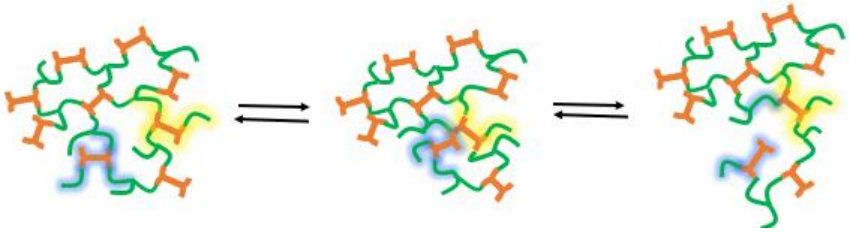

Figure I-20. Associative exchange reaction.

Implementing these two different networks could overcome important issues as the re-processing of crosslinked networks for diverse applications such as a structural material, which might present good mechanical, thermal, and chemical properties.

1.2 Vitrimers

1.2.1 Vitrimer concept

Almost one decade ago, the vitrimer materials were introduced by Leibler *et al.* (2011) as covalent adaptable networks that can rearrange their topology via exchange reactions without depolymerization, showing its processability. These materials do not dissolve in chemically inert solvents even with heating. They only swell like classical thermosets. Nevertheless, they can be recycled under pressure and at high temperatures or by injection after been grounded into a powder because of their covalent reversible networks. Vitrimers share the recyclability properties of thermoplastics. According to Bowman's description, vitrimer networks have been classified as an "**associative CAN**".

Another interesting particularity of vitrimer networks is the progressive variation of viscosity as a function of temperature like vitreous silica: the viscosity follows Arrhenius law. This viscosity evolution is quite different from organic compounds or linear polymers which viscosity varies abruptly near the glass transition temperature following the Williams-Landel-Ferry law (WLF). In other words, the dynamic properties of vitrimers are controlled by the kinetic of chemical exchange reactions, while in a classic crosslinked network, the properties are controlled by a polymer chain diffusion. This particular property is at the origin of the name vitrimer "comme du verre", like glass.

1.2.2 Topology freezing temperature (*T*v)

The viscoelastic behavior of organic polymers is usually described by the glass transition temperature (*T*g) and sometimes by the melting temperature (*T*m). Vitrimer materials are organic networks described at least by one of these both transition temperatures: Tg, but also described by an additional transition temperature, the *T*v or topology freezing temperature. The *T*v is related to the chemical exchange reaction of the adaptable bonds. During this transition, the network has time to rearrange its topology, so it can be deformed due to the fluidity that it acquires. It is a transition from a viscoelastic solid to a viscoelastic liquid.

Inspired by Angell plot 1985 (**Figure I-21a**), *T*v was conventionally chosen at the point where the viscosity is 10^{12} Pa*s, and the dynamics are assumed higher than thermal fluctuation barriers. The plot shows how organic polymers' viscosity (fragile glass) is strongly dependent of temperature near *T*g and slightly modified at high temperatures. For their part, Leibler *et al.* (2011) replayed the Angell plot (**Figure I-21b**), emphasizing the silica glass and vitrimer behaviors (strong glass), showing how the viscosity follows a linear temperature dependency according to Arrhenius law[78, 79].

a)

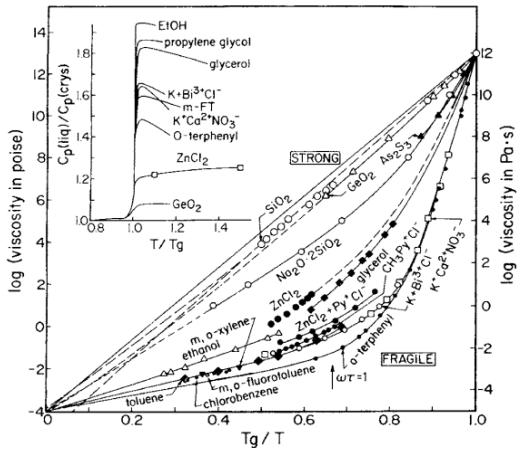

b)

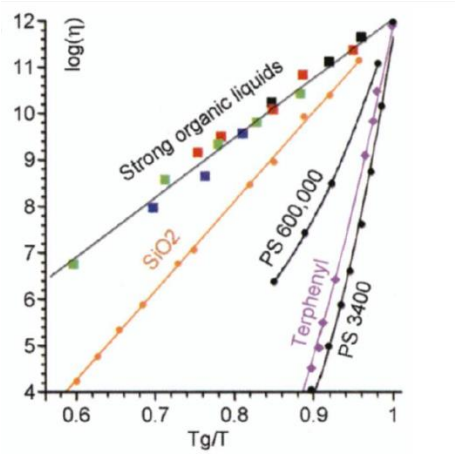

Figure I-21. Viscosity as a function of inverse temperature normalized to 1 at *T*g: a) the original Angell fragility plot (1985) [78], and b) Leibler's representation of the Angell plot[75]. The lower-left corner marks the approximate high-temperature limit to the viscosity that is common to all liquids. The Arrhenian viscosity gives a straight line in the plot.

Since there are two different transition temperatures characteristic of vitrimers, two possibilities exist[70, 80]:

1) The *T*g is lower than *T*v (**Figure I-22a**). Upon heating, the glassy solid goes to the rubbery state in the temperature range between *T*g and *T*v. The exchange bond reaction is very slow and not relevant. In contrast, the segmental motions are the most important at this point. On further heating, the crosslinking exchange kinetic becomes faster and relevant at temperatures above *T*v, obtaining a viscoelastic liquid that flows and whose viscosity decreases following an Arrhenian behavior.

2) The *T*g is higher than *T*v (**Figure I-22b**). Once the *T*v is reached by heating, the crosslinking exchange kinetic is fast but fixed in a rigid polymer matrix due to a lack of segmental motions, limiting and even blocking the exchange reactions. The movements are "frozen". Upon heating at a temperature superior to *T*g, the segmental motions become more important as temperature increases. At a temperature slightly higher than *T*g, the network topology rearrangements are dominated by segmental motions because the diffusion controls the kinetic. Hence, the viscosity follows a WLF law behavior. After further heating, the exchange kinetic becomes more important than diffusion, and the viscosity follows the Arrhenius law. In this case, the *T*v can be calculated via an extrapolation of stress-relaxation or creep experiments.

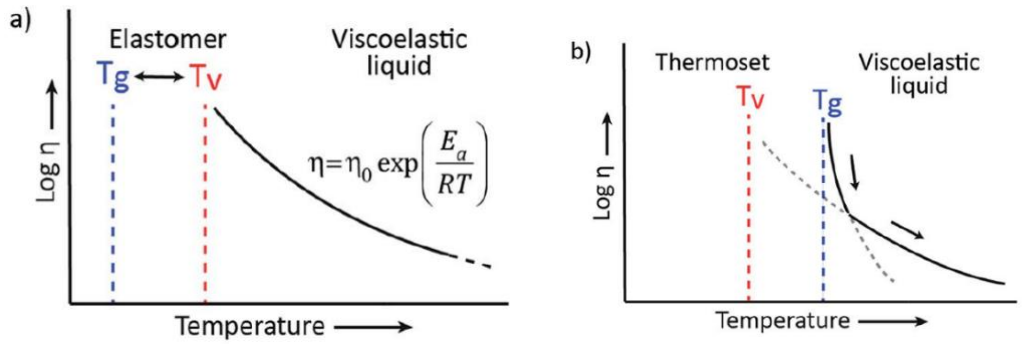

Figure I-22. Representation of the viscoelastic behavior of vitrimers when a) the *T*g is lower than *T*v, exhibiting a clear Arrhenian behavior, and b) the *T*v is lower than *T*g, the viscosity experiments an evolution from a glassy solid to a viscoelastic liquid, controlled through diffusion (WLF) and then by the exchange kinetics (Arrhenius law) [70].

1.2.3 First vitrimer chemistry: transesterification

The transesterification reaction is the rearrangement by thermal activation of an alcohol and an ester, generating new alcohol and a new ester. This interesting exchange behavior was evidenced at the beginning of the XXth century. Some early notable works were performed by Levesque *et al.* (1936)[81], Vromen *et al.* (1949) [49], describing the reversibility of this reaction. Lately, Matějka *et al.* (1984) presented an interesting network based on this interesting chemistry, triggering a deeply research for further application[51, 52, 53]. More recently, Leibler and coworkers (2011) exposed an interesting network based on this chemistry which showed a topology rearrangement behavior with a constant crosslinking density. Leibler and co-workers' networks based on transesterification exchange mechanism constitute the first reported generation of vitrimers. The networks were prepared from epoxy/fatty acid catalyzed by $Zn(Ac)_2$ (**Figure I-23**). The polymerization was performed by simple mixing and generated soft networks. This reaction was guaranteed due to the abundance of free hydroxyl functions and carboxylic esters. The second networks (hard ones) were prepared from epoxy/anhydride monomers and catalyzed by zinc acetylacetonate dihydrate. For this case, the stoichiometry was carefully chosen to assure free hydroxyl groups available throughout the network[54, 75].

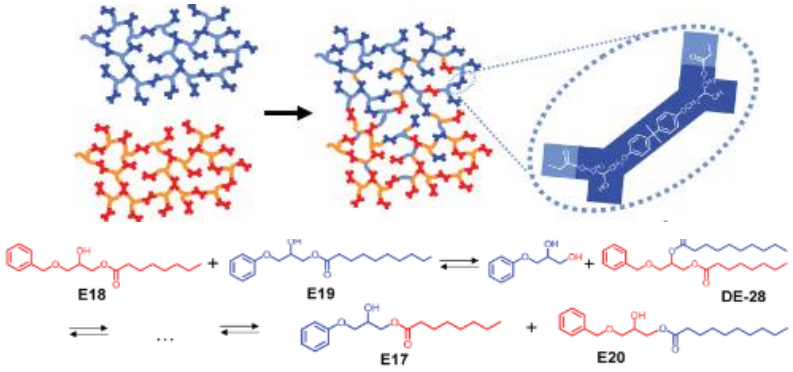

Figure I-23. The schematization of two epoxy resins' welding process via transesterification exchange reaction and molecular model of exchange reaction[54].

In this promising first work, the importance of rearrangement kinetic was also explored, establishing a high dependency of the nature (**Figure I-24 a** and **b**) and quantity of the catalyst (**Figure I-24 c**). The catalysis role is very important since it reduces the activation energy and the *T*v (**Figure I-24 d**) with minimal perturbations of the material properties. i.e., the catalyst accelerates the exchange reaction[82].

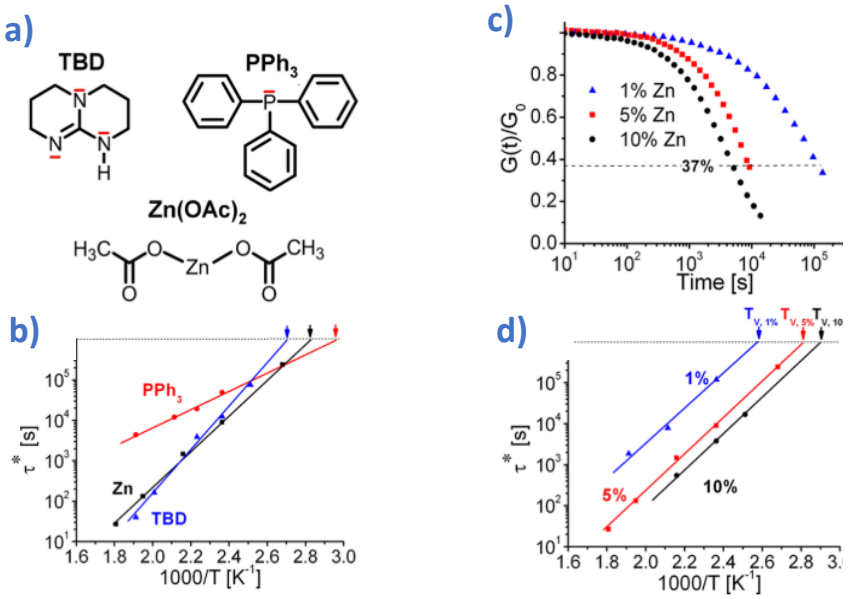

Figure I-24. Catalytic effect control in viscoelastic vitrimer response, a) different employed catalyst, b) Arrhenius plot of the relaxation times for diverse catalysts, c) normalized shear stress relaxation experiments as a function of time at different concentrations of $Zn(OAc)_2$, d) Arrhenius plot of the measured relaxation times at different concentrations of $Zn(OAc)_2$ catalyst[82].

1.2.4. New vitrimers systems

1.2.4.1 Transamination of vinylogous urethanes

Du Prez *et al.* (2015) developed an interesting alternative vitrimer material based on a transamination of vinylogous urethanes without catalyst (**Figure I-25**). The natural intrinsic reactivity of vinylogous urethane moiety as a Michael acceptor facilitates the conjugate nucleophilic addition of an amine group without a catalyst. Vinylogous urethanes are known to undergo associative transamination reactions at temperatures from 100 to 120°C.

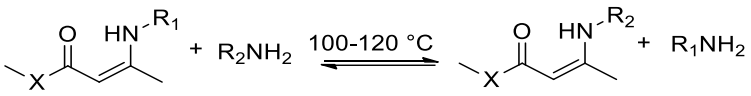

Figure I-25. Schematization of the exchange reaction of vinylogous urethanes and amines via Michael addition[76].

The material performed following this exchange mechanism was prepared through bulk polymerization by a spontaneous condensation reaction between acetoacetate and amine monomers. The reaction was done at a slightly off-stoichiometric condition to have sufficient free amines in the polycondensation network to allow a swift exchange reaction. The mechanical properties were similar to epoxy/acid vitrimers, but with relaxation times shorter. The recyclability was also explored without significant mechanical or chemical degradations up to four times. It was evaluated by consecutive grinding/compression molding. Nevertheless, for a long-term application, the oxidative damage cannot be excluded[76].

To go further, Du Prez and Leibler (2017) explored the possibility of controlling the exchange kinetics of vinylogous urethanes by using neutral, acid, and basic additives (**Figure I-26**). Their results showed that in neutral or acidic conditions (H_2SO_4, pTsOH, and DBTL catalyst), the activation energy was lower than in the uncatalyzed network. They proposed a mechanism of amine exchange via an iminium intermediate. In basic conditions (TBD catalyst), an increment of the activation energy was observed; thus, a very different mechanism must occur. A direct Michael addition was proposed since, at low temperatures, the reaction may start slow but can become fast at higher temperatures. These outcomes open the door to refine the viscoelastic behavior of elastomeric vitrimers[83].

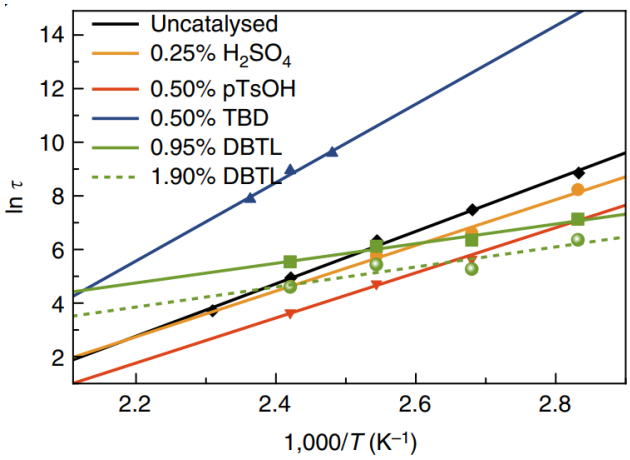

Figure I-26. The Arrhenius plot of vinylogous urethane was loaded with different catalysts and corresponding mol % versus the amine functionalities in the initial monomer mixture[83].

Recently, Leibler *et al.* (2017) synthesized an elastomeric vitrimer-like from PDMS containing pendant amino functional groups (which participate in vinylogous urea exchange reactions) bis-vinylogous urethane as crosslinker via condensation. The networks were not soluble in good solvents of PDMS, but they could be dissolved by selective aminolysis of the vinylogous urethane crosslinking. Due to the dynamic nature of networks, the material could be (re)modeled by temperature and compression[84] .

1.2.4.2 Transalkylation of triazolium salts – ionic vitrimers

Drockenmuller and Montarnal (2015) presented a promising ion-conducting polymer material solvent- and catalyst-free from 1,2,3-triazolium salts (PTILs). The network was easy to obtain in a one-step process by polyaddition of α-azide-ω-alkyne monomers involving a 1,3-dipolar cycloaddition, followed by crosslinking bifunctional alkylating agents. The poly(1,2,3-triazole) network obtained in this process is easy to tune, presents a high ionic content and a slight amount of soluble constituents (4%). In a first approach, the proposed mechanism was a transalkylation between 1,2,3-triazolium and alkyl halides. The reaction was followed by ^{1}H and ^{13}C NMR spectroscopy, confirming a covalent exchange of C-N bonds (**Figure I-27**). Nevertheless, a subsequent study proposes a two-step mechanism: 1) the *N*-alkylation of 1,2,3-triazolium initiated by a nucleophilic attack of the triazolium network by the iodide counteranion, followed by 2) a rapid re-*N*-alkylation of the crosslinked material. This mechanism is related to a dissociative CAN. Like other vitrimer systems, cured networks were insoluble in common solvents and relax following an Arrhenian behavior with temperature and counter-ion function (Br^->> I^- > MsO^-).

Furthermore, the nucleophilicity of the counterion (F^-> Cl^->Br^->I^-) takes importance in a dynamic network, showing a feasible tuning of the viscosity by varying the type of monomer and the amount of cross-linker. This new vitrimer has drawn attention due to its possible malleability and re-processability to ion-conducting solid electrolytes in applications such as supercapacitors, batteries, cells, amount others. It was proposed a nonconcerted and dissociative mechanism, achieving the viscoelastic characteristics of vitrimers. This mechanism suggests that vitrimer materials can follow a simultaneously dissociative/associative covalent mechanism[85, 86, 87].

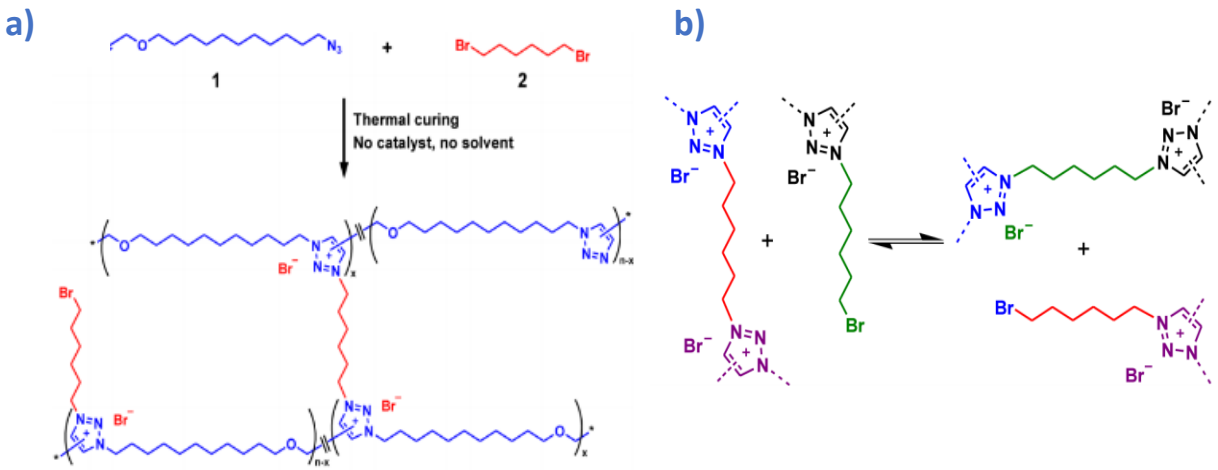

Figure I-27. Schematization synthesis of a) ion-conducting networks by simultaneous polyaddition, resulting in a poly (1,2,3-triazole) by difunctional quaternizing agent, and b) the proposed mechanism for the transalkylation reaction[85].

Rowan *et al.* (2017) performed, almost in simultaneity to Drokenmuller and Montarnal, a poly(alkylurea-urethane) network that followed the Arrhenian behavior at temperatures superior to Tα. The system presents vitrimer-like properties, although a dissociative exchange mechanism related to the bulky urea bonds[88]. More recently, Konkolewicz *et al.* (2020) studied polymer networks with anilinium linkages, which follow a dissociative pathway and a constant bond density in the range of studied temperatures. The system based on anilinium salts showed, like in the systems performed by Rowan and Montarnal, how the associative exchange may not be necessary to achieve vitrimer-like properties[89].

1.2.4.3 Olefin metathesis

Olefin metathesis has proved to be a powerful tool in organic chemistry. It can be classified into diverse categories. The most important are ring-closing metathesis (RCM), ring-opening metathesis (ROM), and cross-metathesis (CM). Since the CM can "rearrange" the topology of polymers, it has

drawn attention to diverse applications (**Figure I-28**). For instance, Guan *et al.* (2012) confirmed an olefin metathesis reaction in crosslinked polybutadiene networks using a second-generation Grubbs catalyst. The viscoelasticity of the network can be controlled via the catalyst concentration. High-efficiency healing was found at sub-ambient temperatures because the exchange reactions are performed at low temperatures in air condition[90, 91].

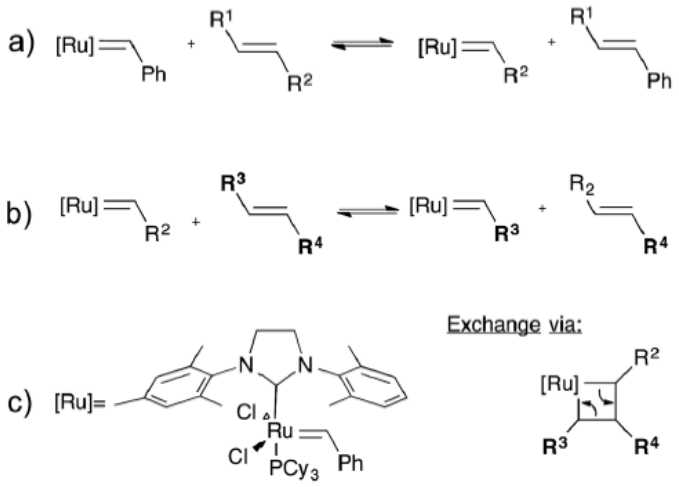

Figure I-28. The schematization of olefin metathesis exchange reaction, a) insertion of the Grubb's catalyst into an alkyl chain, b) exchange of two alkenes, c) the associative exchange mechanism of the metathesis reaction.

1.2.4.4 Dioxaborolane metathesis

Leibler, Nicolaÿ, and coworkers (2017) reported dioxaborolanes' metathesis without catalyst at low temperatures. They prepared vitrimer materials from diverse monomers, obtaining PMMA, PS, and HDPE, all of them able to be re-processed several times by extrusion and/or injection molding. The molecules exhibit reversible exchange fragments linked together by the strong B-O bond of the boronic ester groups.

The commodity polymers were modified in two ways to generate vitrimers, i) by incorporating functional monomers during the polymerization, and ii) by chemical modification of commercial polymers (reactive extrusion), followed by the addition of cross-linkers based on dioxaborolane, which could induce the metathesis reaction. The rheological properties can be tuned by choosing the appropriated molecular parameters: 1) the copolymer molecular weight fraction of pending dioxaborolanes and 2) the cross-linker. Creep tests were carried out to these modified commodity polymers, showing the Arrhenian behavior, which is characteristic of vitrimers. The robustness of dioxoborlate cross-linkers, which induce the vitrimer performance, was evidenced after several reprocessing and immersion in water to promote the hydrolysis of dioxaborolanes. Indeed, the

processed commodity vitrimers exhibit an important melt strength, a dimensional stability, and a solvent and environmental stress-cracking resistance, allowing them to be processed and recyclable like thermoplastics[92]. Similar approaches with commodity polymers such as BR[93], HDPE[94], PE[95] have been carried out.

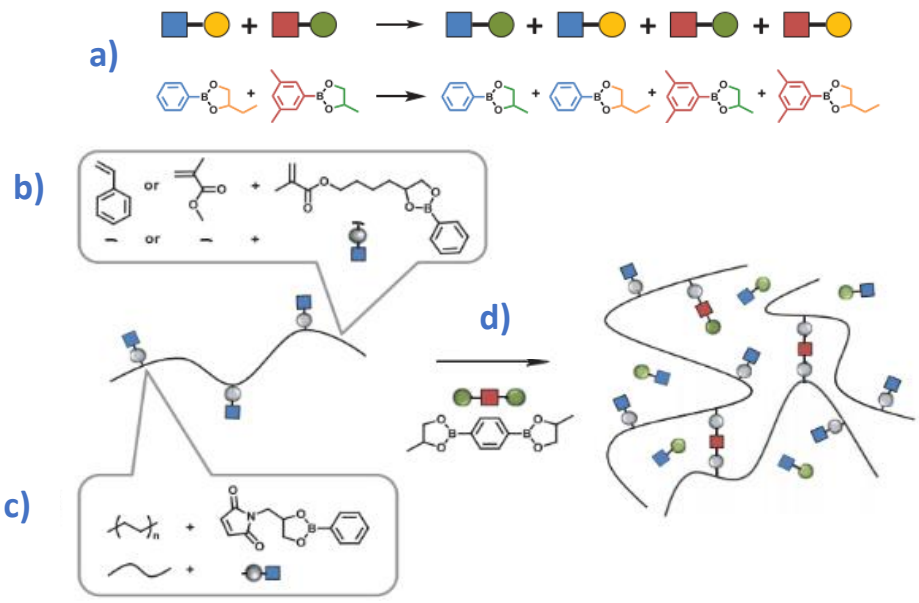

Figure I-29. Vitrimers in thermoplastics, a) general scheme of a metathesis reaction of dioxaborolanes, b) synthesis of copolymers containing pendant dioxaborolanes, c) grafting dioxaborolanes via reactive extrusion onto thermoplastic, d) crosslinking of dioxaborolanes pendant with a bis-dioxaborolane[92].

In the research of thermoplastic commodity vitrimers, Guan *et al.* (2019) described a new silyl ether metathesis reaction. The silyl ether moieties showed an exchanging reaction under anhydrous conditions catalyzed by Bronsted or Lewis acid agent. At this time, the exact mechanism of covalent exchange is not clear. But the authors propose a direct exchange between silyl ethers, presenting some transient reactive intermediates during the process (**Figure I-30**). Low molecular weight poly(ethylene-co-vinyl-acetate) (EVA)s were hydrolyzed, then silylated with a bis trimethylsilyl to yield trimethylsilyl (PE-OTMS), and finally crosslinked with a bis monosilyl and a trisilane. The vitrimer exhibits good thermal stability due to the silyl ether metathesis, which does not generate free hydroxyls susceptible to dehydration or oxidation at high temperatures. Hence good mechanical properties are obtained[96].

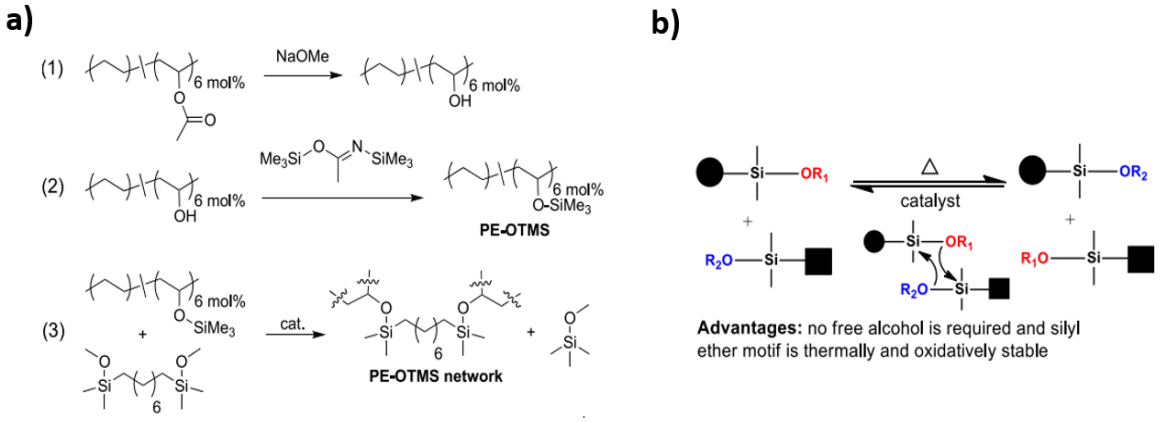

Figure I-30. Silyl ether vitrimers, a) Synthesis of poly(ethylene-co-vinyl-acetate) functionalized with trimethylsilyl, and b) silyl ether metathesis exchange mechanism[96].

1.2.4.5 Siloxane silanol exchange

McCarthy *et al.* (2012) re-drew silicones' attention by "re-discovering" how to prepare truly self-healing materials from silanols on siloxane moieties via addition/elimination. This peculiar behavior has already been reported in several studies and patented in the 1950s by Kantor *et al.* The results of McCarthy showed quantitative healing, and full relaxation of the PDMS networks[77].

Huang *et al.* (2018) have introduced this covalently exchange reaction system as a vitrimer system based on siloxane equilibration chemistry. They synthesized polysiloxane oligomers containing aminopropyl side groups and catalytic potassium silanolate end groups. This last was synthesized and employed as a crosslinker for epoxy prepolymer diglycidyl ether of ethoxylated bisphenol-A (**Figure I-31**). The material was recycled and reprocessed several times without a loss of mechanical or thermal properties at moderated temperatures for approximately 40 min. The Arrhenian behavior was evidenced, and a feasible tuning of the viscoelastic properties was proved by adjusting the amount of potassium ions[97].

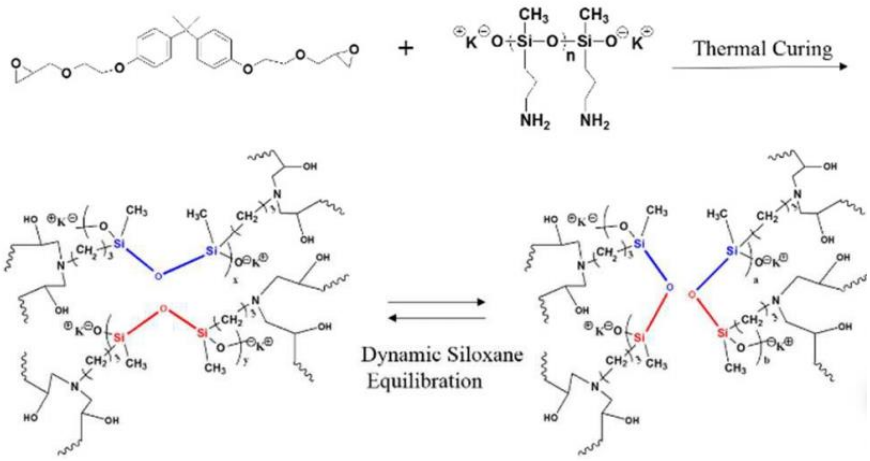

Figure I-31. The schematization of synthesis of dynamic epoxy networks based on siloxane equilibration[97].

1.2.4.6 Disulfide chemical exchange

Disulfide chemical exchange has long been observed in living organisms, thus attracting attention for its application in materials science. Such is the case of the work reported by Tesoro *et al.* (1990) and more recently "retaken" by Klumperman (2011)[60, 61]and Odriozola (2016) [66, 98, 99, 100] (see section 1.2.5.2.3).

This particular exchange mechanism drew the attention of Ruipérez *et al.* (2016) to study the nature of disulfide exchange reactions, particularly for diphenyl disulfide-based compounds[101]. The theoretical calculation to determine the prevalent reaction mechanism indicated a radical-mediated mechanism responsible for the exchange process [2+1]: the most promising amino derivates. The metathesis mechanism [2+2] was also explored, with no computational evidence for its mechanism's existence. In other words, according to the CAN's definition, the disulfide exchange mechanism involves both associative and dissociative exchange mechanisms. The associative mechanism is exemplified in the specie c and the dissociative on the specie d in **Figure I-32**.

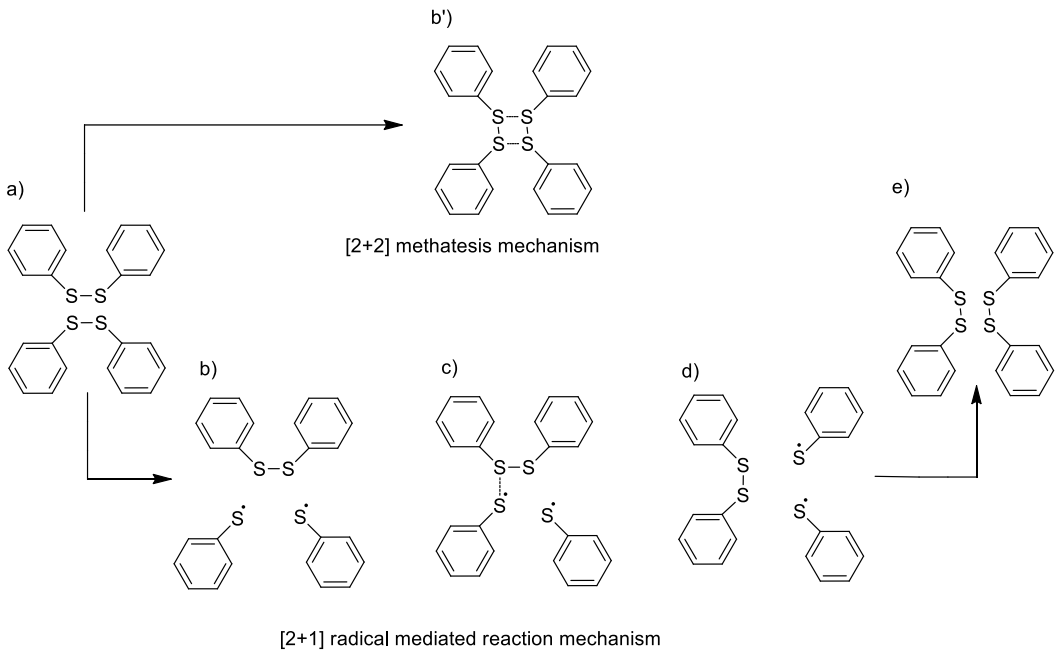

Figure I-32. Schematic representation of a [2+2] metathesis and a [2+1] radical-mediated reaction mechanism[100].

More recently, Odriozola *et al.* (2014) led research on this kind of materials based on disulfide exchange. The first produced material was a poly(urea-urethane) network catalyst-free from isophorone diisocyanate and 4-aminophenyl disulfide (4-APDS). The network did not dissolve in a common solvent. It presented a relaxation at elevated temperatures, a behavior attributed to 1) the disruption of H-bonds at a temperature around 100°C, and 2) the disulfide exchange metathesis, accelerated by temperature. The reprocessability properties were also tested, showing good results after a hot press heating for reshaping. This work presented an innovative strategy to be implemented in industries where polyurethanes are used: its easy process for recovery and recycling could represent an important reduction of waste[98, 99].

Inspired by the promising results of the poly(urea-urethane) systems, Odriozola probed the dynamic hardener employed with DGEBA epoxy prepolymer, like Tesoro and co-workers in the '90s. Odriozola *et al.* (2016) performed a fiber reinforcing polymer composites (FRPCs) of DGEBA - 4-APDS with an excess of amine to quickly relax, and to be able to dissolve the network in a thiol-containing solution to reprocess the material afterward. The network elaborated without reinforcing fibers showed an Arrhenian behavior. It was completely dissolved in mercaptoethanol/DMF solution after 24h. The material promises to be very useful for wind energy applications, where the material can suffer from different kinds of damages such as cracks, impacts, fractures, delaminations, etc. The delamination

damage was especially studied, showing interesting results to overcome this recurring problem and the possibility of reshaping by thermoforming the laminated cured composite.

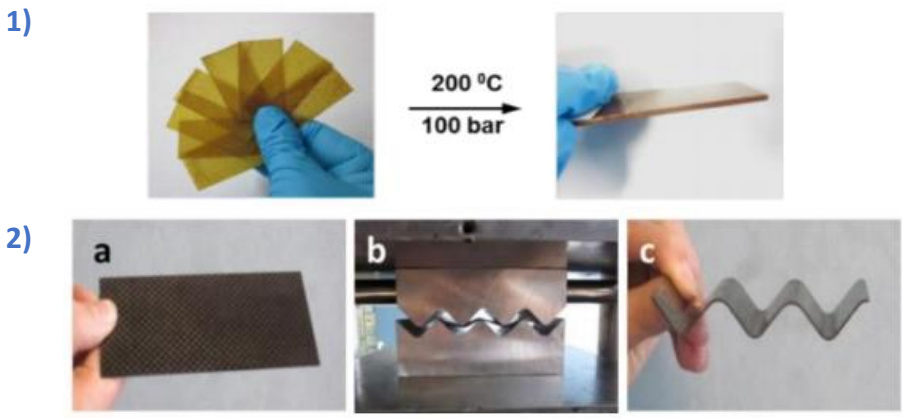

Figure I-33. The potential application for epoxy resins from DGEBA and 4-APDS, 1) sheets of fully cured dynamic epoxy resins before and after being hot-pressed to obtain a compact multilayered composite, 2) thermoformation of cured composite laminated in a zig-zag shape[66].

Odriozola *et al.* (2016) performed an additional mechanochromism study, showing how the network based on DGEBA and 4-APDS presented a coloration due to sulfenyl radicals' formation. This observation is promoted by the mechanical excision of the aromatic disulfide crosslinks (**Figure I-34**). 2-APDS was also used at the place of 4-APDS, but it was impossible to distinguish any change of color by the naked eye. Thus, only the para-substituted network presents mechanochromism. This behavior adds a visual property and facilitates the detection of damage in structural materials[102].

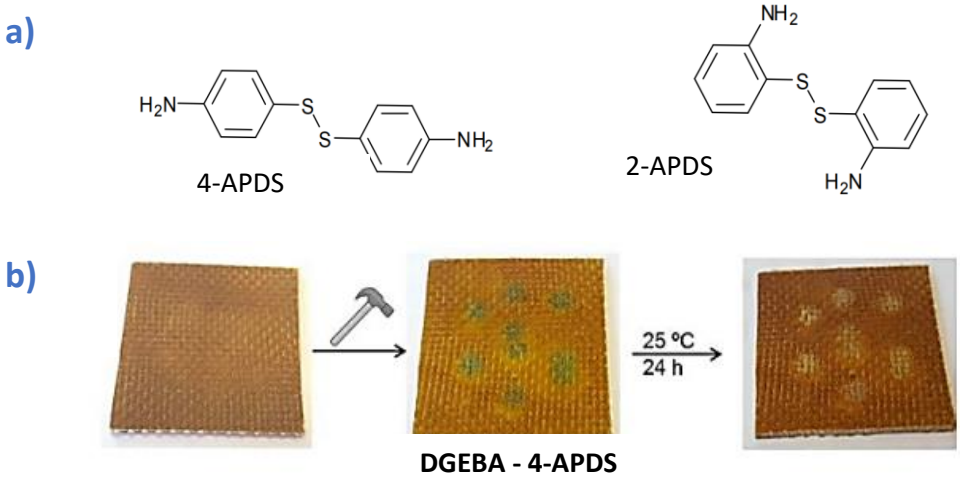

Figure I-34. a) Chemical structure of both employed hardeners, and b) image sequence of a glass-fiber composite based on 4-APDS, then damaged with a hammer showing the apparition of green spots where the damage was injured, and finally, after one day at room temperature, the green color disappears[102].

In the same field of vitrimer composites, Hu *et al.* (2018) elaborated an epoxy network quite similar to that performed by Odriozola's team. They used an epoxy/amine functionality ratio equal to 1, and added unmodified (U-silica), and modified silica by epoxy (EP-silica), and a thiol (SH-silica)[103]. On the one hand, the mechanical properties were increased because of the introduced reinforcement (**Figure I-35a**). On the other hand, the network experimented chain mobility restriction. This limitation is observed in the variation of the relaxation and flowability behaviors, both necessaries for the topological rearrangement (**Figure I-35b**). Finally, an increase in the activation energy was observed (**Figure I-35c**).

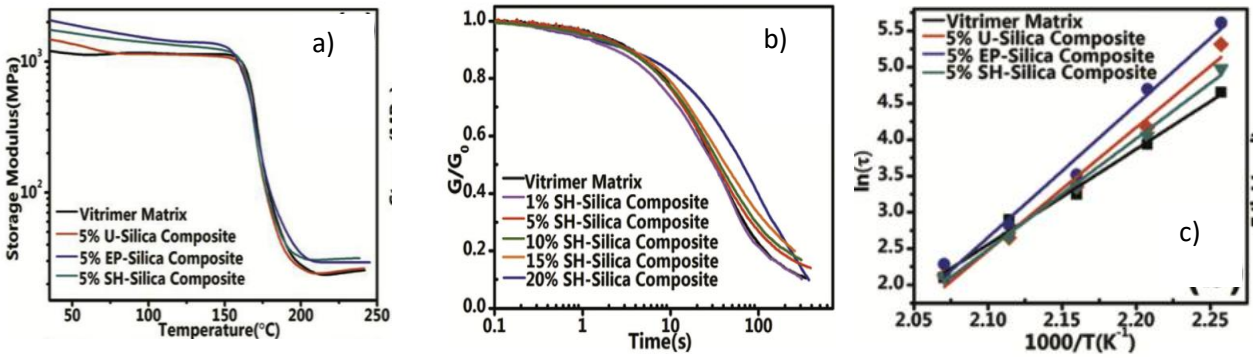

Figure I-35. a) mechanical properties of epoxy-vitrimers with unmodified nano-silica, and modified with epoxy and thiol, b) normalized stress relaxation curves of composite at 180°C and c) fitting of the relaxation times of composites against the inverse of the temperature[103].

Moreover, the healing efficiency was reduced for samples U-silica and EP-silica, but for samples containing SH-silica the efficiency is maintained, most probably due to the presence of thiol in the matrix. So that, both phenomena are present, the disulfide-disulfide and disulfide-thiol exchanges.

1.3.5.7 Imine exchange reaction

The covalently dynamic nature of imines has drawn attention in the vitrimer field. The imines react reversible in water (hydrolysis), with amines (transamination), and with imines (metathesis). Zhang *et al.* (2014) decided to explore the covalently dynamic nature of imines by producing malleable and recyclable polymer networks[104]. The mechanism proposed by the authors was the imine metathesis. Nonetheless, Du Prez suggested a fast imine addition-elimination exchange[76] remarking the work of Di Stefano *et al.* (2013), whom concluded that just little amounts of primary amines effectively catalyze the imine metathesis and not imine metathesis as Zang and co-workers suggested (**Figure I-36**)[105].

In subsequent work, Zhang *et al.* (2018) presented a polyimine vitrimer system based on *m*-xylene diamine, terephthaldehyde, and tris (2-aminoethyl) amine. The re-processability of the vitrimer systems was explored by pressing the sample under heat and water or remolding via amine solvents. This innovative way to reshape is an interesting alternative when elevated temperatures are not possible or convenient. Nevertheless, deterioration of mechanical properties of materials reshaped via the water-pressing method limits their potential applications[106].

To go further, Zhang *et al.* (2019) employed the same synthesis strategy, but they changed the diamine by a polysiloxane oligomer containing amino groups (PDMS-NH_2)[107]. The polysiloxane presented a vitrimer like material properties, reprocessed and reshaped by consecutive grinding/compression molding cycles. It was possible up to three times without losing mechanical properties. It is important to remark that, like in their precedent network, the reshaping can be achieved at a mild temperature after water immersion.

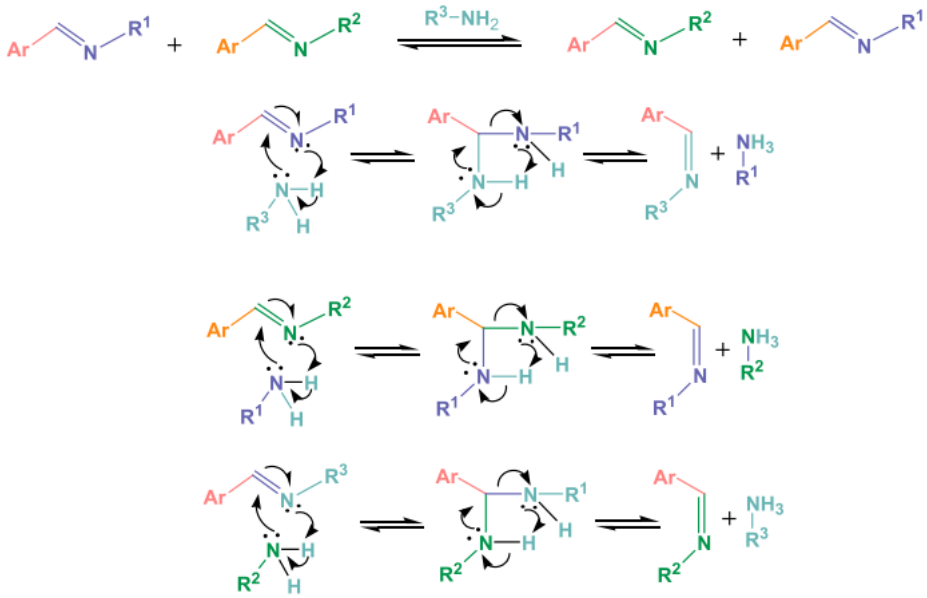

Figure I-36. The schematization of metathesis mediated by primary amines and transamination exchange mechanism[106].

1.2.5 Is it more challenging than expected to identify a vitrimer network?

Following Bowman and coworkers' definition of the different exchange mechanisms, it can be "easy" to differentiate both types of networks. The truth is that it is not so easy-going. The particular viscosity evolution as a function of the temperature, which follows Arrhenius law, has become the "characterization technique key" to assume the "vitrimers" behavior for those networks to show a constant crosslinking density. However, the truth is that vitrimers are not the only network that follows an Arrhenian behavior as a function of the temperature. For instance, Wang and coworkers (2017) elaborated a network based on DA reaction. The network followed an Arrhenian behavior, although the mechanism exchange is clearly dissociative[108].

When a new system is claimed as a vitrimer network, all vitrimer properties must be proved, or at least explored, to provide any possible information that may assist in the description of these materials. The permanent connectivity, which is often omitted, should be included. Nonetheless, proving permanent connectivity is not simple because it is quite complicated to find a good solvent. In agreement with Leibler, Du Prez, and Winne (2019), a rigorous solubility test should always be performed to prove the vitrimer properties of a given polymer network and to show its non-fluctuating crosslink density. Regrettably, the new works claiming new "vitrimer" chemistries do not always address this issue[109].

Furthermore, new reported systems such as poly(alkylurea-urethane)[110] or 1,2,3-triazolium[85] claimed an associative exchange mechanism in a first approach. The networks showed stress relaxation and were able to be reprocessed. Still, for 1,2,3-triazolium subsequent studies showed a more complex pathway nonconcerted and dissociative mechanism exchange by employing different characterization techniques while maintaining the crosslinking density. These particular kinds of CANs networks evidenced how the associative exchange mechanism is not necessarily required to obtain dynamic networks with constant crosslinking. Besides, this particular behavior makes it virtually indistinguishable and not obvious from that genuine vitrimers networks[87, 88, 89]. According to Dichtel *et al.* (2020), several CANs that lose (a low degree) their crosslink density have been described as "vitrimer-like" or erroneously classified as vitrimers. Nonetheless, the authors suggest that the subtle or nonexistent differences in properties between associative and dissociative networks difficult the classification of these materials based on crosslink exchange mechanisms.

From a practical point of view, vitrimer materials exhibit a progressive viscosity variation as a function of temperature, following Arrhenius law. The materials might exhibit a new temperature transition different from the *T*g or *T*m: The *T*v. The *T*g is linked to the segment motion, the *T*m to the crital

temperature point where the crystalline regions in a semycristalline polymers become amorphous, and the *T*v is related to the bond exchange reactions. This new transition temperature is not easy to discern if the *T*g or *T*m is higher that the theorical *T*v *(Tg/Tm>>~~Tv~~)*[111]. Vitrimers materials can rearrange their topology via exchange reactions by *maintaining their crosslink density*, either by an exchange mechanism associative, dissociative, or even a combination of both mechanisms. The temperature at which the chemical exchange occurs is commounly denominated as *T*v. The connectivity of networks has to be proved by both swelling and multifrequency tests varying the temperature. It is important to perform both techniques since finding the correct solvent to evidence the non-fluctuating crosslink density is complicated. Confronting the experimental data from these two different techniques may clarify this critical point for any eventual doubt about the constant network connectivity.

Concerning about the exchange mechanism, another question to ponder is if a network capable of maintaining constant crosslink density has to present an exclusive exchange mechanism. The truth is not. Du Prez and coworkers presented a fluorinated vinylogous urethane vitrimer that exhibits two different exchange mechanism temperature-dependent. A lower energy the pathway entailed is a transamination via an activated iminium intermediate, and to higher energy, the pathway involved is a transamination via conjugate addition reaction to the enaminone. Another interesting case of study displaying both exchange mechanisms is where the networks are based on aryl disulfides. According to Ruipérez *et al.* (2016), a radical-mediated mechanism responsible for the exchange process [2+1]. In such way, both exchange mechanisms are involved.

1.3 Viscoelasticity characterization of CANs

In this section, a brief resume of linear viscosity models to describe the polymer networks and the first molecular theories are listed. Then, a brief introduction of some of the different methods explored to characterize the viscoelasticity behavior of vitrimer materials. The constant evolution of the characterization methods has been sorted chronologically, showing a continual progression to describe these complex networks' rheological behavior.

1.3.1 Linear viscoelasticity

The viscoelasticity behavior of materials can be characterized in the linear domain, i.e., at restricted strains with a low strain rate. The severity of these conditions ensures the linearity degree of materials viscoelasticity behavior.

1.3.1.1 Maxwell model

The Maxwell model results from the direct combination of viscous and elastic behaviors in one constitutive equation combining the Newtonian and Hookean equations.

$$\tau + \frac{\eta_0}{E}\frac{\delta\tau}{\delta t} = -\eta_o \frac{\delta\gamma}{\delta t}$$

$$\tau + \frac{\eta_0}{E}\frac{\delta\tau}{\delta t} = -\eta_o \dot{\gamma}$$

$$\lambda = \frac{\eta_0}{E}$$

$$\tau = \tau_0 * e^{-t/\lambda}$$

Where τ is the stress, λ the characteristic time, η is the viscosity, γ is the deformation, and E is the Young modulus.

Generally, materials are formed by elements that do not necessarily possess a single viscosity nor a single elasticity. That is why it is necessary to consider a set of elements and not a single element to describe real materials' viscoelastic behavior. Different models and theories have been explored to describe the "relaxation time spectrum" of materials throughout the 19th and 20th centuries.

1.3.1.2 Maxwell generalized model

In this model, a set of elements is considered, as displayed in **Figure I-37**. In other words, this model considers a relaxation time spectrum in order to describe the material relaxation more properly, i.e.

$\lambda_i = \frac{\eta_i}{E_i}$. The relaxation modulus can be expressed as:

$$\tau = \sum \tau_i * e^{-t/\lambda_i}$$

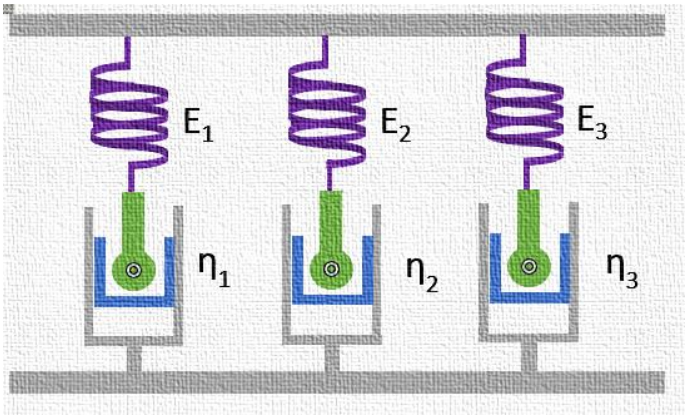

Figure I-37. Generalized Maxwell model.

Divers studies have already employed the Maxwell generalized model, proving a more accurate relaxation time spectrum[112, 113, 114].

1.3.1.3 Rouse model

Rouse model idealizes the polymer chains as a series of elastic dumbbells (**Figure I-38**), suggesting an infinite relaxation modulus series. This model is mainly used in dilute polymer solutions, but it is possible to use it for polymers without solvent[114].

The relaxation time spectrum λ_p can be described as:

$$\lambda_P = \frac{6\eta}{nk_BT\pi^2p^2}$$

Where η is the viscosity, n is the number of polymer chains per volume unit of the polymer, k_B is the Boltzman constant, T is the temperature in K, and p the number of relaxation times.

And the module can be expressed as:

$$G(t) = nk_BT\sum_{p=1}^{z} e^{\left(-\frac{t}{\lambda_P}\right)}$$

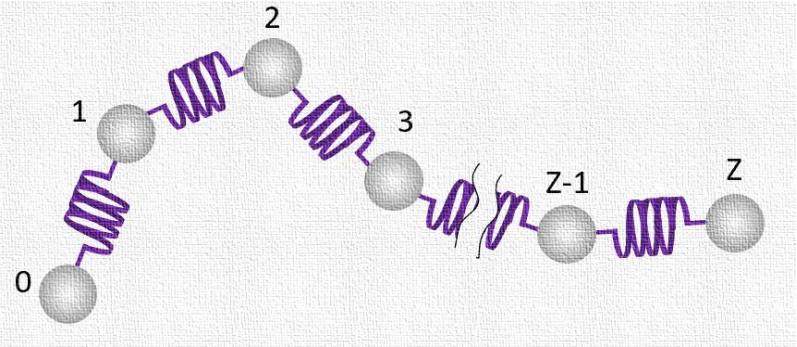

Figure I-38. Rouse model, polymer chains as a series of elastic dumbbells.

Later, in 1971, DeGennes proposed a model considering that the relaxation process was easier in a longitudinal form since the lateral movements are limited. This longitudinal movement was denominated as "reptation". The reptation time is expressed as:

$$t_{rep} = \frac{L^2 N \xi_0}{k_B T}$$

Where L is the molecule length, N is the number of Rouse segments, and ξ_0 is the friction coefficient of each segment.

Soon after, Doi and Edwards considered the dynamic of the chain, keeping in mind longitudinal diffusion. The relaxation modulus was expressed as:

$$G(t) = G_0 \sum_{p,odd}^{z} \frac{8}{p^2 \pi^2} e^{-\frac{t}{\lambda_p}} \quad ; \quad \lambda_p = \frac{t_{rep}}{p^2}$$

1.3.1.4 Unsteady shear flow: Time-temperature superposition principle (TTSP)

Typical single viscoelastic experiments cover over three to five decades of time to fully describe the G(t). The TTSP consists of collecting information at different temperatures, since the curves at different temperatures have similar shapes, and later, shifting the data to one reference temperature. **Figure I-39a** and **b** illustrate the construction of a master curve following TTSP.

According to the work of Williams, Landel and Ferry, the transition from the rubbery to the glassy state for many amorphous polymers follows a dependence of a shifting factor on temperature (**Figure I-39c**).

$$log\ a_T = \frac{-C_1(T - Tg)}{C_2 + T - Tg}$$

Where C1 and C2 are constants and *T*g is the glass transition temperature. This equation holds around the *T*g, and also can be valid for higher temperatures.

The function $a_T(T)$ has been widely studied, showing how the function can give important information about the temperature dependence of material relaxation times. For temperatures within 100 K of the polymer's glass transition temperature, most polymers show Arrhenius dependence.

$$a_T = \exp\left(\frac{-\Delta H}{R}\left(\frac{1}{T} - \frac{1}{T_{ref}}\right)\right)$$

Where ΔH is the activation energy to flow, R is the ideal gas constant, T is the temperature in K and T_{ref} is the reference temperature in K.

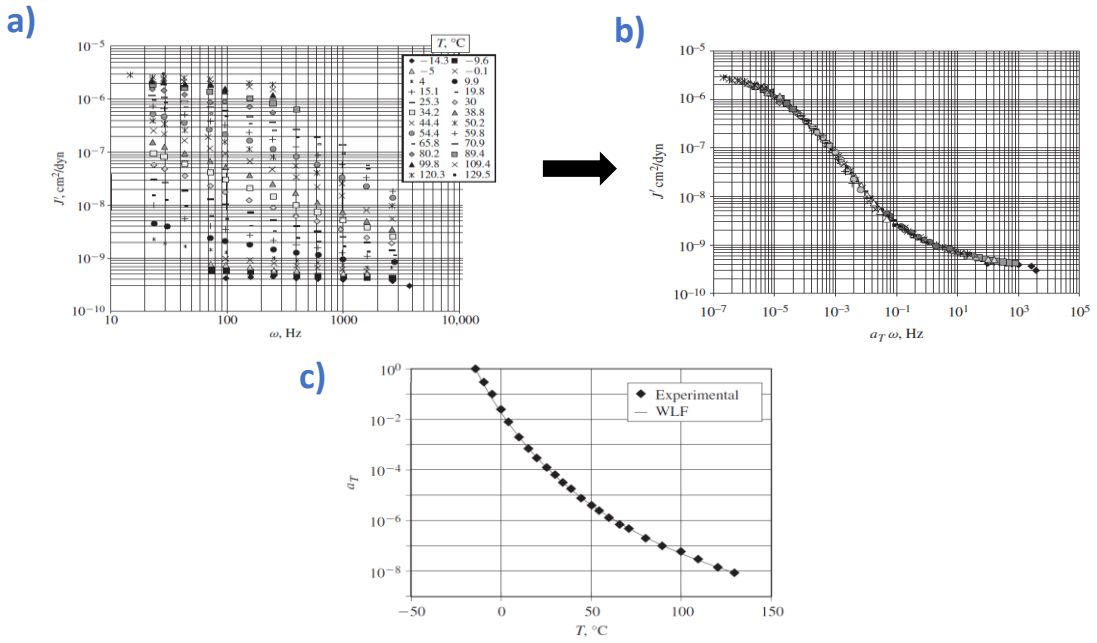

Figure I-39. a) Linear viscoelastic storage compliance J' of poly (n-octyl methacrylate) as a function of frequency and b) temperature and master curve of linear viscoelastic storage compliance at T_{ref} = -14.3 °C as a function of reduced frequency a_T*ω, and c) the shifting factor a_T against the temperature from Dannhauser *et al*. (1958)[112, 115].

1.3.2 Viscoelasticity behavior of vitrimers

Leibler and coworkers (2011) observed how vitrimer materials could completely relax stress at high temperatures and flow. The first approach proposed that the relaxation curve could be described using the single Maxwell model and normalizing the stress relaxations curves. The way to determine the relaxation time at different temperatures was by choosing the value of the maximal slope (1/*e*). The relaxation time at different temperatures showed an evolution that follows the simple Arrhenius law. From this equation, it is possible to determine the activation energy and, by extrapolation, the topology freezing temperature (*T*v).

$$\frac{\tau}{\tau_0} = e^{\left(-\frac{t}{\lambda}\right)}$$

$$\lambda^* = \lambda_0 \, e^{\left(\frac{Ea}{RT}\right)}$$

Nonetheless, as expressed before, materials do not necessarily possess a single viscosity nor a single elasticity. Hence, several research groups have remarked that the single Maxwell model does not properly fit the complex stress relaxation profiles obtained for these materials. That is the main reason why various approaches or theories have been employed to describe the relaxation of vitrimers in recent years.

Smallenburn and Leibler (2013) proposed a patch particle model for vitrimers. The model mimics the bond exchange mechanism of vitrimers, using event-driven molecular dynamics (EDMD) simulation, free calculation, and Wertheim's thermodynamic perturbation theory. The calculation revealed a region of thermodynamic instability in which the vitrimer phase is separated into a more connected phase. The phase behavior is described by Wertheim theory, predicting cluster size distribution in the experimental vitrimer system. The study also shows how high bond-switching rates occur at high T and catalyst concentrations; thus, the maximum number of bonds was formed[116].

Lately, Yu *et al.* (2014) explored a vitrimer system based on transesterification like performed by Leibler and coworkers. The time-temperature superposition principle (TTSP) was used to analyze the relaxation behavior of the networks. The shifting factor a_T was plotted against 1/T, showing a temperature dependence and following Arrhenius law. Yu and coworkers established that their system presented a kinetic *bond exchange reaction* (BERs). This behavior is in accordance with Leibler *et al.* (2011) observations[117].

Continuing in the line of establishing a model to characterize the viscoelastic behavior of CANs, Yu and coworkers (2014) explored a fresh idea to describe the thermo-rheological behavior of shape memory polymers based on ter-butyl acrylate (tBA), poly (ethylene glycol), dimethacrylate (PEGDMA) and 2,2-dimethoxy-2-phenylacetophenone as polymer initiator. The model considers one equilibrium branch and several thermoviscoelastic non-equilibrium branches to represent the polymer's multiple relaxation processes (**Figure I-40a**). Thus, the total stress evolution is expressed as the summation of each branch, quite similar to a Prony series:

$$\tau(t) = E_{eq} + \sum_{i=1}^{n} E_i \exp\left(-\frac{t}{\lambda}\right)$$

E_{eq} and E_i are the elastic moduli in the equilibrium and non-equilibrium branches. The use of E_{eq} may let us think that the network does not fully relax so that the model cannot describe correctly the vitrimer behavior since a vitrimer usually fully relax. Still, the addition of multiple branches illustrates the diversity of relaxation times in the thermoset.

Figure I-40b illustrates the equations mentioned above. Non-equilibrium branches are gradually added in the model (and in the graphs) to improve the accuracy in the description of the experimental stress relaxation master curve.

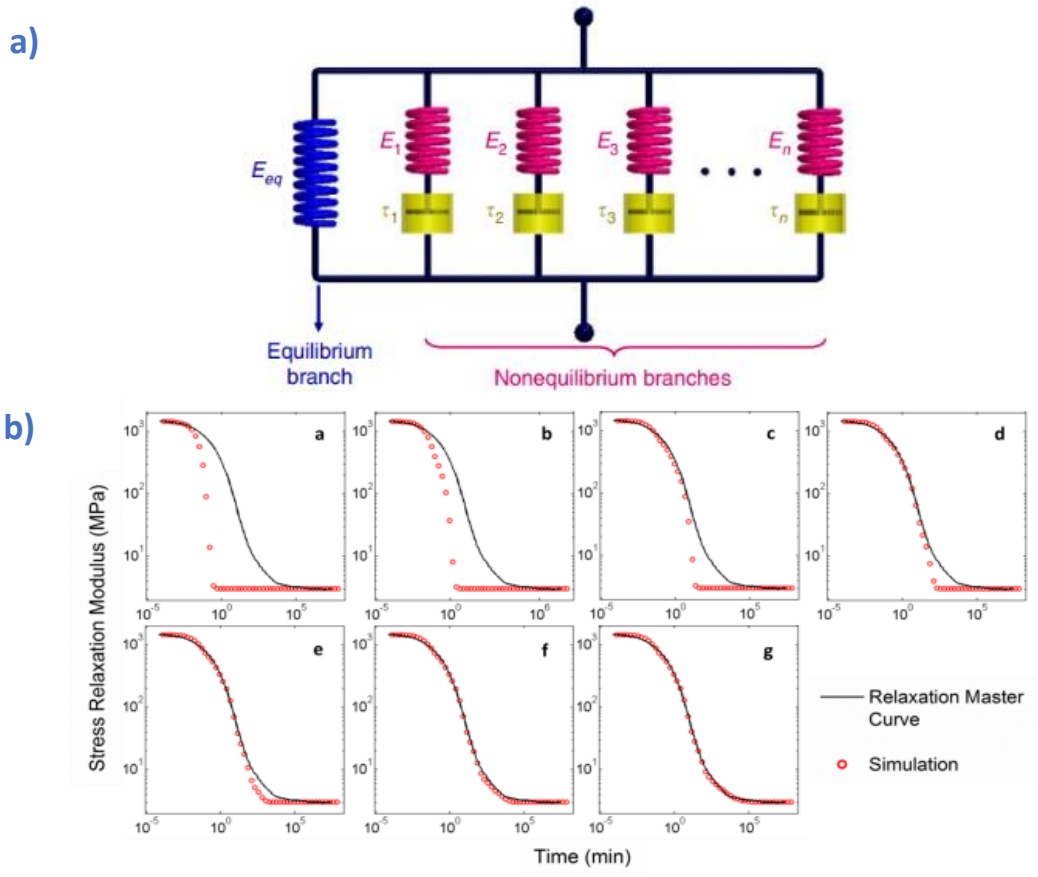

Figure I-40. a) Multi-branch rheological model representation, and b) Simulation curve approaching the experimental relaxation master curve, from a to g the number of non-equilibrium branch increment one by one[118].

The shifting factor achieved from the relaxation master curve was plotted as a function of temperature. The shifting factors displayed a Williams-Landel-Ferry law behavior, and the constant C1 and C2 were quite similar to the universal values. A "key" temperature was established T_s, approximately 20°C below the *T*g, an inflection point between the Arrhenian and WLF behavior. Hence, for temperatures above T_s, the shifting factors follow the classic WLF equation, and below T_s,

the shifting factors follow the Arrhenius-type behavior[118]. Similar approaches were published using systems DGEBA and fatty acids[119] and glutaric anhydride[120].

Snijkers *et al.* (2016) also proved that time-temperature superposition analysis worked well for the vitrimer transesterification system. The shift factor values from the master curve displayed a WLF-dependence on temperature close to *T*g, as observed by Yu and coworkers. The construction of the master curve allowed to glimpse two relaxation behaviors, at high frequencies (ω~ 10^2 rad/s) next to the rubbery plateau and lower frequencies (ω~ 10^{-4} rad/s) before achieving the terminal relaxation (**Figure I-41**). One explanation about this interesting phenomenon is attributed to the performed temperature range, since stress relaxation experiments were carried out at temperatures close to the *T*g. The authors also remarked that the theories for the dynamics of vitrimer explored at that moment do not predict a double relaxation behavior; thus, they suggest that "some ingredients might be missing from the theories", inviting to explore the double relaxation behavior[121].

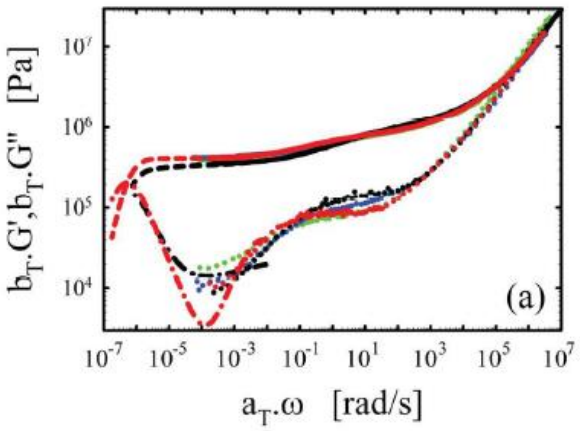

Figure I-41. Master curves of the oscillatory data of G' and G''. G' displays a double relaxation behavior with two apparent plateau moduli at high and low frequencies[121].

A high proportion of works describing the viscoelasticity characterization of vitrimers are performed at temperatures well above the *T*g. Only a few works look into the viscoelasticity of vitrimer near the *T*g. This information gap was explored by Yu *et al.* (2018), who synthesized a polyimine presenting reversible bonds. Yu and coworkers' pioneering work remark the importance of distinguishing the two-relaxation mechanism present in vitrimer networks (the effect of the bond exchange reaction and the chain relaxation) and predicting their contribution to the thermomechanical behavior. In their work, both phenomena are studied in a short temperature range, contrary to most study cases where only the terminal relaxation is observed at high temperatures. A nonlinear thermo-viscoelastic

constitutive model based on the Bernstein-Kearsley-Zapas (BKZ) theory was established. The model's true stress is the summation of the two different stress branches, one linked to the BER branches and the second linked to the viscoelastic branches. It can be written in terms of the relaxation modulus and relaxation time as:

$$\sigma = \sigma_{BER} + \sigma_{Viscoelastic}$$

$$G = \sum_{i=1}^{m} G_{BER_i} \exp\left(-\frac{t}{\lambda_{BER_i}}\right) + \sum_{j=1}^{n} G_{Viscoelastic_j} \exp\left(-\frac{t}{\lambda_{Viscoelastic_j}}\right)$$

The equation's experimental parameters were determined in two steps: 1) determination of the BER relaxation, 2) determination of the viscoelastic relaxation. The contribution linked to the BER was possible to perform at a temperature well above *T*g to ensure that the BER behavior was predominant. The contribution attributed to the viscoelasticity was achieved by studying the relaxation behavior at several temperatures around the *T*g. The induced stress relaxation of the BERs was first predicted and then subtracted from the relaxation curves **Figure I-42a** and **b**). The new relaxation curves were plotted using the TTSP to build the relaxation master curve (**Figure I-42c**). Finally, non-equilibrium branches were gradually added to simulate the experimental relaxation master curve (**Figure I-42d** and **e**)[122, 123].

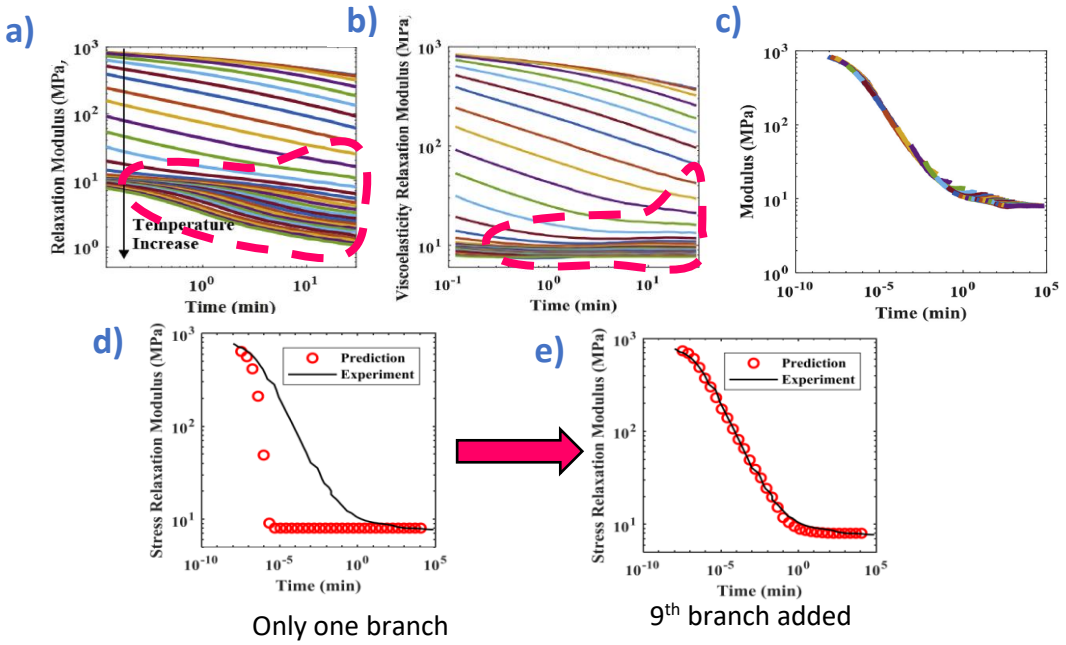

Figure I-42. a) Stress relaxation curves of polyimine at temperatures from 9-75°C with 2°C intervals, b) stress relaxation curves of viscoelastic branches after subtraction of the BER stress relaxation component, c) relaxation master curve at reference temperature of 37°C, d) and e) evolution of master curve fitting from one branch to nine branches[122].

Previous research working with thermoset and elastomers without dynamic bonds have shown how stress relaxation does not properly follow Maxwell's equation but can be described by using a stretched exponent decay, i.e., the Kohlraush-Williams-Watts equation (KWW)[11, 124, 125, 126]. Inspired by this remark, Torkelson and coworkers (2018) re-took KWW equation to describe the stress relaxation behavior of their vitrimer system[127].

$$\frac{G(t)}{G_0} = \frac{G_{perm}}{G_0} + \left(1 - \frac{G_{perm}}{G_0}\right) e^{\left(-\left(\frac{t}{\lambda}\right)^{\beta}\right)}$$

Where $\tau(t)/\tau_0$ is the normalized stress at time t, λ is the characteristic relaxation time, and β (0< β <1) is the stretched exponent that controls the shape. The exponential β reflects the width of the relaxation distribution, i.e., the heterogeneity of the multiple relaxation times presented in the network. A quite similar approach was performed by Terentjev *et al*. (2016). They observed how the stress relaxation of networks based on SIS (styrene-isoprene-styrene) could be described using a stretched exponent [128, 129, 130]. The average relaxation time can be calculated by following the relation, where Γ is the Gamma function[131].

$$\bar{\lambda} = \frac{\lambda\, \Gamma\left(\frac{1}{\beta}\right)}{\beta}$$

Terentjev and coworkers (2019) proposed a model to describe how the full or partial vitrimers respond upon deformation. The model considers a network consisting of N_0 crosslinked chains at time t=0. After an infinitesimal time Δt, the number of cross-linked chains at t=0 decreases, but at the same time, some chains will be re-crosslinked back into the network. These infinitesimal changes were expressed in a continuum model, proving how the theoretical results describe well the experimental stress relaxation and the uniaxial deformation[132].

Montarnal *et al*. (2020) also explored the time-temperature superposition principle of 1,2,3-triazolium-based poly(ionic liquid)s (TPILs) networks. Two different TPILs crosslink were explored, the first presents a dissociative behavior and an absence of the sol-gel transitions (TPIL6). The second displays a constant crosslink density in a range of temperature, characteristic behavior of vitrimers (TPIL7). To clearly compare the viscoelastic behavior of each network, the master curve for both systems were built throughout the time-temperature superposition by performing small amplitude oscillatory shear (SAOS) experiments. Two shifting factors were considered and not only one like Yu and coworkers (2014). The shift factors $a_{T,\ Network}$ indicate the average variation of relaxation times with temperature. The shift factors $b_{T,\ Network}$ indicate the variation of crosslink density with temperature. The shift factors $b_{T,\ Network}$ is frequently omitted after normalizing stress relaxation

curves.

$$a_{T,Nework} = \frac{\lambda_{Network}(T)}{\lambda_{Network}(T_{ref})}$$

$$b_{T,Nework} = \frac{G_{Network}(T)}{G_{Network}(T_{ref})}$$

The shift factors $a_{T,\,Network}$ were calculated from the stress relaxation data, revealing an Arrhenius-type behavior $a_{T,\,Nework}=Ae^{\frac{Ea_\lambda}{RT}}$. Similarly, the shift factors $b_{T,\,Network}$ were determined and followed an exponential law $b_{T,\,Nework}=Ae^{\frac{Ea_{Network}}{RT}}$

The viscosity can be described as follows, allowing to determine properly the activation energy (Ea):

$$\frac{\eta_0(T)}{\eta_0(T_{ref})} = \frac{G_{Network}(T)\,\lambda_{Network}(T)}{G_{Network}(T_{ref})\,\lambda_{Network}(T_{ref})}$$

$$\frac{\eta_0(T)}{\eta_0(T_{ref})} = a_{T,Nework} * b_{T,Nework}$$

$$\frac{\eta_0(T)}{\eta_0(T_{ref})} = e^{\frac{Ea_\lambda}{RT}} * e^{\frac{Ea_{Network}}{RT}}$$

$$Ea_\eta = Ea_\lambda + Ea_{network}$$

This approach allows considering the crosslink density evolution throughout the temperature of CANs to afford a trustworthy insight into their overall rheological behavior[133]. Khabaz and Perego (2021) proposed the use of molecular dynamics (MD) and Monte Carlo (MC) simulations to insight into the relationship between structure and flow. A non-dimensional analysis was carried out based on the shifted Lennard-Jones potential and finite extensible nonlinear elastic (FENE) bond model. The MD/MC simulations predict two transition temperatures based on the *T*g and the *T*v's volumetric data. The system employed displays a higher *T*v than its *T*g, approximately 40°C difference. Besides, the rheology spectrum with the aid of non-equilibrium molecular dynamics (NEMD) simulations and using the TTS principle can be extended, contrary to the classic rheological experiments where only a small part of the terminal regime is observed due to the long experimental data acquisition times. The extended rheology spectrum was employed to describe the behavior of thermosets and vitrimers at low frequencies. The thermoset shows the typical transition from the rubbery to the glassy state, while the vitrimer showed two transition regimes, corresponding to the transition from viscoelastic liquid to rubbery and from rubbery to glassy (**Figure I-43**). These transitions are quite similar to those

expressed by Snijkers *et al. (*2017). The model offers a simple way for modeling and simulating vitrimers behavior. The authors suggest that this model could be used to investigate the impact of later factors or the bond exchange reaction's kinetics[134].

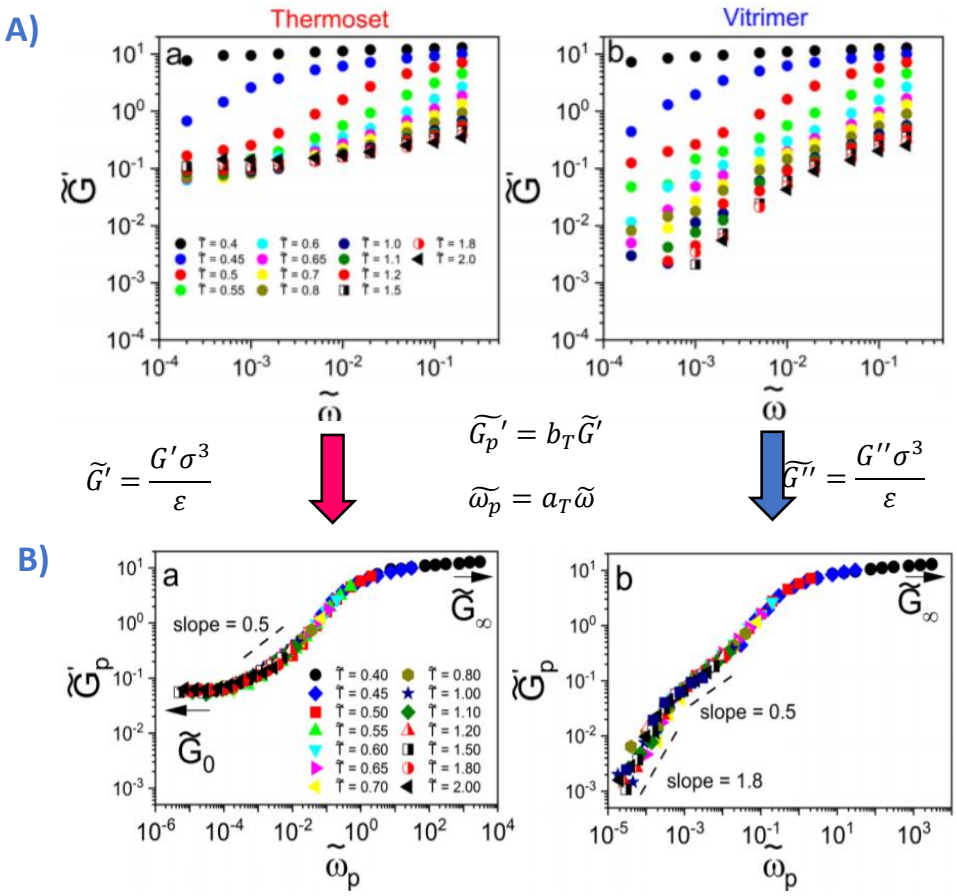

Figure I-43. A) Elastic and loss moduli of the model thermoset and vitrimer as a function of reduced frequency $\tilde{\omega} = \omega\sqrt{\sigma^2 m/\varepsilon}$ at different temperatures $\tilde{T} = T/k_B\varepsilon$, and B) Master curves of elastic and lost moduli non-dimensional[134].

1.4 Cellulose

1.4.1 Historical discovering

Cellulose has been used over the centuries in several applications such as textile, paper, fuel, among others. However, it was not until the 18th century when the French chemist Anselme Payen discovers a resistant fibrous solid substance after treating plant tissues in acid and ammonia, followed by extraction with water, alcohol, and ether. In subsequent experimentation, Payen decided to experiment with concentrated sulfuric, transforming "the fibrous substance" into dextrose. That fact allowed him to determine that the fibrous solid discovered, the starch, and the glucose had the same chemical composition. In 1839 this fibrous substance was recognized as a chemical compound named "cellulose" in a report of the French Academy[135, 136. 137].

1.4.2 Industrial development

Cellulose is the most abundant naturally renawake organic compound, present in all advanced plants, from 40 to 99% in dry weight. Since the discovery of cellulose as a chemical compound, diverse chemical reactions have been explored. Such is the case of cellulose nitrate, which triggered the modern rayon industry's development in the 19th century. Another important chemical reaction was cellulose with ethers, discovered and patented in the earlier 20th century. In 1935, carboxymethylcellulose (CMC) was discovered, acquiring economic importance due to its numerous uses. A few years later, the manufacture of hydroxyethyl cellulose (HEC) and hydroxypropyl cellulose (HPC), water-soluble cellulose ethers used to the present, are proof of the importance of these natural fibers. Since 1950, the production and application of cellulose and modified cellulose have been strongly expanded on a global scale[136].

Today the global cellulose market size is the amount to 300 billion USD according to fortune business insight. Cellulose fibers are mainly used in the paper, textile, construction, pharmaceutical, and chemical industries. The high demand from these industries suggests steady growth in the coming years[138, 139].

1.4.3 Chemical structure

In 1811, Gay-Lussac and Thenard showed that glucose and starch contained 45% of C, 49% of O, and 6% of H in weight, obtaining an empirical formula $(CH_2O)_n$, named *carbohydrate*. A few years later, in 1842, Payen determined cellulose's elemental composition (44-45% of C, 6-6.5% of H, and 48.5- 50% of O w/w). This fact triggered the subsequent works to elucidate the structure of cellulose.

Ost and Wilkening (1910) established a qualitative relationship between cellulose and glucose. A

couple of years later, in 1913, Ost's work was followed by Willstatter and Zechmeister, completing the hydrolysis of cellulose by acid. But it was not until 1921 that Monier-William described this relationship as a nearly quantitative one, according to the following expression:

$$(C_6H_{10}O_5)_n + nH_2O - nC_6H_{10}O_5$$

In subsequent years, several statements were made to clarify the chemical structure of cellulose[140]:

- The presence of three alcoholic hydroxyl groups on positions 2, 3, and 6, evidenced by esterification (Ost (1919), Hess and Ljubits (1928)).
- The existence of covalent bonds between the glucose units. The cellobiose studies allow determining a 4-glucopyranosylglucose structure (Haworth *et al.* (1925), Charlton *et al.* (1926), Haworth and Leaner (1928)) (see **Figure I-44**).
- The glycosidic bond nature 1,4 β rather than an α, or a 1,5 as imagined initially (Ficher and Zemplen (1909), Richtmyer and Hudson (1939)). Moreover, the theory of molecular chains received big support from Staudinger and Lütky (1925).

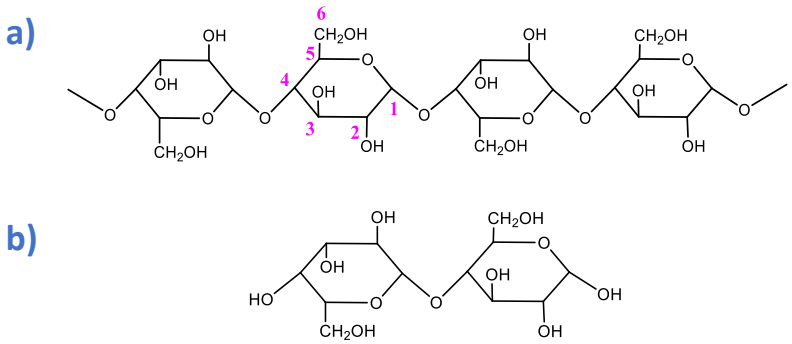

Figure I-44. a) Haworth representation of chemical constitution of cellulose as 1-4 linked beta D-anhydro glucopyranose, and b) cellobiose unit.

Thanks to the X-ray crystallography and NMR techniques, the cellulose conformation was determined. Brown and Ley (1965), Chu and Jeffrey (1968), and Berman and Kim (1968) demonstrated that the D-glucopyranose showed the $^4C_1$ chair conformation, being the lowest conformation energy[137, 141] (**Figure I-45**).

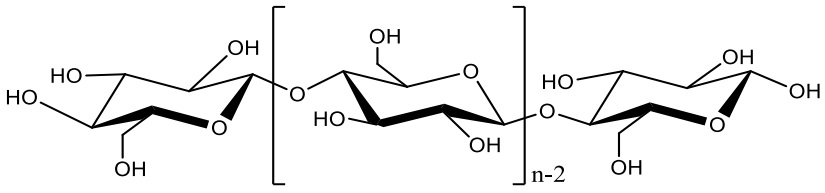

Figure I-45. Chair conformation of cellulose.

1.4.4 Molecular structure

In cellulose structure, it is possible to find two main regions, the first, an amorphous region of low order, and the second, a crystalline region of high order. Still, it is important to consider a small region with an intermediate order[137, 141, 149]. Moreover, cellulose is known for being a polymorph that can adopt various crystal lattice structures. They depend on the origin and the condition during isolation or conversion. Cellulose presents six allomorphs (I, II, III_I, III_{II}, IV_I, IV_{II}).

To determine the polymorphs, and according to several researchers, *Valonia alga*, which has the highest crystalline cellulose degree, is largely used in polymorphs studies and consequently considered as the native cellulose or the cellulose I[137]. The cellulose II is prepared by a mercerization process (soaking cellulose in aqueous NaOH 17-20% w/v), this process is generally irreversible (Kolpak *et al.*, 1978). Cellulose III is obtained from native cellulose decomposition by ammonia and followed by washing with alcohol. Two sub-modification celluloses III_I and III_{II} exist with small differences in lattice dimensions. Cellulose IV is obtained from regenerated cellulose fibers treated in a hot bath and under tension to stretch the fibers (**Figure I-46**) [135].

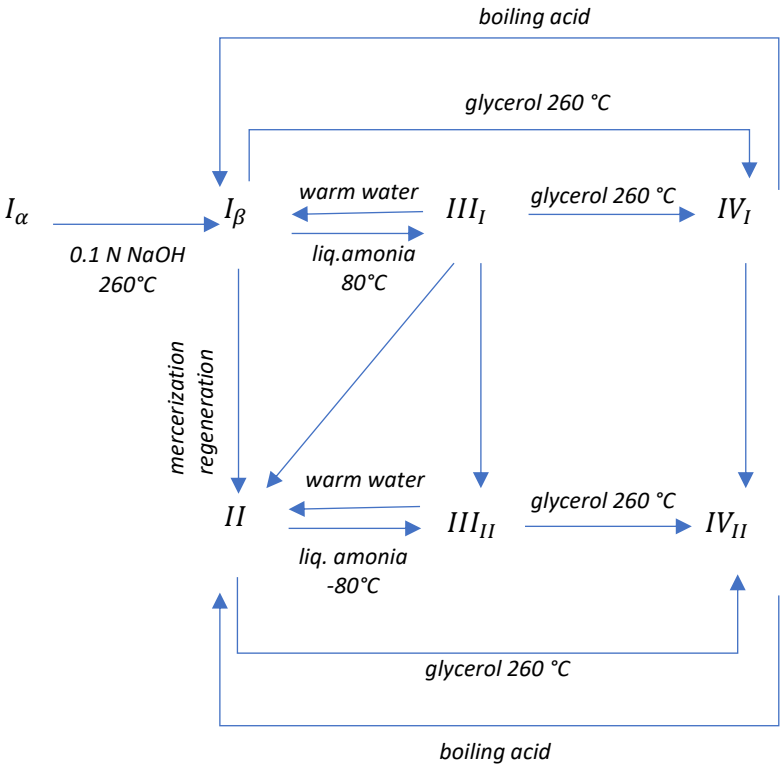

Figure I-46. Phase diagram of cellulose polymorphs and the different pathways to achieve them[143].

Sarko and Muggli (1974) studied cellulose by X-ray analysis, suggesting a triclinic lattice cell with two different cellulose chain segments. Years later, solid-state ^{13}C NMR analysis showed differences in the resonance of the C1 atoms attributed to two different crystal structures, cellulose I_α and I_β, according to VanderHart and Atalla (1984). Cellulose I_α is metastable and can be transformed by annealing into cellulose I_β (Yamamoto and Horii; 1993) [135, 142, 143].

1.4.5 Cellulose morphology

The three-free hydroxyl groups of each D-glucose unit can react with each other, forming hydrogen bonds in two different ways. At first, intramolecular hydrogen bonds are formed between the hydroxyl group C3 and the ring oxygen atom O5 and between the atoms C2 and C6. Second, the intermolecular hydrogen bonds are formed with the hydroxyl groups in adjacent cellulose molecules (**Figure I-47**). The hydrogen bonds produce a strong internal cohesion of the cellulose molecules in the unit cells, reducing the relative reactivity. Kolpak and Backwell (1976) gave the most accepted representation of these chemical bonds (**Figure I-47**).

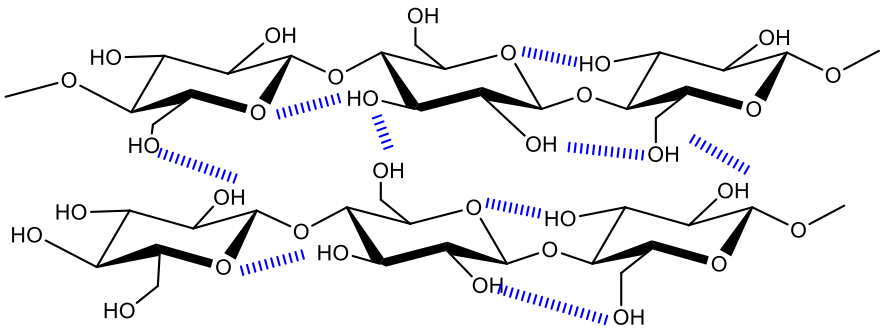

Figure I-47. The schematic representation of inter and intramolecular hydrogen bonds within the cellulose.

These hydrogen interactions permit a high molecular organization into crystallites in parallel chain arrangements. The basic elements of the supramolecular structure of cellulose fibers called "elementary fibrils" was described by Frey-Wyssling, Hess, and Kratky (1954, 1957).

Several models for the supramolecular and morphological structures of cellulose fibers were created, like the micellar model and the fringe fibrillar structure. The second one is the most accepted, and both were proposed by Hearle *et al.* in the 1950s.

The fringe fibrillar model is described as a network of elementary fibrils and random associations. The crystallites have an elongated shape and contain flat blocks (**Figure I-48**).

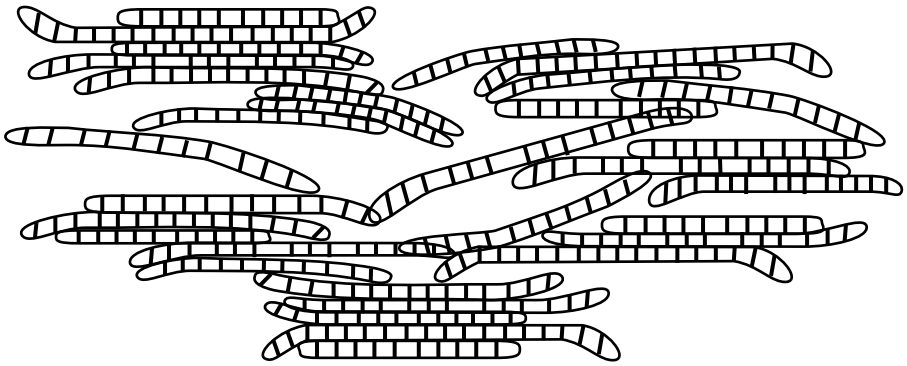

Figure I-48. Fringe fibrillar model of the fiber structure according to Hearle[144].

A few decades later, Chanzy *et al.* (1990) carried out a detailed microscopy electronic analysis. Parallelly, Fink *et al.* (1990) carried out WAXS and transmission electron microscopy experiments, showing a non-uniformity of the diameter range of the elementary fibrils depending on the cellulose source[136, 143, 144].

1.4.6 Cellulose reactivity

The hydroxyl groups OH (2), OH (3), and OH (6) are the main reactive groups susceptible to be chemically modified (**Figure I-44**). Rowland *et al.* (1994) described cellulose's surface in terms of its local reactivity by developing a chemical and microstructural analysis.

Rowland defined an availability ratio as OH (2): OH (3): OH (6), and according to his observations and measurements, the ratio of crystalline microfibrillar cellulose is 1:0:0.5. The OH (3) groups are unreactive due to strong intramolecular hydrogen bonds with O (5). For amorphous cellulose, the ratio founded was 1:1:1. Other factors that can enhance cellulose substrates' reactivity are swelling, solvent exchange, and degradation, among others[145, 146].

The swelling in water or other polar liquids opens the interfibrillar interstices. The solvent penetrates into the less ordered surfaces and interlinking regions of the fibrillar elements between the elementary crystallites[136]. The solvent exchange allows the introduction of medias that are inert in subsequent reactions, thus maintaining the cellulose molecules in their reactive water-swollen state. Some inorganic acids (o-phosphoric, sulfonic or hydrochloric acid), salts solutions (sodium chloride or calcium chloride), and strong alkaline solutions (tetramethylammonium or ethyltrimethylammonium hydroxide) can also penetrate the fiber through capillaries and pores by opening the fibrillar interstices, and entering the interlinking regions between the crystallites, forcing them to open[136, 147].

1.4.7 Nanocellulose

Nanocellulose generally refers to cellulosic materials having dimensions in the nanometer range. In the field of nanotechnology, two general types of nanocellulose are recognized:

1) Nanofibrillated cellulose (NFC) or microfibrillated cellulose (MFC), generally produced from wood, including both amorphous and crystalline regions, with a typical diameter of 5-60 nm and a length of several micrometers.

2) Cellulose nanocrystal (CNC) or whiskers, generally produced from cotton, which does not contain an amorphous region, with a typical diameter of 2-20 nm and a wide length distribution from 100 to 600 nm.

The pioneers in the isolation of nanocellulose were Turbak and Herrick (1983) by the mechanical process of homogenization. The wood fibers pass through a small nozzle with high-pressure that delaminates fibers' cell walls, liberating the nanofibrils. Nevertheless, due to the high energy requirement, pretreatments have become a useful technique to delaminate the fibrils. Some pretreatment examples are the enzymatic or mechanical pretreatments. More recently, Isogai *et al.* (2011) explored the introduction of charged groups like TEMPO as a stabilized radical used as the oxidant 148.

Homogenization is not the only nanocellulose isolation techniques. The following techniques have been explored throughout the cellulose history, among others [149, 150, 151].

- Grinding, where a 5-10 wt% natural fiber suspension passes through a grinder 10 times and the NFC were obtained (Masuko Sangyo Co. Ltd., Japan)
- Ultrasonication is a mechanical method that uses hydrodynamic forces. Ultrasonic waves create strong mechanical stress due to cavitation, causing disaggregation of cellulosic fibers to nanofibers (Cheng *et al*., 2009).
- Cryocrushing consists of freezing the cellulose using liquid nitrogen and further crushed it by applying high shear forces. (Dufresne *et al*., 1997).
- Steam explosion, where a high-pressure steam penetrates into cellulose fibers through diffusion, and pressure suddenly releases, creating shearing forces, hydrolyses the glycosidic and hydrogen bonds. (Mason *et al.*, 1927)

The nanocellulose suspensions are not usually homogenous; they are constituted of various structural components like cellulose nanofibrils and nanofibril bundles[151]. This behavior is attributed to the strong interactions between the nanofibrils that tend to agglomerate them irreversibly during a drying process. This phenomenon is denominated hornification, and it is the main reason why

nanocellulose fibers are founded in the market in aqueous suspensions of 2-5% dry mass.

A recurrent problem of NFC after a drying process is the re-dispersibility, which is limited by the inter-fiber bonds, producing a negative impact on the properties of the dried fibrils. Several strategies have been explored to overcome this problem. For instance, Missoum *et al.* (2012) used sodium chloride to limit fibrils' aggregation during the drying process, allowing a re-dispersion by an Ultra-Turrax disperser[142, 152].

1.4.8 Cellulose modifications

Since the discovery of cellulose as a chemical compound, several modification pathways have been explored. The cellulosic materials elaborated have shown suitable properties like hydrophobic character, water insolubility, among others. These desirable properties have drawn the attention of numerous researching works to add new functionalities to cellulosic materials.

The most common modifications of cellulose are the esterification and etherification of the hydroxy groups of cellulose. Other modifications, less explored, are ionic and radical grafting, oxidation, acetylation, deoxyhalogenation, etc. **Figure I-49** summarizes different cellulose modifications[153].

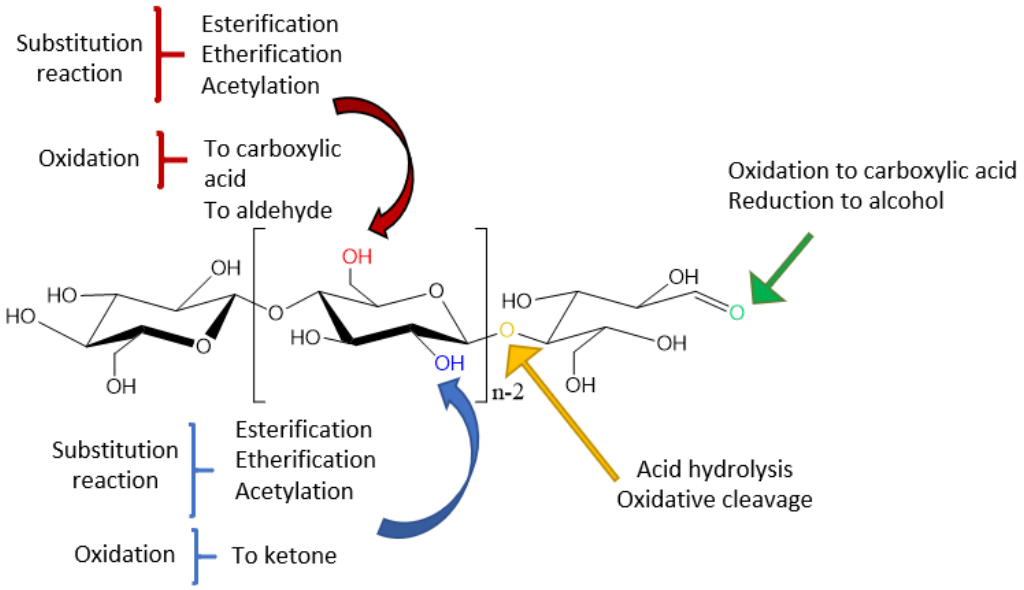

Figure I-49. Chemical modifications of cellulose structure according the OH ring position

1.4.9 Nano Fibrillated Cellulose surface modifications

The promising results of NFC in nanotechnology have generated significant interest in the modification of NFC, either by improving its hydrophilic nature or by increasing the compatibility with diverse matrices. Different reactions have been explored to modify the surface properties, like,

acetylation, grafting with silane coupling agents, coupling with acid and anhydrides, and coupling with isocyanates.

1.4.9.1 Oxidation

The oxidation of cellulose is used to convert the hydroxymethyls into carboxylic groups. The main technique used is by TEMPO or 2,2,6,6-tetramethylpiperidine-1-oxyl in the presence of NaBr and NaOCl. The reaction has a high selectivity for primary alcohol and is easy to implement [154]. The oxidation produces a softening NFC by breaking the intramolecular hydrogen bonds.

Subsequent works performed by Isogai *et al.* (2010) have shown that 4-acetamide-TEMPO and 4-methoxy-TEMPO were more efficient than TEMPO[155]. Also, it was observed by several authors that various degrees of oxidation could be achieved by using specific amounts of oxidizing agent (**Figure I-50**) [148, 156,169].

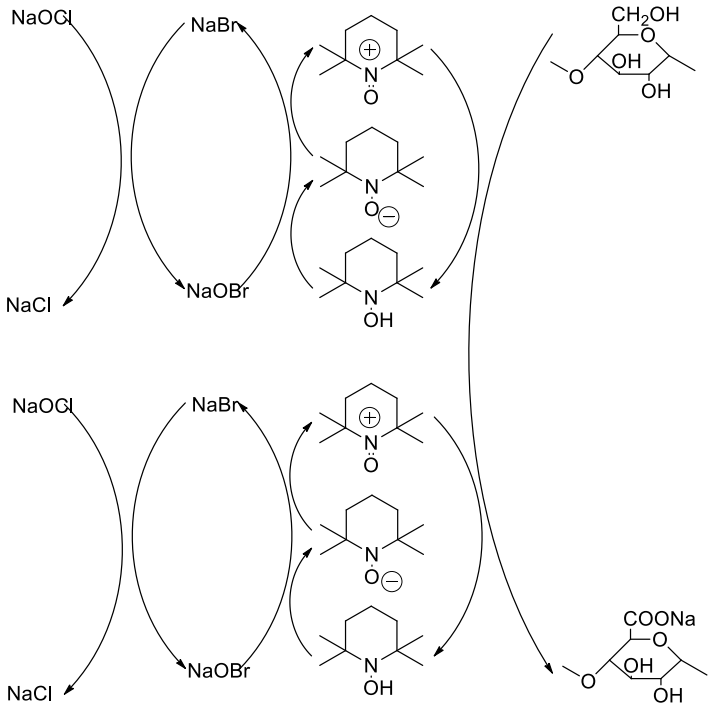

Figure I-50. Regioselective oxidation of C6 primary hydroxyls of cellulose to C6 carboxylate groups by TEMPO/NaBr/NaOCl oxidation in the water at pH 10-11[148].

1.4.9.2 Acetylation

The acetylation of nanocellulose with acetic anhydride is a simple and effective method to introduce hydrophobic moieties onto the nanocellulose surface. This method was discovered by Paul Schützenberger (1895). It consists of adding an excess of acetic anhydride in an inert atmosphere[157] (**Figure I-51**).

The acetylation takes place in two steps. In the first stage, the most accessible hydroxyl groups located on the surface of nanocellulose react, creating new accessible surfaces. In the second one, the reaction is kinetically limited; the acetylation proceeds onto the less accessible hydroxyl groups by diffusion[150].

To enhance the acetylation, Tang *et al.* (2013) showed that the acetylated CNC could be produced directly from wood pulp by coupling the reaction with ultrasonication[158]. Kim *et al.* (2002) reported a partially acetylated cellulose surface preserving the microfibrillar morphology[159,160].

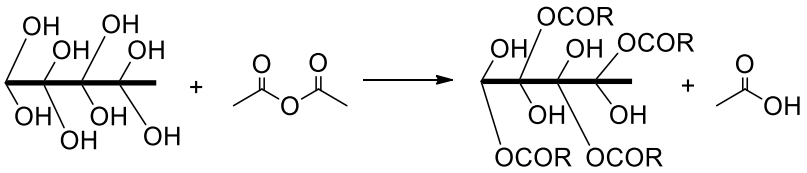

Figure I-51. Acetylation reaction of nanocellulose with acetic anhydride[160].

1.4.9.3 Esterification of nanocellulose with carboxylic acid

This technique consists of attaching long-chain hydrocarbons onto the surface of the nanocellulose to give them a hydrophobic character. The esterification with chains of less than four carbons could be easily produced using acid anhydrides or sulfuric acid. For esterification with longer chains, other methods are required.

Herrick *et al.* (1983) reached acetylated NFC by mixing acetic acid and acetic anhydride with sulfuric acid [161]. McCormick *et al.* (1987) used *N,N*-dimethylacetamide (DMAc), and lithium chloride (LiCl) to produce esterification with long chains[162]. Different authors have largely explored the system LiCl/DMAc, but the use of lithium chloride and its recycling are undesirable for processing industries[163, 164].

The cellulose esterification has also been explored with acid chlorides in DMF by using sulfonic acids[165, 166]. Another technique explored by Jarunda *et al.* (2000) using saturated and unsaturated organic acid in Py/TsCl[167]. A few years later, Vaca-Garcia *et al.* (2006) incorporated fatty acids and fatty acid salts to proceed with acetylation in an emulsion at 195°C [168].

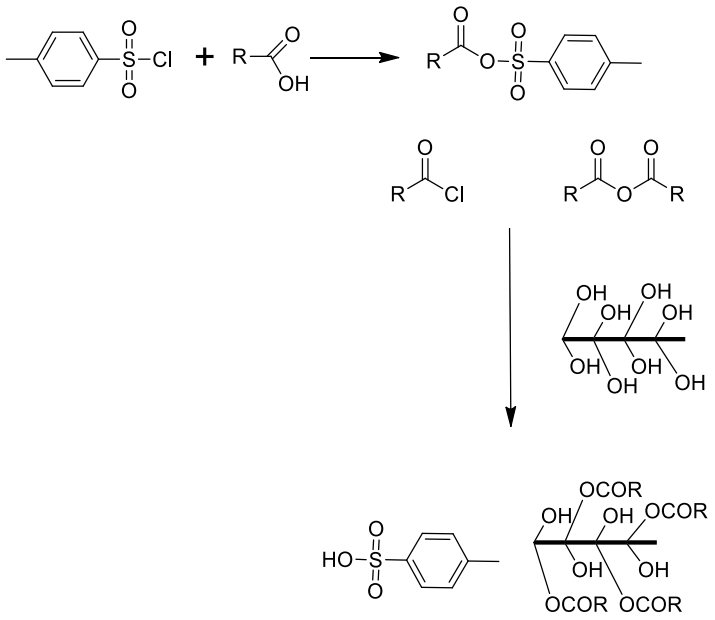

Figure I-52. Esterification of nanocellulose with carboxylic acids[160].

1.4.9.4 Amidation

Amidation in cellulose surface is usually realized by coupling after a pre-oxidized reaction. Habibi *et al.* (2014) have displayed various amine derivatives such as 4-amino-TEMPO, benzylamine, hexylamine, dodecyl amine via a carbodiimidediated amidation. *N*-hydroxysuccinimide (NHS) is often added to prevent unstable rearrangement intermediate o-acylisourea[169].

1.4.9.5 Urethanization

Urethanization or carbonylation takes place when an isocyanate reacts with a hydroxyl group of the nanocellulose surface. Siqueira *et al.* (2010) have reported NFC hydrophobic modification by adding an excess of *n*-octadecyl isocyanate in toluene at temperatures over 100°C with an efficiency around 48%[149, 170].

Lately, Weder *et al.* (2014) presented an isocyanate coupling carried out by reacting nanocellulose with 2-(6-isocyanatohexylaminocarbonylamino)-6-methyl in DMF, using dibutyltin dilaurate as a catalyst[171].

Incorporating nanocellulose with isocyanates into polyurethane matrix has been reported, promoting the physical association with hard segments, and so enhancing the stiffness and the dimensional stability[169, 172].

1.4.9.6 Sulfonation

The sulfonation helps to nano fibrillate the cellulose pulp due to the addition of anionic charge, generating stable dispersion with fibers of diameters that oscillates between 10-60 nm. The cellulose pulp is reacted with sodium periodate ($NaIO_4$) to oxidize the hydroxyl groups. The generating 2,3-dialdehyde cellulose is treated with sodium metabisulfite ($Na_2S_2O_5$). Liimatainen *et al.* (2013) remarked that the concentration of acid groups obtained in sulfonated nanocellulose is higher than that obtained in the sulfonated cellulose pulps, because the hydroxyl groups of nanocellulose are more exposed for peroxide oxidation cleavage and sulfonation than those of cellulose pulp[149, 173] (**Figure I-53**).

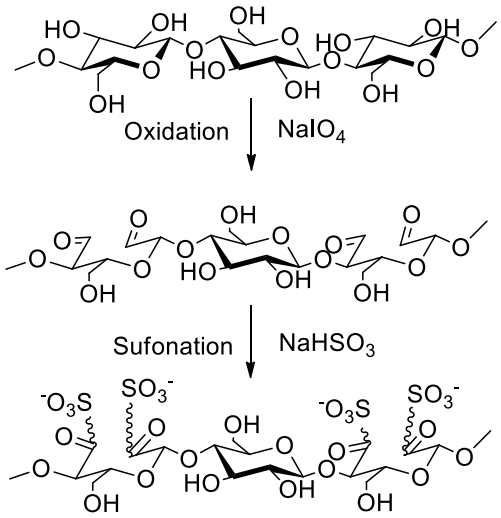

Figure I-53. Regioselective peroxide oxidation and sulfonation of cellulose.

1.4.9.7 Silylation

Silylation, known as silane grafting, is an efficient way to modify nanocellulose surfaces. Chanzy *et al.* (2002) introduced chlorosilane reagents such as isopropyldimethylchlorosilane (IPDMSiCl), *n*-butyldimethylchlorosilane (BDMSiCl) onto the surface of cellulose nanocrystals to confer them a hydrophobic character[174]. Their methodology consists of using cellulose microfibrils in an aqueous suspension. The microfibrils were solvent exchanged to acetone and then flocculated in dry toluene. Chlorosilanes are added in quantity required for the derivation, and imidazole is used for catching the HCl liberated by silanes in equimolar quantity. The reaction has a duration of 16h at room temperature. Finally, the samples are washed with methanol and THF to dissolve the imidazolium chloride formed and to remove the physisorbed disilyl ether.

The samples presented a degree of substitution (DS), i.e., the number of substituent groups attached per hydroxyl unit, that oscillates between 0.2 to 0.6. The integrity of nanocellulose was maintained,

and nanocellulose was easily dispersed in various organic solvents of low polarity such as toluene or THF. Stronger silylation conditions were also explored, and the destruction of nanocellulose was observed, which allowed establishing a limit to derivatization. Figure I-54 describes three levels of surface silylation of cellulose whiskers, remarked by Chanzy *et al.* (2002). **Figure I-54a** relates to a very low DS with a few silyl groups randomly distributed. **Figure I-54b** describes a sample with a high DS between 0.4 to 0.6 per hydroxyl unit depending on the silane used, the number of silyl group at this point is enough to confer the fibrils a hydrophobic character. **Figure I-54c** displays a situation when the DS is equal to 1 or superior, the chains become solubilized, losing the integrity of whiskers.

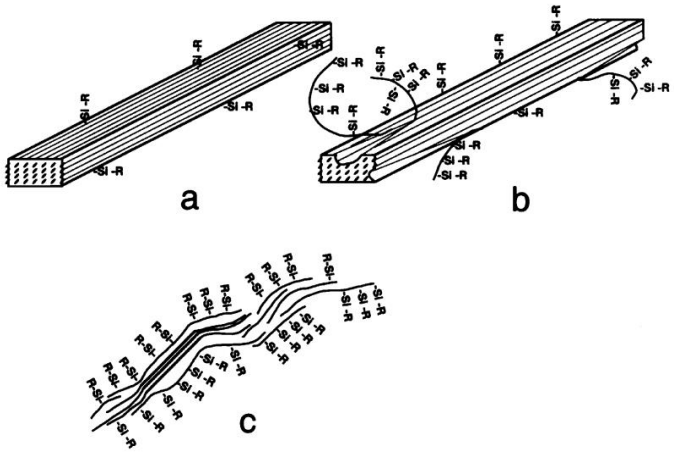

Figure I-54. Models of silylated surface cellulose whiskers. a) onset of surface silylation, b) whisker silylated with a low degree of substitution, c) whisker silylated with a high degree of substitution[174].

Parallelly, Belgacem *et al.* (2004) experimented with various silylation reagents such as *γ*-methacryloxypropyltrimethoxysilane (MPS), *γ*-aminopropyltriethoxysilane (APS), *γ*-mercaptopropytrimethoxysilane (MRPS), among others[32, 33, 34 175]. The silanes were pre-hydrolyzed and then added to a cellulose suspension in ethanol/water showing the presence of silanes into the cellulose surface. The promising work of Belgacem and coworkers has drawn attention due to the eco-friendly method used and the easy reaction conditions.

Figure I-55 illustrates the different steps of chemical functionalization:

a. ***hydrolysis:*** The silane alkoxy groups are catalyzed in acid conditions forming the silanol species.
b. ***physisorption:*** the adsorption of silanol groups onto the hydroxyl groups of cellulose surfaces.
c. ***condensation:*** the chemical sorption of **Si-O**-Cellulose takes place[176,177]. Nonetheless, a self-condensation Si-O-Si cannot be dismissed[178].

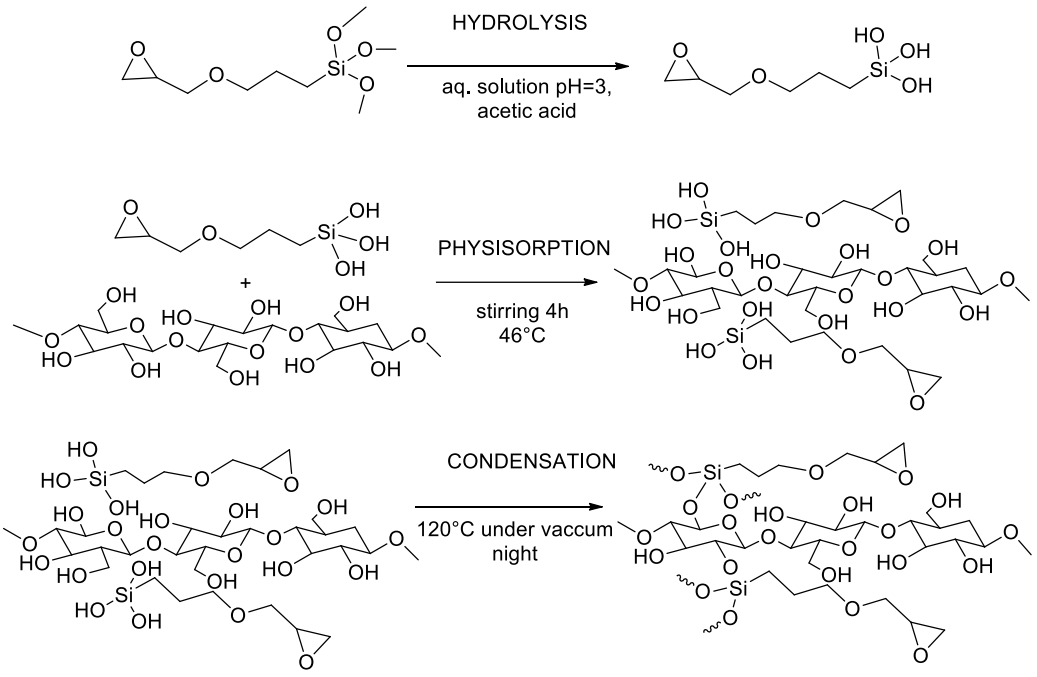

Figure I-55. Silane grafting steps onto nanocellulose surface.

The tri-alkoxysilanes employed by Belgacem *et al.* (2002) have been explored before to modify silica surfaces, and to improve adhesion with surfaces for many purposes like alumina surface modification[179], silica gel polymerization[180] , or glass fiber surface modification [181]. Interestingly, in glass fiber composites, the surface modification enhances not only the adhesion between reinforcing fillers and matrix but also the water resistance of composite[34]. This observation has caught the attention of Drzal *et al.* (2008) to replicate the adhesion improvement of natural fibers[27].

Despite the numerous works about silane coupling agents in cellulose, only a few of them provides a clear explanation of the grafting morphology onto the surface, like Salon *et al.* (2007) and Griesser *et al.* (2018). On the other hand, the large list of experiments carried out on silica gel exposes the construction of a tridimensional covalent network onto the silica surface, supporting silica networks' results onto fibril surfaces[182, 183]. These promising results have evidenced the necessity of deep knowledge of silane morphology, which may have an important role in the interphase of a biocomposite.

The eco-friendly strategy of cellulose silylation triggered by Belgacem *et al.* (2002) allows incorporating a large list of silane coupling agents that may provide diverse functional groups to the cellulose surface, like amine or epoxy function, desirable for epoxy resins composites to enhance the properties of bio-composites.

1.5. Objectives

Epoxy resins are the object of numerous researches, including the emerging field of vitrimers. The DGEBA-APDS epoxy resin has been considered as a recyclable material with good mechanical properties and a high thermal resistance. The reversible disulfide exchange mechanism has been proved as a [2+1] metathesis mechanism, i.e., it undergoes both an associative and dissociative exchange mechanism. The path of a specific bond exchange and the lack of experiments in the literature to support a genuinely vitrimer behavior question the classification of the DGEBA-APDS system as a vitrimer or not. Due to all these considerable doubts, ***the first objective of this work is to highlight the vitrimer properties of the DGEBA-APDS system, and to display all the characteristics that define it***.

The second objective of this thesis is to study the stress relaxation of this epoxy vitrimer just above its glass transition temperature **and to model its behavior.** The proximity of both transition temperatures (*T*g and *T*v) might imply a particular viscoelastic behavior with a partially restricted exchange reactions which cannot be correctly describe by the Maxwell's model.

The third objective of this work is to verify that a composite of nano fibrillated cellulose (NFC) with the previous matrix continues to have a vitrimer behavior and to model its stress relaxation behavior.

The fourth objective is to establish an environmentally friendly protocol to modify the surface of the nano fibrillated cellulose and to study in details the surface of the functionalized NFC in order to prepare composite with an improved durability.

Bibliography

1 Grand Viwe Reserarch (2016) Epoxy Resin Market Size, Share, and Trends Analysis Report, By Application (Paints & Coatings, Wind Turbine, Composites, Construction, Electrical & Electronics, Adhesives) And Segment Forecast to 2024. Recurperated from https://www.grandviewresearch.com/industry-analysis/epoxy-resins-market [March 2021]

2 Gibson, G. (2017). Epoxy Resins. In *Brydson's Plastics Materials* (pp. 773-797). Butterworth-Heinemann.

3 Ellis, B. (Ed.). (1993). *Chemistry and technology of epoxy resins* (1st ed., pp. 24-26). London: Blackie Academic & Professional.

4 Goodman, S. H. (1999). 6-Epoxy Resins. *Handbook of thermoset plastics*, 193-268.

5 Brydson, J. A. (1999). *Plastics materials*. Elsevier.

6 Tcharkhtchi, A., Nony, F., Khelladi, S., Fitoussi, J., & Farzaneh, S. (2015). Epoxy/amine reactive systems for composites materials and their thermomechanical properties. In *Advances in Composites Manufacturing and Process Design* (pp. 269-296). Woodhead Publishing.

7 Shimbo, M., Ochi, M., & Shigeta, Y. (1981). Shrinkage and internal stress during curing of epoxide resins. *Journal of Applied Polymer Science*, *26*(7), 2265-2277.

8 Ochi, M., Yamashita, K., & Shimbo, M. (1991). The mechanism for occurrence of internal stress during curing epoxide resins. *Journal of Applied Polymer Science*, *43*(11), 2013-2019.

9 RJ, R. J. C., & Throne, J. L. (2002). Rotational Molding Technology, Plastics design Library.

10 Pascault, J. P., Sautereau, H., Verdu, J., & Williams, R. J. (2002). *Thermosetting polymers* (Vol. 64). CRC press.

11 Saiter, J. M., Grenet, J., Dargent, E., Saiter, A., & Delbreilh, L. (2007, November). Glass transition temperature and value of the relaxation time at *T*g in vitreous polymers. In *Macromolecular symposia* (Vol. 258, No. 1, pp. 152-161). Weinheim: WILEY-VCH Verlag.

12 Moynihan, C. T. (1993). Correlation between the width of the glass transition region and the temperature dependence of the viscosity of high-*T*g glasses. *Journal of the American Ceramic Society*, *76*(5), 1081-1087.

13 Gupta, V. B., Drzal, L. T., Lee, C. C., & Rich, M. J. (1985). The temperature-dependence of some mechanical properties of a cured epoxy resin system. *Polymer Engineering & Science*, *25*(13), 812-818.

14 Calventus, Y., Montserrat, S., & Hutchinson, J. M. (2001). Enthalpy relaxation of non-stoichiometric epoxy-amine resins. *Polymer*, *42*(16), 7081-7093.

15 Vallo, C. I., Frontini, P. M., & Williams, R. J. J. (1991). The glass transition temperature of nonstoichiometric epoxy–amine networks. *Journal of Polymer Science Part B: Polymer Physics*, *29*(12), 1503-1511.

16 Morgan, R. J., Kong, F. M., & Walkup, C. M. (1984). Structure-property relations of polyethertriamine-cured bisphenol-A-diglycidyl ether epoxies. *Polymer*, *25*(3), 375-386.

17 Mathijsen, D. (2016). Leading the way in thermoplastic composites. *Reinforced Plastics*, *60*(6), 405-407.

18 GAO. Aviation safety, Status of FAA's Actions to Oversee the Safety of Composite Airplanes, 2011.

19 Boeing 787 from the Ground Up. Recuperated from: https://www.boeing.com/commercial/aeromagazine/articles/qtr_4_06/AERO_Q406_article4.pdf [March 2021].

20 https://www.airbus.com/newsroom/news/en/2017/08/composites--airbus-continues-to-shape-the-future.html

21 Seymour, R. B. (1978, January). Nonreinforcing Fillers for Plastics. In *ABSTRACTS OF PAPERS OF THE AMERICAN CHEMICAL SOCIETY* (Vol. 175, No. MAR, pp. 6-6). 1155 16TH ST, NW, WASHINGTON, DC 20036: AMER CHEMICAL SOC.

22 Favier, V., Chanzy, H., & Cavaillé, J. (1995). Polymer nanocomposites reinforced by cellulose whiskers. *Macromolecules*, *28*(18), 6365-6367.

23 Matos Ruiz, M., Cavaille, J. Y., Dufresne, A., Gerard, J. F., & Graillat, C. (2000). Processing and characterization of new thermoset nanocomposites based on cellulose whiskers. *Composite Interfaces*, *7*(2), 117-131.

24 Šturcová, A., Davies, G. R., & Eichhorn, S. J. (2005). Elastic modulus and stress-transfer properties of tunicate cellulose whiskers. *Biomacromolecules*, *6*(2), 1055-1061.

25 Ansari, F., Galland, S., Johansson, M., Plummer, C. J., & Berglund, L. A. (2014). Cellulose nanofiber network for moisture stable, strong and ductile biocomposites and increased epoxy curing rate. *Composites Part A: Applied Science and Manufacturing*, *63*, 35-44.

26 Tang, L., & Weder, C. (2010). Cellulose whisker/epoxy resin nanocomposites. *ACS applied materials & interfaces*, *2*(4), 1073-1080.

27 Lu, J., Askeland, P., & Drzal, L. T. (2008). Surface modification of microfibrillated cellulose for epoxy composite applications. *Polymer*, *49*(5), 1285-1296.

28 Xiao, X., Lu, S., Qi, B., Zeng, C., Yuan, Z., & Yu, J. (2014). Enhancing the thermal and mechanical properties of epoxy resins by addition of a hyperbranched aromatic polyamide grown on microcrystalline cellulose fibers. *RSC Advances*, *4*(29), 14928-14935.

29 Peng, S. X., Shrestha, S., Yoo, Y., & Youngblood, J. P. (2017). Enhanced dispersion and properties of a two-component epoxy nanocomposite using surface modified cellulose nanocrystals. *Polymer*, *112*, 359-368.

30 Zhao, J., Li, Q., Zhang, X., Xiao, M., Zhang, W., & Lu, C. (2017). Grafting of polyethylenimine onto cellulose nanofibers for interfacial enhancement in their epoxy nanocomposites. *Carbohydrate polymers*, *157*, 1419-1425.

31 Lu, T., Jiang, M., Jiang, Z., Hui, D., Wang, Z., & Zhou, Z. (2013). Effect of surface modification of bamboo cellulose fibers on mechanical properties of cellulose/epoxy composites. *Composites Part B: Engineering*, *51*, 28-34.

32 Gousse, 7. C., Chanzy, H., Cerrada, M. L., & Fleury, E. (2004). Surface silylation of cellulose microfibrils: preparation and rheological properties. *Polymer*, *45*(5), 1569-1575.

33 Khanjanzadeh, H., Behrooz, R., Bahramifar, N., Gindl-Altmutter, W., Bacher, M., Edler, M., & Griesser, T. (2018). Surface chemical functionalization of cellulose nanocrystals by 3-aminopropyltriethoxysilane. *International journal of biological macromolecules*, *106*, 1288-1296.

34 Salon, M. C. B., Abdelmouleh, M., Boufi, S., Belgacem, M. N., & Gandini, A. (2005). Silane adsorption onto cellulose fibers: Hydrolysis and condensation reactions. *Journal of colloid and interface science*, *289*(1), 249-261.

35 White, S. R., Sottos, N. R., Geubelle, P. H., Moore, J. S., Kessler, M. R., Sriram, S. R., ... & Viswanathan, S. (2001). Autonomic healing of polymer composites. *Nature*, *409*(6822), 794-797.

36 Brown, E. N., Sottos, N. R., & White, S. R. (2002). Fracture testing of a self-healing polymer composite. *Experimental mechanics*, *42*(4), 372-379.

37 Kumar, R., Hynes, N. R. J., Manju, R., Senthamaraikannan, P., Saravanakumar, S. S., Khan, A., ... & Verpoort, F. (2020). Self-healing fiber-reinforced epoxy composites. In *Self-Healing Composite Materials* (pp. 393-404). Woodhead Publishing.

38 Caruso, M. M., Delafuente, D. A., Ho, V., Sottos, N. R., Moore, J. S., & White, S. R. (2007). Solvent-promoted self-healing epoxy materials. *Macromolecules*, *40*(25), 8830-8832.

39 Caruso, M. M., Blaiszik, B. J., White, S. R., Sottos, N. R., & Moore, J. S. (2008). Full recovery of fracture toughness using a nontoxic solvent-based self-healing system. *Advanced Functional Materials*, *18*(13), 1898-1904.

40 Hia, I. L., Chan, E. S., Chai, S. P., & Pasbakhsh, P. (2018). A novel repeated self-healing epoxy composite with alginate multicore microcapsules. *Journal of Materials Chemistry A*, *6*(18), 8470-8478.

41 Yuan, Y. C., Rong, M. Z., Zhang, M. Q., Yang, G. C., & Zhao, J. Q. (2010). Healing of fatigue crack in epoxy materials with epoxy/mercaptan system via manual infiltration. *Express Polymer Letters*, *4*(10).

42 Xiao, D. S., Yuan, Y. C., Rong, M. Z., & Zhang, M. Q. (2009). Self-healing epoxy based on cationic chain polymerization. *Polymer*, *50*(13), 2967-2975.

43 Chen, X., Dam, M. A., Ono, K., Mal, A., Shen, H., Nutt, S. R., ... & Wudl, F. (2002). A thermally re-mendable cross-linked polymeric material. *Science*, *295*(5560), 1698-1702.

44 Min, Y., Huang, S., Wang, Y., Zhang, Z., Du, B., Zhang, X., & Fan, Z. (2015). Sonochemical transformation of epoxy–amine thermoset into soluble and reusable polymers. *Macromolecules*, *48*(2), 316-322.

45 Liu, Y. L., & Chuo, T. W. (2013). Self-healing polymers based on thermally reversible Diels–Alder chemistry. *Polymer Chemistry*, *4*(7), 2194-2205.

46 Chen, X., Dam, M. A., Ono, K., Mal, A., Shen, H., Nutt, S. R., ... & Wudl, F. (2002). A thermally re-mendable cross-linked polymeric material. *Science*, *295*(5560), 1698-1702.

47 Kuang, X., Liu, G., Dong, X., Liu, X., Xu, J., & Wang, D. (2015). Facile fabrication of fast recyclable and multiple self-healing epoxy materials through diels-alder adduct cross-linker. *Journal of Polymer Science Part A: Polymer Chemistry*, *53*(18), 2094-2103.

48 Turkenburg, D. H., & Fischer, H. R. (2015). Diels-Alder based, thermo-reversible cross-linked epoxies for use in self-healing composites. *Polymer*, *79*, 187-194.

49 Farkas, L., Schachter, O., & Vromen, B. H. (1949). On the rate of the acid-catalyzed trans-esterification of butyl alcohol and ethyl acetate. *Journal of the American Chemical Society*, *71*(6), 1991-1994.

50 Otera, J. (1993). Transesterification. *Chemical reviews*, *93*(4), 1449-1470.

51 DUŠEK, K., & MATĚJKA, L. (1984). Transesterification and gelation of polyhydroxy esters formed from diepoxides and dicarboxylic acids.

52 Hoppe, C. E., Galante, M. J., Oyanguren, P. A., & Williams, R. J. (2005). Epoxies Modified by Palmitic Acid: From Hot-Melt Adhesives to Plasticized Networks. *Macromolecular Materials and Engineering*, *290*(5), 456-462.

53 Altuna, F. I., Pettarin, V., & Williams, R. J. (2013). Self-healable polymer networks based on the cross-linking of epoxidised soybean oil by an aqueous citric acid solution. *Green Chemistry*, *15*(12), 3360-3366.

54 Capelot, M., Montarnal, D., Tournilhac, F., & Leibler, L. (2012). Metal-catalyzed transesterification for healing and assembling of thermosets. *Journal of the american chemical society*, *134*(18), 7664-7667.

55 Yang, Y., Pei, Z., Zhang, X., Tao, L., Wei, Y., & Ji, Y. (2014). Carbon nanotube–vitrimer composite for facile and efficient photo-welding of epoxy. *Chemical Science*, *5*(9), 3486-3492.

56 Kolšek, K., Aponte-Santamaría, C., & Gräter, F. (2017). Accessibility explains preferred thiol-disulfide isomerization in a protein domain. *Scientific reports*, *7*(1), 1-10.

57 Tesoro, G. C., & Sastri, V. (1990). Reversible crosslinking in epoxy resins. I. Feasibility studies. *Journal of applied polymer science*, *39*(7), 1425-1437.

58 Sastri, V. R., & Tesoro, G. C. (1990). Reversible crosslinking in epoxy resins. II. New approaches. *Journal of applied polymer science*, *39*(7), 1439-1457.

59 Engelberg, P. I., & Tesoro, G. C. (1990). Mechanical and thermal properties of epoxy resins with reversible crosslinks. *Polymer Engineering & Science*, *30*(5), 303-307.

60 Canadell, J., Goossens, H., & Klumperman, B. (2011). Self-healing materials based on disulfide links. *Macromolecules*, *44*(8), 2536-2541.

61 Pepels, M., Filot, I., Klumperman, B., & Goossens, H. (2013). Self-healing systems based on disulfide–thiol exchange reactions. *Polymer Chemistry*, *4*(18), 4955-4965.

62 An, S. Y., Noh, S. M., Nam, J. H., & Oh, J. K. (2015). Dual Sulfide–Disulfide Crosslinked Networks with Rapid and Room Temperature Self-Healability. *Macromolecular rapid communications*, *36*(13), 1255-1260.

63 Nevejans, S., Ballard, N., Miranda, J. I., Reck, B., & Asua, J. M. (2016). The underlying mechanisms for self-healing of poly (disulfide) s. *Physical Chemistry Chemical Physics*, *18*(39), 27577-27583.

64 Takahashi, A., Ohishi, T., Goseki, R., & Otsuka, H. (2016). Degradable epoxy resins prepared from diepoxide monomer with dynamic covalent disulfide linkage. *Polymer*, *82*, 319-326.

65 Memon, H., & Wei, Y. (2020). Welding and reprocessing of disulfide-containing thermoset epoxy resin exhibiting behavior reminiscent of a thermoplastic. *Journal of Applied Polymer Science*, *137*(47), 49541.

66 de Luzuriaga, A. R., Martin, R., Markaide, N., Rekondo, A., Cabanero, G., Rodriguez, J., & Odriozola, I. (2016). Epoxy resin with exchangeable disulfide crosslinks to obtain reprocessable, repairable and recyclable fiber-reinforced thermoset composites. *Materials Horizons*, *3*(3), 241-247.

67 Kloxin, C. J., Scott, T. F., Adzima, B. J., & Bowman, C. N. (2010). Covalent adaptable networks (CANs): a unique paradigm in cross-linked polymers. *Macromolecules*, *43*(6), 2643-2653.

68 Bowman, C. N., & Kloxin, C. J. (2012). Covalent adaptable networks: reversible bond structures incorporated in polymer networks. *Angewandte Chemie International Edition*, *51*(18), 4272-4274.

69 Kloxin, C. J., & Bowman, C. N. (2013). Covalent adaptable networks: smart, reconfigurable and responsive network systems. *Chemical Society Reviews*, *42*(17), 7161-7173.

70 Denissen, W., Winne, J. M., & Du Prez, F. E. (2016). Vitrimers: permanent organic networks with glass-like fluidity. *Chemical science*, *7*(1), 30-38.

71 Chang, J. Y., Do, S. K., & Han, M. J. (2001). A sol–gel reaction of vinyl polymers based on thermally reversible urea linkages. *Polymer*, *42*(18), 7589-7594.

72 Iyer, N. P., Gnanarajan, T. P., & Radhakrishnan, G. (2002). Mechanical and thermal properties of networks prepared from reactive poly (urethane-imide) s and blocked polyurethane prepolymer. *Macromolecular Chemistry and Physics*, *203*(4), 712-717.

73 Zuo, Y., Gou, Z., Zhang, C., & Feng, S. (2016). Polysiloxane-Based Autonomic Self-Healing Elastomers Obtained through Dynamic Boronic Ester Bonds Prepared by Thiol–Ene "Click" Chemistry. *Macromolecular rapid communications*, *37*(13), 1052-1059.

74 Dodge, L., Chen, Y., & Brook, M. A. (2014). Silicone boronates reversibly crosslink using Lewis acid–Lewis base amine complexes. *Chemistry–A European Journal*, *20*(30), 9349-9356.

75 Montarnal, D., Capelot, M., Tournilhac, F., & Leibler, L. (2011). Silica-like malleable materials from permanent organic networks. *Science*, *334*(6058), 965-968.

76 Denissen, W., Rivero, G., Nicolaÿ, R., Leibler, L., Winne, J. M., & Du Prez, F. E. (2015). Vinylogous urethane vitrimers. *Advanced Functional Materials*, *25*(16), 2451-2457.

77 Zheng, P., & McCarthy, T. J. (2012). A surprise from 1954: siloxane equilibration is a simple, robust, and obvious polymer self-healing mechanism. *Journal of the American Chemical Society*, *134*(4), 2024-2027.

78 Dyre, J. C. (2006). Colloquium: The glass transition and elastic models of glass-forming liquids. *Reviews of modern physics*, *78*(3), 953.

79 Angell, C. A. (1985). Strong and fragile liquids. *Relaxations in complex systems*, *3*(11).

80 Van Zee, N. J., & Nicolaÿ, R. (2020). Vitrimers: Permanently crosslinked polymers with dynamic network topology. *Progress in Polymer Science*, 101233.

81 Elek, Adalbert, and Robert A. Harte. "The microestimation of acetyl groups." *Industrial & Engineering Chemistry Analytical Edition* 8.4 (1936): 267-269.

82 Capelot, M., Unterlass, M. M., Tournilhac, F., & Leibler, L. (2012). Catalytic control of the vitrimer glass transition. *ACS Macro Letters*, *1*(7), 789-792.

83 Denissen, W., Droesbeke, M., Nicolaÿ, R., Leibler, L., Winne, J. M., & Du Prez, F. E. (2017). Chemical control of the viscoelastic properties of vinylogous urethane vitrimers. *Nature communications*, *8*(1), 1-7.

84 Stukenbroeker, T., Wang, W., Winne, J. M., Du Prez, F. E., Nicolaÿ, R., & Leibler, L. (2017). Polydimethylsiloxane quenchable vitrimers. *Polymer Chemistry*, *8*(43), 6590-6593.

85 Mudraboyina, B. P., Obadia, M. M., Allaoua, I., Sood, R., Serghei, A., & Drockenmuller, E. (2014). 1, 2, 3-Triazolium-based poly (ionic liquid) s with enhanced ion conducting properties obtained through a click chemistry polyaddition strategy. *Chemistry of Materials*, *26*(4), 1720-1726.

86 Obadia, M. M., Mudraboyina, B. P., Serghei, A., Montarnal, D., & Drockenmuller, E. (2015). Reprocessing and recycling of highly cross-linked ion-conducting networks through transalkylation exchanges of C–N bonds. *Journal of the American Chemical Society*, *137*(18), 6078-6083.

87 Obadia, M. M., Jourdain, A., Cassagnau, P., Montarnal, D., & Drockenmuller, E. (2017). Tuning the Viscosity Profile of Ionic Vitrimers Incorporating 1, 2, 3-Triazolium Cross-Links. *Advanced Functional Materials*, *27*(45), 1703258.

88 Zhang, L., & Rowan, S. J. (2017). Effect of Sterics and Degree of Cross-Linking on the Mechanical Properties of Dynamic Poly (alkylurea–urethane) Networks. *Macromolecules*, *50*(13), 5051-5060.

89 Chakma, P., Morley, C. N., Sparks, J. L., & Konkolewicz, D. (2020). Exploring How Vitrimer-like Properties Can Be Achieved from Dissociative Exchange in Anilinium Salts. *Macromolecules*, *53*(4), 1233-1244.

90 Lu, Y. X., & Guan, Z. (2012). Olefin metathesis for effective polymer healing via dynamic exchange of strong carbon–carbon double bonds. *Journal of the American Chemical Society*, *134*(34), 14226-14231.

91 Lu, Y. X., Tournilhac, F., Leibler, L., & Guan, Z. (2012). Making insoluble polymer networks malleable via olefin metathesis. *Journal of the American Chemical Society*, *134*(20), 8424-8427.

92 Röttger, M., Domenech, T., van der Weegen, R., Breuillac, A., Nicolaÿ, R., & Leibler, L. (2017). High-performance vitrimers from commodity thermoplastics through dioxaborolane metathesis. *Science*, *356*(6333), 62-65.

93 Breuillac, A., Kassalias, A., & Nicolaÿ, R. (2019). Polybutadiene Vitrimers Based on Dioxaborolane Chemistry and Dual Networks with Static and Dynamic Cross-links. *Macromolecules*, *52*(18), 7102-7113.

94 Caffy, F., & Nicolaÿ, R. (2019). Transformation of polyethylene into a vitrimer by nitroxide radical coupling of a bis-dioxaborolane. *Polymer Chemistry*, *10*(23), 3107-3115.

95 Ricarte, R. G., Tournilhac, F., Cloître, M., & Leibler, L. (2020). Linear viscoelasticity and flow of self-assembled vitrimers: the case of a polyethylene/dioxaborolane system. *Macromolecules*, *53*(5), 1852-1866.

96 Tretbar, C. A., Neal, J. A., & Guan, Z. (2019). Direct Silyl Ether Metathesis for Vitrimers with Exceptional Thermal Stability. *Journal of the American Chemical Society*, *141*(42), 16595-16599.

97 Wu, X., Yang, X., Yu, R., Zhao, X. J., Zhang, Y., & Huang, W. (2018). A facile access to stiff epoxy vitrimers with excellent mechanical properties via siloxane equilibration. *Journal of Materials Chemistry A*, *6*(22), 10184-10188.

98 Rekondo, A., Martin, R., de Luzuriaga, A. R., Cabañero, G., Grande, H. J., & Odriozola, I. (2014). Catalyst-free room-temperature self-healing elastomers based on aromatic disulfide metathesis. *Materials Horizons*, *1*(2), 237-240.

99 Martin, R., Rekondo, A., de Luzuriaga, A. R., Cabañero, G., Grande, H. J., & Odriozola, I. (2014). The processability of a poly (urea-urethane) elastomer reversibly crosslinked with aromatic disulfide bridges. *Journal of Materials Chemistry A*, *2*(16), 5710-5715.

100 Azcune, I., & Odriozola, I. (2016). Aromatic disulfide crosslinks in polymer systems: Self-healing, reprocessability, recyclability and more. *European Polymer Journal*, *84*, 147-160.

101 Matxain, J. M., Asua, J. M., & Ruipérez, F. (2016). Design of new disulfide-based organic compounds for the improvement of self-healing materials. *Physical Chemistry Chemical Physics*, *18*(3), 1758-1770.

102 de Luzuriaga, A. R., Matxain, J. M., Ruipérez, F., Martin, R., Asua, J. M., Cabañero, G., & Odriozola, I. (2016). Transient mechanochromism in epoxy vitrimer composites containing aromatic disulfide crosslinks. *Journal of Materials Chemistry C*, *4*(26), 6220-6223.

103 Huang, Z., Wang, Y., Zhu, J., Yu, J., & Hu, Z. (2018). Surface engineering of nanosilica for vitrimer composites. *Composites Science and Technology*, *154*, 18-27.

104 Taynton, P., Yu, K., Shoemaker, R. K., Jin, Y., Qi, H. J., & Zhang, W. (2014). Heat-or Water-Driven Malleability in a Highly Recyclable Covalent Network Polymer. *Advanced materials*, *26*(23), 3938-3942.

105 Ciaccia, M., Cacciapaglia, R., Mencarelli, P., Mandolini, L., & Di Stefano, S. (2013). Fast transimination in organic solvents in the absence of proton and metal catalysts. A key to imine metathesis catalyzed by primary amines under mild conditions. *Chemical Science*, *4*(5), 2253-2261.

106 Zheng, H., Liu, Q., Lei, X., Chen, Y., Zhang, B., & Zhang, Q. (2018). A conjugation polyimine vitrimer: Fabrication and performance. *Journal of Polymer Science Part A: Polymer Chemistry*, *56*(22), 2531-2538.

107 Feng, Z., Yu, B., Hu, J., Zuo, H., Li, J., Sun, H., ... & Zhang, L. (2019). Multifunctional Vitrimer-Like Polydimethylsiloxane (PDMS): Recyclable, Self-Healable, and Water-Driven Malleable Covalent Networks Based on Dynamic Imine Bond. *Industrial & Engineering Chemistry Research*, *58*(3), 1212-1221.

108 Kuang, X., Liu, G., Dong, X., & Wang, D. (2017). Correlation between stress relaxation dynamics and thermochemistry for covalent adaptive networks polymers. *Materials Chemistry Frontiers*, *1*(1), 111-118.

109 Winne, J. M., Leibler, L., & Du Prez, F. E. (2019). Dynamic covalent chemistry in polymer networks: a mechanistic perspective. *Polymer Chemistry*, *10*(45), 6091-6108.

110 Brutman, J. P., Fortman, D. J., De Hoe, G. X., Dichtel, W. R., & Hillmyer, M. A. (2019). Mechanistic study of stress relaxation in urethane-containing polymer networks. *The Journal of Physical Chemistry B*, *123*(6), 1432-1441.

111 Hammer, L., Van Zee, N. J., & Nicolaÿ, R. (2021). Dually Crosslinked Polymer Networks Incorporating Dynamic Covalent Bonds. *Polymers*, *13*(3), 396.

112 Morrison, F. A. (2001). *Understanding rheology*. Oxford University Press, USA.

113 Manero-Brito, O. (2014). Lecture 1: Viscoelasticidad lineal [document]. Retrieved from National Autonomus University of Mexico.

114 Bird, R. B., Armstrong, R. C., & Hassager, O. (1987). Dynamics of polymeric liquids. Vol. 1: Fluid mechanics.

115 Dannhauser, W., Child Jr, W. C., & Ferry, J. D. (1958). Dynamic mechanical properties of poly-n-octyl methacrylate. *Journal of Colloid Science*, *13*(2), 103-113.

116 Smallenburg, F., Leibler, L., & Sciortino, F. (2013). Patchy particle model for vitrimers. *Physical review letters*, *111*(18), 188002.

117 Yu, K., Taynton, P., Zhang, W., Dunn, M. L., & Qi, H. J. (2014). Influence of stoichiometry on the glass transition and bond exchange reactions in epoxy thermoset polymers. *Rsc Advances*, *4*(89), 48682-48690.

118 Yu, K., Ge, Q., & Qi, H. J. (2014). Reduced time as a unified parameter determining fixity and free recovery of shape memory polymers. *Nature communications*, *5*(1), 1-9.

119 Shi, X., Soule, D., Mao, Y., Yakacki, C., Lu, H., & Yu, K. (2020). A multiscale chemomechanics theory for the solvent–Assisted recycling of covalent adaptable network polymers. *Journal of the Mechanics and Physics of Solids*, *138*, 103918.

120 Zhang, B., Yuan, C., Zhang, W., Dunn, M. L., Qi, H. J., Liu, Z., ... & Ge, Q. (2019). Recycling of vitrimer blends with tunable thermomechanical properties. *RSC advances*, *9*(10), 5431-5437.

121 Snijkers, F., Pasquino, R., & Maffezzoli, A. (2017). Curing and viscoelasticity of vitrimers. *Soft Matter*, *13*(1), 258-268.

122 Luo, C., Shi, X., Lei, Z., Zhu, C., Zhang, W., & Yu, K. (2018). Effects of bond exchange reactions and relaxation of polymer chains on the thermomechanical behaviors of covalent adaptable network polymers. *Polymer*, *153*, 43-51.

123 Luo, C., Lei, Z., Mao, Y., Shi, X., Zhang, W., & Yu, K. (2018). Chemomechanics in the moisture-induced malleability of polyimine-based covalent adaptable networks. *Macromolecules*, *51*(23), 9825-9838.

124 Kim, D. O., Keum, S. W., Lee, J. H., Lee, J. H., & Nam, J. D. (2006). Thermally-expandable elastomer molding process for thermoset composite materials. *Composites Part A: Applied Science and Manufacturing*, *37*(11), 2121-2127.

125 Lee, A., & McKenna, G. B. (1990). Viscoelastic response of epoxy glasses subjected to different thermal treatments. *Polymer Engineering & Science*, *30*(7), 431-435.

126 Lee, A., & Lichtenhan, J. D. (1999). Thermal and viscoelastic property of epoxy–clay and hybrid inorganic–organic epoxy nanocomposites. *Journal of Applied Polymer Science*, *73*(10), 1993-2001.

127 Li, L., Chen, X., Jin, K., & Torkelson, J. M. (2018). Vitrimers designed both to strongly suppress creep and to recover original cross-link density after reprocessing: quantitative theory and experiments. *Macromolecules*, *51*(15), 5537-5546.

128 Jin, K., Li, L., & Torkelson, J. M. (2016). Recyclable Crosslinked Polymer Networks via One-Step Controlled Radical Polymerization. *Advanced Materials*, *28*(31), 6746-6750.

129 Meng, F., Pritchard, R. H., & Terentjev, E. M. (2016). Stress relaxation, dynamics, and plasticity of transient polymer networks. *Macromolecules*, *49*(7), 2843-2852.

130 Li, L., Chen, X., & Torkelson, J. M. (2019). Reprocessable polymer networks via thiourethane dynamic chemistry: recovery of cross-link density after recycling and proof-of-principle solvolysis leading to monomer recovery. *Macromolecules*, *52*(21), 8207-8216.

131 Dhinojwala, A., Hooker, J. C., & Torkelson, J. M. (1994). Retardation of rotational reorientation dynamics in polymers near the glass transition: a novel study over eleven decades in time using second-order non-linear optics. *Journal of non-crystalline solids*, *172*, 286-296.

132 Meng, F., Saed, M. O., & Terentjev, E. M. (2019). Elasticity and relaxation in full and partial vitrimer networks. *Macromolecules*, *52*(19), 7423-7429.

133 Jourdain, A., Asbai, R., Anaya, O., Chehimi, M. M., Drockenmuller, E., & Montarnal, D. (2020). Rheological Properties of Covalent Adaptable Networks with 1, 2, 3-Triazolium Cross-Links: The Missing Link between Vitrimers and Dissociative Networks. *Macromolecules*, *53*(6), 1884-1900.

134 Perego, A., & Khabaz, F. (2021). Rheology of Vitrimers: A Hybrid Molecular Dynamics-Monte Carlo Simulation Study. *Bulletin of the American Physical Society*.

135 Klemm, D., Philpp, B., Heinze, T., Heinze, U., & Wagenknecht, W. (1998). *Comprehensive cellulose chemistry. Volume 1: Fundamentals and analytical methods*. Wiley-VCH Verlag GmbH.

136 Wüstenberg, T. (2014). Cellulose and cellulose derivatives in the food industry: fundamentals and applications. John Wiley & Sons.

137 Zugenmaier, P. (2008). Crystalline cellulose and derivatives: characterization and structures. Springer Science & Business Media.

138 Cellulose Marke Size, Share & Industry Analysis, By Derivative Type (Commodity Cellulose Pulp, Cellulose Fibers, Cellulose Ethers, Cellulose Esters, Microcyrstalline Cellulose, Nanocellulose, and Others By End-Use Industry (Textile, Food, Chemical Synthesis, Pharmaceuticals, Construction, Paper & Pulp, Paints & Coating, and Others), and Regional Forecast, 2019-2026. Recuperated from: https://www.fortunebusinessinsights.com/cellulose-market-102062 [March 2021].

139 Cellulose Fiber Market Size, Share & Trends Analysis By Product Type (Natural, Synthetic), By Application (Textile, Hygiene, Industrial), By Regions And Segment Forecast, 2018-2025 Recuperated from: https://www.grandviewresearch.com/industry-analysis/cellulose-fibers-market [March 2021].

140 Zugenmaier, P. (2009). Contribution to the historical development of macromolecular chemistry—exemplified on cellulose. *Cellulose Chemistry & Technology*, *43*(9), 351.

141 Krässig, H., Schurz, J., Steadman, R.G., Schliefer, K. and Albrecht, W. (2004) *Cellulose, in Ullmann's Encyclopedia of Industrial Chemistry,* Wiley-VCH Verlag GmbH, Weinheim.

142 Rosenau, T., Potthast, A., & Hell, J. (Eds.). (2018). *Cellulose Science and Technology: Chemistry, Analysis, and Applications*. John Wiley & Sons.

143 Kroon-Batenburg, L. M. J., Bouma, B., & Kroon, J. (1996). Stability of cellulose structures studied by MD simulations. Could mercerized cellulose II be parallel? *Macromolecules*, *29*(17), 5695-5699.

144 Giraud-Guille, M. M., Chanzy, H., & Vuong, R. (1990). Chitin crystals in arthropod cuticles revealed by diffraction contrast transmission electron microscopy. *Journal of structural biology*, *103*(3), 232-240.

145 Verlhac, C., Dedier, J., & Chanzy, H. (1990). Availability of surface hydroxyl groups in Valonia and bacterial cellulose. *Journal of Polymer Science Part A: Polymer Chemistry*, *28*(5), 1171-1177.

146 Tasker, S., Badyal, J. P. S., Backson, S. C. E., & Richards, R. W. (1994). Hydroxyl accessibility in celluloses. *Polymer*, *35*(22), 4717-4721.

147 Zhang, Y. H. P., Cui, J., Lynd, L. R., & Kuang, L. R. (2006). A transition from cellulose swelling to cellulose dissolution by o-phosphoric acid: evidence from enzymatic hydrolysis and supramolecular structure. *Biomacromolecules*, *7*(2), 644-648.

148 Isogai, A., Saito, T., & Fukuzumi, H. (2011). TEMPO-oxidized cellulose nanofibers. *nanoscale*, *3*(1), 71-85.

149 Kargarzadeh, H., Ahmad, I., Thomas, S., & Dufresne, A. (Eds.). (2017). *Handbook of nanocellulose and cellulose nanocomposites*. Wiley-VCH Verlag GmbH & Company

150 Islam, M. N., & Rahman, F. (2019). Production and modification of nanofibrillated cellulose composites and potential applications. In *Green Composites for Automotive Applications* (pp. 115-141). Woodhead Publishing.

151 Chinga-Carrasco, G. (2011). Cellulose fibres, nanofibrils and microfibrils: the morphological sequence of MFC components from a plant physiology and fibre technology point of view. *Nanoscale research letters*, *6*(1), 417.

152 Missoum, K., Bras, J., & Belgacem, M. N. (2012). Water redispersible dried nanofibrillated cellulose by adding sodium chloride. *Biomacromolecules*, *13*(12), 4118-4125.

153 Isogai, A. (2000). Chemical modification of cellulose. *Wood and cellulosic chemistry*.

154 De Nooy, A. E. J., Besemer, A. C., & Van Bekkum, H. (1994). Highly selective TEMPO mediated oxidation of primary alcohol groups in polysaccharides. *Recueil des Travaux Chimiques des Pays-Bas*, *113*(3), 165-166.

155 Iwamoto, S., Kai, W., Isogai, T., Saito, T., Isogai, A., & Iwata, T. (2010). Comparison study of TEMPO-analogous compounds on oxidation efficiency of wood cellulose for preparation of cellulose nanofibrils. *Polymer Degradation and Stability*, *95*(8), 1394-1398.

156 Habibi, Y., Chanzy, H., & Vignon, M. R. (2006). TEMPO-mediated surface oxidation of cellulose whiskers. *Cellulose*, *13*(6), 679-687.

157 Gilbert, M. (2017). Cellulose Plastics. In *Brydson's Plastics Materials* (pp. 617-630). Butterworth-Heinemann.

158 Tang, L., Huang, B., Lu, Q., Wang, S., Ou, W., Lin, W., & Chen, X. (2013). Ultrasonication-assisted manufacture of cellulose nanocrystals esterified with acetic acid. *Bioresource technology*, *127*, 100-105.

159 Kim, D. Y., Nishiyama, Y., & Kuga, S. (2002). Surface acetylation of bacterial cellulose. *Cellulose*, *9*(3-4), 361-367.

160 Lee, K. Y., & Bismarck, A. (2014). Green Chemical Modifications of Nanocellulose for Use in Composites. In *HANDBOOK OF GREEN MATERIALS: 2 Bionanocomposites: processing, characterization and properties* (pp. 7-21).

161 Herrick, F. W., Casebier, R. L., Hamilton, J. K., & Sandberg, K. R. (1983, January). Microfibrillated cellulose: morphology and accessibility. In *J. Appl. Polym. Sci.: Appl. Polym. Symp.;(United States)* (Vol. 37, No. CONF-8205234-Vol. 2). ITT Rayonier Inc., Shelton, WA.

162 McCormick, C. L., & Callais, P. A. (1987). Derivatization of cellulose in lithium chloride and NN-dimethylacetamide solutions. *Polymer*, *28*(13), 2317-2323.

163 Vaca-Garcia, C., Thiebaud, S., Borredon, M. E., & Gozzelino, G. (1998). Cellulose esterification with fatty acids and acetic anhydride in lithium chloride/N, N-dimethylacetamide medium. *Journal of the American Oil Chemists' Society*, *75*(2), 315-319.

164 Dawsey, T. R., & McCormick, C. L. (1990). The lithium chloride/dimethylacetamide solvent for cellulose: a literature review. *Journal of Macromolecular Science—Reviews in Macromolecular Chemistry and Physics*, *30*(3-4), 405-440.

165 Wang, P., & Tao, B. Y. (1995). Synthesis of cellulose-fatty acid esters for use as biodegradable plastics. *Journal of environmental polymer degradation*, *3*(2), 115-119.

166 Satgé, C., Verneuil, B., Branland, P., Granet, R., Krausz, P., Rozier, J., & Petit, C. (2002). Rapid homogeneous esterification of cellulose induced by microwave irradiation. *Carbohydrate Polymers*, *49*(3), 373-376.

167 Jandura, P., Kokta, B. V., & Riedl, B. (2000). Fibrous long-chain organic acid cellulose esters and their characterization by diffuse reflectance FTIR spectroscopy, solid-state CP/MAS 13C-NMR, and X-ray diffraction. *Journal of Applied Polymer Science*, *78*(7), 1354-1365.

168 Peydecastaing, J., Girardeau, S., Vaca-Garcia, C., & Borredon, M. E. (2006). Long chain cellulose esters with very low DS obtained with non-acidic catalysts. *Cellulose*, *13*(1), 95-103.

169 Habibi, Y. (2014). Key advances in the chemical modification of nanocelluloses. *Chemical Society Reviews*, *43*(5), 1519-1542.

170 Siqueira, G., Bras, J., & Dufresne, A. (2010). New process of chemical grafting of cellulose nanoparticles with a long chain isocyanate. *Langmuir*, *26*(1), 402-411.

171 Biyani, M. V., Foster, E. J., & Weder, C. (2013). Light-healable supramolecular nanocomposites based on modified cellulose nanocrystals. *ACS Macro Letters*, *2*(3), 236-240.

172 Rueda, L., d'Arlas, B. F., Zhou, Q., Berglund, L. A., Corcuera, M. A., Mondragon, I., & Eceiza, A. (2011). Isocyanate-rich cellulose nanocrystals and their selective insertion in elastomeric polyurethane. *Composites science and technology*, *71*(16), 1953-1960.

173 Liimatainen, H., Visanko, M., Sirviö, J., Hormi, O., & Niinimäki, J. (2013). Sulfonated cellulose nanofibrils obtained from wood pulp through regioselective oxidative bisulfite pre-treatment. *Cellulose*, *20*(2), 741-749.

174 Goussé, C., Chanzy, H., Excoffier, G., Soubeyrand, L., & Fleury, E. (2002). Stable suspensions of partially silylated cellulose whiskers dispersed in organic solvents. *Polymer*, *43*(9), 2645-2651.

175 Abdelmouleh, M., Boufi, S., Belgacem, M. N., Duarte, A. P., Salah, A. B., & Gandini, A. (2004). Modification of cellulosic fibres with functionalised silanes: development of surface properties. *International Journal of Adhesion and Adhesives*, *24*(1), 43-54.

176 Singha, A. S., & Rana, A. K. (2013). Effect of Aminopropyltriethoxysilane (APS) treatment on properties of mercerized lignocellulosic grewia optiva fiber. *Journal of Polymers and the Environment*, *21*(1), 141-150.

177 Castellano, M., Gandini, A., Fabbri, P., & Belgacem, M. N. (2004). Modification of cellulose fibres with organosilanes: Under what conditions does coupling occur?. *Journal of Colloid and Interface science*, *273*(2), 505-511.

178 Salon, M. C. B., Gerbaud, G., Abdelmouleh, M., Bruzzese, C., Boufi, S., & Belgacem, M. N. (2007). Studies of interactions between silane coupling agents and cellulose fibers with liquid and solid-state NMR. *Magnetic Resonance in Chemistry*, *45*(6), 473-483.

179 Underhill, P. R., Goring, G., & DuQuesnay, D. L. (2000). The effect of humidity on the curing of 3-glycidoxypropyltrimethoxy silane. *International journal of adhesion and adhesives*, *20*(3), 195-199.

180 Horr, T. J., & Reynolds, G. D. (1997). The reactions of 3-glycidoxypropyltrimethoxysilane in acidic solutions on polymerization and in the presence of silica. *Journal of adhesion science and technology*, *11*(7), 995-1009.

181 Park, S. J., & Jin, J. S. (2001). Effect of silane coupling agent on interphase and performance of glass fibers/unsaturated polyester composites. *Journal of Colloid and Interface Science*, *242*(1), 174-179.

182 Zaper, A. M., Cholli, A., & Koenig, J. L. (1985). Applications of Solid-State Magic Angle NMR Spectroscopy to Fiber Reinforced Composites. In *Molecular Characterization of Composite Interfaces* (pp. 299-312). Springer, Boston, MA.

183 Bayer, E., Albert, K., Reiners, J., Nieder, M., & Müller, D. (1983). Characterization of chemically modified silica gels by 29Si and 13C cross-polarization and magic angle spinning nuclear magnetic resonance. *Journal of Chromatography A*, *264*, 197-213.

Chapter II : Materials and analysis methods

2. Materials and analysis methods

2.1 Raw materials characterization

2.1.1 Epoxy prepolymer

Epoxy resin is described as "any molecule containing one or more 1,2-epoxy groups" capable of being converted into a thermoset after a curing cycle in the presence of a hardener, forming a three-dimensional network structure. The important versatility of these thermosets has been the object of numerous studies where the epoxy resins chemistry has been largely reviewed [1, 2, 3, 4, 5] .

For this study, commercial Diglycidy Ether of Bisphenol A (DGEBA), Epikote 828, was acquired from Delta Resins Ltd. **Scheme II-1** represents the chemical structure of DGEBA; it possesses two reactive groups.

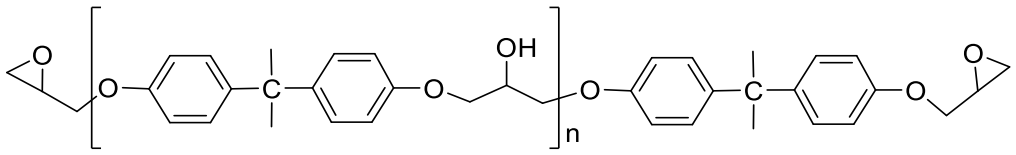

Scheme II-1. Chemical structure of Diglycidy Ether of Bisphenol A (DGEBA).

Usually, DGEBA is slightly homopolymerizated; to properly use the epoxy prepolymer, it is necessary to determine the polymerization degree *n*. This value is easily obtained from ^{1}H-NMR [6,7, 8] by using the following relations:

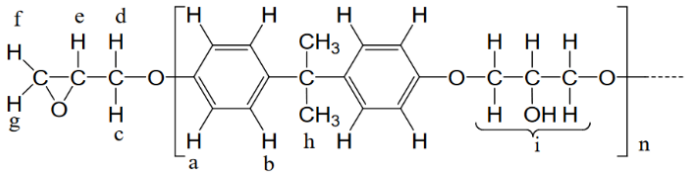

$$R_p = \frac{Integral\ of\ peak\ a,b}{Integral\ of\ peak\ e,f,\ g}$$

$$R_T = \frac{Number\ of\ Aromatical\ protons}{Number\ of\ protons\ in\ oxyrane} = \frac{8}{6} = 1.33$$

$$n = \frac{R_P - R_T}{R_T}$$

$$M_n = 280n + 340$$

According to our information (**Figure II-1**) and the equations described above, *n* is equal to 0.09, and the corresponding molecular weight is 365.33 g/mol.

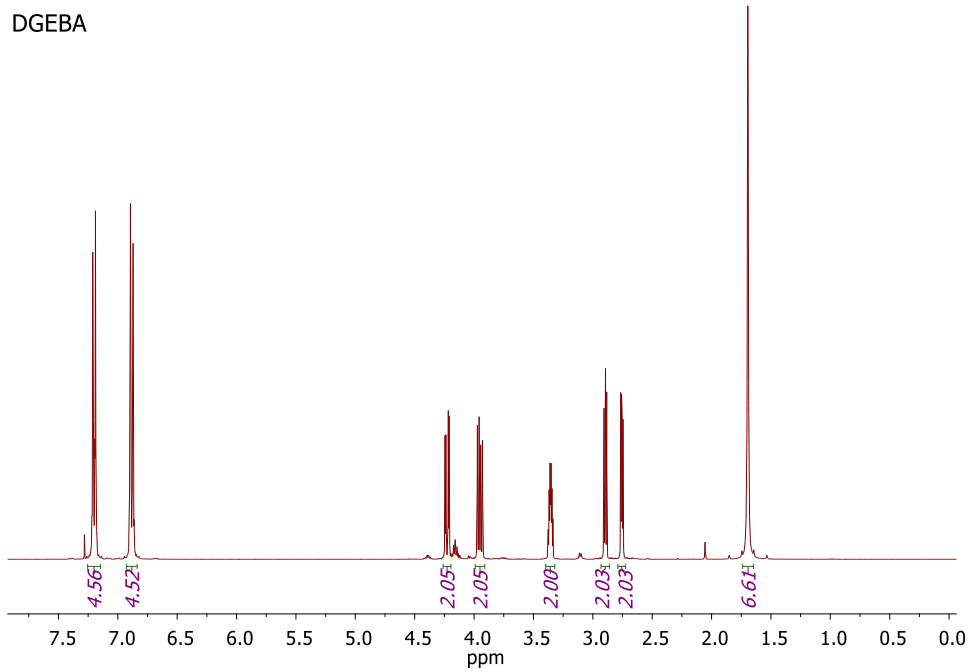

Figure II-1. ^{1}H-NMR spectra in $CDCl_3$ of DGEBA.

DGEBA was also characterized by FTIR spectroscopy (**Figure II-2**) to identify the characteristic infrared absorption bands of the epoxy prepolymer. Based on the literature, **Table II-1** lists the functional groups of the resin.

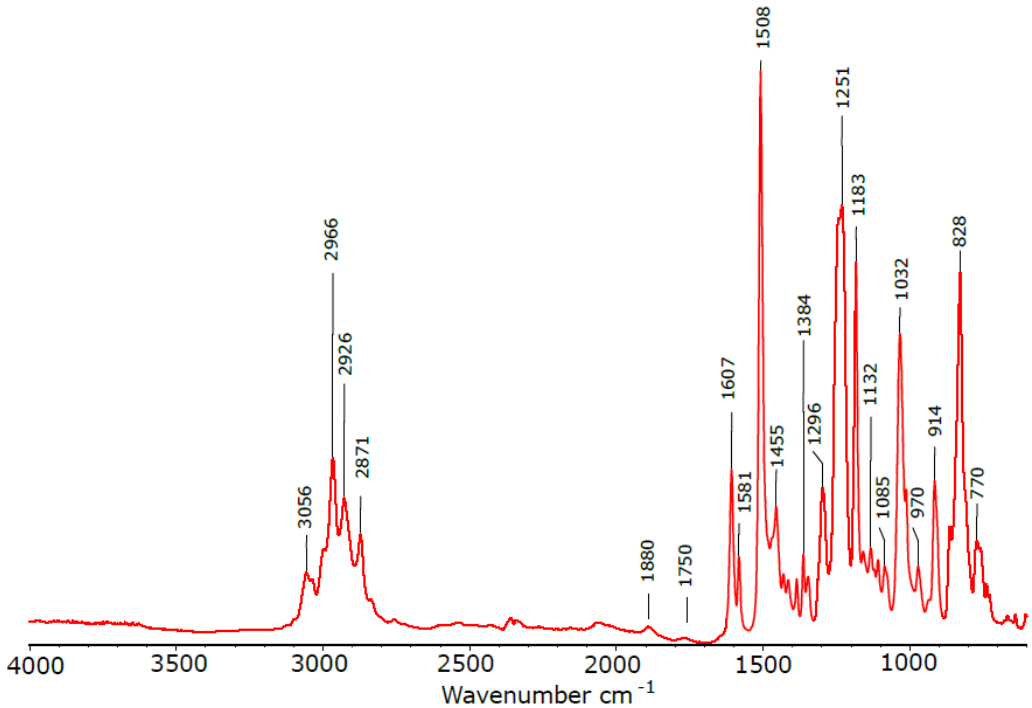

Figure II-2. The mid-infrared spectrum of DGEBA prepolymer.

Wavenumber cm^{-1}	Assignment	Wavenumber cm^{-1}	Assignment
3060-3030	=C-H, stretching, aromatic	**1184**	C-O, stretching, aromatic ring
2970-2950 **2880-2860**	$-CH_3$, asymmetric stretching, methyl $-CH_3$, symmetric stretching, methyl	**1132**	C-O, stretching, epoxide ring
1880, 1750, 1720	C-C, torsion, 1-4 substituted Bz	**1107**	-OH, stretching, secondary alcohol
1600-1580	C=C, stretching, aromatic nucleus	**1085**	C-H, scissoring, benzenic C-O, stretching
1455	$-CH_3$, scissoring, methyl	**1032**	C-O-C, stretching, ether, -CH, scissoring, 1-4 Bz
1384	$-CH_3$, scissoring, isopropyl	**915**	CH_2, scissoring, oxirane
1296	$-CH_2$, twisting and wagging	**840-790**	$-CH_2$, 1-4 substituted Bz
1251	C-O-C, stretching, ether	**770**	$-CH_3$, rocking, methyl

Table II-1. DGEBA absorption bands in the mid-IR[26. 9, 10, 11, 12].

2.1.2 Hardener agents

The good properties of epoxy resins like toughness, chemical resistance, and mechanical properties are strongly linked to the employed hardener. Therefore, it is important to choose the correct curing agent, and the curing conditions to reach the wished properties. In this work, two aromatic amines as hardener agents were selected. Their chemical structure is similar, but one of them presents a dynamic bond. The 4,4'-diaminodiphenylmethane (DDM) was chosen as the reference hardener, while 4-aminophenyl disulfide (4-APDS) is the dynamic hardener. The chemical structures are presented in **Scheme II-2**.

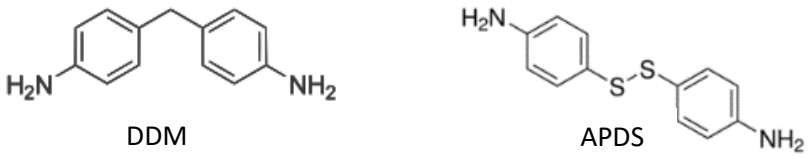

DDM APDS

Scheme II-2. Chemical structure of 4,4'-diaminodiphenylmethane (DDM) and 4-aminophenyl disulfide (4-APDS).

Figure II-3 displays the mid-infrared spectrum of 4-APDS, and **Table II-2** lists its absorption bands.

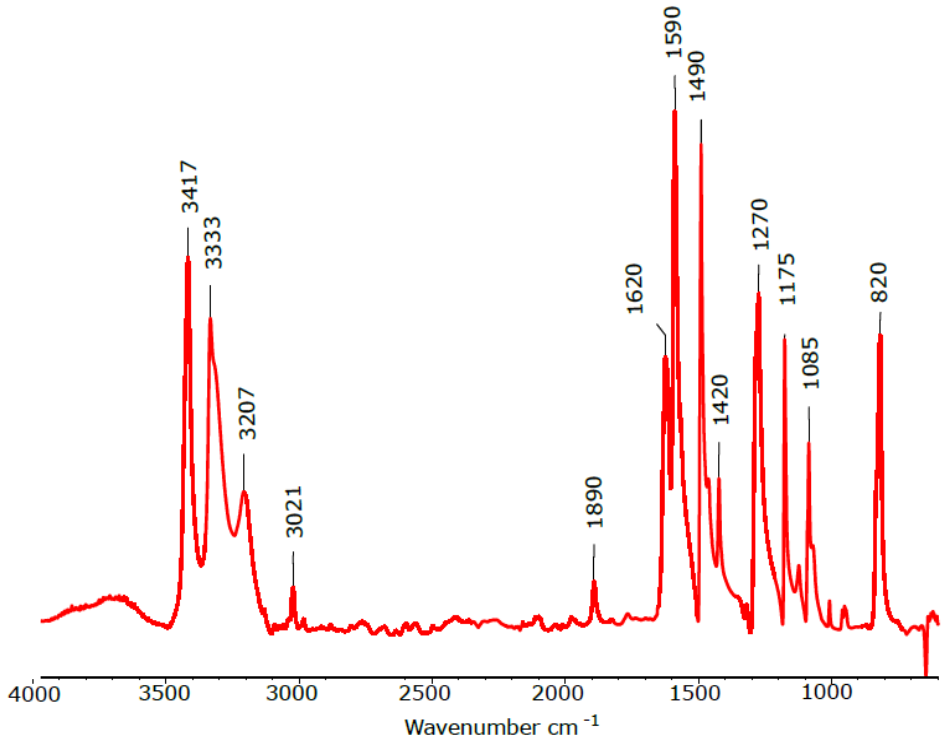

Figure II-3. The mid-infrared spectrum of 4-APDS.

Wavenumber cm^{-1}	Assignment	Wavenumber cm^{-1}	Assignment
3420	-NH_2, symmetric stretching, amine	**1440-1410**	C=C, stretching, aromatic nucleus
3350	-NH_2, symmetric stretching, amine	**1280-1240**	-N-C, stretching, aromatic amine
3100-3000	=C-H, stretching, aromatic	**1225-1165**	-N-C, scissors, aromatic amine
1890, 1750	C-C, torsion, 1-4 substituted Bz	**840-790**	-CH_2, 1-4 substituted Bz
1640-1600	-NH_2, scissors, amine	**1085**	C-C, stretching, Bz C-N, stretching, amine
1600-1560	C=C, stretching, aromatic nucleus	**650**	C-S, stretching
1500-1480	C=C, scissors, aromatic nucleus		

Table II-2. 4-APDS absorption bands in the mid-IR.

Parallelly, FTIR characterization of DDM was carried out. **Figure II-4** displays the mid-infrared spectrum of DDM, and **Table II-3** lists its corresponding absorption bands in the mid-IR.

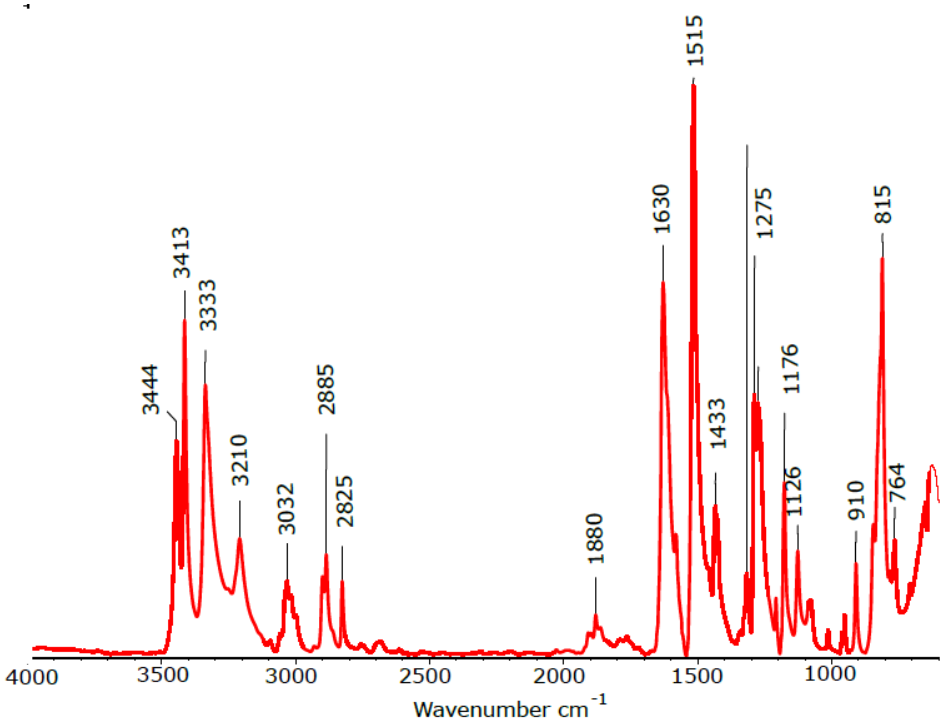

Figure II-4. The mid-infrared spectrum of DDM[13, 14, 15. 26].

Wavenumber cm^{-1}	Assignment	Wavenumber cm^{-1}	Assignment
3500-3400	-NH2, symmetric and asymmetric stretching, amine	**1600-1580**	C=C, stretching, aromatic nucleus
3200-3100	=C-H, stretching, aromatic	**1280-1240**	-N-C, stretching, aromatic amine
2880-2830	-CH, symmetric and asymmetric stretching, methyl	**1225-1175**	-N-C, scissoring, aromatic amine
1880, 1750, 1720	C-C, torsion, 1-4 substituted Bz	**840-790**	$-CH_2$, 1-4 substituted Bz
1640-1560	$-NH_2$, scissors, amine	**650**	C-S, stretching

Table II-3. DDM absorption bands in the mid-IR [15, 16, 17, 26].

2.1.3 Nano Fibrillated Cellulose (NFC)

Nano Fibrillated Cellulose 1% (w/w) in aqueous and ethanol suspensions were supplied by INOFIB (Grenoble, France). The fiber's diameter was estimated by SEM microscopy. It varies from 20 to 70 nm (**Figure II-5**).

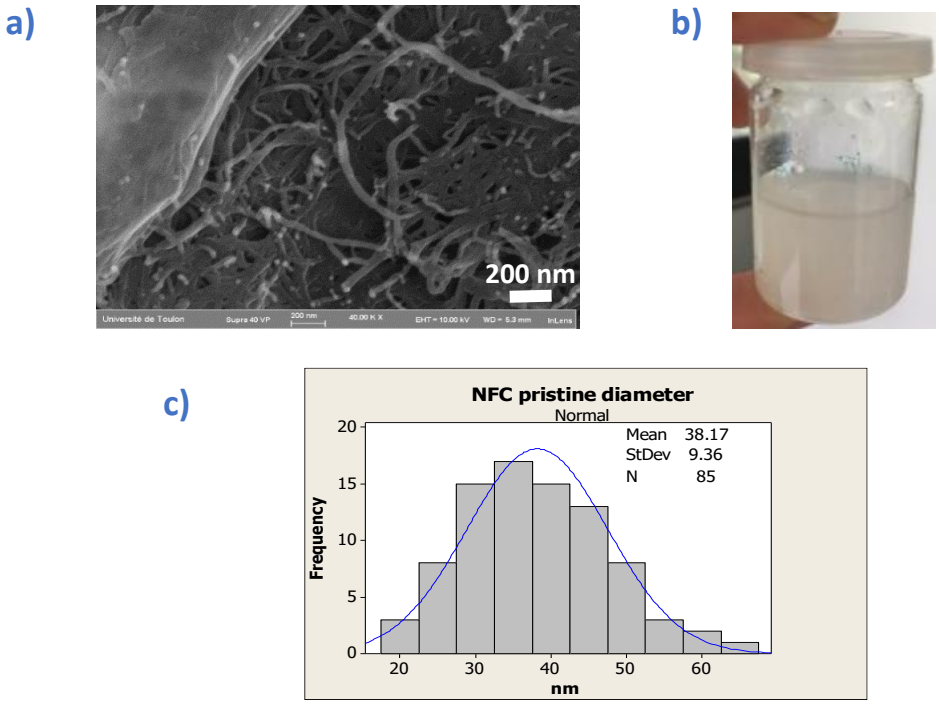

Figure II-5. a) Surface morphology of nano fibrillated cellulose obtained by SEM microscopy, and b) histogram of diameters recorded by SEM.

NFC fibrils were characterized by infrared spectroscopy to elucidate the structure before any chemical treatment. **Figure II-6a** shows an infrared spectrum of pristine NFC, while **Figure II-6b** shows a deconvolution of the spectrum in the range of 800-1200 cm^{-1}, according to the work performed by Maréchal and Chanzy (2000). **Table II-4** summarizes vibrations bands of pristine NFC [18, 19, 20, 21].

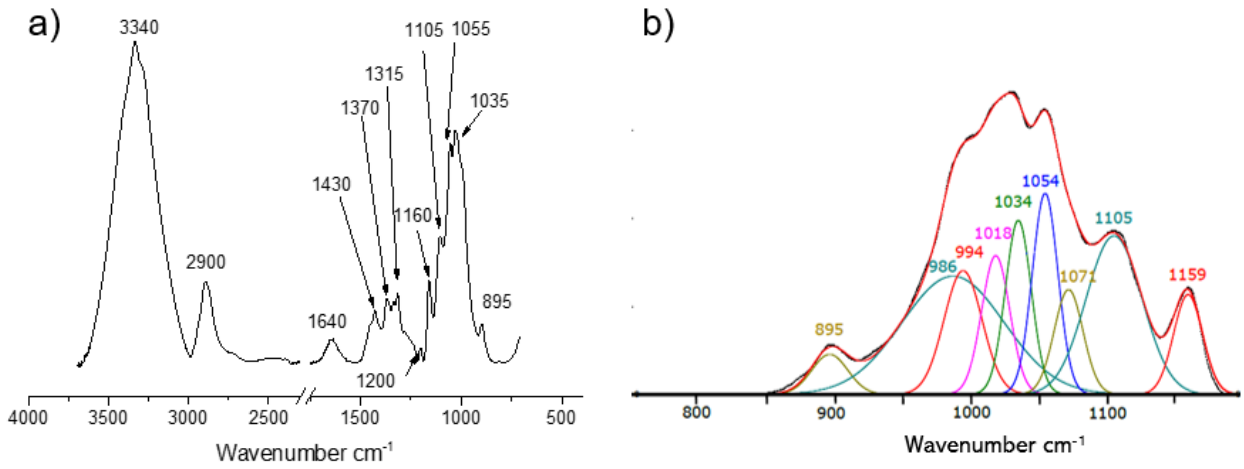

Figure II-6. a) Infrared spectrum of pristine NFC from 4000 to 700 cm^{-1} and b) infrared spectra of pristine NFC deconvoluted from 1200 to 800 cm^{-1}.

Wavenumber cm^{-1}	Assignment	Wavenumber cm^{-1}	Assignment
3340	ν_{OH}, alcohols mainly secondary alcohols	**1105**	C-OH antisymmetric in-plane stretch band of secondary alcohols
2850-3000	CH and CH_2 asymmetrical and symmetrical stretching	**1071**	C-O-C ring mode
1640	OH bending of adsorbed water	**1054**	C-O of secondary alcohols
1430	CH_2 symmetric bending	**1034**	C-O primary alcohols, dominant conformation
1370	CH bending	**1018**	C-O primary alcohol, minor conformation
1315	CH_2 rocking	**994**	C-O primary alcohol, secondary conformation
1200	C-O symmetric stretching glycoside	**968**	C-O ring stretching mode
1160	Anti-symmetrical bridge C-O-C, glycosidic deformation	**895**	Glycosidic deformation, characteristic of β-glycosidic linkage

Table II-4. IR bands vibration of pristine NFC and its assignments.

NFC was also characterized by solid-state ^{13}C NMR. **Figure II-7** shows solid-state ^{13}C NMR of pristine NFC and the corresponding signals attribution[22, 23, 24].

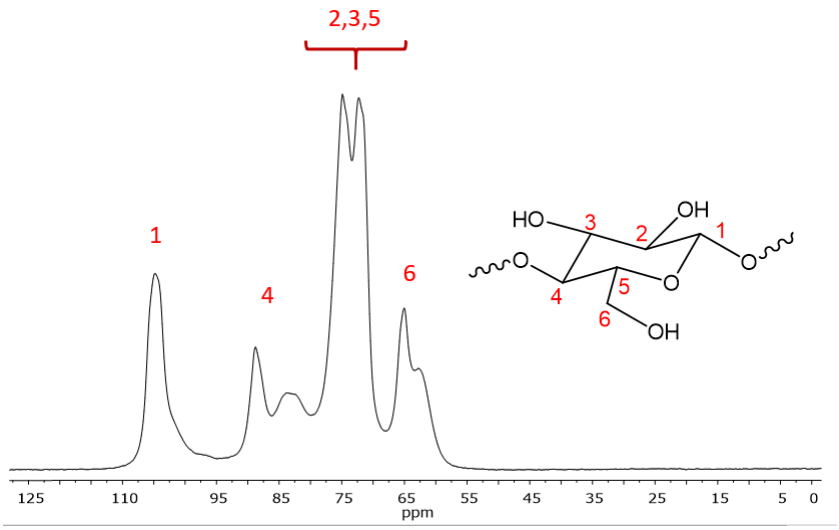

Figure II-7. Solid-state ^{13}C NMR spectra of pristine NFC.

Figure II-8 shows the thermal stability of pristine NFC. The fibrils exhibit a good thermal behavior since the decomposition takes place over 300°C under N_2. Samples were dried at 100°C for 1h to eliminate any possible trace of water.

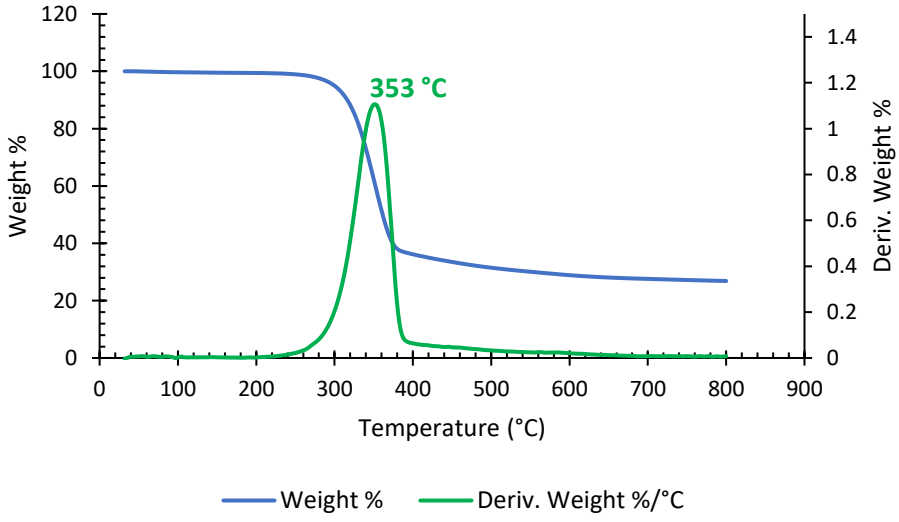

Figure II-8. Thermogravimetric analysis of pristine NFC.

2.1.4 Silanes

3-Glyxidoxypropyltrimethoxysilane; 98% (GPS) and 3-glycidoxypropyldimethylethoxysilane, 97% (GPMES) were purchased from ABCR. Both chemical structures are represented in **Scheme II-3**.

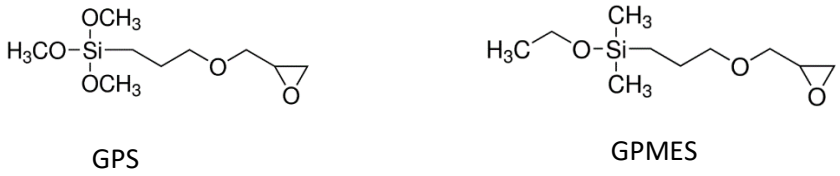

Scheme II-3. Chemical structure of 3-glyxidoxypropyltrimethoxysilane (GPS) and 3-glycidoxypropyldimethylethoxysilane (GPMES).

GPS infrared spectrum is showed in **Figure II-9**, and **Table II-5** of GPS silane [25, 26, 27].

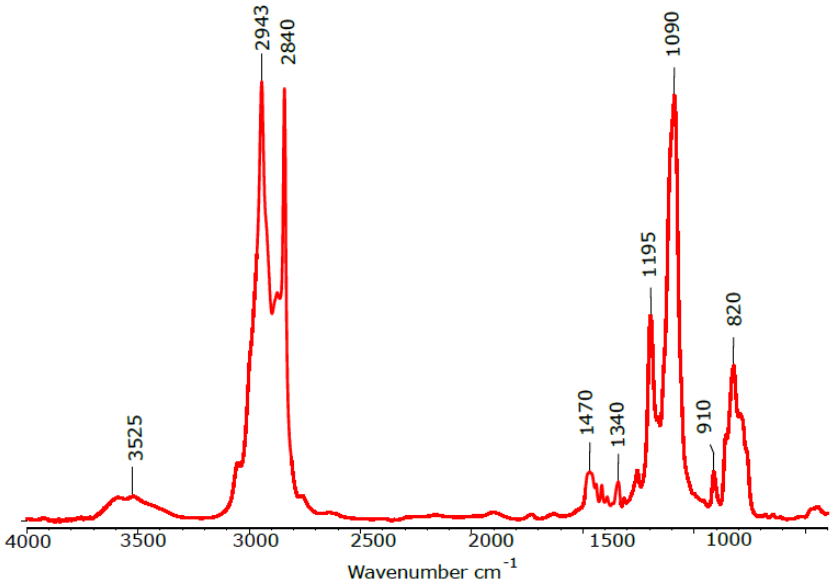

Figure II-9. 3-Glyxidoxypropyltrimethoxysilane infrared spectrum (spectrum from NIST)[27].

Wavenumber cm^{-1}	Assignment	Wavenumber cm^{-1}	Assignment
3550-3500	OH- stretching, methoxy	**995**	CH_2 rock, CC stretching, CO stretching, glycidoxy
2950-2915	CH_2, stretching, glycidoxy	**962**	CH_2 twisting, CH_2 rocking, propyl chain
2840	CH_3 stretching, methoxy	**953**	CH_2 rocking, CO stretching glycidoxy
1470	CH_2 scissoring, glycidoxy	**910**	C-O stretching, C-C stretching, C-O torsion, Epoxy
1340	CH_2 wagging, CH rock, CC stretching, propyl chain	**856**	C-O torsion, C-C stretching Epoxy
1196	CH_2 wagging, propyl chain	**822**	CH_2 rocking, Si-O stretching, propyl chain
1090	C-O stretching, CH_2 wagging, glycidoxy SiO, stretching	**793**	Si-C stretching, Si-O stretching
1085	C-O stretching, Si-O stretch, CH_3 rocking, methoxy	**762**	C-O stretching, C-C-O scissoring, epoxy

Table II-5. IR band vibrations of GPS silane and its assignments [25, 26, 27].

GPS silane was also characterized by ^{13}C NMR. **Figure II-10** shows a ^{13}C NMR spectrum of GPS silane in $CDCl_3$ and their corresponding attribution signals.

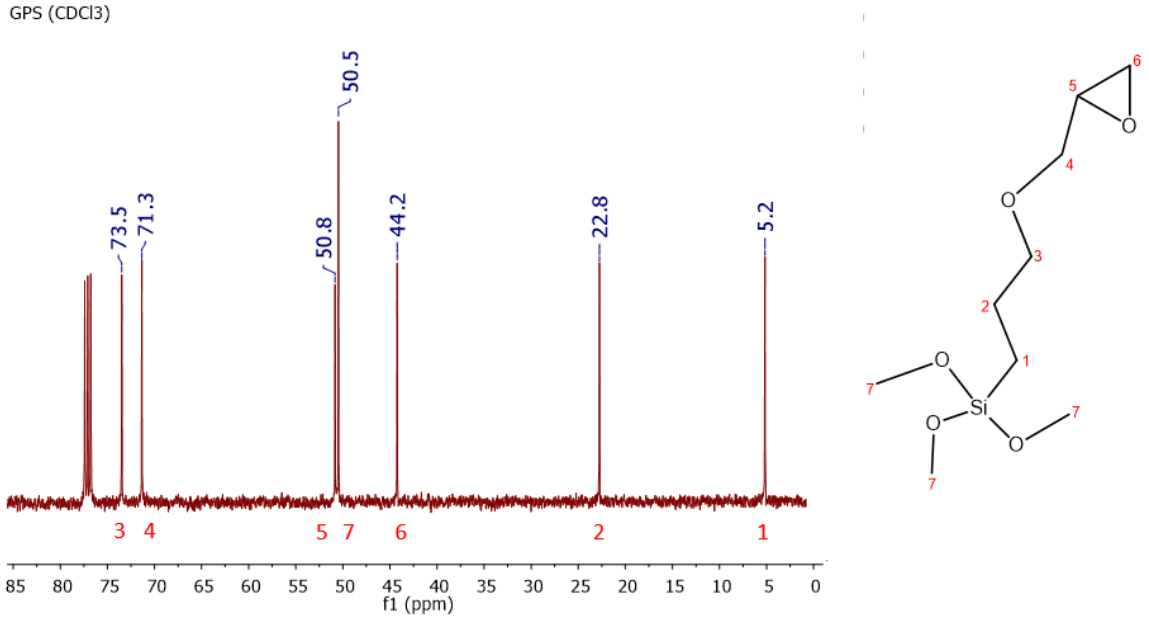

Figure II-10. ^{13}C NMR spectrum of GPS silane in $CDCl_3$.

2.1.5 Solvents and other reactives

- Ethanol, 95% v/v purchased from Fisher Scientific.
- Acetone, purchased from VWR chemicals.
- Acetic acid purchased from Sigma-Aldrich (60.05 g/mol).
- Ethyl 2- Mercaptopropionate (EMP) from TCI (purity > 97%, 134.20 g/mol).
- Tetrahydrofuran (THF) from Sigma-Aldrich (purity > 99%, 72.11 g/mol).
- N, N-Dimethylformamide (DMF) from Sigma-Aldrich (purity > 99%, 73.09 g/mol).
- 1,2,4-Trichlorobenzene (TCI) (purity > 98%, 181.44 g/mol).

2.2 Analysis methods

2.2.1 Attenuated Total Reflection Infrared Spectroscopy (ATR -IR)

Infrared spectroscopy (IR) is a technique that deals with the infrared region of the electromagnetic spectrum based on atomic vibrations. IR provides the characteristic vibrations of functionals groups which allow to elucidate the molecular structure of a sample[28].

Infrared spectroscopy is divided in three regions:

1) The near-IR (14 000- 4000 cm^{-1}) measures broad overtones and some fundamental vibrations.
2) The mid-IR (4000-400 cm^{-1}) is used to measure the fundamental vibration associated with the rational-vibrational structure.
3) The far-IR (400-10 cm^{-1}) is used for rotational spectroscopy.

Attenuated Total Reflection (ATR) is a technique in Fourier Transform Infrared Spectroscopy. ATR takes place when a beam hits an interface between two adjacent media, reflecting a light beam. At an angle of incidence above the critical θ, all the intensity is internally reflected (total reflection). When light is directed over a distance with hard loss and if the refractive index n_2 is absorbed, the electric field will be attenuated due to absorption; hence, less intensity is reflected, resulting in an Attenuated Total Reflection (**Figure II-11**)[29].

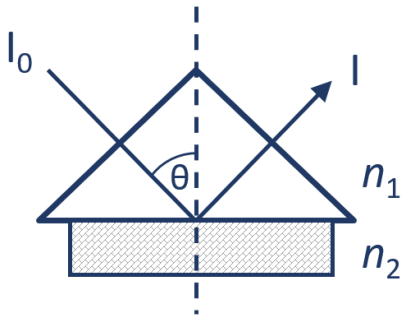

Figure II-11. Schema of attenuated total reflection, where I_0 and I are the intensity of the incident and transmitted radiation, θ is the angle of incidence and n_1, and n_2 are the refractive indices of internal reflection element and sample[29].

Untreated and treated nano fibrillated cellulose were characterized by Fourier transform infrared (FTIR). A spectrometer Nicolet IS50 FT-IR (Thermo Nicolet) with an ATR universal accessory was used. Samples were analyzed in absorbance mode in the range of 700 to 4000 cm^{-1}, a scanning resolution of 1 cm^{-1}, and 32 scans for each sample. Epoxy resins were also characterized in absorbance mode in the range of 700 to 4000 cm^{-1}, a scanning resolution of 4 $cm^{-1,}$ and 32 scans for each sample. All samples were dried at 100°C for 1h before the analysis to discard the presence of water.

2.2.2 X-ray photoelectron spectroscopy (XPS)

X-ray photoelectron spectroscopy is a valuable technique for analyzing the surface chemical composition of samples. XPS could detect almost all elements (except H and He) on the surface layers thanks to ionization from the core electron orbitals of atom in the outermost 2-10 nm of surface, on an area from 1x1 cm^2 to 70x70 μm^2 [30, 31].

In XPS, samples are irradiated by X-rays penetrating at a depth from 5 to 10 nm. Photoelectrons are emitted from core levels of the surface elements; XPS measures the kinetic energy distribution of these emitted photoelectrons. The electron binding energy (BE_x) is defined as the difference between the energy of the primary photon (*hv*) and the kinetic energy of the photoelectron (KE_P)[32]. After X-ray radiation, the atom emits a photoelectron, and a vacancy remains in its inner orbital, and so the atom becomes unstable. Then, an outer-orbital electron is transferred to the inner vacancy orbital (Auger electron). XPS measures the photoelectron and the Auger electron energies. Some electrons escape from the sample's surface, losing their kinetic energy through inelastic scattering and so giving rise to the background in an XPS spectrum[33, 34].

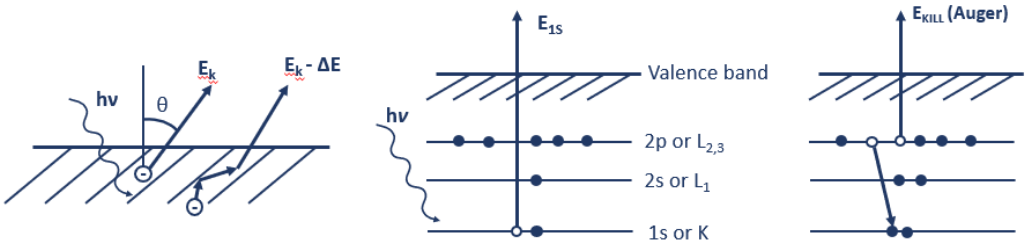

Figure II-12. General schematization of the XPS experiments a) excitation surface process, b) representation of the electron energy levels, and c) the Auger emission relaxation process[34].

XPS experiments were done on an Axis Nova spectrometer (Kratos Analytical) using the Al K(alpha) line (1486.6 eV) as the excitation source. The analysis chamber was maintained below 2 x 10^{-7} Pa, and the analysis area was 700 × 300 µm^2. For survey spectra, the analyzer operated in constant pass energy of 80 eV. The core-level spectra (C (1s), O (1s)) were acquired with an energy step of 0.1 eV and using a constant pass energy mode of 20 eV (energy resolution of 0.48 eV). The binding energies of the spectra were calibrated by setting the C1s peak at 284.8eV. The chemical composition (expressed in atom percentage) was determined using the integrated peak areas of each component, and the peak fitting was made with mixed Gaussian–Lorentzian (70-30%) components.

2.2.3 Nuclear Magnetic Resonance Spectroscopy (NMR)

NMR spectroscopy is a helpful technique for the identification and structure clarification of a chemical compound. All isotopes have an intrinsic nuclear magnetic moment, i.e., a nonzero nuclear spin. Once the nuclei of a sample are under a constant magnetic field, they respond by producing an electromagnetic signal (**Figure II-13**) [35, 36, 37].

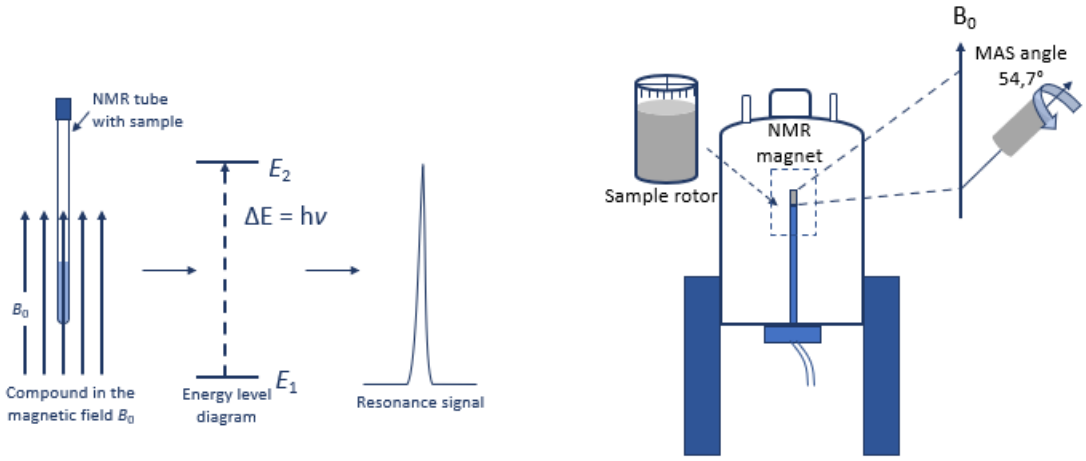

Figure II-13. The schematization of RMN acquisition process, a) the sample is subjected to a magnetic field B_0, the nucleus energy is modified and restricted to certain discrete values E_i, the absorption of the energy is detected in a radiofrequency and recorded as a spectral line, and b) illustrate the CP-MAS by applying the so-called magic angle spin[37].

For solid-state NMR, to obtain a stronger NMR signal and reduce acquisition time, cross-polarization (CP) is a valuable tool. The principle is a polarization of an abundant nucleus like ^{1}H, which transfers to diluted nuclei like ^{13}C or ^{29}Si. In association with cross-polarization, the magic-angle spinning technique (MAS) is highly used. This technique allows increasing the signal intensities by suppressing the band's broadening due to dipolar couplings [36, 38, 39]. The samples were submitted to a rapid rotation and subjected to a magnetic field (B_0) of 54.44° relative to the applied magnetic field, allowing to achieve good spectra' quality.

The solid-state ^{13}C NMR was carried out at a resonance frequency of 100.61 MHz on a Bruker Avance III 400 Ultrashield spectrometer, furnished with a 4 mm dual broadband CP-MAS probe (around 100 mg). The spinning speed was set at 12 kHz.

The liquid-state ^{1}H NMR experiments were carried out at 400.13 MHz on a Bruker Avance III. The solvents employed were $CDCl_3$ and D_2O.

The solid-state ^{29}Si NMR was carried out at a resonance frequency of 79.49 MHz on a Bruker Avance IV HD 400 spectrometer (Rheinstetten, Germany), furnished with a 7 mm dual broadband CP-MAS probe (around 250 mg), a spinning rate of 5kHz, a cross-polarization (CP) with a contact time of 5 ms, a recycle delay of 2s, a SPINAL64 ^{1}H decoupling at 64 kHz and an acquisition time of 43 ms.

2.2.4 Scanning Electron Microscopy (SEM)

Scanning Electron Microscopy is performed with an electronic microscope that employed a focused beam of electrons that *scans* the surface of sample to produce a morphological image. SEM is composed of three major parts: the column, the sample chamber, and the cabinet.

At the top of the column, an electron gun generates an electron beam, accelerating the electrons at voltages from 0.5 to 30 kV. A vacuum is required in the electron column and inside the sample chamber. Electrons traverse through the column until they reached the sample in the chamber, where the scattered signals were captured by different detectors.

The detectors capture the scattered signals and act as a transducer of these signals into an electrical signal (**Figure II-14**). Among these signals, there are electrons (auger electrons, secondary electrons (SE), and backscattered electrons), X-rays (characteristic X-rays and Bremsstrahlung X-ray radiation), light (Ultraviolet, visible, and infrared), heat, electrons conducted through the sample, and electrons absorbed by the sample [40, 41, 42].

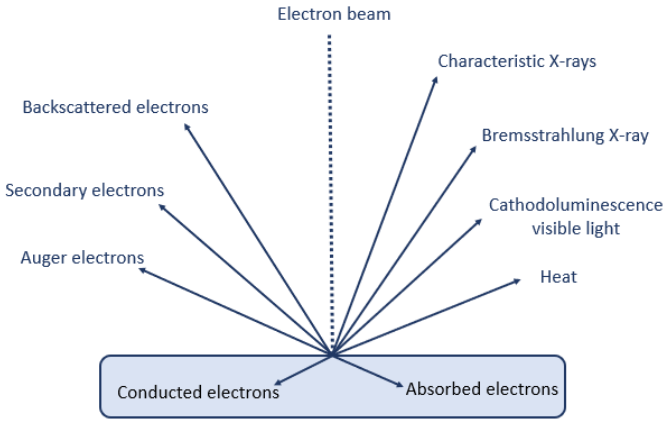

Figure II-14. Main signals emitted after the electron beam emission in sample [30].

In this work, a SEM microscope (Zeiss Supra 40VP Field Emission) was used in secondary electron mode to observe the samples' morphology.

For NFC samples, an aqueous suspension of pristine and modified NFC (0.01% wt) was prepared and deposed onto silicon wafers. The water was evaporated at room temperature, and a carbon conductive layer was applied on the surface before SEM imaging. For epoxy resin and NFC reinforced epoxy composite, samples were cut after being immersed in liquid nitrogen (cryofracture) to see the transversal morphology. Then, samples were covered by a carbon conductive layer for imaging SEM studies. In both cases, experiments were carried out using secondary electron detection mode, with a field emission gun of 3 kV, a work distance of 8 mm, and a vacuum of 10^{-5} mbar.

2.2.5 Energy-Dispersive X-ray spectroscopy (EDX)

The Energy-dispersive X-ray technique is used to determine the chemical composition of the samples analyzed in the SEM microscope. This analysis technique performs a microanalysis with a resolution of 1µm^3. The results could be correlated to the image of the morphology of the samples. It provides local chemical composition data (only a few micrometers of the surface).[42]

The characteristic X-ray emitted, after the samples were hit with the primary electrons beam, possess a *distinguishing* energy value for each chemical element from the different electronic layers (K, L, M) and electronic transitions (α, β, χ, δ)[43] (**Figure II-15**), so the element determination is possible.

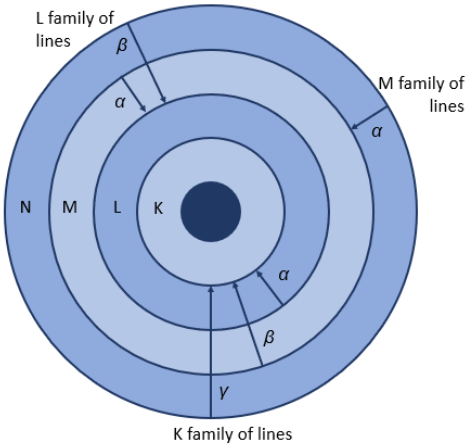

Figure II-15. Families K, L, M of characteristic X-ray[43].

For EDX experiments, the samples were fixed on carbon conductive supports, and the analysis was handled under a field emission gun of 20 kV and a work distance of 8 mm.

2.2.6 Atomic Force Microscopy (AFM)

Atomic Force Microscopy is a very useful technique to obtain quantitative and qualitative databases on topography, texture, adhesion, and mechanical properties of materials at micro and sub-micrometric scale. AFM consists of a microscale cantilever with a probe positioned at its end. This probe is used to scan the sample surface (**Figure II-16**). The cantilever and the tip are typically manufactured as one unit from silicon. The force between the sharp probe and the sample surface is measured by reflecting a laser beam by the "beam bounce" method, where a laser beam is reflected off the cantilever into a segmented photodetector. Thus, the surface topography is directly measured by the deflection of the cantilever [44, 45, 46].

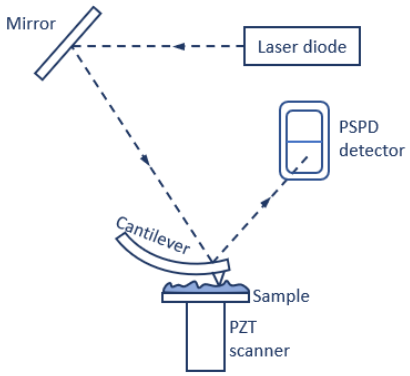

Figure II-16. Schematic representation of AFM[46].

AFM possesses several imaging modes [47, 48]:

- **Contact mode.** A continuous bend in the cantilever is upheld while the scanning between the tip and the sample occurs. The cantilever is positioned above the sample until the tip touches the surface. Any movement toward the sample surface will result in a deflection of lever or sample deformation.
- **Tapping mode:** the tip touches the surface only for a short time. The cantilever oscillates near the sample surface (typical amplitudes in the range of tens of nanometers, small compared to the cantilever length). The short contact time allows to protect both the sample and the tip. A frequency close to the cantilever resonance is selected, and the tip-sample spacing is changed to maintain a constant cantilever amplitude without changing the drive frequency.
- **PeakForce Tapping and PeakForce QNM modes**. The cantilever oscillates near the sample surface like in tapping mode but at frequencies well below the cantilever resonance, non-resonant mode. The z-position of the cantilever is modulated by a sine wave, avoiding unwanted resonances. **Figure II-17** displays a schematize of the interaction of the periodically modulated probe with the surface. When the tip is far from the surface sample (**Figure II-17 i-A/E**), no force on the tip is detected. As the tip approaches the surface, the cantilever is pulled down toward the surface due to Van der Waals's attractive forces (**Figure II-17 i-B**). Then, the force increases while the tip stays on the surface until the Z position of modulation (**Figure Figure II-17 i-C**). The force during the interaction period is kept constant. Later, the probe starts to withdraw, and the force decreases until it reaches a minimum point (**Figure II-17 i-D**); the force is due to the adhesion. Since the Z position of the modulation is controlled as a function of time, and the cantilever deflection is also measured, it is feasible to eliminate the time variable and plot the force against the Z position. Therefore, quantitative mechanical properties such as adhesion, modulus, dissipation, and deformation at the nanoscale can be measured (Peakforce QNM).

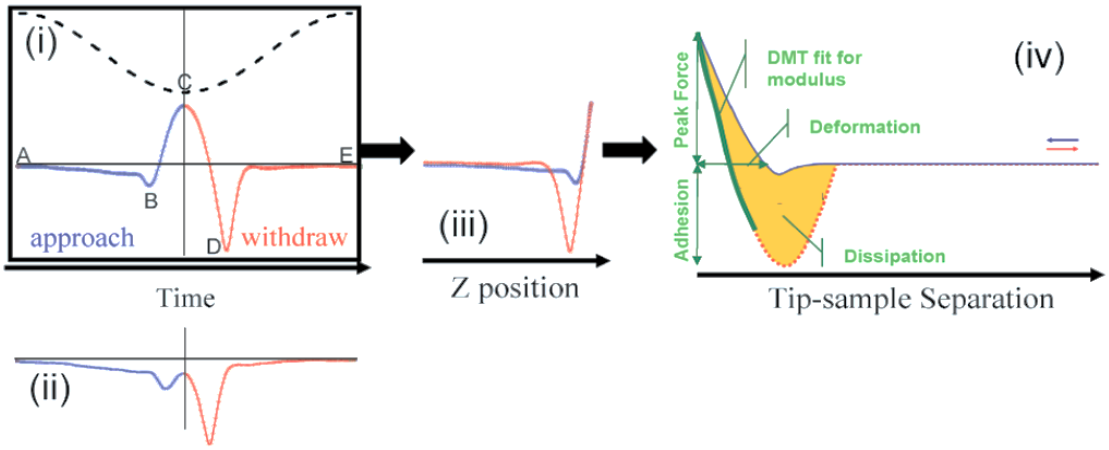

Figure II-17. Schematic representation of the force curve and information obtained applying Peak force QNM: i) plot of force and piezo Z position as a function of time. Where B) is the jump-to-contact, C) the peak force, and D) the adhesion, ii) plot of force vs time, iii) plot force vs Z piezo position, iv) plot force vs separation calculated from the Z piezo position and the cantilever deflection[47, 48].

The determination of the elastic modulus using the PeakForce QNM is achieved by fitting the curve of **Figure II-17 iv** and using the Derjaguin-Muller-Tporov (DMT) model:

$$F - F_{adh} = \frac{4}{3} E^* \sqrt{r(d - d_0)^3}$$

Where $F\text{-}F_{adh}$ is the relative cantilever force due to the adhesion force between the sample and cantilever, r is the tip end rations, and $d\text{-}d_0$ is the deformation of the sample. The result is the reduced modulus E^*, and lately, if the Poisson's rate (v) is known, the Young's modulus can be calculated following the relation:

$$E^* = \left[\frac{1 - \nu_s^2}{E_s}\right]^{-1}$$

AFM experiments were operated on a Multimode 8 microscope (Bruker). For NFC characterization, AFM imaging was done by using the PeakForce tapping mode. For the epoxy resin and epoxy composite material, the samples were analyzed by using the PeakForce QNM mode.

NFC Samples were prepared by placing a drop of 0.001 wt. % of an aqueous suspension of pristine or modified NFC onto mica surfaces, then the water was evaporated at room temperature. The scans were performed on an area of 1 µm x 1 µm, with 512 pixels collecting images at a scan rate of 0.8 Hz. The nominal spring constant of the cantilever was 0.4 N/m. All measurements were carried out under ambient conditions.

The epoxy-vitrimer and epoxy-vitrimer-composite cross-section surfaces for AFM studies were polished in P100, P320, P600, and P1200 discs, each one during 2-3 min. Then a polishing in a

diamond suspension of 6µm, 3µm, and 1µm for 2-3 min. Finally, samples were rinsed with water and dried before the analysis. The sample treatment allows studying the surface properties like adhesion and elastic modulus.

2.2.7 Differential Scanning Calorimetry (DSC)

Differential Scanning Calorimetry is the most popular thermal analysis technique used for characterizing the different thermal transitions of materials. The principle of DSC is based on the measure of the heat flow rate difference between a substance and a reference as a function of temperature; meanwhile, the sample is subjected to a controlled temperature program [49,50].

Figure II-18. Schematic representation of servo cell of DSC. Two sensors are involved to determine the heat flux of sample, the reference, and the sample sensor.

Experiments were carried out in DSC-Q100 TA Instruments in standard alumina capsules. DSC experiments were performed using 5-10 mg of sample, previously dried at 100 °C for 1h to eliminate as much as possible traces of water. The analysis was carried out using a temperature ramp of 10°C/min under a nitrogen flow of 50 mL/min.

2.2.8 Thermogravimetric Analysis (TGA)

Thermogravimetric Analysis consists of a continuous recording of the mass of a sample heated in a furnace with a controlled environment. Some applications of this analysis method in the polymers field are 1) the determination of the thermal stability of polymers, 2) composition analysis, and 3) identification of polymers from their decomposition patterns [49].

Experiments were run using a TA instrument (Q600) in a range of 25°C to 800°C with a heating rate of 20°C/min under a nitrogen flow of 100 mL/min. Approximately 5-10 mg of sample was used for each experiment. Samples were dried at 100°C for 1h to eliminate any possible trace of water.

2.2.9 Dynamic Mechanical Analysis (DMA)

The dynamic mechanical analysis is a technique used to characterize materials and specially to describe the viscoelastic behavior of polymers. It allows to determine the mechanical properties of

materials and study the molecular relaxation processes as a function of time and temperature. The dynamic mechanical analysis consists of applying a small cyclic strain on a sample, measuring the stress response[49].

DMA has different measurement modes (**Figure II-19**); these methods are useful to characterize the materials in many applications. The following list briefly discusses their advantages[51, 52]:

1. Shear mode. The only mode that allows determining the shear modulus G'. Ideal for soft samples in a modulus range from 0.1 kPa to 10 MPa.
2. Three-point bending mode. The sample is pre-stressed, so it remains in contact with the three supports during the measurement. This method is ideal for sample modulus range from 10 MPa to 1000 GPa.
3. Dual cantilever mode. The sample is clamped at three positions, anchored on both ends by stationary clamps, and a moveable clamp at the sample midpoint. The effective free sample length is difficult to determine due to clamping effects. A length correction considers that the effective mechanical stressed sample length is greater than the free clamped length. These effects lead to incorrect modulus values. The modulus measurement range is from 1 MPa to 100 GPa.
4. Single cantilever mode. Contrary to dual cantilever mode, thermal expansion or contraction is eliminated, but determining the free sample length is not easy due to the clamping effects since the sample often deformed after the test. The sample is immovable on one end by a stationary clamp and affixed to a mobile clamp on the other side. Through this moveable clamp, a controlled force is applied by the motor of the machine. The modulus measurement range is from 1 MPa to 100 GPa.
5. Tension mode. The sample is pre-stressed to prevent buckling, ideal for films, fibers, and samples in the shape of thin rods. The modulus measurement range is from 1 kPa to 200 GPa.
6. Compression mode. The sample is placed on a fixed flat surface, and a force is applied. This mode is suitable for low to moderate modulus materials. This mode can also be used to make measurements of expansion or penetration by using a static force.

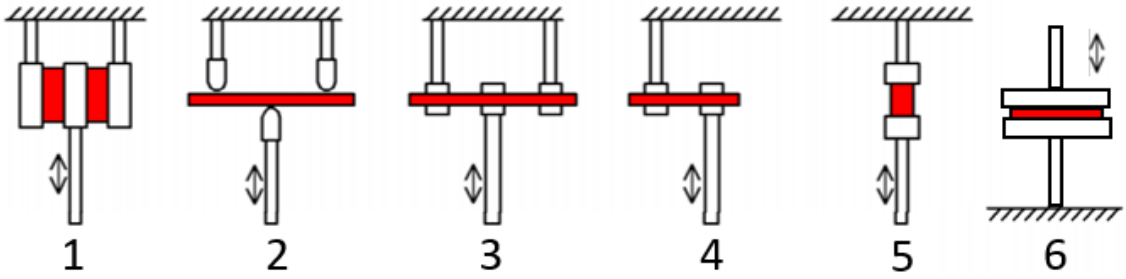

Figure II-19. DMA measurement modes 1) shear, 2) three-point bending, 3) dual cantilever, 4) single cantilever, 5) tension, and 6) compression [51].

2.2.9.1 Dynamic Temperature Program

The dynamic mechanical analysis is a reliable method to evaluate the viscoelastic response of materials subjected to a mechanical stimulus as a function of temperature and frequency. The DMA data are usually expressed with a complex modulus, obtained from a complex variable treatment of the sinusoidal deformation, which is defined as the ratio of the sinusoidal stress to strain:

$$E^* = \frac{\sigma_0}{\epsilon_0}(\cos(\delta) + i sin(\delta))$$

$$E^* = E' + E''$$

Where $E' = \frac{\sigma_0}{\epsilon_0}(\cos(\delta))$ $E'' = \frac{\sigma_0}{\epsilon_0}(\mathrm{i}\sin(\delta))$

$$\tan\delta = \frac{E''}{E'} = \frac{\sin(\delta)}{\cos\delta}$$

E' is the *storage modulus*. It measures the elastic character (solid-like nature of the material). *E''* is the *loss modulus*. It measures the viscous character (liquid-like nature of the material). Tan δ is known as the material loss factor or loss tangent, representing the ratio of the energy dissipated to the energy stored per deformation cycle [49, 53].

The experiments were carried out using a TA Instrument (Q800) by employing a single cantilever. For the dynamic temperature program test, experiments were conducted over the temperature range of 25°C to 220°C with a heating rate of 3°C/min, a frequency of 1Hz and an oscillation amplitude of 20 µm. The sample dimensions were 17.5 x 8 x 0.7 mm^3. Samples were pre-heated at 100 °C/1h before each experiment to eliminate any possible traces of water.

2.2.9.2 Stress Relaxation

The stress relaxation test consists of applying an instantaneous deformation to the sample and measuring the stress variation as a function of time. When the sample is in steady-state flow, the test is performed by ceasing the movement and measuring stress decay. In Maxwell's model, this

means to make $\frac{\delta\gamma}{\delta t}$ equal to zero. Maxwell model is the following:

$$\tau + \lambda \frac{\delta\tau}{\delta t} = \eta_o \frac{\delta\gamma}{\delta t}$$

Where τ is the stress, λ is the characteristic relaxation time, η is the viscosity, and γ is the deformation.

$$\tau + \lambda \frac{\delta\tau}{\delta t} = 0$$

$$\frac{\tau}{\tau_o} = e^{-\frac{t}{\lambda}}$$

Experiments were carried out at different temperatures (from 180 to 220 °C) in a single cantilever mode. The program begins with 30 min of an isotherm before the relaxation stress measurement, a displacement of 1%, and a static force of 0.001N*. Sample's dimension was 17.5 x 8 x 0.7 mm^3. Before each analysis, samples were pre-heated at T=Tα-30°C for 1h to remove any possible traces of water.

2.2.9.3 Dilatometry test

Dilatometry tests were carried out using a TA Instrument (Q800) in compression and tensile mode. Experiments were carried out from 50 to 220°C at a heating rate of 3°C/min at a controlled force of 0.010 N. The sample's dimensions in compression mode were cylinders of 6.13 mm of diameter and 5.5 mm of thickness. For tensile mode, the sample shape was rectangular, the dimension was 9x7x0.7 mm^3.

2.2.9.4 Frequency sweep experiments

Frequency sweep tests is a useful test which allows to determine viscoelastic properties and the inner structure of polymers as a function of time scale. The experiments were carried out using a TA Instrument (Q800) in compression mode under a controlled strain of 0.1%. The temperatures explored were from 180 to 230°C in a frequency range from 30 to 0.05 Hz. The sample shape was a cylinder of 6.13 mm of diameter and 5.5 mm of thickness.

* The displacement in the composite material was changed to 0.1%.

2.2.9.5 Multi-frequency strain

Multi-frequency experiments allow describing the time-dependent behavior of a sample. The experiments were carried out using a TA Instrument (Q800) by employing a single cantilever. For the dynamic temperature program test, experiments were conducted over the temperature range of 100°C to 230°C with a heating rate of 1°C/min and a frequency of 1, 2, 5, 10 and 20 Hz. The sample dimensions were 17.5 x 8 x 0.7 mm^3. Samples were pre-heated at 100 °C/1h before each experiment to eliminate any possible traces of water.

2.2.10 Other equipment

- Ultraturrax, T 18 digital, dispersing tool S 18 N- 19G. It was used to change the solvent of suspension or redispersing pristine and modified NFC.
- Hettich centrifugen EBA 20. It was used when performing NFC solvent exchange.
- Bransonic Ultrasonic cleaner, 2510E-DTH. It was used for redispersing the NFC for SEM and AFM spectroscopy analysis.
- Polisher ESC 300 GTL (ESCIL 69689-CHASSIEU-FRANCE). It was used to prepare the sample surfaces for AFM studies and DMA analysis.

Bibliography

1 May, C. (Ed.). (1998). *Epoxy resins: chemistry and technology*. Routledge.

2 Ellis, B. (Ed.). (1993). *Chemistry and technology of epoxy resins* (1st ed., pp. 24-26). London: Blackie Academic & Professional.

3 Hodgkin, J. H., Simon, G. P., & Varley, R. J. (1998). Thermoplastic toughening of epoxy resins: a critical review. *Polymers for advanced technologies*, *9*(1), 3-10.

4 Jin, F. L., Li, X., & Park, S. J. (2015). Synthesis and application of epoxy resins: A review. *Journal of Industrial and Engineering Chemistry*, *29*, 1-11.

5 Dodiuk, H., & Goodman, S. H. (Eds.). (2013). *Handbook of thermoset plastics*. William Andrew.

6 Garea, S. A., Corbu, A. C., Deleanu, C., & Iovu, H. (2006). Determination of the epoxide equivalent weight (EEW) of epoxy resins with different chemical structure and functionality using GPC and 1H-NMR. *Polymer testing*, *25*(1), 107-113.

7 Garcia, F. G., & Soares, B. G. (2003). Determination of the epoxide equivalent weight of epoxy resins based on diglycidyl ether of bisphenol A (DGEBA) by proton nuclear magnetic resonance. *Polymer Testing*, *22*(1), 51-56.

8 Dornbusch, M., Christ, U., & Rasing, R. (2016). *Epoxy resins*. Hanover: Vincentz Network.

9 González, M. G., Cabanelas, J. C., & Baselga, J. (2012). Applications of FTIR on epoxy resins-identification, monitoring the curing process, phase separation and water uptake. *Infrared Spectroscopy-Materials Science, Engineering and Technology*, *2*, 261-284.

10 Cholake, S. T., Mada, M. R., Raman, R. S., Bai, Y., Zhao, X. L., Rizkalla, S., & Bandyopadhyay, S. (2014). Quantitative analysis of curing mechanisms of epoxy resin by mid-and near-fourier transform infrared spectroscopy. *Defence Science Journal*, *64*(3), 314.

11 Ghosal, A., & Ahmad, S. (2017). High performance anti-corrosive epoxy–titania hybrid nanocomposite coatings. *New Journal of Chemistry*, *41*(11), 4599-4610.

12 Cherdoud-Chihani, A., Mouzali, M., & Abadie, M. J. M. (2003). Study of crosslinking acid copolymer/DGEBA systems by FTIR. *Journal of applied polymer science*, *87*(13), 2033-2051.

13 NIST, 4,4' Methylenedianiline infrared spectrum. Recuperated from: https://webbook.nist.gov/cgi/cbook.cgi?ID=C101779&Type=IR-SPEC&Index=0#IR-SPEC [November 2020].

14 Kortaberria, G., Arruti, P., Gabilondo, N., & Mondragon, I. (2004). Curing of an epoxy resin modified with poly (methylmethacrylate) monitored by simultaneous dielectric/near infrared spectroscopies. *European polymer journal*, *40*(1), 129-136.

15 Hopewell, J. L., George, G. A., & Hill, D. J. T. (2000). Quantitative analysis of bismaleimide-diamine thermosets using near infrared spectroscopy. *Polymer*, *41*(23), 8221-8229.

16 Nyquist, R. A. (2001). Thiols, Sulfides and Disulfides, Alkanethiols, and Alkanedithiols (S− H Stretching). *Interpreting infrared, Raman, and nuclear magnetic resonance spectra*, *2*, 65-83.

17 NIST, 4-Aminophenyl disulfide Infrared spectrum. Recuperated from: https://webbook.nist.gov/cgi/inchi?ID=C722270&Type=IR-SPEC&Index=0 [November 2020].

18 Vasiljević, J., Tomšič, B., Jerman, I., Orel, B., Jakša, G., & Simončič, B. (2014). Novel multifunctional water-and oil-repellent, antibacterial, and flame-retardant cellulose fibres created by the sol–gel process. *Cellulose*, *21*(4), 2611-2623.

19 Oh, S. Y., Yoo, D. I., Shin, Y., & Seo, G. (2005). FTIR analysis of cellulose treated with sodium hydroxide and carbon dioxide. *Carbohydrate research*, *340*(3), 417-428.

20 Maréchal, Y., & Chanzy, H. (2000). The hydrogen bond network in Iβ cellulose as observed by infrared spectrometry. *Journal of molecular structure*, *523*(1-3), 183-196.

21 Colom, X., Carrillo, F., Nogués, F., & Garriga, P. (2003). Structural analysis of photodegraded wood by means of FTIR spectroscopy. *Polymer degradation and stability*, *80*(3), 543-549.

22 Moulthrop, J. S., Swatloski, R. P., Moyna, G., & Rogers, R. D. (2005). High-resolution 13C NMR studies of cellulose and cellulose oligomers in ionic liquid solutions. *Chemical communications*, (12), 1557-1559.

23 Wickholm, K., Larsson, P. T., & Iversen, T. (1998). Assignment of non-crystalline forms in cellulose I by CP/MAS 13C NMR spectroscopy. *Carbohydrate Research*, *312*(3), 123-129.

24 Kono, H., Yunoki, S., Shikano, T., Fujiwara, M., Erata, T., & Takai, M. (2002). CP/MAS 13C NMR study of cellulose and cellulose derivatives. 1. Complete assignment of the CP/MAS 13C NMR spectrum of the native cellulose. *Journal of the American Chemical Society*, *124*(25), 7506-7511.

25 Šapić, I. M., Bistričić, L., Volovšek, V., Dananić, V., & Furić, K. (2009). DFT study of molecular structure and vibrations of 3-glycidoxypropyltrimethoxysilane. *Spectrochimica Acta Part A: Molecular and Biomolecular Spectroscopy*, *72*(4), 833-840.

26 Rojo Callejas, F., Tablas de Espectroscopía Infrarroja, Facultad de Química, UNAM. Recuperated from: http://depa.fquim.unam.mx/amyd/archivero/TablasIR_34338.pdf [November 2020].

27 NIST, 3(Glycidoxy) propyl Trimethoxy Silane. Infrared spectrum. Recuperated from: https://webbook.nist.gov/cgi/cbook.cgi?ID=C2530838&Units=SI&Mask=80#IR-Spec [November 2020].

28 Larkin, P. (2017). Infrared and Raman spectroscopy: principles and spectral interpretation. Elsevier.

29 Bürgi, T., & Baiker, A. (2006). Attenuated total reflection infrared spectroscopy of solid catalysts functioning in the presence of liquid-phase reactants. *Advances in Catalysis*, *50*, 227-283.

30 Buschow, K. J., Cahn, R. W., Flemings, M. C., Ilschner, B., Kramer, E. J., & Mahajan, S. (2001). Encyclopedia of materials. *Science and technology*, *1*, 11.

31 Oswald, S. (2006). X-Ray Photoelectron Spectroscopy in Analysis of Surfaces. *Encyclopedia of Analytical Chemistry: Applications, Theory and Instrumentation*.

32 Konno, H. (2016). X-ray Photoelectron Spectroscopy. In *Materials Science and Engineering of Carbon* (pp. 153-171). Butterworth-Heinemann.

33 Rafiee, Z., Nejatian, M., Bodbodak, S., & Jafari, S. M. (2020). Surface composition of nanoencapsulated food ingredients by X-ray photoelectron spectroscopy (XPS). In *Characterization of Nanoencapsulated Food Ingredients* (pp. 243-268). Academic Press.

34 Tougaard, S. M. (2013). X-ray Photoelectron Spectroscopy-Elsevier Reference Module in Chemistry, Molecular Sciences and Chemical Engineering. In J. Reedijk (Ed.), Elsevier Reference Module in Chemistry, Molecular Sciences and Chemical Engineering.

35 Lindon, J. C., Tranter, G. E., & Koppenaal, D. (2016). *Encyclopedia of spectroscopy and spectrometry*. Academic Press.

36 Gutmann, T., Groszewicz, P. B., & Buntkowsky, G. (2019). Solid-state NMR of Nanocrystals. *ANNUAL REPORTS ON NMR SPECTROSCOPY, VOL 97*, *97*, 1-82.

37 Gunther, H., & Gunther, H. (1994). NMR spectroscopy: basic principles, concepts, and applications in chemistry. Chichester, UK: John Wiley & Sons.

38 Fujiwara, T., & Ramamoorthy, A. (2006). How far can the sensitivity of NMR be increased?. In *Annual Reports on NMR Spectroscopy* (Vol. 58, pp. 155-175). Academic Press.

39 Andrew, E. R., Bradbury, A., & Eades, R. G. (1958). Nuclear magnetic resonance spectra from a crystal rotated at high speed. *Nature*, *182*(4650), 1659-1659.

40 Mutalib, M. A., Rahman, M. A., Othman, M. H. D., Ismail, A. F., & Jaafar, J. (2017). Scanning electron microscopy (SEM) and energy-dispersive X-ray (EDX) spectroscopy. In *Membrane Characterization* (pp. 161-179). Elsevier.

41 Barkay, Z. (2017). Scanning Electron Microscopy Under Gaseous Environment. In *Microscopy Methods in Nanomaterials Characterization* (pp. 85-103). Elsevier.

42 de Assumpção Pereira-da-Silva, M., & Ferri, F. A. (2017). Scanning Electron Microscopy. In *Nanocharacterization Techniques* (pp. 1-35). William Andrew Publishing.

43 Goldstein, J. I., Newbury, D. E., Michael, J. R., Ritchie, N. W., Scott, J. H. J., & Joy, D. C. (2017). *Scanning electron microscopy and X-ray microanalysis*. Springer.

44 Nasrollahzadeh, M., Atarod, M., Sajjadi, M., Sajadi, S. M., & Issaabadi, Z. (2019). Plant-Mediated Green Synthesis of Nanostructures: Mechanisms, Characterization, and Applications. In *Interface Science and Technology* (Vol. 28, pp. 199-322). Elsevier.

45 Dejous, C., Hallil, H., Raimbault, V., Rukkumani, R., & Yakhmi, J. V. (2017). Using microsensors to promote the development of innovative therapeutic nanostructures. In *Nanostructures for Novel Therapy* (pp. 539-566). Elsevier.

46 Yan, Y. (2010). Tribology and tribo-corrosion testing and analysis of metallic biomaterials. In *Metals for Biomedical Devices* (pp. 178-201). Woodhead Publishing.

47 Bruker, AFM applications notes 133, Recuperated from: https://www.bruker.com/fileadmin/user_upload/8-PDF-Docs/SurfaceAnalysis/AFM/ApplicationNotes/Introduction_to_Brukers_ScanAsyst_and_PeakForce_Tapping_Atomic_Force_Microscopy_Technology_AFM_AN133.pdf [November 2020]

48 Bruker, AFM applications notes 128. Recuperated from: https://www.bruker.com/fileadmin/user_upload/8-PDF-Docs/SurfaceAnalysis /AFM/ ApplicationNotes /AN128-RevB0-Quantitative_Mechanical_Property_Mapping_at_the_ Nanoscale_with_PeakForceQNM-AppNote.pdf [November 2020].

49 Menczel, J. D., & Prime, R. B. (Eds.). (2009). *Thermal analysis of polymers: fundamentals and applications*. John Wiley & Sons.

50 Chartoff, R. P., & Sircar, A. K. (2002). Thermal analysis of polymers. *Encyclopedia of polymer science and technology*.

51 Wagner, M. (Ed.). (2017). *Thermal Analysis in Practice: Fundamental Aspects*. Carl Hanser Verlag GmbH Co KG.

52 Henriques, I. R., Borges, L. A., Costa, M. F., Soares, B. G., & Castello, D. A. (2018). Comparisons of complex modulus provided by different DMA. *Polymer Testing*, *72*, 394-406.

53 Jayanarayanan, K., Rasana, N., & Mishra, R. K. (2017). Dynamic mechanical thermal analysis of polymer nanocomposites. In *Thermal and Rheological Measurement Techniques for Nanomaterials Characterization* (pp. 123-157). Elsevier.

Chapter III : Epoxy vitrimer resin based on exchangeable disulfide crosslinks

3. Epoxy vitrimer resin based on exchangeable disulfide crosslinks.

3.1 Introduction

Throughout the last decades, the growing manufacturing volume and market size predictions of epoxy resins have proved the importance of their production and led to the requirement for innovative researches. In 2015, the global market size was USD 8 billion in growing industries such as coating, transport, aerospace, electrical and electronic, composites, and decorative coating. This growing trend positions of epoxy resins suggest that this material becomes to have an important position on the market sales of tomorrow[1, 2]. By varying the curing agent's chemical structure and the curing conditions during the manufacturing process, it is possible to obtain desirable properties such as toughness, chemical resistance, good mechanical properties (from extreme flexibility to high strength), high thermal, and electrical resistance. These suitable properties have drawn many researchers and industries' attention due to their versatility in numerous domains, from adhesives to polymer matrices with composites[3,4].

Despite the excellent properties of the epoxy resins, the markets need new sustainable and high-performance materials to deal not only with industry requirements but also with the growing production of waste materials. Numerous researchers have found inspiration from biological systems that can repair themselves after suffering [5, 6] to face these challenges. Self-healing behavior offers considerable potential for solving some of the most limiting problems of thermosetting materials, such as re-processability. Many strategies to introduce self-healing behavior into the epoxy resins have been explored, from the incorporation of the microcapsules to heal the materials until the incorporation of reversible covalent bonds into the epoxy matrix[5,7, 8, 9, 10, 11].

The reversible covalent bonds have been studied for a long time, both in the study of biological systems[12] and in the development of crosslinked networks [13, 14]. More recently, Bowman *et al.* (2010) defined as ***Covalent Adaptable Networks*** *(CANs) the networks which contain a sufficient number and a topology of reversible covalent bonds so as to enable the crosslinked network structure to respond chemically to an applied stimulus*. The CANs are divided in two main groups depending on their exchange mechanism[15, 16, 17]. In the first mechanism, dissociative one, the crosslink exchange follows a bond-breaking and bond-forming reaction sequence such as Diels-Alder reactions[10, 18]. In the second mechanism, the associative one, the crosslink exchange follows a bond-forming and bond-breaking sequences, such as transesterification catalyst to epoxy/acid or epoxy anhydride[19,20].

Vitrimer materials were introduced by Leibler *et al.* (2011) and have been presented as a new kind of crosslinked material *able to flow, fully relax, and heal*[21]. Vitrimers have been described as a covalent adaptable network that can rearrange its topology via exchange reaction without

depolymerization. Hence, according to Bowman and coworkers' definition, vitrimers follow an "associative" mechanism, showing healing properties[22]. In other words, vitrimers *show a permanent connectivity at all temperatures*. Nonetheless, more recently, it has been found that vitrimers could also pursue a "dissociative" mechanism during the re-forming bond process[23, 24]. The nature of the mechanism associative/dissociative in vitrimer materials has drawn many research groups' attention, and diverse works have launched new debates about vitrimer definition as a result of new interesting observations[25, 26].

In addition to the glass transition temperature (*T*g), or melting temperature (*T*m), vitrimer materials may have a different transition temperature called *T*v *or topology freezing temperature*. This *T*v derives from the chemical exchange mechanism, being *the temperature* at which these *exchanges become significant* for a rearrangement of the topology of the material.

Furthermore, in an Angell fragility plot, the thermal behavior of vitrimers displays a progressive viscosity variation as a function of the temperature like vitreous silica[27]. This variation follows Arrhenius law, like vitreous silica materials and not William-Landel-Ferry law (WLF) like other polymers whose viscosity varies brusquely near the glass transition temperature. One way to explore the viscosity variation of vitrimers is via dynamic mechanical analyses. The stress relaxation analysis allows the determination of the characteristic relaxation time (λ) at different temperatures by using the Maxwell model. Then, plotting λ against 1/T to prove the Arrhenian-like behavior, and to determine the activation energy and the topology freezing temperature of the vitrimer material[21,28,29].

Maxwell's constitutive model is the most recurrent method to describe the relaxation behavior of a wide list of polymer materials, including vitrimers. However, the truth is that the Maxwell model does not correctly describe the stress relaxation of reals materials, including the vitrimers, which display a very complex viscoelastic behavior. Indeed, different vitrimers may require different models to describe their behavior more accurately. Therefore, new models and characterization methods have emerged to fill this gap, providing a more accurate description of their viscoelastic behavior and new methods to determine their activation energy [23, 30, 31, 32, 33, 34, 35].

From the first vitrimer based on transesterification, the list of new vitrimers systems with different chemistries such as trans carbonation[36], transamination of vinylogous urethanes[28, 37, 38], transamination of imines[39, 40], boronic ester exchange[41, 42], olefin metathesis[43, 44], disulfide exchange[45, 46], transalkylation of sulfonium salts[47, 48], silyl ether exchange[49, 50], among others grows day by day. Consistent with this view, Odriozola and coworkers presented a new epoxy vitrimer

without catalyst, possessing good mechanical properties with solving processability, reparability, and recyclability of thermosets materials. This *new epoxy vitrimer* was prepared by mixing diglycidyl ether of bisphenol A (DGEBA) with the dynamic hardener 4-aminophenyl disulfide (4-APDS) *containing aromatic disulfides.* Besides, this new thermoset exhibits an Arrhenian behavior and self-healing properties. According to Ruipérez *et al.*, the bonding reformation *mechanism* proceeds *via* a radical-mediated [2+1] mechanism[51] , i.e., *an associative/dissociative* exchange reaction. Hence, the system was considered as a vitrimer according to the definition[22].

Vitrimers works based on transesterification or transamination chemistry have shown the modulation of the covalent exchange kinetic by introducing different catalysts and at different concentrations to tune the viscoelastic behavior[20, 37]. These findings may pave the way toward tuning the viscoelastic behavior of vitrimers without catalysts. This way consists in varying the dynamic agent in the network, like in the epoxy vitrimer containing dynamic hardeners. Different research groups have explored the system DGEBA–4-APDS separately; both described different viscoelastic behaviors by using different dynamic hardener concentrations[45, 52]. Consequently, it can be assumed that the hardener concentration plays a crucial role in tuning the viscoelastic behavior of the vitrimer and modifying the thermo- mechanical properties of the epoxy-based resins.

3.2 Objectives

3.2.1 General objective

The main objective of this Chapter is to evidence the vitrimer behavior of the DGEBA–4-APDS system varying the quantity of added hardener. The classical characterizations described in the literature are employed, and a new approach to interpret the complex viscoelastic behavior of this system is studied. The hardener concentration leads to the presence of adaptable covalent bonds in the vitrimer system. Hence, the hardener concentration plays an essential role in relaxation and network structuration to achieve good mechanical and thermal properties.

3.2.2 Particular objectives

- To optimize the curing cycle of three different epoxy vitrimer resins based on an epoxy prepolymer EPON 828 (DGEBA) and a hardener 4-aminophenyl disulfide (4-APDS). The difference between these three systems is the amine/epoxy stoichiometric ratio, $r = \frac{amine\ equivalent}{epoxy\ equivalent}$. The hardener will be in excess when r=1.2, in scarcity when r=0.8, and in balanced stoichiometric when r=1.
- To determine the thermal and the thermomechanical properties of the three epoxy vitrimers elaborated at different amine/epoxy ratios.
- To evidence and evaluate the vitrimer properties (permanent connectivity, ability to flow and fully relax, and the presence of two different relaxation temperatures) of the three different DGEBA–4-APDS stoichiometry systems.
- To discuss and propose an adapted relaxation model able to describe more accurately the viscoelasticity behavior of the DGEBA–4-APDS systems at different amine-epoxy ratios.

3.3 Experimental section

The epoxy vitrimer samples were prepared by mixing DGEBA and 4-APDS at 60 °C. The resulting viscous homogeneous liquid was cast into silicon molds and cured in an oven following a temperature ramp under different conditions. Three different samples were prepared by varying the amine among used, DGEBA–4-APDS r=1, DGEBA–4-APDS r=0.8, and DGEBA–4-APDS r=1.2, where r is $r=\frac{4*\ n_{amine}}{2*\ n_{epoxy}}$.

Where n is the number of moles (the 4 is due to the number of functional reactive sites of the amine 4-APDS, and 2 for the epoxy reactive sites of DGEBA).

Different curing cycles were performed to determine the optimal conditions to reach the maximal

Tg for each system. The different curing cycles are described in **Table III-1**.

Amine/epoxy ratio	Curing cycle	Curing cycle condition
r=1	DGEBA–4-APDS r=1**a**	**80 °C/1h + 120°C/2h + 150°C/2h**
	DGEBA–4-APDS r=1**b**	**25°C/1h + 50°C/1h + 75°C/45 min + 110°C/30min**
	DGEBA–4-APDS r=1**c**	**80 °C/1h + 130°C/2h + 150°C/2h + 180°C/1h vacuum**
	DGEBA–4-APDS r=1**d**	**60 °C/1h + 80 °C/1h + 130°C/2h + 150°C/2h + 180°C/1h vacuum**
r=0.8	DGEBA–4-APDS r=0.8**a**	**60 °C/1h + 80 °C/1h + 130°C/2h + 150°C/2h + 180°C/1h vacuum**
	DGEBA–4-APDS r=0.8**b**	**60 °C/1h + 80 °C/1h + 130°C/2h + 150°C/2h + 180°C/4h vacuum**
	DGEBA–4-APDS r=0.8**c**	**60 °C/1h + 80 °C/1h + 130°C/2h + 150°C/2h + 180°C/4h under Ar**
r=1.2	DGEBA–4-APDS r=1.2**a**	**60 °C/1h + 80 °C/1h + 130°C/2h + 150°C/2h + 180°C/1h vacuum**
	DGEBA–4-APDS r=1.2**b**	**60 °C/1h + 80 °C/1h + 130°C/2h + 150°C/2h + 180°C/4h vacuum**
	DGEBA–4-APDS r=1.2**c**	**60 °C/1h + 80 °C/1h + 130°C/2h + 150°C/2h + 180°C/4h under Ar**

Table III-1. Different curing conditions performed for the different stoichiometries of the DGEBA-4-APDS resin.

The thermo-mechanical properties were studied by carrying out a dynamic ramp temperature in a DMA Q800 TA instrument, determining the storage modulus (E') at 30°C and in the rubbery plateau at T=*Tg*+30°C, the mechanical damping factor (tan δ) and to calculate the crosslink density (ρ) of the different samples.

The present Chapter is divided in three main parts. The first explores different curing cycles to achieve a highest *Tg* to then evaluate the thermo-mechanical properties of the epoxy resins performed at different stoichiometry ratios.

In the second part of this Chapter, the vitrimer properties of the networks are evidenced. Properties such as: 1) the permanent connectivity, 2) the presence of another transition temperature (*Tv*) in addition to the *Tg* or *Tm*, and 3) the fully relaxation of the network and its ability to flow which leads to a rearrangement of its topology controlled by the exchange reaction kinetics (it viscosity follows an Arrhenian behavior).

In the third part of this Chapter, the data of the stress relaxation experiments obtained at different stoichiometric ratios in a temperature range from 180 to 220°C invites to propose a more adapted model able to describe the complex relaxation behavior of the epoxy vitrimer DGEBA–4-APDS. Inspired by the work of Torkelson *et al.*[31] and Yu *et al.*[30], the model explored suggest the use of stretched exponential decays and two main relaxation branches. The proposed model considers a

first relaxation branch induced by the bond exchange reactions (BER) and a second relaxation branch linked to the polymer network segmental motions.

3.4 Characterization results and discussion

3.4.1 Curing cycle optimization

In the literature, two different curing cycles for the epoxy vitrimer DGEBA–4-APDS systems were found, and both deal with different stoichiometric ratios (**Figure III-1**). These differences make it challenging to establish which process is the best. Thus, the first aim of this section work was to optimize the curing cycles of DGEBA–4-APDS for the three explored stoichiometries.

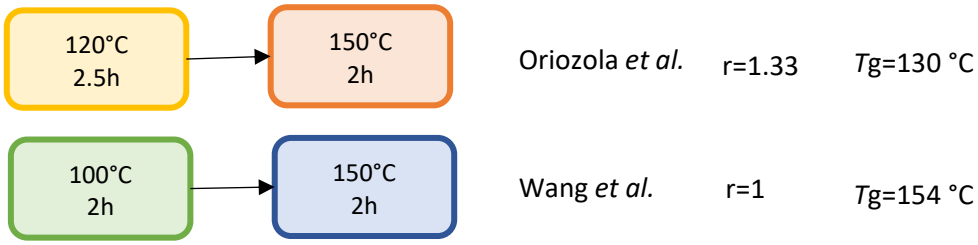

Figure III-1. Curing cycle performed by Odriozola *et al.* and Wang *et al.* by using different stoichiometric ratios of DGEBA and 4-APDS.

However, the chemical structure of 4-APDS is quite similar to another hardener widely studied with DGEBA prepolymer, the 4,4'-diaminodiphenylmethane, DDM (**Scheme III-1**). Mondragon *et al.* performed an interesting study on the importance of the correct curing conditions to obtain the optimal properties for the DGEBA-DDM system[53]. The highest mechanical properties of the epoxy resin are achieved at the highest curing rate, which in turn, is associated with a high *Tg*[54, 55, 56].

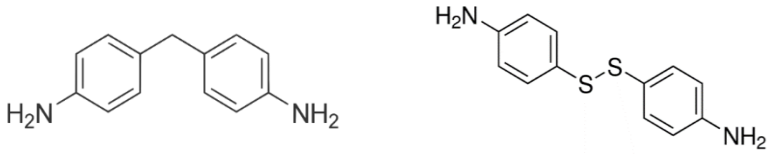

DDM 4-APDS

Scheme III-1. Chemical structure of 4,4'-diaminodiphenylmethane (DDM) and 4-aminophenyl disulfide (4-APDS).

Differential Scanning Calorimetry (DSC) experiments were performed to determine which curing cycle allows achieving the maximal *Tg* to guarantee, as much as possible, a complete curing, hence, good mechanical properties. Two consecutive temperature ramps were carried out to evaluate a possible post-curing during the first cycle and to authenticate the *Tg* value on the second ramp.

- *DGEBA–4-APDS **r=1a**, 80°C/1h, 120°C/2h, and 150°C/2h;*
- *DGEBA–4-APDS **r=1b**, 25°C/1h, 50°C/1h, 75°C/45min, 110°C/30 min.*

The curing cycle **r=1a** and **r=1b,** proposed for the system DGEBA–4-APDS r=1, are inspired by two quite different approaches. The curing cycle **r=1a** considers the references of **Figure III-1**[45, 52]. The curing cycle **r=1b** performs a slow curing cycle inspired by a previous work based on the system DGEBA-DDM at different amine/epoxy ratios. The cycle **r=1b** explores a gradual temperature ramp to promote a high organizing degree of the network structure due to the long gelation stage[57].

The epoxy cured following the cycle **r=1a** displays a *T*g around 161°C in both cycles carried out, while the epoxy cured with cycle **r=1b** displays two different *T*g. The first ramp of cycle **r=1b** displays a *T*g at 138 °C, and the second ramp a *T*g at 161 °C. This difference on cycle **r=1b** indicates a post-curing process during the first temperature ramp of the DSC experiment (**Figure III-2**). Although the curing cycle **r=1b** considers multiples stages at low temperatures to reduce the thermal stresses, the cycle does not offer a complete curing process. This behavior might be related to the duration of the different steps of the curing cycle. The step at high temperature is not long enough to achieve a complete curing. For this reason, the cycle **r=1a** which offers longer curing times at high temperatures was retained.

- *DGEBA–4-APDS **r=1c**, 80°C/1h, 130°C/2h, 150°C/2h, and 180°C/1h under vacuum.*

In previous work, Ochi *et al.* have shown the importance of a post-curing temperature to guarantee a complete reaction[58]. Thus, a third curing cycle (DGEBA–4-APDS **r=1c**) was proposed based on the curing cycle **r=1a** and considering Ochi *et al.* observations. The post-curing stage under vacuum and a slow cooling process from 150°C to room temperature to avoid thermal stresses were added to the cycle. The post-curing step was performed under vacuum to prevent as much as possible the oxidation phenomenon of the sample. The *T*g of curing cycle **r=1c** was of 164°C, an increase of 3°C compared to cycle **r=1a**.

- *DGEBA–4-APDS **r=1d**, 60°C/1h, 80°C/1h, 130°C/2h, 150°C/2h, and 180°C/1h under vacuum.*

A fourth curing cycle was also proposed by increasing the gelation time process of the cycle **r=1c.** A pre-heat step (60°C/1h) was added to promote a high cured density and avoid the possible residual thermal stresses [59, 60]. The *T*g of curing cycle **r=1d** was 167°C, displaying a minor increase on the glass transition temperature.

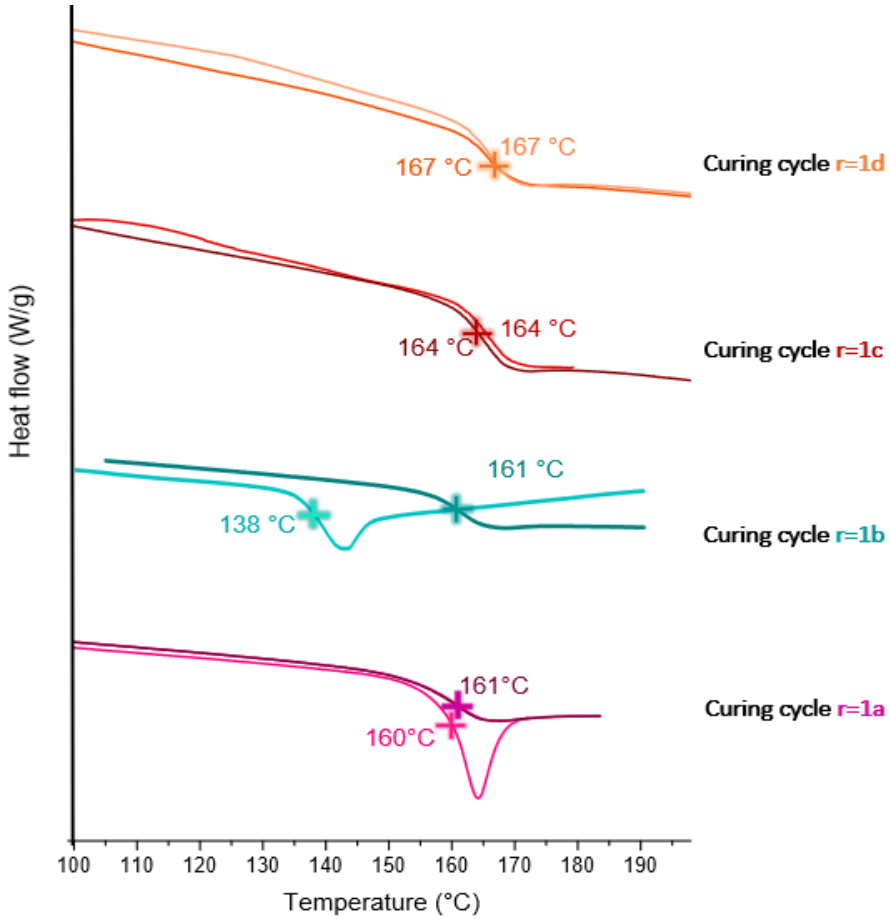

Figure III-2. DSC curves of DGEBA– 4-APDS resin r=1 prepared according to different curing cycles, r=1a (pink), r=1 (bleu), r=1c (red), and r=1d (orange). The light color represents the first temperature ramp, the dark color the second temperature ramp. The values of *Tg* are determined at mid-point on DSC curves.

The curing cycle **r=1d**, which considers a slow ramp temperature, and a post-curing stage was selected as the optimal curing cycle. A gradual temperature ramp allows the network structure to organize during the gelation stage, promoting a high cured density.

Furthermore, the samples were analyzed by FTIR spectroscopy. **Figure III-3** shows the FTIR spectra of the different DGEBA–4-APDS epoxy resins. The spectra were normalized by taking the band linked to aromatics at 830 cm^{-1} as a reference[61, 62, 63].

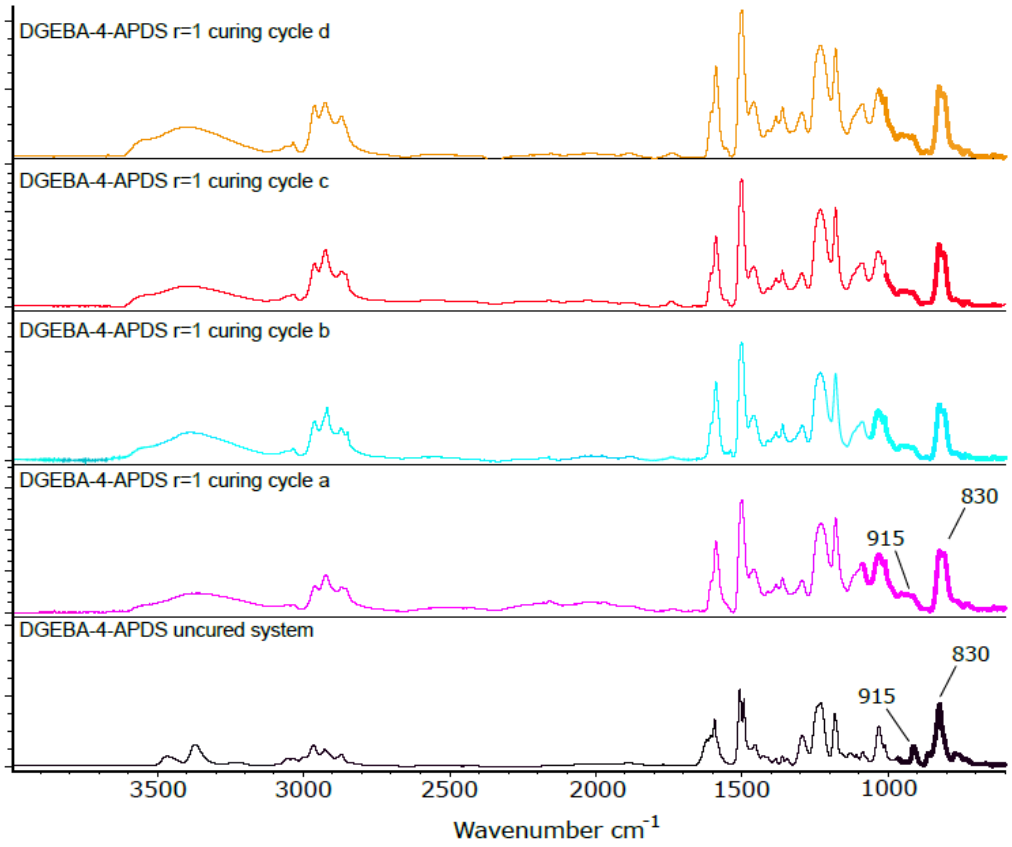

Figure III-3. FTIR spectra of uncured DGEBA-4-APDS system r=1 (black) and DGEBA-4-APDS systems cured according to the four curing cycles proposed. Cycles r=1a (pink), r=1b (bleu), r=1c (red), r=1d (orange).

The main studied signal in the spectra corresponds to the oxirane absorption band at 915 cm^{-1}, which is easy to observe in the uncured spectrum of the epoxy resin DGEBA–4-APDS. The FTIR spectra of four cured systems show a vanishing of the band at 915 cm^{-1}, even for the sample cured under the conditions **r=1b**. Although FTIR is a valuable tool to characterize the polymer and epoxy resins, in this case, it is not enough precise to determine the complete curing. Indeed, the determination of the *Tg* has shown to be more sensitive than the characterization of free functional groups using IR spectroscopy[64].

For the system rich in epoxy (DGEBA–4-APDS r=0.8), the first explored curing cycle was the optimal one of the systems at amine/epoxy ratio equal to 1 (DGEBA–4-APDS **r=0.8a**). Two consecutive temperature ramps were carried out on the DSC experiment to apprehend any possible post-curing during the first ramp (**Figure III-4**).

- *DGEBA–4-APDS **r=0.8a**, 60°C/1h, 80°C/1h, 130°C/2h, 150°C/2h, and 180°C/1h under vacuum.*

The DSC analysis of the system obtained with the curing cycle **r=0.8a** revelated a *Tg* of 144 °C in the first cycle and a *Tg* of 149°C in the second cycle. This behavior evidenced a post-curing reaction during the first DSC cycle, suggesting that the network was not completely cured under these conditions.

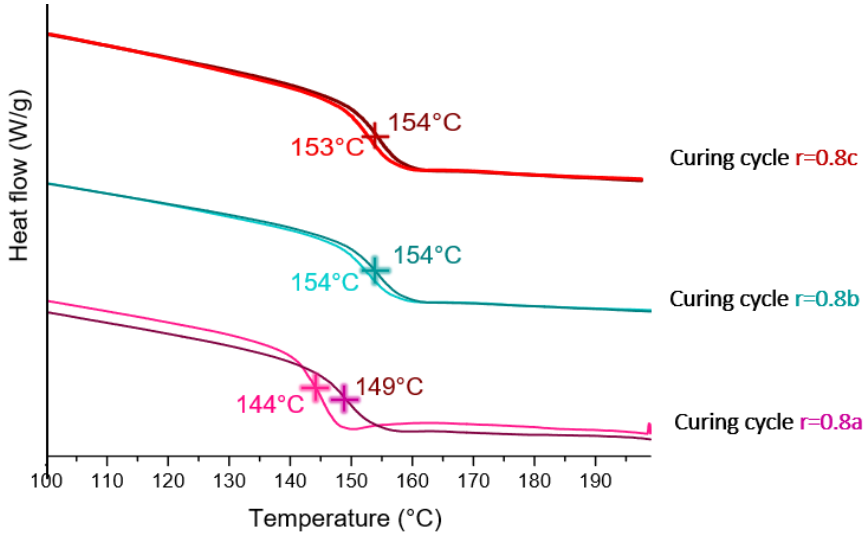

Figure III-4. DSC curves of DGEBA-4-APDS systems r=0.8 prepared according to three curing cycles explored, r=0.8a (pink), r=0.8b (bleu), and r=0.8c (red). The light color curves correspond to the first temperature ramp and the dark color to the second one. The *Tg* values were determined at mid-point on DSC curves.

In the light of this information, a longer post-curing seemed necessary to achieve the maximal *Tg* for the DGEBA–4-APDS system r=0.8.

- *DGEBA–4-APDS **r=0.8b**, 60°C/1h, 80°C/1h, 130°C/2h, 150°C/2h, and 180°C/4h under vacuum.*

The new curing cycle propose an increasement on the post-curing time (from 1h to 4h under vacuum conditions)**.** The DSC results of this new cycle displayed in **Figure III-4** reveal two consecutive cycles almost overlapped, with a maximal *Tg* at 154°C.

- *DGEBA–4-APDS **r=0.8c**, 60°C/1h, 80°C/1h, 130°C/2h, 150°C/2h, and 180°C/4h under Ar.*

A third curing cycle, DGEBA–4-APDS **r=0.8c**, was also proposed by only changing the atmosphere condition for an inert atmosphere with Argon during the post-curing stage. No change was remarked, obtaining a *Tg*=154 °C.

FTIR studies were also carried out to verify the complete curing of samples by evaluating the fading of the oxirane absorption band at 915 cm^{-1}. Results are displayed in **Figure S.III- 1** in the annex of Chapter III.

The optimal curing conditions for the system rich in amine (DGEBA–4-APDS r=1.2) were also explored. Two consecutive ramps were carried out in DSC to verify the complete curing.

- *DGEBA–4-APDS **r=1.2a**, 60°C/1h, 80°C/1h, 130°C/2h, 150°C/2h, and 180°C/1h under vacuum.*

The first cycle explored was optimal for the system in stoichiometry. The reached *T*g was 141°C (**Figure III-5**). Nonetheless, based on the precedent sample's experience, a longer post-curing, from 1 to 4h, was carried out to observe the change in *T*g.

- *DGEBA–4-APDS **r=1.2b**, 60°C/1h, 80°C/1h, 130°C/2h, 150°C/2h, and 180°C/4h under vacuum.*

The DSC curves of this cycle**,** with a longer post-curing time, display a minor increase of 2°C (*T*g=143°C) than the curing cycle **r=1.2a**, suggesting a higher curing.

- *DGEBA–4-APDS **r=1.2c**, 60°C/1h, 80°C/1h, 130°C/2h, 150°C/2h, and 180°C/4h under Ar.*

A different curing cycle was explored by changing the post-curing conditions from 4h under constant vacuum to 4h under an inert atmosphere of Ar. This consideration was examined under the premise that the unreacted amines inside the matrix could be removed if the system is under a constant vacuum. The result revealed an increase of the *T*g from 143°C to 149°C.

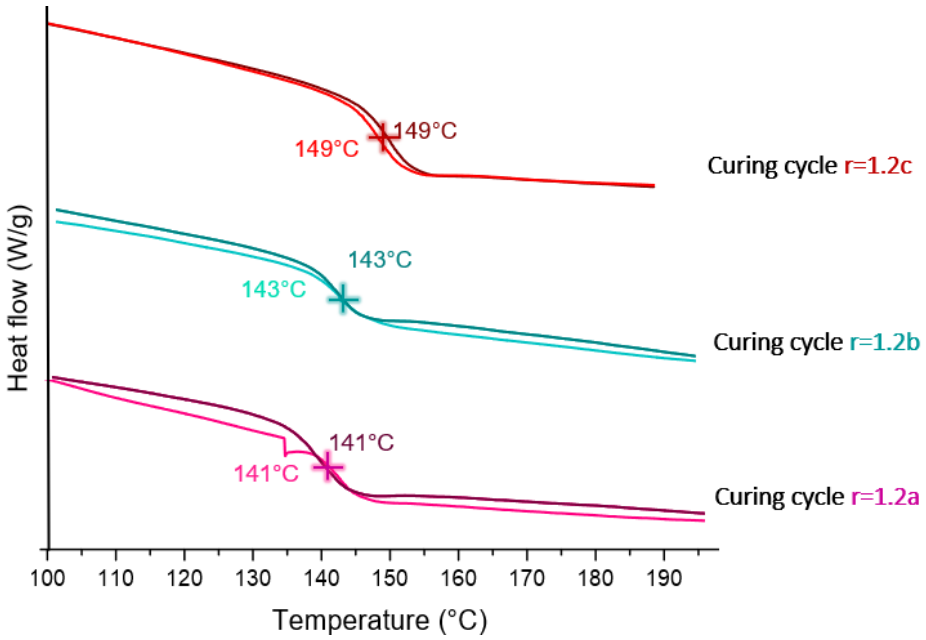

Figure III-5. DSC curves of DGEBA–4-APDS systems r=1.2 prepared according to three curing cycles explored, r=1.2a (pink), r=1.2b (bleu), and r=1.2c (red). The light color curves correspond to the first temperature ramp and the dark color correspond to the second one. The values of *T*g are determined at mid-point on DSC curves.

As for the two precedent systems, FTIR studies were carried out to corroborate the complete curing. The results are displayed in **Figure S.III- 2** in the annex of Chapter III.

In this first part, an optimal curing cycle for the three systems was established. **Table III-2** summarizes the *Tg* values measured for each explored curing cycle and the degradation temperature for the best curing cycle. Like in other systems, it is possible to remark that the highest *Tg* is achieved in the stoichiometric ratio (r=1)[65]. Based on this information, it can be concluded the following statements:

- In the system where the amine and epoxy functions are in stoichiometry (r=1), the best curing cycle was the **r=1d**, **60 °C/1h + 80 °C/1h + 130°C/2h + 150°C/2h + 180°C/1h vacuum**. The curing cycle performs a gradual increase of temperature and a post-curing stage at a temperature superior to the *Tg*.

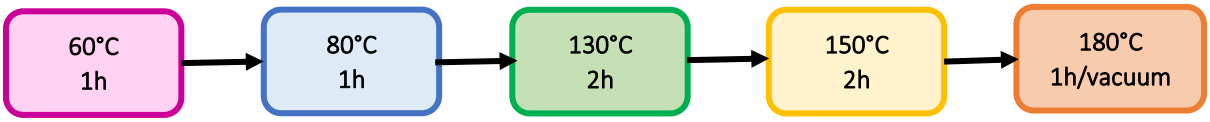

- In the system where the amine functions were in scarcity (r=0.8), the best curing cycle was the **r=0.8b**, **60 °C/1h + 80 °C/1h + 130°C/2h + 150°C/2h + 180°C/4h vacuum.** A longer post-curing stage promoted a high conversion of oxiranes groups present in this system. The effect of an inert atmosphere or the exposition of the sample to vacuum does not present an important factor for reaching the maximal *Tg*.

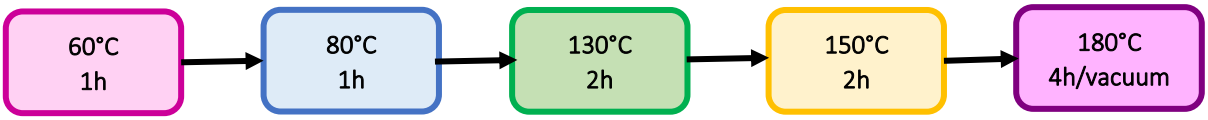

- In the system where the amine was in excess (r=1.2), the best curing cycle was the **r=1.2*c*, 60 °C/1h + 80 °C/1h + 130°C/2h + 150°C/2h + 180°C/4h under Ar**. The longer post-curing stage helped to reach a high conversion. The results showed the importance to do not disturb the post-curing conditions with vacuum, since the amines in excess may migrate to the surface and be eliminated by the vacuum effect, and so changing the thermal properties. This fact may perturb the mechanical and vitrimer behavior since the hardener employed for this system possesses a covalent bond of a broad interest in this work.

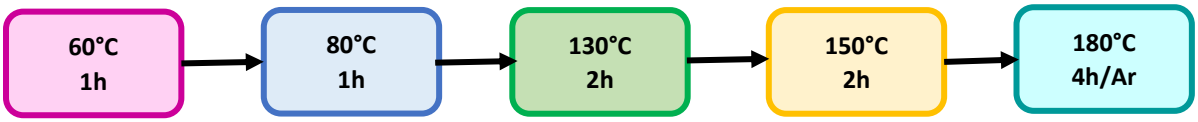

System	Curing cycle	*Tg* (°C)	Degradation temperature (°C)
DGEBA–4-APDS r=1	DGEBA–4-APDS r=1**a**	161 ± 1	
	DGEBA–4-APDS r=1**b**	145 ± 9	
	DGEBA–4-APDS r=1**c**	164 ± 2	
	DGEBA–4-APDS r=1**d**	167 ± 1	359 ± 1
DGEBA–4-APDS r=0.8	DGEBA–4-APDS r=0.8**a**	144 / 149	
	DGEBA–4-APDS r=0.8**b**	155 ± 1	364 ± 1
	DGEBA–4-APDS r=0.8**c**	154 ± 2	
DGEBA–4-APDS r=1.2	DGEBA–4-APDS r=1.2**a**	142	
	DGEBA–4-APDS r=1.2**b**	143 ±1	
	DGEBA–4-APDS r=1.2**c**	148 ± 1	360 ± 4
DGEBA-DDM r=1	DGEBA–4-APDS r=1**d**	177 ± 1	396 ± 2

Table III-2. Glass transition temperatures (*Tg*) and degradation temperature values achieved from the different curing cycles explored for the three different ratios amine/epoxy of the system DGEBA–4-APDS. In this table, a reference without dynamic bonds DGEBA-DDM is also presented. TGA curves are summarized in the annex of Chapter III (Figure S-III-3).

3.4.2 Thermo-mechanical performance

The thermo-mechanical properties of DGEBA–4-APDS systems are strongly linked to their maximal glass transition temperature *Tg*. Therefore, once the optimum curing cycles of epoxy resins were established, the thermo-mechanical properties can be determined easily by carrying out a dynamic temperature ramp with DMA, as shown in **Figure III-6, Figure III-7**, and Figure III-8.

Figure III-6 displays the samples of DGEBA–4-APDS and DGEBA-DDM, both at amine/epoxy stoichiometry ratios. Both samples' storage modulus are quite similar, 2.6 GPa for the DGEBA–4-APDS and 2.7 GPa for the DGEBA-DDM system. These results indicate that using a dynamic hardener (4-APDS) might confer the same mechanical properties as a network cured with a non-dynamic hardener (DDM). Similar behavior is observed for the *Tα*; both values are quite similar, 170 °C and 176 °C for the sample with dynamic and no dynamic hardener, respectively. The E' at the rubbery plateau of the systems with and without dynamic bonds are quite similar. The first displays a modulus of 268 MPa, and the second of 225 MPa.

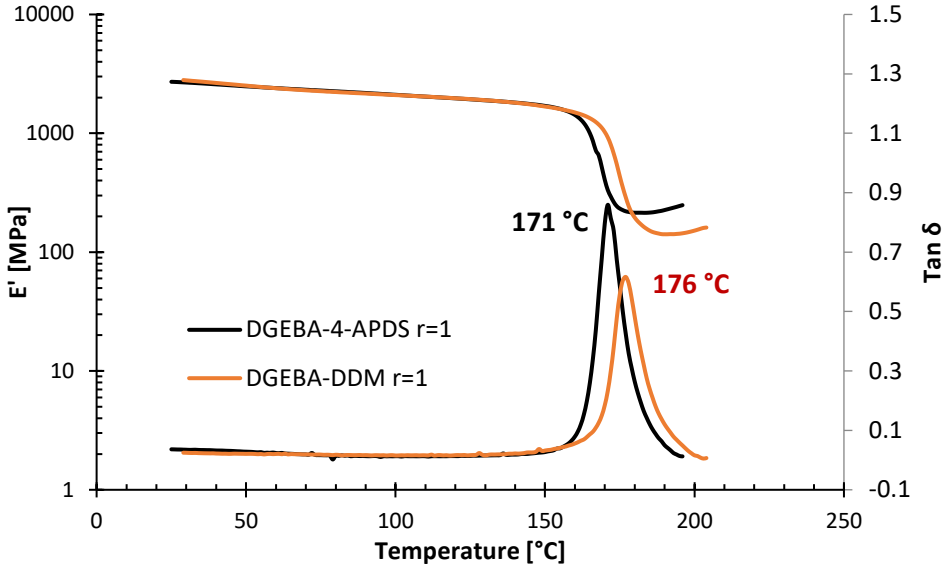

Figure III-6. Storage Modulus (E') and damping factor (tan δ) as a function of the temperature of DGEBA–4-APDS (black) and DGEBA-DDM (red). The amine/epoxy ratio for both systems is equal to 1.

Figure III-7 displays the storage modulus of DGEBA–4-APDS systems at different stoichiometry ratios. The higher storage modulus was for the system in stoichiometry (DGEBA–4-APDS r=1) with a storage modulus of 2.7 GPa. For the systems rich in amine (DGEBA–4-APDS r=1.2), a similar storage modulus was registered, 2.6 GPa and the lower value at 2.3 GPa corresponds to the system rich in epoxy (DGEBA–4-APDS r=0.8). The results are consistent with the literature where the highest storage modulus is obtained for systems in stoichiometry (r=1) [53, 66]. The systems rich in epoxy presented undoubtedly the lowest strength. This is due to the network's imperfections like holes or uncrosslinked chain-ends. These phenomena are also present for the systems rich in amine but to a lesser extent, so that, the storage modulus is less impacted.

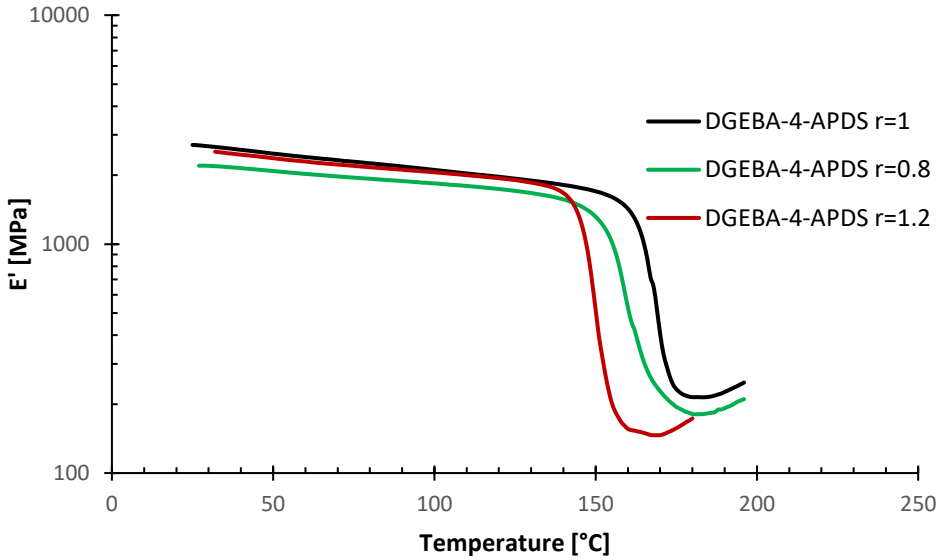

Figure III-7. Storage Modulus (E') as a function of the temperature of DGEBA-4-APDS systems at amine/epoxy ratio of 1 (black), 0.8 (green), and 1.2 (red)[†].

Figure III-8 displays the α-relaxation of all systems cured with 4-APDS. The α-relaxation is associated with the thermal history of samples during the curing cycle and its breadth with the heterogeneity of the network. These two facts suggest a lower crosslink density network commonly observed in literature for off-stoichiometry systems[68, 67].

The following equation (1) derived from the rubberlike elasticity theory can be used to determine the crosslinking density[68].

$$\rho = \frac{G_r}{3RT} \quad \text{(1)}$$

Where ρ is the crosslink density, G_r is the rubber modulus at T=*T*g+30°C.

[†] The increase of the modulus in the rubbery plateau is linked to an artefact derived from the dimensions of the analyzed samples (a thickness of about 0.7mm). At the end of the test, at high temperatures, the deformation becomes relevant, modifying sample dimensions. Thus, an increase of the storage modulus is recorded. This phenomenon is not only observed for the systems with dynamic bonds, but also for the system without dynamic bonds as shown in **Figure III-6**. To verify the constant behavior of the rubbery plateau, an analysis in tension mode was performed (**Figure S.III-4**). The tests under tension allowed to reduce the deformation during the time. The results showed a constant behavior of the modulus at the rubbery plateau. The evaluation of E' and E" in tension mode were not explored in detail in the present work because of the experimental difficulties to obtain homogeneous samples for numerous required analyses for the stress relaxation study as explored in section 3.4.3.3.

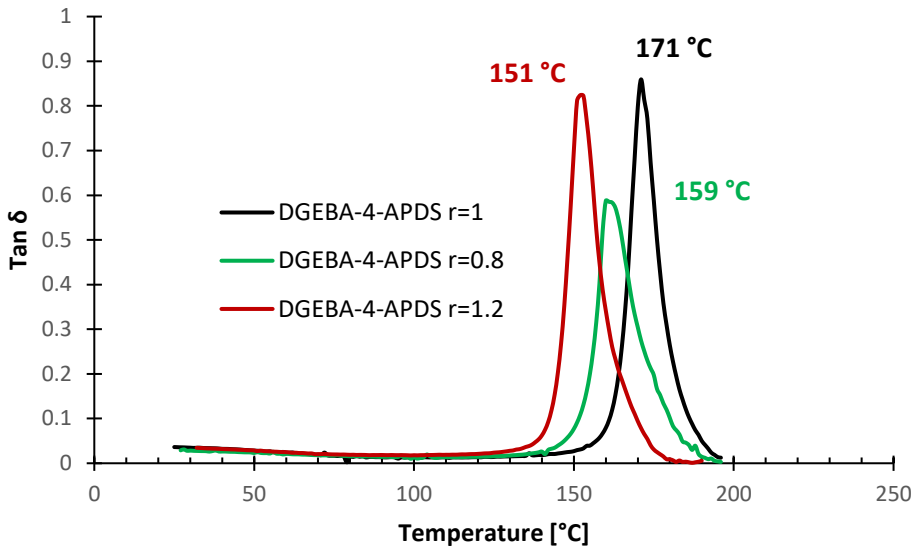

Figure III-8. Damping factor (tan δ) of DGEBA-4-APDS systems at amine/epoxy ratio of 1 (black), 0.8 (green) and 1.2 (red).

The crosslink densities have been calculated and presented in **Table III-3**. The results show that the crosslink density decreases for non-stoichiometric ratio systems (1.48E+04 mol/m^3) compared to the stoichiometric one (2.29E+04 mol/m^3). These results are consistent with those obtained by Mondragon and coworkers[68, 69]. The elaborated DEGBA–4-APDS r=1 displays the highest crosslink density, followed by the system rich in amine (r=1.2) and finally by the system rich in epoxy (r=0.8). In both last cases, the network architecture is altered. In the first case (r=0.8), the alteration of the structure is due to the etherification and homopolymerization of the prepolymer, i.e., the hydroxyl groups react with an oxirane ring[69, 70]. The epoxide condensation is promoted during the gelation and post-curing process. In the second case (r=1.2), the network will always contain a significant number of unreacted species and a large percentage of the softer phase[71].

Table III-3 summarizes the storage modulus (E'), the α-relaxation (Tα), and the crosslink density (ρ) of different studied systems.

System	E' at 30°C (MPa)	E_r' at *T*g + 30°C (MPa)	*T*α (°C)	ρ (mol/m³)
DGEBA-4-APDS r=0.8	2261 ± 100	219 ± 34	159 ± 3	1.92E+04
DGEBA-4-APDS r=1	2681 ± 121	268 ± 98	171 ± 3	2.29E+04
DGEBA-4-APDS r=1.2	2574 ± 97	166 ± 26	151 ± 1	1.48E+04
DGEBA-DDM r=1	2692 ± 144	225 ± 82	176 ± 1	1.88E+04

Table III-3. Values of storage modulus (E') at 30°C and at *T*g + 30°C, and of *T*α and the crosslink density at *T*g + 30°C (ρ) of the different elaborated epoxy resins.

This small section shows that the thermo-mechanical properties of the system DGEBA–4-APDS, which uses a dynamic amine, do not seem to differ from the system without a dynamic hardener in the same amine/ epoxy stoichiometry ratio. Moreover, the non-stoichiometric systems have shown a significant rise in heterogeneity, which could be linked to a diminution of the crosslinked density[74].

3.4.3 Vitrimer characterization of DGEBA–4-APDS systems

According to the pioneering work of Leibler and coworkers, vitrimer materials can be defined by some criteria such as:

- permanent connectivity;
- the presence of a different transition temperature to the *T*g or *T*m;
- ability to flow and fully relax

Therefore, these criteria were explored to prove the vitrimer behavior of the elaborated epoxy vitrimer systems. First, vitrimers are permanent networks with permanent connectivity at all temperatures. Therefore, in according with Du Prez *et al.* (2016), these materials swell but do not dissolve in chemically inert solvents. To prove this first criterion in DGEBA–4-APDS systems, swelling tests and frequency sweep experiments are performed.

Second, vitrimers present a new transition temperature the *T*v. The topology freezing temperature is associated with the rearrangement of the topology network derived from the chemical exchange mechanism of the network. Dilatometry analyses were carried out to evidence this new transition temperature.

Third, at temperatures superior to the *T*g, the vitrimers viscosity decreases by following the Arrhenius law, like typical inorganic silica materials. Stress relaxation experiments were recorded to evaluate the characteristic viscoelastic behavior of vitrimers materials.

3.4.3.1 Permanent connectivity: constant crosslink density

Swelling tests are the most common test to prove the permanent connectivity of vitrimer networks. Thus, three different solvents were used at room temperature and the fourth one at a high temperature. Nonetheless, in agreement with Leibler, Du Prez, and Winne (2019), finding the correct solvent to evidence the permanent connectivity of networks might be difficult[72]. A second characterization method is necessary to demonstrate this crucial behavior of a vitrimer material. For this reason, frequency sweep experiments were performed to confront the information achieved from the swelling test.

3.4.3.1.1 Swelling test

Inspired from the literature, four different solvents were employed: THF, a classical solvent used for the swelling test; DMF, a solvent which has proved to solubilize similar networks based on disulfide chemistry[73]; ethyl 2-mercaptopropionate (EMP), a reactive solvent that possesses a thiol group that might react with the disulfide bonds of the networks and alters the network structure; and 1,2,4-Trichlorobenzene, a solvent that allows proving the permanent connectivity at high temperatures[78]. The swelling test allows to evidence the permanent connectivity. It provides valuable information about the crosslink density and the soluble fraction of the network.

A swelling study was done using the first three solvents, the THF, DMF, and EMP. The tests were recorded at different times (1 day, 2 days, 3 days, and 1 week) at a controlled temperature of 25°C. The results are summarized in **Figure III-9**.

The following equations express the percentage of swelling and the sample soluble fraction.

$$Swelling\ (\%) = \frac{(m_w - m_0)}{m_0} x100 \quad \text{..... (2)}$$

$$Soluble\ fraction\ (\%) = \left[\frac{m_d}{m_0} - 1\right] x\ 100 \quad \text{..... (3)}$$

Where m_w is the swollen mass, m_0 is the initial mass, and m_d is the dry mass after the swelling test.

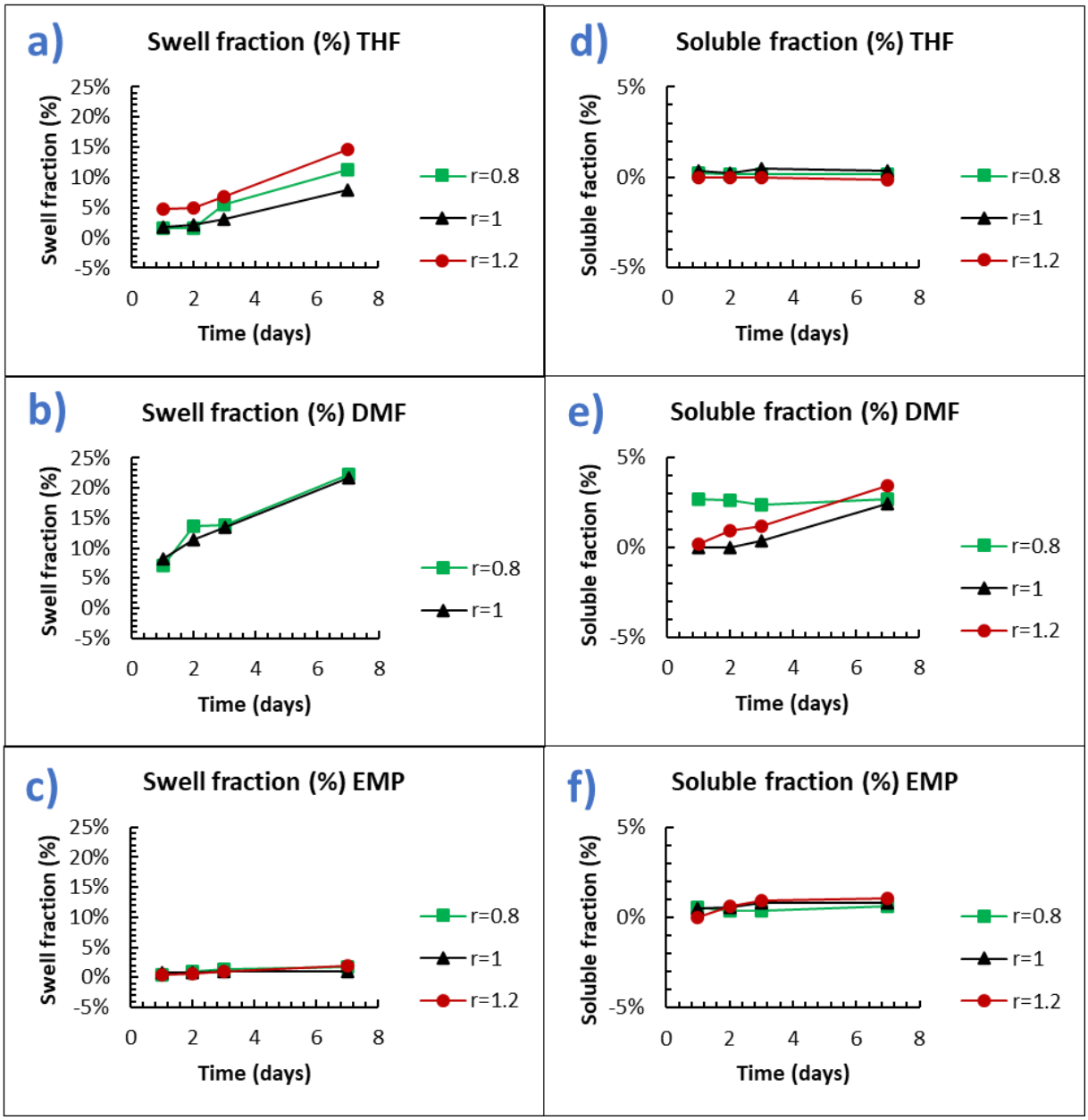

Figure III-9. Linear swelling percent and soluble fraction of DGEBA–4-APDS networks prepared with different amine/epoxy ratios in THF a) and d), DMF b) and e), and EMP c) and f).

Figure III-9a, b and **c** display a linear win of mass due to the swelling of the sample, while **Figure III-9d, e**, and **f** indicate the soluble fraction.

The results displayed in **Figure III-9a,** and **c** show that the three stoichiometry samples swell but do not dissolve as expected in a solvent as THF and in a reactive such as EMP. In both cases a slight weight loss was observed (less than 1% as **Figure III-9d,** and **f** show). Besides, the swelling show that the system DGEBA–4-APDS r=1.2 won more weight during the swelling, followed by the system

DGEBA–4-APDS r=0.8, and finally the system DGEBA–4-APDS r=1. This behavior has been observed for different systems[74] and is attributed to the crosslink density of the networks. The networks with high crosslink densities have a shorter distance between crosslink nodes[75], hence, the distance between the crosslink nodes of non-stoichiometric networks (r=0.8 and r=1.2) is expected to be higher, allowing a greater solvent diffusion and then a higher swelling ratio. The observation seen in **Figure III-9a,** and **c** go hand in hand with the results of section 3.4.2, where the non-stoichiometric systems showed lower crosslink densities than the stoichiometry system.

The swelling tests in DMF solvent followed a different pathway, displaying a loss of network integrity for the off-stoichiometry systems (**Figure III-10**). The system rich in dynamic bonds (DGEBA–4-APDS r=1.2) began to lose its connectivity from the second day of immersion (**Figure III-10a**), and the system in scarcity of dynamic bonds (DGEBA–4-APDS r=0.8) started to lose its connectivity after a week (**Figure III-10b**).The integrity loss of samples with ratios r=0.8 and r=1.2 in DMF might be explained by the low crosslink density of these samples and a selective scission of disulfide groups. The low crosslink density of the non-stoichiometric systems facilitates the deep penetration of solvents inside the matrix. Once the DMF penetrates, a selective scission of disulfide groups is initiated since DMF can act as a solvent and nucleophilic reagent[73 76, 77]. The network rich in amino groups, presenting a high concentration of disulfide bonds, loses its integrity network in a shorter time than the network in a deficit of disulfide bonds.

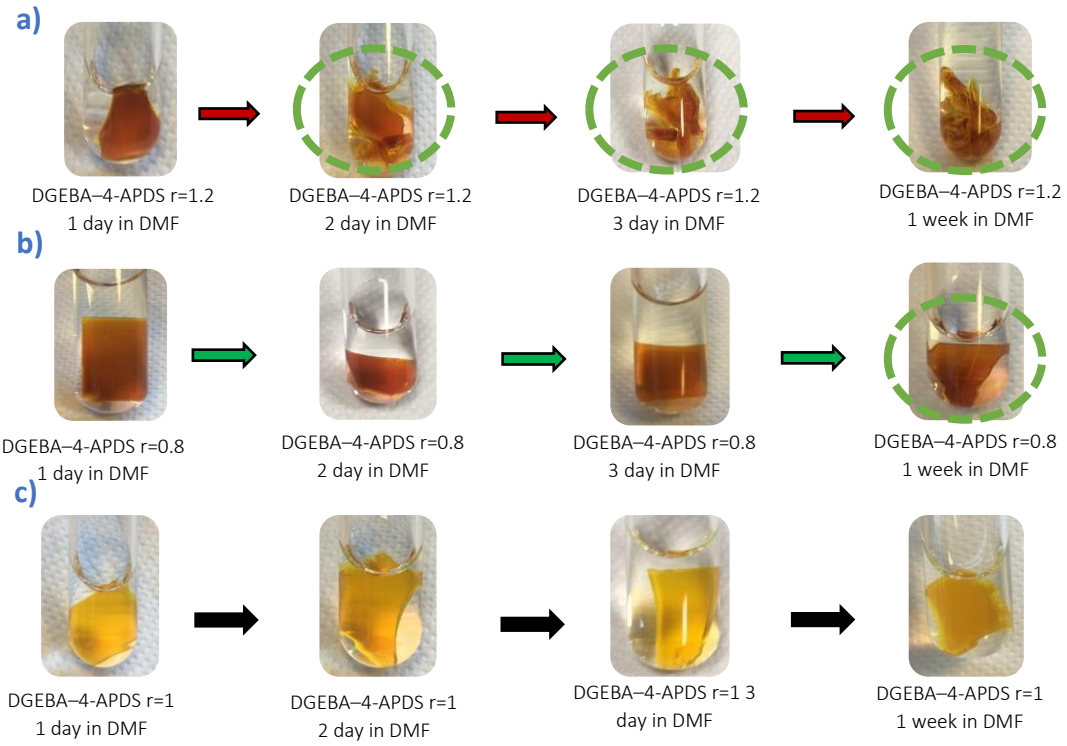

Figure III-10. Swelling tests throughout a week in DMF solvent of systems a) DGEBA-4-APDS r=1.2, b) r=0.8, and c) r=1.

The permanent connectivity was also tested at high temperatures, employing 1,2,4-trichlorobenzene as solvent at a high temperature (190°C) for 1 h. As shown in **Figure III-11**, no loss of connectivity was observed, but an important win of mass was recorded (**Figure III-12**), like for other vitrimer systems [78].

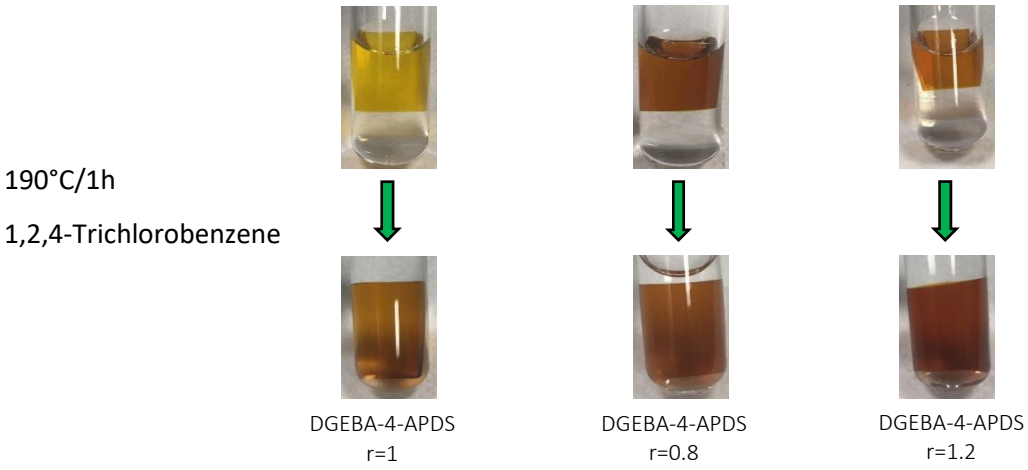

Figure III-11. Swelling test in 1,2,4-trichlorobenzene at 190 °C/1h of the DGEBA–4-APDS r=1, r=0.8, and r=1.2.

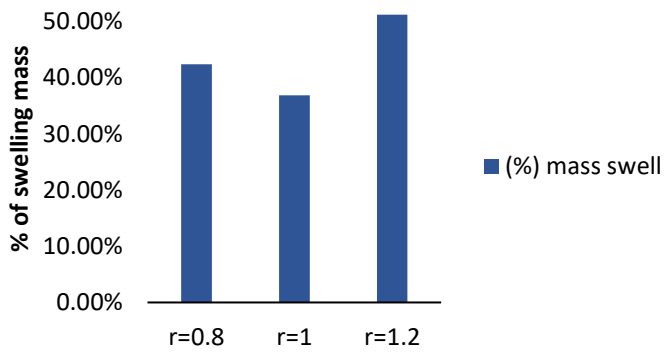

Figure III-12. Swelling mass won after samples' immersion in 1,2-4 trichlorobenzene for 1h.

The swelling tests allow proving the permanence of networks. Vitrimer materials swell but do not dissolve in good solvents, even after immersion at high temperature[22]. Nonetheless, the fact that the swelling tests are the unique method to determine the permanent connectivity of vitrimer materials, is quite questionable. For instance, many authors have specified the difficulties of finding a good solvent and conditions to evidence the permanent connectivity, hindering and slowing the task. Moreover, more recently Nicolaÿ and coworkers (2019) have shown how vitrimers can be dissolved in solvents such as THF under condition where the cross-links are dynamics, leading to inaccurate assessment of the actual crosslink density of vitrimers[26]. To overcome this issue, a different method to prove the permanent connectivity must be explored. Frequency sweep tests might be an option to evaluate this vitrimer criteria.

3.4.3.1.2 Frequency sweep

The constant crosslink density claimed for vitrimer materials can also be evidenced by studying the stability of storage modulus at different temperatures and frequencies[23,73 79, 80]. Frequency sweep experiments allow studying the crosslink density from another point of view. They were carried out at frequencies ranging from 30Hz to 0.01 Hz to test the network's permanence at different temperatures corresponding to the rubbery state (from 190 to 230°C). **Figure III-13** displays the frequency sweep analyses performed on the different samples of DGEBA–4-APDS and a reference sample without dynamic bonds (DGEBA-DDM r=1).

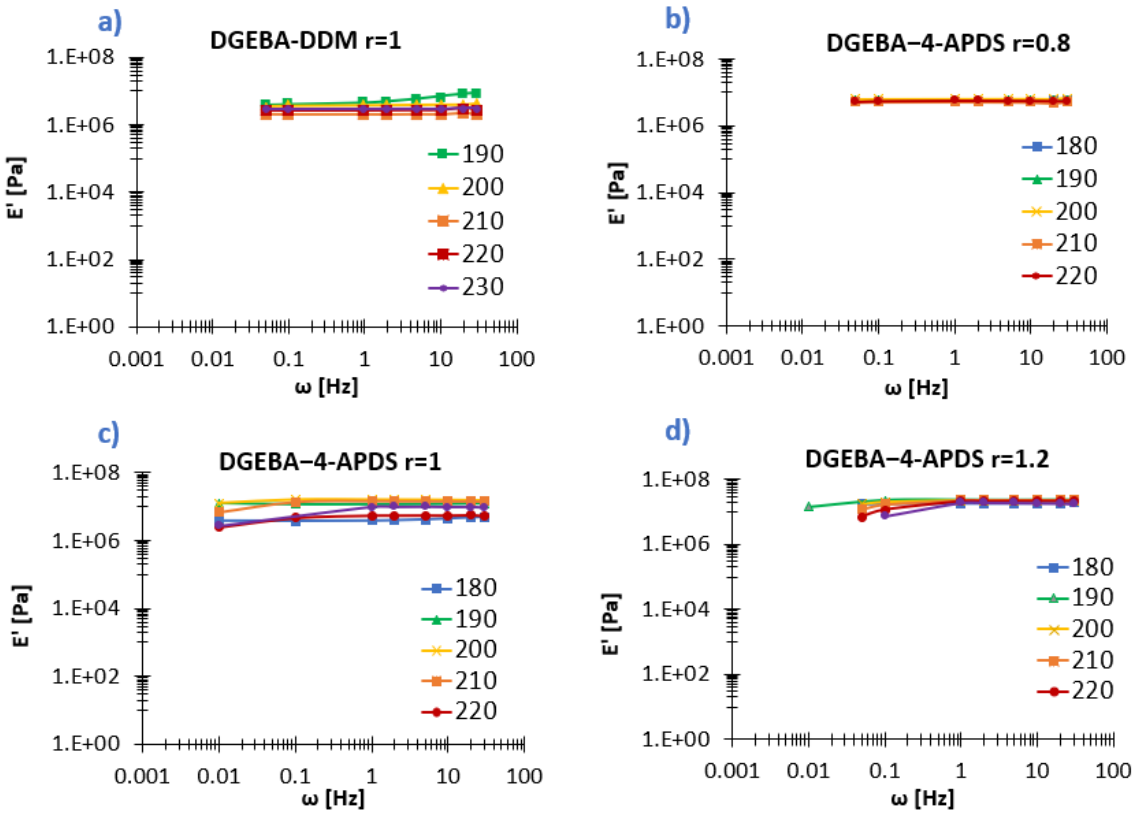

Figure III-13. Frequency sweep experiments of a DGEBA–4-APDS r=1, b) DGEBA–4-APDS r=1.2, c) DGEBA–4-APDS r=0.8, and d) DGEBA-DDM r=1 at different temperatures from 180 to 230 °C. The test was carried out from high to low frequencies[‡].

For the two systems DGEBA–4-APDS r=1 and r=1.2 (**Figure III-13c** and **d**, the elastic modulus seems independent of the frequency at the different temperatures, indicating permanent connectivity. Nonetheless, it must be noted that, at very low frequencies (0.05 Hz and 0.1 Hz), or long-timescale, the modulus is slightly reduced, suggesting a loss in connectivity at extreme conditions.

Furthermore, **Figure III-13b** corresponds to the DGEBA–4-APDS system r=0.8. In this case, the elastic modulus looks entirely independent of the frequency like the reference system prepared with DDM (as shown in **Figure III-13a**.

The earlier definition of a vitrimer suggests a "permanent connectivity" of the network. This is observed at high frequencies and start to be lost for the systems at DGEBA–4-APDS r=1 and r=1.2 at

[‡] These experiments were performed on a DMA Q800 TA in compression mode. We respectfully ask the reader to omit the magnitude of the E' value in the experiments. The compression mode is recommended for the analysis of foam with low modulus (10^2 to 10^7 Pa), and is not particularly suitable for the systems in question with moderated modulus (10^6 to 10^9 Pa). The unique purpose of these tests is to evaluate the evolution of the modulus as a function of the frequency.

low frequencies. Indeed, this definition is in continuous evolution thanks to the effort of many research groups[26, 33].

The loss of connectivity in sweep frequency tests is often seen at extreme conditions (low frequency and high temperatures). Other works have reported similar behaviors to those obtained in **Figure III-13c** and **d** for chemistries associated with vitrimer systems[73, 76]. Snijkers and coworkers (2016) performed an interesting analysis by applying the time-temperature superposition principle and building a master curve for a system based on transesterification. Their study showed two relaxation behaviors: one at high frequencies next to the rubbery plateau ($\omega \sim 10^2$ rad/s) and a second at lower frequency before achieving the terminal relaxation ($\omega \sim 10^{-4}$ rad/s). This particular behavior has been suggested as a possible "fingerprint" of vitrimers [33]. Like Snijkers *et al.*, the range of temperatures used throughout this work is close to the *T*g. By contrast, in many study cases, the viscoelastic behavior of vitrimers is explored at temperatures well above their *T*g.

More recently, Khabaz *et al.* (2020) performed a very outstanding work proposing the use of molecular dynamics, a Monte Carlo simulation, a non-equilibrium molecular dynamics simulation, and the TTS principle to analyze the terminal regime. This last is difficult to achieve on a simple frequency sweep experiment. This study showed that the vitrimers present two transition regimes. The authors analyzed the slope's evolution as a function of the frequency observed at very low frequencies. They suggested a behavior that follows a power-law, and the Rouse theory could describe that[81].

Without a doubt, the frequency sweep experiments can offer invaluable information about vitrimers. A more detailed study might be considered to see properly the relaxation phenomena explained by a molecular relaxation theory or an effect of the dissociative exchange mechanism of the network at low frequencies, which probably becomes more relevant that the associative exchange mechanism, triggering a loss of connectivity.

3.4.3.2 A new transition temperature: The Tv

Vitrimer materials are characterized by presenting a different transition temperature, the *Tv*, in addition to the *T*g or *T*m. The *T*g is briefly defined as a transition temperature from the glassy to the rubbery state, leading to a major change in physical properties such as elastic modulus, dielectric constant, specific heat capacity, or thermal expansion coefficient. The *T*m is known as the critical temperature point where the crystalline regions in a semicrystalline polymer become amorphous

and are able to flow[82]. The theorical *T*v or topology freezing temperature is defined as the temperature at which the melt viscosity is equal to 10^{12} Pa*s, but also at this temperature the chemical exchange reaction becomes sufficiently fast to allow macroscopic flow, rearranging its topology. This new transition temperature is not easy to discern if the *T*g or *T*m is higher that the theorical *T*v *(T*g*/T*m*>>~~T~~v)*[83]

On the one hand, the *T*g has been largely studied, and many determination techniques have been developed, such as DSC, TMA, specific volume determination, and dilatometry.

On the other hand, the recent introduction of topology freezing temperature has generated multiple questions about its definition and determination. To the best of our knowledge, there are only four methods to determine the *T*v of vitrimer materials, 1) stress-relaxation experiments and extrapolation, 2) creep test and extrapolation, 3) dilatometry test, and recently 4) aggregation-induced emission (AIE) luminogens into vitrimer. The most commonly used is the extrapolation from the stress relaxation experiments, followed by dilatometry studies. Both were explored.

In the first promising work of Leibler *et al.* (2011), the *T*v has been introduced as a transition temperature above which chemical exchanges become significant, considering the viscosity value 10^{12} *Pa*s* as reference for its determination via extrapolation. This extrapolation is based on the premise that the viscosity will follow the same temperature dependency in the analyzed range. The truth is that both physical and chemical factors might affect the viscosity profile and originate off-linear deviation. Therefore, an unprecise determination of the topology freezing temperature may occur by using the Arrhenian law[84]. Due to these deviation factors, a second method must be used to confront the information obtained from the extrapolation of stress relaxation experiments. Previous works have shown that dilatometry analysis may allow to determine the evolution of specific volume with temperature and evidence the transition temperatures and the thermal history dependence of polymers [27, 85, 86]. Thus, a dilatometry study may provide valuable information to characterize vitrimer materials and confront the *T*v obtained from stress relaxation experiments.

Dilatometry analyses were carried out on the DGEBA–4-APDS systems prepared with different amine/epoxy stoichiometries and for the reference system DGEBA-DDM (without dynamic bonds). **Figure III-14** displays the dilatometry curves obtained for the four samples. The sample without dynamic bonds DGEBA-DDM displays a single transition temperature illustrated by an inflection point around 174°C. The systems with dynamic bonds show two inflection points associated with two different transition temperatures for the different stoichiometry cases. These transition temperatures are summarized in **Table II-4**.

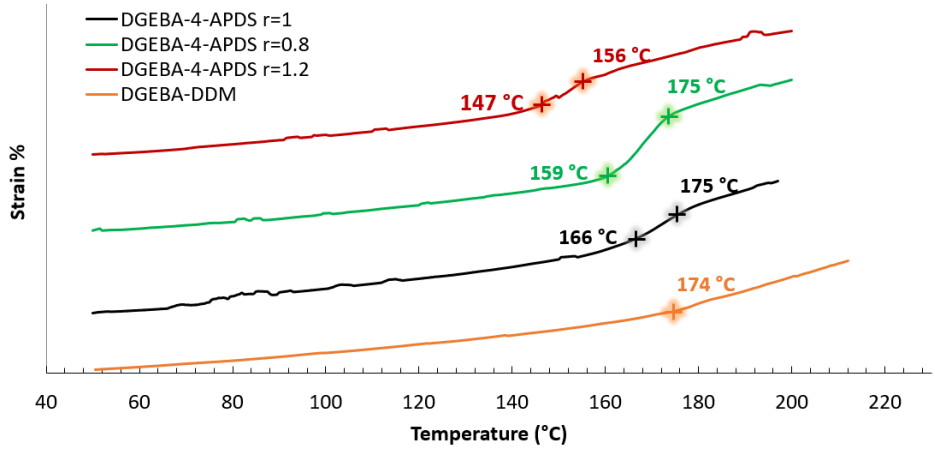

Figure III-14. Dilatometry curves obtained for DGEBA–4-APDS r=1 (black), r=0.8 (green), r=1.2 (red), and the reference DGEBA-DDM (orange). The test was carried out in compression mode. The detailed curves are present in the annex of Chapter III in Figure S.III-4.

System	*Tg* (°C) dilatometry	*Tg* (°C) DSC	*Tv* (°C) dilatometry
DGEBA–4-APDS r=0.8	159 ± 3	155 ± 1	175 ± 1
DGEBA–4-APDS r=1	165 ± 1	167 ± 1	175 ± 2
DGEBA–4-APDS r=1.2	147 ± 1	149 ± 1	156 ± 1
DGEBA-DDM r=1	174 ± 2	177 ± 1	----------

Table III-4. Values of glass transition temperature (*Tg*) and topology freezing temperature (*Tv*) of the three DGEBA–4-APDS stoichiometry systems and the reference system DGEBA-DDM.

The first transition temperature for systems DGEBA–4-APDS is associated with the *Tg*, in line with DSC results reported in section 3.4.2. The second transition temperature is associated with *Tv*.

3.4.3.3 Stress relaxation behavior

Stress relaxation experiments prove that the networks elaborated with reversible covalent bonds can relax and flow; hence, the network's topology can be modified by controlling the exchange reaction kinetics.

Stress relaxation experiments were carried out for all the dynamic systems, as shown in **Figure III-15**. Likewise, the stress relaxation of the system without reversible bonds (DGEBA-DDM) was carried out, as is shown in **Figure III-16**. In all experiments, a constant strain of 1% was applied. The results were normalized $G(t)/G_0$ for easier comparison between the different temperatures in **Figure III-15** and under the premise of a constant crosslink density as shown in **Figure III-13**.

This kind of curves is typically fitted by using the Maxwell model (equation 4) in a range of 10^1-10^6 s at high temperatures. This equation expresses that the relaxation process can be described by only using a single relaxation time and not a multiplicity of time relaxation like other studies[87, 88].

$$\frac{E(t)}{E_o} = e^{-\frac{t}{\lambda}} \quad \text{(4)}$$

Where $\frac{E(t)}{E_0}$ is the normalized stress, t is the experimental time, and λ is the characteristic relaxation time determined from the maximal relaxation according to the Maxwell model (E/Eo= 1/e).

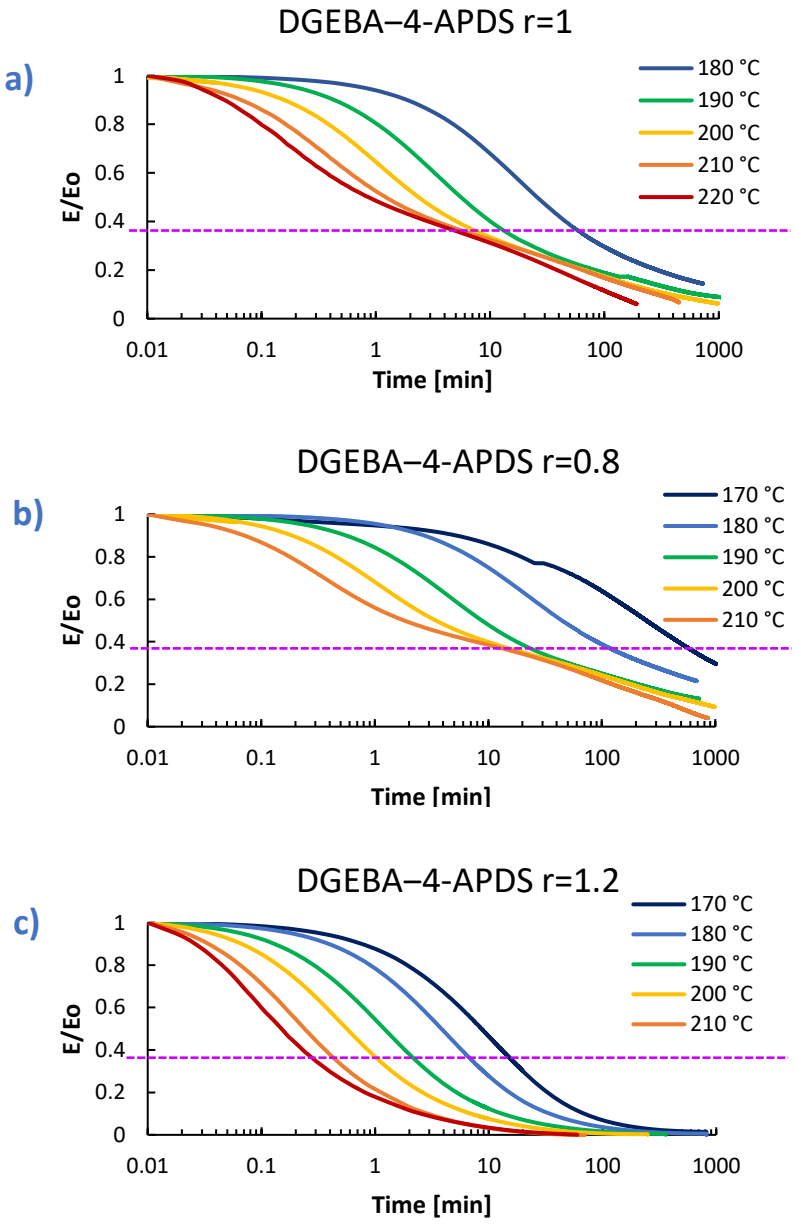

Figure III-15. Normalized stress relaxation curves of DGEBA–4-APDS systems a) r=1, b) r=0.8, and c) r=1.2 under 1% strain.

The experimental curves in **Figure III-15** containing a dynamic hardener can relax at high temperatures and flow like a viscoelastic liquid, contrary to the network with non-dynamic networks displayed in **Figure III-16**.

The analysis of the stress relaxation behavior of networks with a dynamic hardener (**Figure III-15**) reveals that the relaxation is not only temperature-dependent, but also dependent on the hardener (or reversible covalent bonds) concentration. For instance, at 180 °C the system rich in epoxy r=0.8 (**Figure III-15b**) fully relaxes not to far from 1000 min, while the system rich in amine r=1.2 (**Figure III-15c**) fully relaxes in the first 100 min. Williams and coworkers[19] have reported similar behavior by increasing the number of reactive dynamics sites of a crosslinking system based on the transesterification exchange chemistry. So that, an excess of amine promotes fast deformation upon stress as a result of a better ability of the network to rearrange its structure.

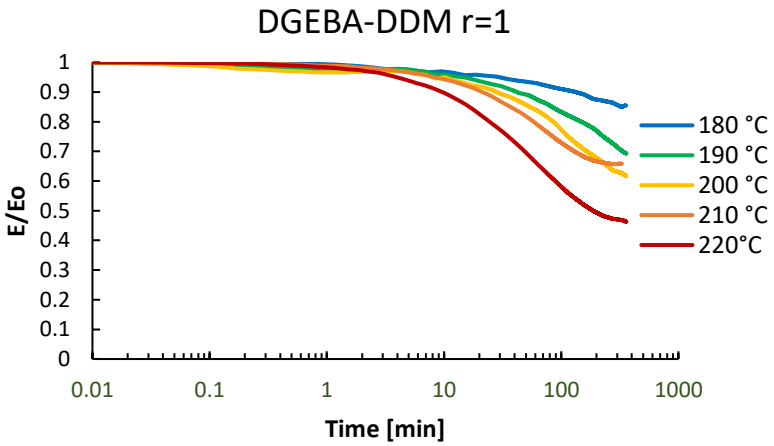

Figure III-16. Normalized stress relaxation curves of the DGEBA-DDM system r=1 under a strain of 1%.

A fundamental characteristic of vitrimer materials is the viscoelastic behavior that resembles silica viscosity profile and has been evidenced in the so-called "Angell plot". This plot explores the viscosity variation against the inverse of the temperature normalized (*T*g/T) displays an Arrhenius-like behavior for the strong liquids like vitrimers[21].

The stress relaxation experiment can afford a quite similar response since the viscosity can be expressed in terms of relaxation time (equation (7)). Leibler *et al.* in their first promising work concerning vitrimer materials, exposed the clever argument to determine the relaxation time as the maximal slope of the Maxwell model., i.e., when the experimental time (t) is equal to the characteristic relaxation time (λ), $\frac{E(t)}{E_0}=e^{-1}$.

Following the same logic as Leibler *et al.*, the relaxation times at $E(t)/E_0=1/e$ were plotted in **Figure**

III-17. The three systems display an Arrhenius-type behavior like classical vitrimer systems.

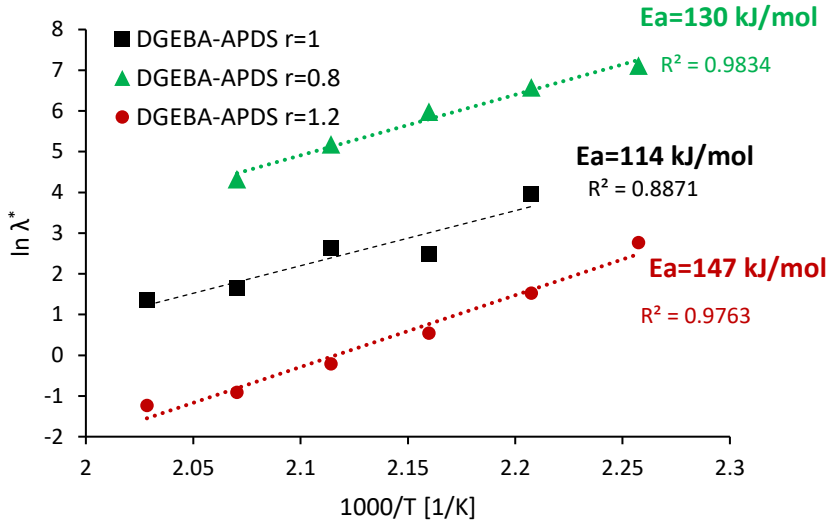

Figure III-17. Variation of the relaxation time as a function of the inversed temperature of the systems DGEBA–4-APDS r=1 (black), DGEBA–4-APDS r=0.8 (green), and DGEBA–4-APDS r=1.2 (red).

Following the Arrhenius model expressed in equations (5) and (6), it is easy to determine the activation energy (Ea), and by extrapolation, the topology freezing temperature (*T*v).

$$\lambda = \lambda_0 \, e^{\left(\frac{Ea}{RT}\right)} \quad \text{..... (5)}$$

$$\ln(\lambda) = \frac{Ea}{R}\left(\frac{1}{T}\right) + \ln \lambda_0 \quad \text{..... (6)}$$

$$\lambda^* = \frac{\eta}{E_{rubbery}} \quad \text{..... (7)}$$

Generally, when the viscosity becomes higher than 10^{12} Pa*s, the transition temperature from liquid to glass occurs[27]. Hence, this viscosity has been chosen to determine the *T*v according to equations (6) and (7), where λ is the relaxation time, Ea the activation energy, R the universal gas constant (8.314 $JK^{-1}mol^{-1}$), T the temperature (comprising between 180 to 220 °C), η the viscosity according to the vitrimer definition (10^{12} Pa*s), $E_{rubbery}$ the elastic modulus at the rubbery plateau, and λ^* the characteristic relaxation time related to the viscosity of the vitrimer definition (10^{12} Pa*s). **Table III-5** recapitulates the Ea and *T*v calculated by following the Arrhenian law and considering a single relaxation time for each temperature.

System	Ea (kJ/mol)	*Tv* (°C) Maxwell model
DGEBA–4-APDS r=0.8	130 ± 7	205 ± 17
DGEBA–4-APDS r=1	114 ± 1	175 ± 3
DGEBA–4-APDS r=1.2	147 ± 3	154 ± 5

Table III-5. Calculated values of activation energy (Ea) and topology freezing temperature (*Tv*) of DGEBA–4-APDS networks elaborated at different amine/epoxy ratios.

As shown in the table, *Tv decreases as a function of amine concentration* in the cross-linked networks. Therefore, it can be assumed that when the concentration of reversible covalent bonds is high, the probabilities of approximation of different dynamic bonds for a subsequent exchange reaction is equally high. Resulting in a lower topology freezing temperature.

Concerning the activation energy, a linear evolution as a function of the dynamic bonds concentration like other promising works such as the performed by Guo *et al.* or Nicolaÿ *et al.* is not observed. Indeed, the results show that the Ea calculated from the Maxwell model seems to be higher for non-stoichiometry systems. Faced with these controversial results compared to other outstanding works, and on the base of many research works that have already questioned the Maxwell model's accuracy, we must ask: can Maxwell's model provide an accurate description of the relaxation behavior of this vitrimer systems? This point is crucial for the determination of the activation energy of the exchange reaction and could allow to obtain a good approximation of the the topology freezing temperature. To fill this gap, several works have begun to explore and propose models capable of describing the complex relaxation behavior of vitrimers. The models must include 1) the chemical reactions due to the reversible bonds in the material, inducing a fast local relaxation, and 2) the cooperative relaxation at a larger time scale.

Table III-6 summarizes the *T*v determined by the dilatometry test and the extrapolation of the Arrhenian like behavior obtained from the Maxwell model relaxation results. To our knowledge, the *T*v values of the DGEBA–4-APDS systems at the amine/epoxy ratios r=1, r=0.8, and r=1.2 have not been reported. Nonetheless, Odriozola *et al.* obtained a *T*v value of 75°C for a system with an amine-epoxy ratio equal to 1.33, which is quite different from those found in this work[45].

System	*Tv* (°C) dilatometry	*Tv* (°C) Maxwell model
DGEBA–4-APDS r=0.8	175 ± 1	205 ± 17
DGEBA–4-APDS r=1	175 ± 2	175 ± 3
DGEBA–4-APDS r=1.2	156 ± 1	154 ± 5

Table III-6. The topology freezing temperature of the system DGEBA–4-APDS at stoichiometry was determined by dilatometry test and by the extrapolation of the Arrhenian-like behavior obtained from Maxwell model results.

The *T*v determination by extrapolating stress relaxation results is similar to that obtained by dilatometry experiments presented in section 3.4.3.2 for samples r=1 and r=1.2. For samples rich in epoxy (r=0.8), the *T*v determined by the Maxwell relaxation model resulted in a large difference from the dilatometry results. This remark might be explained by an interesting hypothesis of a deviation factor of the Arrhenian behavior expressed by Guerre *et al.* (2020). The deviation is associated with two possible phenomena, 1) a decrease in the mobility of chains due to the cooling rate, or 2) a different mechanism that "surpassed" the extrapolated exchange pathway[84]. Likewise, Guerre and coworkers suggested that "*the Tv should not be treated as a temperature belonging to a material but rather as a temperature belonging to the specific dynamic exchange mechanism,"* A physical change (volume expansion) is remarked. It belongs to the dynamic exchange mechanism. *T*v value is only treated as a conceptual value in numerous works, and only a few demonstrate a physical change experimented by the network.

3.4.3.4 The DGEBA–4-APDS system might be called "vitrimer"?

Different experiments were carried out throughout the vitrimer characterization section of DGEBA–4-APDS systems to highlight the system vitrimer behavior. The **permanent connectivity** of the epoxy network was **evidenced by the frequency sweep experiments and by the swelling tests**. The results showed that the elastic modulus remains quite independent of frequency at the rubbery plateau, suggesting permanent connectivity in the rubbery plateau till T=*T*v+50. Swelling tests were also carried out showing how the network integrity was preserved in an inert solvent (THF), a reagent (EMP) and in a reactive solvent (DMF) at room temperature for one week for system in stoichiometry. An inert solvent at high temperatures (trichlorobenzene) was also tested, showing a permanent connectivity at a temperature superior to its *T*v.

The nomination of the system DGEBA–4-APDS as vitrimer material has been questioned because it has not been suficiently explored. The swelling and frequency sweep results evidenced the crucial

criteria of the constant crosslink despite its associative/dissociative exchange mechanism. The dissociative chemistry might occur extremely fast, like in other chemistries[89], and might coincide with the associative chemistry so that the permanent connectivity is not impacted. Thus, from our perspective, defining a vitrimer material with a unique exchange mechanism (associative) to guarantee the permanent connectivity should be re-discussed to include cases where different exchange mechanisms are involved without perturbing the permanent connectivity of a network.

A new transition temperature different to the *T*g or *T*m was **evidenced by carrying out dilatometry studies**. The test evidenced a *T*v slightly superior to the *T*g. The *T*v values obtained by the dilatometry tests are similar to those obtained from the extrapolation information of the stress relaxation experiments. The behavior observed in this work is consistent with other studies [85, 86, 90].

The **stress relaxation experiments** also **evidenced** the vitrimer properties. The analysis showed **how the network relaxed** and **flowed**, an important characteristic of vitrimer material. The relaxation rate increased with the concentration of the disulfide bonds. Similar results have already been obtained by Williams *et al.* by increasing the reactive groups in their system[19]. Even though the Maxwell model faces difficulties in accurately reflecting the viscoelastic behavior of DEGBA–4-APDS network, especially for lower 4-APDS concentration, in a first approximation at a short time scale, the network displayed **a viscoelastic character that follows an Arrhenian-like behavior**, resembling silica material like Leibler and coworkers showed in their first promising work. In other words, this behavior is expected for vitrimer materials.

Moreover, the ***T*v** seems **to decrease as a function of the concentration of dynamic bonds**, i.e., the sample rich in amine (excess of disulfide bonds) shows the lowest *T*v, while the sample rich in epoxy (scarce of disulfide bonds) displays the highest *T*v. Nevertheless, it is essential to remark that a decrease in the *T*v can also be impacted by the crosslink density of the material (equation (6) and (7)). To our knowledge, this behavior has not been explored yet for epoxy resins with disulfide exchange chemistry. Still, after comparing three independent works, all of them working with the same system (DGEBA–4-APDS) but different stoichiometric ratios, a decrease of the *T*v as a function of disulfide concentration in the thermoset was remarked [45, 52, 91]. The behavior observed of the system DGEBA-4-APDS is the opposite to other commodity-vitrimer chemistries where an increase of the *T*v as a function of the covalent adaptable bonds is explored[26]. This last work, performed by Nicolaÿ *et al*., evidenced the possibility of changing the *T*v or the activation energy by manipulating the crosslinking density, the topology, and the functionality of the network. Nontheless, the difference between both cases might be related to the polymer nature, the first a thermoset

(DGEBA-4-APDS), and the second a thermoplastic (polybutadiene-vitrimer).

Based on the different obtained results and the above discussion, the DGEBA–4-APDS system meets the characteristic properties of a vitrimer material. Hence, this system can be classified as epoxy vitrimer resin with exchangeable disulfide bonds.

3.5 Stress relaxation modeling

Several works have reported that the Maxwell model does not correctly describe the relaxation behavior of vitrimers. Therefore, many efforts and research works have explored different approaches to afford a better strategy or models to analyze the complex stress relaxation of the vitrimer materials. To achieve this objective, the modeling using the Kohlrausch-Williams-Watts model (KWW) has been explored to describe the thermoset's relaxation behavior[92, 93, 94]. In the field of vitrimer materials, Torkelson and coworkers (2018) have performed interesting works "re-taken" this interesting model to describe the relaxation behavior of vitrimer materials[95, 96]. The model considers a stretched exponential factor that determines the relaxation curve's shape, reflecting the relaxation time distribution.

Furthermore, Yu and coworkers used a different approach to explain the stress relaxation of covalent adaptable networks (CANs). The theory of Bernstein-Kearsley-Zapas inspired their approach. It describes two different relaxation modes: 1) a relaxation mode linked to the bond exchange reaction (BER) and 2) a relaxation related to the viscoelastic polymer network[30].

As a result of close *T*g and *T*v for DGEBA–4-APDS systems, the relaxation might be well described by combining these two relaxation modes. In this section, the modeling proposed by Torkelson *et al.* is explored alone and in combination with the approach proposed by Yu *et al.* to provide a model capable of describing the complex relaxation behavior of DGEBA–4-APDS systems.

3.5.1 Kohlrausch-Williams-Watts (KWW) modeling

The modeling of relaxation behaviors by using the Kohlrausch-Williams-Watts model (KWW), equation (8), has a good acceptance by many groups working with vitrimers[31, 97, 98, 99, 100, 101]. The KWW equation seems to the Maxwell models (equation 4), but this considers a stretched exponential decay β able to control the curve shape. The exponential β takes values 0<β<1, reflecting the relaxation time distribution. Hence when β→1, it indicates a single relaxation time, and in turn, the average relaxation time can be calculated by following the relation (9), where **Γ** is the Gamma function[95].

$$\frac{G(t)}{G_0} = E * e^{\left(-\left(\frac{t}{\lambda}\right)^{\beta}\right)} \quad \text{..... (8)}$$

$$\bar{\lambda} = \frac{\lambda\,\Gamma\left(\frac{1}{\beta}\right)}{\beta} \quad \text{..... (9)}$$

Inspired by all these works and showing how the use of a stretched exponential decay can

potentially describe the stress relaxation behavior of vitrimers, more precisely, the KWW equation was explored for the system DGEBA–4-APDS.

The experimental data recorded during the stress relaxation experiments were normalized. Since the crosslinking density at the rubbery state is constant (**Figure III-13**), it was assumed that the elastic modulus value is the same for all curves at different temperatures. The modeling work was carried out employing Origin® 9 and equation (8).

3.5.1.1 Modeling of the DGEBA–4-APDS system r=1 using the KWW equation.

The DGEBA–4-APDS r=1 was the first system studied at different temperatures using the KWW equation. The results are displayed in **Figure III-18** on the left. The performed fits try to describe the entire relaxation curve using equation (8). The simulated curves clearly show that it is impossible to correctly describe the relaxation by using this equation, as proposed by Torkelson *et al.* for their transcarbamoylation[95] and thiol-epoxy click chemsitry[31] systems. Indeed, their works consider systems where the stress relaxation analyses are carried out well about the *T*g, more than 100°C.

Since stress relaxation experiments exploited in **Figure III-15** or **Figure III-18** display what be called *a staged relaxation behavior,* a description of the relaxation behavior only employing the equation (8) seems not to be a good approach. The observed overlapped relaxation is linked to the close temperature range of both transition temperatures (*T*g and *T*v). For this reason, the fitting was divided into two main study zones. The analysis of these two zones is plotted in **Figure III-18** on the right. The first fit corresponds to the first minutes of the relaxation and the second to the last minutes of the relaxation.

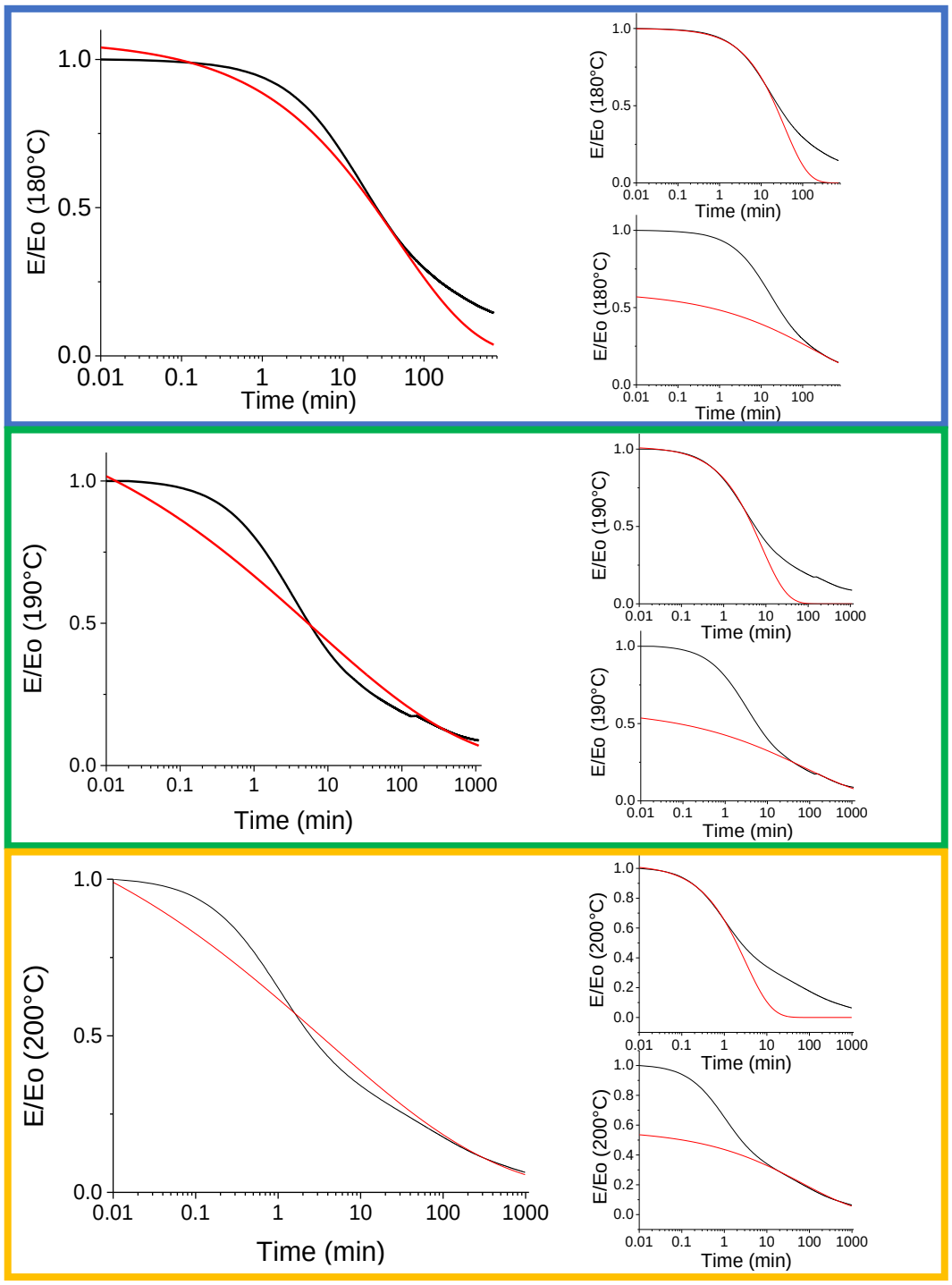

Figure III-18. Normalized and modeled stress relaxation curves of DGEBA–4-APDS system r=1 by using the KWW equation at different temperatures. To the left, the modeling considering the entire recorded relaxation. To the right, the modeling is divided into two study zones: 1) the first relaxation zone and 2) the second relaxation zone. The black line corresponds to experimental data, and the red line to the modeling achieved.

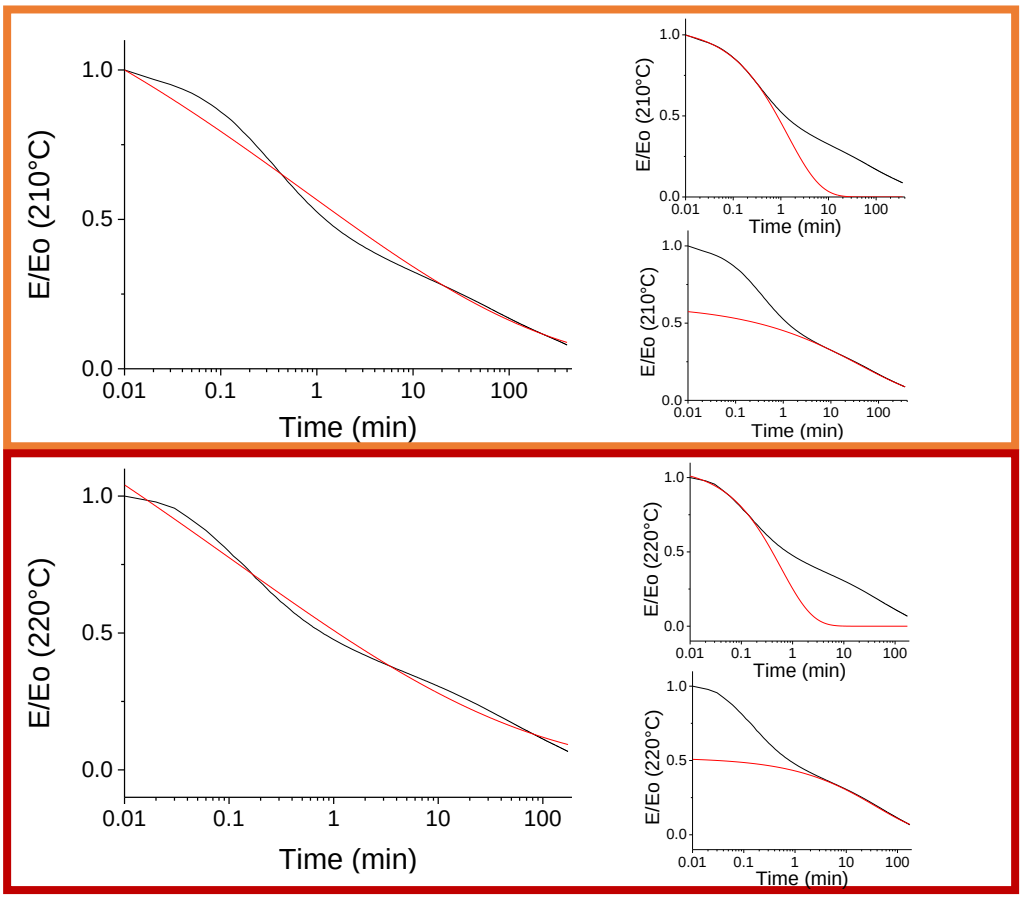

Figure III-18. Normalized and modeled stress relaxation curves of DGEBA–4-APDS system r=1 by using the KWW equation at different temperatures. To the left, the modeling considering the entire recorded relaxation. To the right, the modeling is divided into two study zones: 1) the first relaxation zone and 2) the second relaxation zone. The black line corresponds to experimental data, and the red line to the modeling achieved.

T (°C)	Parameters from the complete curve				Parameters from the first part of the curve				Parameters from the last part of the curve			
	E	λ (min)	β	$\bar{\lambda}$	E	λ (min)	β	$\bar{\lambda}$	E	λ (min)	B	$\bar{\bar{\lambda}}$
180	1.07	46.8	0.44	122	1.00	36.1	0.75	43	0.61	196.7	0.28	2417
190	1.32	6.1	0.21	532	1.02	7.8	0.72	10	0.59	71.3	0.26	1434
200	1.62	3.5	0.20	351	1.05	3.1	0.70	5	0.62	67.7	0.31	530
210	1.62	0.8	0.17	431	1.05	1.4	0.62	2	0.62	41.0	0.31	335
220	2.08	0.1	0.15	203	1.07	0.6	0.70	1	0.52	37.9	0.46	92

Table III-7. Modeling parameters of the normalized stress relaxation curves of the DGEBA–4-APDS r=1 system with equation (8). The cases explored are the relaxation of: 1) the whole relaxation spectrum, 2) the first relaxation zone, and 3) the second relaxation zone. The parameters correspond to those of the equation (8), where E is the prefactor, λ the relaxation time yielded by the simulation, β the stretched exponent decay and $\bar{\lambda}$ the average relaxation time yielded by the gamma function.

The simulation analysis has been done by fitting: 1) the complete stress relaxation curve, 2) the first relaxation zone, and 3) the second relaxation zone (**Table III-7**). The results of the three studied cases show that the relaxation time decreases as the temperature rises. This behavior is generally expected for polymer systems. Moreover, the stretched decay exponent (β) for the complete relaxation curve follows a decreasing trend. In contrast, when the simulation analysis of stress relaxation is divided into two regimes (short and long times), the β and the prefactor (E) are quite similar regardless of the temperature (**Table III-7**). The entire simulation results are noted in **Table S.III-1, Table S.III- 2,** and **Table S.III- 3**.

Dividing the relaxation curve into two study zones, as proposed in **Figure III-18 - right**, the modeling offers a good approximation of two different phenomena seen during the relaxation. A first phenomenon that induce a fast local relaxation, and a second at a larger time scale inducing a cooperative relaxation of the network. A variation of stoichiometry might clarify these phenomena and evaluate the prefactors and the stretched decay exponent evolution as a function of the amine concentration. Therefore, the same analysis was carried out for the off-stoichiometric systems (r=0.8 and r=1.2).

3.5.1.2 Modeling of the DGEBA–4-APDS system r=0.8 using the KWW equation.

The first explored off-stoichiometric system was the system DGEBA–4-APDS r=0.8. **Table III-8** summarizes the parameters obtained from the simulation analysis of the system r=0.8. The simulated curves and all the simulation data are noted in **Figure S.III-6**, **Table S.III- 4**, **Table S.III- 5**, and **Table S.III- 6** on the annex of Chapter III.

The single exponent decay cannot correctly describe the relaxation behavior of the DGEBA–4-APDS systems r=1 nor r=0.8. For this reason, the simulation analysis using the KWW equation was carried out to fit the first and the second relaxation zones of the relaxation behavior. The fitting carried out separately accentuates the double relaxation behavior. The results of these two independent simulations are summarized in **Table III-8**.

As observed for system r=1, the stretched decay exponent (β) for the complete relaxation curve follows a decreasing trend. Concerning the simulation analysis on the two relaxation zones, at short relaxation times, the exponent β is slightly stable regardless of the temperature. At long relaxation times, the exponent β displays an increasing trend.

T (°C)	Parameters from the complete curve				Parameters from the first part of the curve				Parameters from the last part of the curve			
	E	λ (min)	β	$\bar{\lambda}$	E	λ (min)	B	$\bar{\lambda}$	E	λ (min)	B	$\bar{\bar{\lambda}}$
180	1.01	730.2	0.46	1699	0.99	314.5	0.59	483	0.73	4104.0	0.32	28119
190	1.03	274.7	0.35	1434	1.01	86.4	0.65	118	0.68	3629.6	0.30	33829
200	1.02	166.4	0.41	518	1.01	33.4	0.58	52	0.62	2239.4	0.38	8373
210	1.05	93.4	0.34	513	1.02	14.8	0.63	21	0.63	738.7	0.41	2230
220	1.07	72.9	0.32	526	1.02	5.5	0.63	8	0.70	391.7	0.54	677

Table III-8. Modeling parameters of the normalized stress relaxation curves of the DGEBA–4-APDS r=0.8 system with equation (8). The cases explored are the relaxation of: 1) the whole relaxation spectrum, 2) the first relaxation zone, and 3) the second relaxation zone. The parameters correspond to those of the equation (8), where E is the prefactor, λ the relaxation time yielded by the simulation, β the stretched exponent decay and $\bar{\lambda}$ the average relaxation time yielded by the gamma function.

3.5.1.3 Modeling of the DGEBA–4-APDS system r=1.2 using the KWW equation.

Like for the other systems, the simulated curves and all the simulation data are noted in **Figure S.III-7** and in **Table S.III- 7**, **Table S.III- 8,** and **Table S.III- 9** in the annex of Chapter III. **Table III-9** summarizes the parameters found of the simulation of system r=1.2.

Following the same analysis for the system in excess of epoxy (r=0.8), we can again look at **Figure III-15c**, which displays the normalized experimental stress relaxation curves of the DGEBA–4-APDS system r=1.2. Contrary to the system rich in epoxy, the relaxation behavior seems to indicate a unique relaxation and is not staged as in the precedent cases. Nonetheless, the three different simulation cases were carried out, like for both former systems.

The simulation of the complete relaxation curve using a single stretched decay exponent describes moderately well the relaxation behavior as shown in **Figure S.III-7**. This simulation differs significantly from that obtained for systems r=1 and r=0.8. Still, regarding in detail, the KWW equation cannot accurately describe the relaxation behavior either at short or long relaxation times.

Hence, the analyses dividing the relaxation into two zones were also carried out. The results are summarized in **Table III-9**. Like in the two precedent cases, the exponent β follows a decreasing tendency by fitting the entire relaxation curve. Concerning the fitting performed separately in the two relaxation zones, once again the parameter β seems constant regardless of the temperature, as seen for the two precedent cases r=1 and r=0.8.

T (°C)	Parameters from the complete curve				Parameters from the first part of the curve				Parameters from the last part of the curve			
	E	λ (min)	β	$\bar{\lambda}$	E	λ (min)	β	$\bar{\lambda}$	E	λ (min)	B	$\bar{\bar{\lambda}}$
170	1.07	13.6	0.61	20	1.01	14.0	0.74	17	0.23	53.6	0.45	132
180	1.10	5.8	0.59	9	1.02	6.2	0.71	8	0.27	28.8	0.55	49
190	1.10	1.9	0.52	4	1.03	2.0	0.73	2	0.30	9.5	0.50	19
200	1.09	1.0	0.56	2	1.05	0.8	0.72	1	0.32	4.3	0.47	10
210	1.33	0.3	0.46	1	1.09	0.3	0.70	0.4	0.36	1.7	0.49	4
220	1.96	0.1	0.31	0.45	1.14	0.2	0.70	0.2	0.34	1.67	0.46	3

Table III-9. Modeling parameters of the normalized stress relaxation curves of the DGEBA–4-APDS r=1.2 system with equation (8). The cases explored are the relaxation of: 1) the whole relaxation spectrum, 2) the first relaxation zone, and 3) the second relaxation zone. The parameters correspond to those of the equation (8), where E is the prefactor, λ the relaxation time yielded by the simulation, β the stretched exponent decay and $\bar{\lambda}$ the average relaxation time yielded by the gamma function.

3.5.1.4 Stretched exponential decay modeling conclusions of the stress relaxation behavior

From this first experience of simulation analysis using the KWW model, we can point out two key behaviors to develop a model capable of describing the stress relaxation of DGEBA–4-APDS systems.

1. More than one relaxation phenomenon occurs according to this time scale
2. The shape of the curve, i.e., the stretched decay exponent β, seems constant regardless of the temperature once the relaxation is divided into two relaxation zones.

More than one relaxation phenomenon

The experimental stress relaxation curves recorded in this work present more than one relaxation. In agreement with Leibler *et al.* (2020), it can be said that a "*stress relaxation experiment is actually a convolution of several relaxation modes occurring over a wide range of time scales and with different temperature dependencies*."[102] Thus, analyzing the relaxation behavior separately into two relaxation zones, at short and at long relaxation times, could lead to distinguish two different relaxation behaviors and attribute them to a specific phenomenon. But, which are these relaxation phenomena?

Yu *et al.* (2018) used a thermo-viscoelastic constitutive model based on the Bernstein -Kearsley-Zapas (BKZ) theory[30]. The objective was to separate the contributions of the bond exchange reactions (BER) and the viscoelastic relaxation of the network in which glass transition temperature is close to the bond exchange operating temperature. Their approach inspired the following study

since the glass transition temperature is close to the topology freezing temperature (less than 20 °C of difference even varying the stoichiometric ratio, **Table III-6**).

Based on the interesting work performed by Yu *et al.*, and the observation of two presumably overlapped relaxation behaviors, it can be hypothesized that one relaxation behavior is attributed to the covalent exchange bonds and the other to the network segmental relaxation common for crosslink networks. To prove this last assertion, we must refer to the relaxation of the reference system DGEBA-DDM (without covalent exchange bonds) displayed in **Figure III-16**. The reference system does not fully relax, and the relaxation occurs for a long time. The long relaxation time observed for the reference system is associated with the relaxation time of the network segmental motions. Therefore, for the DGEBA–4-APDS system, the short relaxation times can be attributed to the pure exchange mechanism. The long times are related to the network segmental relaxation, which can encompass covalent dynamic bonds not involved in the exchange mechanism.

The stretched decay exponent β evolution

From a practical point of view, the exponent β drives the "shape" of the relaxation curve. As β decreases, the stress relaxation's shape described by the Maxwell model is lost. Once the relaxation behavior was divided into two relaxation zones, the values of β seem constant and slightly similar for the three-stoichiometry studied, i.e., $0.6 < \beta_{\text{short times}} < 0.75$ and $0.25 < \beta_{\text{long times}} < 0.5$. These values are relatively stable compared to other works where the exponent β changes drastically as temperature function [103, 104].

From these two key behaviors, it was decided to explore an approach considering two relaxation zones. The first domain is associated with the BER relaxation, and the second is linked to segmental relaxation. The BER contribution is only linked to the reaction exchange mechanisms, while the network motion segmental relaxation considers the segment relaxations, including the disulfides that do not participate in the exchange mechanism. Each part is described by the KWW equation, meaning the stretched decay exponent, as shown in equation (10).

$$\frac{E(t)}{E_0} = \underbrace{E_1 * e^{\left(-\left(\frac{t}{\lambda_1}\right)^{\beta_1}\right)}}_{\text{Bond Exchange Reaction}} + \underbrace{E_2 * e^{\left(-\left(\frac{t}{\lambda_2}\right)^{\beta_2}\right)}}_{\text{Network segmental motion}} \quad \text{(10)}$$

3.5.2 Bernstein- Kearsley-Zapas theory (BKZ)

The equation (10) was employed for the modeling based on the BKZ theory explored in this section[30]. It considers: 1) the bond exchange reaction, achieved at short relaxation times, and 2) the segmental

relaxation movements of the network, reached at long relaxation times. The aim is to identify both overlapped phenomena on the experimental stress relaxation data recorded for the three stoichiometric systems. Like modeling using only a single stretched decay exponent, the relaxation curves were normalized. The modeling was carried out using Origin® 9.

3.5.2.1 Modeling of the DGEBA–4-APDS system using two branches: Application of the BKZ theory

3.5.2.1.1 Modeling of the DGEBA–4-APDS system r=1 using two stretched exponential decay factors

The first case of study was the system on stoichiometry r=1. The modeling is displayed in **Figure III-19**, and the parameters for this fitting are summarized in **Table III-10**. The entire parameters yielded from the simulation are noted in **Table S.III- 10**.

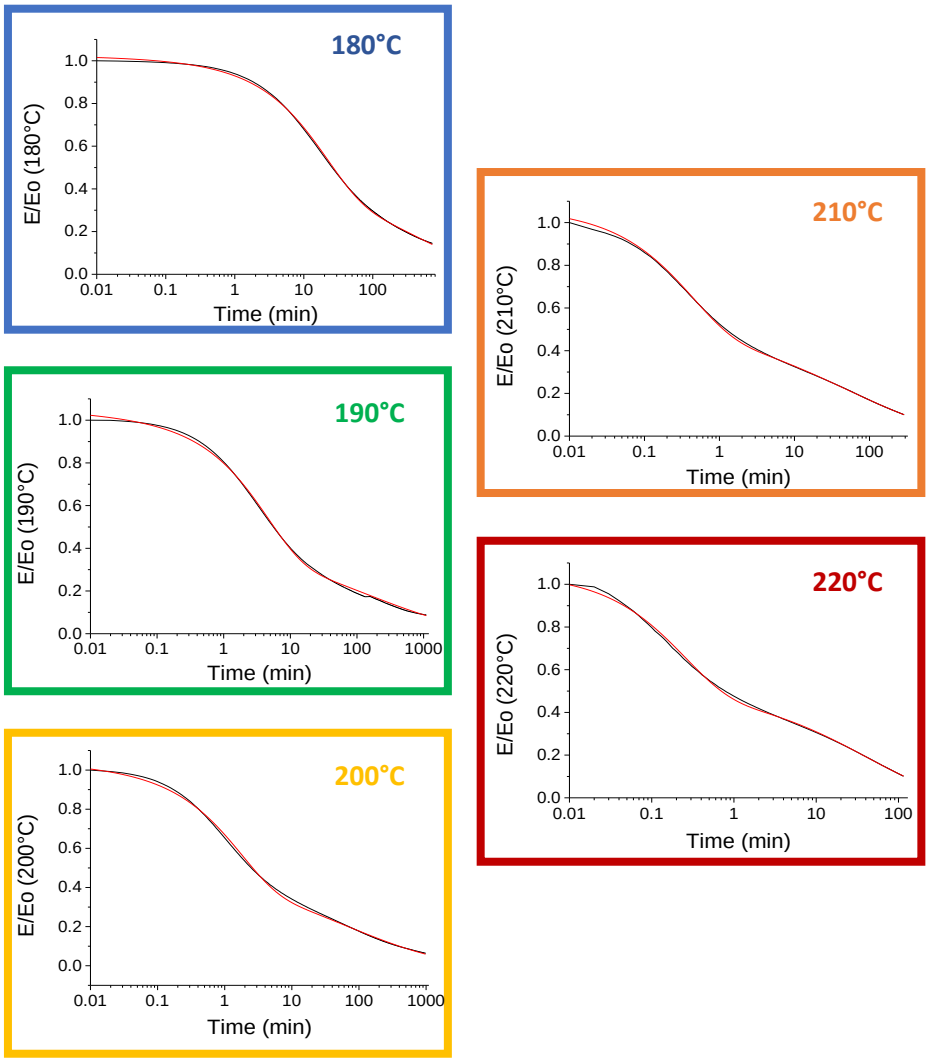

Figure III-19. Modeling of the normalized stress relaxation curves of the DGEBA–4-APDS r=1 system with equation (10) at different temperatures from 180 to 220 °C. The black line corresponds to experimental data, and the red line to the modeling achieved.

T (°C)	Bond Exchange Reaction					Segmental relaxation movements				
	E_1	E_1%	λ_1 (min)	β_1	$\bar{\lambda}$	E_2	E_2%	λ_2 (min)	β_2	$\bar{\lambda}$
180	0.51	0.50	20.4	0.81	23	0.51	0.50	359.4	0.37	1458
190	0.54	0.50	4.5	0.79	5	0.53	0.50	116.9	0.30	1137
200	0.49	0.46	1.7	0.77	2	0.57	0.54	59.4	0.29	642
210	0.50	0.46	0.4	0.75	0.5	0.59	0.54	51.7	0.33	322
220	0.53	0.51	0.2	0.77	0.3	0.52	0.49	40.8	0.47	93

Table III-10. Parameters of the fit by using two stretched exponential decay functions for the stress relaxation description of the normalized DGEBA–4-APDS r=1 system. The parameters correspond to those of equation (10), where E_i are the prefactors, λ_i, the relaxation times yielded by the simulation, β_i the stretched exponents decay and $\bar{\lambda}_i$ the average relaxation time yielded by the Γ_i function. i=1,2, where 1 is related to the BER relaxation and 2 is associated with the segmental relaxation movements of the network.

From the information of **Table III-10**, it may be noted that:

- The use of the two contributions factors in the stretched exponential decay model allows to describe more accurately the full relaxation than the use of a single stretched decay exponent reported in the previous section.
- The exponent **β_1**, which corresponds to the BER's relaxation, is quite similar and **independent of the temperature**. It ranges **between 0.75 and 0.81**. Thus, the distribution breadth of relaxation times remains constant regardless of temperature. Interestingly, these values are not so far from those found in the modeling of the precedent section at short times by using a single stretched decay exponent (values summarized in **Table III-7**), where the values of the exponent β oscillate between 0.62<β<0.75.
- The exponent **β_2**, related to the network's segmental relaxation movements, is rather **constant** and quite similar to those found in the modeling at long relaxation times of the previous section (**Table III-7**). The value of the exponent β_2 in both cases **oscillates between 0.30<β<0.54**.
- The pre-factors of each stretched decay exponent are constant at all temperatures. In percentage terms, the contribution fraction (E%) of the **bond exchange reaction** (**E_1%**) and **the segmental relaxation movements** (**E_2%**) are **equitable and independent of the temperature.**

3.5.2.1.2 Modeling of the DGEBA–4-APDS system r=0.8 using two stretched exponential decay factors

The same simulation analysis was carried out for off-stoichiometric systems. For the case DGEBA–4-APDS r=0.8, the fitted parameters are summarized in **Table III-11**. The modeling and corresponding data yielded by the simulation are noted in **Figure S.III- 9** and **Table S.III- 10**.

T (°C)	Bond Exchange Reaction					Segmental relaxation movements				
	E_1	E_1%	λ_1 (min)	β_1	$\bar{\lambda}$	E_2	E_2%	λ_2 (min)	β_2	$\bar{\lambda}$
170	0.35	0.35	72.4	0.76	85	0.65	0.65	7428.9	0.34	39641
180	0.37	0.36	20.5	0.76	24	0.66	0.65	3474.4	0.34	19311
190	0.31	0.30	5.2	0.81	6	0.72	0.70	1325.2	0.32	9763
200	0.34	0.32	2.6	0.77	3	0.70	0.68	561.6	0.37	2358
210	0.34	0.33	0.6	0.76	1	0.70	0.68	392.5	0.54	698

Table III-11. Parameters of the fit by using two stretched exponential decay functions for the stress relaxation description of the normalized DGEBA–4-APDS r=0.8 system. The parameters correspond to those of equation (10), where E_i are the prefactors, λ_i, the relaxation times yielded by the simulation, β_i the stretched exponents decay and $\bar{\lambda_i}$ the average relaxation time yielded by the Γ_i function. i=1,2, where 1 is related to the BER relaxation and 2 associated to the segmental relaxation movements.

Like in the stoichiometric case, the simulation results show valuable information:

- The modeling with two contributions factors in the stretched exponential decay model describes more precisely the relaxation behavior.
- The values of the exponent **β_1**, are **independent of the temperature**. The values are a bit far away from those values found by only modeling the first relaxation at short times ($0.58<\beta<0.6$), The obtained β of the new modeling oscillates between **$0.76<\beta<0.81$**. Interestingly, these new values of the exponent β_1 are quite similar to those found at r=1.
- The values of the exponent **β_2** oscillate in a short-range **between $0.32<\beta<0.54$**, and they are quite similar to those found in the modeling at long relaxation times of **Table III-8** ($0.30<\beta<0.54$), suggesting independence to the temperature.
- The contribution fractions (**E_i%**) seem to be **dependent on the concentration of dynamic bonds**. Alongside, the contribution is still independent of the temperature.

3.5.2.1.3 Modeling of the DGEBA–4-APDS system r=1.2 using two stretched exponential decay factors

Finally, the samples in excess of amine (or reversible bonds) were explored. The fitted parameters of system DGEBA–4-APDS r=1.2 are summarized in **Table III-12**. The fitted simulations and the values yielded from the simulation are noted in **Figure S.III- 10** and **Table S.III- 12**.

T (°C)	Bond Exchange Reaction					Segmental relaxation movements				
	E_1	E_1%	λ_1 (min)	β_1	$\bar{\lambda}$	E_2	E_2%	λ_2 (min)	β_2	$\bar{\lambda}$
170	0.81	0.80	9.74	0.77	11	0.20	0.20	95.32	0.46	220
180	0.72	0.71	3.84	0.78	4	0.30	0.29	27.24	0.52	51
190	0.71	0.69	1.26	0.76	1	0.33	0.31	10.24	0.51	20
200	0.70	0.67	0.58	0.78	0.7	0.34	0.33	4.91	0.53	9
210	0.72	0.66	0.22	0.78	0.3	0.37	0.34	1.87	0.50	4
220	0.76	0.66	0.11	0.74	0.1	0.40	0.34	1.59	0.50	3

Table III-12. Parameters of the fit by using two stretched exponential decay functions for the stress relaxation description of the normalized DGEBA–4-APDS r=1.2 system The parameters correspond to those of equation (10), where E_i are the prefactors, λ_i, the relaxation times yielded by the simulation, β_i the stretched exponents decay and $\bar{\lambda}_i$ the average relaxation time yielded by the Γ_i function. i=1,2, where 1 is related to the BER relaxation and 2 is associated with the segmental relaxation movements.

According to this information, the following statements can be pointed out:

While it is true that the modeling with a single stretched decay exponent yielded a good fit (**Figure S.III-7**), the use of two contributions factors in the stretched exponential decay model allows to describe much better the complex relaxation of the system rich in amine (**Figure S.III- 10**).

- The values of the exponent **β_1** are again quite **similar regardless of the temperature**. Like in the two previous cases (r=1 and r=0.8), the values are not so far from the values found in the modeling at the first relaxation zone ($0.70<\beta_1<0.74$, **Table III-9**). Besides, the three-stoichiometries display β_1 values quite similar ($0.74<\beta_1<0.81$).
- The values of the exponent **β_2** show similar behavior to β_1 values, **suggesting independence to the temperature**. Besides, the values are not so far from those found in the modeling at long relaxation times, summarized in **Table III-9** ($0.45<\beta_1<0.55$).
- The contribution fractions (**E_i%**) display an increase in BER behavior, contrary to that exposed for the system rich in epoxy. The **change in the contribution fraction is related to** the rise in the **number of reversible bonds** present in this system. This response is consistent with the results observed for the DGEBA–4-APDS system r=0.8.

3.5.2.1.4 Conclusions from modeling stress relaxation using two contributions in the stretched exponential decay model

From the results of the three studied DGEBA–4-APDS systems, it is possible to summarize two main remarks:

- The contribution fractions (E_1 and E_2) are a function of the disulfide bond concentration, and they are independent of the temperature.
- The parameters β_1 and β_2, which control the shape of the relaxation curves, do not change with the reversible bond concentration and are independent of the temperature.

A similar approach to that performed in this work has been recently exposed by Hayashi *et al.* (2020). An elastomer system was studied using the same method of two stretched exponent decay to describe the relaxation behavior of their elastomeric vitrimers. The values of both β's are independent of the temperature. Yet, in their case, the long relaxation behavior was attributed to the BER relaxation and the short for the segmental relaxation movements of the network [105]. This behavior, reversed to that reported for the epoxy-vitrimer studied in this work, is linked to the elastomeric nature of their systems. The elastomeric network relaxes much faster than those of a thermoset.

3.5.2.2 Activation energy and topology freezing temperature determination using two stretched exponential decay contribution factors

The Arrhenian-type behavior is a characteristical property of vitrimers and is strongly associated with the exchange mechanism. Therefore, the relaxation times of both relaxation phenomena were plotted against the temperature to visualize the viscoelastic behavior.

Figure III-20 displays the relaxation behavior BER and the segmental relaxation movements of the network of the three-stoichiometric systems. The BER relaxation displays an Arrhenian-like behavior, a characteristical of CAN's, including vitrimer. The segmental relaxation of the network exhibits a non-Arrhenian phenomenon.

Concerning the BER behavior, the activation energy (Ea) can be calculated by following the equation (6) and the *T*v by combining the equation (6) and (7) and with the premise of a viscosity 10^{12} Pa*s.

$$\ln(\lambda^*) = \frac{Ea}{R}\left(\frac{1}{T}\right) + \ln\lambda_0 \quad \text{..... (6)}$$

$$\lambda^* = \frac{\eta}{E_{rubbery}} \quad \text{..... (7)}$$

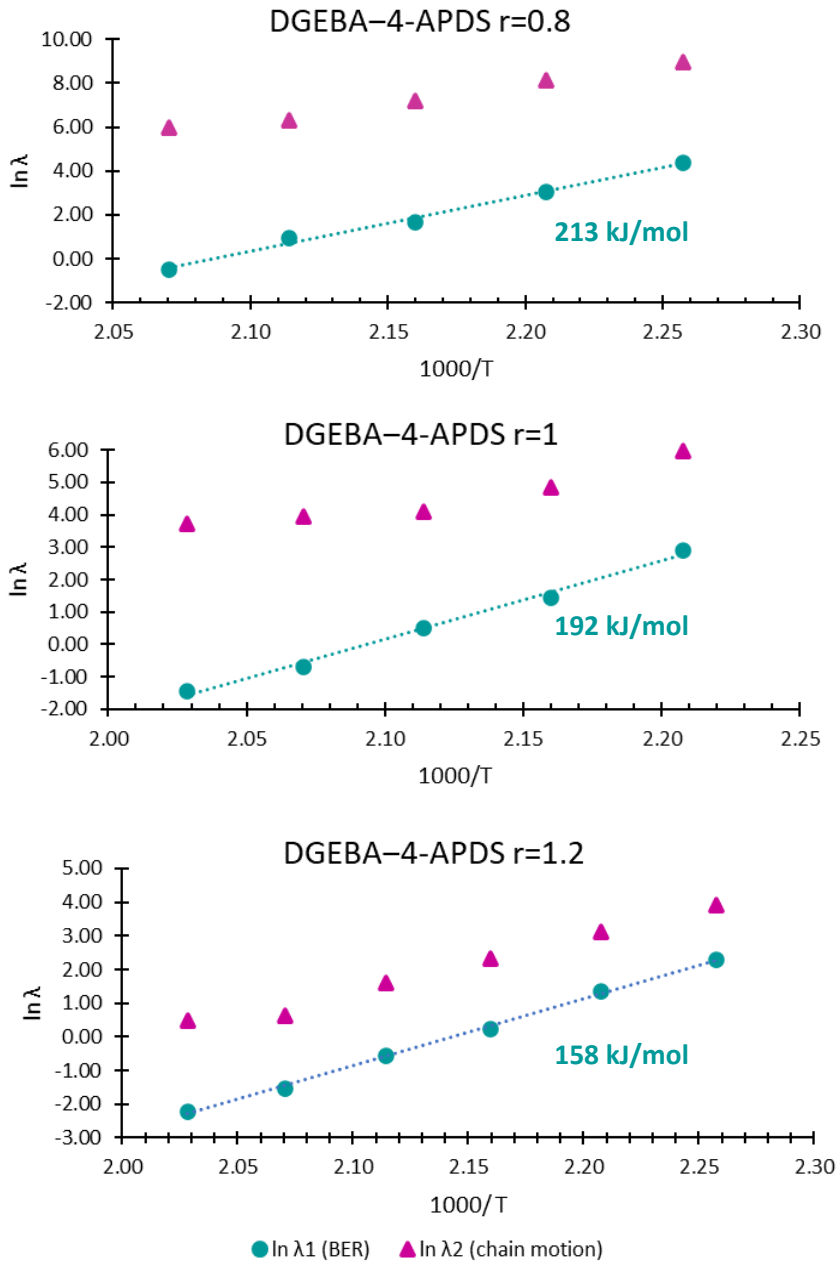

Figure III-20. Arrhenius plot of the characteristic relaxation time of the BER in blue and the segmental relaxation movements of the network in violet against the inverse of temperature.

Table III-13 summarizes the Ea and the *T*v values calculated from equations (6) and (7) and the dilatometry analyses. The calculated values of the activation energies by using the Maxwell model differ from those calculated from the BER behavior. The Ea estimated from the BER behavior is higher than the value found by using the Maxwell equation. Besides, these new values are quite

similar to the bond dissociation energies of disulfides described by Ruipérez and coworkers. The dissociation energy of disulfides varies from 170-210 kJ/mol, depending on the chemical nature of the adjacent functional groups[51].

	Maxwell model		Stretched exponent decay BER		Dilatometry
System	**Ea (kJ/mol)**	*Tv* (°C)	**Ea (kJ/mol)**	*Tv* (°C)	*Tv* (°C)
r=0.8	**130 ± 7**	205 ± 17	**213 ± 3**	172 ± 3	175 ± 1
r=1	**114 ± 1**	175 ± 3	**192 ± 15**	171 ± 3	175 ± 2
r=1.2	**147 ± 3**	154 ± 5	**158 ± 9**	151 ± 6	156 ± 1

Table III-13. Ea and *Tv* values of the different stoichiometries of the DGEBA–4-APDS system determined by Maxwell's model and using the deconvoluted data of the stretched exponent decay due to BER relaxation. The *Tv* determined by the dilatometry test is also summarized.

Furthermore, the information on the Table shows that the **Ea increases when the disulfide bond concentration decreases**. The low concentration of amine reduces the probabilities of adjoined disulfide bonds to achieve an effective exchange; thus, the energy for the rearrangement of the network increases, reflected in the Ea rise. A similar observation has already been remarked by Guo *et al.* (2020) by varying the concentration of imines in a crosslinked elastomeric vitrimer. Their networks showed quite similar crosslink densities and *Tg* despite the increase of crosslinker in the network[106]. Other works have shown the contrary case, a rise on dynamic bonds concentration involves an increase on the Ea. Nonetheless, in these cases a significant increase in *Tg* (even more that 100°C) and with it, the crosslinking density of the network[26]. Guo *et al.* observation are in line with the results in the present work.

The evolution of the activation energy as a function of the concentration of reversible covalent bonds cannot be visualized by only using the Maxwell model since it considers several relaxation modes. Still, after the isolation of the BER relaxation phenomenon, the evolution is clear and consistent with the conditions of the systems.

While it is true that the *Tv* values determined via Arrhenius law extrapolation of relaxation times (Maxwell model) and the BER relaxation are not so far from each other, the *Tv* obtained from BER relaxations is closer to the experimental values found by the dilatometry study (**Table III-13**). Hence, the BER relaxation's isolation allows determining a more accurate estimation of the topology freezing temperature, principally for the epoxy-rich network. The ***Tv*** determined by the three methods showed a **decrease as a function of the number of disulfide bonds** in the network.

3.5.2.3 Time-temperature superposition (TTS) studies

Figure III-20 displayed two different behaviors, one linked to the BER and the other associated with the segmental network's relaxation. This second relaxation showed what appears to be a behavior of WLF-law. To test the WLF behavior on the three different stoichiometries, TTS experiments were carried out at temperatures from *T*g to *T*g ± 30°C. The master curve for the reference network (DGEBA-DDM) is plotted in **Figure S.III- 11**, and the dynamic networks (DGEBA–4-APDS) in Figure S.III- 12, **Figure S.III- 13**, and **Figure S.III- 14**. The shifting factors a_T obtained from the master curves were plotted against the temperature (**Figure III-21**).

The function a_T contains valuable information about the temperature dependence of relaxation times. The shifting factor can take two different functional forms depending on the proximity to the glass-transition temperature[107, 108].

According to the work of Williams, Landel and Ferry, at temperatures near and above the *T*g, the shifting factor follows a dependency on the temperatures following the empirical equation (9), the so-called WLF law.

$$log\ a_T = \frac{-C_1(T-T_{ref})}{C_2+T-T_{ref}} \quad \text{..... (11)}$$

Where C_1 and C_2 are the model parameters determined during the fitting, and T_{ref} is usually the *T*g or the Tα of the material.

Figure III-21 displays the WLF-law behavior at temperatures close and superior to the *T*g, as ascribed by the equations (11). The behavior described by the figure has also been observed by Yu *et al.* (2014)[109]. So, the WLF equation was used to describe the viscoelastic behavior of networks at temperatures near and above *T*g. The corresponding C_1 and C_2 parameters from the WLF law were determined and summarized in **Table III-14** for the four different epoxy systems. The C_1 and C_2 parameters are different from those founded by Williams, Landel, and Ferry for polystyrene. Montarnal *et al*. (2020) have already exposed this remark, presumably related to the broad network dispersity of networks[23].

Moreover, the WLF equation allows determining the apparent activation energy of the relaxation's phenomena at the temperature reference by following the equation (12) [110, 111].

$$Ea = 2.303 * R * T_{ref}^2 \frac{C_1}{C_2} \quad \text{..... (12)}$$

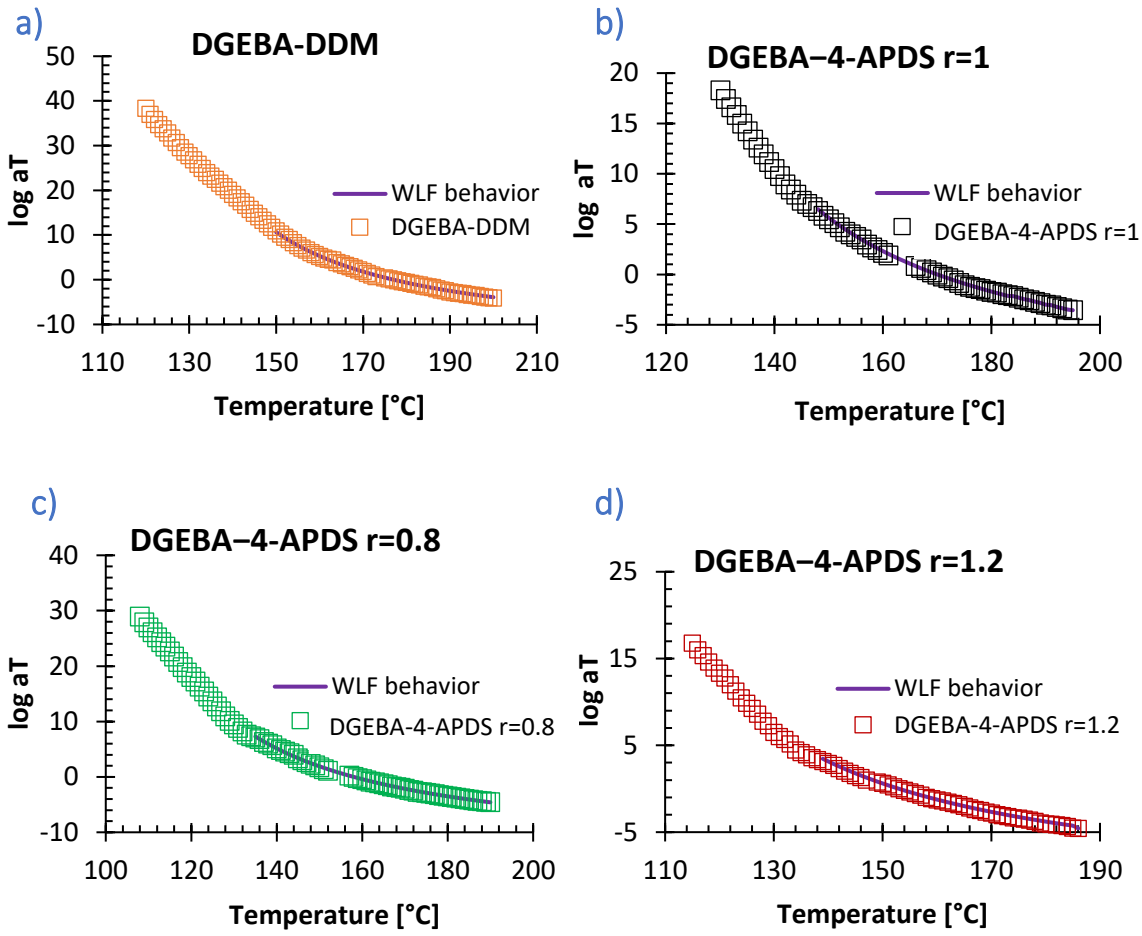

Figure III-21. Plots of the shifting factor a_T and the WLF using equation (11) against the temperature for the system a) DGEBA-DDM r=1 (orange), b) DGEBA–4-APDS r=1 (black), c) DGEBA–4-APDS r=0.8 (green), and d) DGEBA–4-APDS r=1.2 (red).

System	T_{ref} (°C)	C1	C2	Ea $_{apparent}$ (kJ/mol)
DGEBA-DDM	177	14.99	65.05	893
DGEBA-–4-APDS r=0.8	158	14.42	68.50	749
DGEBA–4-APDS r=1	170	12.85	65.62	736
DGEBA–4-APDS r=1.2	153	13.27	67.71	681

Table III-14. C1 and C2 parameters and temperature reference employed in the fitting applying the equation (11), and the apparent activation energy applying equation (12).

Table III-14 also contains the apparent activation energy Ea $_{apparent}$, determined from equation (12). The apparent activation energy decreases as the dynamic bonds' concentration rises. This behavior is consistent with the relaxation rates observed during the stress relaxation experiments. The apparent activation energy of the network mobility over *Tg* is reduced as the presence of reversible

covalent bonds. This apparent activation energy encompasses both the energy due to the chemical exchange between the reversible bonds (BER) and the energy due to the relaxation of the segmental motions of the network.

The TTS experiments allowed evidence the WLF behavior of the epoxy-vitrimer. The parameters C1 and C2 of the dynamic systems (DGEBA–4-APDS) are not so far for the non-dynamic system (DGEBA-DDM). Besides, from the C1 and C2 parameters, it was possible to determine the *apparent activation energy* around the *T*g for the different systems.

So, it is not surprising that the WLF behavior is seen after extracting the segmental network relaxation from the complete relaxation behavior, as shown in **Figure III-20**. Thus, the DGEBA–4-APDS systems present a BER relaxation, which follows an Arrhenian-type behavior, and the relaxation movements of the network follow a WLF-like behavior with an apparent activation energy dependent on bond exchange reaction concentration.

3.6 Conclusions

In this Chapter, we undertook the tasks of 1) determining the optimum curing condition to obtain the best thermomechanical properties of our thermoset, 2) validating the characteristic behaviors that define this thermoset as vitrimer, and 3) providing a model able to describe appropriately the relaxation behavior of the systems DGEBA–4-APDS instead of Maxwell model that does not accurately describe the relaxation behavior.

The first task was to determine the **optimal curing conditions** for the different epoxy systems performed. The best conditions **were established**. A **slow curing ramp** allows to reduce as much as possible **the internal mechanical stresses**, and **a post-curing** step **guarantees as much as possible a complete reaction** of epoxy resins [53,58, 69]. Introducing reversible covalent bonds does not alter the thermomechanical behavior of the epoxy network. Indeed, it followed the same behavior as classical epoxy resins. The off-stoichiometric systems display a low α-transition and a decrease in the crosslink density, presumably linked to the heterogeneity on the network's architecture.

The second primary task was to evidence **the vitrimer behavior of the DGEBA–4-APDS systems**: 1) the permanent connectivity, 2) a relaxation that follows an Arrhenian behavior, and 3) a new transition temperature different to the *T*g or *Tm* was identified: The *T*v[22]. All properties were **proved** and summarized below.

1) **The permanent connectivity** was **demonstrated by** performing **swelling** experiments and testing the crosslink density at different temperatures by **frequency sweep experiments**. In the

swelling tests, the samples swell, but they do not dissolve, even at elevated temperatures, except in DMF. Still, the DMF might have a reactant role and not a solvent role, so we have to be aware of its employment. This observation might be helpful for a further reprocessing process. The frequency sweep experiments displayed a constant crosslink density, and only at a low frequency, a decrease of the density was remarked. This behavior is quite similar to other systems like vinylogous urethanes or transesterification. Indeed, this behavior might represent a characteristical fingerprint of vitrimer behavior.

2) **A new transition temperature different from the *T*g or *T*m** was **evidenced** by performing dilatometry experiments, the *T*g and the *T*v. The *T*g decreases for the off-stoichiometric systems, a very common behavior. The ***T*v** displayed a **diminution as a function of the number of dynamic bonds**.
3) The stress relaxation experiment showed that **the networks relaxed and flowed**, as the vitrimer definition suggests. The observed relaxation rate increases as a function of the concentration of reversible bonds. Besides, the networks based on DGEBA–4-APDS displayed a **relaxation time** evolution that **follows an Arrhenian-like behavior.** Therefore, it **resembles silica materials** or strong liquids, indicating an easy re-processability.

Finally, the third task was to **provide a different relaxation model** to describe the relaxation behavior of the DGEBA–4-APDS systems more accurately than the Maxwell model, which does not correctly describe the relaxation behavior of vitrimer materials. The model proposed in this work **considers two relaxation behaviors**: **1**) the **bond exchange reaction** relaxation, **2**) the **segmental relaxation movements of the network**, both using a stretched exponent decay function, the KWW equation. The use of this model allowed **to provide a more accurate description** of the relaxation behavior. The analysis of the BER component permitted to determine different activation energies and topology freezing temperatures. The robustness of the model was supported by tuning the number of dynamic bonds added to the system. **The Ea** determined by the adapted model **displays a dependence on the number of reversible bonds in the network.** The results were in line with many other works using different vitrimer systems[19, 106]. This behavior was not possible to be predicted when using the Maxwell model because it considers a single relaxation, although, in reality, it is a convolution of multiple relaxations modes[102].

Bibliography

1 Grand Viwe Reserarch (2016) Epoxy Resin Market Size, Share, and Trends Analysis Report, By Application (Paints & Coatings, Wind Turbine, Composites, Construction, Electrical & Electronics, Adhesives) And Segment Forecast to 2024. Recurperated from https://www.grandviewresearch.com/industry-analysis/epoxy-resins-market

2 Mordor Intelligence (2019) Global Epoxy Resins Market (2020-2025). Recuperated from https://samples.mordorintelligence.com/56869/Sample%20-%20Global%20Epoxy%20Resins%20Market%20(2020%20-%202025)%20-%20Mordor%20Intelligence.pdf

3 May, C. (Ed.). (1988). Epoxy resins: chemistry and technology. Second Editions. Routledge.

4 Ellis, B. (Ed.). (1993). Chemistry and technology of epoxy resins. London: Blackie Academic & Professional.

5 White, S. R., Sottos, N. R., Geubelle, P. H., Moore, J. S., Kessler, M. R., Sriram, S. R., Viswanathan, S. (2001). Autonomic healing of polymer composites. Nature, 409(6822), 794-797.

6 Brown, E. N., Sottos, N. R., & White, S. R. (2002). Fracture testing of a self-healing polymer composite. Experimental mechanics, 42(4), 372-379.

7 Kumar, R., Hynes, N. R. J., Manju, R., Senthamaraikannan, P., Saravanakumar, S. S., Khan, A., ... & Verpoort, F. (2020). Self-healing fiber-reinforced epoxy composites. In Self-Healing Composite Materials (pp. 393-404). Woodhead Publishing.

8 Caruso, M. M., Delafuente, D. A., Ho, V., Sottos, N. R., Moore, J. S., & White, S. R. (2007). Solvent-promoted self-healing epoxy materials. Macromolecules, 40(25), 8830-8832.

9 Xiao, D. S., Yuan, Y. C., Rong, M. Z., & Zhang, M. Q. (2009). Self-healing epoxy based on cationic chain polymerization. Polymer, 50(13), 2967-2975.

10 Chen, X., Dam, M. A., Ono, K., Mal, A., Shen, H., Nutt, S. R., & Wudl, F. (2002). A thermally re-mendable cross-linked polymeric material. *Science*, *295*(5560), 1698-1702.

11 Hoppe, C. E., Galante, M. J., Oyanguren, P. A., & Williams, R. J. (2005). Epoxies Modified by Palmitic Acid: From Hot-Melt Adhesives to Plasticized Networks. *Macromolecular Materials and Engineering*, *290*(5), 456-462.

12 Ludueña, R. F., Roach, M. C., Trcka, P. P., & Weintraub, S. (1981). N, N-Bis (α-iodoacetyl)-2, 2′-dithiobis (ethylamine), a reversible crosslinking reagent for protein sulfhydryl groups. *Analytical biochemistry*, *117*(1), 76-80.

13 Sastri, V. R., & Tesoro, G. C. (1990). Reversible crosslinking in epoxy resins. II. New approaches. *Journal of applied polymer science*, *39*(7), 1439-1457.

14 Dušek, K., & Matejka, L. (1984). Transesterification and gelation of polyhydroxy esters formed from diepoxides and dicarboxylic acids in Comstock, J. (Ed.), *Rubber-Modified Thermoset Resin* (Vo. 208, pp. 15-26). Advances in Chemistry Series.

15 Kloxin, C. J., Scott, T. F., Adzima, B. J., & Bowman, C. N. (2010). Covalent adaptable networks (CANs): a unique paradigm in cross-linked polymers. *Macromolecules*, *43*(6), 2643-2653.

16 Bowman, C. N., & Kloxin, C. J. (2012). Covalent adaptable networks: reversible bond structures incorporated in polymer networks. *Angewandte Chemie International Edition*, *51*(18), 4272-4274.

17 Kloxin, C. J., & Bowman, C. N. (2013). Covalent adaptable networks: smart, reconfigurable and responsive network systems. *Chemical Society Reviews*, *42*(17), 7161-7173.

18 Turkenburg, D. H., & Fischer, H. R. (2015). Diels-Alder based, thermo-reversible cross-linked epoxies for use in self-healing composites. *Polymer*, *79*, 187-194.

19 Altuna, F. I., Pettarin, V., & Williams, R. J. (2013). Self-healable polymer networks based on the cross-linking of epoxidised soybean oil by an aqueous citric acid solution. *Green Chemistry*, *15*(12), 3360-3366.

20 Capelot, M., Montarnal, D., Tournilhac, F., & Leibler, L. (2012). Metal-catalyzed transesterification for healing and assembling of thermosets. *Journal of the american chemical society*, *134*(18), 7664-7667.

21 Montarnal, D., Capelot, M., Tournilhac, F., & Leibler, L. (2011). Silica-like malleable materials from permanent organic networks. *Science*, *334*(6058), 965-968.

22 Denissen, W., Winne, J. M., & Du Prez, F. E. (2016). Vitrimers: permanent organic networks with glass-like fluidity. *Chemical science*, *7*(1), 30-38.

23 Jourdain, A., Asbai, R., Anaya, O., Chehimi, M. M., Drockenmuller, E., & Montarnal, D. (2020). Rheological Properties of Covalent Adaptable Networks with 1, 2, 3-Triazolium Cross-Links: The Missing Link between Vitrimers and Dissociative Networks. *Macromolecules*, *53*(6), 1884-1900.

24 Chakma, P., Morley, C. N., Sparks, J. L., & Konkolewicz, D. (2020). Exploring How Vitrimer-like Properties Can Be Achieved from Dissociative Exchange in Anilinium Salts. *Macromolecules*, *53*(4), 1233-1244.

25 Elling, B. R., & Dichtel, W. R. (2020). Reprocessable cross-linked polymer networks: are associative exchange mechanisms desirable?. *ACS Central Science*, *6*(9), 1488-1496.

26 Breuillac, A., Kassalias, A., & Nicolaÿ, R. (2019). Polybutadiene vitrimers based on dioxaborolane chemistry and dual networks with static and dynamic cross-links. *Macromolecules*, *52*(18), 7102-7113.

27 Dyre, J. C. (2006). Colloquium: The glass transition and elastic models of glass-forming liquids. *Reviews of modern physics*, *78*(3), 953.

28 Denissen, W., Rivero, G., Nicolaÿ, R., Leibler, L., Winne, J. M., & Du Prez, F. E. (2015). Vinylogous urethane vitrimers. *Advanced Functional Materials*, *25*(16), 2451-2457.

29 Maxwell equation $\frac{G}{G_o} = e^{-\frac{t}{\lambda}}$ where $\frac{G}{G_o}$ is the stress modulus normalized, t is the relaxation time and λ the characteristically relaxation time.

30 Luo, C., Shi, X., Lei, Z., Zhu, C., Zhang, W., & Yu, K. (2018). Effects of bond exchange reactions and relaxation of polymer chains on the thermomechanical behaviors of covalent adaptable network polymers. *Polymer*, *153*, 43-51.

31 Li, L., Chen, X., Jin, K., & Torkelson, J. M. (2018). Vitrimers designed both to strongly suppress creep and to recover original cross-link density after reprocessing: quantitative theory and experiments. *Macromolecules*, *51*(15), 5537-5546.

32 Hayashi, M., Yano, R., & Takasu, A. (2019). Synthesis of amorphous low T g polyesters with multiple COOH side groups and their utilization for elastomeric vitrimers based on post-polymerization cross-linking. *Polymer Chemistry*, *10*(16), 2047-2056.

33 Snijkers, F., Pasquino, R., & Maffezzoli, A. (2017). Curing and viscoelasticity of vitrimers. *Soft Matter*, *13*(1), 258-268.

34 Wu, J. B., Li, S. J., Liu, H., Qian, H. J., & Lu, Z. Y. (2019). Dynamics and reaction kinetics of coarse-grained bulk vitrimers: a molecular dynamics study. *Physical Chemistry Chemical Physics*, *21*(24), 13258-13267.

35 Zhang, B., Yuan, C., Zhang, W., Dunn, M. L., Qi, H. J., Liu, Z., ... & Ge, Q. (2019). Recycling of vitrimer blends with tunable thermomechanical properties. *RSC advances*, *9* (10), 5431-5437.

36 Snyder, R. L., Fortman, D. J., De Hoe, G. X., Hillmyer, M. A., & Dichtel, W. R. (2018). Reprocessable acid-degradable polycarbonate vitrimers. *Macromolecules*, *51*(2), 389-397.

37 Denissen, W., Droesbeke, M., Nicolaÿ, R., Leibler, L., Winne, J. M., & Du Prez, F. E. (2017). Chemical control of the viscoelastic properties of vinylogous urethane vitrimers. *Nature communications*, *8*(1), 1-7.

38 Guerre, M., Taplan, C., Nicolaÿ, R., Winne, J. M., & Du Prez, F. E. (2018). Fluorinated vitrimer elastomers with a dual temperature response. *Journal of the American Chemical Society*, *140*(41), 13272-13284.

39 Zhang, H., Wang, D., Liu, W., Li, P., Liu, J., Liu, C., ... & Xu, J. (2017). Recyclable polybutadiene elastomer based on dynamic imine bond. *Journal of Polymer Science Part A: Polymer Chemistry*, *55*(12), 2011-2018.

40 Zheng, H., Liu, Q., Lei, X., Chen, Y., Zhang, B., & Zhang, Q. (2018). A conjugation polyimine vitrimer: Fabrication and performance. *Journal of Polymer Science Part A: Polymer Chemistry*, *56*(22), 2531-2538.

41 Zuo, Y., Gou, Z., Zhang, C., & Feng, S. (2016). Polysiloxane-Based Autonomic Self-Healing Elastomers Obtained through Dynamic Boronic Ester Bonds Prepared by Thiol–Ene "Click" Chemistry. *Macromolecular rapid communications*, *37*(13), 1052-1059.

42 Saed, M. O., Gablier, A., & Terentejv, E. M. (2020). Liquid Crystalline Vitrimers with Full or Partial Boronic-Ester Bond Exchange. *Advanced Functional Materials*, *30*(3), 1906458.

43 Lu, Y. X., Tournilhac, F., Leibler, L., & Guan, Z. (2012). Making insoluble polymer networks malleable via olefin metathesis. *Journal of the American Chemical Society*, *134*(20), 8424-8427.

44 Lu, Y. X., & Guan, Z. (2012). Olefin metathesis for effective polymer healing via dynamic exchange of strong carbon–carbon double bonds. *Journal of the American Chemical Society*, *134*(34), 14226-14231.

45 de Luzuriaga, A. R., Matxain, J. M., Ruipérez, F., Martin, R., Asua, J. M., Cabañero, G., & Odriozola, I. (2016). Transient mechanochromism in epoxy vitrimer composites containing aromatic disulfide crosslinks. *Journal of Materials Chemistry C*, *4*(26), 6220-6223.

46 Azcune, I., & Odriozola, I. (2016). Aromatic disulfide crosslinks in polymer systems: Self-healing, reprocessability, recyclability and more. *European Polymer Journal*, *84*, 147-160.

47 Hendriks, B., Waelkens, J., Winne, J. M., & Du Prez, F. E. (2017). Poly (thioether) vitrimers via transalkylation of trialkylsulfonium salts. *ACS Macro Letters*, *6*(9), 930-934.

48 Tang, Z., Liu, Y., Huang, Q., Zhao, J., Guo, B., & Zhang, L. (2018). A real recycling loop of sulfur-cured rubber through transalkylation exchange of C–S bonds. *Green chemistry*, *20*(24), 5454-5458.

49 Tretbar, C. A., Neal, J. A., & Guan, Z. (2019). Direct Silyl Ether Metathesis for Vitrimers with Exceptional Thermal Stability. *Journal of the American Chemical Society*, *141*(42), 16595-16599.

50 Nishimura, Y., Chung, J., Muradyan, H., & Guan, Z. (2017). Silyl ether as a robust and thermally stable dynamic covalent motif for malleable polymer design. *Journal of the American Chemical Society*, *139*(42), 14881-14884.

51 Matxain, J. M., Asua, J. M., & Ruipérez, F. (2016). Design of new disulfide-based organic compounds for the improvement of self-healing materials. *Physical Chemistry Chemical Physics*, *18*(3), 1758-1770.

52 Huang, Z., Wang, Y., Zhu, J., Yu, J., & Hu, Z. (2018). Surface engineering of nanosilica for vitrimer composites. *Composites Science and Technology*, *154*, 18-27.

53 Sanz, G., Garmendia, J., Andres, M. A., & Mondragon, I. (1995). Dependence of dynamic mechanical behavior of DGEBA/DDM stoichiometric epoxy systems on the conditions of curing process. *Journal of applied polymer science*, *55*(1), 75-87.

54 Campana, C., Leger, R., Sonnier, R., Ferry, L., & Ienny, P. (2018). Effect of post curing temperature on mechanical properties of a flax fiber reinforced epoxy composite. *Composites Part A: Applied Science and Manufacturing*, *107*, 171-179.

55 Kumar, D. S., Shukla, M. J., Mahato, K. K., Rathore, D. K., Prusty, R. K., & Ray, B. C. (2015). Effect of post-curing on thermal and mechanical behavior of GFRP composites. *Proceeding of IOP Publishing*, 012012.

56 Wu, C. S. (1992). Influence of post-curing and temperature effects on bulk density, glass transition and stress-strain behaviour of imidazole-cured epoxy network. *Journal of materials science*, *27*(11), 2952-2959.

57 Hong, M. (2017). Application de la spectroscopie de fluorescence 3D a la caractérisation des réseaux polymères thermodurcis : influence de la mobilité macromoléculaire et du vieillissement hydrolytique [Thèse de doctorat non publie], Université de Toulon.

58 Ochi, M., Yamashita, K., & Shimbo, M. (1991). The mechanism for occurrence of internal stress during curing epoxide resins. *Journal of Applied Polymer Science*, *43*(11), 2013-2019.

59 Plepys, A. R., & Farris, R. J. (1990). Evolution of residual stresses in three-dimensionally constrained epoxy resins. *Polymer*, *31*(10), 1932-1936.

60 Kim, S. S., Murayama, H., Kageyama, K., Uzawa, K., & Kanai, M. (2012). Study on the curing process for carbon/epoxy composites to reduce thermal residual stress. *Composites Part A: Applied Science and Manufacturing*, *43*(8), 1197-1202.

61 Xiao, G. Z., & Shanahan, M. E. R. (1998). Irreversible effects of hygrothermal aging on DGEBA/DDA epoxy resin. *Journal of Applied Polymer Science*, *69*(2), 363-369.

62 Cherdoud-Chihani, A., Mouzali, M., & Abadie, M. J. M. (2003). Study of crosslinking acid copolymer/DGEBA systems by FTIR. *Journal of applied polymer science*, *87*(13), 2033-2051.

63 Scherzer, T., Strehmel, V., Tänzer, W., & Wartewig, S. (1992). FTIR spectroscopy studies on epoxy networks. In *Physics of Polymer Networks* (pp. 202-205). Steinkopff.

64 Pascault, J. P., Sautereau, H., Verdu, J., & Williams, R. J. (2002). *Thermosetting polymers* (Vol. 64). CRC press.

65 Fernandez-Nograro, F., Valea, A., Llano-Ponte, R., & Mondragon, I. (1996). Dynamic and mechanical properties of DGEBA/poly (propylene oxide) amine-based epoxy resins as a function of stoichiometry. *European Polymer Journal*, *32*(2), 257-266.

66 De Nograro, F. F., Guerrero, P., Corcuera, M. A., & Mondragon, I. (1995). Effects of chemical structure of hardener on curing evolution and on the dynamic mechanical behavior of epoxy resins. *Journal of applied polymer science*, *56*(2), 177-192.

67 Li, Y. F., Xiao, M. Z., Wu, Z., Peng, K., Han, C. M., Xiang, W., & Dai, J. Y. (2016, July). Effects of epoxy/hardener Stoichiometry on structures and properties of a diethanolamine-cured epoxy encapsulant. In *IOP Conference Series: Materials Science and Engineering* (Vol. 137, No. 1, p. 012012). IOP Publishing.

68 Meyer, F., Sanz, G., Eceiza, A., Mondragon, I., & Mijović, J. (1995). The effect of stoichiometry and thermal history during cure on structure and properties of epoxy networks. *Polymer*, *36*(7), 1407-1414.

69 Frank, K., & Wiggins, J. (2013). Effect of stoichiometry and cure prescription on fluid ingress in epoxy networks. *Journal of Applied Polymer Science*, *130*(1), 264-276.

70 Dušek, K. (1986). Network formation in curing of epoxy resins. In *Advances in Polymer Science. Epoxy Resins and Composites III* (Vol. 78, pp. 1-59). Springer, Berlin, Heidelberg.

71 Vanlandingham, M. R., Eduljee, R. F., & Gillespie Jr, J. W. (1999). Relationships between stoichiometry, microstructure, and properties for amine-cured epoxies. *Journal of Applied Polymer Science*, *71*(5), 699-712.

72 Winne, J. M., Leibler, L., & Du Prez, F. E. (2019). Dynamic covalent chemistry in polymer networks: a mechanistic perspective. *Polymer Chemistry*, *10*(45), 6091-6108.

73 Canadell, J., Goossens, H., & Klumperman, B. (2011). Self-healing materials based on disulfide links. *Macromolecules*, *44*(8), 2536-2541.

74 Morgan, R. J., Kong, F. M., & Walkup, C. M. (1984). Structure-property relations of polyethertriamine-cured bisphenol-A-diglycidyl ether epoxies. *Polymer*, *25*(3), 375-386.

75 Nouailhas, H., Aouf, C. Le Guerneve, C., Caillol, S., Bouevin, B., & Fulcrand, H. (2011). Synthesis and properties of biobased epoxy resins. Part 1. Glycidylation of flavonoids by epichlorohydrin. *Journal of Polymer Science Part A: Polymer Chemistry, 49* (10), 2261-2270.

76 Heravi, M. M., Ghavidel, M., & Mohammadkhani, L. (2018). Beyond a solvent: triple roles of dimethylformamide in organic chemistry. *RSC advances*, *8*(49), 27832-27862.

77 Rajan, V. V., Dierkes, W. K., Joseph, R., & Noordermeer, J. W. (2006). Science and technology of rubber reclamation with special attention to NR-based waste latex products. *Progress in polymer science*, *31*(9), 811-834.

78 Mathieu Capelot, (2013), *Chimie de Polycondensation, Polymères Supramoléculaires et Vitrimères. Polymères.* [Thèse doctoral, Université Pierre et Marie Curie - Paris VI].

79 Denissen, W., De Baere, I., Van Paepegem, W., Leibler, L., Winne, J., & Du Prez, F. E. (2018). Vinylogous urea vitrimers and their application in fiber reinforced composites. *Macromolecules*, *51*(5), 2054-2064.

80 Taplan, C., Guerre, M., Winne, J. M., & Du Prez, F. E. (2020). Fast processing of highly crosslinked, low-viscosity vitrimers. *Materials Horizons*, *7*(1), 104-110.

81 Perego, A., & Khabaz, F. (2020). Volumetric and Rheological Properties of Vitrimers: A Hybrid Molecular Dynamics and Monte Carlo Simulation Study. *Macromolecules*, *53*(19), 8406-8416.

82 Shrivastava, A. (2018). *Introduction to plastics engineering*. William Andrew.

83 Hammer, L., Van Zee, N. J., & Nicolaÿ, R. (2021). Dually Crosslinked Polymer Networks Incorporating Dynamic Covalent Bonds. *Polymers*, *13*(3), 396.

84 Guerre, M., Taplan, C., Winne, J. M., & Du Prez, F. E. (2020). Vitrimers: directing chemical reactivity to control material properties. *Chemical Science*, *11*(19), 4855-4870.

85 Capelot, M., Unterlass, M. M., Tournihac, F., & Leibler, L. (2012). Catalytic control of the vitrimer glass transition. *ACS Macro Letters*, 1 (7), 789-792.

86 Yang, Y., Zhang, S. Zhang, X., Gao, L., Wei, Y., & Ji, Y. (2019). Detecting topology freezing transition temperature of vitrimers by AIE luminogens. *Nature communications*, 10 (1), 1-8.

87 Zhang, B., Yuan, C., Zhang, W., Dunn, M. L., Qi, H. J., Liu, Z., ... & Ge, Q. (2019). Recycling of vitrimer blends with tunable thermomechanical properties. *RSC advances*, *9*(10), 5431-5437.

88 Murata, H., Shigeto, N., & Hamada, T. (1990). Viscoelastic properties of tissue conditioners—stress relaxation test using Maxwell model analogy. *Journal of oral rehabilitation*, *17*(4), 365-375.

89 Obadia, M. M., Mudraboyina, B. P., Serghei, A., Montarnal, D., & Drockenmuller, E. (2015). Reprocessing and recycling of highly cross-linked ion-conducting networks through transalkylation exchanges of C–N bonds. *Journal of the American Chemical Society*, *137*(18), 6078-6083.

90 Yang, Y., Pei, Z., Zhang, X., Tao, L., Wei, Y., & Ji, Y (2014). Carbon nanotube-vitrimer composite for facile and efficent photo-welding of epoxy. *Chemical Science*, 5 (9), 3486-3492.

91 Drozdov, A. D., & Chistiansen, J. D. (2020). Thermo-mechanical behavior of elastomers with Dynamic covalent bonds. *International Journal of Engineering Science*, 147, 103200.

92 Li, S., Shen, J., Chen, X., Chen, R., & Luo, X. (1997). Studies on relaxation and thermal expansion behavior of polysiloxane-modified epoxy resin. *Journal of Macromolecular Science, Part B: Physics*, *36*(3), 357-366.

93 Alig, I., Lellinger, D., Nancke, K., Rizos, A., & Fytas, G. (1992). Dynamic light scattering and ultrasonic investigations during the cure reaction of an epoxy resin. *Journal of applied polymer science*, *44*(5), 829-835.

94 Lee, A., & Lichtenhan, J. D. (1999). Thermal and viscoelastic property of epoxy–clay and hybrid inorganic–organic epoxy nanocomposites. *Journal of Applied Polymer Science*, *73*(10), 1993-2001.

95 Chen, X., Li, L., Wei, T., Venerus, D. C., & Torkelson, J. M. (2018). Reprocessable polyhydroxyurethane network composites: effect of filler surface functionality on cross-link density recovery and stress relaxation. *ACS applied materials & interfaces*, *11*(2), 2398-2407.

96 Dhinojwala, A., Hooker, J. C., & Torkelson, J. M. (1994). Retardation of rotational reorientation dynamics in polymers near the glass transition: a novel study over eleven decades in time using second-order non-linear optics. *Journal of non-crystalline solids*, *172*, 286-296.

97 Hayashi, M., Yano, R., & Takasu, A. (2019). Synthesis of amorphous low T g polyesters with multiple COOH side groups and their utilization for elastomeric vitrimers based on post-polymerization cross-linking. *Polymer Chemistry*, *10*(16), 2047-2056.

98 Li, Z., Wang, J., Li, X., Wang, Y., Fan, L. J., Yang, S., ... & Tu, Y. (2020). Supramolecular and Physically Double-Cross-Linked Network Strategy toward Strong and Tough Elastic Fibers. *ACS Macro Letters*, *9*(11), 1655-1661.

99 Ishibashi, J. S., Pierce, I. C., Chang, A. B., Zografos, A., El-Zaatari, B. M., Fang, Y., ... & Kalow, J. A. (2021). Mechanical and structural consequences of associative dynamic cross-linking in acrylic diblock copolymers. *Macromolecules*, *54*(9), 3972-3986.

100 El-Zaatari, B. M., Ishibashi, J. S., & Kalow, J. A. (2020). Cross-linker control of vitrimer flow. *Polymer Chemistry*, *11*(33), 5339-5345.

101 Song, Z., Wang, Z., & Cai, S. (2021). Mechanics of vitrimer with hybrid networks. *Mechanics of Materials*, *153*, 103687.

102 Ricarte, R. G., Tournilhac, F., Cloître, M., & Leibler, L. (2020). Linear viscoelasticity and flow of self-assembled vitrimers: The case of a polyethylene/dioxaborolane system. *Macromolecules*, *53*(5), 1852-1866.

103 Meng, F., Saed, M. O., & Terentjev, E. M. (2019). Elasticity and relaxation in full and partial vitrimer networks. *Macromolecules*, *52*(19), 7423-7429.

104 Lessard, J. J., Scheutz, G. M., Sung, S. H., Lantz, K. A., Epps III, T. H., & Sumerlin, B. S. (2019). Block copolymer vitrimers. *Journal of the American Chemical Society*, *142*(1), 283-289.

105 Hayashi, M., & Chen, L. (2020). Functionalization of triblock copolymer elastomers by cross-linking the end blocks via trans-N-alkylation-based exchangeable bonds. *Polymer Chemistry*, *11*(10), 1713-1719.

106 Liu, Y., Tang, Z., Chen, J., Xiong, J., Wang, D., Wang, S., ... & Guo, B. (2020). Tuning the mechanical and dynamic properties of imine bond crosslinked elastomeric vitrimers by manipulating the crosslinking degree. *Polymer Chemistry*, *11*(7), 1348-1355.

107 Ferry, J. D. (1980). *Viscoelastic properties of polymers*. John Wiley & Sons.

108 Morrison, F. A. (2001). *Understanding rheology*. Oxford University Press, USA.

109 Yu, K., Ge, Q., & Qi, H. J. (2014). Reduced time as a unified parameter determining fixity and free recovery of shape memory polymers. *Nature communications*, *5*(1), 1-9.

110 Gerard, J. F., Galy, J., Pascault, J. P., Cukierman, S., & Halary, J. L. (1991). Viscoelastic response of model epoxy networks in the glass transition region. *Polymer Engineering & Science*, *31*(8), 615-621.

111 Shangguan, Y., Chen, F., Jia, E., Lin, Y., Hu, J., & Zheng, Q. (2017). New insight into time-temperature correlation for polymer relaxations ranging from secondary relaxation to terminal flow: Application of a universal and developed WLF equation. *Polymers*, *9*(11), 567.

Chapter IV : Epoxy-vitrimer resin reinforced with nano fibrillated cellulose

4. Epoxy vitrimer resin reinforced with nano fibrillated cellulose

4.1 Introduction

The use of composite materials has been widely documented throughout the history of humankind. Nowadays, composites materials are found in our daily lives, such as packaging, construction, automobile, or even in the aerospace industry.[1] For this reason, the interest in composite materials grows day by day. Parallelly, the growing need for more and more environment-friendly materials to reduce polymer waste production has triggered diverse studies to propose an eco-friendly solution without compromising the good performance of these materials.

Natural fibers, such as plant fibers containing cellulose fibrils, have drawn the attention as fillers in polymer matrices due to their highly desirable properties such as lightweight, biodegradability, recyclability, renewability, low density, high specific strength, Young's modulus, and last but not least, low-cost[2, 3]. Hence, numerous works using cellulose as reinforcement have been explored, showing that nanocellulose can afford high strength and modulus to composite materials[4, 5, 6, 7].

Numerous works have been focused on the study of cellulose whiskers and nanofibrillated cellulose. The cellulose whiskers have diameters in the range of 2-20 nm and a length that could go to several tens of microns; thus, they have a significant load-carrying capability with this high aspect ratio. Nonetheless, the production of cellulose whiskers is costly and time-consuming. These disadvantages have triggered nano fibrillated cellulose (NFC) studies as fillers, which display advantages such as low cost and easy preparation compared to cellulose whiskers. The diameter range of NFC goes from 10 to 60 nm, exhibiting excellent mechanical properties up to 150 GPa[8, 9]. Indeed, several composite materials based on a polymer matrix with NFC reinforcement have shown promising results. That is the case of acrylic resins[10], PBD[11], polypropylene[12] polyurethane[13], polylactic acid[14], melamine-formaldehyde resins [15], or epoxy resins reinforced by cellulose fibers [16].

In the field of epoxy resin composites, the incorporation of nano fibrillated cellulose into the resin is not always easy. Hence diverse incorporation methods have been developed like cellulose aerogels impregnation[17], cellulose surface modification[18], high-speed mechanical stirrer[19], or pre-impregnated cellulose suspensions[20, 21]. The last incorporation technique adapted by Berglund *et al.* has shown favorable results. They aimed to preserve the higher mechanical performance that the NFC might confer in the glassy and rubbery state of the material. The technique consists of a prepreg process that leads to an advantageous distribution into the matrix, allowing the epoxy to diffuse into the cellulose structure. In this way, the fibers are embedded in the epoxy polymer matrix during the curing process.

On the other hand, vitrimer materials with their self-healing behavior can reduce polymer waste.

Therefore, several vitrimer-based composites with glass fibers[22], carbon fibers[23, 24], carbon nanotubes[25], silica[26, 27], and cellulose have been explored recently[28]. While it is true that, in the beginning, the use of fibers for reinforcing vitrimer-based composites was focused on carbon and glass fibers, the use of natural ones is not far behind. Indeed, notable works explore the use of cellulose fibers based on transesterification chemistry, where the cellulose fibers play a filler role and a reactive role in the exchange reaction[29, 30, 31]. For instance, Walther *et al.* (2019) have explored the manufacture of vitrimer composites reinforced with cellulose fibers under aqueous conditions. Their protocol allows the polymeric matrix to diffuse into the fibrils and benefit from most of the natural filler properties. This challenging technique has also been proved by incorporating nano-clays for further promising applications like flame retardants[32].

While the works using cellulose in a vitrimeric matrix based on transesterification exchanges are promising, other exchange chemistries may be worth exploring with retaining the NFC as reinforcement. DGEBA–4-APDS system has kept the attention as an advantageous crosslink due to its high-temperature resistance with a *T*g superior to 100°C (depending on the stoichiometry ratio). Indeed, this system has been explored by using fillers such as carbon fibers and surface-modified nano-silicas. Both cases display promising results, either by increasing the elastic modulus or modifying the stress relaxation spectrum. The present work explores the use of NFC in the vitrimer system DGEBA–4-APDS and studies the effect of the NFC as fillers on the thermo-mechanical and vitrimer properties.

4.2 Objectives

4.2.1 General objective

The general objective of this Chapter is to provide a vitrimer-based composite that combines a high *T*g with enhanced mechanical properties by incorporating nano fibrillated cellulose without perturbing the vitrimer properties of the composite material. On the one hand, the incorporation of fibrils in the epoxy matrix promotes a load-carrying capability improving the mechanical properties. On the other hand, natural fibers as fillers may confer flexibility to the material that inorganic fillers cannot afford.

4.2.2 Particulars objectives

- To determine the optimal conditions to manufacture NFC templates impregned in an epoxy resin DGEBA–4-APDS with an amine/epoxy stoichiometric ratio of 1.

- To characterize the thermal and thermomechanical properties of the elaborated NFC reinforced composite materials.
- To characterize the morphology of the elaborated DGEBA–4-APDS-NFC template.
- To verify the vitrimeric properties of the composite DGEBA–4-APDS-NFC: the permanent connectivity, a new transition temperature different to the *Tg* or *T*m, and the relaxation behavior.
- To describe the vitrimer composite's relaxation behavior more accurately by applying a relaxation model considering the bond exchange relaxation mechanism and the segmental movements of the network relaxation.

4.3 Experimental section

Two approaches to produce NFC reinforced composites were explored. The first protocol is inspired by Drzal *et al.* process, and the second protocol is inspired by the methodology of Berglund *et al*. Both protocols were used with some modifications.

The first protocol, inspired by Drzal *et al.* works, is summarized in **Figure IV-1**. This method uses cellulose in acetone suspension (1% w/w). Solvent exchanges were performed using an ultraturrax, ten changes, each one of 5min at 10k rpm, to ensure a complete solvent exchange. The DGEBA was added to the NFC suspension in acetone for 30 min at room temperature. Then the hardener was added and mixed for 30 min. The mixture was cast in silicone molds.
The mixture was degassed to eliminate as much as possible the acetone. Finally, the samples were cured at 60°C/ 1h + 80°C/1h + 130°C/2h +150°C/2h.

The obtained samples were not homogeneous, soft, and containing many empty spaces at the material's interior. Tests with acetone and ethanol solvent were carried out to obtain better results, but the same behavior was remarked using both solvents.

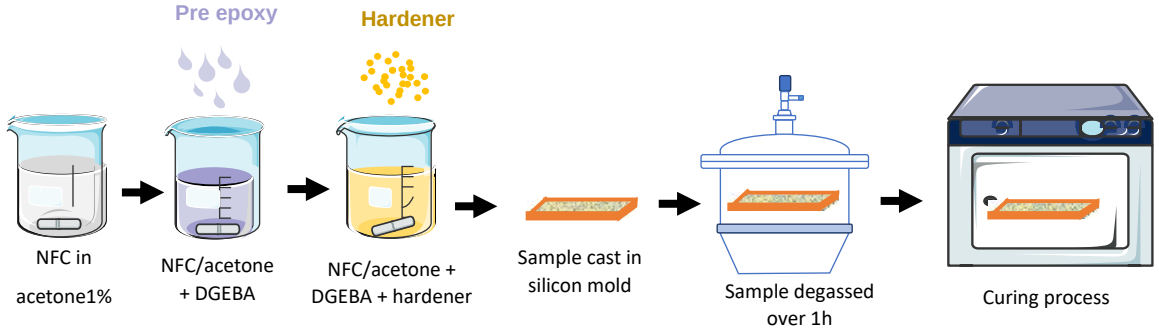

Figure IV-1. The protocol of NFC incorporation into resin (inspired by Drzal *et al.*)[18].

The second protocol, inspired by Berglund *et al.* work, suggests producing cellulose/water templates, avoiding the NFC's agglomeration, and allowing an advantageous diffusion of the epoxy matrix into the fibrils. The elaborated composites contain 10% of pristine NFC and 90% of epoxy vitrimer DGEBA–4-APDS. **Figure IV-2** summarizes the employed methodology for the template's elaboration and the employed curing cycle.

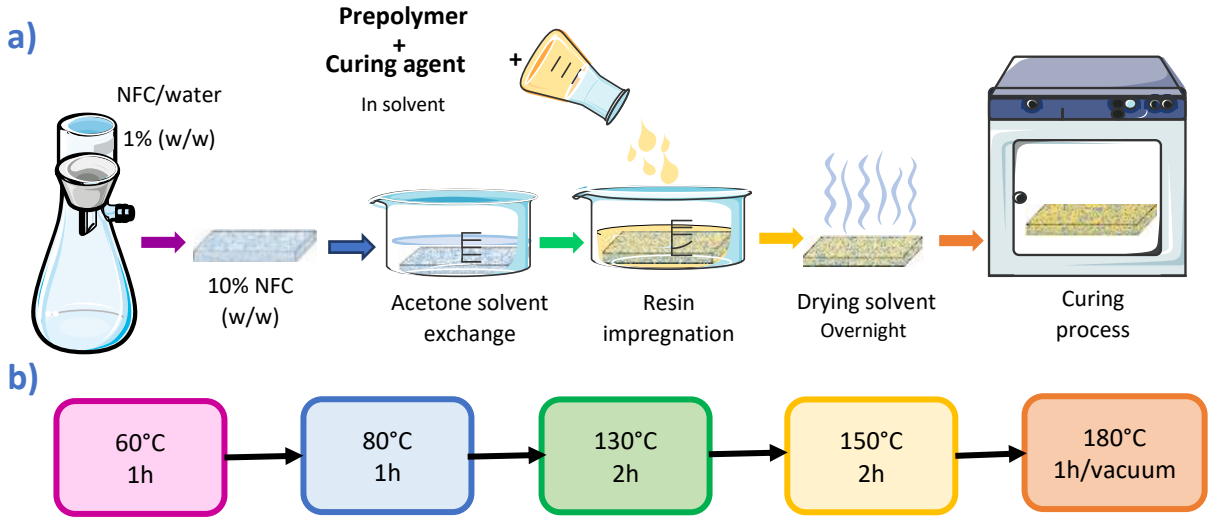

Figure IV-2. a) the protocol of NFC incorporation into epoxy resin (inspired by Berglund *et al.*[11] and b) the used curing cycle.

The first step of this method is the elaboration of a cellulose template. A filter net of polyamide with a diameter pore of 1 µm was employed to filter the cellulose in an aqueous suspension (1% w/w). The elaborated template contains 10% of NFC and 90 % of water. Four to five solvent exchanges in acetone were carried out, each one of 4h.

The second step was the preparation of the epoxy resin. Prepolymer and hardener were blended in acetone on a dilution of 70 % of w/w. Then, the template is immersed in the epoxy resin in acetone over a night.

Finally, the samples are cured employing the optimal curing cycle for system DGEBA–4-APDS r=1 (described in Chapter III), 60°C/1h + 80°C/1h +130°C/2h + 150°C/2h + 180°C/1h under vacuum.

The thermo-mechanical properties were studied with DMA by carrying out a dynamic ramp temperature, determining the storage modulus (E') at 30°C and in the rubbery plateau (at T=*T*g+30°C), and the mechanical damping factor (Tan δ).

The vitrimer properties of the composite material were demonstrated by testing: 1) the permanent connectivity by carrying out a swelling test, 2) the relaxation and the flowability of the networks, which lead to a rearrangement of their topology, 3) the evidence of two different transition temperatures, the *T*g and the *T*v.

Finally, the relaxation behavior of the composite was described with the model that combines the relaxation linked to the BER and the segmental relaxations of polymer chains developed for the epoxy vitrimer DGEBA—4-APDS. The model uses two stretched exponential decays allowing to fit the main relaxation branches. The analysis was executed based on the stress relaxation data of the two systems (with and without NFC) using OriginPro® 9.

4.4 Characterization results and discussion

4.4.1 Thermo-mechanical performance

The thermo-mechanical behavior of composite DGEBA—4-APDS-NFC was studied in detail and compared with the vitrimer system (DGEBA–4-APDS) at the same stoichiometry ratio.

The resin's degradation temperature (**Figure IV-3**) does not display a significant change after incorporating NFC into the polymer matrix. The glass transition temperature of the composite samples, determined by the DSC technique, drops by 5 degrees comparing to the polymer matrix **(Figure IV-4**). The *T*g diminution may be linked to a secondary reaction of esterification between the hydroxyl groups of cellulose and the epoxide ring of the DGEBA. Indeed, Berglund and co-workers[11] and Lin *et al.* [31] observed that their epoxy-cellulose resin composites at a stoichiometry ratio displayed similar behavior to that observed for the epoxy resin system DGEBA–4-APDS. Besides, Berglund's work showed that the *T*g of epoxy-cellulose resin composite is quite dependent on the cellulose concentration added. The cellulose concentration in this work was 10% and not 30%, like the previous works[11]; therefore, the decrease in *T*g recorded for the present work is lower than for a high cellulose content system.

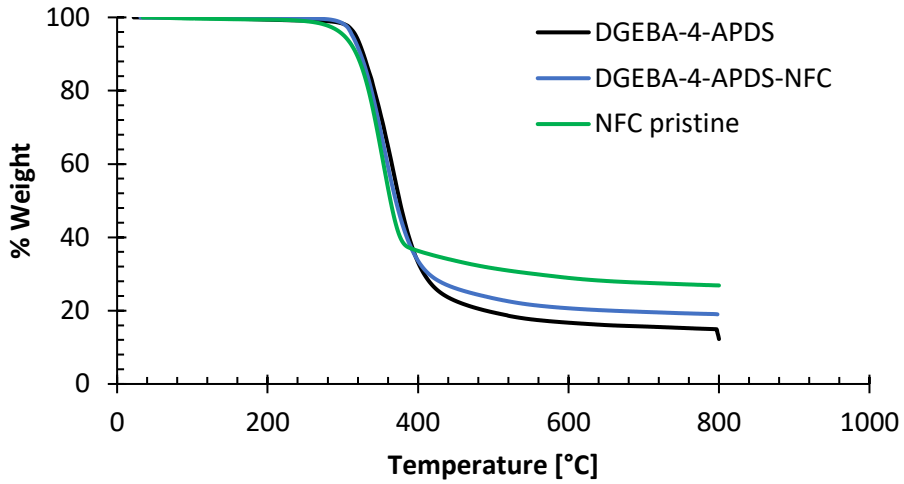

Figure IV-3. Degradation temperature of DGEBA—4-APDS (black), DGEBA–4-APDS-NFC (blue), and NFC pristine (green).

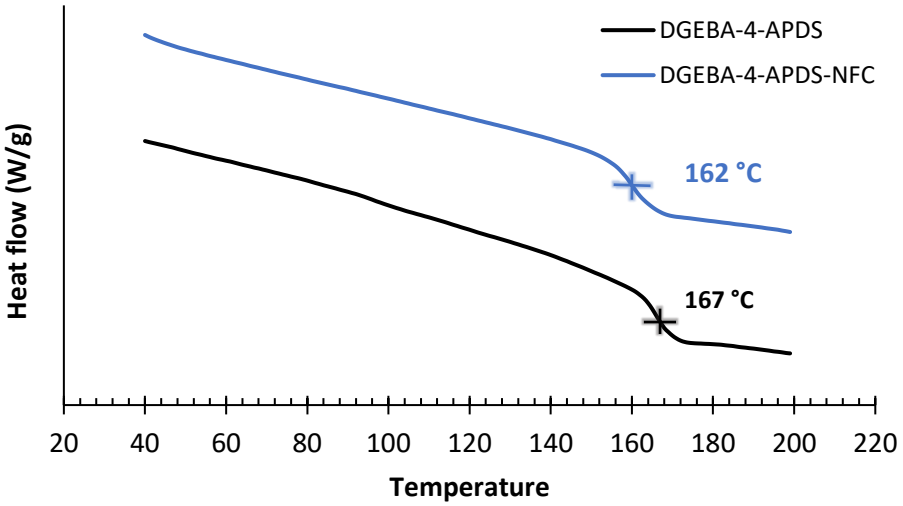

Figure IV-4. DSC curves showing the glass transition *Tg* of DGEBA—4-APDS (black) and the composite with NFC (blue). The amine/epoxy stoichiometric ratio is equal to 1.

Figure IV-5 displays the storage modulus (E') of systems DGEBA–4-APDS, DGEBA–4-APDS-NFC. The increase of storage modulus in the composite is remarkable for the glassy or rubbery state due to the presence of NFC in the composite.

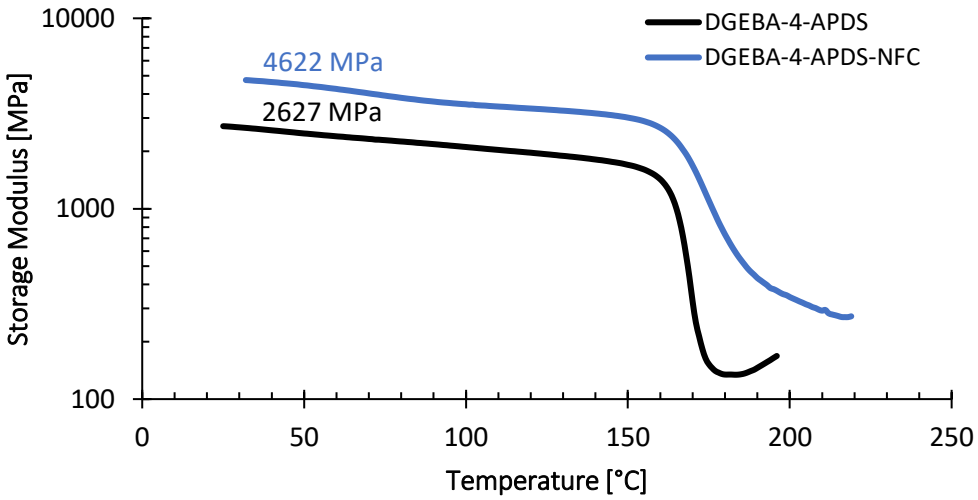

Figure IV-5. Storage Modulus (E') as a function of the temperature of the systems DGEBA–4-APDS and DGEBA–4-APDS-NFC.

The storage modulus of the composite, determined at 30°C, displays an increase of approximately 76% by only adding 10% (w/w) of NFC. The addition of natural fibers could lead to a restriction in the mobility of the polymer. These segmental restrictions could induce a rise of storage modulus[33, 34]. The enhancement of storage modulus of the composite DGEBA–4-APDS-NFC is consistent with other composites employing inorganic reinforced fibers[35, 36], and natural fibers[37, 38, 39] in epoxy resins. Despite the increase in the storage modulus, the obtained value is lower than those expected from a mixing law between the NFC and the epoxy-vitrimer. The storage modulus of NFC fibers reported in the literature varies between 30 and 150 GPa[40, 41], depending on the source of the nanocellulose and its preparation. Applying the mixing law for a composite based on NFC fibers and a vitrimer epoxy would result in a storage modulus between 5 and 17 GPa, with 10% of NFC. This theorical modulus was not obtained in our case. A lower modulus suggests a weak interfacial adhesion between the cellulose fibers and the epoxy vitrimer. The composite material displayed also a rise on the rubbery plateau (**Figure IV-5**), most probably a product of the presence of the high NFC modulus (even at high temperature), and the potential reactions and interactions between the filler and the epoxy [18, 42, 43].

Figure IV-6 shows the Tan δ of the vitrimer system with and without NFC. An important change is appreciated on the intensity and the width of the damping factor. The increase of the width means that the elaborated composite is less homogenous; hence, the material could comprise zones with different crosslinking degrees. So, the Tan δ distribution observed is constituted of a wide range of

mobility areas that the epoxy resin by itself. Furthermore, the intensity decrease of Tan δ reflects a reduction in the segmental motions of the composite (also reflected in the increase of storage modulus of **Figure IV-5**).

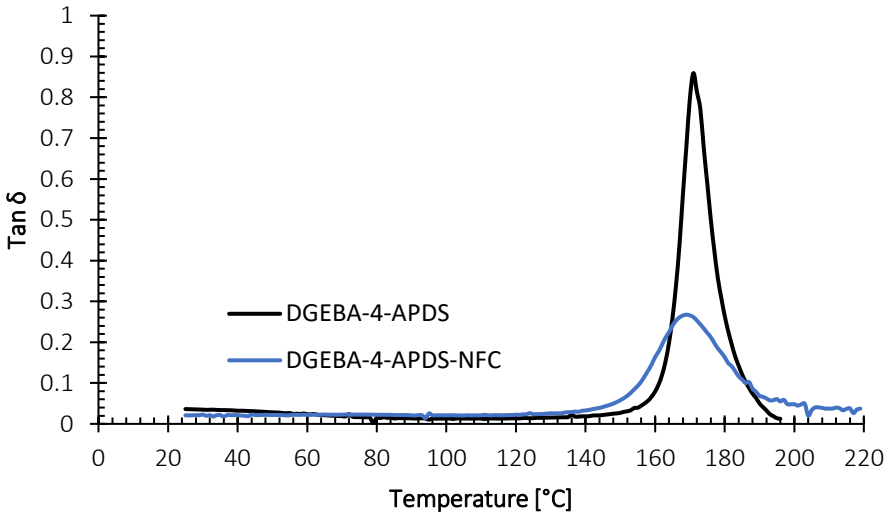

Figure IV-6. Damping factor (Tan δ) of the systems DGEBA–4-APDS with and without NFC.

System	*Tg* (°C)	Degradation temperature (°C)	E' at 30°C (MPa)	E' at *Tg* + 30°C (MPa)	*Tα* (°C)	ρ (mol/m³)
DGEBA–4-APDS	167 ± 1	359 ± 1	2627 ± 69	179 ± 40	170 ± 1	1.53E+04
NFC template	----------	351 ± 3	8123 ± 132	735 ± 40	324 ± 6	---------
DGEBA–4-APDS-NFC	162 ± 2	354 ± 1	4622 ± 57	313 ± 52	169 ± 1	---------

Table IV-1. Glass transition temperature (*Tg*) measured by DSC, degradation temperature, elastic modulus (E') measured at 30 °C, and at *Tg* + 30°C, Tα values and crosslink density (ρ) of DGEBA–4-APDS, DGEBA–4-APDS-NFC, and pristine NFC. The epoxy resin and the composite were measured in single cantilever mode, while the NFC was measured in tensile mode.

Table IV-1 summarizes the glass transition temperature (*Tg*) measured by DSC, the storage modulus (E') in the glassy and rubbery plateau, the α-relaxation (*Tα*) measured by DMA experiments, the degradation, and the crosslink density of the pristine NFC and of the systems DGEBA–4-APDS with and without NFC.

In this work, the challenging impregnation protocol already described by Berglund and co-workers was modified to allow producing a vitrimer composite based on the system DGEBA–4-APDS and nano fibrillated cellulose. Interestingly, the results showed an enhancement of the mechanical properties while maintaining an elevated *Tg*.

4.4.2 Morphology characterization

Figure IV-7 displays the SEM cross-section images of NFC pristine and DGEBA–4-APDS-NFC composite. In both cases, it is possible to appreciate the nanofibrils and their entangled morphology. The composite displays fibrils' aggregates (zone A) and well-dispersed fibrils (zone B). Zone A displays important branch-like fibrils aggregates (microfiber bunches), probably formed by flocculation during the filtration step. So, the resin probably does not diffuse suitably during the impregnation step. Zone B displays white dots, which could be attributed to the section of fractured branches of NFC. The pull-out lengths in numerous areas on zone B suggest a weak interfacial adhesion. Zone B also exhibits a poor interaction area, which is possible to remark due to the presence of a "nanofiber bunch" (showed in the area enclosed by the dashed line). This morphological observation probably explains the limited mechanical reinforcement of the composite.

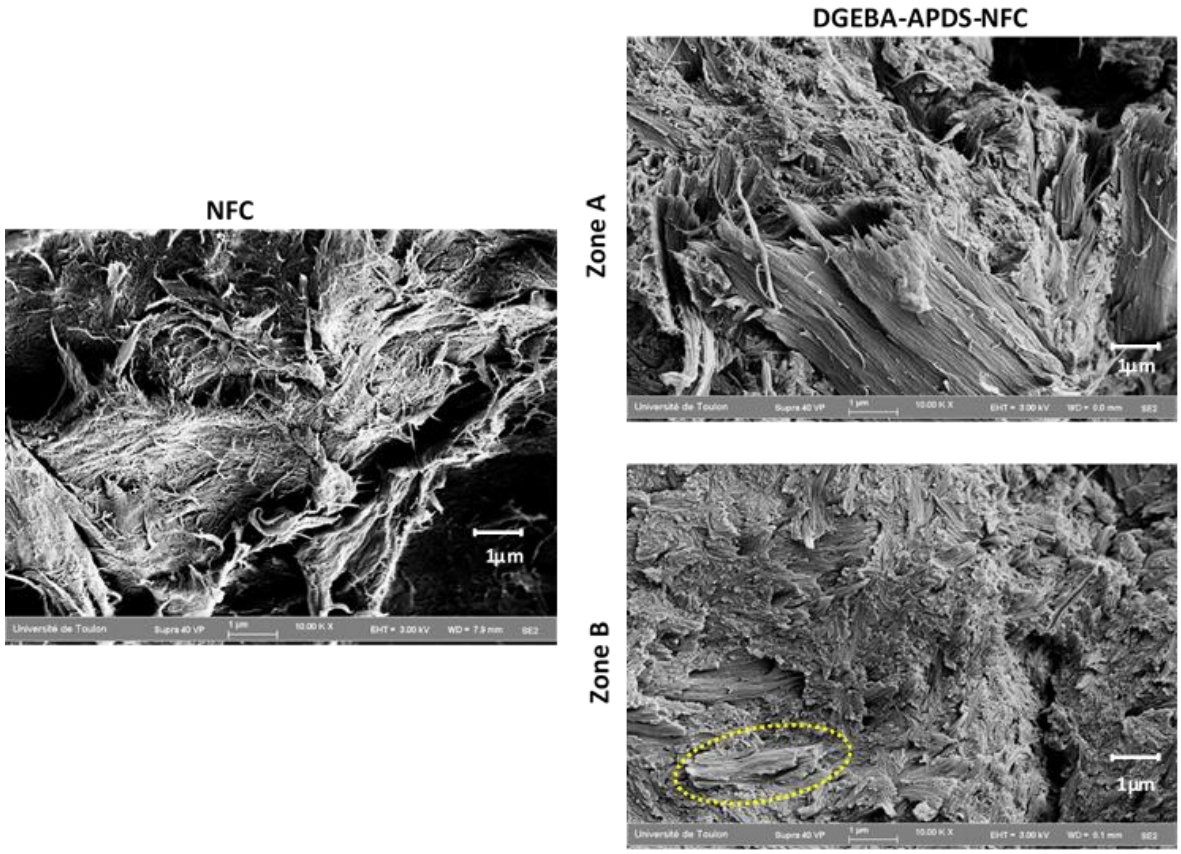

Figure IV-7. SEM cross-section images displaying the pristine NFC and two zones of epoxy resin reinforced with NFC. Zone A shows the NFC surrounded by the DGEBA-APDS; zone B displays a mix of both phases.

Figure IV-8 displays the AFM cross-section topography, elastic modulus, and adhesion maps (1 µm x 1 µm) of the pure resin and the NFC-reinforced composite. In the recorded topography images, it

is possible to appreciate some nanofibrils present in the epoxy matrix (**Figure IV-8d**). The elastic modulus cartography displays diverse modulus obtained for the epoxy resins and the composites. The resin by itself displays a homogeneous mechanical mapping (**Figure IV-8b**) which oscillates between 1- 4 GPa, while the composite material shows a heterogenous mechanical mapping (**Figure IV-8e**) oscillating between 3-15 GPa. The white dots represent the high elastic modulus recorded, most probably due to the presence of NFC as observed by SEM characterizations. Finally, the adhesion cartography displays a significant increase of the adhesion force in the composite, from 15nN for the resin itself (**Figure IV-8c**) to 90 nN for the composite material (**Figure IV-8e**). The increase in the adhesion force allows illustrating the high hydrophilic nature of the NFC. The use of cellulose as a filler could lead to a detrimental impact of composite material in the presence of water if the filler is not previously treated.

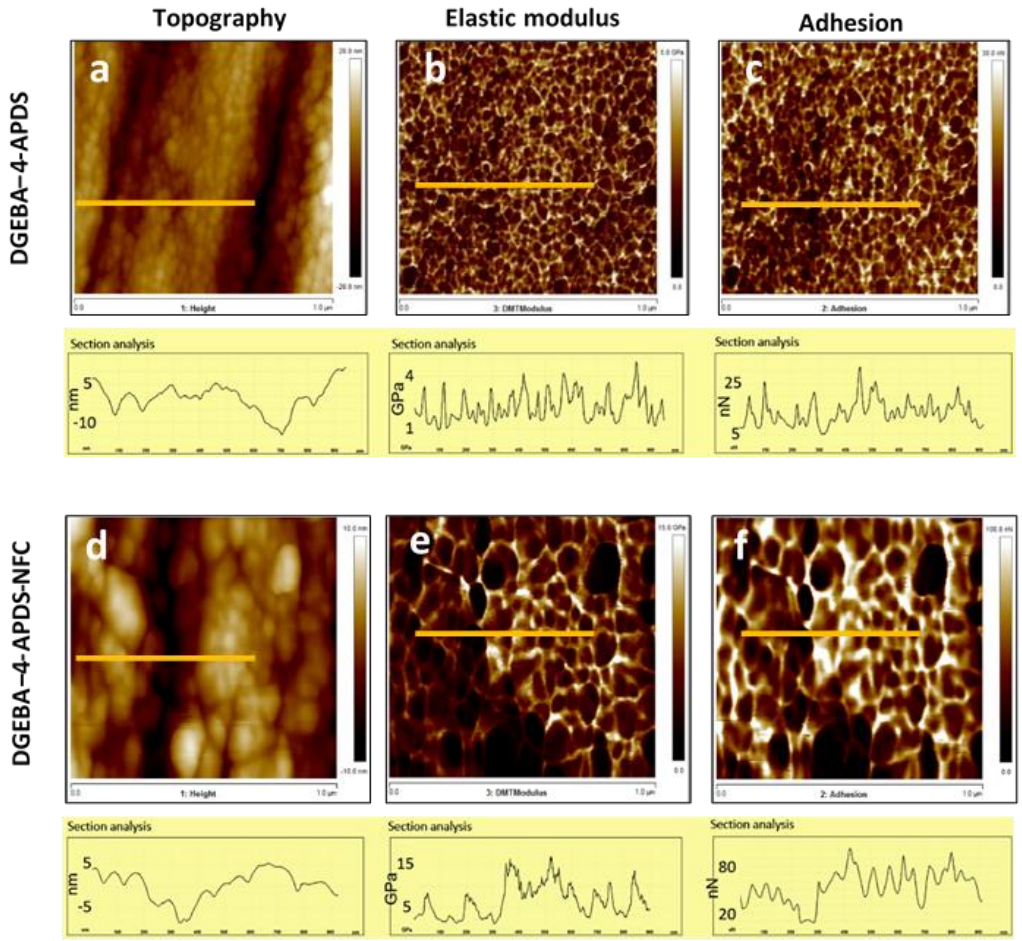

Figure IV-8. AFM topography (a and d), elastic modulus (b and e), and adhesion (c and f) maps (with its respective section analysis) of DGEBA–4-APDS and DGEBA–4-APDS-NFC. AFM analysis has been performed on the samples' cross-sections.

Although the NFC incorporation into epoxy resin seems to provide promising results, several works have revealed how the NFC surface modification might improve the interfacial adhesion[18, 44, 45] resulting in an even more significant increase in the material's mechanical properties. It will be the purpose of the Chapter V.

4.4.3 Vitrimer characterization

4.4.3.1 Permanent connectivity

As for the DGEBA–4-APDS resin, the permanent connectivity on the composite material was explored to prove the true permanence of the constant crosslink density, eliminating any possible doubt about the true vitrimer behavior of the composite. Although the permanent connectivity was explored for the neat epoxy vitrimer, it is crucial to prove that NFC does not annul one of the properties that characterize a vitrimer material before calling it vitrimer. The permanent connectivity was examined for the composite epoxy vitrimer by performing swelling tests.

The swelling tests of NFC-reinforced composite were carried out under four different solvents: THF, DMF, EMP, and 1,2,4-Trichlorobenzene. The first three solvents, THF, DMF, EMP, were employed throughout one week at room temperature and 1,2,4-Trichlorobenzene 1h at 190 °C. As for the DGEBA–4-APDS system, the composite does not display any loss of connectivity in the four used solvents.

The swelling test at room temperature for one week in THF, DMF, and EMP solvent is summarized in **Figure IV-9**. The results showed that the won mass during the swelling tests was inferior in the composite than in the pure resin. In the composite, the fibrils restrict the diffusion throughout the sample; and therefore, the swelling is inferior in the composite. Likewise, a weak mass loss was noted, less than 0.5% in the pure resin and less than 1.5% in the composite. In both cases, the mass loss is explained due to uncured segments. The higher mass loss in the composite could be explained by the fact that NFC disturbs the crosslinking reaction, thus generating a slight increase in non-crosslinked sections.

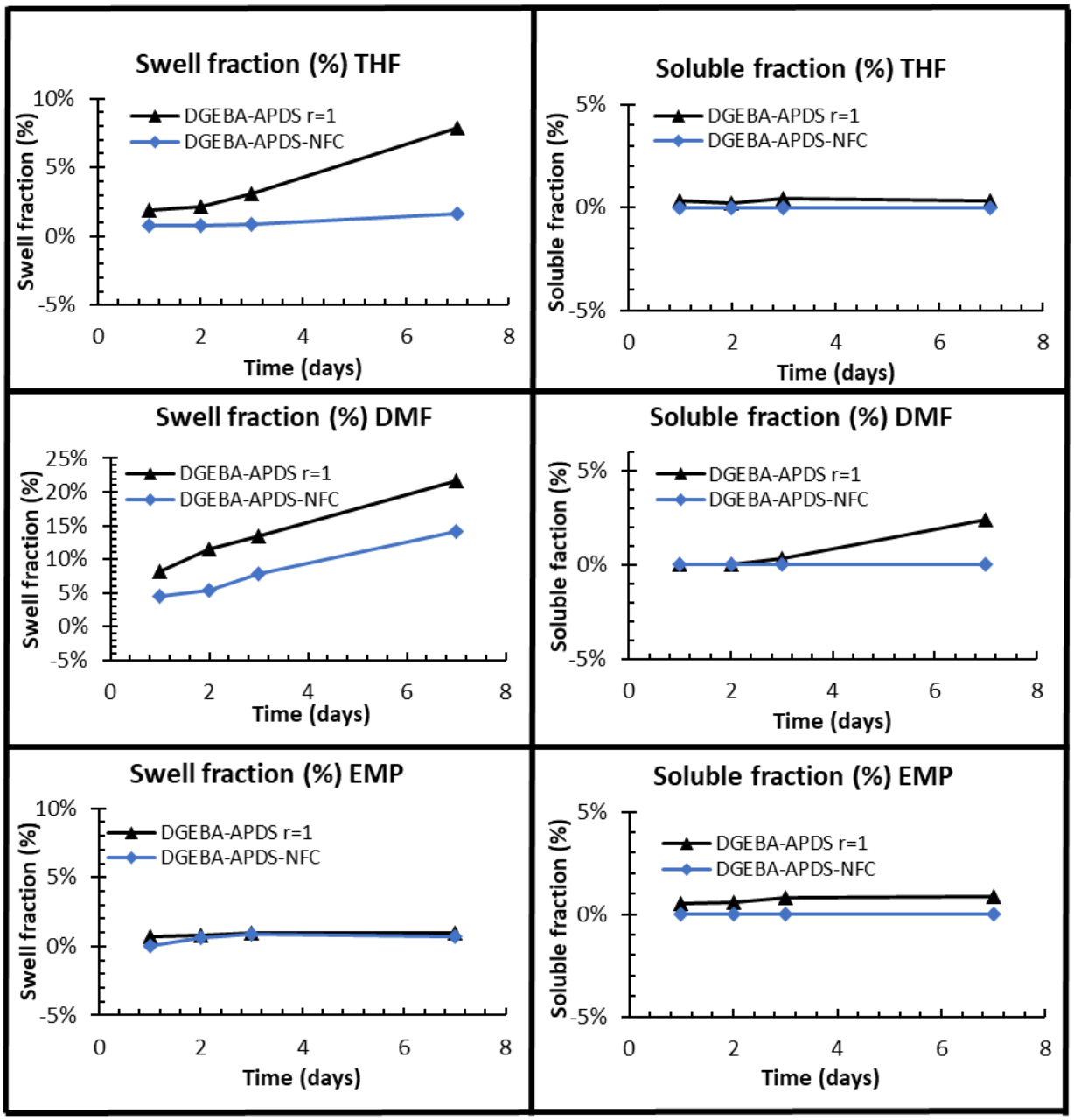

Figure IV-9. Linear swelling of networks DGEBA–4-APDS and DGEBA–4-APDS-NFC in solvents THF, DMF, and EMP. At the left, the mass percentage won during the test, and at the right, the mass loss registered after solvent drying.

Figure IV-10 displays how the network connectivity of NFC-reinforced composite remains constant in an inert solvent at high temperatures. The NFC incorporation to this system does not seem to alter the constant connectivity of vitrimer since no physical changes or weight losses were remarked, just a win of mass, due to difficulties of the drying process due to the elevated boiling point of the solvent.

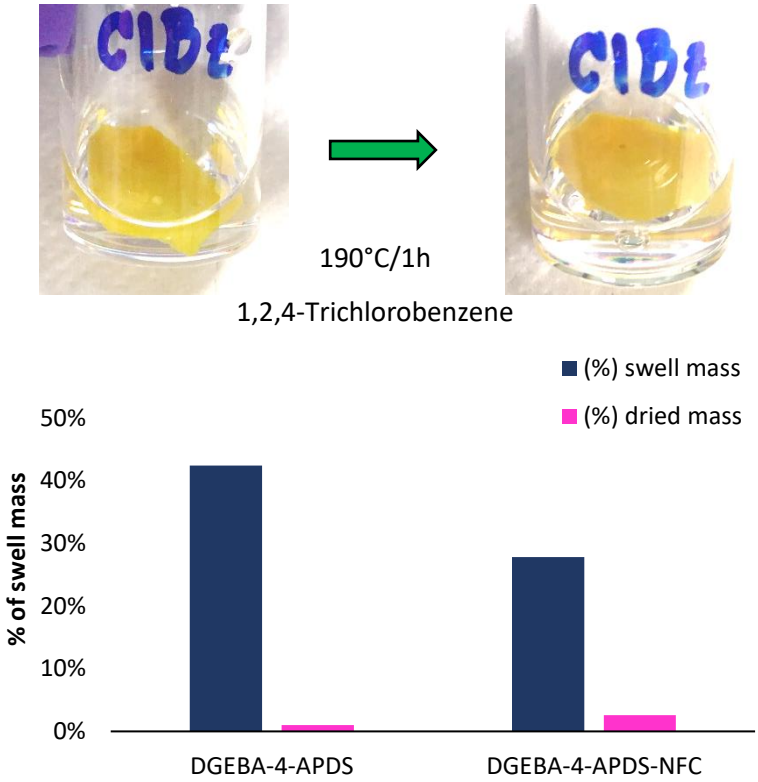

Figure IV-10. Swelling mass won after samples' immersion during 1h in 1,2-4 trichlorobenzene (blue) and after drying the solvent on samples for 10 days.

4.4.3.2 Stress relaxation behavior

The relaxation behavior of either system, DGEBA–4-APDS, and DGEBA–4-APDS-NFC, were performed in **Figure IV-11**. As a first approximation, the Maxwell model (equation (1)) was employed to describe the relaxation behavior.

$$\frac{E(t)}{E_0} = e^{\left(-\frac{t}{\lambda}\right)} \quad \text{..... (1)}$$

Figure IV-11 displays the stress relaxation behavior of the vitrimer pure and the NFC reinforced vitrimer. This figure illustrates how the relaxation described for the composite is much important than the pure epoxy system. This delayed relaxation may be explained by the restriction of the network's mobility generated by the fillers. For instance, the maximal relaxation time achieved for the pure system, according to the maximal relaxation of Maxwell model (E/Eo= 1/e), at 180 °C is less than 30 min, while for the composite, it is above 100 min. Similar behavior was reported by Wang *et al*. by adding nano-silica to their vitrimer system, suggesting restricted network mobility which alters the relaxation behavior and flowability for the further topological rearrangement[27].

The relaxation times were plotted against the inverse of the temperature (**Figure IV-11c** and **d**),

displaying an Arrhenius-like behavior. Applying the Arrhenius law, illustrated in equations (2), (3), and (4), it is easy to determine the activation energy (Ea), and by extrapolation, the topology freezing temperature (*T*v).

$$\lambda = \lambda_0 \, e^{\left(\frac{Ea}{RT}\right)} \quad \text{..... (2)}$$

$$\ln(\lambda^*) = \frac{Ea}{R}\left(\frac{1}{T}\right) + \ln \lambda_0 \quad \text{..... (3)}$$

$$\lambda^* = \frac{\eta}{E_{rubbery}} \quad \text{..... (4)}$$

Where λ is the relaxation time determined from the maximal relaxation according to the Maxwell model (E/Eo= 1/e), Ea, the activation energy, R the universal gas constant, T the temperature (comprising between 180 to 220 °C), η the viscosity according to the vitrimer definition (10^{12} Pa*s), $E_{rubberty}$ the elastic modulus at the rubbery plateau, and λ^* the characteristical relaxation time related to the viscosity of the vitrimer definition (10^{12} Pa*s).

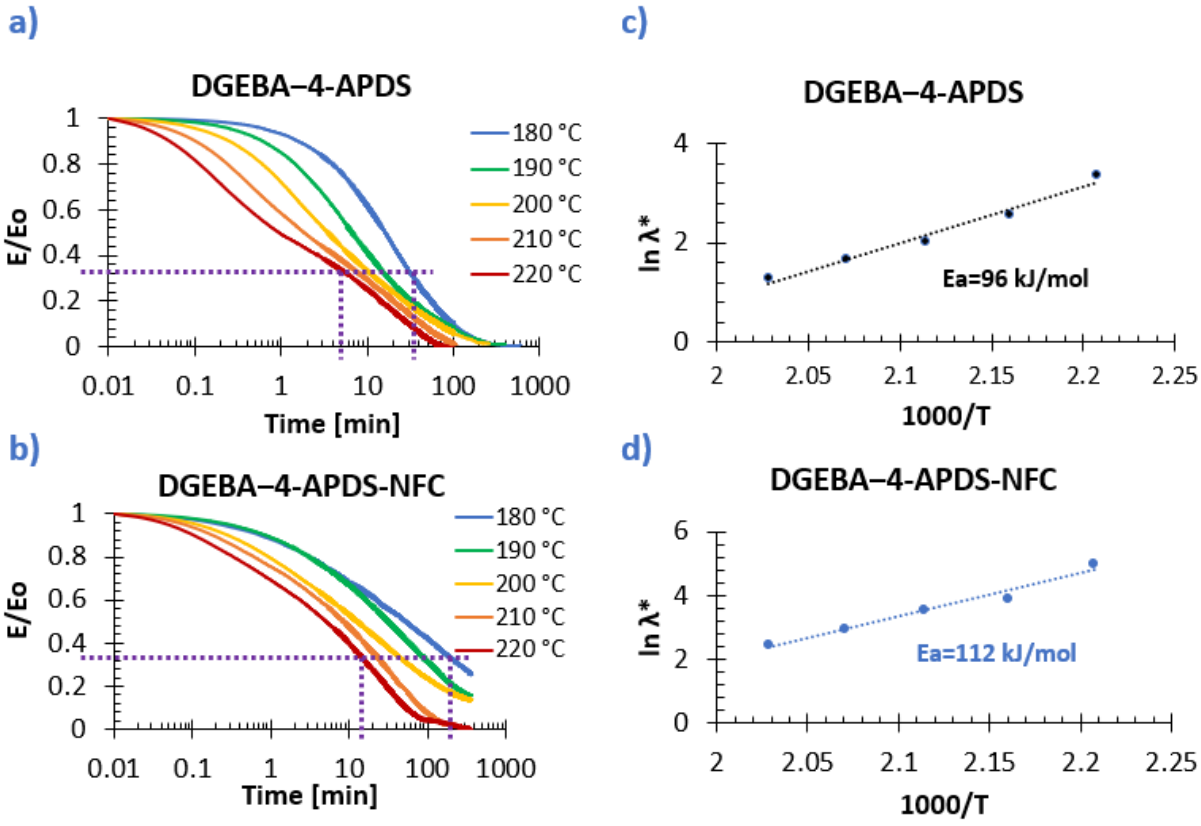

Figure IV-11. Stress relaxation behavior and Arrhenius plot of a) DGEBA–4-APDS b) DGEBA-APDS–4-NFC under a strain of 0.1%. Arrhenius-like behavior of the c) DGEBA–4-APDS and d) DGEBA–4-APDS-NFC.

System	Ea (kJ/mol)	*Tv* (°C)
DGEBA–4-APDS	96	169
DGEBA–4-APDS-NFC	112	212

Table IV-2. The activation energy (Ea) and topology freezing temperature (*T*v) of DGEBA–4-APDS with and without NFC at an amine/epoxy ratio equal to 1 under a strain of 0.1%[§].

Table IV-2 recapitulates the Ea and *T*v calculated by following the Arrhenian law and considering a single relaxation time for each temperature. The activation energy seems to be slightly impacted by nanofillers' addition, and the relaxation is delayed, as shown in **Figure IV-11**. Concerning the topology freezing temperature, a meaningful difference is remarked, a rise of 43°C after the NFC adding, probably due to the rubbery plateau modulus rise.

In Chapter III, it was discussed how the Maxwell model does not accurately describe the relaxation behavior of the vitrimer system; hence, the information related in **Table IV-2** probably does not display the correct information concerning the activation energy or the *T*v, because the recorded and exploited data is a convolution of several relaxation phenomena[46], and not a single relaxation as the Maxwell model describes. Therefore, even though the results of the NFC composite are contrary to the work reported by Wang and co-workers using nanosilica [27], showing an increase of the activation energy, they cannot be further discussed because of the questionable model used to determine the activation energy and *T*v.

Therefore, to discuss deeper the relaxation behavior, the adapted model developed in Chapter III was employed to describe the complex relaxation behavior of the performed NFC reinforced vitrimer composite.

4.4.3.2.1 Stress relaxation modeling

The stress relaxation model proposed for the pure epoxy vitrimer system considers two primary relaxation behaviors linked to the bond exchange reaction (BER) and the segmental motion relaxation. This model was applied for the composite material by following equation (5)[47, 48, 49].

[§] We ask the reader to consider that these results were obtained under a different deformation than those used for pure resins (in Chapter III). The results are different (but not so far) from values obtained under a higher deformation.

Figure IV-12 displays the simulation carried out using two decay exponents of the equation (5) and the respective deconvolution of both relaxation phenomena.

$$\frac{E(t)}{E_0} = \underbrace{E_1 * e^{\left(-\left(\frac{t}{\lambda_1}\right)^{\beta_1}\right)}}_{\text{Bond Exchange Reaction}} + \underbrace{E_2 * e^{\left(-\left(\frac{t}{\lambda_2}\right)^{\beta_2}\right)}}_{\text{Network segmental motion}} \quad \text{..... (5)}$$

$$\bar{\lambda} = \frac{\lambda\,\Gamma\left(\frac{1}{\beta}\right)}{\beta} \quad \text{..... (6)}$$

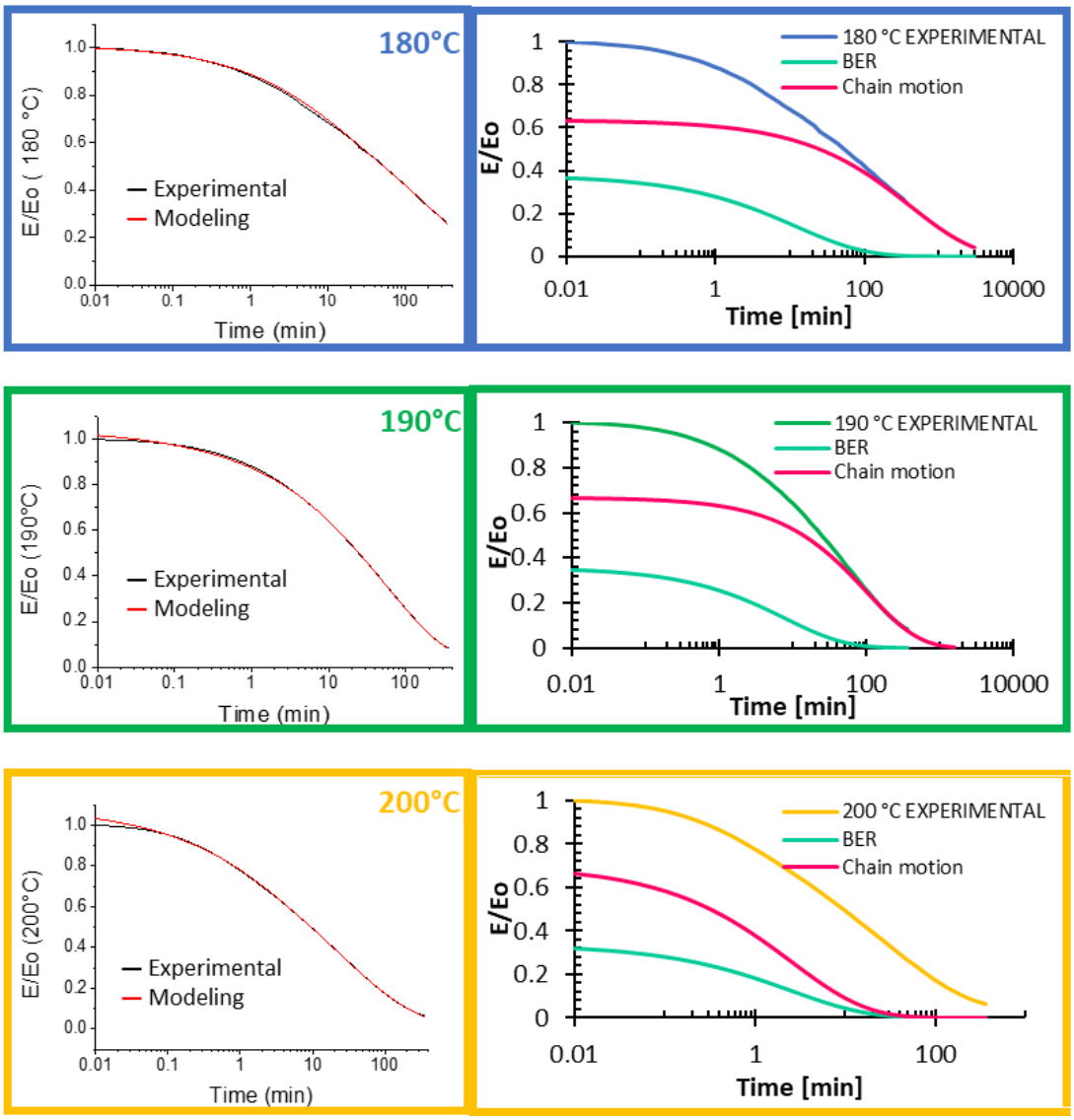

Figure IV-12. Stress relaxation experiments normalized of the NFC-reinforced vitrimer. To the left, the modeling by using two stretched exponential functions displayed in equation (5) at different temperatures from 180 to 220°C.To the right, the deconvolution of both relaxation phenomena.

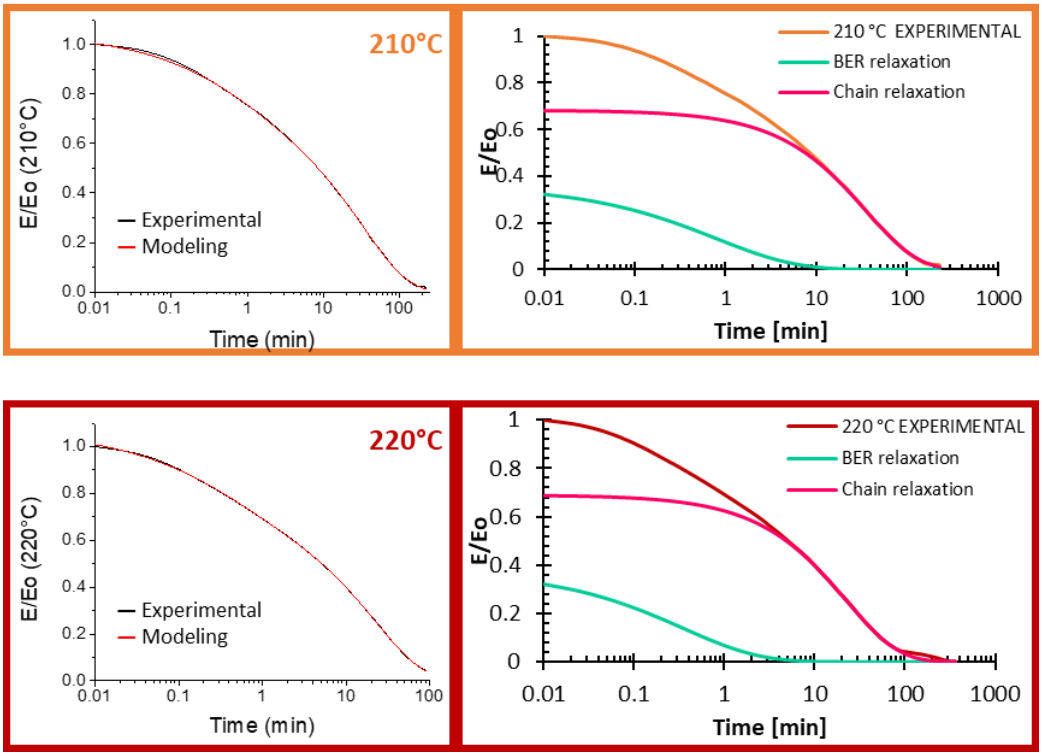

Figure IV-12. Stress relaxation experiments normalized of the NFC-reinforced vitrimer. To the left, the modeling by using two stretched exponential functions displayed in equation (5) at different temperatures from 180 to 220°C.To the right, the deconvolution of both relaxation phenomena.

T [°C]	Bond Exchange Reaction					Segmental motions				
	E_1	E_1%	λ_1 (min)	β_1	$\overline{\lambda_1}$	E_2	E_2%	λ_2 (min)	β_2	$\overline{\lambda_2}$
180	0.38	0.37	12.2	0.47	27	0.63	0.63	420.1	0.51	817
190	0.36	0.35	7.9	0.53	14	0.67	0.65	103.1	0.62	149
200	0.34	0.32	2.5	0.52	5	0.70	0.68	50.5	0.47	113
210	0.36	0.35	0.8	0.50	2	0.68	0.65	35.5	0.76	42
220	0.38	0.35	0.4	0.51	1	0.69	0.65	22.4	0.74	27

Table IV-3. Main adjustment parameters of equation (5) for the DGEBA–4-APDS-NFC system. E_i% represents the relaxation contribution, λ_i is the characteristic relaxation times of each phenomenon, β_i is the stretched exponent decay, $\overline{\lambda_i}$ the average relaxation times using the stretched exponents decay and the gamma function. Where i=1 correspond to the BER relaxation and i=2 correspond to the segmental motion relaxation.

T [°C]	Bond Exchange Reaction					Segmental motions				
	E_1	E_1%	λ_1 (min)	β_1	$\bar{\lambda}$	E_2	E_2%	λ_2 (min)	β_2	$\bar{\lambda}$
180	0.52	0.51	15	0.78	18	0.49	0.49	54.8	0.79	62
190	0.51	0.50	5	0.78	6	0.52	0.50	33.2	0.58	52
200	0.51	0.50	2	0.79	2	0.50	0.50	29.7	0.67	39
210	0.52	0.51	0.6	0.80	0.7	0.50	0.49	23.8	0.79	27
220	0.53	0.51	0.3	0.81	0.3	0.50	0.49	17.9	0.78	21

Table IV-4. Main adjustment parameters of equation (5) for the DGEBA–4-APDS system. E_i% represents the relaxation contribution, λ_i is the characteristic relaxation times of each phenomenon, β_i is the stretched exponent decay, $\bar{\lambda}_i$ the average relaxation times using the stretched exponents decay and the gamma function. Where i=1 correspond to the BER relaxation and i=2 the segmental motion relaxation.

Table IV-3 summarizes the main parameters of the DGEBA–4-APDS-NFC simulations carried out from equations (5) and (6), and **Table IV-4** summarizes the main parameters of the DGEBA–4-APDS simulation, both obtained with a strain of 0.1%. The detailed parameters yielded by the simulation are described in the annex of Chapter IV (**Table S.IV- 1** and **Table S.IV- 2**)

Concerning the relaxation time associated with **the BER (λ_1),** the relaxation time values are not so different between both explored vitrimer systems, the pure and the reinforced. Thus, the use of the NFC as reinforcement **does not highly modify** the relaxation times associated with the bond exchange mechanism. A contrary behavior is observed for the relaxation times associated with **the segmental motion relaxation (λ_2),** which **relaxes over a longer time**. For instance, the characteristical relaxation time due to the segmental motion relaxation at 180°C is 55 min for the epoxy vitrimer pure and 420 min for the reinforced epoxy vitrimer (**Table IV-3** and **Table IV-4**). The longer relaxation times probably involve the relaxation of the DGEBA–4-APDS covalent network and the NFC relaxation.

Moreover, the values of **β_1 remain constant, around 0.51**. Although it is not an elevated value as the system without NFC (0.79), the values are constants. Compared to the pure vitrimer resin, the decrease of the stretched exponents means an increase in the relaxation times distribution. It is reflected in the relaxation curve's shape in **Figure IV-12**. This observation can be explained by the presence of NFC, which induces a more heterogeneous network. This is consistent with the width increases of the damping factor of **Figure IV-6**. Therefore, the increase in the time distribution of the first relaxation branch (BER) can be ascribed to: 1) less mobility of some dynamic covalent bonds and 2) a wider distribution of these bonds in the network.

Another interesting detail noted in **Table IV-3** and **Table IV-4** was the change of the contribution

fractions (E%). The DGEBA–4-APDS system displays similar contribution fractions for both relaxation phenomena, i.e., both the BER and the segmental network relaxation contribution are present in the same proportions. Samples with NFC display a **reduction of the contribution fraction linked to the BER relaxation (E_1%)**. The first supposition explaining this change is a probable reduction in the number of dynamic covalent bonds available to effectuate the exchange since the NFC restricts the mobility of dynamic bonds. The second hypothesis, and highly probable, is the own NFC contribution to the network relaxation explaining the contribution increase of the segmental relaxation branch. The relaxation times found in the simulations of systems DGEBA–4-APDS with and without NFC were plotted against the inverse of temperature (**Figure IV-13**). The plot shows two different behaviors as observed for the pure epoxy vitrimer system seen in Chapter III, section 3.5.2.2.

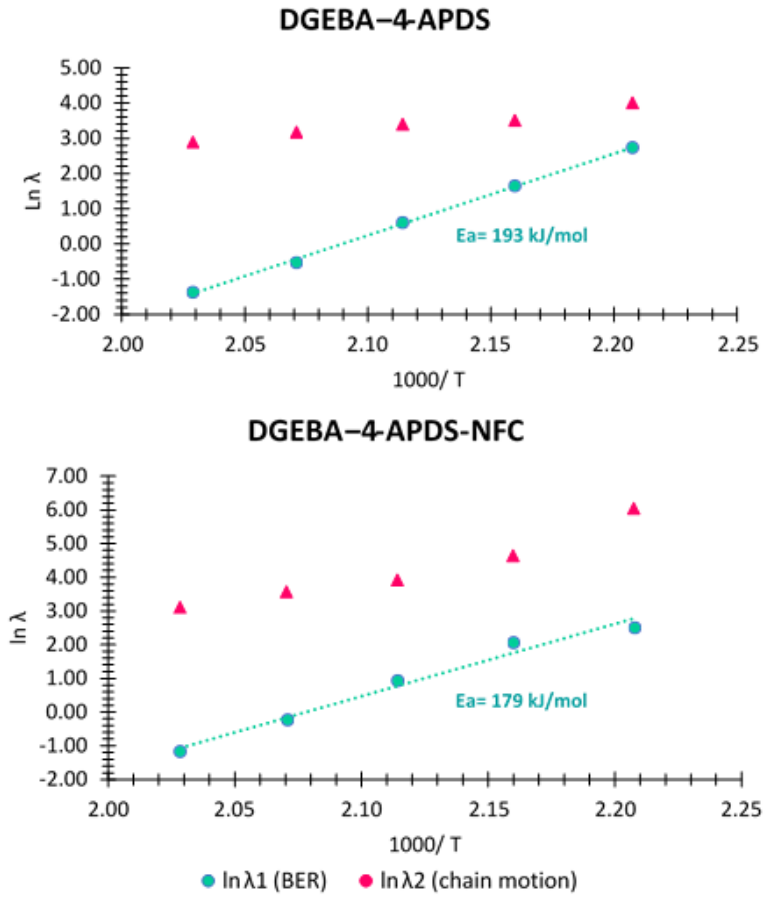

Figure IV-13. The characteristic relaxation time against the inverse of the temperature of the BER behavior (blue) and the segmental motion relaxation (violet). The data was collected from Table IV-3 and Table IV-4.

The green plot of **Figure IV-13** is linked to the BER relaxation; it follows an Arrhenian-like behavior. The pink plot is associated with the segmental motion relaxation, and it does not seem to follow an

Arrhenian behavior.

Since the BER relaxation plot follows the Arrhenian law, the Ea and *T*v were estimated by following the equation (3) and (4).

$$\ln(\lambda^*) = \frac{Ea}{R}\left(\frac{1}{T}\right) + \ln\lambda_0 \quad \text{..... (3)}$$

$$\lambda^* = \frac{\eta}{E_{rubbery}} \quad \text{..... (4)}$$

Hence *T*v=*T*v(Ea, λ_0, $E_{\text{rubbery plateau}}$).

The results are summarized in **Table IV-5**. The Ea of system DGEBA–4-APDS-NFC is slightly decreased to the pure vitrimer system. This slight decrease might be attributed to a possible excess of disulfide bonds less cured into the network. The assumption is the possible esterification reaction between the hydroxyl groups of cellulose and the epoxide ring of DGEBA[31] inducing local amine-epoxide off-stoichiometry.

	Maxwell model		**Stretched exponent decay BER**	
System	**Ea (kJ/mol)**	***T*v (°C)**	**Ea (kJ/mol)**	***T*v (°C)**
DGEBA–4-APDS	96	189	193	170
DGEBA–4-APDS-NFC	112	212	174	180

Table IV-5. Ea and *T*v of DGEBA–4-APDS and DGEBA–4-APDS-NFC employing the Maxwell model, the BER relaxation behavior, and the *T*v determined by dilatometry test.

4.4.3.3 A new transition temperature: The Tv

Dilatometry tests were performed to evidence a different transition temperature from the *T*g: The *T*v. This last transition temperature is characteristic of vitrimer materials. In Chapter III, this test was carried out in compression mode. For the composite material, an exception had to be made due to the shape of the composite (templates), so the experiments were carried out in tensile mode. The mechanical solicitation in tensile mode is not optimal to carry out dilatometry experiments because the weight of the mobile section might generate confusion on the terminal transition. Therefore, terminal relaxation values should be taken with caution. Indeed, in literature, different dilatometry tests measured in DMA in tensile mode have been exploited, showing that the terminal transitions are not very clear[50, 51, **]. **Figure IV-14** shows the dilatometry test in the tensile mode of the epoxy-

** Dilatometry experiments in tensile mode were also carried out for the off-stoichiometric systems, the results are noted in **Figure S.IV- 1**. Deviations in the terminal relaxation were also observed, thus showing how the deviations are a product of the mechanical stress applied to the sample.

vitrimer and the reinforced NFC-vitrimer. The *T*g and *T*v are related to the observed displacement inflections. The *T*g for the epoxy-vitrimer is 164 °C, while for the composite, it is 162°C. Both results are consistent with the information found by the DSC technique. The *T*v for the epoxy-vitrimer is 183°C, while for the NFC-reinforced vitrimer it is 188°C[††].

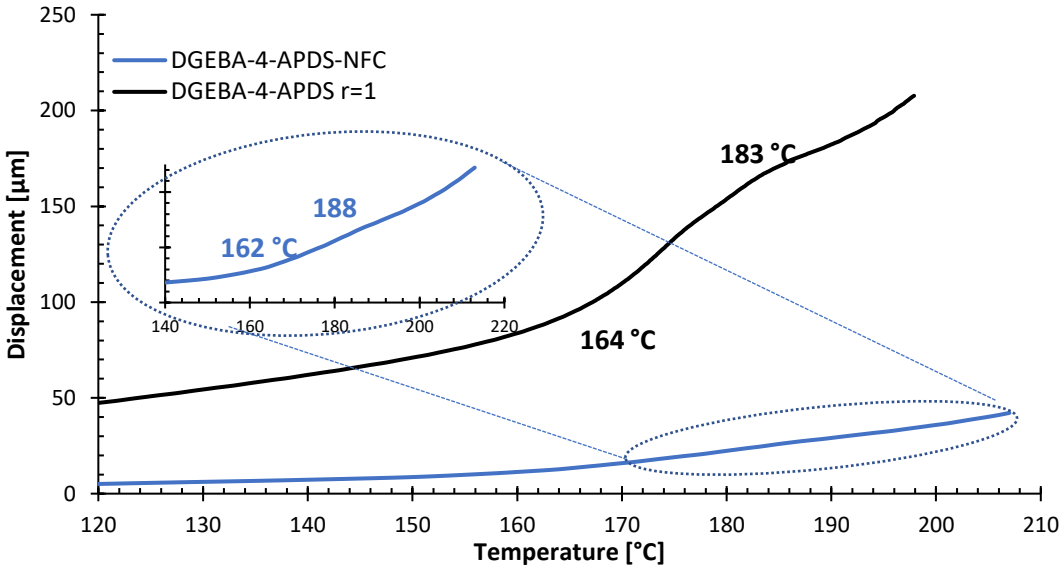

Figure IV-14. Dilatometry test of systems DGEBA–4-APDS (black) and DGEBA–4-APDS-NFC (blue). An increase of 50 nm of sample without NFC was added to the curve.

Table IV-6 summarizes the transition temperatures determined by different techniques (DSC experiments and dilatometry in tensile mode). Concerning the *T*g, the DSC experiments and the dilatometry results are consistent. Regarding the *T*v results obtained by dilatometry in tensile mode, they slightly differ from those found by the Arrhenius law's extrapolation. Since the mechanical stress employed for the determination of *T*v in the used technique is not the same, the *T*v values of both methods slightly differ. However, the values are in a very close temperature range between 171 and 183°C for the system DGEBA–4-APDS and between 180°C and 188°C for the system DGEBA–4-APDS-NFC.

[††] The results obtained by dilatometry tests on the terminal relaxation in both compression and tensile mode are quite questionable to compare. Even though these analyses have allowed us to find a second transition temperatura (presumably attributed to the *T*v), the test carried out on a DMA cannot replace the information that a dilatometer can provide. In particular, the tests in tension mode can generate an important deviation in the terminal relaxation, attributed to the weight of the movable clamp of the DMA.

	Dilatometry tensile mode		DSC	Extrapolation of the relaxation time (BER)
System	*Tg* (°C)	*Tv* (°C)	*Tg* (°C)	*Tv* (°C)
DGEBA–4-APDS	164 ± 2	183 ± 1	167 ± 1	171
DGEBA–4-APDS- NFC	162 ± 2	188 ± 1	162 ± 2	180

Table IV-6. *Tg* and *Tv* values of the systems DGEBA–4-APDS with and without NFC. The *Tg* is determined by dilatometry and DSC experiments. The *Tv* is determined by the dilatometry test and the extrapolation of the relaxation times determined by employing two stretched exponent decay contributions.

Furthermore, the *Tv* of the composite (188°C) is higher than for the pure resin (183°C), both recorded by dilatometry test in tensile mode. The increase of *Tv* is linked to the rise of the crosslink density of the composite since the topology freezing temperature is a function of it. The presence of NFC blocks the segment relaxation of the network slightly disturbing the activation energy, as seen in section 4.4.3.2. Thus, a slight increase in the topology freezing temperature to achieve the bond exchange can be expected.

The creep behavior is an undesired phenomenon for polymer materials. The responsiveness of vitrimers to creep substantially has been referred to as the Achilles heel of vitrimer materials[47]. This has led to the search for alternatives to reduce creep. In **Figure IV-14**, a significant reduction of creep is remarked since the samples, both under the same conditions and dimensions, displayed a quite different displacement in the dilatometry test. This advantageous remark and the increase of mechanical properties might encourage the study for further applications of vitrimer-composites.

4.5 Conclusions

Throughout this Chapter, a new vitrimer-composite was explored. A protocol that allows to produce a vitrimer composite based on DGEBA–4-APDS and 10% (w/w) NFC used as reinforcement was achieved. The morphology of produced templates was also studied. In general, a medium dispersion is observed, with NFC well-dispersed and several areas with important bunch-like fibrils' aggregates. In these areas, the interactions with the matrix are low, and some detachments of fibers were observed. This composite combines a high *Tg* and an enhanced storage modulus compared to the pure epoxy resin in the glassy and rubbery plateau.

The vitrimer properties like the permanent network connectivity evidenced by swelling tests were maintained. The vitrimer properties are not highly impacted despite the incorporation of NFC as

fillers. The activation energy of the dynamic covalent bonds is quite similar to those of the resin whereas the *T*v is higher, it is most likely due to the presence of NFC. Because of the lack of a good interphase between NFC and the matrix, the stress relaxation model based on two main contributions from Bond Exchange Reaction and polymer network relaxation can be applied to describe the material stress relaxation. Also, the dilatometry tests revealed a significant creep reduction after incorporating the NFC as fillers. The creep diminution might be interesting to explore for further applications where this behavior is undesirable like in the aerospace industry.

Bibliography

1 Vinson, J. R., & Sierakowski, R. L. (2006). *The behavior of structures composed of composite materials* (Vol. 105). Springer.

2 Parbin, S., Waghmare, N. K., Singh, S. K., & Khan, S. (2019). Mechanical properties of natural fiber reinforced epoxy composites: A review. *Procedia Computer Science*, *152*, 375-379.

3 Azizi Samir, M. A. S., Alloin, F., & Dufresne, A. (2005). Review of recent research into cellulosic whiskers, their properties and their application in nanocomposite field. *Biomacromolecules*, *6*(2), 612-626.

4 Siró, I., & Plackett, D. (2010). Microfibrillated cellulose and new nanocomposite materials: a review. *Cellulose*, *17*(3), 459-494.

5 Kalia, S., Dufresne, A., Cherian, B. M., Kaith, B. S., Avérous, L., Njuguna, J., & Nassiopoulos, E. (2011). Cellulose-based bio-and nanocomposites: a review. *International journal of polymer science*, *2011*.

6 Miao, C., & Hamad, W. Y. (2013). Cellulose reinforced polymer composites and nanocomposites: a critical review. *Cellulose*, *20*(5), 2221-2262.

7 Lee, K. Y., Aitomäki, Y., Berglund, L. A., Oksman, K., & Bismarck, A. (2014). On the use of nanocellulose as reinforcement in polymer matrix composites. *Composites Science and Technology*, *105*, 15-27.

8 Nakagaito, Antonio Norio, and Hiroyuki Yano. "Novel high-strength biocomposites based on microfibrillated cellulose having nano-order-unit web-like network structure." *Applied Physics A* 80.1 (2005): 155-159.

9 Azizi Samir, M. A. S., Alloin, F., & Dufresne, A. (2005). Review of recent research into cellulosic whiskers, their properties and their application in nanocomposite field. *Biomacromolecules*, *6*(2), 612-626.

10 Iwamoto, S., Nakagaito, A. N., & Yano, H. (2007). Nano-fibrillation of pulp fibers for the processing of transparent nanocomposites. *Applied Physics A*, *89*(2), 461-466.

11 Ansari, F., Galland, S., Johansson, M., Plummer, C. J., & Berglund, L. A. (2014). Cellulose nanofiber network for moisture stable, strong and ductile biocomposites and increased epoxy curing rate. *Composites Part A: Applied Science and Manufacturing*, *63*, 35-44.

12 Suzuki, K., Homma, Y., Igarashi, Y., Okumura, H., & Yano, H. (2017). Effect of preparation process of microfibrillated cellulose-reinforced polypropylene upon dispersion and mechanical properties. *Cellulose*, *24*(9), 3789-3801.

13 Seydibeyoğlu, M. Ö., & Oksman, K. (2008). Novel nanocomposites based on polyurethane and micro fibrillated cellulose. *Composites Science and Technology*, *68*(3-4), 908-914.

14 Jonoobi, M., Harun, J., Mathew, A. P., & Oksman, K. (2010). Mechanical properties of cellulose nanofiber (CNF) reinforced polylactic acid (PLA) prepared by twin screw extrusion. *Composites Science and Technology*, *70*(12), 1742-1747.

15 Henriksson, M., & Berglund, L. A. (2007). Structure and properties of cellulose nanocomposite films containing melamine formaldehyde. *Journal of Applied Polymer Science*, *106*(4), 2817-2824.

16 Bruce, D. M., Hobson, R. N., Farrent, J. W., & Hepworth, D. G. (2005). High-performance composites from low-cost plant primary cell walls. *Composites Part A: Applied Science and Manufacturing*, *36*(11), 1486-1493.

17 Nissilä, T., Hietala, M., & Oksman, K. (2019). A method for preparing epoxy-cellulose nanofiber composites with an oriented structure. *Composites Part A: Applied Science and Manufacturing*, *125*, 105515.

18 Lu, J., Askeland, P., & Drzal, L. T. (2008). Surface modification of microfibrillated cellulose for epoxy composite applications. *Polymer*, *49*(5), 1285-1296.

19 Saba, N., Safwan, A., Sanyang, M. L., Mohammad, F., Pervaiz, M., Jawaid, M., ... & Sain, M. (2017). Thermal and dynamic mechanical properties of cellulose nanofibers reinforced epoxy composites. *International journal of biological macromolecules*, *102*, 822-828.

20 Capadona, J. R., Van Den Berg, O., Capadona, L. A., Schroeter, M., Rowan, S. J., Tyler, D. J., & Weder, C. (2007). A versatile approach for the processing of polymer nanocomposites with self-assembled nanofibre templates. *Nature Nanotechnology*, *2*(12), 765-769.

21 Ansari, F., Galland, S., Johansson, M., Plummer, C. J., & Berglund, L. A. (2014). Cellulose nanofiber network for moisture stable, strong and ductile biocomposites and increased epoxy curing rate. *Composites Part A: Applied Science and Manufacturing*, *63*, 35-44.

22 Denissen, W., De Baere, I., Van Paepegem, W., Leibler, L., Winne, J., & Du Prez, F. E. (2018). Vinylogous urea vitrimers and their application in fiber reinforced composites. *Macromolecules*, *51*(5), 2054-2064.

23 Chabert, E., Vial, J., Cauchois, J. P., Mihaluta, M., & Tournilhac, F. (2016). Multiple welding of long fiber epoxy vitrimer composites. *Soft Matter*, *12*(21), 4838-4845.

24 de Luzuriaga, A. R., Matxain, J. M., Ruipérez, F., Martin, R., Asua, J. M., Cabañero, G., & Odriozola, I. (2016). Transient mechanochromism in epoxy vitrimer composites containing aromatic disulfide crosslinks. *Journal of Materials Chemistry C*, *4*(26), 6220-6223.

25 Yang, Y., Pei, Z., Zhang, X., Tao, L., Wei, Y., & Ji, Y. (2014). Carbon nanotube–vitrimer composite for facile and efficient photo-welding of epoxy. *Chemical Science*, *5*(9), 3486-3492.

26 Legrand, A., & Soulié-Ziakovic, C. (2016). Silica–epoxy vitrimer nanocomposites. *Macromolecules*, *49*(16), 5893-5902.

27 Huang, Z., Wang, Y., Zhu, J., Yu, J., & Hu, Z. (2018). Surface engineering of nanosilica for vitrimer composites. *Composites Science and Technology*, *154*, 18-27.

28 Zhao, W., Feng, Z., Liang, Z., Lv, Y., Xiang, F., Xiong, C., ... & Ni, Y. (2019). Vitrimer-Cellulose Paper Composites: A New Class of Strong, Smart, Green, and Sustainable Materials. *ACS applied materials & interfaces*, *11*(39), 36090-36099.

29 Lossada, F., Guo, J., Jiao, D., Groeer, S., Bourgeat-Lami, E., Montarnal, D., & Walther, A. (2018). Vitrimer chemistry meets cellulose nanofibrils: bioinspired nanopapers with high water resistance and strong adhesion. *Biomacromolecules*, *20*(2), 1045-1055.

30 Jouyandeh, M., Tikhani, F., Hampp, N., Yazdi, D. A., Zarrintaj, P., Ganjali, M. R., & Saeb, M. R. (2020). Highly curable self-healing vitrimer-like cellulose-modified halloysite nanotube/epoxy nanocomposite coatings. *Chemical Engineering Journal*, *396*, 125196.

31 Xu, C., Zheng, Z., Wu, W., Fu, L., & Lin, B. (2019). Design of healable epoxy composite based on β-hydroxyl esters crosslinked networks by using carboxylated cellulose nanocrystals as crosslinker. *Composites Science and Technology*, *181*, 107677.

32 Lossada, F., Jiao, D., Yao, X., & Walther, A. (2019). Waterborne methacrylate-based vitrimers. *ACS Macro Letters*, *9*(1), 70-76.

33 Nair, S. S., Chen, H., Peng, Y., Huang, Y., & Yan, N. (2018). Polylactic acid biocomposites reinforced with nanocellulose fibrils with high lignin content for improved mechanical, thermal, and barrier properties. *ACS Sustainable Chemistry & Engineering*, *6*(8), 10058-10068.

34 Tingaut, P., Zimmermann, T., & Lopez-Suevos, F. (2010). Synthesis and characterization of bionanocomposites with tunable properties from poly (lactic acid) and acetylated microfibrillated cellulose. *Biomacromolecules*, *11*(2), 454-464.

35 McGrath, L. M., Parnas, R. S., King, S. H., Schroeder, J. L., Fischer, D. A., & Lenhart, J. L. (2008). Investigation of the thermal, mechanical, and fracture properties of alumina–epoxy composites. *Polymer*, *49*(4), 999-1014.

36 Rahman, M. M., Zainuddin, S., Hosur, M. V., Robertson, C. J., Kumar, A., Trovillion, J., & Jeelani, S. (2013). Effect of NH2-MWCNTs on crosslink density of epoxy matrix and ILSS properties of e-glass/epoxy composites. *Composite Structures*, *95*, 213-221.

37 Nissilä, T., Karhula, S. S., Saarakkala, S., & Oksman, K. (2018). Cellulose nanofiber aerogels impregnated with bio-based epoxy using vacuum infusion: Structure, orientation and mechanical properties. *Composites Science and Technology*, *155*, 64-71.

38 Yue, L., Liu, F., Mekala, S., Patel, A., Gross, R. A., & Manas-Zloczower, I. (2019). High performance biobased epoxy nanocomposite reinforced with a bacterial cellulose nanofiber network. *ACS Sustainable Chemistry & Engineering*, *7*(6), 5986-5992

39 Tang, L., & Weder, C. (2010). Cellulose whisker/epoxy resin nanocomposites. *ACS applied materials & interfaces*, *2*(4), 1073-1080.

40 Mohammadi, P., Toivonen, M. S., Ikkala, O., Wagermaier, W., & Linder, M. B. (2017). Aligning cellulose nanofibril dispersions for tougher fibers. *Scientific reports*, *7*(1), 1-10.

41 Wang, W., Sabo, R. C., Mozuch, M. D., Kersten, P., Zhu, J. Y., & Jin, Y. (2015). Physical and mechanical properties of cellulose nanofibril films from bleached eucalyptus pulp by endoglucanase treatment and microfluidization. *Journal of Polymers and the Environment*, *23*(4), 551-558.

42 Chen, Y., Zhang, Y., Xu, C., & Cao, X. (2015). Cellulose nanocrystals reinforced foamed nitrile rubber nanocomposites. *Carbohydrate polymers*, *130*, 149-154.

43 Yue, L., Maiorana, A., Khelifa, F., Patel, A., Raquez, J. M., Bonnaud, L., ... & Manas-Zloczower, I. (2018). Surface-modified cellulose nanocrystals for biobased epoxy nanocomposites. *Polymer*, *134*, 155-162.

44 Abdelmouleh, M., Boufi, S., Belgacem, M. N., Dufresne, A., & Gandini, A. (2005). Modification of cellulose fibers with functionalized silanes: effect of the fiber treatment on the mechanical performances of cellulose–thermoset composites. *Journal of applied polymer science*, *98*(3), 974-984.

45 Herrera-Franco, P., & Valadez-Gonzalez, A. (2005). A study of the mechanical properties of short natural-fiber reinforced composites. *Composites Part B: Engineering*, *36*(8), 597-608.

46 Ricarte, R. G., Tournilhac, F., Cloître, M., & Leibler, L. (2020). Linear viscoelasticity and flow of self-assembled vitrimers: The case of a polyethylene/dioxaborolane system. *Macromolecules*, *53*(5), 1852-1866.

47 Li, L., Chen, X., Jin, K., & Torkelson, J. M. (2018). Vitrimers designed both to strongly suppress creep and to recover original cross-link density after reprocessing: quantitative theory and experiments. *Macromolecules*, *51*(15), 5537-5546.

48 Luo, C., Shi, X., Lei, Z., Zhu, C., Zhang, W., & Yu, K. (2018). Effects of bond exchange reactions and relaxation of polymer chains on the thermomechanical behaviors of covalent adaptable network polymers. *Polymer*, *153*, 43-51.

49 Hayashi, M., & Chen, L. (2020). Functionalization of triblock copolymer elastomers by cross-linking the end blocks via trans-N-alkylation-based exchangeable bonds. *Polymer Chemistry*, *11*(10), 1713-1719.

50 Capelot, M., Unterlass, M. M., Tournilhac, F., & Leibler, L. (2012). Catalytic control of the vitrimer glass transition. *ACS Macro Letters*, *1*(7), 789-792.

51 Yang, Y., Zhang, S., Zhang, X., Gao, L., Wei, Y., & Ji, Y. (2019). Detecting topology freezing transition temperature of vitrimers by AIE luminogens. *Nature communications*, *10*(1), 1-8.

Chapter V : NFC modification

5. Chemical functionalization of Nano Fibrillated Cellulose Surface by glycidyl silane coupling agents

5.1 Introduction

Nano fibrillated cellulose (NFC) has drawn the attention of several types of research because of its excellent mechanical properties[1, 2.] By virtue of its excellent properties, the NFC has been used as reinforcement fillers[3, 4, 5, 6, 7, 8,.] Nonetheless, the strong tendency for self-agglomeration due to numerous hydroxyl groups restricts the good dispersion into an epoxy resin. Like many others[5, 8], this work displayed a deficient interfacial adhesion of fibrils inside the vitrimer epoxy resin. Besides, the high hygroscopic character of NFC negatively impacts the durability of composite material by the hydrolytic aging acceleration. To overcome these difficulties and promote covalent bonds between the fibrils and the resin, the surface chemical modification of NFC has been explored. Reactions such as nucleophilic substitution[9], oxidation[6, 9], amidation[9], silylation[10, 11], or polymer grafting[6] have shown promising results in different matrices[5, 12, 13, 14]. The modified NFC might acquire a nature quite different from the original. Therefore, different properties of the composite material, such as mechanical, thermal, or even rheological, might be expected.

Since NFC is an eco-friendly material, the surface modification should be as far as possible a sustainable method, including low energy cost, eco-friendly solvent conditions, low cost, and no adverse effect on the mechanical properties. The silylation achieves these requirements and has proved to be an efficient method to modify the NFC surface [11, 15].

Many silylation protocols have been described in the literature to achieve a good functionalization[16, 17, 18, 19, 20], changing the surface with a wide variety of functional groups for further uses or applications [5], [21, 22, 23, 24]. The most accepted grafting process has been divided into three main steps, summarized in **Figure V-1**[25, 26, 27, 28]. The steps are:

1) The **hydrolysis** of alkoxy groups of the silane.
2) The **physical adsorption** of silanol groups onto the hydroxyl groups of cellulose surfaces.
3) The **chemical sorption** (grafting) onto the cellulose, i.e., the bond Si-O-Cellulose is formed. This step is carried out at high temperatures and under vacuum. A siloxane **self-condensation** cannot be dismissed[29].

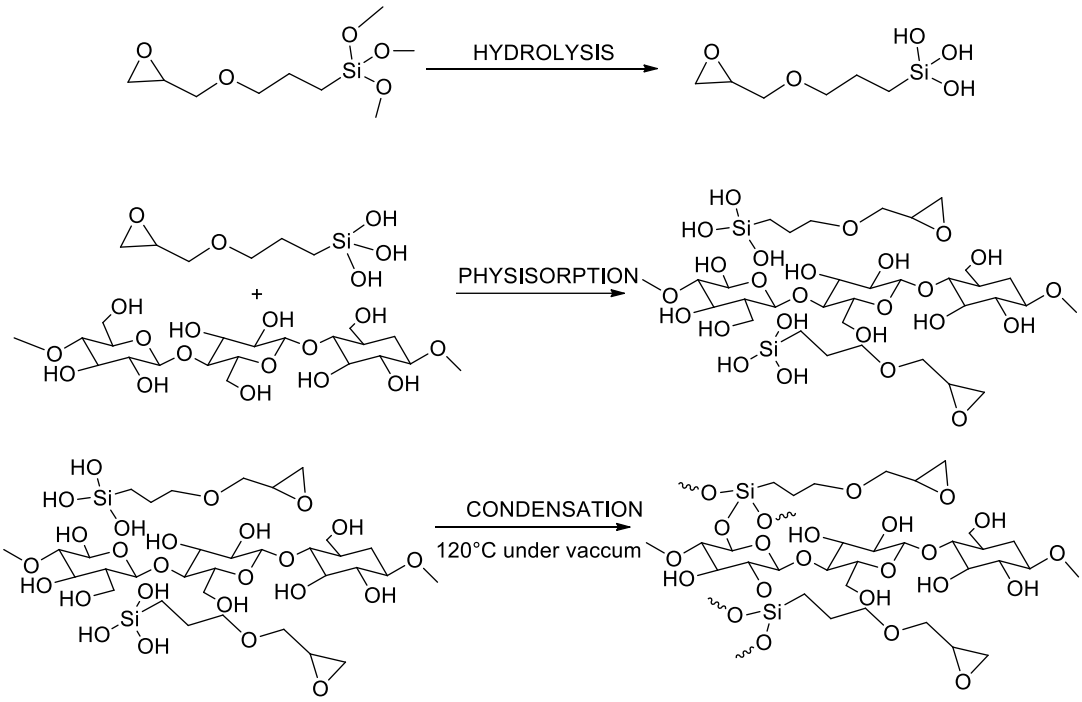

Figure V-1. Functionalization steps of the NFC surface by a silane coupling agent.

Despite the great efforts to clarify the reactions and phenomena on the surface, many questions concerning the siloxane network remain unanswered. For instance, the silane self-condensation forms a dense siloxane network surrounding NFC with a probably incomplete condensation[29, 30] or a physisorbed condensed structure far away from cellulose. The presence of weak adsorbed self-condensed structures reduces the load transfer of fibrils and weakens the interfacial adhesion between the NFC and the matrix. Since the interface between the fibrils and the matrix plays an important role in improving the performance of a composite, a weak adsorbed structure might limit the possible generation of covalent bonds between the filler and the resin. In that context, the Soxhlet extraction might be an interesting method to remove the weakly adsorbed silanes. The effects of the extraction have not been discussed profoundly in the literature.

5.2 Objectives

5.2.1 General objective

The main objective of this Chapter is to produce a Nano Fibrillated Cellulose with epoxy groups onto its surface. The modified NFC will improve the diffusion and the interfacial adhesion of fibrils with the epoxy vitrimer resin, DGEBA–4-APDS. Besides, a modification of the NFC surface might enhance the durability of the composite.

5.2.2 Particular objectives

- To establish an easy NFC surface modification protocol by using glycidoxy silanes.
- To characterize the chemical, morphological, and thermal properties of the modified fibrils.
- To evaluate the nature of self-condensed structures adsorbed and grafted on the NFC by using Soxhlet extraction.

5.3 Experimental section

The chosen silane coupling agents were the 3-glycidyloxypropyl trimethoxysilane (GPS) and the 3-glycidoxyloxyproyl dimethylethoxysilane (GPMES), shown in **Scheme V-1**. With three potential reaction sites, the GPS has a high probability to form a network surrounding the fibrils. However, with a single reaction site, the GPMES forms a monolayer chemically grafted to the surface.

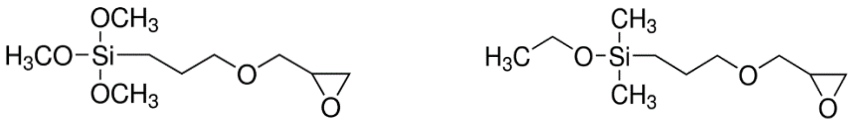

GPS GPMES

Scheme V-1. Chemical structure of 3-glycidyloxypropyl trimethoxysilane (GPS) and the 3-glycidoxyloxypropyl dimethylethoxysilane (GPMES).

In this study, four different protocols were explored for grafting GPS silane on NFC. These protocols were inspired by previous works in the literature[5, 18, 20, 21, 23, 31, 32]. There are many similitudes between these protocols, like the mass percentage of NFC suspensions, the quantity of added silane (2-3% w/w), and the heating at temperatures superior to 100°C under vacuum after the hydrolysis reaction.

Table V-1 summarizes the performed methods using the GPS silane in a concentration of 3%. After each reaction, the sample was washed with an EtOH/H_2O mixture (8:2, v/v) and acetone to remove the weakly absorbed silanes and the acetic acid in excess (protocols 1 and 4 of **Table V-1**). Then, the samples were dried under vacuum at 120 °C for 12 h. The obtained compound was a white powder.

	Protocol	pH	m_{NFC} (g) (1% m/m)	V_{GPS} (µL)	Reaction time	Temperature (°C)
1	**NFC-GPS** - H^+/H_2O	3	10	300	4h	46
2	**NFC- GPS** - EtOH	Neutral				80
3	**NFC – GPS** - Acetone	Neutral				25
4	**NFC –GPS** - EtOH/H^+/ H_2O (7:3)	3				80

Table V-1. Protocols explored for NFC-GPS grafting.

After each reaction, a Soxhlet extraction during 48h in acetone was carried out to eliminate any possible residue of weakly absorbed silanes onto the modified NFC surface and any external pollution before characterization.

5.4 Characterization results

The NFC functionalized with silane coupling agents was first characterized by Attenuated Total Reflection Infrared Spectroscopy to corroborate the presence of GPS and GPMES absorbed at the surface. Then the silanes present on the surface were characterized in detail. Energy Dispersive X-ray (EDX) and X-ray Photoelectron Spectroscopy (XPS) were used to quantitatively evaluate the silane present on the surface. The effect of Soxhlet extraction was then studied to evidence the presence of weakly adsorbed silane on the NFC surface. ^{13}C and ^{29}Si solid-state NMR experiments were conducted to understand the chemical grafting of the silane coupling agents and their network structure on the NFC fibrils.

In order to observe the changes in NFC morphology, Scanning Electron Microscopy (SEM) and Atomic Force Microscopy (AFM) were performed. Thermogravimetric Analysis (TGA) was also used to verify the thermal stability of the modified NFC.

5.4.1 Chemical Characterization

5.4.1.1 Characterization of pristine and modified NFC by infrared spectroscopy

Attenuated Total Reflection-Infrared (ATR-IR) studies were used to ascertain the NFC modification by following the absorption peaks of the NFC [20, 33]. **Figure V-2** shows the infrared spectra of the pristine NFC and the different modified NFC. The spectra are normalized using the peak at 1160 cm^{-1} as a reference. This last peak corresponds to the glycosidic vibration of cellulose, which has no interaction with the silanes during the grafting process.

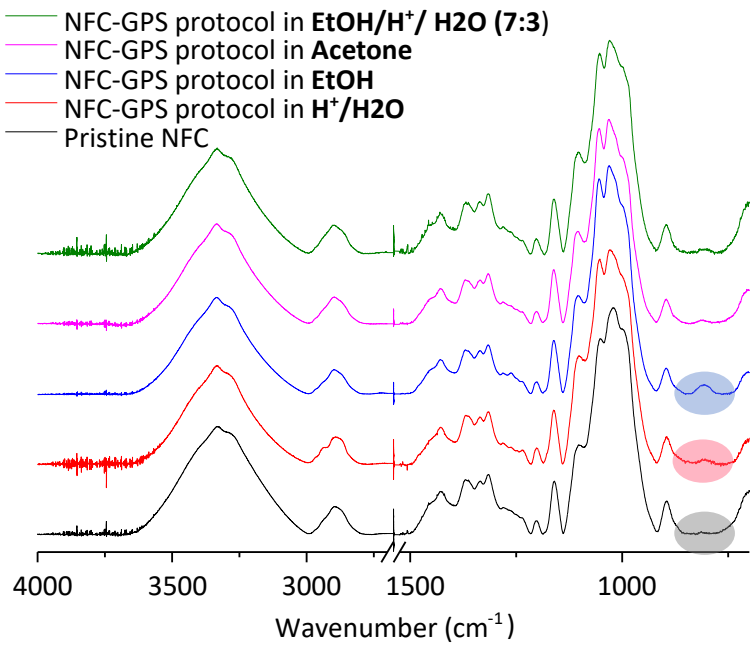

Figure V-2. Infrared spectra of pristine and modified NFC under the different conditions established in Table V-1.

The most relevant vibrations attributed to the grafting process are found in the region between 822 and 793 cm^{-1}, where no vibration linked to the pristine NFC is present[34]. In this region, the vibration bands are related to the Si-O-C absorption band[5, 23, 35]. This vibration constitutes the first test to evidence of GPS adsorbed to the NFC surface. Based on the results of **Figure V-2,** the experimental conditions of the two first methods (under the acid condition at pH=3 and in ethanol) were kept to continue a detailed characterization.

The region between 1200-700 cm^{-1} comprises various bands corresponding to the hydroxy groups of cellulose [34] and the Si-O-C[35] of silanes. Therefore, this area was analyzed in detail, as shown in **Figure V-3**. The figure shows modified NFC's spectra (red and blue) overlapped to the pristine NFC (black). Several areas display slight differences between the pristine and the two modified NFC. The most remarkable ones are enclosed in the dashed lines.

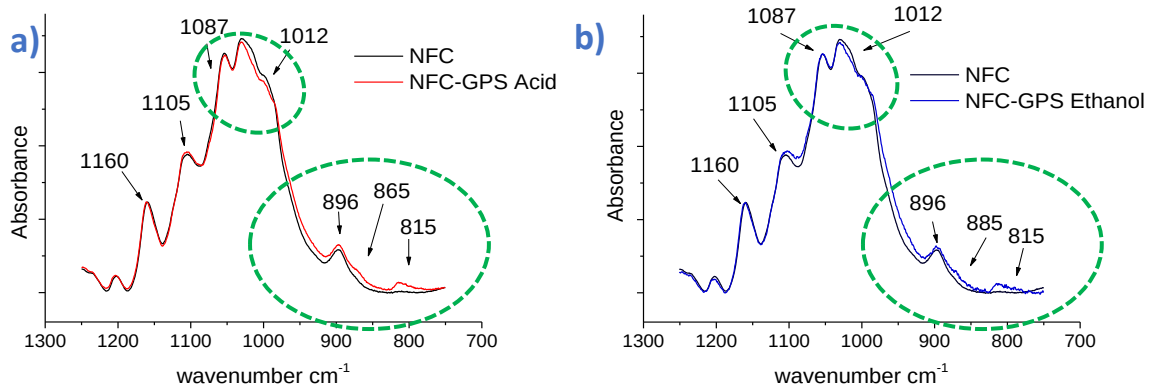

Figure V-3. Infrared spectra of modified NFC overlapped to the pristine NFC spectrum in the region of 1200-700 cm^{-1}. a) NFC-GPS acid, b) NFC GPS-EtOH.

A detailed deconvolution of all vibration bands in the region between 1200-700 cm^{-1} was carried out to go further in this analysis. **Figure V-4** displays the deconvoluted spectra of pristine and modified NFC. The black line corresponds to the experimental data, and the red line to the summation of all deconvoluted signals. To achieve the deconvolution analysis properly, it was realized into three stages.

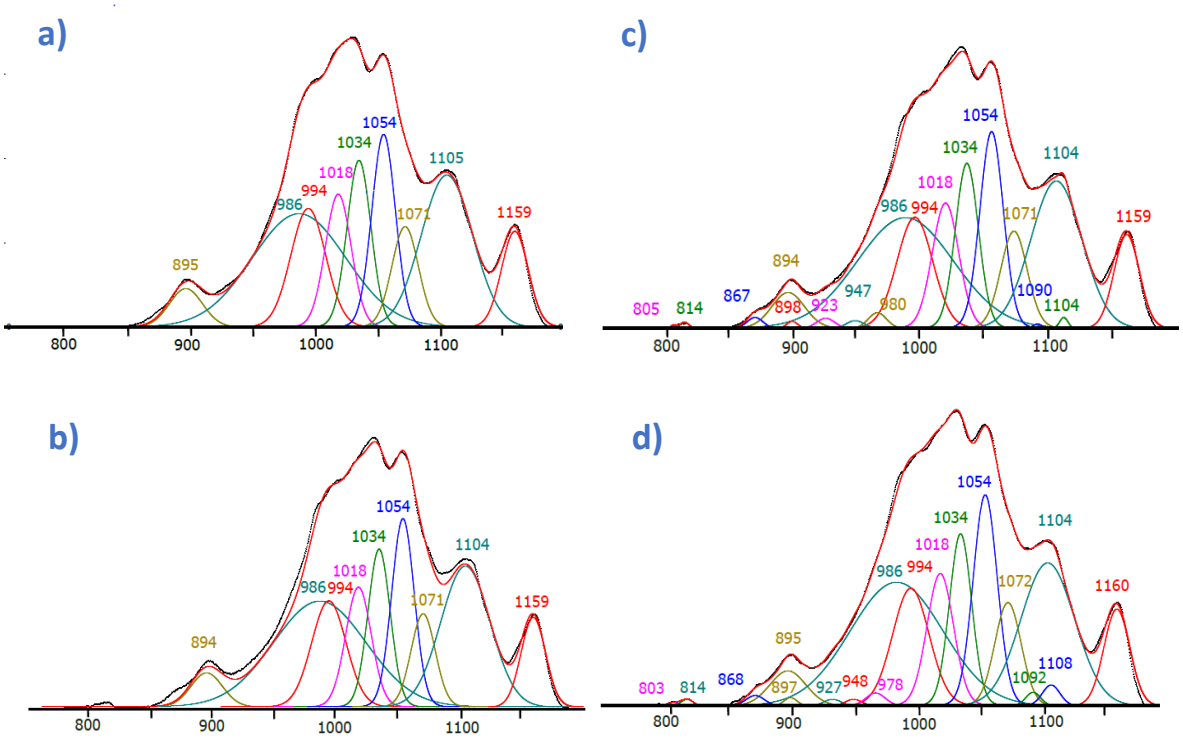

Figure V-4. Infrared spectra of a) NFC after Soxhlet extraction and its deconvoluted bands, b) NFC-GPS acid overlapped by pristine NFC deconvoluted bands, c) NFC-GPS acid overlapped by NFC and GPS deconvoluted bands, and d) NFC-GPS EtOH deconvoluted spectrum displays the presence of GPS vibration and similar intensities like in sample performed under acid conditions.

The first stage represented in **Figure V-4a** displays the deconvolution of all vibration bands of the pristine NFC. The peaks at 1034, 1018, 994, and 986 cm^{-1} correspond to the primary alcohols and 1105 and 1054 cm^{-1} to the secondary alcohols. The band at 1160, 1070, and 895 cm^{-1} are related to the glycosidic deformation.

The second stage is shown in **Figure V-4b** displays the summation of all deconvoluted signals of pristine NFC (the red line) normalized by using the band at 1160 cm^{-1}. This red spectrum is overlapped on the NFC-GPS under the acid condition spectrum (the black line). Two regions show significant differences: 940-1054 cm^{-1} and 800-930 cm^{-1}. These differences are explained due to GPS grafting. Therefore, to fill this information gap, the bands referring to the GPS must be added, triggering the third stage.

The third stage is shown in **Figure V-4c**. In this stage, the objective is to attribute the vibrations that do not correspond to the NFC and are presumably attributed to GPS. The bands added at 805 and 815 cm^{-1} are the primary references for the grafting because of the non-overlapping with the pristine NFC. These bands are attributed to Si-O-C and Si-O-Si and are presumably linked to a silicon network[23, 37]. The other bands are in overlapping areas with the pristine NFC. The vibration at 813, 965, and 1096 cm^{-1} correspond to the propyl chain of GPS. The signals at 867 and 926 cm^{-1} are related to the epoxy group. Finally, multiple GPS vibration bands at 951, 1109, and 1143 cm^{-1} are associated with the glycidoxy [4, 16, 19, 36, 37]. Conversely, the vibration bands at 940 and 1054 cm^{-1} linked to alcohol vibrations from the NFC decrease slightly after the treatment under acid conditions.

In **Figure V-4d**, the deconvoluted spectrum of the NFC-GPS under ethanol conditions is presented. It shows similar intensities as displayed in **Figure V-4c**.

5.4.1.2 The silanes onto NFC surface: adsorption, reactions, and network structure

The literature rarely explores the kind of adsorption achieved after a silane grafting. Since the *grafting* will constitute the interface between the fibrils and the epoxy-vitrimer resin, it is necessary to know in detail different aspects such as the quantification of the adsorbed silane molecules, the possible reaction between the silanes and fibrils, and the condensed structure around the fibrils.

5.4.1.2.1 Quantitative characterization of modified NFC after Soxhlet extraction

EDX experiments on NFC samples were carried out before and after Soxhlet extraction to confirm the presence of silanes onto NFC surface, presumably chemically grafted. **Figure V-5** displays the spectrum of modified NFC with GPS silane performed under acid conditions. Three different signals

are present at 0.277, 0.525, and 1.75 keV, associated with C, O, and Si Kα elements respectively. This analysis confirms the presence of silane in the modified NFC.

Table V-2 summarizes the relative percentages of C, O, and Si present in pristine and modified NFC samples before and after Soxhlet extraction.

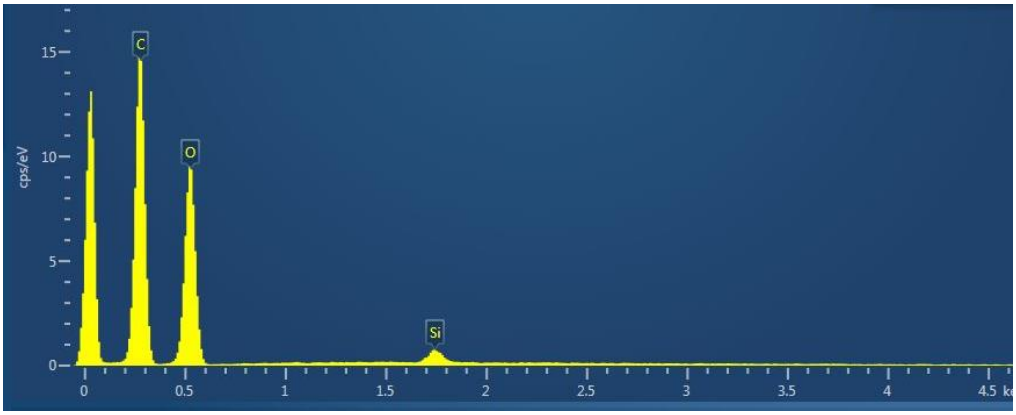

Figure V-5. EDX spectrum of the modified NFC-GPS under acid conditions and treated with a Soxhlet extraction.

Sample	Atomic % of C	Atomic % of O	Atomic % of Si
Pristine NFC	56.7	43.3	0
NFC- GPS- acid *before* Soxhlet extraction	55.7	42.2	2.1
NFC- GPS- acid after Soxhlet extraction	58.4	41.0	0.6
NFC- GPS- EtOH *before* Soxhlet extraction	61.0	38.6	0.4
NFC-GPS-EtOH after Soxhlet extraction	60.3	39.4	0.3

Table V-2. The relative percentages of C, O, and Si present at the NFC surface determined by EDX analysis.

As observed in **Table V-2**, EDX analysis allow asserting that a quantity of GPS is weakly adsorbed onto fibrils surfaces and can be eliminated after a soxhlet extraction. For the modified NFC under acid conditions, two-thirds of the silanes were weakly adsorbed, while the modified NFC under ethylic condition, only a quarter were weakly adsorbed. The eliminated silanes are presumably purely physical adsorbed onto the NFC.

As observed in **Table V-2**, the functionalization protocol conducted under acid conditions promotes a higher concentration of silanes than that performed under EtOH conditions. The acid condition might catalyze the reaction, allowing to generate the silanols faster than under ethylic conditions[38].

To go further on the surface analysis of NFC fibrils, X-ray photoelectron spectroscopy analysis was performed. This technique allows to quantify and analyze the chemical composition of the

functionalized NFC surface. The samples are irradiated by X-rays, penetrating a depth from 2 to 10 nm[39].

Figure V-6 shows the XPS spectra of pristine and different samples of modified NFC after Soxhlet extraction. The survey spectrum of the pristine NFC possesses only two peaks, at 532 and 286 eV, corresponding respectively to oxygen (O 1s) and carbon (C 1s)[40, 41, 42]. The NFC modified with silanes present a third peak at 102 eV, corresponding to the Si element of the silane coupling agent.

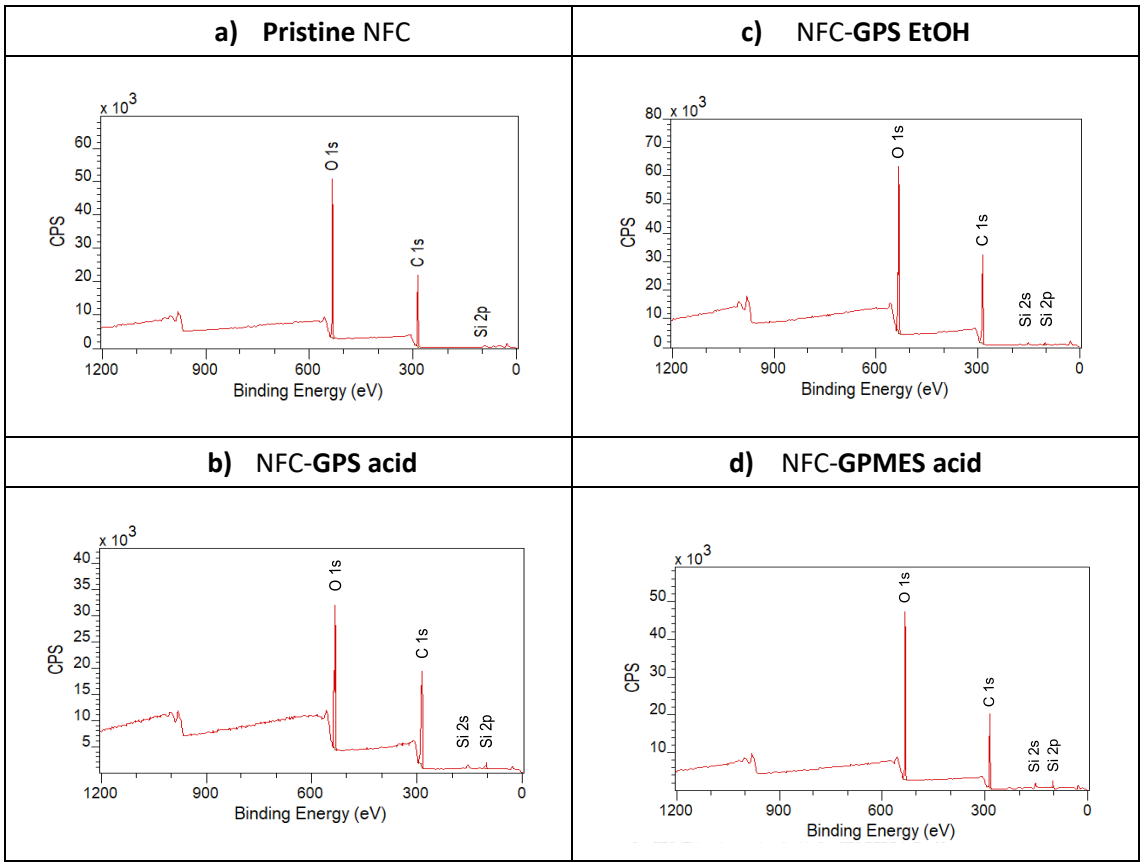

Figure V-6. XPS survey spectra of different NFC samples after Soxhlet extraction. a) pristine NFC, b) NFC-GPS under acid conditions, c) NFC-GPS under EtOH conditions, and NFC-GPMES under acid conditions.

Table V-3 presents the relative atomic concentration of the chemical elements and the oxygen/carbon ratios for each sample. As observed by EDX analysis, XPS measurements reveal that the relative percentage of silicon element is higher by using the first protocol (H^+/H_2O, acid conditions) than the second one (EtOH). In light of the EDX and XPS results, the first protocol was chosen as the best functionalization method. Therefore, the detailed surface analysis considers the grafting condition under acid conditions. Besides, the subsequent analyses also include the use of

the GPMES as a monofunctional silane coupling agent to understand the silicon grafting mechanism on the NFC surface.

The O/C atomic ratio analysis can be used as a parameter to confirm the GPS on the surface. The results for the pristine ($C_6H_{10}O_5$) and modified NFC are presented in **Table V-3**. While it is true that the theoretical atomic ratio O/C of the cellulose, considering the chemical formula, must be 0.83, the experimental result was 0.67. This difference has been attributed to surface contaminants and some other components on the surface, such as adventitious carbon [19, 40]. Besides, different studies have exposed the possible adaptation of the NFC surface due to the solvent used previously or during the manufacturing of nanofibrils, leading to the difference between the experimental and theoretical results of O/C atomic ratio[43].

For samples with GPS as the silane coupling agent, the O/C atomic ratio slightly changes and shows a decreasing tendency from 0.67 to 0.64. This trend is explained because of the addition of GPS to the NFC surface, changing the O/C ratio at the surface (**Scheme V-2**). Likewise, for GPMES grafting, the atomic ratio variation is also observed. The O/C value decreased from 0.67 to 0.62. In this last case, the change is more remarked due to the chemical structure of the GPMES, which possesses eight carbons and not six like GPS.

Sample	C 1s	O 1s	Si 2p	O/C
Pristine NFC	59.8	39.9	0.3	0.67
NFC-GPS Acid	57.7	37.1	5.1	0.64
NFC-GPS EtOH	59.5	37.4	3.1	0.64
NFC-GPMES	61.2	37.9	1	0.62

Table V-3. Relative atomic concentration obtained by XPS analysis of pristine and modified NFC after Soxhlet extraction.

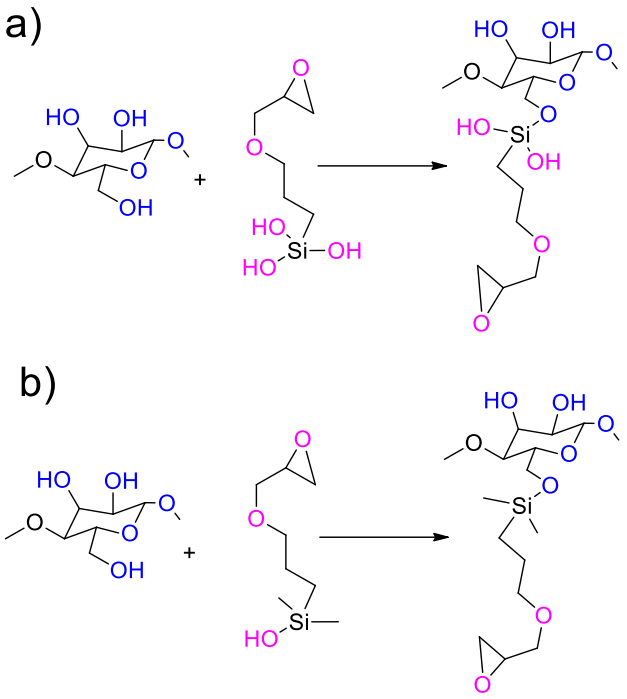

Scheme V-2. Schematization of a) GPS and b) GPMES grafting onto the NFC surface.

From the information reported in **Table V-3**, it is possible to estimate the quantity of silane coupling agents present in the surface of fibrils. A quick calculation shows that an average of one silane grafted per one saccharide unit in the surface is obtained when the GPS is grafted under acid conditions. The grafting under ethylic conditions, an average of one silane grafted per two saccharide units is obtained. The calculus is detailed in the annex of Chapter V (**Table S.V- 1**).

The band of C1s in the XPS characterization was analyzed in detail to go further in the analysis. The C1s peak in **Figure V-6** is a convolution of different types of carbons, so after a chemical grafting, it is possible to appreciate significant differences and new types of carbons present on the surface. These results are presented in **Figure V-7**and **Table V-4**.

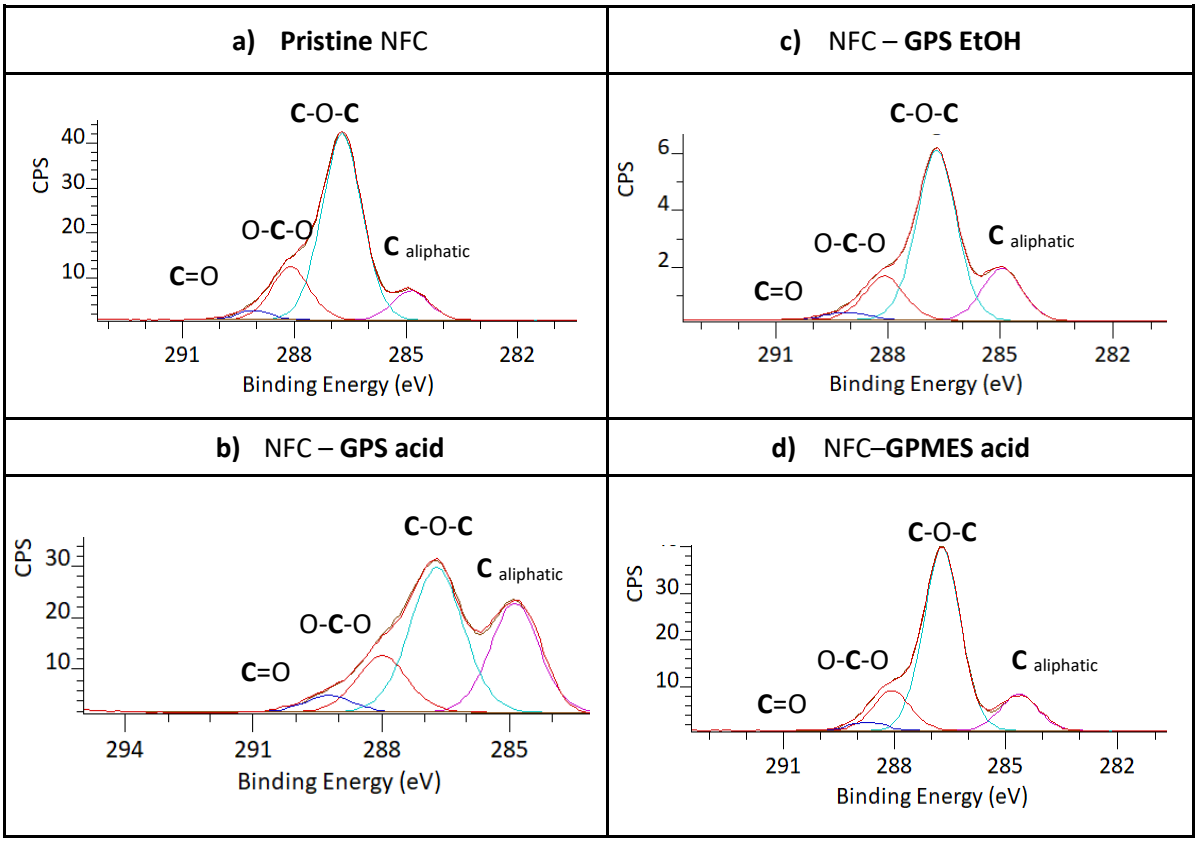

Figure V-7. Deconvolution of C1s XPS spectra of NFC samples after Soxhlet extraction a) pristine NFC, b) NFC-GPS under acid conditions, c) NFC-GPS under EtOH conditions, and e) NFC-GPMES under acid conditions.

Sample	C1 at 284.8 eV	C2 at 286.7 eV	C3 at 288.0 eV	C4 at 289.0 eV
	C aliphatic	**C**-O-**C**	O-**C**-O	**C**=O
Pristine NFC	11	69	17	3
NFC-GPS - *EtOH*	16	61	19	3
NFC-GPS - *acid*	26	48	21	5
NFC-GPMES - *acid*	13	65	18	4

Table V-4. Positions and intensities (%) of the C1s sub-peaks of pristine NFC and GPS-modified NFC.

The deconvolution study performed in **Figure V-7** shows four sub-peaks at 284.8, 286.7, 288.0, and 289.0 eV attributed to C1 (C-H), C2(C-O-C), C3 (O-C-O), and C4 (C=O) [44, 45, 46]. The sub-peak C1s at 284.8 eV is the most relevant for this analysis and linked to the aliphatic carbons present in the pristine and modified NFC. In the pristine NFC case, these aliphatic carbons are attributed to

chemical defects and the surface pollution by hydrocarbons adsorbed at nanofibers' surface[43]. For the modified NFC, these carbons are attributed to the same defects as those of the pristine NFC and the propyl group of the GPS and the GPMES. The relative intensity of the sub-peak increases from 11% for pristine to 16% for NFC-GPS EtOH, and up to 26% for NFC-GPS- acid, according to **Table V-4**. In the case of the GPMES, a minor increase of propyl groups is remarked (from 11 to 13%). The minor increase is explained due to the chemical nature of GPMES that only allows to generate a monolayer and not a self-condensed structure and then more propyl groups onto the surface.

The sub-peak with the minor intensity at 289 eV (C4) is related to the carbonyl group [37, 47], and provides information related to the robustness of fibrils, i.e., oxidation due to the acid treatment. Since the sub-peak is already present in NFC pristine, it can be assumed that a small number of carbonyls were probably formed during the fibrils' manufacturing process (some process uses strong acids that might slightly oxidate the fibrils surfaces, Chapter I). The intensity evolution of this peak was analyzed, displaying a minor increase (1%), so the acid conditions induce limited oxidation.

5.4.1.2.3 Chemical grafting of silanes coupling agents on the surface of the NFC

^{13}C solid-state NMR experiments were carried out to prove the presence of GPS and GPMES on the cellulose fibrils and evaluate the possible reaction that might occur on the two potential reactive sites of glycidoxy silanes: the silanols and the epoxy ring[38]. The analyzed spectra were previously treated under Soxhlet extraction to eliminate as much as possible the siloxanes physiosorbed onto the fibrils. **Figure V-8** shows the ^{13}C NMR spectra of the pristine and modified NFC with GPS and GPMES under acid conditions.

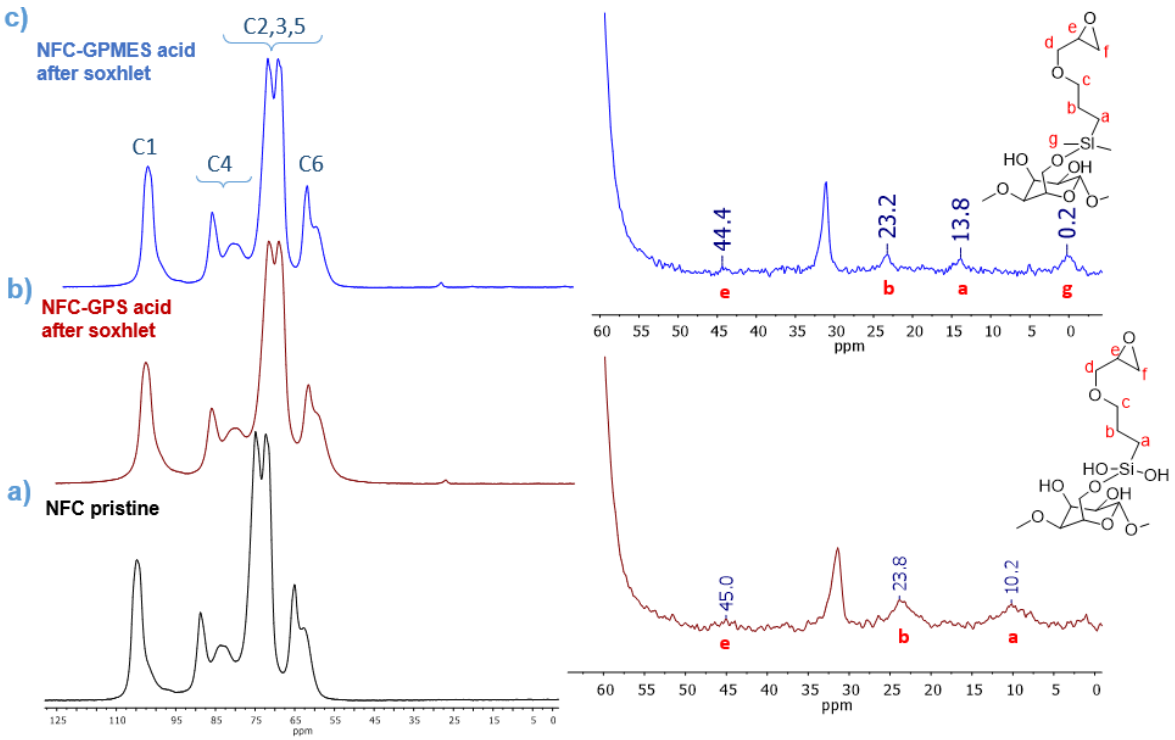

Figure V-8. ^{13}C solid-state NMR spectra of a) pristine NFC, b) NFC-GPS, and c) NFC-GPMES, both grafting under acid conditions.

Figure V-8a displays the cellulose chemical shifts, which have been widely studied and identified in numerous works[48, 49,50, 51, 52]. The region from 62 to 66 corresponds to C_6; from 71 to 77, the peaks are attributed to C_2, C_3, and C_5; from 85 to 90 ppm, the signal is assigned to C_4; finally, from 104 to 108 ppm, the band corresponds to C_1. The corresponding spectrum of the NFC-GPS (**Figure V-8b**) displays the cellulose bands and three new chemical shifts at 8.2, linked to **C**H_2-O-Si, at 22.4 ppm to **C**H_2-CH_2-O-Si, and at 45 ppm to the tri-substituted carbon of the oxirane group (C_e). The small intensity of the peak at 45 ppm is attributed to the resonance structures generated by the different self-condensation forms. Finally, **Figure V-8c** corresponds to the spectrum of NFC-GPMES, showing four new peaks which are easy to identify. The first at 0.2 ppm is linked to the methylene next to Si (C_g), and the last three peaks are related to the same carbons as those described before for the GPS. The peak at 31.1 ppm in both spectra corresponds to the acetone that was not eliminated with the drying protocol of the samples.

Moreover, the spectra of the modified NFC by silane coupling agent correspond correctly to a chemical grafting between the silanol and the hydroxyl groups of cellulose as suggested the **Scheme V-2**. The chemical shifts registered of C_a (10.2 and 13.8 ppm for GPS and GPMES) discard the hypothesis of a possible reaction between the hydroxyl groups of the cellulose and the epoxy ring

of glycidoxy. If a chemical reaction had taken place between the epoxy ring and hydroxyl groups of the cellulose, the C_a of the chemical structure in **Figure V-8** would display a chemical shift to low fields. That chemical shift was not seen. A simulation was carried out to verify the hypothesis (**Figure S.V- 1**).

The chemical shifts of silane coupling agents were corroborated by making a blank test of both silanes under the same pH and temperature conditions. **Figure V-9a** and **c** display the ^{13}C NMR of silanes coupling agents in $CDCl_3$, and **Figure V-9b** and **d** the silanes after the blank test. The complete hydrolysis of both silanes is remarked since the peaks linked to the **methoxy group of the GPS at 50.8 ppm of C_h** (**Figure V-9a**) and to the **ethoxy group of the GPMES at 18.5 and 58.2 ppm** (**Figure V-9b**) disappeared (C_h and C_i). Besides, the hydrolyzed silanes revealed a ring-opening of the oxirane group on the spectra of the hydrolyzed GPS and GPMES. This **ring-opening** is linked to the signals at **62.7 and 70.4 ppm** for the GPS and at **64.2 and 70.5 ppm for the GPMES** (C_e and C_f)**.**

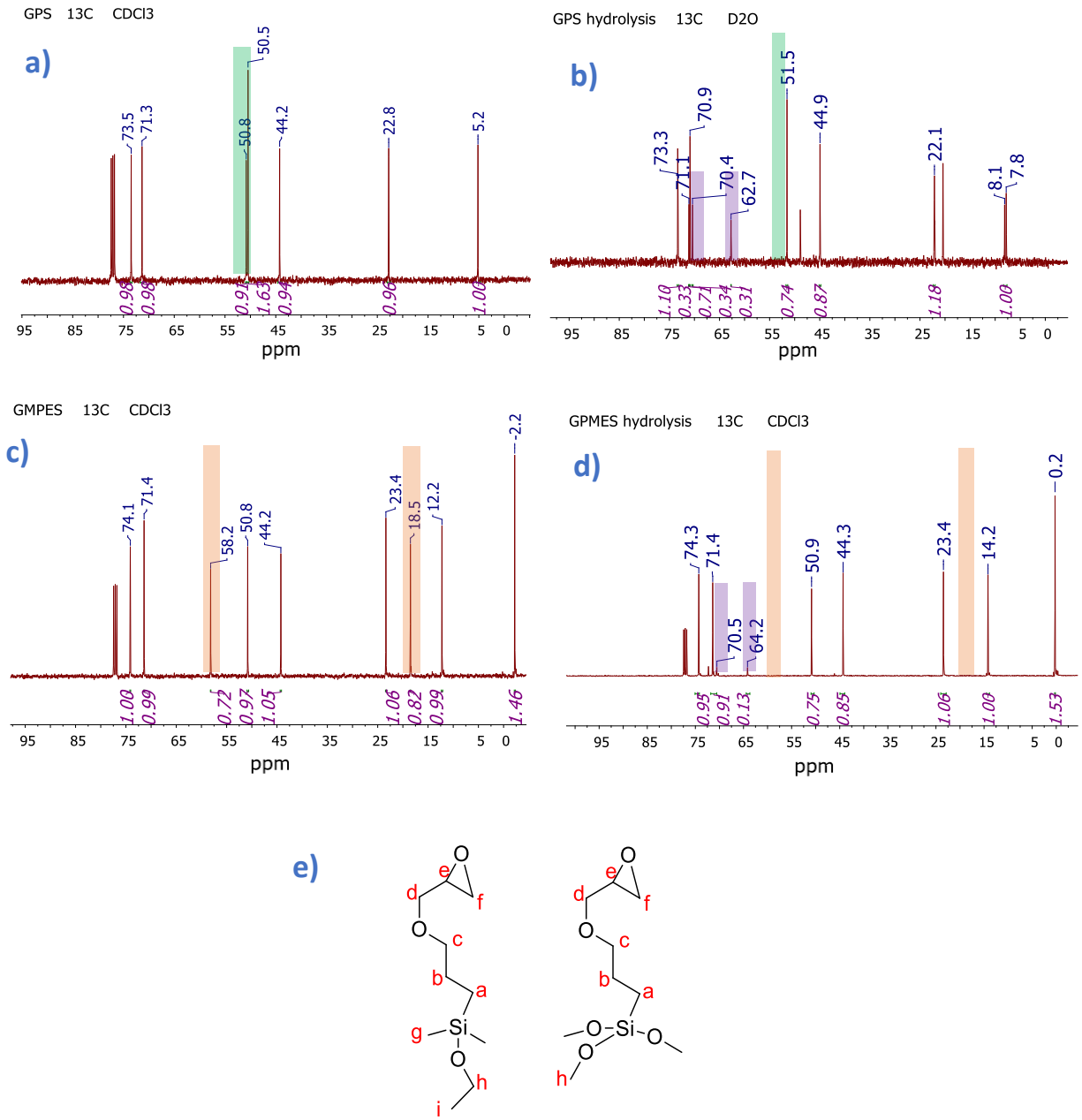

Figure V-9. ^{13}C NMR spectra of a) GPS, c) hydrolyzed GPS, b) GPMES, d) hydrolyzed GPMES and e) chemical structure of GPS and GPMES.

In addition, an integration of these new peaks was performed, exposing a relative presence between 26% and 32% of ring-opened GPS after the treatment at 4h at 46°C at pH 3 (C_e, C_f, $C_{e'}$ and $C_{f'}$,). **Scheme V-3** and **Table V-5** summarize the chemical shifts and the integration values of each carbon of hydrolyzed GPS.

The spectra of **Figure V-9c** and **d** do not show evidence of a possible reaction between the silanol and the oxirane. If that reaction had taken place, the C_f should experiment a chemical shift to high

fields not observed (**Figure S.V-2**).

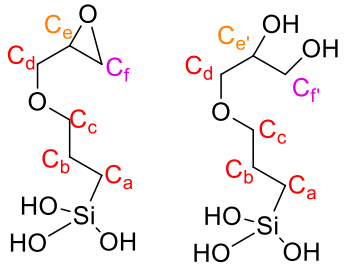

Scheme V-3. GPS after hydrolysis of methoxy, a) GPS with its unreacted oxirane ring, b) GPS with a ring-opening oxirane.

Carbon	Chemical shift	Integral
C_a	7.86/8.12	1
C_b	22.16	1.18
C_c	73.39	1.1
C_d	70.9 (and 71.13)	1.04 (0.71+0.33)
C_e	**51.61**	**0.74**
C_f	**44.95**	**0.87**
$C_{e'}$	**70.39**	**0.34**
$C_{f'}$	**62.7**	**0.31**

Table V-5. Chemical shift values of the different carbons of the GPS and their respective integration values. The detailed calculus of these values is described in detail in the annex of Chapter V.

5.4.1.2.4 Siloxane network structures around the NFC fibrils.

^{29}Si solid-state NMR experiments were carried out to prove the presence of a self-condensed structure onto the NFC surface, as hypothesized in the infrared analysis. The chemical shifts of signals related to the silicon network formed on the surface are determined by the number of siloxane bridges attached to the silicon atoms[29].

The self-condensation evolution from a dimer to a network is illustrated in **Figure V-10a**, showing four possible structures denominated T0, T1, T2, and T3. The structure T0 corresponds to the GPS directly grafted onto the NFC surface (δ ≈-40 ppm), while T1, T2, and T3 correspond to the different self-condensation degrees (δ ≈ -48, -56, -68 ppm respectively). The chemical shifts slightly vary as a function of the silane grafted and of the nature of the analyzed surface[15, 29, 53].

Figure V-10b displays the spectra of NFC-GPS acid before and after the soxhlet extraction. Both spectra display the different silane configurations related to the self-condensation of GPS onto the cellulose surface. The chemical shifts are δ≈-39, -48, -58, and -66 ppm, corresponding to T0, T1, T2,

and T3, respectively[29, 54, 55]. These chemical shifts are quite similar to those described in the literature and ratified by using MestReNova software. The spectra predict by MestReNova are shown in **Figure S.V- 3**, and the chemical shifts are summarized in **Table S.V- 2**.

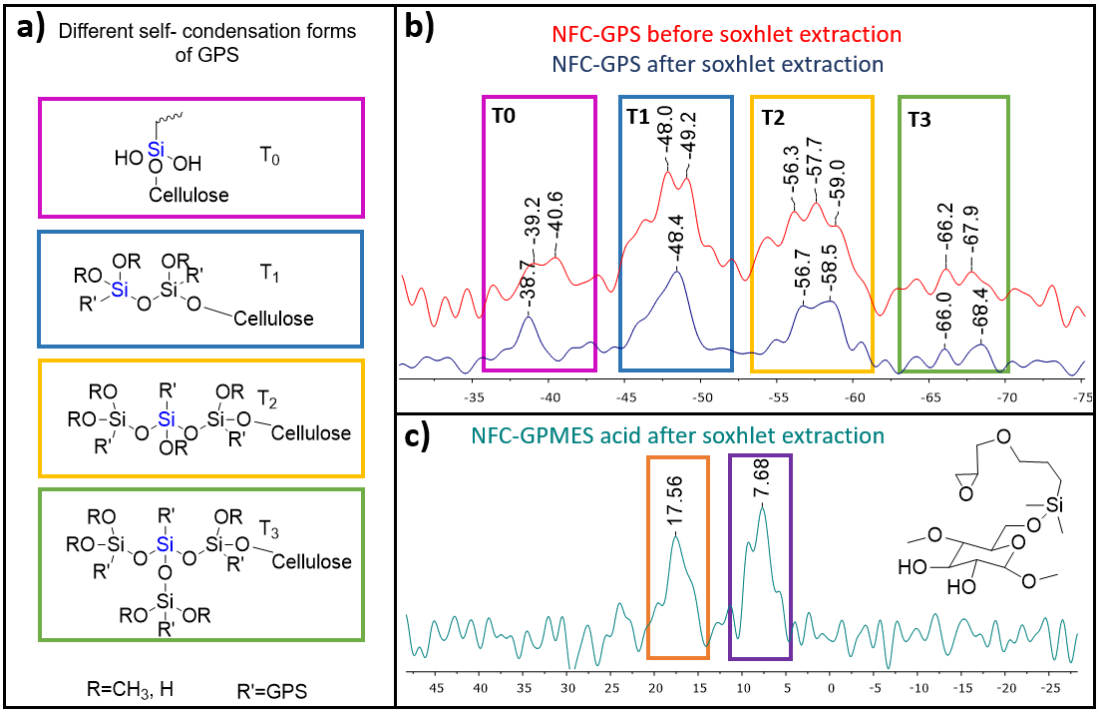

Figure V-10. Solid-state ^{29}Si NMR spectra of NFC functionalized with GPS under acid conditions. A) Different condensation forms of GPS silane, b) NFC-GPS under acid conditions before and after Soxhlet extraction and c) NFC-GPMES under acid conditions after Soxhlet extraction.

Figure V-10b also displays the effect of the Soxhlet extraction, overlapping the spectra before and after Soxhlet extraction. Before the extraction, the spectrum shows more than one peak, while after Soxhlet extraction, the peaks are narrower, and the intensity is slightly reduced. Both samples were analyzed with the same acquisition time. The narrowness and the reduced intensity of peaks overlapped in the same area can be attributed to two main factors: 1) The diversity of reactive sites of the cellulose (C1, C3, and C6) and 2) A GPS self-condensed physiosorbed networks. The signals of the chemically and physically grafted siloxane chains are overlapped, displaying chemical shifts slightly different. The extraction eliminates preferentially T3 structures that presumably are weakly grafted onto NFC. Silanes grafted structures T0, and T1 showed an apparent increase after Soxhlet extraction. This result suggests that the functionalized NFC possesses a significant amount of the siloxane networks surrounding the fibrils without covalent bonds to the cellulose.

Moreover, the simulated spectra of the self-condensed structures and the grafting of these structures was carried out by using MestReNova software. The simulation results are presented in

Figure S.V- 3 and summarized in **Table S.V- 2**. The chemical shift of the structures grafted or not to the NFC surface are quite similar. The minor difference is due to the grafting process.

From the spectra presented in **Figure V-10b**, it was also possible to obtain the relative concentration values of each structure grafted to the NFC surface. These results are summarized in **Table V-6**. The GPS grafted directly to the cellulose surface, T0, is approximately 20%. More than 70% is related to linear grafting (T1 and T2). Finally, less than 10% are related to a three-dimensional siloxane network.

Signal	Before Soxhlet extraction (%)	After Soxhlet extraction (%)
T0	15	19
T1	40	45
T2	35	32
T3	10	4

Table V-6. Values of the relative concentration of GPS networks before and after Soxhlet extraction.

These relative proportions show a contrary behavior to those reported in the literature concerning natural fibers grafting[19, 20, 29]. As discussed before, the study showed how self-condensed structure T3 was not the most abundant structure neither before nor after Soxhlet extraction. The explanation is attributed to the low kinetic of GPS. Indeed, Kretschmer *et al.*[55] described a low GPS kinetic and showed how their network's concentration T3 was directly linked to the epoxy ring-opening, the temperature, and the reaction time. In some previous works, the reaction time occurs over one reaction day[5, 53].

Furthermore, the use of silane with a single silanol reactive site was explored by using the GPMES. **Figure V-10c** shows the spectrum of NFC-GPMES after the Soxhlet extraction of the modified NFC. This silane allows generating a monolayer of silane onto the NFC surface. Compared to the GPS spectrum, the GPMES spectrum shows only two signals, δ=18 and 8 ppm, attributed to a linkage between the NFC and the GPMES and the self-condensed dimer. These chemical shifts were validated by using MestReNova software (**Figure S.V- 4**). Even after a Soxhlet extraction, the self-condensed physiosorbed structures remained on the surface, contrary to GPS, where an important quantity of self-condensed physiosorbed structures was eliminated. This behavior might be explained by a strong surface interaction between the GPMES and cellulose surface. Since the dimers formed by using GPMES are smaller than the oligomers or the networks formed by GPS, the surface interaction of GPMES and cellulose could be more important. So that, the contact surface

leads to an incomplete elimination of the physiosorbed dimers on the surface even after Soxhlet extraction.

5.4.3 Morphological characterization

SEM images of nano fibrillated cellulose were recorded before and after chemical functionalization to determine the effect of silane coupling agents on the NFC morphology (**Figure V-11**).

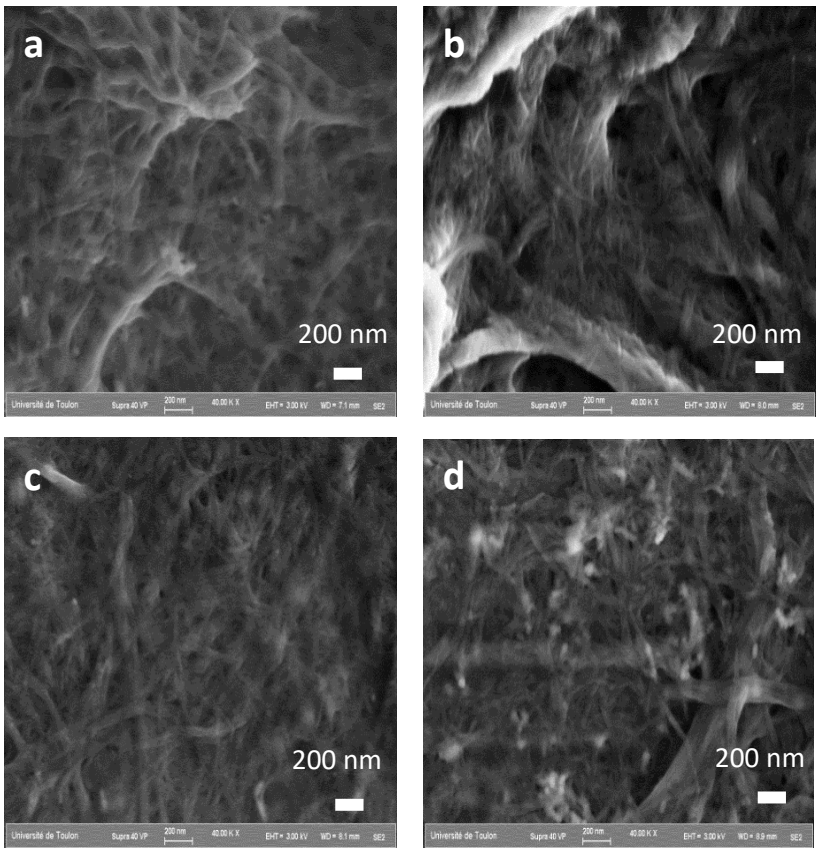

Figure V-11. Surface morphology recorded by SEM microscopy of a) pristine NFC, b) NFC-GPS EtOH, c) NFC treated with GPS in acid conditions acid, and d) NFC treated with GPMES in acid conditions.

Figure V-12 summarizes the diameter measured of SEM images of the **Figure V-11**. The results show an increase of the NFC diameter after modification. The NFC diameter before and after Soxhlet extraction is still higher than in NFC pristine. It is important to remark that before the Soxhlet extraction, the standard deviation is higher than after extraction. These results suggest the presence of a siloxane network physiosorbed onto the modified NFC, which is partially removed after the Soxhlet extraction, inducing an NFC surface covered by a heterogenous siloxane network. **Figure S.V- 5** displays the histograms of the fibrils diameter and the standard deviation reported in **Figure V-12**.

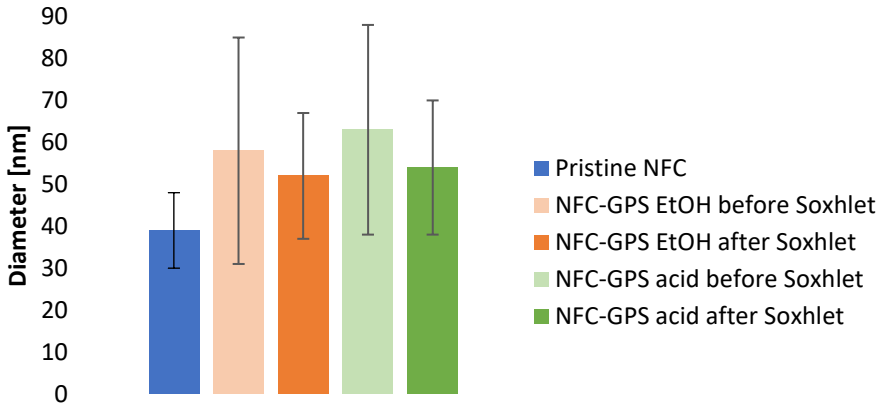

Figure V-12 Measured diameter of pristine NFC and modified NFC.

The chemical functionalization with silane coupling agents slightly alters the width dimensions. The NFC's morphological aspect at the microscale does not seem to be strongly modified. Similar results have been obtained by Herrera-Franco *et al.*[8]

AFM analysis was executed on the pristine and modified NFC samples to get more insight into the NFC morphology. **Figure V-13** displays AFM topographical images. No change in the NFC organization after modification is observed, which is consistent with SEM observations.

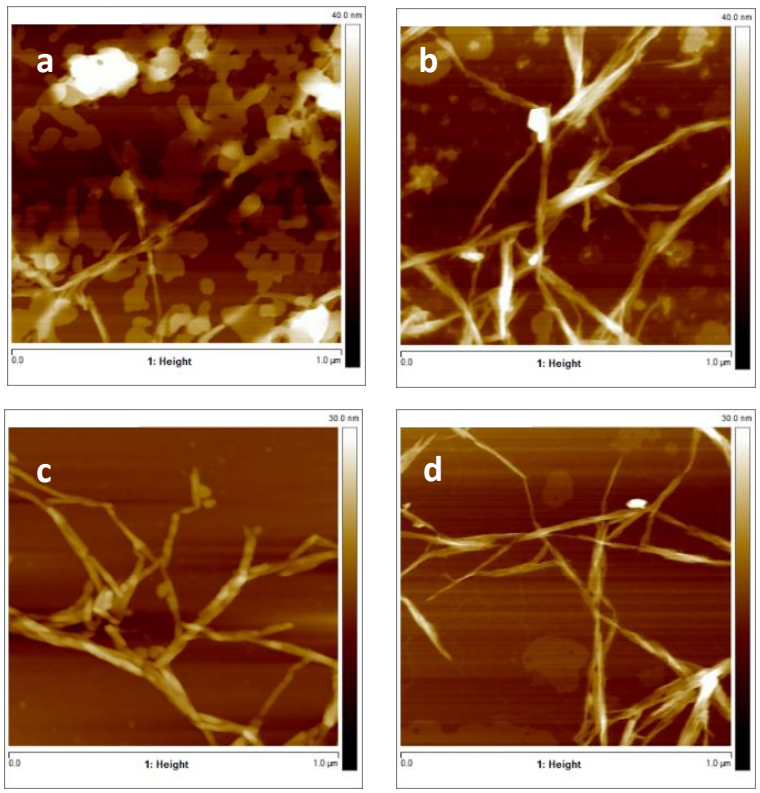

Figure V-13. AFM topographical images (1 µm x 1 µm) of a) pristine NFC, b) NFC-GPS EtOH, c) NFC-GPS in acid conditions, d) NFC GPMES in acid conditions.

5.4.4 Thermal characterization

The thermal stability of the modified NFC was evaluated by TGA analysis. The stability of this filler might improve the thermal stability of the composite reinforced with the modified fibrils. **Figure V-14** shows the thermal resistance of pristine and modified NFC. Before 250°C, the weight loss is similar and very small, attributed to water weight loss. At temperature superior to 250°C, the thermal stability of the modified NFC is higher than those of pristine NFC. This behavior could be associated with a polysiloxane layer formed onto the NFC surface, delaying the thermal decomposition[23]. The result strengthens the assumption of a siloxane network that surrounds the NFC. Indeed, the inorganic components do not decompose at the working temperatures in the **Figure V-14**. Besides, a delayed thermal decomposition has been observed in different silane coupling agent systems like APS[23], CPTES[56], and MPS[57].

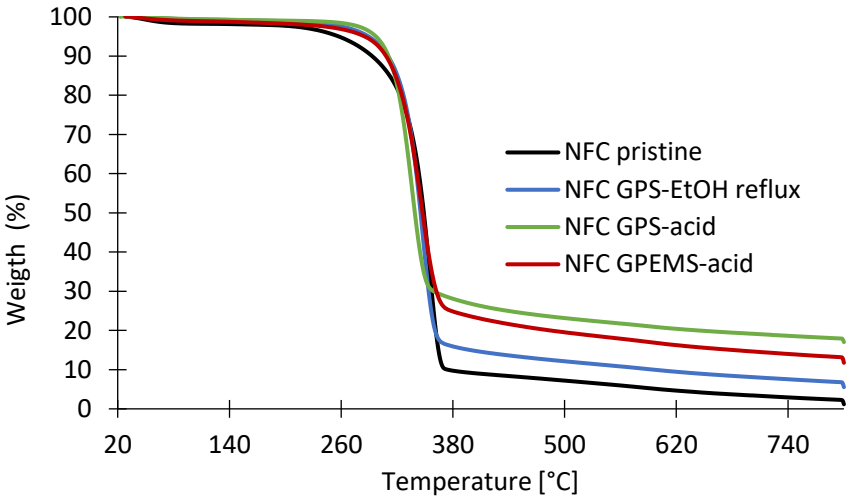

Figure V-14. Thermogravimetric analysis of pristine and modified NFC.

5.5 Conclusions

The chemical functionalization of nano fibrillated cellulose (NFC) with 3-(glycidyloxypropyl) trimethoxysilane (GPS) and 3-(glycidoxypropyl) dimethylethoxysilane (GPMES) was successfully achieved by using a simple protocol. Physical and chemical adsorptions onto the NFC surface were evidenced by the use of the Soxhlet extraction, keeping epoxy groups available on the surface for further applications.

The chemical reactions of the glycidyl silane coupling agents on the NFC surface were evidenced, and a reaction between the silanol and the hydroxyl groups of cellulose was successfully achieved. The chemical characterization showed a not fully self-condensation of silanes onto the fibrils in the case of the GPS silane. The silanes surrounding the NFC are mainly constituted by linear pending

chains and a few tridimensional structures. The 3D structures were majority eliminated by performing a Soxhlet extraction.

The morphology analysis of the modified NFC was done by SEM and AFM microscopic observations. The results showed how the morphological structure was not abruptly modified after any treatment, but an increase in the diameter of the fibrils was remarked.

Furthermore, the NFC functionalization with GPS or GPMES improved thermal stability. This behavior is associated with silanes' presence.

This study elaborates a bio-filler containing epoxy groups that can promote an easier diffusion of resin inside the fibrils, a better dispersion, and further covalent reactions between the NFC and the epoxy-vitrimer resin DGEBA–4-APDS. Besides, the results allow to clear up the silanes network's condensation state at the surface of fibrils. The silane network will play an important role in the interphase adhesion, and so in the mechanical properties and durability of the vitrimer based composite reinforced with NFC fibrils. Since new chemical reactions between the modified NFC fibrils and epoxy-vitrimer are anticipated, one can expect changes in the morphology and the rheological behavior of the composite materials.

Bibliography

1 Jawaid, M. H. P. S., & Khalil, H. A. (2011). Cellulosic/synthetic fibre reinforced polymer hybrid composites: A review. *Carbohydrate polymers*, *86*(1), 1-18.

2 Dufresne, A. (2013). Nanocellulose: a new ageless bionanomaterial. *Materials today*, *16*(6), 220-227.

3 Kalia, S., Dufresne, A., Cherian, B. M., Kaith, B. S., Avérous, L., Njuguna, J., & Nassiopoulos, E. (2011). Cellulose-based bio-and nanocomposites: a review. *International journal of polymer science*, *2011*.

4 Singha, A. S., & Rana, A. K. (2013). Effect of Aminopropyltriethoxysilane (APS) treatment on properties of mercerized lignocellulosic grewia optiva fiber. *Journal of Polymers and the Environment*, *21*(1), 141-150.

5 Lu, J., Askeland, P., & Drzal, L. T. (2008). Surface modification of microfibrillated cellulose for epoxy composite applications. *Polymer*, *49*(5), 1285-1296.

6 Gericke, M., Trygg, J., & Fardim, P. (2013). Functional cellulose beads: preparation, characterization, and applications. *Chemical reviews*, *113*(7), 4812-4836.

7 Mohanty, A. K., Misra, M., & Drzal, L. T. (Eds.). (2005). *Natural fibers, biopolymers, and biocomposites*. CRC press.

8 Herrera-Franco, P., & Valadez-Gonzalez, A. (2005). A study of the mechanical properties of short natural-fiber reinforced composites. *Composites Part B: Engineering*, *36*(8), 597-608.

9 S. Eyley, W. Thielemans, Surface modification of cellulose nanocrystals, Nanoscale. 6 (2014) 7764–7779.

10 Heinze, T., & Liebert, T. (2001). Unconventional methods in cellulose functionalization. *Progress in polymer science*, *26*(9), 1689-1762.

11 Gousse, 7. C., Chanzy, H., Cerrada, M. L., & Fleury, E. (2004). Surface silylation of cellulose microfibrils: preparation and rheological properties. *Polymer*, *45*(5), 1569-1575.

12 Goffin, A. L., Raquez, J. M., Duquesne, E., Siqueira, G., Habibi, Y., Dufresne, A., & Dubois, P. (2011). From interfacial ring-opening polymerization to melt processing of cellulose nanowhisker-filled polylactide-based nanocomposites. *Biomacromolecules*, *12*(7), 2456-2465.

13 Ten, E., Turtle, J., Bahr, D., Jiang, L. & Wolcott, M. (2010). Thermal and mechanical properties of poly(3-hydroxybutyrate-co-3-hydroxyvalerate)/cellulose nanowhiskers composites. *Polymer*, 51(12), 2652-2660.

14 Navarro-Baena, I., Sessini, V., Dominici, F., Torre, L., Kenny, J. M., & Peponi, L. (2016). Design of biodegradable blends based on PLA and PCL: From morphological, thermal and mechanical studies to shape memory behavior. *Polymer degradation and stability*, *132*, 97-108.

15 Abdelmouleh, M., Boufi, S., ben Salah, A., Belgacem, M. N., & Gandini, A. (2002). Interaction of silane coupling agents with cellulose. *Langmuir*, *18*(8), 3203-3208.

16 Castellano, M., Gandini, A., Fabbri, P., & Belgacem, M. N. (2004). Modification of cellulose fibres with organosilanes: Under what conditions does coupling occur?. *Journal of Colloid and Interface science*, *273*(2), 505-511.

17 Threepopnatkul, P., Kaerkitcha, N., & Athipongarporn, N. (2009). Effect of surface treatment on performance of pineapple leaf fiber–polycarbonate composites. *Composites Part B: Engineering*, *40*(7), 628-632.

18 Abdelmouleh, M., Boufi, S., ben Salah, A., Belgacem, M. N., & Gandini, A. (2002). Interaction of silane coupling agents with cellulose. *Langmuir*, *18*(8), 3203-3208.

19 Khanjanzadeh, H., Behrooz, R., Bahramifar, N., Gindl-Altmutter, W., Bacher, M., Edler, M., & Griesser, T. (2018). Surface chemical functionalization of cellulose nanocrystals by 3-aminopropyltriethoxysilane. *International journal of biological macromolecules*, *106*, 1288-1296.

20 Robles, E., Csóka, L., & Labidi, J. (2018). Effect of reaction conditions on the surface modification of cellulose nanofibrils with aminopropyl triethoxysilane. *coatings*, *8*(4), 139.

21 Abdelmouleh, M., Boufi, S., Belgacem, M. N., Dufresne, A., & Gandini, A. (2005). Modification of cellulose fibers with functionalized silanes: effect of the fiber treatment on the mechanical performances of cellulose–thermoset composites. *Journal of applied polymer science*, *98*(3), 974-984.

22 Girones, J., Méndez, J. A., Boufi, S., Vilaseca, F., & Mutjé, P. (2007). Effect of silane coupling agents on the properties of pine fibers/polypropylene composites. *Journal of Applied Polymer Science*, *103*(6), 3706-3717.

23 Yeo, J. S., Kim, O. Y., & Hwang, S. H. (2017). The effect of chemical surface treatment on the fracture toughness of microfibrillated cellulose reinforced epoxy composites. *Journal of Industrial and Engineering Chemistry*, *45*, 301-306.

24 Urreaga, J. M., Matias, M. C., De la Orden, M. U., Munguía, M. L., & Sánchez, C. G. (2000). Effects of coupling agents on the oxidation and darkening of cellulosic materials used as reinforcements for thermoplastic matrices in composites. *Polymer Engineering & Science*, *40*(2), 407-417.

25 Bayer, E., Albert, K., Reiners, J., Nieder, M., & Müller, D. (1983). Characterization of chemically modified silica gels by 29Si and 13C cross-polarization and magic angle spinning nuclear magnetic resonance. *Journal of Chromatography A*, *264*, 197-213.

26 Nishiyama, N., Horie, K., & Asakura, T. (1987). Hydrolysis and condensation mechanisms of a silane coupling agent studied by 13C and 29Si NMR. *Journal of Applied Polymer Science*, *34*(4), 1619-1630.

27 Plueddemann, E. P. (1991). Nature of adhesion through silane coupling agents. In *Silane coupling agents* (pp. 115-152). Springer, Boston, MA.

28 Waddell, T. G., Leyden, D. E., & DeBello, M. T. (1981). The nature of organosilane to silica-surface bonding. *Journal of the American Chemical Society*, *103*(18), 5303-5307.

29 Salon, M. C. B., Gerbaud, G., Abdelmouleh, M., Bruzzese, C., Boufi, S., & Belgacem, M. N. (2007). Studies of interactions between silane coupling agents and cellulose fibers with liquid and solid-state NMR. *Magnetic Resonance in Chemistry*, *45*(6), 473-483.

30 Salon, M. C. B., Abdelmouleh, M., Boufi, S., Belgacem, M. N., & Gandini, A. (2005). Silane adsorption onto cellulose fibers: Hydrolysis and condensation reactions. *Journal of colloid and interface science*, *289*(1), 249-261.

31 Valadez-Gonzalez, A., Cervantes-Uc, J. M., Olayo, R., & Herrera-Franco, P. J. (1999). Chemical modification of henequen fibers with an organosilane coupling agent. *Composites Part B: Engineering*, *30*(3), 321-331.

32 Yue, L., Maiorana, A., Khelifa, F., Patel, A., Raquez, J. M., Bonnaud, L., ... & Manas-Zloczower, I. (2018). Surface-modified cellulose nanocrystals for biobased epoxy nanocomposites. *Polymer*, *134*, 155-162.

33 Qing, W., Wang, Y., Wang, Y., Zhao, D., Liu, X., & Zhu, J. (2016). The modified nanocrystalline cellulose for hydrophobic drug delivery. *Applied Surface Science*, *366*, 404-409.

34 Maréchal, Y., & Chanzy, H. (2000). The hydrogen bond network in Iβ cellulose as observed by infrared spectrometry. *Journal of molecular structure*, *523*(1-3), 183-196.

35 Šapić, I. M., Bistričić, L., Volovšek, V., Dananić, V., & Furić, K. (2009). DFT study of molecular structure and vibrations of 3-glycidoxypropyltrimethoxysilane. *Spectrochimica Acta Part A: Molecular and Biomolecular Spectroscopy*, *72*(4), 833-840.

36 Bistričić, L., Volovšek, V., Dananić, V., & Šapić, I. M. (2006). Conformational stability and vibrations of aminopropylsilanol molecule. *Spectrochimica Acta Part A: Molecular and Biomolecular Spectroscopy*, *64*(2), 327-337.

37 Šapić, I. M., Bistričić, L., Volovšek, V., & Dananić, V. (2014, May). Vibrational Analysis of 3-glycidoxypropyltrimethoxysilane polymer. In *Macromolecular Symposia* (Vol. 339, No. 1, pp. 122-129).

38 Abel, M. L., Joannic, R., Fayos, M., Lafontaine, E., Shaw, S. J., & Watts, J. F. (2006). Effect of solvent nature on the interaction of γ-glycidoxy propyl trimethoxy silane on oxidised aluminium surface: A study by solution chemistry and surface analysis. *International journal of adhesion and adhesives*, *26*(1-2), 16-27.

39 Oswald, S. (2006). X-Ray Photoelectron Spectroscopy in Analysis of Surfaces. *Encyclopedia of Analytical Chemistry: Applications, Theory and Instrumentation*.

40 Missoum, K., Bras, J., & Belgacem, M. N. (2012). Organization of aliphatic chains grafted on nanofibrillated cellulose and influence on final properties. *Cellulose*, *19*(6), 1957-1973.

41 Johansson, L. S., Campbell, J. M., Koljonen, K., & Stenius, P. (1999). Evaluation of surface lignin on cellulose fibers with XPS. *Applied surface science*, *144*, 92-95.

42 Watts, J. F. (1993). High resolution XPS of organic polymers: The Scienta ESCA 300 database. G. Beamson and D. Briggs. *Surface and Interface Analysis*, *20*(3), 267-267.

43 Johansson, L. S., Tammelin, T., Campbell, J. M., Setälä, H., & Österberg, M. (2011). Experimental evidence on medium driven cellulose surface adaptation demonstrated using nanofibrillated cellulose. *Soft Matter*, *7*(22), 10917-10924.

44 Davies, M. (1994). High resolution XPS of organic polymers: The Scienta ESCA300 database: G. Beamson and D. Briggs John Wiley, Chichester, UK 1992.

45 Ahmed A, Adnot A, Grandmaison JL, Kaliaguine S, Doucet J (1987) ESCA analysis of cellulosic materials. Cellulose Chem Technol 21(5):483–492

46 Hua, X., Kaliaguine, S., Kokta, B. V., & Adnot, A. J. W. S. (1993). Surface analysis of explosion pulps by ESCA Part 1. Carbon (1s) spectra and oxygen-to-carbon ratios. *Wood Science and Technology*, *27*(6), 449-459.

47 Liu, S., Chen, Y., Liu, C., Gan, L., Ma, X., & Huang, J. (2019). Polydopamine-coated cellulose nanocrystals as an active ingredient in poly (vinyl alcohol) films towards intensifying packaging application potential. *Cellulose*, *26*(18), 9599-9612.

48 Atalla, R. H., & Vanderhart, D. L. (1984). Native cellulose: a composite of two distinct crystalline forms. *Science*, *223*(4633), 283-285.

49 Wickholm, K., Larsson, P. T., & Iversen, T. (1998). Assignment of non-crystalline forms in cellulose I by CP/MAS 13C NMR spectroscopy. *Carbohydrate Research*, *312*(3), 123-129.

50 Kalia, S., Kaith, B. S., & Vashistha, S. (2011). Cellulose nanofibers reinforced bioplastics and their applications. *Handbook of Bioplastics and Biocomposites Engineering Applications*, 452-470.

51 Rojas, O. J. (Ed.). (2016). Cellulose chemistry and properties: fibers, nanocelluloses and advanced materials (Vol. 271). Springer.

52 Kono H, Numata Y (2004) Two-dimensional spin-exchange solid-state NMR study of the crystal structure of cellulose II. Polymer 45:4541–4547.

53 Vrancken, K. C., De Coster, L., Van Der Voort, P., Grobet, P. J., & Vansant, E. F. (1995). The role of silanols in the modification of silica gel with aminosilanes. *Journal of colloid and interface science*, *170*(1), 71-77.

54 Daniels, M. W., & Francis, L. F. (1998). Silane adsorption behavior, microstructure, and properties of glycidoxypropyltrimethoxysilane-modified colloidal silica coatings. *Journal of colloid and interface science*, *205*(1), 191-200.

55 Buyl, F. D., & Kretschmer, A. (2008). Understanding hydrolysis and condensation kinetics of γ-glycidoxypropyltrimethoxysilane. *The Journal of Adhesion*, *84*(2), 125-142.

56 Rafieian, F., Mousavi, M., Yu, Q., & Jonoobi, M. (2019). Amine functionalization of microcrystalline cellulose assisted by (3-chloropropyl) triethoxysilane. *International journal of biological macromolecules*, *130*, 280-287.

57 Rachini, A., Le Troedec, M., Peyratout, C., & Smith, A. (2012). Chemical modification of hemp fibers by silane coupling agents. *Journal of applied polymer science*, *123*(1), 601-610.

General conclusions and perspectives

General Conclusions

Vitrimer polymers are promising covalent adaptable networks (CAN) that might offer a potential solution for some of the most limiting problems of thermosetting materials, such as durability and re-processability. These promising materials have been defined as organic networks able to change their topology through dynamic covalent exchange reactions. The rearrangement in their topology network confers them the ability to be reprocessed like thermoplastic polymers.

If we attempt to define a vitrimer briefly, we can state that:

- it is a network with permanent connectivity at all temperatures,
- a new transition temperature different from the *T*g describe it;
- it can fully relax while experimenting a topological rearrangement;
- its viscosity decreases by following an Arrhenius law.

The first chemistry claimed as a vitrimer material was the transesterification reaction one decade ago. Since that moment, the list of exchange chemistries presenting vitrimer properties has grown. One of these chemistries is the disulfide metathesis [2+1], which involves an associative/dissociative mechanism. The disulfide metathesis ascribes the reversible character of system DGEBA–4-APDS explored in the present work.

The DGEBA–4-APDS system has been classified in some works as a vitrimer material and, for others, as a vitrimer-like material because not all the characteristics that define a vitrimer material have been evidenced. The doubts about the real nature of this system come from its particular reversible exchange mechanism (associative and dissociative).

To clarify the correct categorization of this system, all the elements that define a vitrimer were rigorously explored.

Since the CANs can relax and exhibit Arrhenius-type behavior, the study of their stress relaxation behavior is not the best way to determine whether the material is a vitrimer or not. For this reason, the studies allowing to determine **the permanent network connectivity** and **the presence of a different transition temperature to the *T*g** is essential to prove the vitrimer network (***T*v**).

The condition that a covalent adaptable network with permanent connectivity was only achieved under an associative mechanism has evolved in the last years. At the beginning, a purely associative exchange was an essential condition for defining a vitrimer, ensuring in this way constant crosslink density. Today, the list of reversible covalent networks with associative and dissociative chemical exchanges simultaneously allowing to maintain permanent connectivity grows day by day. This is the case for the disulfide metathesis [2+1]. The topology rearrangement of this system follows both

associative and dissociative exchange mechanisms. The maintenance of a constant crosslink density, despite the two different mechanisms, suggests that: 1) associative exchanges are more relevant than dissociative exchanges leading to a permanent connectivity, and 2) dissociative exchanges occur really quickly, restricting the loss of the crosslink density. These two statements are valid in the range of temperature explored in the present work. Nonetheless, an important change could be expected at higher temperatures or at higher times scales. Theses changes could be explored in the future by carrying out a TTS experiments.

The permanent connectivity, which had not been explored in detail for the system DGEBA–4-APDS in the literature, ***was evidenced in a so-called as a good solvent*** (trichlorobenzene) at a temperature higher than its *Tv* ***and*** evaluating the ***independence*** of its ***modulus to the frequency***. The frequency sweep experiments performed in this work ***showed a permanent connectivity despite the disulfide metathesis [2+1],*** at temperatures T=*Tv*+50°C. Although it has been shown that vitrimers can be solubilized, the insolubility may continue to be attractive under certain condition for further uses at temperatures above their *Tv.*

A different transition temperature to the Tg or Tm was evidenced by performing dilatometry tests. The dilatometry study eliminates any possible doubt about the real existence of the topology freezing temperature because usually, the *T*v is only hypothesized by extrapolating the Arrhenian-type behavior. Besides, ***the dilatometry tests allow remarking the proximity between both transition temperatures,*** even varying the stoichiometry ratio. The proximity, thus, between the *T*g and the *Tv* ***supposes essential changes in the viscoelasticity behavior of the vitrimer***, as it was seen on the stress relaxation behavior ascribed in the present work***.***

The variation in amine/epoxy stoichiometry showed that the *T*v is inversely proportional to the number of dynamic covalent bonds, i.e., when ***the amount of reversible bonds increases, the Tv decreases.***

The stress relaxation experiments evidenced that the DGEBA–4-APDS material can flow and fully relax. Since all the characteristics that allow describing a vitrimer were satisfactorily evidenced, it can be concluded that the DGEBA–4-APDS system can be classified as an epoxy vitrimer material.

The stress relaxation behavior of vitrimers is usually evaluated at temperatures well above *T*g, i.e., at temperatures where *T*v can presumably be found, using only Maxwell's model for its analysis. Since the DGEBA–4-APDS system ***displays both transition temperatures in a short temperature range,*** the viscoelastic behavior of this vitrimer ***differs from those with a larger difference*** between both transition temperatures***.*** Therefore, the development of an ***adapted model*** which is ***able to***

describe the relaxation behavior of the DGEBA–4-APDS system was effectuated.

The adapted relaxation model proposed in this work considers two main branches for the relaxation behavior. The first branch is linked to the **bond exchange reaction (BER) relaxation**. The second branch is associated with the **segmental relaxation movements of the network**.

$$\frac{E(t)}{E_0} = E_1 * e^{\left(-\left(\frac{t}{\lambda_1}\right)^{\beta_1}\right)} + E_2 * e^{\left(-\left(\frac{t}{\lambda_2}\right)^{\beta_2}\right)}$$

In this approach, the model allows describing the material in a more integrated way, analyzing its behavior as a vitrimer without neglecting its polymeric nature. Both relaxation behaviors were modelized with a stretched-exponent decay (β), which leads to the relaxation curve's shape and reflects the relaxation time distribution. The main conclusions applying this model were:

- The parameter β_1 ***is a constant closed to 0.8*** within the adapted model for this vitrimer system, is independent to temperature and concentration of dynamic bonds.
- The contribution fractions (E_1 and E_2) are independent to the temperature, but they vary as a function of the concentration of dynamic bonds present in the thermoset.

This noteworthy behavior was only possible to visualize after the convolution of both types of relaxation.

The two deconvoluted behavior (BER and segmental motion) were explored in a similar approach to Angell's plot. ***The BER relaxation follows the behavior of a strong glass-forming liquid***, characteristically of silica and vitrimer materials. The segmental relaxation movements display a non-Arrhenian behavior. The system's ***Ea*** of the BER behavior and the ***Tv*** (determined by extrapolation) ***displayed a remarkable evolution as a function of the concentration of dynamic bonds***. Increasing the number of dynamic bonds in the thermoset resulted in a decrease of the exchange's energy barrier and the topology freezing temperature. The dilatometry tests confirmed the values of the *T*v obtained by the extrapolation of the Arrhenian behavior.

The DGEBA–4-APDS system has good thermal and mechanical properties. Combining this resin with natural fibers is an interesting alternative to produce sustainable lightweight composite with enhanced properties for further applications. Hence, a strategy to produce a ***vitrimer-based composite*** (DGEBA–4-APDS-NFC) ***was developed by incorporating nano fibrillated cellulose*** while taking care ***of not disturbing the vitrimer properties of the network.***

The elaborated ***DGEBA–4-APDS-NFC composite*** displayed:

- An enhancement of the storage modulus
- The thermal behavior is slightly impacted, showing a small decrease in *T*g.
- ***The vitrimer properties with no major changes***, except for the relaxation in a longer time, most probably because the fibrils block the networks relaxation movement and thus the system relaxation.

Moreover, ***the use of NFC might help to reduce the creep,*** which is a real problem for further applications***.***

The robustness of the adapted relaxation model applied to ***vitrimer composite*** was evidenced. The ***curve shape significantly changed*** due to the relaxation times distribution associated with the inhomogeneities generated by the cellulose and confirmed by the morphology characterizations. ***The Ea and the Tv*** values do ***not largely differ from the pure vitrimer*** despite the change of the curve shape. ***The contribution fraction of BER decreases*** significantly, which is consistent with the diminution of the ***number of dynamic bonds.***

The ***morphology of the DGEBA-APS-NFC*** composite ***revealed a regular dispersion*** of fibers, from areas where the nanofibrils are well-dispersed to microfiber bunch***.*** To fix these issues***, a surface modification of the NFC was carried out***.

The NFC modification is not always easy to achieve; indeed, sometimes the use of toxic solvents or multiple steps are necessary to achieve the modification. Thus, ***a simple and environmentally friendly strategy to modify the NFC's surface with silanes was developed*** employing the silanes 3-(glycidyloxypropyl) trimethoxysilane (GPS), and 3-(glycidoxypropyl) dimethylethoxysilane (GPMES). The effect of soxhlet extraction to eliminate weak adsorbed silanes was explored because physical and not chemical adsorption might impact the interphase adhesion between the fibrils and the resin. Chemical characterization supported by FTIR, EDX, XPS, ^{13}C, and ^{29}Si solid-state NMR permits establishing ***the presence of silicon grafted to the fibrils and the configuration of the siloxane network formed onto the surface of the fibrils***. The siloxane network formed at the surface might play an essential role once this modified filler is incorporated into the vitrimer system DGEBA–4-APDS.

The morphology of fibrils modified with silanes was analyzed by SEM and AFM techniques. The fibrils are not sharply modified after both treatments.

Perspectives

The possible applications that vitrimer networks offers are numerous and promising. The chemical and thermal resistance of the DGEBA–4-APDS system makes it suitable in the aerospace industry, as shown in the European project AIRPOXY. Thus, the study of this system has gained relevance. Throughout this work, many questions were answered while new ones were raised. The following is a summary of the points that could provide valuable information based on the results obtained in this work.

A deep study of the adapted relaxation model to evaluate its robustness.

The use of different epoxy prepolymers with the same hardener could allow separating the two transition temperatures of the vitrimer epoxy and at the same time changing the size of the polymeric network to answer the following questions:

- Does parameter β_1 remain constant and identical to that found for the DGEBA–4-APDS system? The response to this question would help conclude that the relaxation due to the BER of the [2+1] disulfide metathesis obeys a value between $0.77<\beta_1<0.81$, which is characteristic of this vitrimer chemistry.
- Does the lattice size of the network influence the prefactors (E%)? The present work demonstrated how the values of the prefactors of the adapted Maxwell's model are dependent on the number of reversible bonds in the matrix. A different lattice size of the network could promote (or not) significant changes and display a dominance of one relaxation over the other.
- Does the found activation energy of the BER relaxation is genuinely due to S-S bonding? A change in the matrix chemistry would slightly modify the electronegativity surrounding the S-S bonds. Therefore, the activation energy should remain very similar to those found in this work over this new hypothesized system.

Improvement of vitrimer material properties and durability by using natural fibers.

In the present work, many areas of the composite material presented poor interfacial adhesion, leading to a decrease in mechanical properties. Several works have shown that surface modifications of cellulose fibrils could increase the interfacial interactions between these and a polymer matrix. Thus, the ***modified NFC with silanes*** could ***increase the interfacial properties*** of the ***NFC- reinforced vitrimer***. Moreover, modifications of the fibril's surface ***could increase*** the water

resistance property of cellulose and improve ***the durability*** of the composite material.

On the other hand, the composite material displayed a longer relaxation behavior than the pure resin, thus, the reprocessing might be highly impacted. To resolve this drawback, a ***variation of the vitrimer stoichiometry*** by increasing the number of reversible bonds could ***lead to a faster relaxation***. It could be ***helpful for the reprocessing*** of the vitrimer-composite. This variation in stoichiometry and the use of modified fibers could give a performing material with 1) enhanced mechanical properties due to an improvement in the interfacial interactions and 2) an important creep reduction due to the presence of NFC into the matrix that blocks the possible reptation phenomena.

Annex Chapter III

FTIR spectra of non-stoichiometric systems

FTIR spectrum of the DGEBA–4-APDS r=0.8 system

Figure S.III- 1 displays the spectra of samples of the DGEBA–4-APDS r=0.8 system uncured and cured by following the three curing cycles. At a glance, the three curing cycles show a fading of the oxirane absorption band at 915 cm^{-1}. In detail, the curing cycle's spectrum **r=0.8a** displays a slight but undeniable intensity in the oxirane region, which could be interpreted as a not completed cured system. **Figure S.III- 1** also explores the curing cycles b and c. The signal at 915 cm^{-1}, which corresponds to the oxiranes, disappears in both cases.

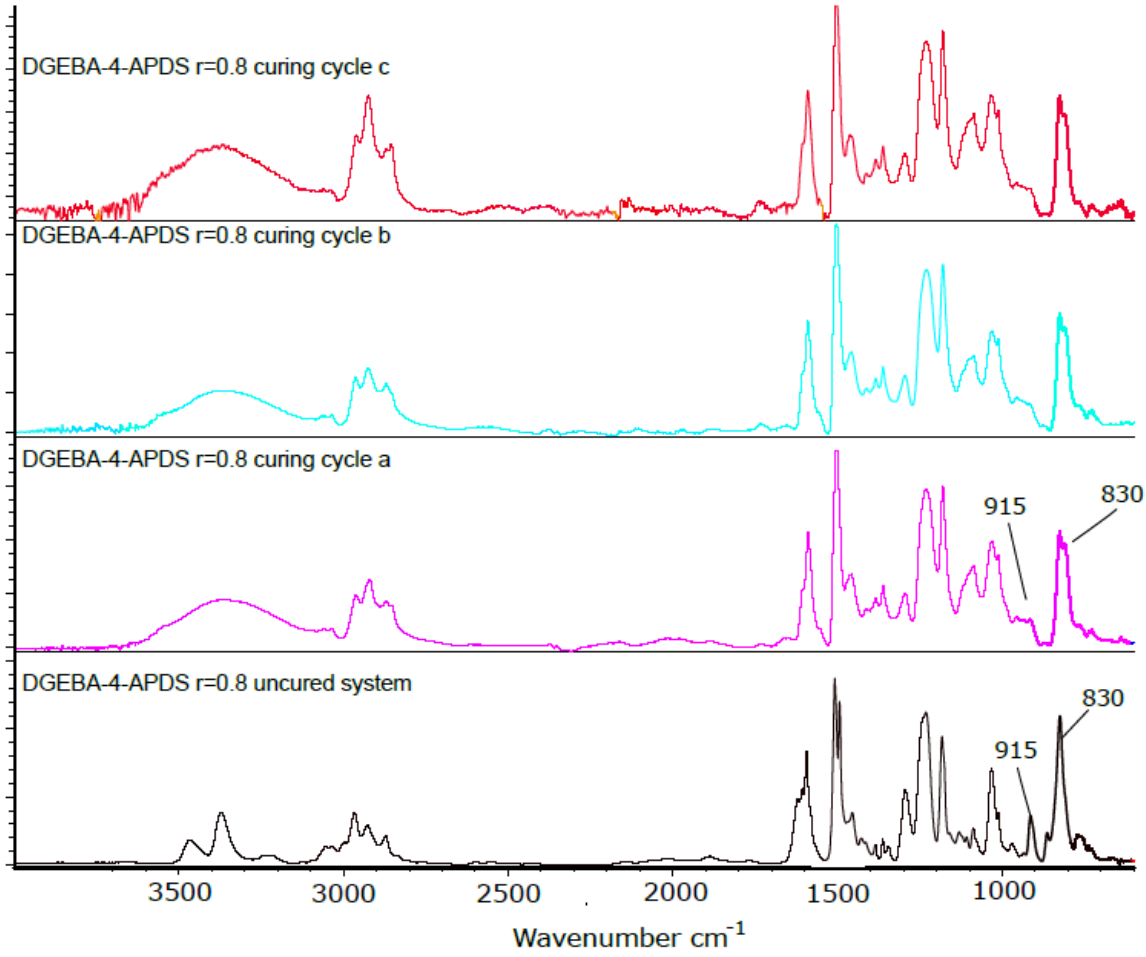

Figure S.III- 1. FTIR spectra of uncured DGEBA–4-APDS system r=0.8 (black) and the cured systems according to the three curing cycles explored r=0.8a (pink), r=0.8b (bleu), and r=0.8c (red).

FTIR spectrum of the DGEBA–4-APDS r=1.2 system

Figure S.III- 2 displays the spectra of the DGEBA–4-APDS r=1.2 system uncured and cured under three different curing conditions. The three cured spectra display fading of the oxirane absorption band. The changes observed by carrying out DSC experiments in **Figure III-5** suggest that a limited number of epoxy functions remains unreacted, which is not possible to evidence by the FTIR technique as observed for the system in stoichiometry.

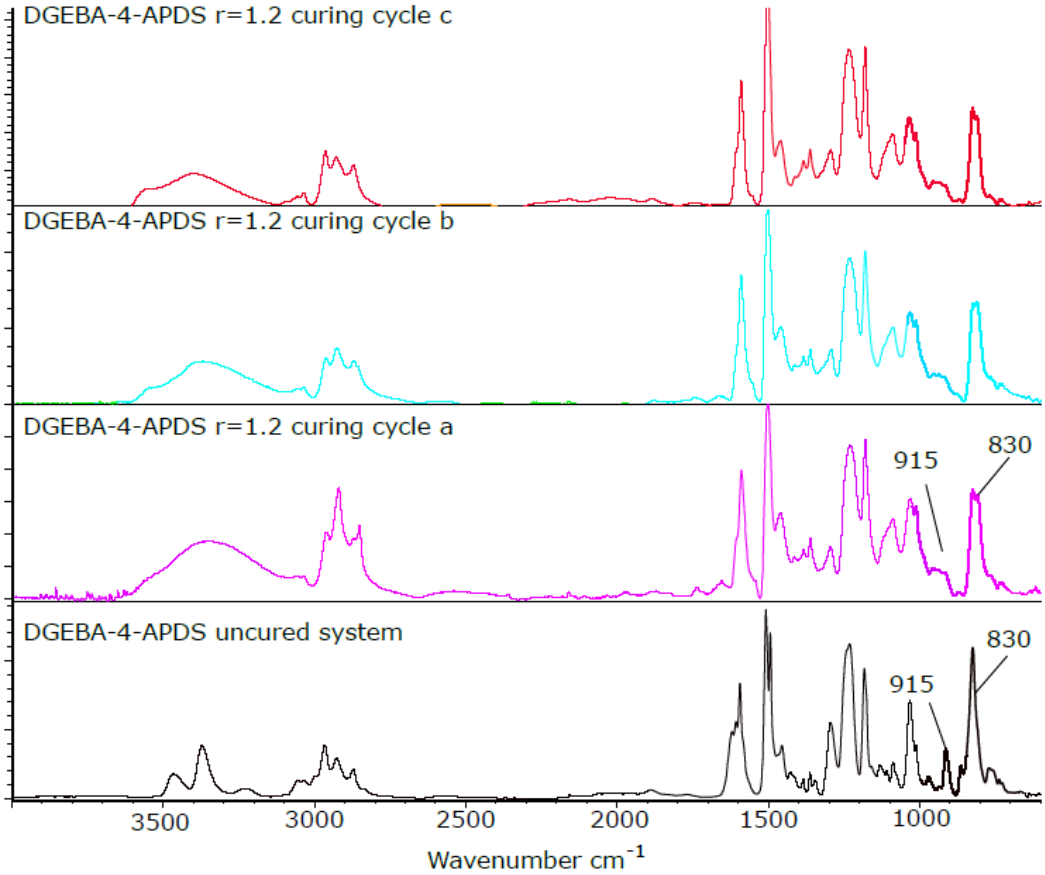

Figure S.III- 2. FTIR spectra of uncured DGEBA–4-APDS system r=1.2 (black) and the cured systems according to the three curing cycles explored. Cycles r=1.2a (pink), r=1.2b (bleu), and r=1.2c (red).

Thermal resistance of systems with and without dynamic hardener

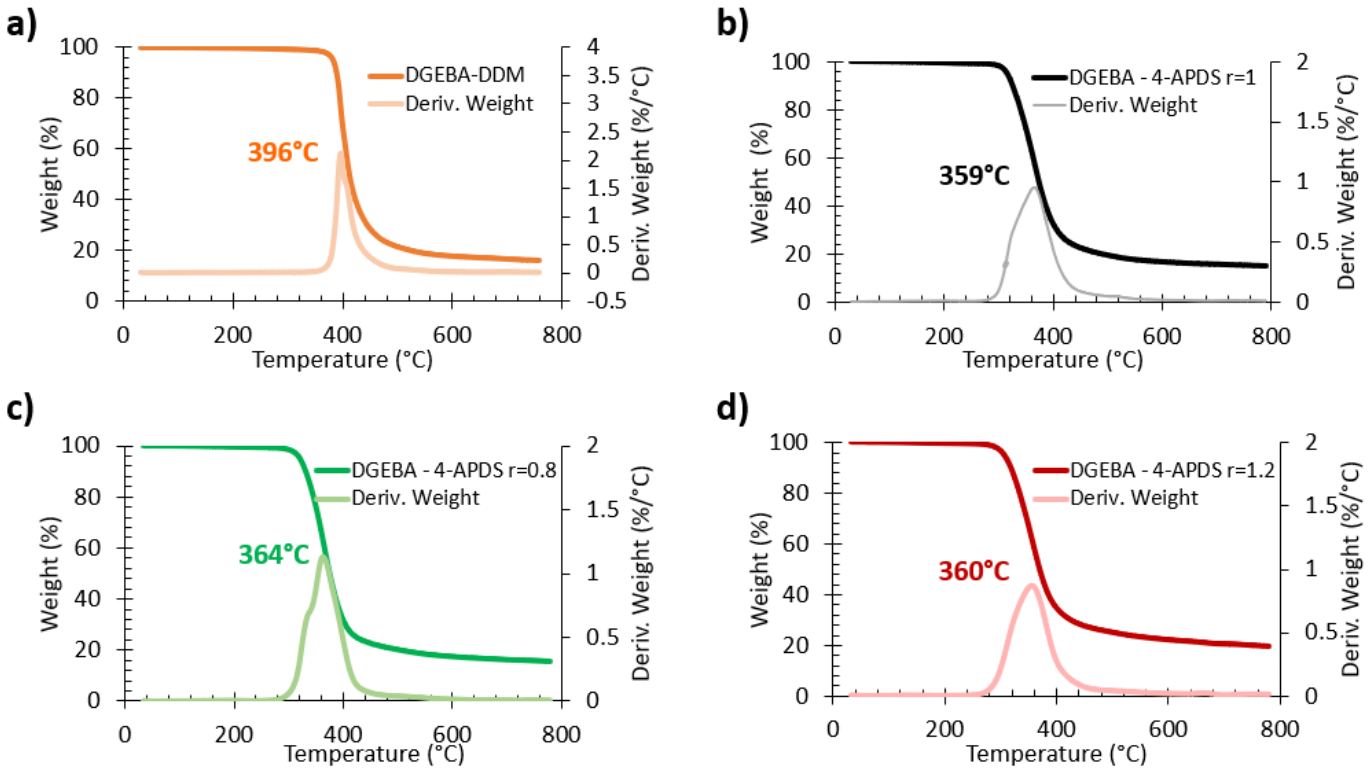

Figure S.III- 3. TGA studies of a) DGEBA-DDM, b) DGEBA–4-APDS r=1, c) DGEBA–4-APDS r=0.8, and d) DGEBA–4-APDS r=1.2.

Tensile mode study

Evaluation of thermomechanical properties of DGEBA-4-APDS r=1 in tensil mode. The dynamic temperature test was conducted over the temperature range of 25 to 220 °C with a heating rate of 3°C/min and a frequency of 1Hz. The sample dimensions were 12 x 8 x 0.35 mm^3. OscAmp 20 µm and a StaticF 0.01N. Sample was pre-heated at 100°C/1h before the test to eliminate any posible trace of water.

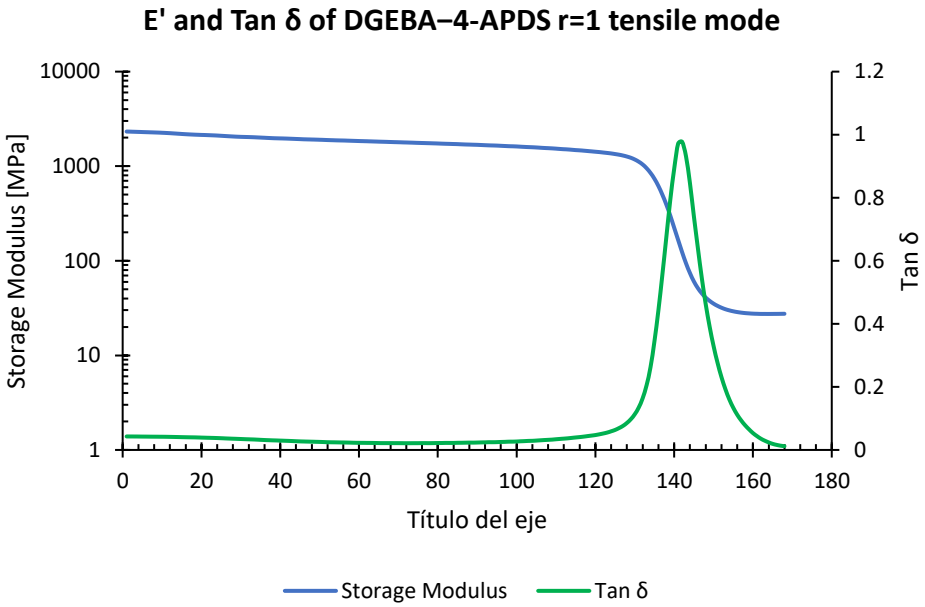

Figure S.III- 4. Storage modulus (E') and damping factor (tan δ) as function of temperature of the system DGEBA—4-APDS in tensile mode.

Dilatometry test

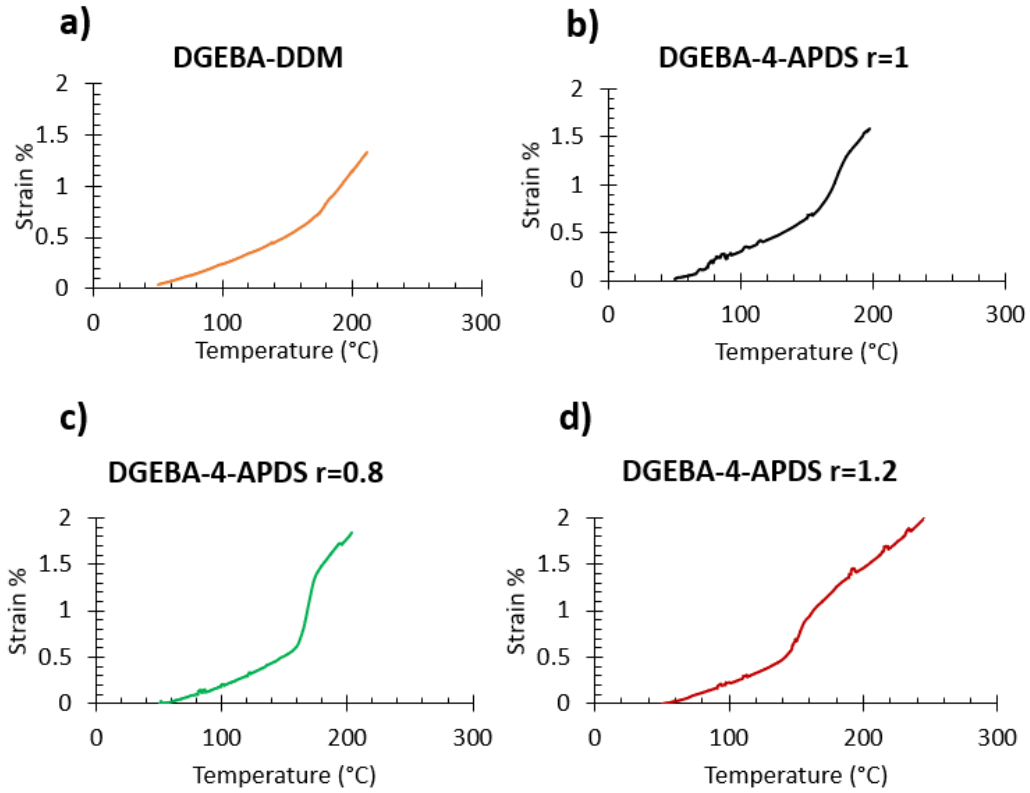

Figure S.III- 5. Dilatometry test of systems a) DGEBA-DDM, b) DGEBA–4-APDS r=1, c) DGEBA–4-APDS r=0.8, and d) DGEBA–4-APDS r=1.2 under compression mode.

Kohlrausch-Williams-Watts model (KWW)

Modeling of stress relaxation of DGEBA–4-APDS r=1 system by using a single stretched exponential decay

Parameters found from all recorded data of the stress relaxation curve of system DGEBA–4-APDS r=1.

180 °C	Value	Standard Error
E	1.07	0.0140
λ	46.79	1.7719
β	0.44	0.0067
Adj. R-Squ	0.60	
Reduced Chi-Sqr	7.29E-03	

190 °C	Value	Standard Error
E	1.32	0.0130
λ	6.13	0.3024
β	0.21	0.0015
Adj. R-Squ	0.94	
Reduced Chi-Sqr	4.64E-04	

200 °C	Value	Standard Error
E	1.34	0.0089
λ	3.51	0.1182
β	0.20	0.0010
Adj. R-Square	0.98	
Reduced Chi-Sqr	1.52E-04	

210 °C	Value	Standard Error
E	1.62	0.0146
λ	0.75	0.0397
β	0.17	0.0010
Adj. R-Square	0.99	
Reduced Chi-Sqr	7.78E-05	

220 °C	Value	Standard Error
E	2.08	0.0677
λ	0.11	0.0215
β	0.15	0.0029
Adj. R-Square	0.98	
Reduced Chi-Sqr	3.24E-04	

Table S.III- 1. Parameters yielded from the simulation carried out in Origin ® 9 using a single stretched exponent over all the recorded data of the stress relaxation of system DGEBA–4-APDS r=1 at temperatures between 180 and 220 °C, where E is the prefactor, λ, the relaxation time yielded by the simulation, and β the stretched decay exponent.

Parameters found from the first minutes of the stress relaxation curve of the system DGEBA–4-APDS r=1.

180 °C	Value	Standard Error
E	1.00	0.0197
λ	36.06	1.4737
β	0.75	0.0259
Adj. R-Squ	-0.57	
Reduced Chi-Sqr	2.83E-02	

200 °C	Value	Standard Error
E	1.03	0.0389
λ	3.09	0.2814
β	0.70	0.0487
Adj. R-Squ	-0.80	
Reduced Chi-Sqr	1.33E-02	

220 °C	Value	Standard Error
E	1.07	0.1156
λ	0.59	0.1112
β	0.70	0.1245
Adj. R-Squ	-0.60	
Reduced Chi-Sqr	2.59E-02	

190 °C	Value	Standard Error
E	1.02	0.0259
λ	7.83	0.4971
β	0.72	0.0379
Adj. R-Squ	-0.90	
Reduced Chi-Sqr	1.57E-02	

210 °C	Value	Standard Error
E	1.05	0.0823
λ	1.37	0.2414
β	0.62	0.0711
Adj. R-Squ	-1.19	
Reduced Chi-Sqr	2.39E-02	

Table S.III- 2. Parameters yielded from the simulation carried out in Origin ® 9 using a single stretched exponent over the first minutes recorded of the stress relaxation of system DGEBA–4-APDS r=1 at temperatures between 180 and 220 °C. Where E is the prefactor, λ, the relaxation time yielded by the simulation, and β the stretched exponent decay.

Parameters found from the last minutes of the stress relaxation curve of the system DGEBA–4-APDS r=1.

180 °C	Value	Standard Error
E	0.61	0.0180
λ	196.71	22.4521
β	0.28	0.0119
Adj. R-Squ	0.68	
Reduced Chi-Sqr	5.82E-03	

190 °C	Value	Standard Error
E	0.59	0.0123
λ	71.33	6.3507
β	0.26	0.0056
Adj. R-Squ	0.77	
Reduced Chi-Sqr	1.91E-03	

200 °C	Value	Standard Error
E	0.57	0.0073
λ	67.70	3.1961
β	0.31	0.0043
Adj. R-Squ	0.85	
Reduced Chi-Sqr	1.09E-03	

210 °C	Value	Standard Error
E	0.62	0.0098
λ	41.03	2.4628
β	0.31	0.0062
Adj. R-Squ	0.90	
Reduced Chi-Sqr	1.06E-03	

220 °C	Value	Standard Error
E	0.52	0.0083
λ	37.95	1.7091
β	0.46	0.0124
Adj. R-Squ	0.89	
Reduced Chi-Sqr	1.71E-03	

Table S.III- 3. Parameters yielded from the simulation carried out in Origin ® 9 using a single stretched exponent over the last minutes recorded of the stress relaxation of system DGEBA–4-APDS r=1 at temperatures between 180 and 220 °C, where E is the prefactor, λ, the relaxation time yielded by the simulation, and β the stretched exponent decay.

Modeling of stress relaxation of DGEBA–4-APDS r=0.8 system by using a single stretched exponential decay

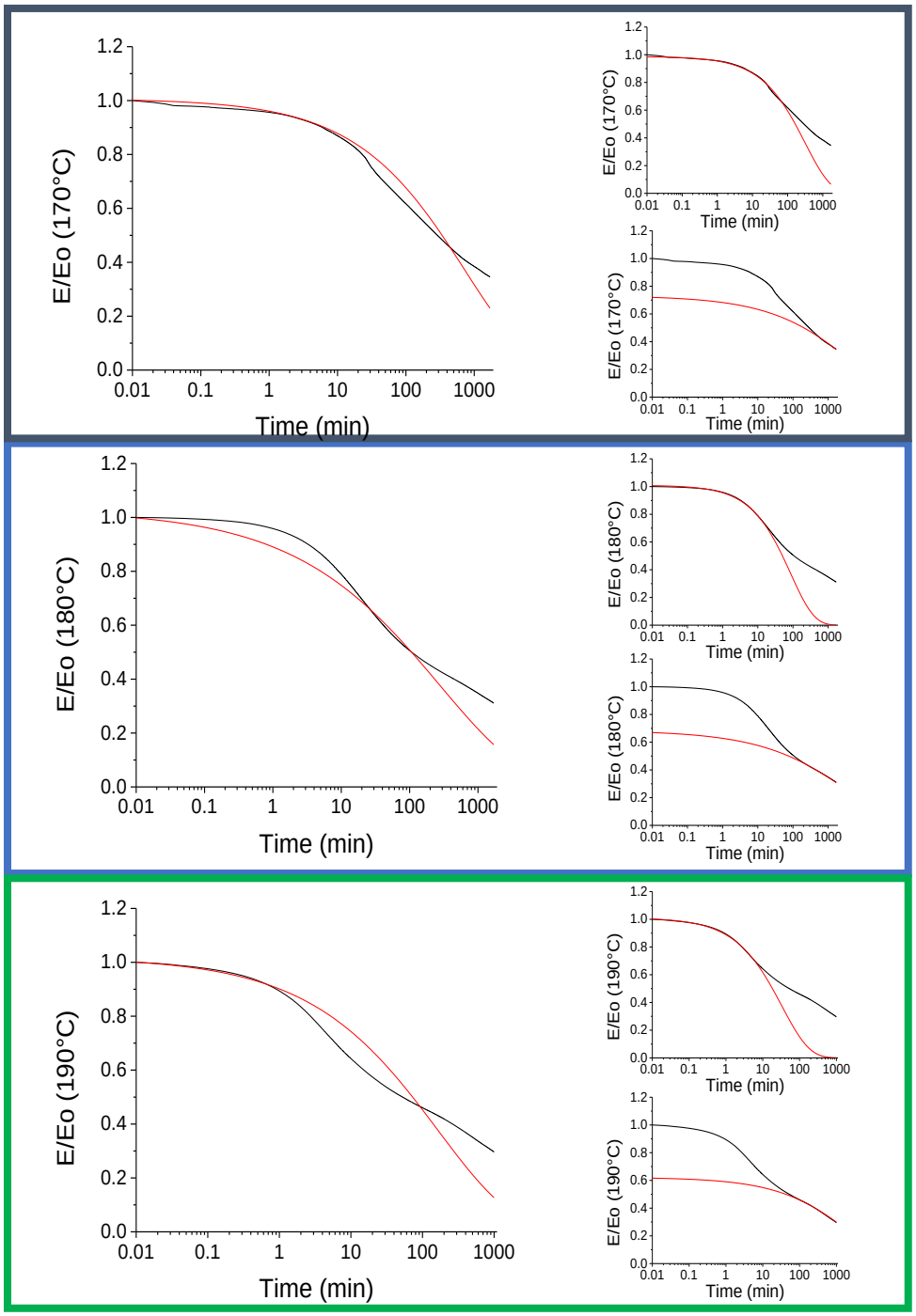

Figure S.III- 6. Normalized and modeled stress relaxation curves of DGEBA–4-APDS system r=0.8 by using the KWW equation at different temperatures. To the left, the modeling considering the entire recorded relaxation. To the right, the modeling is divided into two study zones: 1) the first relaxation zone and 2) the second relaxation zone. The black line corresponds to the experimental data, and the red line to the modeling achieved.

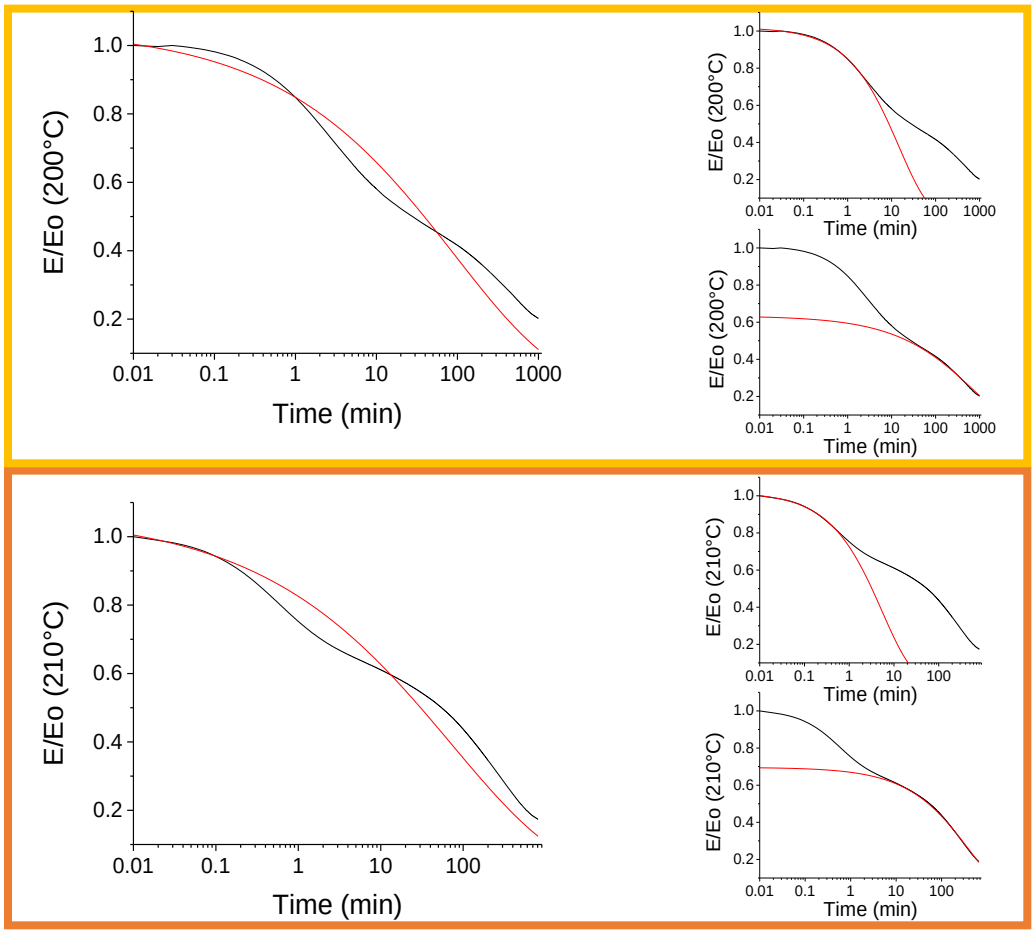

Figure S.III- 6. Normalized and modeled stress relaxation curves of DGEBA–4-APDS system r=0.8 by using the KWW equation at different temperatures. To the left, the modeling considering the entire recorded relaxation. To the right, the modeling is divided into two study zones: 1) the first relaxation zone and 2) the second relaxation zone. The black line corresponds to the experimental data, and the red line to the modeling achieved.

Parameters found from the entire stress relaxation curve of system DGEBA–4-APDS r=0.8.

170 °C	Value	Standard Error
E	1.01	0.0027
λ	730.18	4.6137
β	0.46	0.0028
Adj. R-Square	0.90	
Reduced Chi-Sqr	2.54E-03	

180 °C	Value	Standard Error
E	1.03	0.0054
λ	274.65	4.4813
β	0.35	0.0031
Adj. R-Square	0.87	
Reduced Chi-Sqr	2.43E-03	

190 °C	Value	Standard Error
E	1.02	0.0103
λ	166.38	4.9100
β	0.41	0.0083
Adj. R-Square	0.72	
Reduced Chi-Sqr	7.32E-03	

200 °C	Value	Standard Error
E	1.05	0.0117
λ	93.41	3.5900
β	0.34	0.0060
Adj. R-Square	0.86	
Reduced Chi-Sqr	3.96E-03	

210 °C	Value	Standard Error
E	1.07	0.0137
λ	72.93	3.1200
β	0.32	0.0053
Adj. R-Square	0.36	
Reduced Chi-Sqr	5.43E-03	

Table S.III- 4. Parameters yielded from the simulation carried out in Origin ® 9 using a single stretched exponent over all the recorded data of the stress relaxation of system DGEBA–4-APDS r=0.8 at temperatures between 180 and 220 °C, where E is the prefactor, λ, the relaxation time yielded by the simulation, and β the stretched decay exponent.

Parameters found from the first minutes of stress relaxation curve of system DGEBA–4-APDS r=0.8.

180 °C	Value	Standard Error
E	0.99	0.0063
λ	314.48	4.7199
β	0.59	0.0069
Adj. R-Square	0.21	
Reduced Chi-Sqr	2.11E-02	

190 °C	Value	Standard Error
E	1.01	0.0109
λ	86.38	1.5166
β	0.65	0.0152
Adj. R-Square	-0.23	
Reduced Chi-Sqr	2.26E-02	

200 °C	Value	Standard Error
E	1.01	0.0331
λ	33.38	2.7500
β	0.58	0.0316
Adj. R-Square	-1.62	
Reduced Chi-Sqr	6.82E-02	

210 °C	Value	Standard Error
E	1.02	0.0427
λ	14.80	1.3600
β	0.63	0.04
Adj. R-Square	-1.80	
Reduced Chi-Sqr	7.90E-02	

220 °C	Value	Standard Error
E	1.02	0.0825
λ	5.49	0.8780
β	0.63	0.0558
Adj. R-Square	-19.36	
Reduced Chi-Sqr	1.74E-01	

Table S.III- 5. Parameters yielded from the simulation carried out in Origin ® 9 using a single stretched exponent over the first minutes recorded of the stress relaxation of system DGEBA–4-APDS r=0.8 at temperatures from 170 to 210 °C, where E is the prefactor, λ, the relaxation time yielded by the simulation, β the stretched exponent.

Parameters found from the last minutes of stress relaxation curve of system DGEBA–4-APDS r=0.8.

180 °C	Value	Standard Error
E	0.73	0.0089
λ	4104.01	112.4057
β	0.32	0.0119
Adj. R-Square	0.57507	
Reduced Chi-Sqr	1.13E-02	

190 °C	Value	Standard Error
E	0.68	0.0116
λ	3629.59	212.2662
β	0.30	0.01495
Adj. R-Square	0.34	
Reduced Chi-Sqr	1.21E-02	

200 °C	Value	Standard Error
E	0.62	0.0956
λ	2239.39	167.00
β	0.38	0.0243
Adj. R-Square	0.59	
Reduced Chi-Sqr	1.07E-02	

210 °C	Value	Standard Error
E	0.63	0.0070
λ	738.73	22.91
β	0.41	0.0141
Adj. R-Square	0.79	
Reduced Chi-Sqr	6.06E-03	

220 °C	Value	Standard Error
E	0.70	0.0008
λ	391.73	0.0795
β	0.54	0.0019
Adj. R-Square	0.98	
Reduced Chi-Sqr	1.75E-04	

Table S.III- 6. Parameters yielded from the simulation carried out in Origin ® 9 using a single stretched exponent over the last minutes recorded of the stress relaxation of system DGEBA–4-APDS r=0.8 at temperatures from 170 to 210 °C, where E is the prefactor, λ, the relaxation time yielded by the simulation, β the stretched exponent decay and $\bar{\lambda}$ the average relaxation time yielded by the gamma function.

Modeling of stress relaxation of DGEBA–4-APDS r=1.2 system by using a single stretched exponential decay

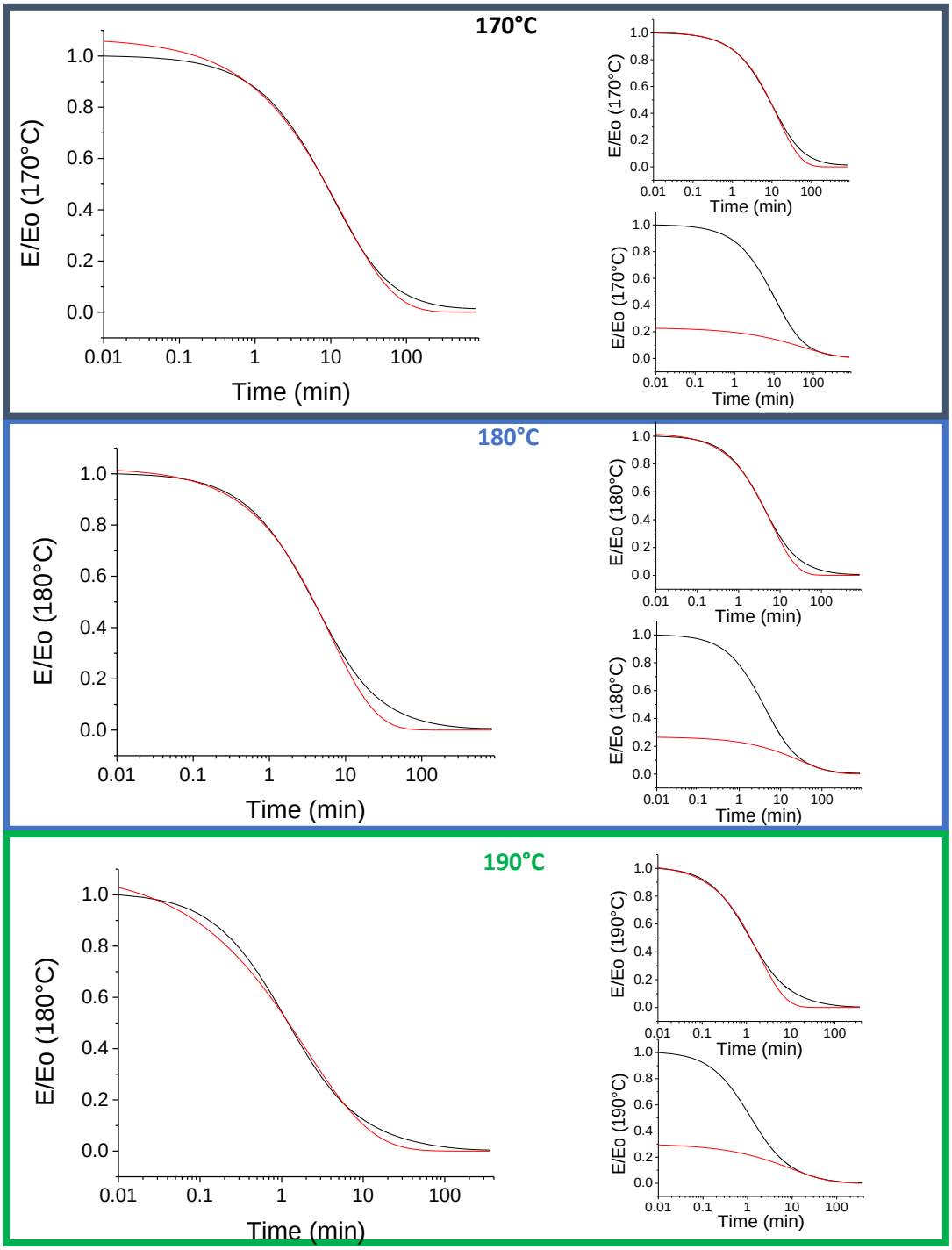

Figure S.III- 7. Normalized and modeled stress relaxation curves of DGEBA–4-APDS system r=1.2 by using the KWW equation at different temperatures. To the left, the modeling considering the entire recorded relaxation. To the right, the modeling is divided into two study zones: 1) the first relaxation zone and 2) the second relaxation zone. The black line corresponds to the experimental data, and the red line to the modeling achieved.

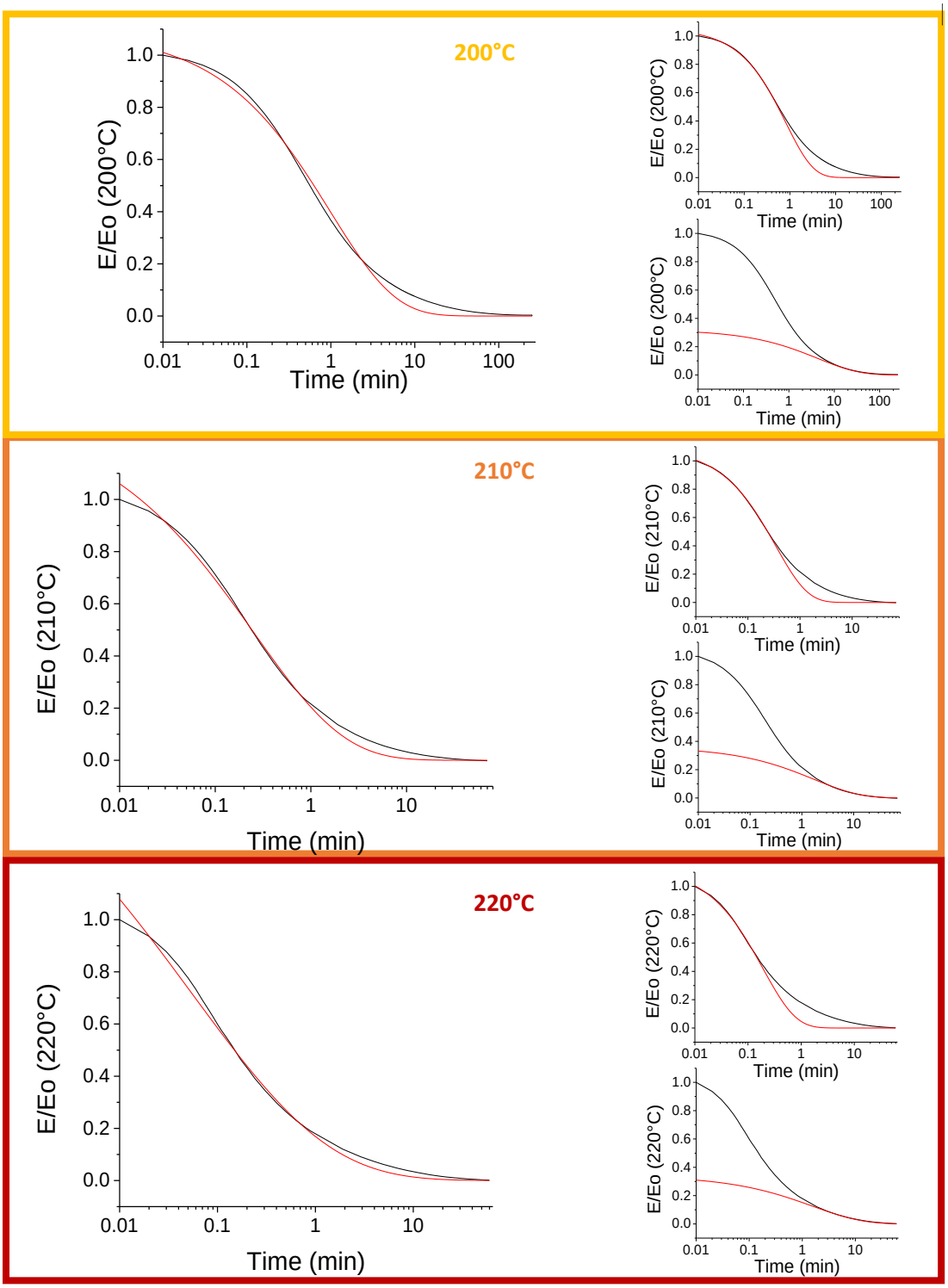

Figure S.III- 7. Normalized and modeled stress relaxation curves of DGEBA–4-APDS system r=1.2 by using the KWW equation at different temperatures. To the left, the modeling considering the entire recorded relaxation. To the right, the modeling is divided into two study zones: 1) the first relaxation zone and 2) the second relaxation zone. The black line corresponds to the experimental data, and the red line to the modeling achieved.

Parameters found from the entire stress relaxation curve of system DGEBA–4-APDS r=1.2.

170 °C	Value	Standard Error
E	1.07	0.0024
λ	13.56	0.0539
β	0.61	0.0026
Adj. R-Square	0.9978	
Reduced Chi-Sqr	1.55E-04	

180 °C	Value	Standard Error
E	1.10	0.0037
λ	5.82	0.0363
β	0.59	0.0036
Adj. R-Square	0.9979	
Reduced Chi-Sqr	1.53E-04	

190 °C	Value	Standard Error
E	1.10	0.0072
λ	1.93	0.0287
β	0.52	0.0041
Adj. R-Square	0.9941	
Reduced Chi-Sqr	2.23E-04	

200 °C	Value	Standard Error
E	1.09	0.0182
λ	0.98	0.0352
β	0.56	0.0097
Adj. R-Square	0.9569	
Reduced Chi-Sqr	0.00104	

210 °C	Value	Standard Error
E	1.33	0.0271
λ	0.25	0.0126
β	0.46	0.0113
Adj. R-Square	0.9975	
Reduced Chi-Sqr	1.57E-04	

220 °C	Value	Standard Error
E	1.96	0.0893
λ	0.05	0.0082
β	0.31	0.0107
Adj. R-Square	0.9963	
Reduced Chi-Sqr	1.75E-04	

Table S.III- 7. Parameters yielded from the simulation carried out in Origin ® 9 using a single stretched exponent over all the recorded data of the stress relaxation of system DGEBA–4-APDS r=1.2 at temperatures between 180 and 220 °C, where E is the prefactor, λ, the relaxation time yielded by the simulation and β the stretched decay exponent.

Parameters found from the first minutes of stress relaxation curve of system DGEBA–4-APDS r=1.2.

170 °C	Value	Standard Error
E	1.01	0.0027
λ	14.03	0.0569
β	0.74	0.0043
Adj. R-Square	0.9955	
Reduced Chi-Sqr	3.19E-04	

180 °C	Value	Standard Error
E	1.02	0.0039
λ	6.19	0.0370
β	0.71	0.0054
Adj. R-Square	0.9964	
Reduced Chi-Sqr	2.71E-04	

190 °C	Value	Standard Error
E	1.03	0.0174
λ	1.95	0.0590
β	0.73	0.0164
Adj. R-Square	0.9236	
Reduced Chi-Sqr	2.90E-03	

200 °C	Value	Standard Error
E	1.05	0.0375
λ	0.82	0.0521
β	0.72	0.0313
Adj. R-Square	0.7525	
Reduced Chi-Sqr	5.96E-03	

210 °C	Value	Standard Error
E	1.09	0.0386
λ	0.34	0.0207
β	0.70	0.0386
Adj. R-Square	0.9778	
Reduced Chi-Sqr	1.37E-03	

220 °C	Value	Standard Error
E	1.14	0.0974
λ	0.19	0.0293
B	0.70	0.0759
Adj. R-Square	0.8803	
Reduced Chi-Sqr	5.57E-03	

Table S.III- 8. Parameters yielded from the simulation carried out in Origin ® 9 using a single stretched exponent over the first minutes recorded of the stress relaxation of system DGEBA–4-APDS r=1.2 at temperatures from 170 to 220 °C, where E is the prefactor, λ, the relaxation time yielded by the simulation, and β the stretched decay exponent.

Parameters found from the last minutes of stress relaxation curve of system DGEBA–4-APDS r=1.2.

170 °C	Value	Standard Error
E	0.23	0.0493
λ	53.57	34.1109
β	0.45	0.1560
Adj. R-Square	-0.5972	
Reduced Chi-Sqr	1.12E-01	

180 °C	Value	Standard Error
E	0.27	0.0405
λ	28.82	12.2413
β	0.55	0.1589
Adj. R-Square	0.1360	
Reduced Chi-Sqr	6.43E-02	

190 °C	Value	Standard Error
E	0.30	0.0453
λ	9.50	3.0868
β	0.50	0.1309
Adj. R-Square	0.3196	
Reduced Chi-Sqr	2.58E-02	

200 °C	Value	Standard Error
E	0.32	0.0484
λ	4.30	1.5219
β	0.47	0.1056
Adj. R-Square	0.4590	
Reduced Chi-Sqr	1.30E-02	

210 °C	Value	Standard Error
E	0.36	0.1413
λ	1.70	1.7477
β	0.49	0.3159
Adj. R-Square	0.4176	
Reduced Chi-Sqr	3.60E-02	

220 °C	Value	Standard Error
E	0.34	0.1303
λ	1.57	1.6039
β	0.46	0.2787
Adj. R-Square	0.4419	
Reduced Chi-Sqr	2.60E-02	

Table S.III- 9. Parameters yielded from the simulation carried out in Origin ® 9 using a single stretched exponent over the last minutes recorded of the stress relaxation of system DGEBA–4-APDS r=1.2 at temperatures from 170 to 220 °C, where E is the prefactor, λ, the relaxation time yielded by the simulation, and β the stretched decay exponent.

Bernstein-Kearsley-Zapas theory (BZK)

Stress relaxation modeling of the DGEBA–4-APDS r=1 system analyzing two different branches: the use of two stretched exponential decay contribution factors.

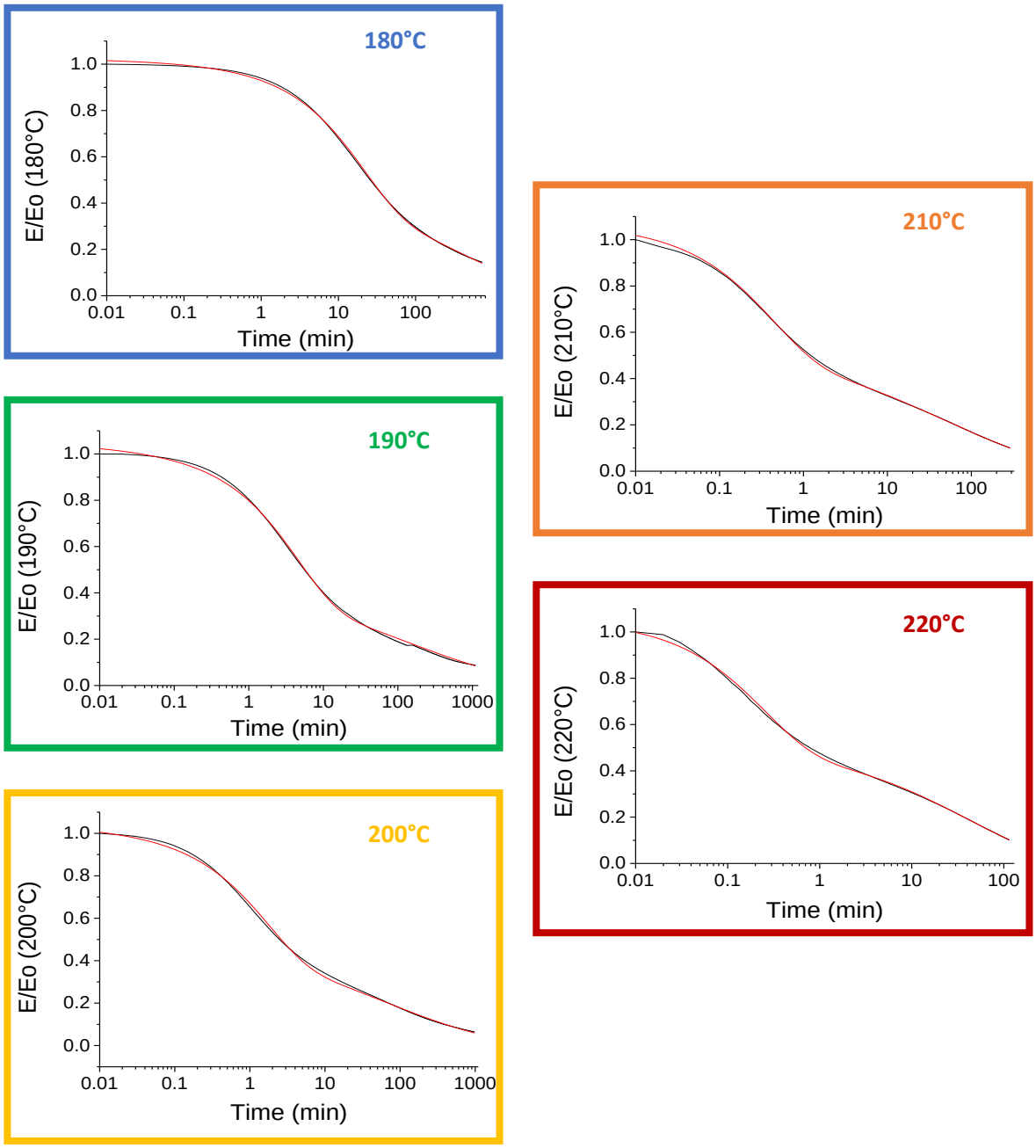

Figure S.III- 8. Modeling of the normalized stress relaxation curves of the DGEBA–4-APDS r=1 system with equation (10) at different temperatures from 180 to 220 °C. The black line corresponds to the experimental data, and the red line to the modeling achieved.

Parameters found from the complete stress relaxation curve analyzing two different branches: the use of two stretched decay exponents for system DGEBA–4-APDS r=1.

180 °C	Value	Standard Error
$E_{1\ BER}$	0.51	0.0064
$E_{2\ Segmental\ network\ relaxation}$	0.51	0.0083
$\lambda_{1\ BER}$	20.37	0.0934
$\lambda_{2\ Segmental\ network\ relaxation}$	359.35	15.6070
$\beta_{1\ BER}$	0.81	0.0054
$\beta_{2\ Segmental\ network\ relaxation}$	0.37	0.0058
Adj. R-Square	0.9994	
Reduced Chi-Sqr	1.17E-05	

190 °C	Value	Standard Error
$E_{1\ BER}$	0.54	0.0054
$E_{2\ Segmental\ network\ relaxation}$	0.52	0.0071
$\lambda_{1\ BER}$	4.17	0.0304
$\lambda_{2\ Segmental\ network\ relaxation}$	126.14	5.8350
$\beta_{1\ BER}$	0.82	0.0082
$\beta_{2\ Segmental\ network\ relaxation}$	0.29	0.0033
Adj. R-Square	0.9946	
Reduced Chi-Sqr	4.42E-05	

200 °C	Value	Standard Error
$E_{1\ BER}$	0.49	0.0035
$E_{2\ Segmental\ network\ relaxation}$	0.57	0.0041
$\lambda_{1\ BER}$	1.68	0.0109
$\lambda_{2\ Segmental\ network\ relaxation}$	59.41	1.4643
$\beta_{1\ BER}$	0.77	0.0058
$\beta_{2\ Segmental\ network\ relaxation}$	0.29	0.0015
Adj. R-Square	0.9980	
Reduced Chi-Sqr	1.47E-05	

210 °C	Value	Standard Error
$E_{1\ BER}$	0.49	0.0020
$E_{2\ Segmental\ network\ relaxation}$	0.59	0.0015
$\lambda_{1\ BER}$	0.41	0.0017
$\lambda_{2\ Segmental\ network\ relaxation}$	51.69	0.4373
$\beta_{1\ BER}$	0.75	0.0036
$\beta_{2\ Segmental\ network\ relaxation}$	0.33	0.0009
Adj. R-Square	0.9998	
Reduced Chi-Sqr	2.36E-06	

220 °C	Value	Standard Error
$E_{1\ BER}$	0.53	0.0048
$E_{2\ Segmental\ network\ relaxation}$	0.52	0.0025
$\lambda_{1\ BER}$	0.24	0.0026
$\lambda_{2\ Segmental\ network\ relaxation}$	40.84	0.4552
$\beta_{1\ BER}$	0.77	0.0083
$\beta_{2\ Segmental\ network\ relaxation}$	0.47	0.0029
Adj. R-Square	0.9994	
Reduced Chi-Sqr	1.11E-05	

Table S.III- 10. Parameters yielded from the simulation carried out in Origin ® 9 using two stretched exponents over the all-recorded data of the stress relaxation normalized of system DGEBA–4-APDS r=1 at temperatures from 180 to 220 °C. The parameters in the table correspond to those of equation (10), where E_i are the prefactors, λ_i, the relaxation times yielded by the simulation, and β_i the stretched exponents decay.

Stress relaxation modeling of the DGEBA–4-APDS r=0.8 system analyzing two different branches: the use of two stretched exponential decay contribution factors.

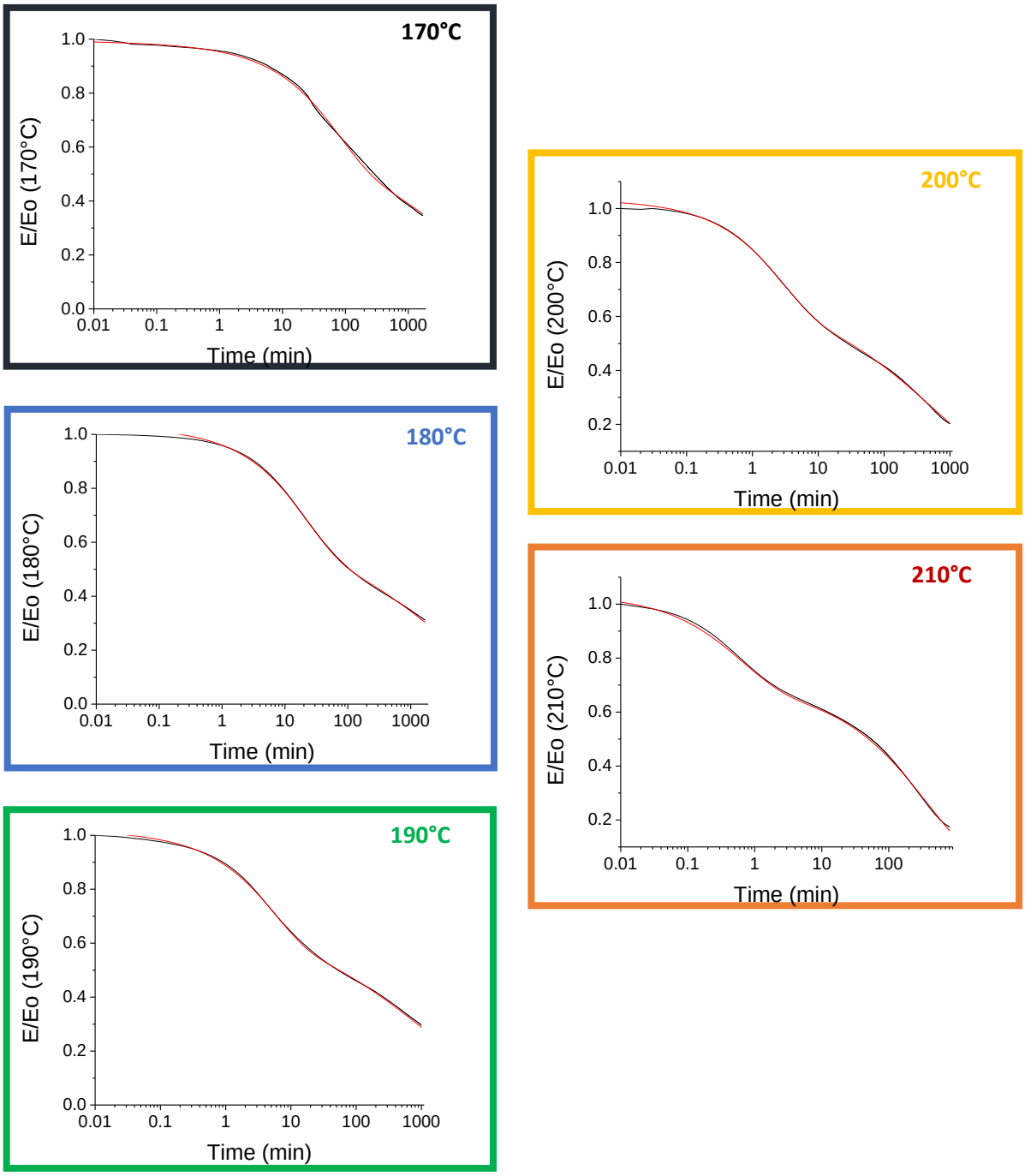

Figure S.III- 9. Modeling of the normalized stress relaxation curves of the DGEBA–4-APDS r=0.8 system with equation (10) at different temperatures from 180 to 220 °C. The black line corresponds to the experimental data, and the red line to the modeling achieved.

Parameters found from the complete stress relaxation curve analyzing two different branches: the use of two stretched decay exponents for system DGEBA–4-APDS r=0.8.

170 °C	Value	Standard Error
$E_{1\ BER}$	0.35	0.0068
$E_{2\ Segmental\ network\ relaxation}$	0.65	0.0091
$\lambda_{1\ BER}$	80.27	0.4063
$\lambda_{2\ Segmental\ network\ relaxation}$	7819.63	272.2559
$\beta_{1\ BER}$	0.76	0.0075
$\beta_{2\ Segmental\ network\ relaxation}$	0.32	0.0084
Adj. R-Square	0	
Reduced Chi-Sqr	0.9969	

180 °C	Value	Standard Error
$E_{1\ BER}$	0.37	0.0033
$E_{2\ Segmental\ network\ relaxation}$	0.66	0.0044
$\lambda_{1\ BER}$	20.51	0.0381
$\lambda_{2\ Segmental\ network\ relaxation}$	3474.41	51.9119
$\beta_{1\ BER}$	0.76	0.0035
$\beta_{2\ Segmental\ network\ relaxation}$	0.34	0.0042
Adj. R-Square	0.9995	
Reduced Chi-Sqr	9.01E-06	

190 °C	Value	Standard Error
$E_{1\ BER}$	0.31	0.0032
$E_{2\ Segmental\ network\ relaxation}$	0.72	0.0040
$\lambda_{1\ BER}$	5.21	0.0215
$\lambda_{2\ Segmental\ network\ relaxation}$	1325.16	19.8353
$\beta_{1\ BER}$	0.81	0.0061
$\beta_{2\ Segmental\ network\ relaxation}$	0.32	0.0031
Adj. R-Square	0.9998	
Reduced Chi-Sqr	5.03E-06	

200 °C	Value	Standard Error
$E_{1\ BER}$	0.34	0.0023
$E_{2\ Segmental\ network\ relaxation}$	0.70	0.0021
$\lambda_{1\ BER}$	2.64	0.0136
$\lambda_{2\ Segmental\ network\ relaxation}$	561.64	4.5089
$\beta_{1\ BER}$	0.77	0.0047
$\beta_{2\ Segmental\ network\ relaxation}$	0.37	0.0017
Adj. R-Square	0.9995	
Reduced Chi-Sqr	1.38E-05	

210 °C	Value	Standard Error
$E_{1\ BER}$	0.31	0.0039
$E_{2\ Segmental\ network\ relaxation}$	0.71	0.0005
$\lambda_{1\ BER}$	0.59	0.0117
$\lambda_{2\ Segmental\ network\ relaxation}$	395.57	0.4404
$\beta_{1\ BER}$	0.78	0.0087
$\beta_{2\ Segmental\ network\ relaxation}$	0.49	0.0010
Adj. R-Square	0.9941	
Reduced Chi-Sqr	4.77E-05	

Table S.III- 11. Parameters yielded from the simulation carried out in Origin ® 9 using two stretched exponents over all recorded data of the stress relaxation normalized of system DGEBA–4-APDS r=0.8 at temperatures from 170 to 210 °C. The parameters in the table correspond to those of equation (10), where E_i are the prefactors, λ_i, the relaxation times yielded by the simulation, and β_i the stretched decay exponents.

Stress relaxation modeling of the DGEBA–4-APDS r=1.2 system analyzing two different branches: the use of two stretched exponential decay contribution factors.

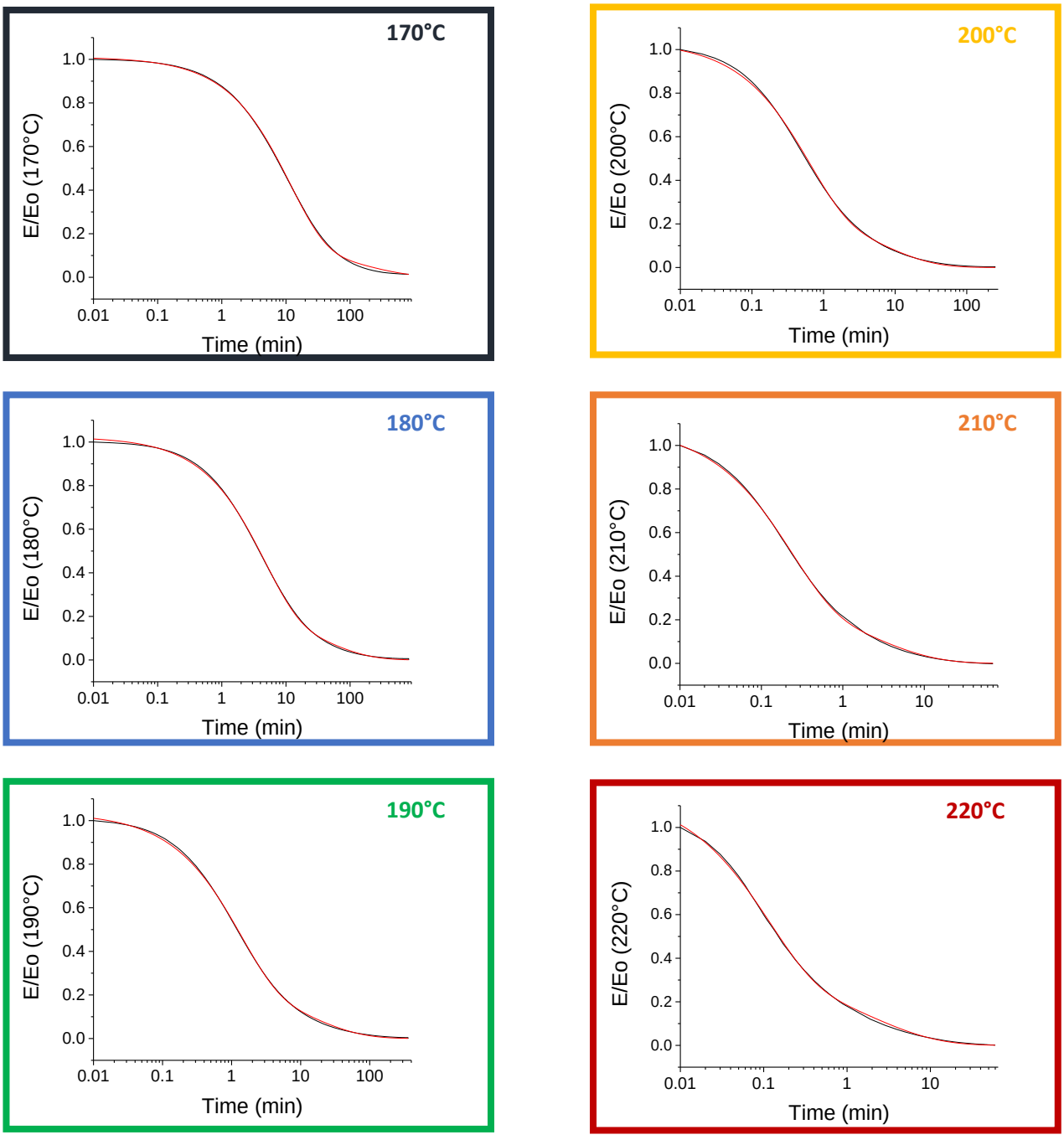

Figure S.III- 10. Modeling of the normalized stress relaxation curves of the DGEBA–4-APDS r=1.2 system with equation (10) at different temperatures from 180 to 220 °C. The black line corresponds to the experimental data, and the red line to the modeling achieved.

Parameters found from the complete stress relaxation curve analyzing two different branches: the use of two stretched decay exponents for system DGEBA–4-APDS r=1.2.

170 °C	Value	Standard Error
$E_{1\ BER}$	0.81	0.0204
$E_{2\ Segmental\ network\ relaxation}$	0.20	0.0231
$\lambda_{1\ BER}$	11.22	0.0445
$\lambda_{2\ Segmental\ network\ relaxation}$	95.32	21.3357
$\beta_{1\ BER}$	0.77	0.0077
$\beta_{2\ Segmental\ network\ relaxation}$	0.47	0.0311
Adj. R-Square	0.9996	
Reduced Chi-Sqr	2.90E-05	

180 °C	Value	Standard Error
$E_{1\ BER}$	0.72	0.0241
$E_{2\ Segmental\ network\ relaxation}$	0.30	0.0261
$\lambda_{1\ BER}$	4.35	0.0186
$\lambda_{2\ Segmental\ network\ relaxation}$	27.24	3.8525
$\beta_{1\ BER}$	0.78	0.0091
$\beta_{2\ Segmental\ network\ relaxation}$	0.52	0.0211
Adj. R-Square	0.9998	
Reduced Chi-Sqr	1.28E-05	

190 °C	Value	Standard Error
$E_{1\ BER}$	0.71	0.0215
$E_{2\ Segmental\ network\ relaxation}$	0.33	0.0233
$\lambda_{1\ BER}$	1.26	0.0042
$\lambda_{2\ Segmental\ network\ relaxation}$	10.24	1.3481
$\beta_{1\ BER}$	0.76	0.0077
$\beta_{2\ Segmental\ network\ relaxation}$	0.52	0.0213
Adj. R-Square	0.9997	
Reduced Chi-Sqr	9.70E-06	

200 °C	Value	Standard Error
$E_{1\ BER}$	0.70	0.0238
$E_{2\ Segmental\ network\ relaxation}$	0.34	0.0252
$\lambda_{1\ BER}$	0.58	0.0036
$\lambda_{2\ Segmental\ network\ relaxation}$	4.91	0.6497
$\beta_{1\ BER}$	0.78	0.0102
$\beta_{2\ Segmental\ network\ relaxation}$	0.53	0.0254
Adj. R-Square	0.9993	
Reduced Chi-Sqr	1.72E-05	

210 °C	Value	Standard Error
$E_{1\ BER}$	0.72	0.0727
$E_{2\ Segmental\ network\ relaxation}$	0.37	0.0788
$\lambda_{1\ BER}$	0.22	0.0031
$\lambda_{2\ Segmental\ network\ relaxation}$	1.87	0.7367
$\beta_{1\ BER}$	0.78	0.0302
$\beta_{2\ Segmental\ network\ relaxation}$	0.51	0.0612
Adj. R-Square	0.9997	
Reduced Chi-Sqr	2.01E-05	

220 °C	Value	Standard Error
$E_{1\ BER}$	0.76	0.0417
$E_{2\ Segmental\ network\ relaxation}$	0.39	0.0423
$\lambda_{1\ BER}$	0.11	0.0017
$\lambda_{2\ Segmental\ network\ relaxation}$	1.59	0.3576
$\beta_{1\ BER}$	0.75	0.0190
$\beta_{2\ Segmental\ network\ relaxation}$	0.49	0.0371
Adj. R-Square	0.9997	
Reduced Chi-Sqr	1.64E-05	

Table S.III- 12. Parameters yielded from the simulation carried out in Origin ® 9 using two stretched exponents over all recorded data of the stress relaxation normalized of system DGEBA–4-APDS r=1.2 at temperatures from 170 to 220 °C. The parameters in the table correspond to those of equation (10), where E_i are the prefactors, λ_i, the relaxation times yielded by the simulation, and β_i the stretched decay exponents.

Time-temperature superposition: WLF behavior.

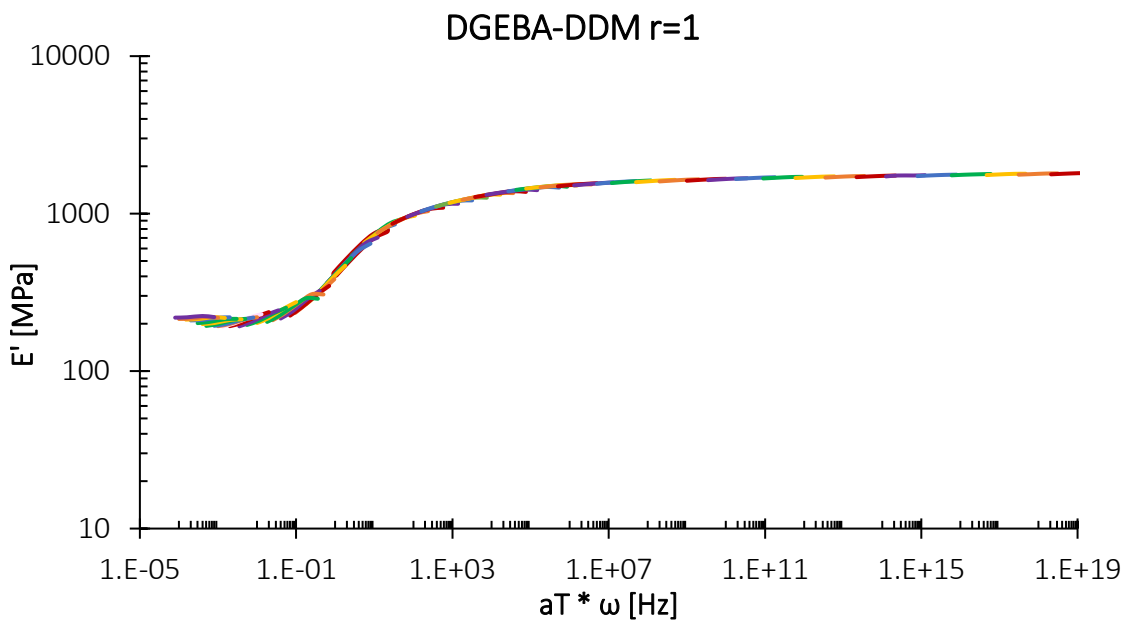

Figure S.III- 11. Master curve of network DGEBA-DDM r=1 at ± 30 °C T_{ref}, where T_{ref} = 177 °C.

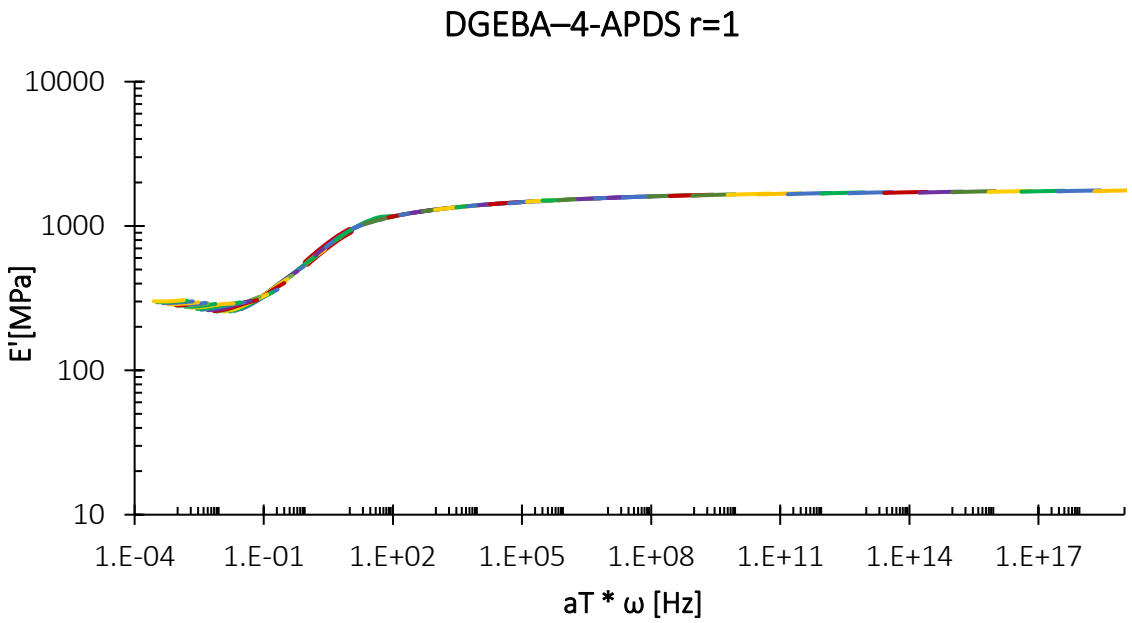

Figure S.III- 12. Master curve of network DGEBA–4-APDS r=1 at ± 30 °C Tref, where Tref = 170 °C.

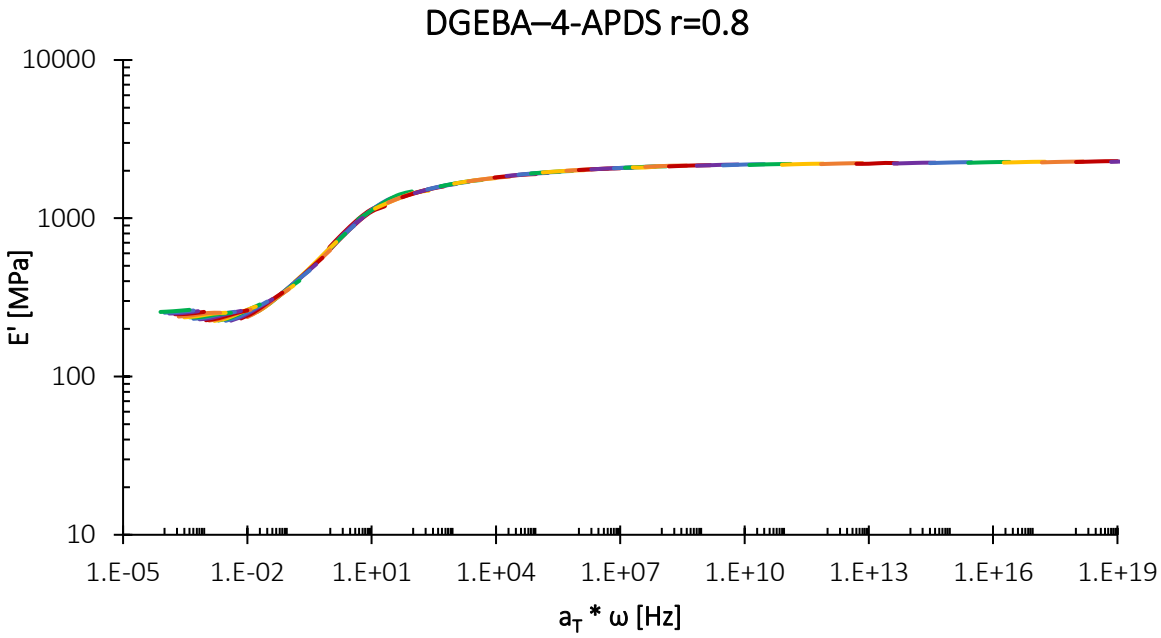

Figure S.III- 13. Master curve of network DGEBA–4-APDS r=0.8 at ± 30 °C T_{ref}, where T_{ref} = 158 °C.

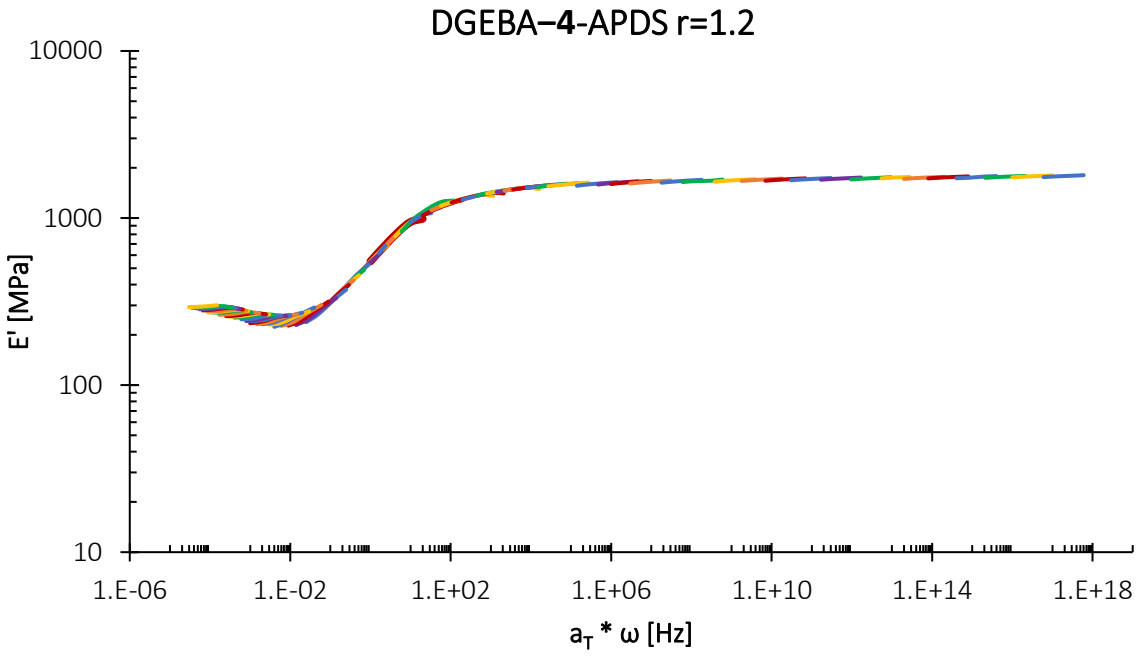

Figure S.III- 14. Master curve of network DGEBA–4-APDS r=1.2 at ± 30 °C T_{ref}, where T_{ref} = 153 °C.

Annex Chapter IV

Parameters found from the complete stress relaxation curve using two stretched decay exponents for the system DGEBA–4-APDS-NFC.

180 °C	Value	Standard Error
$E_{1\ BER}$	0.379	0.0417
$E_{2\ segmental\ motion}$	0.634	0.0408
$\lambda_{1\ BER}$ (min)	12.218	0.9691
$\lambda_{2\ Segmental\ motion}$ (min)	420.096	50.1204
$\beta_{1\ BER}$	0.471	0.0064
$\beta_{2\ Segmental\ motion}$	0.508	0.0275
Adj. R-Square	0.9991	
Reduced Chi-Sqr	1.28E-05	

190 °C	Value	Standard Error
$E_{1\ BER}$	0.357	0.0132
$E_{2\ Segmental\ motion}$	0.667	0.0125
$\lambda_{1\ BER}$ (min)	7.869	0.2491
$\lambda_{2\ Segmental\ motion}$ (min)	103.107	2.5120
$\beta_{1\ BER}$	0.531	0.0030
$\beta_{2\ Segmental\ motion}$	0.619	0.0055
Adj. R-Square	0.9997	
Reduced Chi-Sqr	1.00E-05	

200 °C	Value	Standard Error
$E_{1\ BER}$	0.338	0.0088
$E_{2\ Segmental\ motion}$	0.703	0.0079
$\lambda_{1\ BER}$ (min)	2.528	0.0291
$\lambda_{2\ Segmental\ motion}$ (min)	50.455	1.0684
$\beta_{1\ BER}$	0.521	0.0052
$\beta_{2\ Segmental\ motion}$	0.471	0.0030
Adj. R-Square	0.9989	
Reduced Chi-Sqr	1.63E-05	

210 °C	Value	Standard Error
$E_{1\ BER}$	0.361	0.0042
$E_{2\ Segmental\ motion}$	0.682	0.0020
$\lambda_{1\ BER}$ (min)	0.793	0.0114
$\lambda_{2\ Segmental\ motion}$ (min)	35.508	0.1253
$\beta_{1\ BER}$	0.499	0.0052
$\beta_{2\ Segmental\ motion}$	0.756	0.0013
Adj. R-Square	0.9995	
Reduced Chi-Sqr	1.00E-05	

220 °C	Value	Standard Error
$E_{1\ BER}$	0.377	0.0028
$E_{2\ Segmental\ motion}$	0.689	0.0010
$\lambda_{1\ BER}$ (min)	0.351	0.0037
$\lambda_{2\ Segmental\ motion}$ (min)	22.436	0.0429
$\beta_{1\ BER}$	0.515	0.0037
$\beta_{2\ Segmental\ motion}$	0.742	0.0008
Adj. R-Square	0.9999	
Reduced Chi-Sqr	2.78E-06	

Table S.IV- 1. Parameters yielded from the simulation carried out in Origin ® 9 using two stretched exponents of the normalized stress relaxation of system DGEBA–4-APDS-NFC from 180 - 220 °C.

Parameters found from the complete stress relaxation curve using two stretched decay exponents for system DGEBA–4-APDS.

180 °C	Value	Standard Error
$E_{1\ BER}$	0.5179	0.4503
$E_{2\ Segmental\ motion}$	0.4892	0.4506
$\lambda_{1\ BER}$ (min)	15.3948	2.9703
$\lambda_{2\ Segmental\ motion}$ (min)	54.7799	44.3271
$\beta_{1\ BER}$	0.7808	0.0588
$\beta_{2\ Segmental\ motion}$	0.7865	0.2461
Adj. R-Square	0.9953	
Reduced Chi-Sqr	2.07E-04	

190 °C	Value	Standard Error
$E_{1\ BER}$	0.5106	0.0056
$E_{2\ Segmental\ motion}$	0.5202	0.0059
$\lambda_{1\ BER}$ (min)	5.1807	0.0050
$\lambda_{2\ Segmental\ motion}$ (min)	33.2223	0.5782
$\beta_{1\ BER}$	0.7841	0.0025
$\beta_{2\ Segmental\ motion}$	0.5850	0.0039
Adj. R-Square	0.9999	
Reduced Chi-Sqr	1.80E-06	

200 °C	Value	Standard Error
$E_{1\ BER}$	0.5097	0.0028
$E_{2\ Segmental\ motion}$	0.5043	0.0023
$\lambda_{1\ BER}$ (min)	1.8288	0.0062
$\lambda_{2\ Segmental\ motion}$ (min)	29.7021	0.2101
$\beta_{1\ BER}$	0.7872	0.0031
$\beta_{2\ Segmental\ motion}$	0.6664	0.0025
Adj. R-Square	0.9995	
Reduced Chi-Sqr	9.31E-06	

210 °C	Value	Standard Error
$E_{1\ BER}$	0.5180	0.0043
$E_{2\ Segmental\ motion}$	0.5014	0.0014
$\lambda_{1\ BER}$ (min)	0.5884	0.0066
$\lambda_{2\ Segmental\ motion}$ (min)	23.7958	0.0971
$\beta_{1\ BER}$	0.7989	0.0086
$\beta_{2\ Segemental\ motion}$	0.7948	0.0023
Adj. R-Square	0.9974	
Reduced Chi-Sqr	4.08E-05	

220 °C	Value	Standard Error
$E_{1\ BER}$	0.5286	0.0177
$E_{2\ Segmental\ motion}$	0.5010	0.0031
$\lambda_{1\ BER}$ (min)	0.2530	0.0125
$\lambda_{2\ Segmental\ motion}$ (min)	17.8850	0.1753
$\beta_{1\ BER}$	0.8113	0.0359
$\beta_{2\ Segmental\ motion}$	0.7798	0.0054
Adj. R-Square	0.9762	
Reduced Chi-Sqr	3.36E-04	

Table S.IV- 2. Parameters yielded from the simulation carried out in Origin ® 9 using two stretched exponents of normalized stress relaxation of the system DGEBA–4-APDS from 180 to 220 °C.

Dilatometry test of systems off-stoichiometry in tensile mode

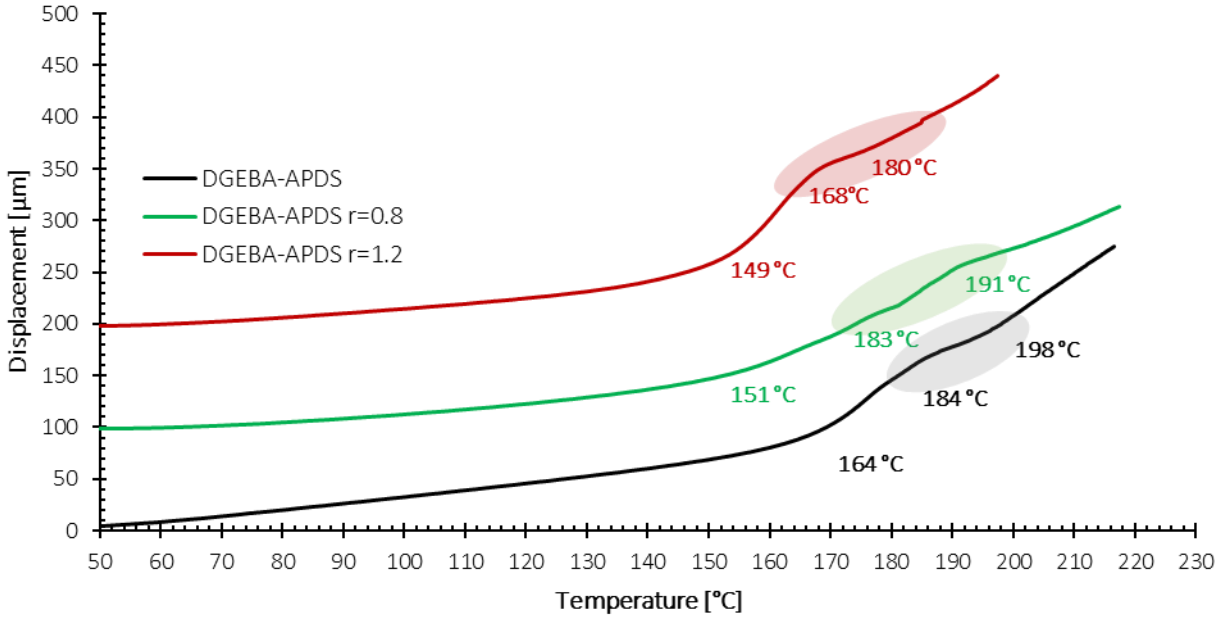

Figure S.IV- 1. Dilatometry test of systems DGEBA-APDS r=1 (black), r=0.8 (green), and r=1.2 (red). An increasement of 100 and 200 µm for system r=0.8 and r=1.2, respectively, was added.

Annex Chapter V

XPS calculus

Sample	C 1s	O 1s	Si 2p	O/C
Pristine NFC	59.8 ± 0.4	39.9 ± 0.6	0.3 ± 0.3	0.67 ± 0.01
NFC-**GPS Acid**	57.7 ± 0.8	37.1 ± 1.8	5.1 ± 2.4	0.64 ± 0.02
NFC-**GPS EtOH**	59.5 ± 1.7	37.4 ± 1.5	3.1 ± 0.2	0.64 ± 0.04
NFC-**GPMES**	61.2 ± 1.8	37.9 ± 1.6	1 ± 0.2	0.62 ± 0.04

Table V-3. Relative atomic concentration obtained by XPS analysis of pristine and modified NFC after Soxhlet extraction.

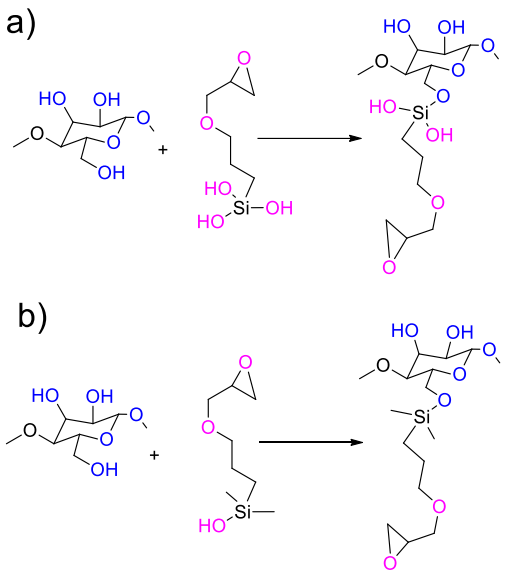

Scheme V-2. Schematization of a) GPS and b) GPMES grafting onto the NFC surface.

Pristine NFC formula: $(C_6H_{10}O_5)$

GPS hydrolyzed and grafted to NFC formula $(C_6H_{13}O_4Si)$

Sample	Si	C_{GPS}(Si*6) C_{GPMES}(Si*8)	$C_{NFC-GPS}$ From Table V-3	C_{NFC} = $C_{NFC-GPS}$ - C_{GPS}	Saccharide= C_{NFC}/6	Silane:saccharide (column 2 and 6)
NFC-GPS Acid	5.1	30.6	57.70	27.1	4.5	1:1
NFC-GPS EtOH	3.1	18.6	59.50	40.9	6.8	1:2
NFC-GPMES	1	8	61.20	55.2	9.2	1:9

Table S.V- 1. Calculus of the silane coupling agents per saccharide unit.

[13]C NMR simulation of a grafting of NFC-GPS. Reaction between the oxyrane groups of GPS and the hydroxy groups of the cellulose.

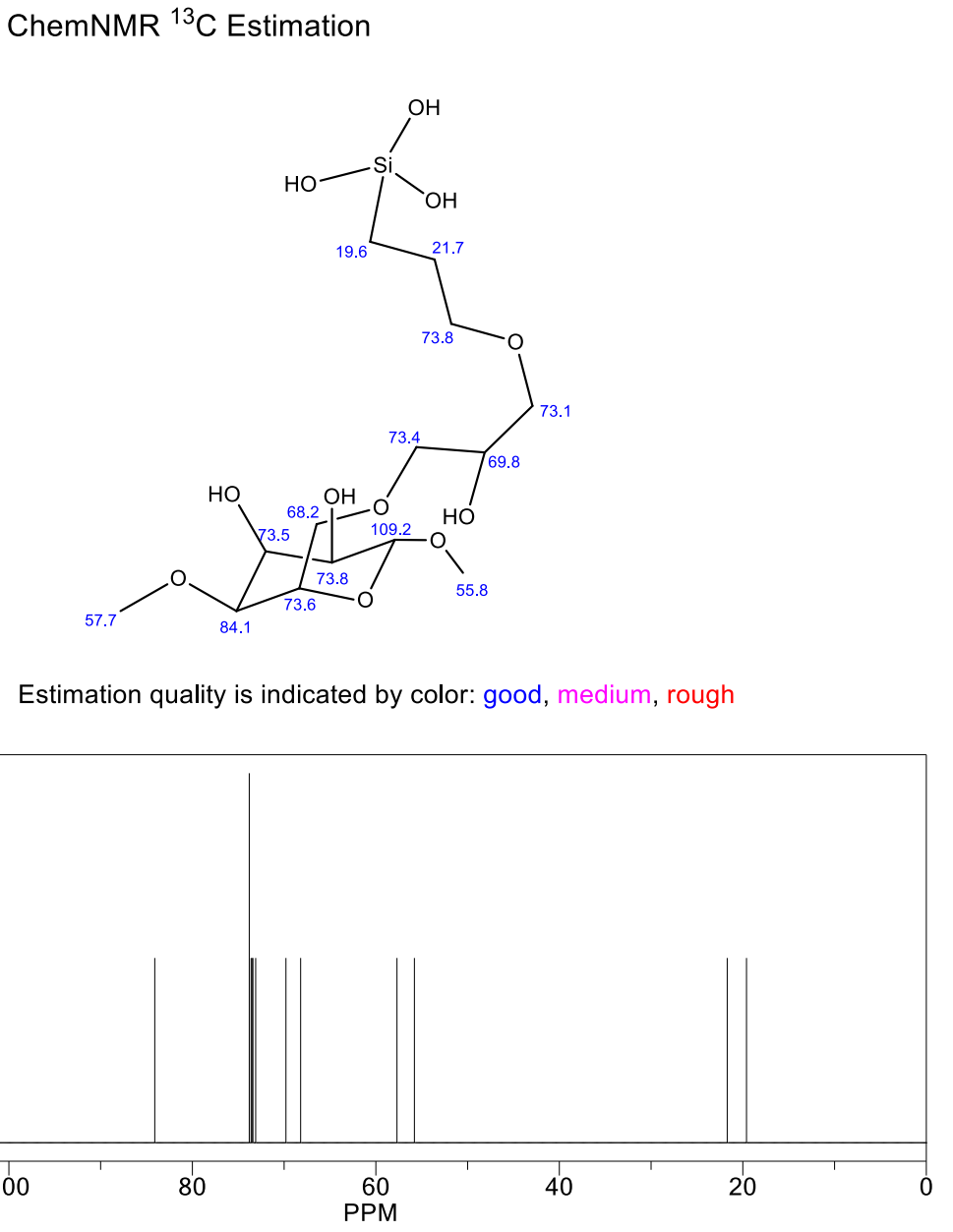

Figure S.V- 1. [13]C NMR simulation of the reaction between the oxirane group of the GPS and the hydroxy groups of the cellulose.

^{13}C NMR simulation of a reaction between the oxirane groups of a GPS and a siloxane

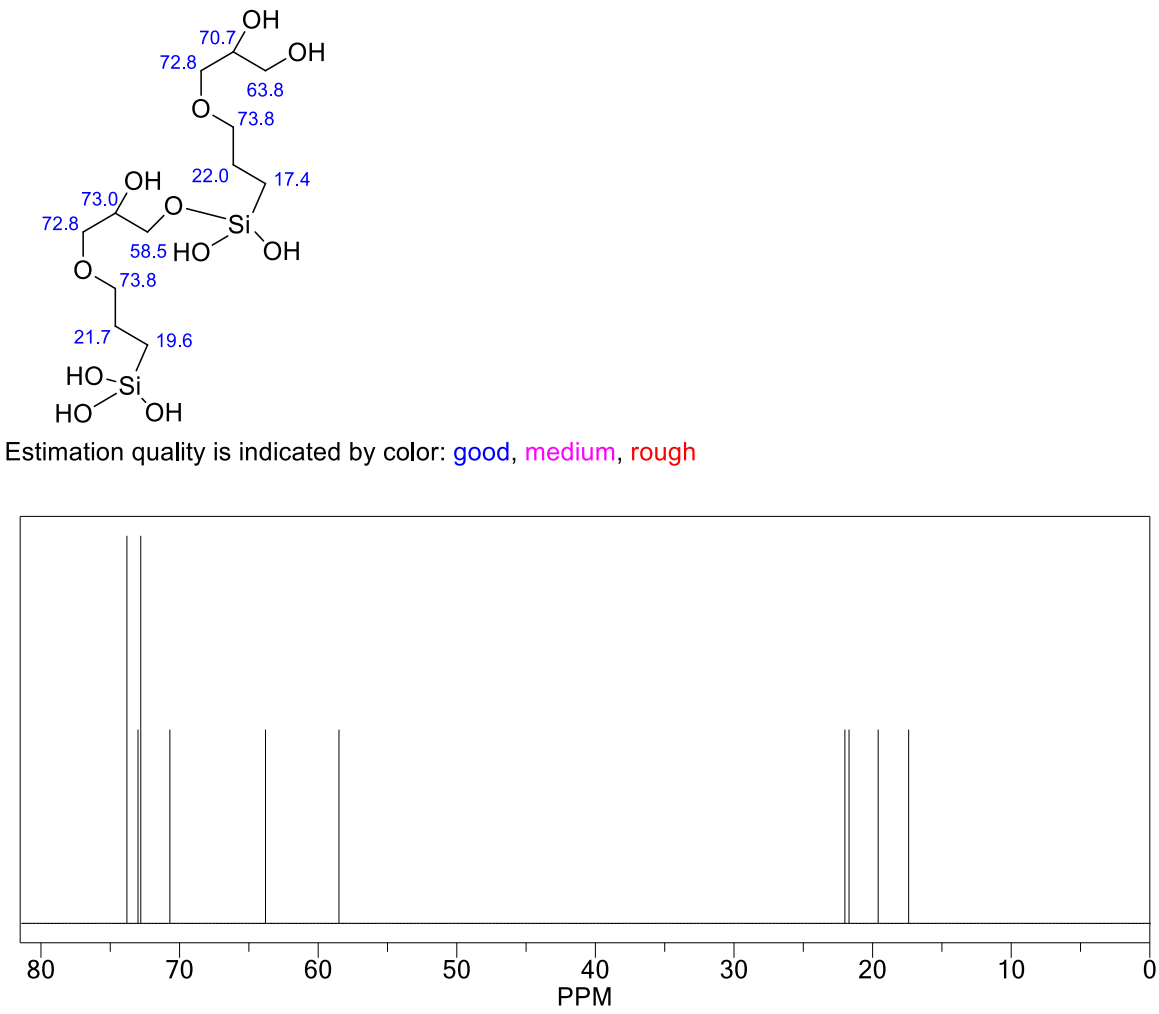

Figure S.V- 2. 13C NMR simulation of the reaction between the oxirane group of a GPS and a siloxane

^{13}C NMR integration calculus after GPS and GPMES hydrolysis

$$Ce_T = Ce + Ce' = 0.74 + 0.34 = 1.08$$

$$\frac{Ce}{Ce_T} = \frac{0.73}{1.08} = 68\%$$

$$\frac{Ce}{Ce_T} = \frac{0.34}{1.08} = 32\%$$

$$Cf_T = Cf + Cf' = 0.87 + 0.31 = 1.18$$

$$\frac{Cf}{Cf_T} = \frac{0.87}{1.18} = 74\%$$

$$\frac{Cf'}{Cf_T} = \frac{0.31}{1.18} = 26\%$$

^{29}Si NMR simulation carried out with MestReNova software

Predicted ^{29}Si NMR spectra of different networks with a) two condensation degrees, b) three condensation degrees, c) two condensation degrees grafted to cellulose C6, and d) three condensation degrees grafted to cellulose C6.

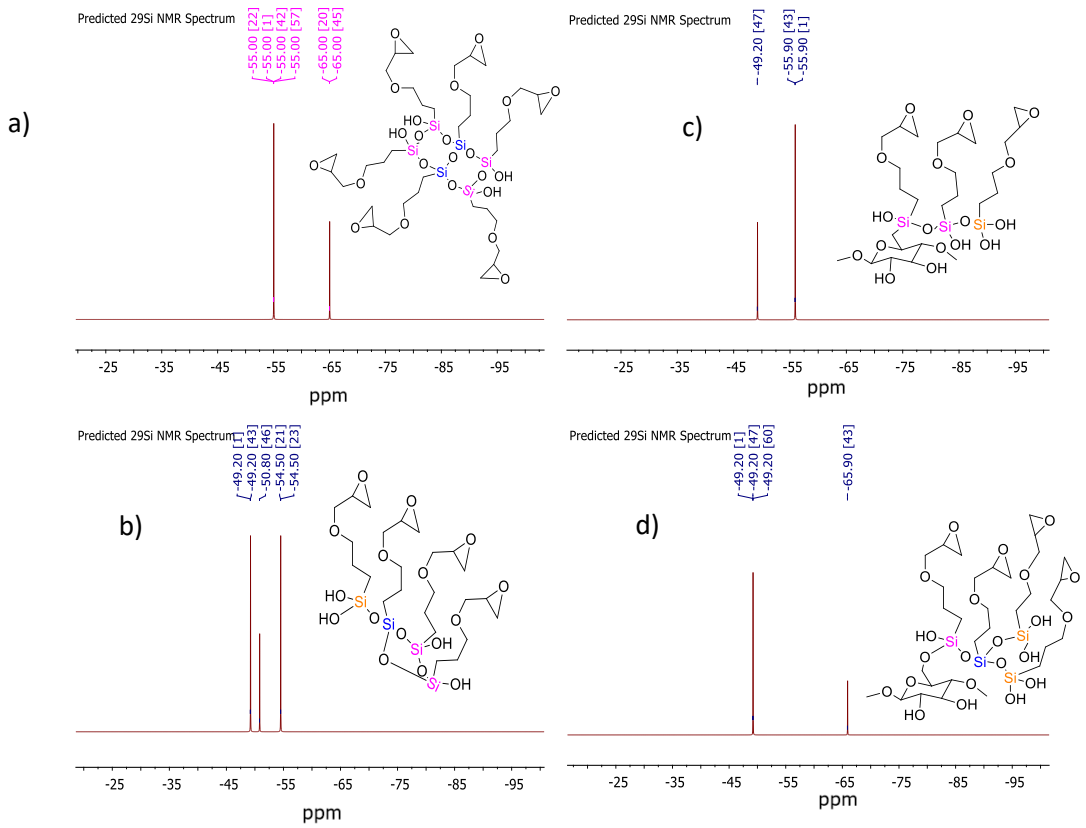

Figure S.V- 3. Predicted ^{29}Si NMR spectra of different networks with a) two condensation degrees, b) three condensation degrees, c) two condensation degrees grafted to cellulose C6, and d) three condensation degrees grafted to cellulose C6.

Signal	Predicted spectrum a)	Predicted spectrum b)	Predicted spectrum c)	Predicted spectrum d)
T1	--	-49.2	49.2	49.2
T2	-55.0	-50.8	55.9	--
T3	-65.0	-54.5	--	65.9

Table S.V- 2. Chemical shifts of silicon of the different predicted spectra displayed in **Figure S.V- 3**.

Predicted ^{29}Si NMR spectra of a) GPMES grafted to the fibrils surface, b) the dimer formed by the self-condensation of the GPMES.

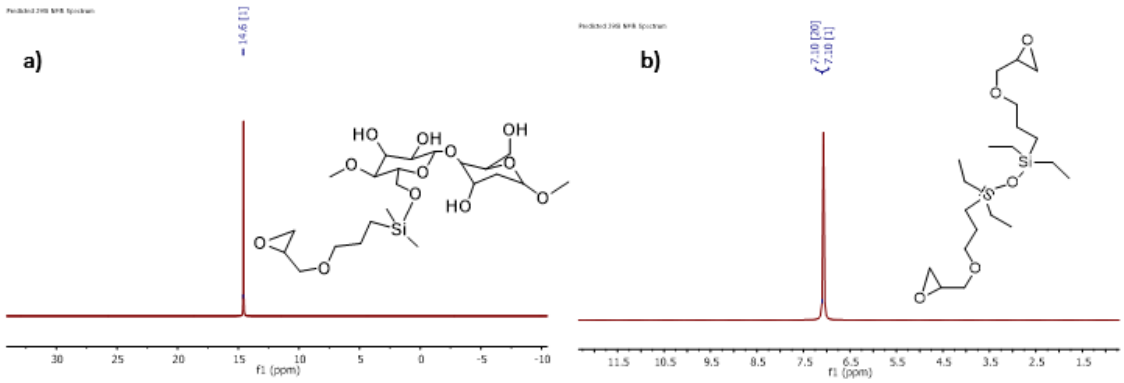

Figure S.V- 4. Predicted ^{29}Si NMR spectra of a) the GPMES grafted to the NFC C6 surface, b) the dimer formation between two GPMES silanes.

SEM histograms of pristine and modified NFC after Soxhlet extraction

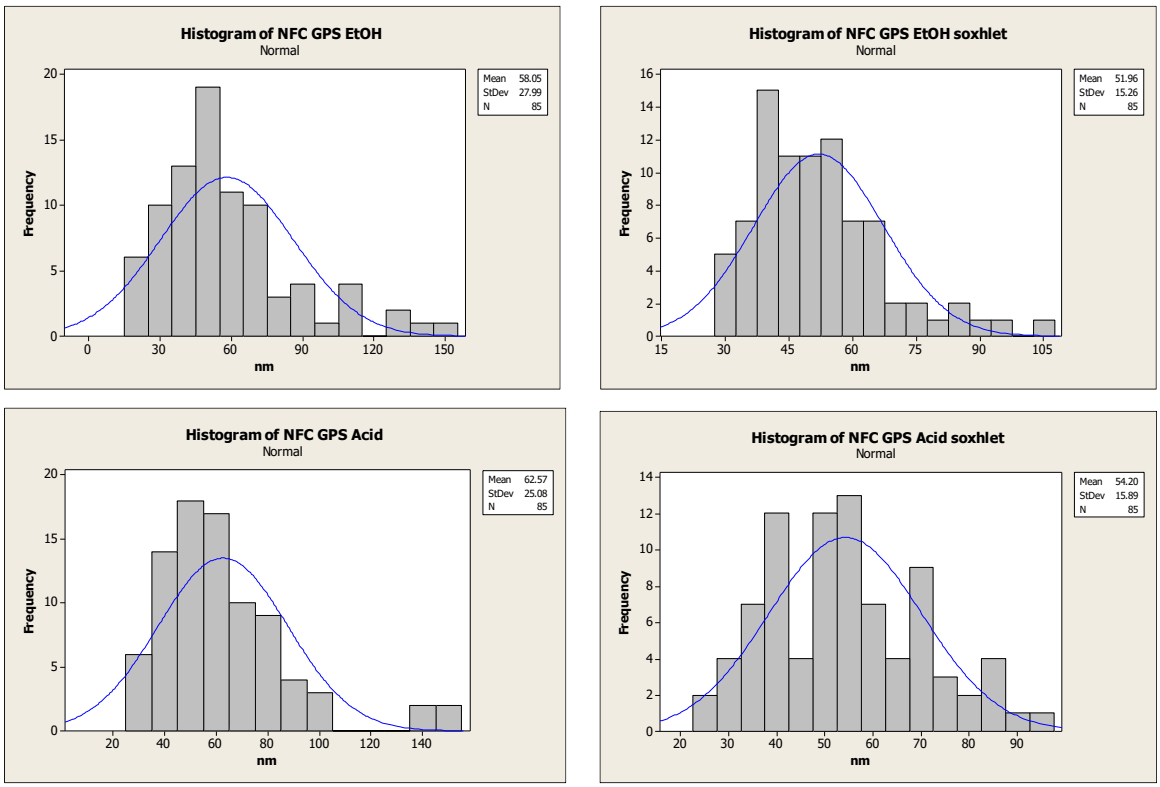

Figure S.V- 5. Histograms of pristine and modified NFC, before and after Soxhlet extraction.

Résumé

Ce travail est divisé en quatre parties. La première est destinée à l'étude de la résine époxy DGEBA–4-APDS comme matériau vitrimère. La deuxième est focalisée sur le développement d'un modèle adapté afin de décrire la relaxation de contrainte plus correctement. La troisième concerne l'étude d'un matériau composite basé sur DGEBA-APDS et des NFC. La quatrième vise à modifier la surface des NFC pour qu'elles puissent ensuite être incorporées dans la résine époxy vitrimère.

1. Résines époxy comme matériau vitrimère.

1.1 Introduction

Au cours des dernières décennies, la croissance du volume de production des résines époxy et les prévisions de la demande du marché pour des composites hautes performances, expliquent l'importance des recherches innovantes sur ces résines. En faisant varier la structure chimique de la résine ou du durcisseur et les conditions de réticulation, il est possible de moduler les propriétés obtenues.[1] Malgré la grande polyvalence des résines époxy, les marchés ont besoin de nouveaux matériaux durables et performants pour répondre aux exigences de l'industrie tout en limitant la production croissante de déchets non recyclables. De nombreux chercheurs se sont inspirés de systèmes biologiques, capables de se réparer après avoir subi des dommages, pour proposer des solutions innovantes en termes de durabilité. De nombreuses stratégies visant à introduire un comportement auto réparateur dans les résines époxy ont été explorées comme l'insertion de liaisons covalentes réversibles dans le matériau[2, 3].

Les liaisons covalentes réversibles ont été étudiées depuis longtemps, dans des systèmes biologiques, et dans des réseaux réticulés[4]. Récemment, Bowman *et al.* (2010) ont défini comme réseaux adaptables covalents (CAN) les réseaux qui contiennent un nombre suffisant de liaisons covalentes réversibles permettant une modification du réseau réticulé. On peut les classer en deux groupes principaux en fonction de leur mécanisme d'échange. Le premier mécanisme dit dissociatif, la réaction d'échange chimique, suit une séquence de réaction de rupture de liaison suivie d'une formation de liaison. Le second mécanisme, dit associatif, la rupture et la formation de liaison interviennent simultanément, ce qui assure une densité de réticulation constante. C'est le cas de la transestérification[5, 6, 7, 8, 9].

La définition des matériaux vitrimères a été introduite par Leibler *et al.* (2011) comme un nouveau type de matériau réticulé capable de changer sa topologie et de s'autoréparer[10]. Les vitrimères ont été décrits comme des réseaux covalents adaptables qui peuvent réarranger leur topologie par une réaction d'échange de liaisons sans dépolymérisation. On parle de mécanisme associatif[11]. Néanmoins, plus récemment, il a été découvert que les vitrimères pouvaient également suivre un mécanisme dissociatif sans dépolymérisation [12, 13]. Depuis la première étude sur les vitrimères, qui était basée sur la transestérification[14, 15], le nombre de nouveaux systèmes vitrimères avec une chimie différente comme la transcarbonation, la transamination d'uréthanes vinyliques[16], la transamination d'imines[17], l'échange d'esters boroniques[18], la métathèse d'oléfines[19], l'échange de disulfures[20], la transalkylation de sels de sulfonium[21], entre autres, augmente constamment. On peut citer le travail d'Odriozola *et al.* qui ont présenté un nouvel vitrimère époxy sans catalyseur,

possédant de bonnes propriétés mécaniques. Cet vitrimère époxy a été préparé en mélangeant de la DGEBA avec un durcisseur dynamique contenant des disulfures aromatiques (4-Aminophenyl disulfide (4-APDS))[20].

Une autre caractéristique des vitrimères est la présence d'une nouvelle température de transition differente de *T*g ou *T*m : la température de gel topologique, *T*v.

1.2 Objectif

L'objectif de cette partie est d'une part, déterminer les conditions optimales pour la réticulation du système DGEBA-APDS à différentes stœchiométries, et d'autre part, mettre en évidence les propriétés vitrimères caractéristiques du système en utilisant en première ligne les techniques classiques décrites dans la littérature.

1.3 Section expérimentale

Des échantillons d'époxy vitrimère ont été préparés en mélangeant du DGEBA et du 4-APDS à 60°C. Le liquide homogène visqueux obtenu a été coulé dans des moules en silicone et réticulé dans une étuve suivant différents programmes de températures/temps. Trois types d'échantillons ont été préparés avec différentes stœchiométries : DGEBA–4-APDS r=1, DGEBA–4-APDS r=0.8 et DGEBA–4-APDS r=1.2, avec r défini comme étant $r = \frac{f_{amine}\ x\ n_{amine}}{f_{epoxy}\ x\ n_{epoxy}}$; avec f, le nombre de fonctions (f=4 pour les amines et f=2 pour l'époxy), et n, le nombre de moles.

Systèmes	**Cycle de cuisson**	**Conditions**
r=1	DGEBA-APDS r=1**a**	80 °C/1h + 120°C/2h + 150°C/2h
	DGEBA-APDS r=1**b**	25°C/1h + 50°C/1h + 75°C/45 min + 110°C/30min
	DGEBA-APDS r=1**c**	80 °C/1h + 130°C/2h + 150°C/2h + 180°C/1h vide
	DGEBA-APDS r=1**d**	60 °C/1h + 80 °C/1h + 130°C/2h + 150°C/2h + 180°C/1h vide
r=0.8	DGEBA-APDS r=0.8**a**	60 °C/1h + 80 °C/1h + 130°C/2h + 150°C/2h + 180°C/1h vide
	DGEBA-APDS r=0.8**b**	60 °C/1h + 80 °C/1h + 130°C/2h + 150°C/2h + 180°C/4h vide
	DGEBA-APDS r=0.8**c**	60 °C/1h + 80 °C/1h + 130°C/2h + 150°C/2h + 180°C/4h sous Ar
r=1.2	DGEBA-APDS r=1.2**a**	60 °C/1h + 80 °C/1h + 130°C/2h + 150°C/2h + 180°C/1h vide
	DGEBA-APDS r=1.2**b**	60 °C/1h + 80 °C/1h + 130°C/2h + 150°C/2h + 180°C/4h vide
	DGEBA-APDS r=1.2**c**	60 °C/1h + 80 °C/1h + 130°C/2h + 150°C/2h + 180°C/4h sous Ar

Tableau 1-1. Cycles de réticulation pour les systèmes DGEBA-APDS avec 3 rapports amine/époxy différents.

La caractérisation des propriétés thermomécaniques a été effectué en utilisant l'analyse dynamique mécanique avec une rampe de température. Elle a permis de déterminer le module de stockage (E')

à 30°C et sur le plateau caoutchoutique à T=*Tg*+30°C, et le facteur d'amortissement mécanique (Tan δ).

Les propriétés caractéristiques des vitrimères à mettre en évidence sont 1) la connectivité permanente (évaluée par un test de gonflement et des expériences DMA en balayage de fréquence), 2) les relaxations des réseaux, qui conduisent à un réarrangement de leur topologie, 3) la mise en évidence d'une nouvelle température de transition : la *Tv*.

1.4 Résultats de la caractérisation et discussion

1.4.1 Optimisation du cycle de cuisson

A partir de la littérature, deux cycles de réticulation ont été explorés[22, 23] (r=1**a** et r=1**b**) et après différents essais d'optimisation pour le système en stœchiométrie (r=1**c** et r=1**b**)[24, 25], et pour les autres stœchiométries du système DGEBA–4-APDS (r=0.8**b** et r=1.2**c**) ont été étudiés.

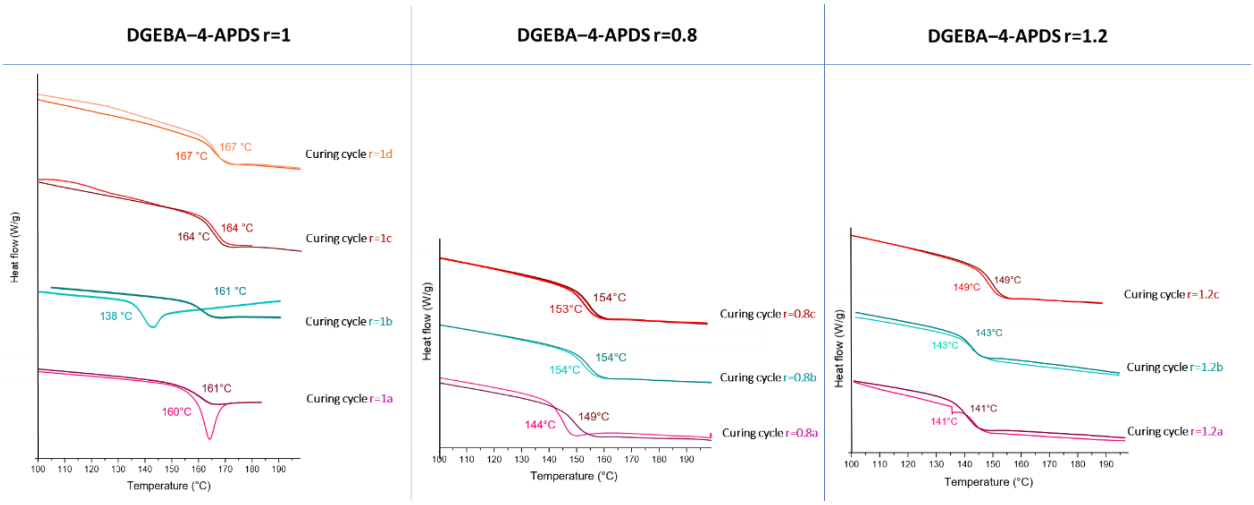

Figure 1-1. Expériences de calorimétrie à balayage différentiel des différents cycles de durcissement pour DGEBA–4-APDS des trois stichométries explores (r=1, 0.8 et 1.2).

La **Figure 1-1** montre des thermogrammes DSC effectués à différentes stœchiométries et selon plusieurs cycles de cuisson suivis. Les cycles de réticulation r=1**d**, r=0.8**b** et r=1.2**c** présentent les températures de transition vitreuse les plus élevées, ce qui suggère que ce sont ces conditions de réticulation qui permettront d'atteindre les propriétés mécaniques maximales. Les trois cycles sont proches avec des différences mineures mais importantes pour juger du taux de réticulation le plus élevé. Cela nous a permis de déterminer les cycles optimaux.

1.4.2 Performance thermomécanique

Une fois que le cycle de réticulation optimal a été établi pour les différentes résines époxy, les propriétés thermomécaniques ont pu être déterminées en effectuant une rampe de température dynamique, par analyse dynamique mécanique (DMA), comme le montre la **Figure 1-2**.

La **Figure 1-2c** montre les propriétés thermomécaniques du système DGEBA–4-APDS, qui utilise un durcisseur amine permettant la formation de liaisons réversibles. Il ne semble pas différer du système élaboré avec un durcisseur classique (DDM)) si l'on se place dans le même rapport stœchiométrique amine/époxy (r=1).

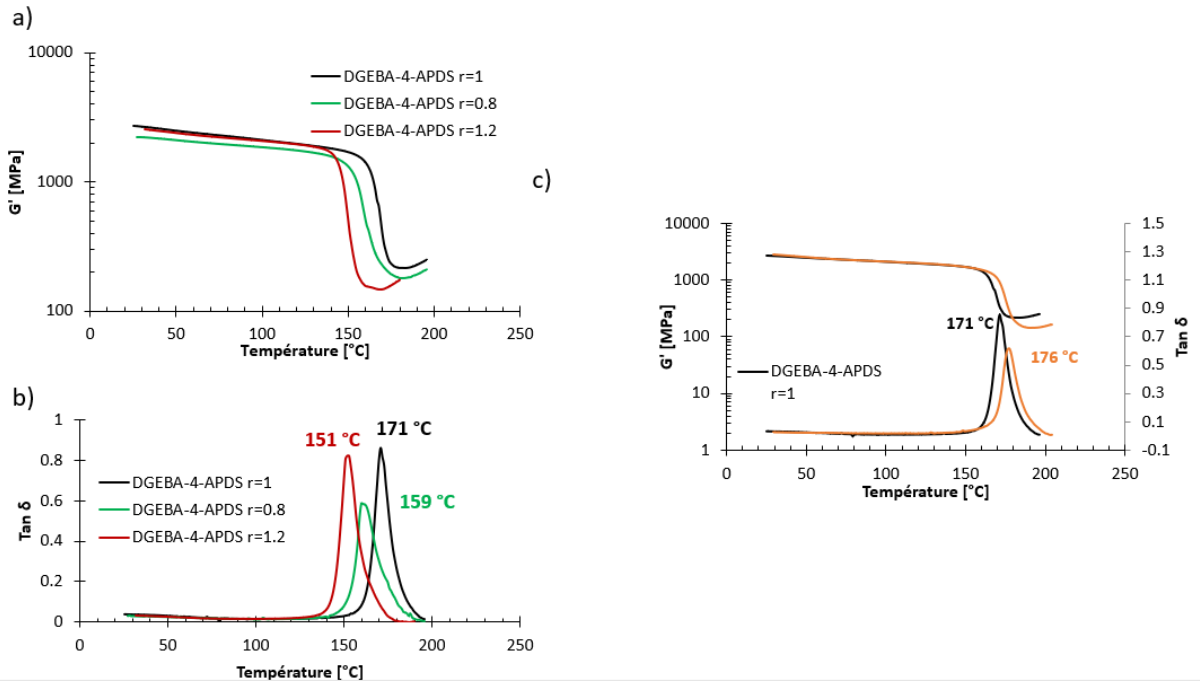

Figure 1-2. a) module de stockage (E') en fonction de la température des systèmes DGEBA–4-APDS, b) facteur d'amortissement (Tan δ) en fonction de la température pour les différents systèmes avec un rapport amine/époxy de 1 (noir), 0.8 (vert) et 1.2 (rouge), et c) Courbes de E' et de Tan δ du DGEBA–4-APDS (noir) et DGEBA-DDM (rouge).

Système	E' à 30°C (MPa)	E_r' à *Tg* + 30°C (MPa)	Tα (°C)	ρ (mol/m^3)
DGEBA–4- APDS r=0.8	2261 ± 100	219 ± 34	159 ± 3	1.92E+04
DGEBA–4- APDS r=1	2681 ± 121	268 ± 98	171 ± 3	2.29E+04
DGEBA–4-APDS r=1.2	2574 ± 97	166 ± 26	151 ± 1	1.48E+04
DGEBA-DDM r=1	2692 ± 144	225 ± 82	176 ± 0.5	1.88E+04

Tableau 1-2. Valeurs des modules de conservation (E') mesurés à 30 °C et à *Tg* + 30 °C, les valeurs de *Tα* et de la densité de réticulation (ρ) des systèmes DGEBA–4-APDS et DGEBA-DDM à différents rapports amine/époxy.

Le **Tableau 1-2** regroupe les valeurs des modules de conservation (E') et des températures de relaxation (*T*α) pour les différents systèmes réticulés. Le module de conservation le plus élevé est obtenu pour le système en stichométrie et le plus bas pour les autres systèmes amine/époxy à différentes stœchiométries[26, 27.] En ce qui concerne la relaxation α, une baisse de *T*α a été observée pour les deux systèmes hors-stœchiométries, ce qui suggère une densité de réticulation plus faible[28].

Les conditions optimales de réticulation pour le système époxy étudié aux différentes stœchiométries ont été trouvées. Une rampe lente pour la réticulation permet de réduire les contraintes mécaniques internes, et une étape de post-réticulation garantit une réaction complète des résines époxy en et hors rapport stœchiométrique. Une *T*g supérieure à celles rapportées dans la littérature a été obtenue en optimisant le cycle de réticulation. L'introduction de liaisons covalentes réversibles ne modifie pas significativement le comportement thermomécanique du réseau époxy. Le module élastique et la transition α sont très similaires dans les deux cas. Les systèmes hors-stœchiométrie présentent une température de transition α plus faible et une diminution de la densité de réticulation.

1.4.3. Propriétés vitrimères

Selon les premiers travaux de Leibler et de ses collègues, les vitrimères peuvent être définis par certains critères. Ces critères ont été explorés pour prouver le comportement vitrimère des systèmes DGEBA–4-APDS élaborés. Les vitrimères sont des réseaux avec une densité de réticulation constante à toutes les températures, ce qui implique que ces matériaux gonflent mais ne se dissolvent pas dans les solvants chimiquement inertes, même à températures élevées. Les vitrimères subissent une baisse de viscosité avec la température et qui suit la loi d'Arrhenius, à l'instar des matériaux de type « silice inorganique ». Enfin, les vitrimères présentent (en général) une nouvelle température de transition, la *T*v.

1.4.3.1 Connectivité permanente : densité de réticulation constante.

La connectivité permanente a été explorée en utilisant deux techniques différentes : des tests de gonflement et des expériences de balayage en fréquence réalisées par analyse DMA.

Pour les tests de gonflement, quatre solvants différents ont été employés : THF, DMF, 2-mercaptopropionate d'éthyle (EMP), et 1,2,4-Trichlorobenzène. Les trois premiers ont été testés pendant une semaine à température ambiante, et le tri chlorobenzène à 190 °C pendant 1h.

L'étude de gonflement montre que les trois systèmes (r=1, 0.8 et 1.2) gonflent mais ne se dissolvent

pas dans le THF et le EMP. Le gonflement avec le DMF a mis en évidence la perte d'intégrité du réseau pour le système DGEBA–4-APDS r=1.2 dès le deuxième jour d'immersion, et après une semaine pour le système DGEBA–4-APDS r=0.8. Pour le système à rapport stœchiométrique (r=1), aucune perte de l'intégrité du réseau n'a été observée. La perte d'intégrité du réseau avec le DMF est expliquée par une réaction de scission sélective des groupes disulfures, car le DMF peut avoir le rôle de solvant réactif vis-à-vis des liaisons disulfures.[29, 30].

La « connectivité permanente » a également été testée à haute température. Ainsi, un test de gonflement a été effectué dans 1,2,4-Trichlorobenzène à haute température (190°C) pendant 1 h. Aucune perte visible de connectivité n'a été constatée, mais un gain de masse important a été enregistré comme pour les autres systèmes vitrimères décrits dans la littérature[31].

La stabilité du réseau des matériaux vitrimères peut également être mise en évidence en étudiant l'évolution du module de conservation en fonction de la fréquence de sollicitation du matériau à différentes températures. Le balayage en fréquence a été effectué de 30 à 0.05 Hz pour tester la stabilité de la densité de réticulation à l'état caoutchoutique à différentes températures : de 190 à 230°C par pallier de 10°C. Les résultats montrent que le module élastique semble indépendant de la fréquence aux différentes températures, ce qui indique une densité de réticulation constante[32,33].

1.4.3.2 Relaxation de contrainte

Les expériences de relaxation de contraintes permettent de montrer que les réseaux présentant des liaisons covalentes réversibles peuvent relaxer et présenter une certaine fluidité.

Les résultats ont été normalisés pour faciliter la comparaison entre les relaxations sous différentes températures comme le présente la **Figure 1-3**. Ce type de courbes sont classiquement ajustées en utilisant le modèle de Maxwell dans une gamme de 10^1-10^6 s pour des températures supérieures à la *T*g du matériau[34].

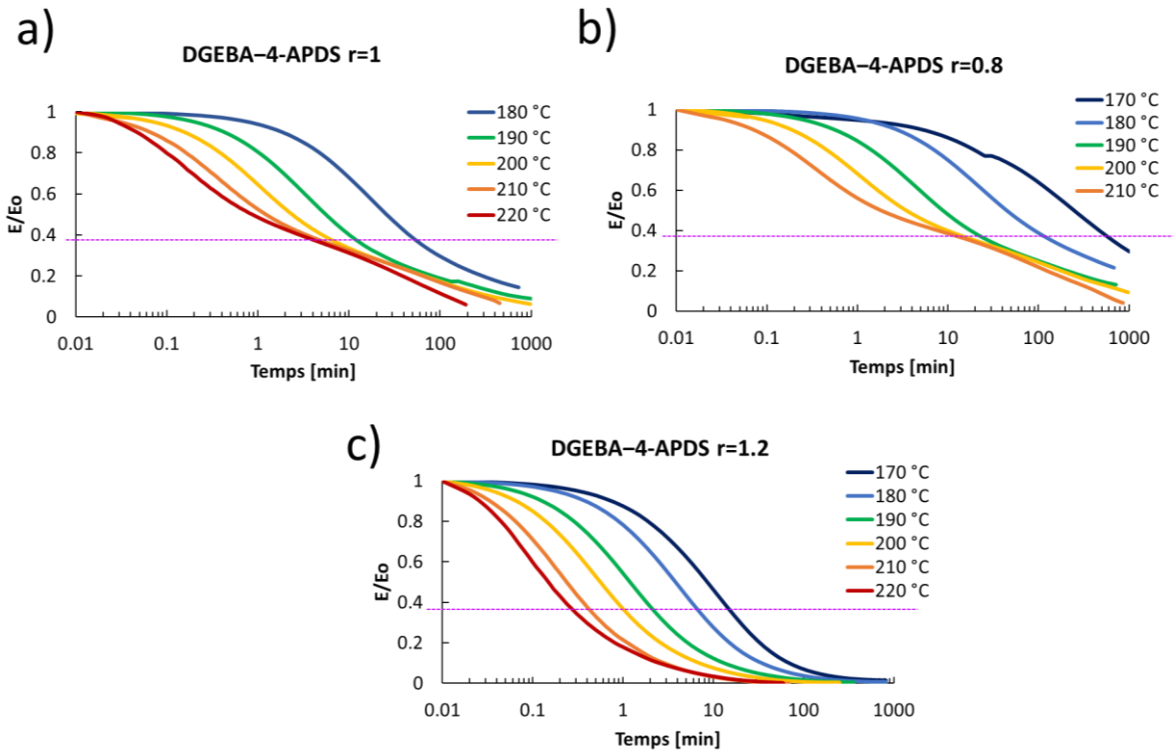

Figure 1-3. Comportement de relaxation sous contrainte normalisé du systèmes époxy sous une déformation de 1% a) DGEBA–4-APDS r=1, b) DGEBA–4-APDS r=0.8, et c) DGEBA–4-APDS r=1.2.

Les résultats montrent que le temps de relaxation dépend fortement de la température et de la concentration relative en durcisseur 4-APDS.

Une caractéristique fondamentale des vitrimères est le comportement viscoélastique qui ressemble à celui de la silice. Ce comportement a été mis en évidence dans le diagramme d'Angell, représentant la variation de la viscosité en fonction de l'inverse de la température normalisée par rapport à la *Tg* (*Tg*/T), et montrant un comportement de type Arrhenius[35]. En suivant l'équation d'Arrhenius, il est possible de déterminer l'énergie d'activation (Ea), et par extrapolation, la température de gel topologique (*Tv*). Les résultats sont résumés dans le **Tableau 1-3**.

Système	Ea (kJ/mol)	*Tv* (°C) modèle de Maxwell
DGEBA–4-APDS r=0.8	130 ± 6	205 ± 17
DGEBA–4-APDS r=1	114 ± 1	175 ± 3
DGEBA–4-APDS r=1.2	147 ± 3	154 ± 5

Tableau 1-3. L'énergie d'activation (Ea) et la température de gel topologique (*Tv*) des réseaux DGEBA–4-APDS variant le rapport amine/époxy.

1.4.3.3 Mise en évidence d'une nouvelle transition thermique : La Tv

La récente introduction de la température de gel topologique a généré de multiples questions sur sa définition et sa détermination. À notre connaissance, il existe trois méthodes pour déterminer la *T*v des vitrimères, 1) les expériences de relaxation sous contrainte et leur extrapolation, 2) les expériences fluage et leur extrapolation, 3) l'essai de dilatométrie, et 4) l'utilisation de luminogènes d'émission induite par agrégation (AIE) dans le vitrimère[36]. La méthode la plus utilisée est l'extrapolation à partir des expériences de relaxation sous contrainte, suivie par les études de dilatométrie.

Des études de dilatométrie ont été réalisées pour les systèmes DGEBA–4-APDS à différentes stœchiométries et pour le système de référence sans liaisons chimiques dynamiques (DGEBA-DDM). L'échantillon sans liaisons dynamiques (DGEBA-DDM) présente une seule température de transition, alors que les systèmes avec liaisons dynamiques présentent deux températures de transition différentes. Les températures de transition sont résumées dans le **Tableau 1-4**.

System	*Tg* (°C) dilatométrie	*Tg* (°C) DSC	*Tv* (°C) dilatométrie	*Tv* (°C) Modèle de Maxwell
DGEBA–4-APDS r=0.8	159 ± 3	155 ± 1	175 ± 1	205 ± 17
DGEBA–4-APDS r=1	165 ± 1	167 ± 1	175± 2	175 ± 3
DGEBA–4-APDS r=1.2	147± 1	148 ± 1	156 ± 1	154 ± 5
DGEBA-DDM r=1	174 ± 2	177 ± 1	----------	----------

Tableau 1-4. Températures de transition vitreuse (*Tg*) et températures de gel topologique (*Tv*) du DGEBA–4-APDS pour 3 rapports amine/époxy différents et d'un système sans liaisons dynamiques DGEBA-DDM à r=1.

1.5 Conclusion

Les propriétés caractéristiques des vitrimères pour les systèmes DGEBA–4-APDS ont été étudiées. On peut noter trois points essentiels :

1) La connectivité permanente a été mise en évidence en réalisant des mesures de gonflement par des solvants. Les échantillons gonflent mais ne se dissolvent pas, même à des températures élevées, pour les solvants inertes. Les expériences de balayage en fréquence en DMA ont confirmé une densité de réticulation constante.
2) Une nouvelle température de transition a été mise en évidence en réalisant des expériences de dilatométrie. Les valeurs des *T*g obtenues par cette méthode de caractérisation sont cohérentes à celles obtenues par DSC. Les valeurs de *T*v trouvées sont en accord avec les résultats obtenus par l'extrapolation des résultats des expériences de relaxation de contraintes réalisées en DMA.

3) Les expériences de la relaxation de contraintes ont montré comment les réseaux relaxent et fluent, comme le suggère la définition des vitrimères. La vitesse de relaxation observée augmente au fur et à mesure que la concentration en liaisons réversibles augmente. De plus, les réseaux DGEBA–4-APDS ont montré un comportement viscoélastique qui suit un comportement Arrhenien. Ce comportement peut être comparé au tracé dit "d'Angell" et ressemble à celui des matériaux à base de silice ou aux liquides forts, indiquant une remise en œuvre facile.

2. Modélisation de la relaxation des contraintes

2.1 Introduction

Les vitrimères ont la capacité de se relaxer et présentent de la fluidité aux températures supérieures à leurs *T*g, de sorte que la relaxation de contrainte suit le modèle de Maxwell. Bien que le modèle de Maxwell ait été le plus utilisé pour déterminer le comportement de relaxation de contraintes, il ne décrit pas correctement la relaxation de contraintes de polymères, même pour des systèmes vitrimères[13, 37]. Par conséquent, de nouveaux modèles et de nouvelles méthodes de caractérisation sont apparus pour mieux appréhender ce phénomène de relaxation[38, 39, 40 40, 41, 42, 43].

Pour atteindre cet objectif, la modélisation a été explorée en utilisant le modèle de Kohlrausch-Williams-Watts (KWW). Torkelson et son équipe (2018) ont réalisé des travaux intéressants en appliquant ce modèle pour décrire le comportement de relaxation des matériaux vitrimères. Le modèle considère une fonction exponentielle étirée qui détermine la forme de la courbe de relaxation[41]. De même, Yu et ses collègues (2014) ont employé une approche différente pour expliquer la relaxation de contrainte de ces types des réseaux, inspirée de la théorie de Bernstein-Kearsley-Zapas[42]. Leur approche décrit deux modes de relaxation différents : 1) un mode de relaxation lié à la réaction d'échange des liaisons réversibles (BER) et 2) et une relaxation liée au caractère viscoélastique des chaines polymères.

Pour aller plus loin dans cette analyse, un modèle permettant de décrire la relaxation complexe de ce type de réseaux est exposé. Ce modèle consiste à utiliser des fonctions exponentielles décroissantes étirées et s'appuie sur deux relaxations principales distinctes : une première relaxation liée aux réactions d'échange des liaisons réversibles (BER) et une seconde relaxation liée aux mouvements des chaînes polymères. Les analyses ont été réalisées sur la base des données de relaxation des contraintes enregistrées pour les différents systèmes en utilisant OriginPro® 9.

2.2 Objectif

Utilisation d'une approche innovante pour interpréter le comportement viscoélastique complexe de ce système.

2.3 Modélisation du comportement de relaxation des contraintes en utilisant une décroissance exponentielle à étirement unique

Dans cette section, la modélisation proposée par Torkelson *et al*. est utilisée. Elle considère une fonction exponentielle étirée (β) qui détermine la forme de la courbe de relaxation. Il s'agit du modèle de Kohlraush-Williams-Watts (KWW) [41] décrit par l'équation (1).

$$\frac{E(t)}{E_0} = e^{\left(-\left(\frac{t}{\lambda}\right)^{\beta}\right)} \quad \text{..... (1)}$$

Dans ce résumé, seules les courbes de relaxation du système en stœchiométrie seront discutées.

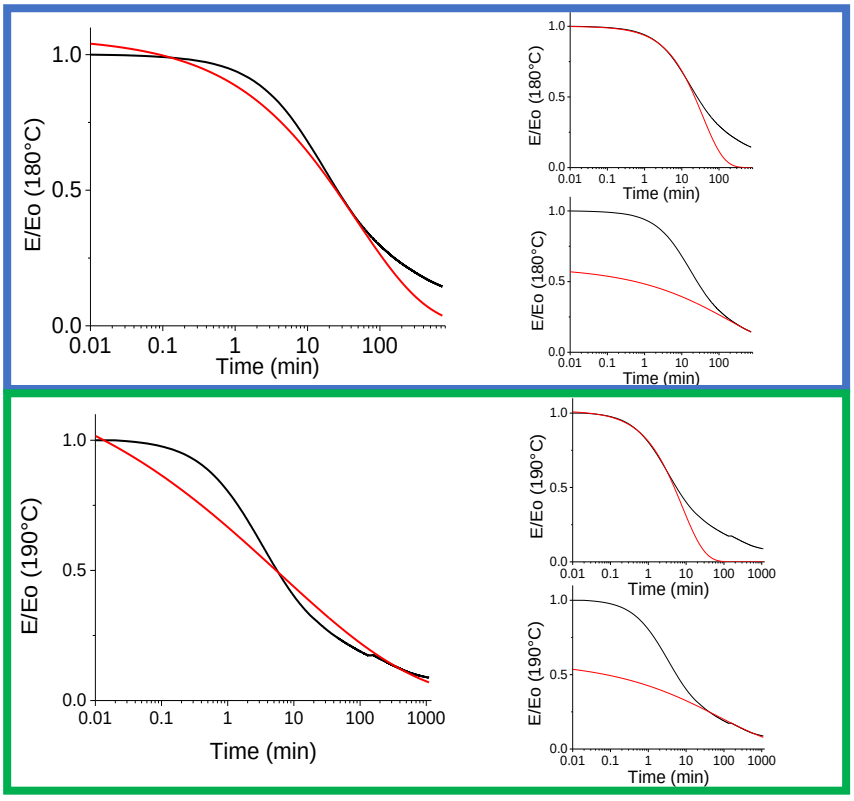

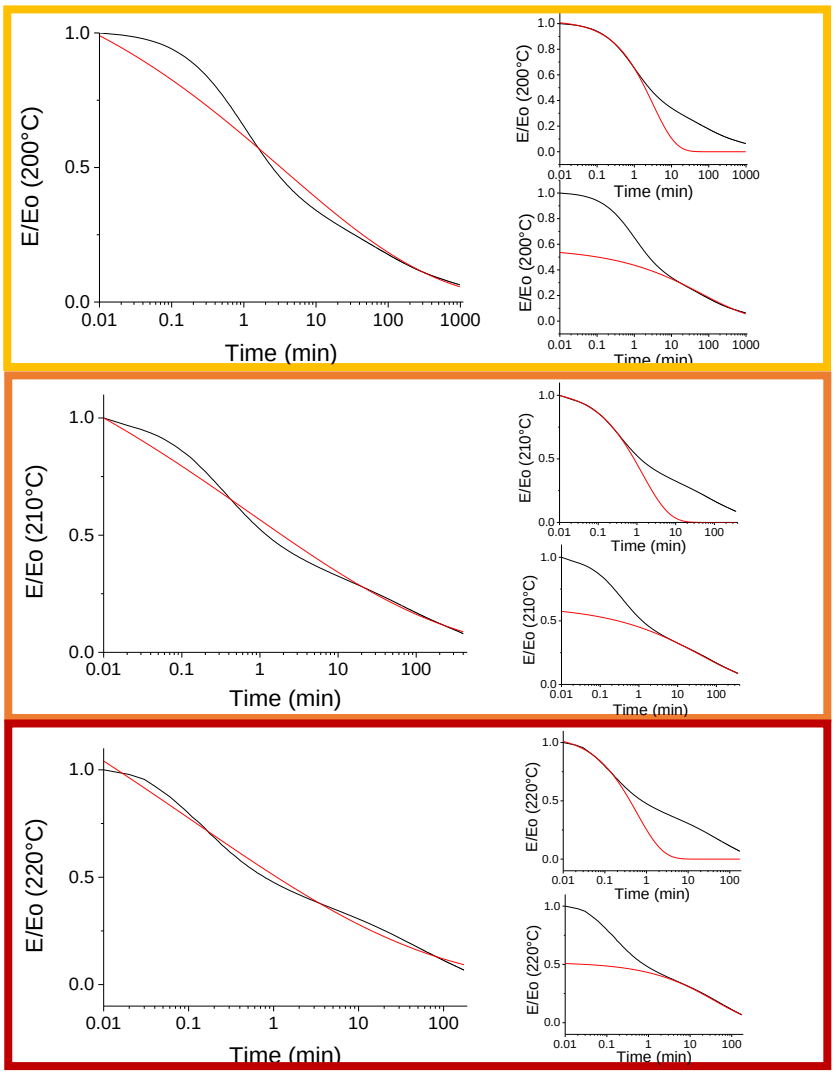

Figure 2-1. Modélisation de la relaxation de contrainte du système DGEBA–4-APDS r=1 en utilisant l'équation KWW à différentes températures. A gauche la modélisation considérant la relaxation entière, à droite la modélisation divisée en deux zones d'étude : 1) a court temps de relaxation et 2) a longs temps de relaxation.

La modélisation des courbes selon l'équation KWW montrent qu'il est impossible de décrire correctement la totalité de la relaxation en utilisant cette équation. En effet, l'observation des courbes de relaxation expérimentales normalisées présentées dans la **Figure 2-1**, montrent que deux comportements distincts sont probablement superposés. L'existence de ces deux comportements semble d'autant plus marquée que la température de test est élevée. Par conséquent, un ajustement permettant de prendre en compte la première partie et la dernière partie de la courbe de relaxation séparément a été effectué : les courbes modélisées sont présentées dans la **Figure 2-1** à droite. En séparant la courbe en deux parties, on fait l'hypothèse de

deux relaxations différentes : 1) une au court temps de relaxation et 2) et l'autre au long temps de relaxation.

T (°C)	Paramètres de la courbe complète				Paramètres des premières minutes de la courbe				Paramètres des dernières minutes de la courbe			
	E	λ	β	$\bar{\lambda}$	E	λ	β	$\bar{\lambda}$	E	λ	β	$\bar{\lambda}$
180	1.07	46.79	0.44	122.45	1.00	36.06	0.75	42.76	0.61	196.71	0.28	2417.36
190	1.32	6.13	0.21	532.28	1.02	7.83	0.72	9.64	0.59	71.33	0.26	1433.68
200	1.62	3.51	0.20	351.15	1.05	3.09	0.70	3.91	0.62	67.70	0.31	529.76
210	1.62	0.75	0.17	431.26	1.05	1.37	0.62	1.99	0.62	41.03	0.31	334.52
220	2.08	0.11	0.15	203.49	1.07	0.59	0.70	0.75	0.52	37.95	0.46	90.51

Tableau 2-1. Paramètres d'ajustement de l'équation KWW du système DGEBA–4-APDS r=1 en faisant la modélisation selon trois gammes : 1) la relaxation dans sa totalité, 2) à court temps de relaxation, et 3) à long temps de relaxation.

De cette première expérience de simulation résumée dans le **Tableau 2-1**, deux comportements semblent apparaitre pour les systèmes DGEBA–4-APDS. Par ailleurs, l'exposant de décroissance étiré β qui dicte la forme de la courbe, reste constant quelle que soit la température.

À partir des comportements observés, il a été décidé d'explorer l'approche donnée par Yu *et al.* en séparant le comportement thermo-viscoélastique en un domaine associé à la relaxation du BER et un autre lié aux mouvements classiques de la relaxation des chaînes[42]. Chaque partie est décrite par l'équation KWW, c'est-à-dire par une fonction exponentielle étirée, comme le montre l'équation (2).

$$\frac{E(t)}{E_0} = \underbrace{E_1 * e^{\left(-\left(\frac{t}{\lambda_1}\right)^{\beta_1}\right)}}_{\text{Echange des liaisons réversibles}} + \underbrace{E_2 * e^{\left(-\left(\frac{t}{\lambda_2}\right)^{\beta_2}\right)}}_{\text{Relaxation des réseaux}} \quad \text{..... (2)}$$

2.4 Modélisation du comportement de relaxation de contrainte en utilisant deux décroissances exponentielles à étirement

L'équation (2) a été utilisée pour cette modélisation, en considérant : 1) la réaction d'échange des liaisons dynamiques, obtenue à des temps de relaxation courts, et 2) le mouvement de relaxation des chaînes de polymères du réseau, atteint à des temps de relaxation longs. L'objectif est d'identifier les deux phénomènes de relaxation à partir des contraintes obtenues expérimentalement pour les différents systèmes DGEBA–4-APDS. La **Figure 2-2** présente les résultats de la modélisation ; les paramètres de cet ajustement sont résumés dans le **Tableau 2-2** pour le système en condition stœchiométrique.

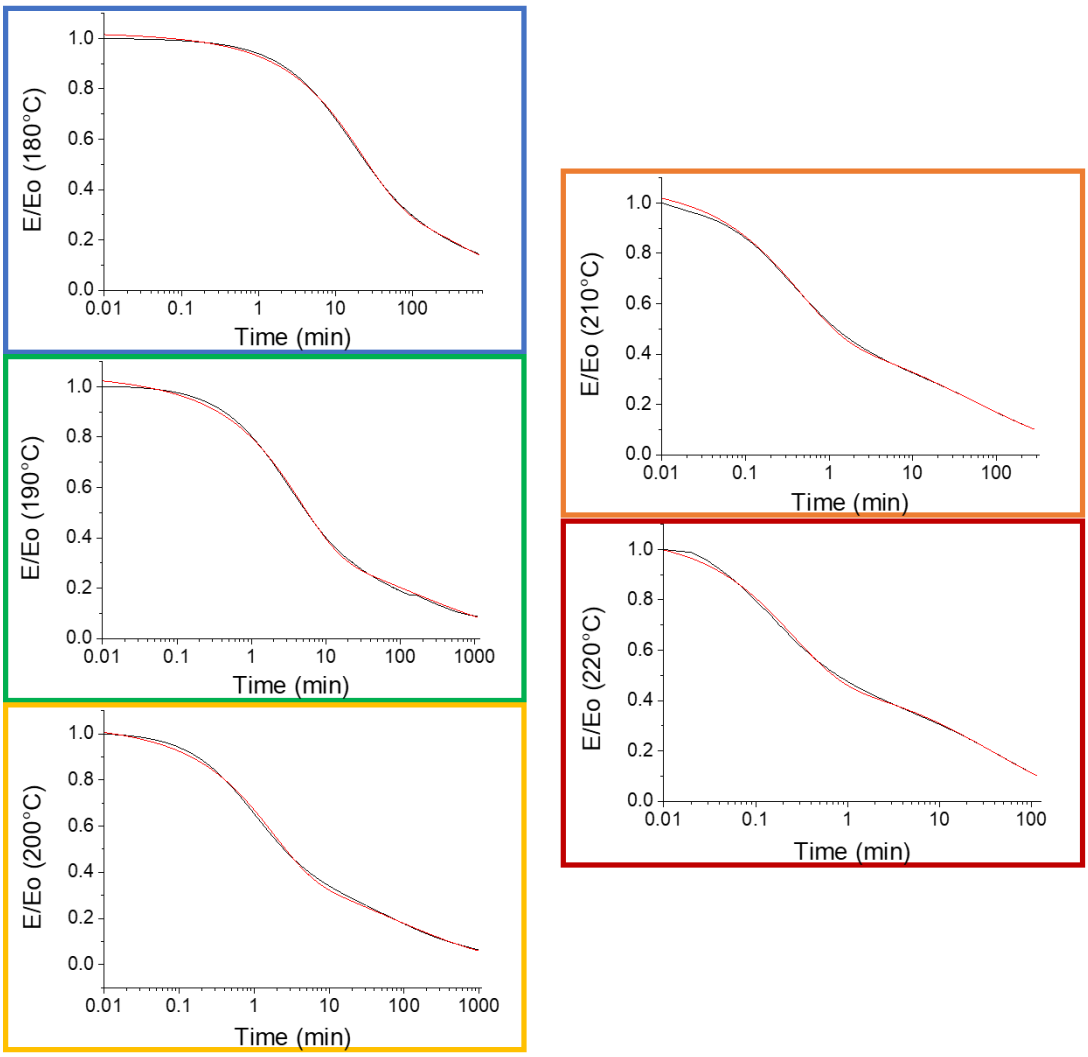

Figure 2-2. Modélisation des courbes de relaxation de contrainte obtenues expérimentalement pour le système DGEBA–4-APDS r=1 en utilisant deux fonctions exponentielles étirées à différentes températures de 180 à 220°C par palier de 10°C.

T [°C]	Echange des liaisons réversibles					Relaxation de la chaine				
	E_1	E_1%	λ_1	β_1	$\bar{\lambda}$	E_2	E_2%	λ_2	β_2	$\bar{\lambda}$
180	0.51	0.50	20.4	0.81	22.91	0.51	0.50	359.3	0.37	1458.3
190	0.54	0.50	4.5	0.79	5.1	0.53	0.50	116.9	0.27	1136.6
200	0.49	0.46	1.7	0.77	1.9	0.57	0.54	59.4	0.29	641.7
210	0.50	0.46	0.4	0.75	0.5	0.59	0.54	51.7	0.33	321.7
220	0.53	0.51	0.2	0.77	0.3	0.52	0.49	40.8	0.47	92.6

Tableau 2-2. Paramètres d'ajustement en utilisant deux fonctions exponentielles étirées pour le système DGEBA–4-APDS r=1.

A partir des informations du **Tableau 2-2** on peut noter que :

- L'utilisation de deux fonctions exponentielles étirées permet de décrire plus précisément la relaxation que l'utilisation d'une seule exponentielle étirée.
- L'exposant β_1, qui correspond à la relaxation du BER, est apparemment indépendant de la température.
- Les pré-facteurs de chacune des fonctions exponentielles étirées sont constants pour les différentes températures testées. La contribution de la réaction d'échange des liaisons (E_1%) et de la relaxation des chaines polymères du réseau (E_2%) sont équitables et indépendantes de la température.

2.5 Comportement Arrhenien : détermination de l'énergie d'activation et de la température de gel topologique

Après avoir isolé la relaxation liée aux liaisons réversibles, les temps de relaxation ont été tracés en fonction de la température pour visualiser le comportement Arrhenien caractéristique des vitrimères. Le même tracé a été effectué pour la relaxation du mouvement des chaînes polymères du réseau. Le BER suit un comportement Arrhenien tandis que la relaxation du mouvement des chaînes polymères du réseau ne le suit pas (**Figure 2-3**).

Concernant le comportement du BER, l'énergie d'activation (Ea) et la *T*v peuvent être calculées par extrapolation. Le **Tableau 2-3** résume les valeurs de Ea et de *T*v de l'équation.

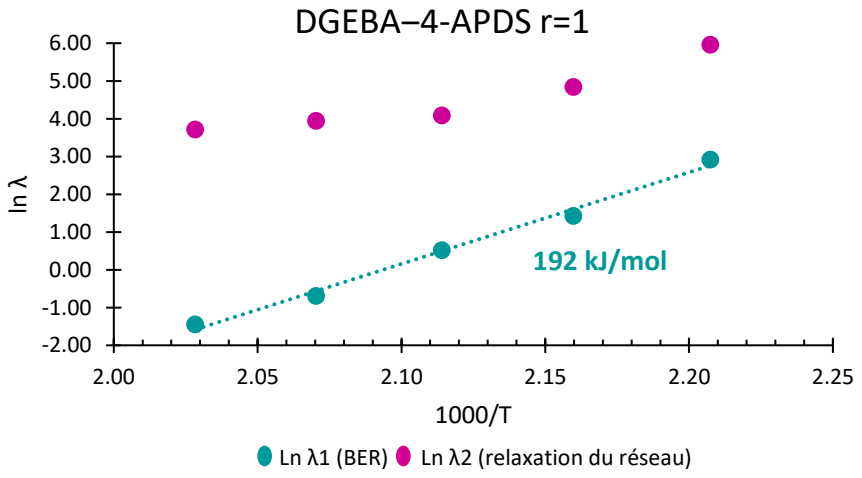

Figure 2-3. Variation des temps de relaxation caractéristiques de BER (bleu) et du mouvement des chaînes (violet) en fonction de l'inverse de la température.

	Modèle de Maxwell		Décroissance de l'exposant BER	
Système	**Ea (kJ/mol)**	***Tv* (°C)**	**Ea (kJ/mol)**	***Tv* (°C)**
r=0.8	130 ± 7	205 ± 17	213 ± 3	172 ± 3
r=1	114 ± 1	175 ± 3	192 ± 15	171 ± 3
r=1.2	147 ± 3	154 ± 5	158 ± 9	151 ± 6

Tableau 2-3. Valeurs des Ea et *T*v du système DGEBA–4-APDS à différentes stœchiométries déterminées en utilisant le modèle de Maxwell ; Ea et *T*v estimées à partir des données déconvoluées de la fonction exponentielle étirée du BER.

L'énergie d'activation estimée à partir du comportement isolé du BER est supérieure à celles trouvées en utilisant l'équation de Maxwell pour les trois stœchiométries étudiées. Les nouvelles valeurs d'énergie d'activation trouvées sont en accord avec les travaux de Ruipérez et ses collègues. Ils ont déterminé plusieurs énergies de dissociation des liaisons pour les systèmes disulfures, avec une énergie variante entre 170 à 210 kJ/mol[44].

2.6 Superposition temps-température (TTS)

La **Figure 2-3** montre deux comportements différents, l'un lié à la relaxation du BER et l'autre associé au mouvement de relaxation des chaînes du réseau. Pour tester le comportement global de la matrice vitrimère, des expériences TTS en DMA ont été réalisées sur les différents systèmes à des températures de ± 30°C autour de la *T*g. Les courbes maîtresses ont été construites et les facteurs de décalage a_T déterminés à partir des courbes multifréquences ont été tracés en fonction de la température pour les différents réseaux. Les **Figure 2-4** et **Figure 2-5** montrent, respectivement, un exemple de courbe maîtresse et la dépendance des facteurs de décalage en fonction de la température pour le système DGEBA–4-APDS r=1.

Selon les travaux de Williams, Landel et Ferry, à des températures proches de la *T*g et supérieure, la dépendance du facteur de décalage a_T à la température est décrite par l'équation empirique suivante (3)[34, 45].

$$log\ a_T = \frac{-C_1(T-T_{ref})}{C_2+T-T_{ref}} \quad \text{..... (3)}$$

Où C_1 et C_2 sont les paramètres du modèle déterminés par l'ajustement par rapport aux données expérimentales, et T_{ref} est généralement la *T*g ou la *T*α du matériau.

De plus, l'équation WLF permet de déterminer l'énergie apparente d'activation des phénomènes de relaxation à la température de référence en suivant l'équation (4).

$$Ea_{apparente} = 2.303 * R * T_{ref}^2 \frac{C_1}{C_2} \quad \text{..... (4)}$$

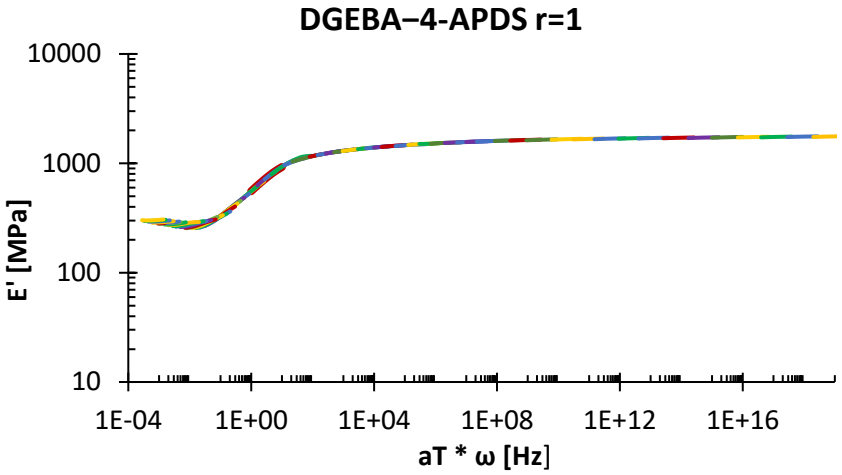

Figure 2-4. Courbe maîtresse du réseau DGEBA–4-APDS r=1 à ± 30 °C T_{ref}, où T_{ref} = 170 °C.

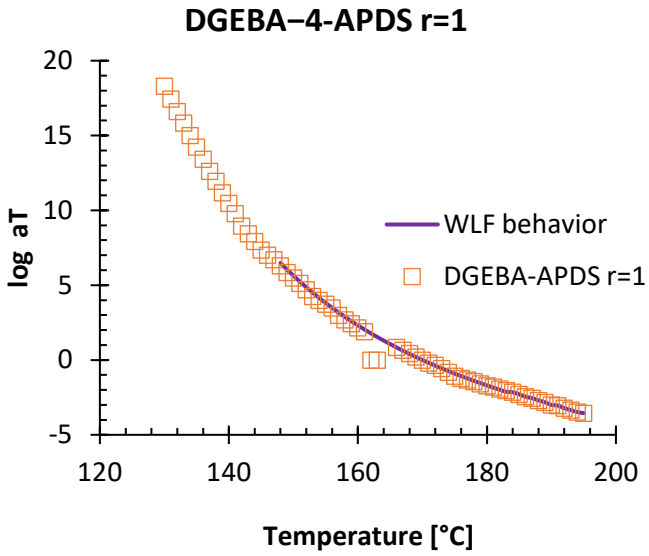

Figure 2-5. Le facteur de décalage correspondant a_T et l'équation (3) en fonction de la température pour le système DGEBA–4-APDS r=1.

Les paramètres C_1 et C_2 correspondants de la loi WLF ont été déterminés ainsi que l'énergie d'activation de la transition vitreuse des différents réseaux. Les paramètres sont regroupés dans le **Tableau 2-4**.

Système	T_{ref} (°C)	C1	C2	$Ea_{apparent}$ (kJ/mol)
DGEBA–4-APD r=0.8	158	14.42	68.50	736
DGEBA–4-APD r=1	170	12.85	65.62	749
DGEBA–4-APD r=1.2	153	13.27	67.71	681
DGEBA-DDM	177	14.99	65.05	893

Tableau 2-4. Paramètres C1 et C2 et référence de température utilisée dans l'ajustement.

Les paramètres C_1 et C_2 sont différents de ceux fondés par Williams, Landel, et Ferry pour le polystyrène, mais de tels comportements ont déjà été observés. Ils sont probablement liés à la grande dispersion des chaînes des réseaux par rapport au polystyrène[13]. En ce qui concerne $Ea_{apparente}$, elle diminue lorsque la concentration en liaisons dynamiques augmente.

2.7 Conclusions

Un modèle de relaxation capable de mieux décrire le comportement de relaxation des systèmes DGEBA–4-APDS que le modèle de Maxwell a été établi. Le modèle considéré est composé de deux modes de relaxation : la relaxation de la réaction d'échange des liaisons réversibles (BER), et la relaxation des chaînes du réseau. Les relaxations ont été modélisées en utilisant l'équation KWW avec des fonctions exponentielles étirées. L'utilisation de ce modèle a permis de fournir une description plus précise du comportement de relaxation des contraintes. L'isolement du comportement BER a permis de déterminer une énergie d'activation et une température de gel topologique différentes de celles trouvées par le modèle de Maxwell. Le modèle adapté a été aussi appliqué pour les systèmes hors-stœchiométrie. En ce qui concerne l'énergie d'activation, une diminution de sa valeur a été constatée lorsque la quantité de liaisons covalentes réversibles augmente dans le réseau, ce qui est en accord avec de nombreux autres travaux employant différents systèmes vitrimères. Il n'aurait pas été possible d'observer ce comportement en utilisant simplement le modèle de Maxwell car celui-ci considère une seule relaxation, alors qu'en réalité il s'agit d'une superposition de plusieurs relaxations distinctes.

3. Résine époxy vitrimère renforcée par des substrats de nano fibrilles de cellulose

3.1 Introduction

Les matériaux composites sont présents dans notre vie quotidienne, comme dans l'emballage, la construction, l'automobile, ou même dans l'industrie aérospatiale[46]. Le besoin croissant de matériaux de plus en plus respectueux de l'environnement a déclenché diverses recherches pour proposer des solutions écologiques sans compromettre les bonnes performances des matériaux.

Les fibres naturelles telles que les fibres végétales, comme les fibrilles de cellulose, ont attiré l'attention en tant que renfort dans les matrices polymères en raison de leurs propriétés telles que leur biodégradabilité, leur recyclabilité, leur faible densité, leur module et, et leur coût. Par conséquent, de nombreux travaux utilisant la cellulose comme renfort ont été menés. Ces recherches ont montré comment l'utilisation de la nanocellulose peut offrir une résistance mécanique et un module élevé aux matériaux composites[47, 48, 49].

De nombreux travaux ont été consacrés à l'étude des whiskers et des nanofibrilles de cellulose. Les whiskers de cellulose ont une capacité de renfort élevée mais leur production est coûteuse et prend du temps. Cet inconvénient a déclenché la nécessité d'explorer l'utilisation de nanofibrilles de cellulose (NFC) qui sont plus faciles à préparer à la place des whiskers.

Dans le domaine des composites à base de résine époxy, l'incorporation des nanofibrilles de cellulose n'est pas toujours facile[50]. Donc, diverses méthodes d'incorporation ont été développées, comme l'imprégnation d'aérogels de cellulose, la modification de surface de la cellulose pour améliorer leur dispersion, l'agitation mécanique à grande vitesse ou des suspensions de cellulose pré-imprégnées[51, 52, 53]. La dernière technique d'incorporation, adaptée par Berglund *et al.*[54], a donné des résultats favorables. La technique consiste en imprégner de résine un substrat de microfibrilles partiellement séché ce qui conduit à une diffusion de la résine dans la structure des microfibrilles.

D'autre part, les matériaux vitrimères qui présentent un comportement auto-réparateur, peuvent réduire les déchets en termes de matériaux mais leur résistance mécanique reste assez faible. C'est pourquoi, plusieurs composites à base de vitrimères ont été récemment étudiés[11]. On note l'utilisation de fibres de verre[32], de fibres de carbone[20], de nanotubes de carbone[55], de silice[22] et de la cellulose[56, 57]. Il existe en particulier des travaux explorant l'utilisation de fibres de cellulose basées sur la chimie de transestérification[58]. Dans ces travaux, les fibres de cellulose jouent non seulement un rôle de renfort mais aussi un rôle actif dans la réaction d'échange. Walther *et al.* ont exploré la fabrication de composites vitrimère-cellulose dans des conditions aqueuses permettant la diffusion optimale de la matrice polymérique dans les fibrilles[57].

Si les travaux utilisant la cellulose et une matrice vitrimère basée sur l'échange par transestérification sont prometteurs, il peut être intéressant d'explorer d'autres méthodes avec les NFC comme renfort. Le système DGEBA–4-APDS a retenu l'attention en tant que structure prometteuse en raison de sa résistance à haute température avec une *T*g supérieure à 100°C (en fonction du rapport stœchiométrique). En effet, ce système a été exploré en utilisant des renforts tels que des fibres de carbone et de la nano-silice modifiée en surface. Les deux cas montrent des résultats prometteurs, se traduisant soit par une augmentation du module élastique, soit par une amélioration de la relaxation des contraintes.

3.2 Objectif

- ⇨ Elaborer un composite vitrimère qui combine une *T*g élevée avec des propriétés mécaniques améliorées en incorporant des nanofibrilles de cellulose sans perturber les propriétés vitrimères du matériau.
- ⇨ L'utilisation de fibrilles dispersées dans la matrice époxy peut améliorer les propriétés mécaniques comme le module d'Young ou la résistance à la rupture.

3.3 Approche expérimentale

L'approche inspirée par Berglund *et al.* a été retenue car elle permet d'obtenir des matrices époxy vitrimères tout en préservant la distribution des NFC[54]. Cette approche consiste à élaborer un substrat cellulosique (10%) imprégné de solvant et à incorporer ensuite la résine (90%) (**Figure 3-1**). Le solvant est ensuite lentement remplacé par de la matrice époxy dans le substrat, réduisant ainsi les éventuelles concentrations de contraintes. Le cycle de réticulation utilisé est le même que celui optimisé pour le système DGEBA–4-APDS, cycle r=1d exposé dans la section 1.4.1.

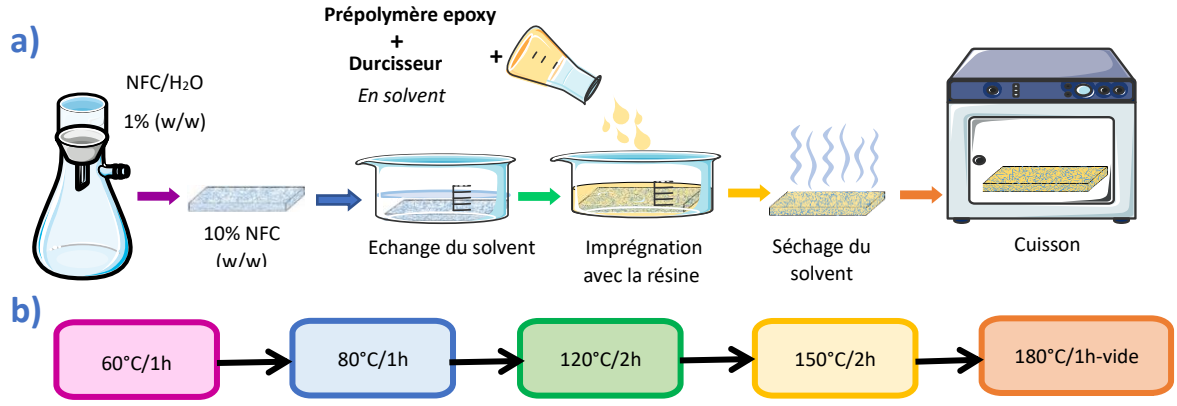

Figure 3-1. a) le protocole d'incorporation du NFC dans la résine époxy (modifié à partir de celui de Berglund *et al.*) et b) le cycle de réticulation utilisé.

Les propriétés thermomécaniques ont été étudiées en réalisant une rampe de température, afin de déterminer le module de conservation (E') à 30°C et sur le plateau caoutchoutique à T=*T*g+30°C, le facteur d'amortissement mécanique (tan δ) et la densité de réticulation (ρ) pour les systèmes avec différents rapports amine/époxy.

Les propriétés caractéristiques des vitrimères de ces matériaux composites ont été démontrées en expérimentant 1) la connectivité permanente en réalisant un test de gonflement, 2) la relaxation et la fluidité des réseaux, qui conduisent à un réarrangement de leur topologie et 3) la mise en évidence d'une nouvelle température de transition différente à la *T*g : La *T*v.

Enfin, comme pour les systèmes DGEBA–4-APDS, un modèle qui combine la relaxation liée au BER et la relaxation liée au mouvement des chaînes de polymères a été appliqué. Il est décrit par deux fonctions exponentielles étirées pour modéliser finement les deux branches principales de la relaxation.

3.4 Résultats de la caractérisation et discussion

3.3.1 Performance thermomécanique

Comme pour le système vitrimère DGEBA–4-APDS r=1, les propriétés thermomécaniques du composite ont été étudiées (**Figure 3-2**).

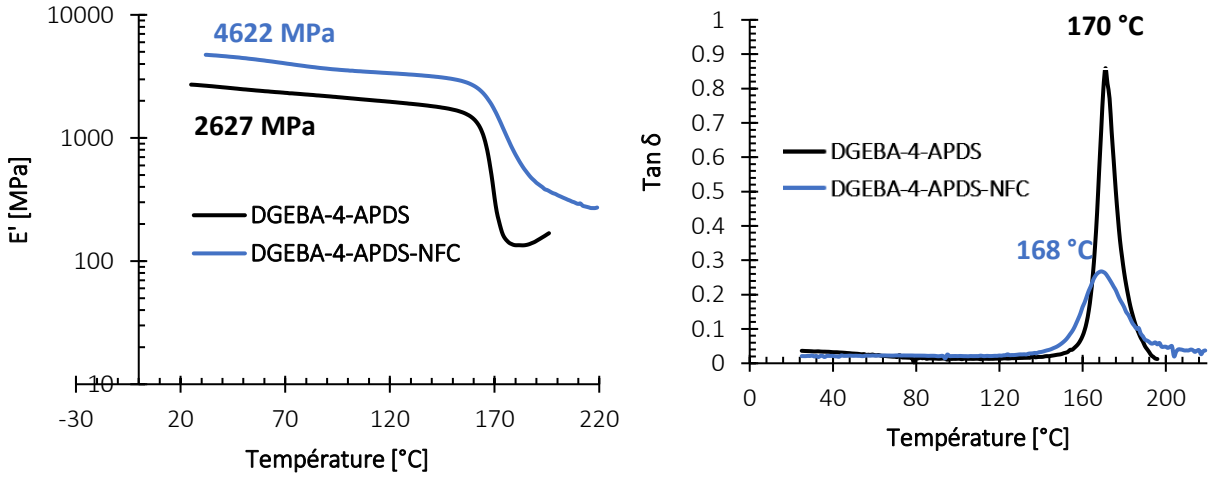

Figure 3-2. Module de stockage (E') et le facteur d'amortissement (tan δ) en fonction de la température pour le système DGEBA–4-APDS r=1 avec et sans NFC.

Le **Tableau 3-1** récapitule les valeurs de *T*g, des modules E' dans les plateaux vitreux et caoutchoutique, des *T*α, des températures de dégradation et les densités de réticulation (ρ) des résines DGEBA–4-APDS avec et sans NFC.

Système	*Tg* (°C)	Température de dégradation (°C)	E' à 30°C (MPa)	E' à *Tg* + 30°C (MPa)	*Tα* (°C)	ρ (mol/m³)
DGEBA–4-APDS	167 ± 0.5	359 ± 1	2627 ± 69	179 ± 40	170 ± 1	1.53E+04
DGEBA–4-APDS-NFC	162 ± 1	354 ± 1	4622 ± 57	313 ± 52	169 ± 0.2	2.71E+04

Tableau 3-1. Température de transition vitreuse (*Tg*), température de dégradation, module élastique (E') mesuré à 30 °C, et à *Tg* + 30°C, valeurs de Tα et densité de réticulation (ρ) du DGEBA–4-APDS r=1 avec et sans NFC.

Le faible changement de la *Tg* observé dans le **Tableau 3-1** peut s'expliquer par des réactions secondaires d'estérification entre les groupes hydroxyles de la cellulose et le cycle époxyde de la DGEBA[58]. L'augmentation du module de conservation est notable (76%). Cette augmentation est cohérente avec d'autres formulations de composites renforcés par des fibres naturelles ou des NFC[59, 60]. On peut noter un changement important de l'intensité et de la largeur de tan δ (**Figure 3-2**), ce qui signifie que le composite élaboré est moins homogène que le système vierge. La diminution de l'intensité de tan δ implique que l'ajout de NFC a restreint la capacité d'amortissement de la matrice polymère.

3.3.2 Caractérisation morphologique

La **Figure 3-3** montre des images MEB en coupe transversale des NFC seules et du composite DGEBA–4-APDS-NFC. Le composite présente des agrégats de fibrilles et des fibrilles bien dispersées. La zone A présente d'importants agrégats de fibrilles qui se sont probablement formés par floculation lors de l'étape de filtration. La zone B présente des points blancs qui semblent correspondre à des extrémités fracturées des NFC, suggérant une bonne adhésion interfaciale. En revanche, la zone B entourée en pointillé montre un interstice entre les fibrilles et la résine ce qui engendre une très faible adhésion interfaciale.

Bien que l'incorporation de la NFC dans la résine époxy semble donner des résultats prometteurs, plusieurs travaux ont révélé que la modification de la surface de la NFC pourrait améliorer l'adhésion interfaciale, et donc la résistance mécanique du matériau[52, 61, 62].

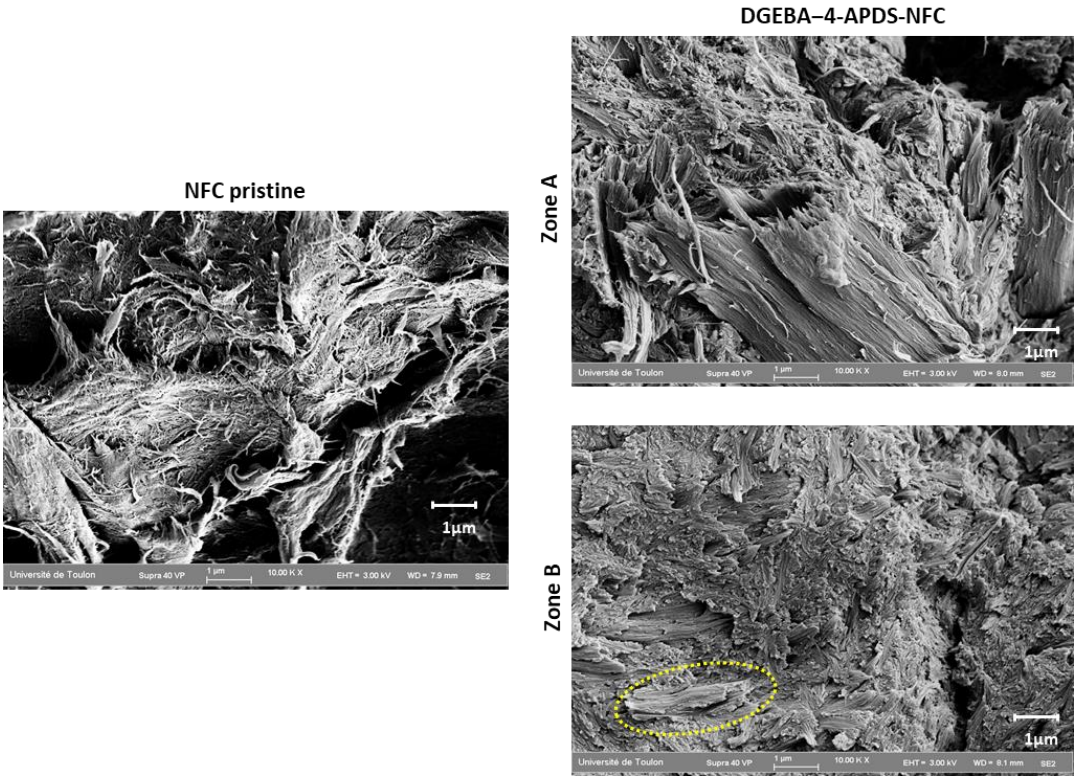

Figure 3-3. Images MEB en coupe transversale de NFC vierge et de composite DGEBA–4-APDS-NFC divisée en deux zones A et B.

3.3.3 Caractérisation des vitrimères

3.3.3.1 Connectivité permanente

Le test de gonflement a été réalisé avec du THF, DMF, EMP, pendant une semaine à température ambiante et avec du 1,2,4-Trichlorobenzène pendant 1h à 190 °C. Comme pour le système DGEBA–4-APDS r=1, le composite ne présente aucune perte de connectivité dans les quatre solvants utilisés. En revanche, une faible perte de masse a été observée (moins de 2%) après séchage des échantillons composites. Cette perte de masse est probablement liée à l'élimination de quelques nanofibrilles de cellulose.

3.3.3.2 Relaxation de contrainte

Des expériences de relaxation de contrainte avec une déformation de 0.1% ont été réalisées sur des systèmes DGEBA–4-APDS et DGEBA–4-APDS-NFC. Les résultats sont présentés dans la **Figure 3-4**, ils montrent que les temps de relaxation du composite sont beaucoup plus longs que pour le système époxy pur. Ce retard au niveau de la relaxation peut être expliqué par la restriction de la mobilité des chaînes générée par les NFC. Un comportement similaire a été rapporté par Wang *et al*. lors de l'ajout de nano-silice à leur système.

En appliquant l'équation d'Arrhenius, l'énergie d'activation (Ea) a pu être déterminée, et par extrapolation, la température de gel topologique (*T*v).

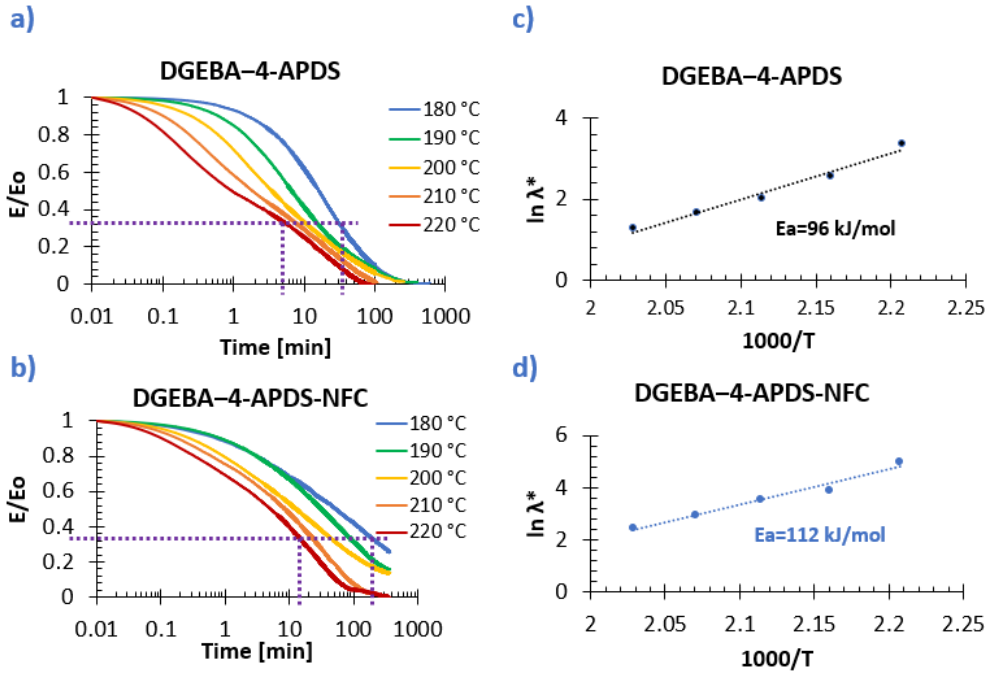

Figure 3-4. Comportement de relaxation de contrainte et tracé d'Arrhenius du DGEBA–4-APDS avec et sans NFC sous une déformation de 0.1%.

Système	Ea (kJ/mol)	*T*v (°C)
DGEBA–4-APDS	96	169
DGEBA–4-APDS-NFC	112	212

Tableau 3-2. L'énergie d'activation (Ea) et la température de de gel topologique (*T*v) du DGEBA–4-APDS avec et sans NFC à un rapport amine/époxy égal à 1 sous une déformation de 0.1%.

Le **Tableau 3-2** récapitule les Ea et *T*v calculées en suivant la loi d'Arrhenius et en considérant une seule relaxation. L'énergie d'activation ne semble pas être impactée par l'ajout des nanofibrilles, mais la relaxation du système prend plus de temps (de 30 min jusqu'à plus de 200 min a une température de 180°C). Contrairement aux travaux rapportés par Wang *et al.*, les nanofibrilles n'augmentent pas la barrière énergétique des liaisons réversibles. Concernant la température de gel topologique, une augmentation de 40°C est mesurée avec l'ajout des NFC.

Néanmoins, l'emploi du modèle de Maxwell pour décrire correctement la relaxation du système vitrimère n'est pas suffisamment, car il s'agit d'une déconvolution de plusieurs phénomènes ; par conséquent, les informations préliminaires de l'énergie d'activation et de la *T*v présentées dans le

Tableau 3-2 doivent être prises avec précaution. De façon à améliorer la modélisation de la relaxation de contraintes, un modèle avec deux relaxations distinctes a été étudié pour le composite.

2.4.3.2.1 Modélisation de la relaxation de contrainte

Le modèle de relaxation de contraintes proposé précédemment, considérant deux relaxations liées à la relaxation des BER et à la relaxation aux mouvements des chaînes polymère, a été testé sur le matériau composite[42]. La **Figure 3-5** montre la modélisation effectuée en utilisant l'équation (2). Les **Tableau 3-3** et **Tableau 3-4** résument les principaux paramètres des simulations pour les systèmes DGEBA–4-APDS-NFC et DGEBA–4-APDS respectivement. Les expériences ont été effectuées sous une déformation de 0.1% et les paramètres décrits correspondent aux équations (2) et (5).

$$\frac{E(t)}{E_0} = \underbrace{E_1 * e^{\left(-\left(\frac{t}{\lambda_1}\right)^{\beta_1}\right)}}_{\text{Echange des liaisons réversibles}} + \underbrace{E_2 * e^{\left(-\left(\frac{t}{\lambda_2}\right)^{\beta_2}\right)}}_{\text{Relaxation des réseaux}} \quad \text{(2)}$$

$$\bar{\lambda} = \frac{\lambda\, \Gamma\left(\frac{1}{\beta}\right)}{\beta} \quad \text{(5)}$$

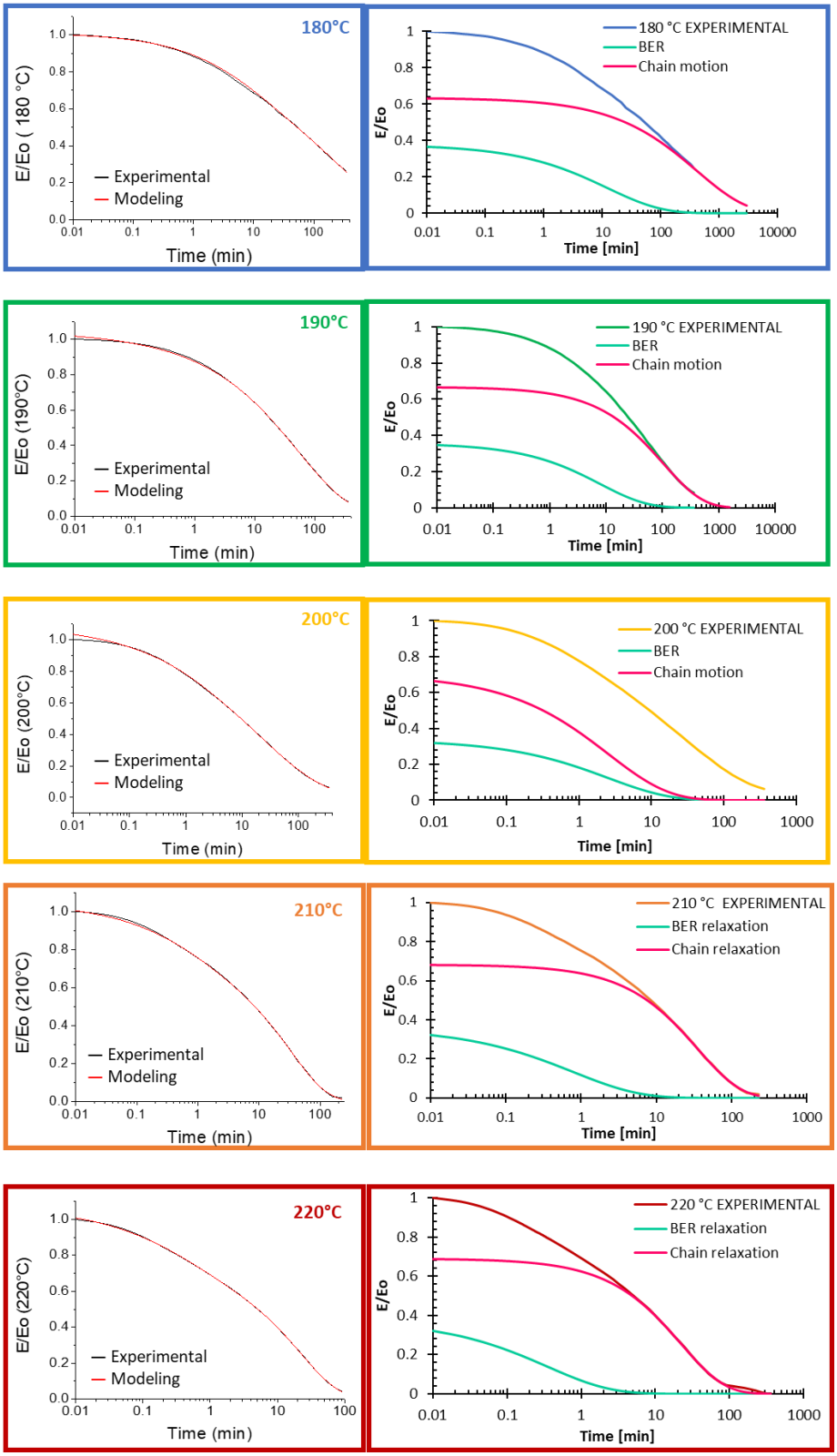

Figure 3-5. A gauche, la modélisation de la relaxation expérimentale de contrainte normalisée du système DGEBA–4-APDS-NFC en utilisant deux fonctions exponentielles étirées à différentes températures de 180 à 220°C. A droite, la déconvolution des deux phénomènes de relaxation.

T[°C]	Echange des liaisons réversibles					Relaxation de la chaine				
	E_1	E_1%	λ_1	β_1	$\bar{\lambda}$	E_2	E_2%	λ_2	β_2	$\bar{\lambda}$
180	0.38	0.37	12.2	0.47	27	0.63	0.63	420.1	0.51	817
190	0.36	0.35	7.9	0.53	14	0.67	0.65	103.1	0.62	149
200	0.34	0.32	2.5	0.52	4.7	0.70	0.68	50.5	0.47	113
210	0.36	0.35	0.8	0.50	1.6	0.68	0.65	35.5	0.76	42
220	0.38	0.35	0.4	0.51	0.7	0.69	0.65	22.4	0.74	27

Tableau 3-3. Paramètres d'ajustement utilisant deux fonctions exponentielles étirées pour le système DGEBA–4-APDS-NFC sous une déformation de 0.1%.

T [°C]	Echange des liaisons réversibles					Relaxation de la chaine				
	E_1	E_1%	λ_1	β_1	$\bar{\lambda}$	E_2	E_2%	λ_2	β_2	$\bar{\lambda}$
180	0.52	0.51	15.4	0.78	17.8	0.49	0.49	54.8	0.79	62.8
190	0.51	0.50	5.2	0.78	5.9	0.52	0.50	33.2	0.58	51.7
200	0.51	0.50	1.8	0.79	2.1	0.50	0.50	29.7	0.67	39.5
210	0.52	0.51	0.6	0.80	0.7	0.50	0.49	23.8	0.79	27.1
220	0.53	0.51	0.3	0.81	0.3	0.50	0.49	17.9	0.78	20.7

Tableau 3-4. Paramètres d'ajustement utilisant deux fonctions exponentielles étirées pour le système DGEBA–4-APDS sous une déformation de 0.1%.

Les résultats exposés dans le **Tableau 3-3** et le **Tableau 3-4** affichent les résultats des données de simulation. Concernant le temps de relaxation lié à la **relaxation des BER (λ1), les valeurs ne sont pas si différentes les unes des autres** entre la résine et le composite. De plus, **les valeurs de β1 restent constantes**. Bien que la valeur ne soit pas aussi élevée que le système sans NFC, les valeurs sont stables.

Un autre détail intéressant observé est le changement de la fraction de contribution (E%). Le composite **montre une réduction de la fraction de la contribution liée à la relaxation BER (E1%) par rapport à la résine.** *Ce résultat s'explique par l'augmentation relative des liaisons non-dynamiques*.

Les temps de relaxation trouvés dans la simulation des systèmes DGEBA–4-APDS avec et sans NFC ont été tracés en fonction de l'inverse de la température (**Figure 3-6**). Le graphique montre deux comportements différents. Le premier suit un comportement de type Arrhenien (bleu), et le second non-Arrhenien (violet). A partir de ces graphiques, l'énergie d'activation et la température de gel topologique peuvent être estimées. Les résultats sont résumés dans le **Tableau 3-5**. L'énergie

d'activation du système composite est proche de celle de la résine. Ainsi, l'utilisation de la NFC ne modifie pas significativement la barrière énergétique du mécanisme d'échange.

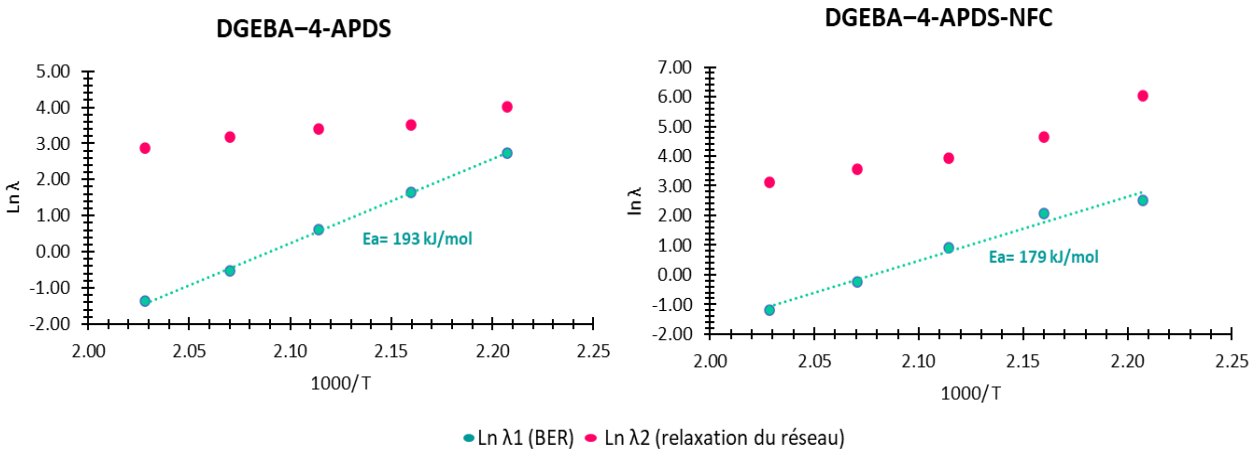

Figure 3-6. Variation du temps de relaxation caractéristiques des BER (en bleu) et du mouvement de la chaîne (en violet) en fonction de l'inverse de la température. Graphes tracés à partir des données présentées dans les Tableau 3-3 et le Tableau 3-4.

	Modèle de Maxwell		Décroissance de l'exposant BER		Dilatométrie en tension
Système	Ea (kJ/mol)	*T*v (°C)	Ea (kJ/mol)	*T*v (°C)	*T*v (°C)
DGEBA–4-APDS	96	169	193	169	184
DGEBA–4-APDS-NFC	112	212	174	180	186

Tableau 3-5. Ea et *T*v du système DGEBA–4-APDS avec et sans NFC en utilisant le modèle de Maxwell, Ea et *T*v à partir des données déconvoluées de la décroissance de l'exposant étiré des BER, et la *T*v déterminée par le test de dilatométrie.

3.3.3.3 Test de dilatométrie

Des tests de dilatométrie ont été réalisés pour mettre en évidence de façon expérimentale une nouvelle température de transition differente de la *T*g et qui est caractéristique d'un vitrimère : la *T*v. Pour le matériau composite, les expériences ont été réalisées en mode tension en raison de la forme de l'échantillon, contrairement à la résine pure qui avait été testée en mode compression. En raison de cette sollicitation mécanique particulière, la transition terminale peut être déroutante. En effet, ce phénomène est également noté dans d'autres travaux utilisant la même sollicitation mécanique en tension[31, 63].

La **Figure 3-7** présente les essais de dilatométrie des systèmes DGEBA–4-APDS avec et sans NFC réalisés en mode tension. Le **Tableau 3-6** regroupe les températures de transition déterminées par

les différentes techniques. Les résultats de *T*v obtenues par dilatométrie en mode tension diffèrent légèrement de celles trouvées par dilatométrie en mode compression et par l'extrapolation de la loi d'Arrhenius.

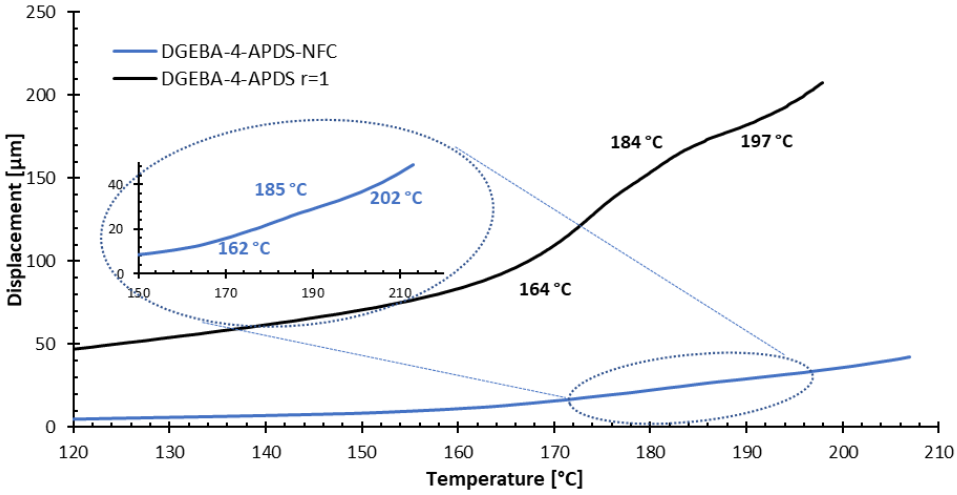

Figure 3-7. Essai de dilatométrie des systèmes DGEBA–4-APDS (noir) et DGEBA–4-APDS-NFC (bleu).

	Dilatométrie en tension		DSC	Décroissance de l'exposant BER
System	***Tg* (°C)**	***Tv* (°C)**	***Tg* (°C)**	***Tv* (°C)**
DGEBA–4-APDS	164 ± 2	183 ± 1	167 ± 1	171
DGEBA–4-APDS-NFC	162 ± 2	188 ± 1	162 ± 2	180

Tableau 3-6. *Tg* et *Tv* des systèmes DGEBA–4-APDS avec et sans NFC par mode de tension, expérience DSC, et à partir des données déconvoluées de la décroissance de l'exposant étiré de la relaxation BER.

En outre, la *T*v enregistrée pour le composite est plus élevée que pour la résine pure. L'augmentation de la *T*v est probablement liée à l'augmentation du module au-delà de la *T*α induite par la présence des NFC. De plus, la présence des NFC bloque les relaxations des chaînes du réseau sans pour autant perturber de façon majeure l'énergie d'activation. Une légère augmentation de la température de gel topologique est remarquée.

Le comportement de fluage est un phénomène indésirable des matériaux vitrimères. Dans la **Figure 3-7**, une diminution significative du fluage est observée. Cette caractéristique pourrait encourager l'étude de ces composites vitrimères.

3.5 Conclusions

Un protocole qui permet d'élaborer un composite-vitrimère à base de DGEBA–4-APDS et des nanofibrilles de cellulose a été établi en incorporant 10% (w/w) des charges. Le composite présente une haute *T*g et des propriétés mécaniques améliorées par rapport à la résine. Une augmentation du module de conservation à l'état vitreux et caoutchoutique a été obtenue.

L'analyse morphologique des échantillons du composite a montré des nanofibrilles de cellulose plus ou moins bien dispersées dans la matrice, ce qui se traduit par une augmentation relativement faible des propriétés mécaniques par rapport à la quantité massique de charge utilisée. Les agrégats de fibrilles observés dans certaines zones ainsi que les faibles interactions mise en évidence par des détachements de fibres en sont probablement l'explication.

Les propriétés caractéristiques des vitrimères ont été maintenues et n'ont pas été fortement impactées malgré l'incorporation de NFC comme renforts. La connectivité permanente a été mise en évidence dans des solvants inertes à température ambiante (THF, et EMP) et à haute température (tri chlorobenzène). Le matériau s'est relaxé à haute température, mais les temps de relaxation étaient beaucoup plus longs que pour la résine pure. En outre, la relaxation a été modélisée en séparant la relaxation liée aux réactions d'échange des liaisons et de la relaxation du réseau époxy. L'énergie d'activation du composite déterminé par la loi d'Arrhenius à partir de la branche de BER est assez similaire à celle de la résine pure. Ainsi, l'incorporation des NFC ne modifie pas l'énergie d'activation. Concernant la *T*v, une augmentation a été remarquée, probablement liée à l'augmentation du module du matériau. Deux températures de transition ont été mises en évidence en effectuant le test de dilatométrie. De plus, les essais de dilatométrie ont révélé une réduction significative du fluage après l'incorporation des NFC.

4 Fonctionnalisation chimique de la surface des nanofibrilles de cellulose par des agents de couplage glycidyl silanes.

4.1 Introduction

Les nanofibrilles de cellulose (NFC) ont attiré l'attention de plusieurs types de recherche en raison de leurs excellentes propriétés mécaniques. Néanmoins, le caractère intrinsèquement hydrophile des NFC limite à l'état vierge leur utilisation dans une résine époxy. La forte tendance à l'auto-agrégation due aux nombreux groupes hydroxyles limite la bonne dispersion dans la matrice. Par ailleurs, la forte sensibilité à l'eau peut être problématique pour certaines applications. Pour pallier à ces difficultés, la modification chimique de surface a été utilisée[48, 51, 52, 62, 64].

Les NFC étant respectueuses de l'environnement, leur modification de surface doit l'être autant que possible avec l'utilisation d'une méthode durable : un faible coût énergétique, l'emploi de solvants non toxiques, et de bonnes propriétés mécaniques permettant la durabilité du matériau. La silylation nous a semblé répondre à ces exigences[65, 66].

De nombreux protocoles de silylation des NFC ont été développés et décrits dans la littérature, dotant la surface des microfibrilles d'une grande variété de groupes fonctionnels pour des utilisations ou des applications futures [52, 67, 68, 69]

Malgré des efforts importants pour mettre en évidence les réactions et les phénomènes en surface, de nombreuses questions concernant la conformation des siloxanes demeurent, tel est le cas de l'auto-condensation des silanes. Cette réaction induit un réseau dense de siloxanes entourant les NFC avec une condensation probablement incomplète[70, 71], et une structure condensée physisorbée. La présence de cette structure pourrait générer une faible adhésion entre les fibrilles et la matrice, entrainant une faible capacité de transfert de charge lors d'une sollicitation mécanique. L'extraction Soxhlet nous a semblé un outil pertinent pour éliminer les silanes faiblement liés, qui peuvent défavoriser l'adhésion fibre/matrice. Les agents de couplage silanes choisis sont le 3-glycidyloxypropyl triméthoxysilane (GPS) et le 3-glycidoxyloxyproyl diméthyléthoxysilane (GPMES). Le GPS, avec ses trois sites réactifs possibles, présente une probabilité élevée de former un réseau autour des fibrilles. Le GPMES, qui n'a qu'un seul site réactif possible, ne peut former qu'une monocouche ou un simple dimère physisorbé à la surface des fibrilles.

4.2 Objectif

⇨ L'objectif principal de cette section est la production des nanofibrilles de cellulose avec des groupes époxy sur leur surface. Cette fonctionnalisation permettra d'améliorer l'adhésion interfaciale des fibrilles dans une résine époxy vitrimère en utilisant des glycidoxy silanes. Pour atteindre cet objectif, la mise en place d'un protocole de modification de surface des NFC a été établi. La caractérisation des réseaux de siloxane sur la surface des NFC a été effectuée.

4.3 Approche expérimentale

A partir de la littérature, quatre protocoles ont été établis et évalués. Le **Tableau 4-1** résume les protocoles de fonctionnalisation suivis. Après chaque réaction, les échantillons ont été lavés avec un mélange EtOH/H_2O et de l'acétone pour éliminer les silanes faiblement adsorbés. Ensuite, les

échantillons ont été séchés sous vide à 120 °C pendant 12 h. Le composé obtenu est sous forme de poudre blanche. La dernière étape consiste en une extraction Soxhlet pendant 48h avec de l'acétone pour les NFC vierges (témoin) et les NFC modifiées.

	Protocole	pH	m_{NFC} (g) (1% m/m)	V_{GPS} (µL)	Temps de réaction	Température (°C)
1	NFC-GPS - **H^+/H_2O**	3	10	300	4h	46
2	NFC- GPS - **EtOH**	Neutre				80
3	NFC – GPS - **Acétone**	Neutre				25
4	NFC –GPS - **EtOH/ H^+/ H_2O (7:3)**	3				80

Tableau 4-1. Protocoles de fonctionnalisation des NFC par GPS inspirées des travaux de la littérature.

4.4 Résultats de la caractérisation et discussion

4.4.1 Caractérisation Chimique

La **Figure 4-1** montre les spectres FTIR des NFC vierges et modifiées suivant les conditions exposées dans le **Tableau 4-1**. Les spectres ont été normalisés par rapport à la bande à 1160 cm^{-1}.

La vibration la plus importante pour cette étude se situe dans la région de 822 à 793 cm^{-1}, liée à la vibration Si-O-C [52, 69, 72, 73, 74] . Les intensités des bandes d'absorption Si-O-C sont plus élevées lors d'une modification en milieu acide et éthanol. Pour cela, les deux premiers protocoles ont été choisis pour continuer la suite de cette étude de fonctionnalisation.

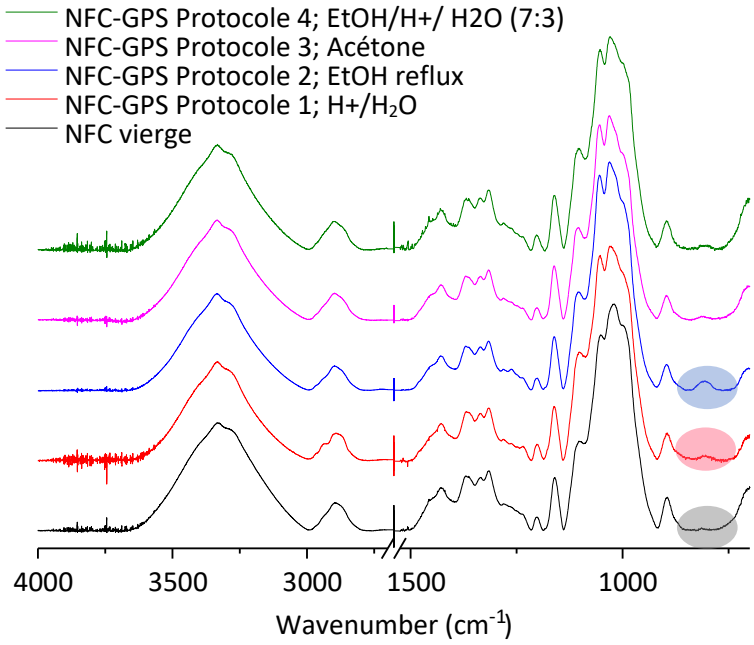

Figure 4-1. Spectres infrarouges de NFC vierge et des NFC modifiées dans les différentes conditions établies dans le Tableau 4-1.

Sur la base de ces premiers résultats, il est possible de supposer que les silanes sont absorbés physiquement et chimiquement à la surface des NFC. De plus, la vibration à 813 cm^{-1}, liée aux réseaux de silicium, suggère une auto-condensation des silanes sur la surface.

Des analyses EDX ont été réalisées avant et après l'extraction Soxhlet pour confirmer l'adsorption du silane. La **Figure 4-2** montre un spectre EDX des NFC-GPS préparées dans un milieu acide. Trois signaux différents sont présents à 0.277, 0.525, et 1.75 keV, associés aux C, O, et Si Kα, respectivement.

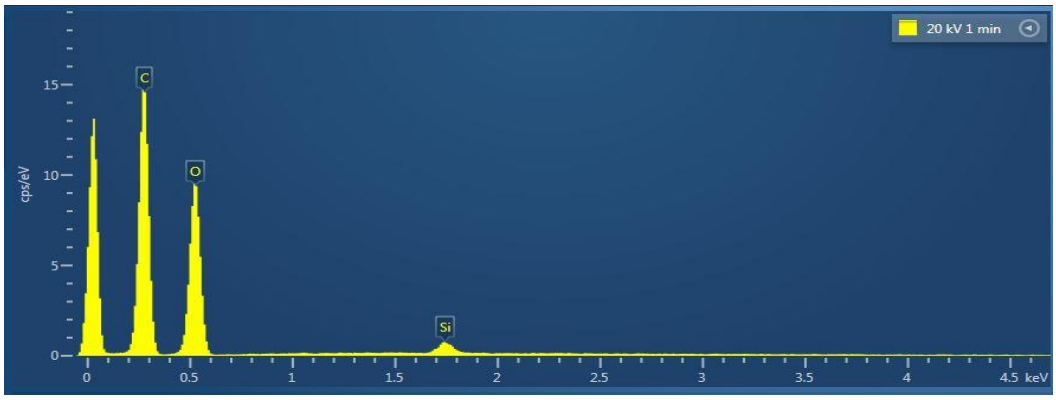

Figure 4-2. Le spectre EDX des NFC-GPS préparées dans un milieu acide (après extraction Soxhlet). Spectre obtenue sous un champ de 20 kV et une distance de travail de 8 mm.

Pour aller plus loin dans l'analyse de surface des fibrilles, des caractérisations par spectroscopie de photoélectrons à rayons X (XPS) ont été réalisées. La **Figure 4-3** présentent les spectres XPS obtenus après extraction Soxhlet, et le Tableau 4-2 regroupe les valeurs des concentrations atomiques relatives et les rapports oxygène/carbone pour chaque échantillon. Le spectre d'étude des NFC vierges ne possède que deux pics à 532 et 286 eV, correspondant respectivement à l'oxygène (O 1s) et au carbone (C1s). Les NFC modifiées avec des silanes présentent un troisième pic à 102 eV, confirmant la présence de l'élément Si.

Le rapport atomique O/C peut être utilisé comme paramètre pour mesurer la présence de GPS sur la surface en mesurant les changements de concentration des atomes à la surface[67]. Les résultats pour les NFC vierges et modifiées sont présentés dans le Tableau 4-2. Pour les échantillons où l'agent de couplage silane est le GPS, le rapport atomique O/C montre une décroissante de 0.67 à 0.64.

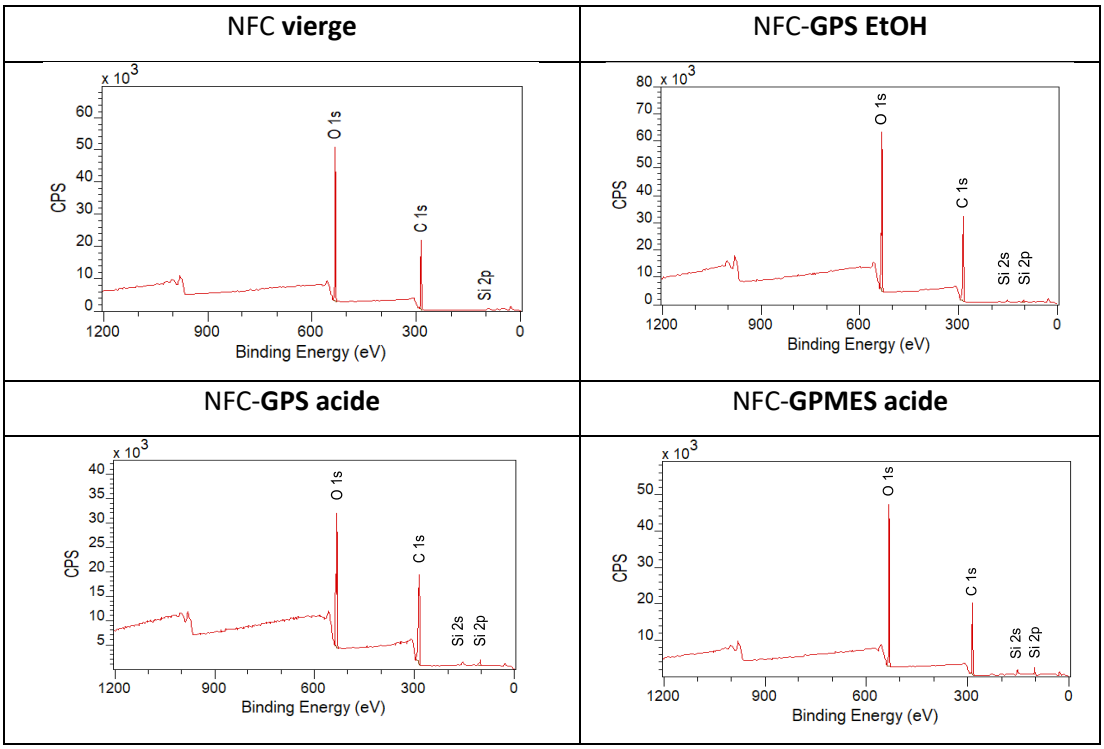

Figure 4-3. Spectres XPS des NFC vierge, NFC-GPS sous conditions EtOH et acide, et NFC-GPMES sous condition acide. Ces spectres ont tous été réalisés sur des échantillons obtenus après extraction Soxhlet.

Échantillon	C 1s	O 1s	Si 2p	O/C
NFC **vierge**	59.8	39.9	0.3	0.67
NFC-**GPS - Acide**	57.7	37.1	5.1	0.64
NFC-**GPS - EtOH**	59.5	37.4	3.1	0.64
NFC-**GPMES - Acide**	61.2	37.9	1	0.62

Tableau 4-2. Concentration atomique relative obtenue par analyse XPS des NFC vierges et modifiées après extraction Soxhlet.

Pour étudier la structure auto-condensée des silanes greffés sur la surface des NFC, des expériences de RMN à l'état solide ^{29}Si ont été réalisées. La **Figure 4-4a** illustre l'évolution de l'auto-condensation d'un dimère à un réseau, montrant quatre degrés possibles d'auto-condensation dénommées T0, T1, T2 et T3. La **Figure 4-4b** présente le spectre des NFC modifiées avec le GPS avant et après l'extraction Soxhlet. Dans les deux cas, les déplacements chimiques sont presque les mêmes, δ=-39, -48, -58, et -66 ppm, correspondant à T0, T1, T2, et T3, respectivement[70, 71, 75].

Après l'extraction Soxhlet (**Figure 4-4b** en bleu), le principal changement est l'intensité des pics des différentes structures auto-condensées. De plus, l'extraction élimine préférentiellement les

structures T3 sur les NFC. Les réseaux greffés de silanes plus proches de la cellulose, T0 et T1, montre une augmentation notable après extraction Soxhlet. Cette remarque laisse penser qu'il y a une quantité significative du réseau avec un degré d'auto-condensation plus élevé (structures T2 et T3) physisorbé a la surface des NFC, et facilement éliminé par l'extraction Soxhlet.

L'utilisation de silanes avec un seul silanol a été étudié en utilisant le GPMES afin d'obtenir une monocouche de silane à la surface des NFC. La **Figure 4-4c** montre les déplacements chimiques du GPMES greffés sur les NFC. En comparaison au greffage effectué avec le GPS, le spectre du GPMES montre deux signaux, δ=18 et 8 ppm, attribués à la liaison entre la NFC-GPMES et au dimère auto-condensé, respectivement. Même après une extraction Soxhlet, les structures auto-condensées physisorbées semblent restées à la surface de la cellulose.

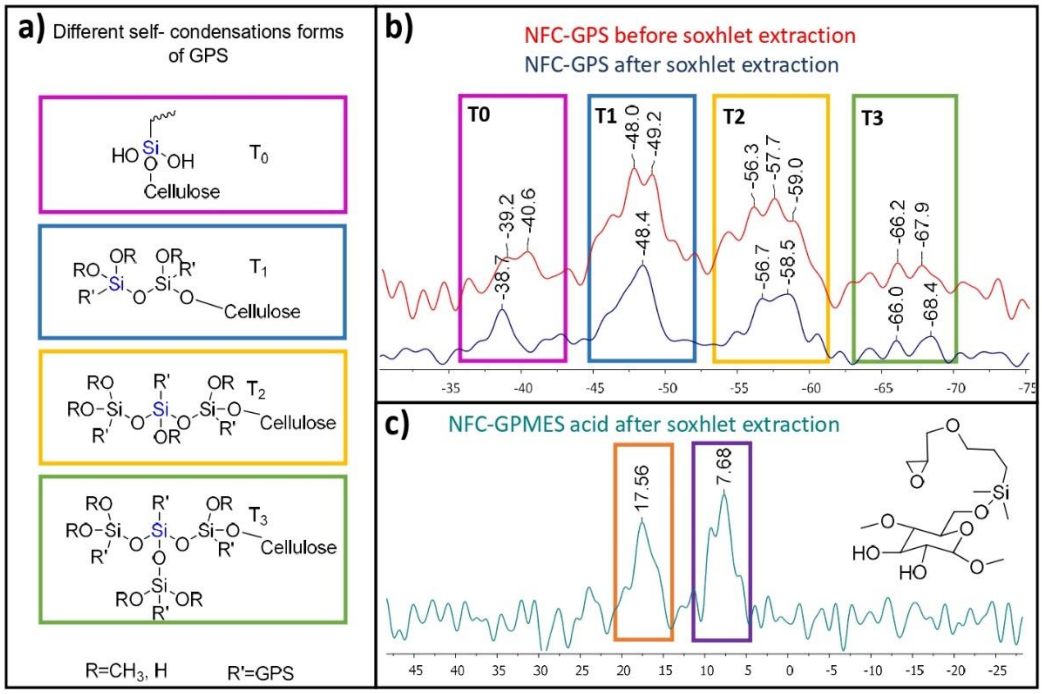

Figure 4-4. Spectres RMN ^{29}Si à l'état solide des NFC fonctionnalisées avec GPS en condition acide. a) Différentes formes de condensation du silane GPS, b) NFC-GPS avant et après extraction Soxhlet en condition acide, et c) NFC-GPMES - acide après extraction Soxhlet.

4.4.2 Caractérisation Morphologique

Afin de voir l'effet des agents de couplage silane sur la morphologie des nanofibrilles de cellulose modifiée, des images MEB ont été réalisées avant et après fonctionnalisation (**Figure 4-5**). Les résultats montrent une légère augmentation du diamètre des fibrilles (**Tableau 4-3**) après la modification, même après l'extraction Soxhlet. Ces observations suggèrent la présence d'un réseau de siloxane physisorbé sur les NFC modifiées, qui semble partiellement éliminé après l'extraction

Soxhlet. La fonctionnalisation chimique avec des agents de couplage silane ne semble pas modifier fortement l'aspect morphologique des NFC à l'échelle microscopique. Des résultats similaires ont été obtenus par Herrera-Franco *et al.*[62].

	NFC vierge	**NFC-GPS EtOH *avant* Soxhlet**	**NFC-GPS EtOH *après* Soxhlet**	**NFC-GPS acide *avant* Soxhlet**	**NFC-GPS acide *après* Soxhlet**
Diamètre (nm)	38 ± 9	58 ± 27	52 ± 15	63 ± 25	54 ± 16

Tableau 4-3. Diamètre mesuré du NFC vierge et du NFC modifié.

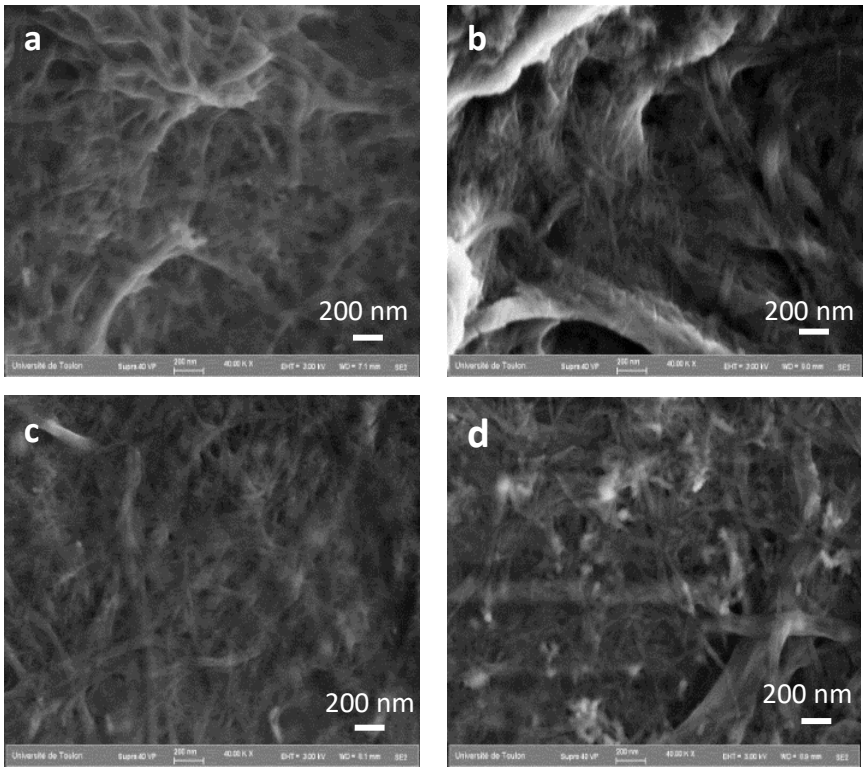

Figure 4-5. Morphologies de surface enregistrées par microscopie MEB des échantillons de NFC après extraction Soxhlet. a) NFC vierge, b) NFC-GPS EtOH, c) NFC-GPS sous condition acide, et d) NFC-GPMES sous condition acide. Les quatre après Soxhlet.

4.4.3 Caractérisation Thermique

La stabilité thermique des NFC modifiées a été évaluée par analyse thermogravimétrique ATG (**Figure 4-6**). En dessous de 380°C, la perte de masse est très similaire et attribuée à l'évaporation de l'eau, mais à des températures supérieures, la stabilité thermique des fibrilles modifiées est supérieure à celle des NFC vierges. Ce comportement pourrait être associé à une couche de polysiloxane formée sur la surface des NFC, ce qui retarde la décomposition thermique.

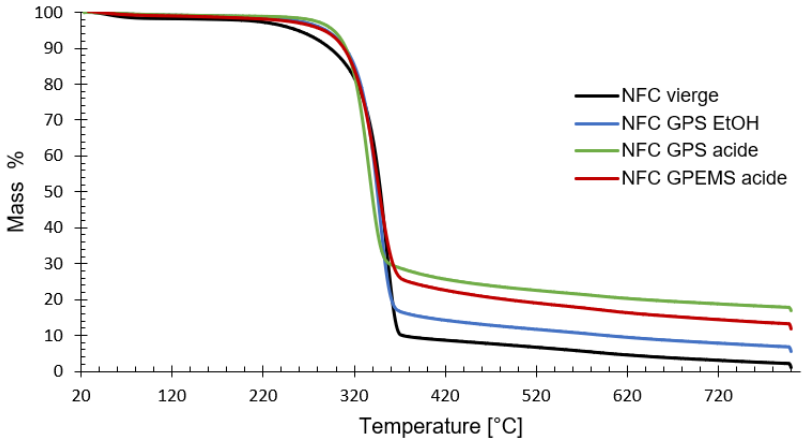

Figure 4-6. Analyse thermogravimétrique des NFC vierge et modifiées.

4.5 Conclusions

La fonctionnalisation chimique des nanofibrilles de cellulose avec le 3-(glycidyloxypropyl) triméthoxysilane et le 3-(glycidoxypropyl) diméthyléthoxysilane a été réalisée avec succès en utilisant un protocole simple. Les analyses par FTIR, EDX, XPS ont permis de mettre en évidence la présence de silicium adsorbés sur la surface des NFC, même après une extraction Soxhlet. La fonctionnalisation dans des conditions acides a été retenue car la quantité de Si déterminé par XPS était la plus élevée.

La formation de structures tridimensionnelles des silanes adsorbées à la surface des NFC a été mise en évidence par la RMN solide ^{29}Si. En outre, les structures auto-condensées de degré supérieur ont été plus facilement éliminées que les oligomères probablement formés par l'extraction par Soxhlet. La morphologie a été caractérisée en utilisant le MEB et l'AFM. Les résultats ont montré que la structure morphologique n'est pas modifiée par le traitement chimique, mais une augmentation de 35% du diamètre des fibrilles a été remarquée. De plus, la présence de silanes a amélioré la stabilité thermique la fonctionnalisation des NFC.

Cette étude a permis d'élaborer un renfort biosourcé avec des groupes époxy, qui peuvent promouvoir des réactions dans le système vitrimère DGEBA–4-APDS. Le composite DGEBA–4-APDS-NFC a montré une adhésion interfaciale moyenne, donc, la modification des NFC peut améliorer :

1) l'adhésion interfaciale fibres-matrice, en favorisant la formation de liaisons covalentes résine-fibres et en améliorant leurs propriétés mécaniques ;
2) la dispersion des fibres, en favorisant la diffusion de la résine dedans les fibrilles ;
3) la durabilité du matériau en diminuant légèrement le caractère hydrophilie des nanofibrilles de cellulose.

Bibliographie

1 Grand View Research (2016) Epoxy Resin Market Size, Share, and Trends Analysis Report, By Application (Paints & Coatings, Wind Turbine, Composites, Construction, Electrical & Electronics, Adhesives) And Segment Forecast to 2024. Recurperated from https://www.grandviewresearch.com/industry-analysis/epoxy-resins-market [March 2021].

2 May, C. (2018). Epoxy Resins: Chemistry and Technology, Second Edition. Boca Raton: Routledge.

3 Ellis, B. (Ed.). (1993). Chemistry and technology of epoxy resins.

4 White, S. R., Sottos, N. R., Geubelle, P. H., Moore, J. S., Kessler, M. R., Sriram, S. R., ... & Viswanathan, S. (2001). Autonomic healing of polymer composites. *Nature*, *409*(6822), 794-797

5 Kloxin, C. J., Scott, T. F., Adzima, B. J., & Bowman, C. N. (2010). Covalent adaptable networks (CANs): a unique paradigm in cross-linked polymers. *Macromolecules*, *43*(6), 2643-2653.

6 Bowman, C. N., & Kloxin, C. J. (2012). Covalent adaptable networks: reversible bond structures incorporated in polymer networks. *Angewandte Chemie International Edition*, *51*(18), 4272-4274.

7 Sastri, V. R., & Tesoro, G. C. (1990). Reversible crosslinking in epoxy resins. II. New approaches. *Journal of applied polymer science*, *39*(7), 1439-1457.

8 DUŠEK, K., & MATĚJKA, L. (1984). Transesterification and gelation of polyhydroxy esters formed from diepoxides and dicarboxylic acids.

9 Turkenburg, D. H., & Fischer, H. R. (2015). Diels-Alder based, thermo-reversible cross-linked epoxies for use in self-healing composites. *Polymer*, *79*, 187-194

10 Montarnal, D., Capelot, M., Tournilhac, F., & Leibler, L. (2011). Silica-like malleable materials from permanent organic networks. *Science*, *334*(6058), 965-968.

11 Denissen, W., Winne, J. M., & Du Prez, F. E. (2016). Vitrimers: permanent organic networks with glass-like fluidity. *Chemical science*, *7*(1), 30-38.

12 Obadia, M. M., Jourdain, A., Cassagnau, P., Montarnal, D., & Drockenmuller, E. (2017). Tuning the Viscosity Profile of Ionic Vitrimers Incorporating 1, 2, 3-Triazolium Cross-Links. *Advanced Functional Materials*, *27*(45), 1703258.

13 Jourdain, A., Asbai, R., Anaya, O., Chehimi, M. M., Drockenmuller, E., & Montarnal, D. (2020). Rheological Properties of Covalent Adaptable Networks with 1, 2, 3-Triazolium Cross-Links: The Missing Link between Vitrimers and Dissociative Networks. *Macromolecules*, *53*(6), 1884-1900.

14 Altuna, F. I., Pettarin, V., & Williams, R. J. (2013). Self-healable polymer networks based on the cross-linking of epoxidised soybean oil by an aqueous citric acid solution. *Green Chemistry*, *15*(12), 3360-3366.

15 Capelot, M., Montarnal, D., Tournilhac, F., & Leibler, L. (2012). Metal-catalyzed transesterification for healing and assembling of thermosets. *Journal of the american chemical society*, *134*(18), 7664-7667.

16 Denissen, W., Rivero, G., Nicolaÿ, R., Leibler, L., Winne, J. M., & Du Prez, F. E. (2015). Vinylogous urethane vitrimers. *Advanced Functional Materials*, *25*(16), 2451-2457.

17 Zheng, H., Liu, Q., Lei, X., Chen, Y., Zhang, B., & Zhang, Q. (2018). A conjugation polyimine vitrimer: Fabrication and performance. *Journal of Polymer Science Part A: Polymer Chemistry*, *56*(22), 2531-2538.

18 Saed, M. O., Gablier, A., & Terentejv, E. M. (2020). Liquid Crystalline Vitrimers with Full or Partial Boronic-Ester Bond Exchange. *Advanced Functional Materials*, *30*(3), 1906458.

19 Lu, Y. X., Tournilhac, F., Leibler, L., & Guan, Z. (2012). Making insoluble polymer networks malleable via olefin metathesis. *Journal of the American Chemical Society*, *134*(20), 8424-8427.

20 de Luzuriaga, A. R., Matxain, J. M., Ruipérez, F., Martin, R., Asua, J. M., Cabañero, G., & Odriozola, I. (2016). Transient mechanochromism in epoxy vitrimer composites containing aromatic disulfide crosslinks. *Journal of Materials Chemistry C*, *4*(26), 6220-6223.

21 Obadia, M. M., Mudraboyina, B. P., Serghei, A., Montarnal, D., & Drockenmuller, E. (2015). Reprocessing and recycling of highly cross-linked ion-conducting networks through transalkylation exchanges of C–N bonds. *Journal of the American Chemical Society*, *137*(18), 6078-6083.

22 Huang, Z., Wang, Y., Zhu, J., Yu, J., & Hu, Z. (2018). Surface engineering of nanosilica for vitrimer composites. *Composites Science and Technology*, *154*, 18-27.

23 Hong, M. (2017). Application de la spectroscopie de fluorescence 3D a la caractérisation des réseaux polymères thermodurcis : influence de la mobilité macromoléculaire et du vieillissement hydrolytique [Thèse de doctorat, Université de Toulon].

24 Ochi, M., Yamashita, K., & Shimbo, M. (1991). The mechanism for occurrence of internal stress during curing epoxide resins. *Journal of Applied Polymer Science*, *43*(11), 2013-2019.

25 Meyer, F., Sanz, G., Eceiza, A., Mondragon, I., & Mijović, J. (1995). The effect of stoichiometry and thermal history during cure on structure and properties of epoxy networks. *Polymer*, *36*(7), 1407-1414.

26 De Nograro, F. F., Guerrero, P., Corcuera, M. A., & Mondragon, I. (1995). Effects of chemical structure of hardener on curing evolution and on the dynamic mechanical behavior of epoxy resins. *Journal of applied polymer science*, *56*(2), 177-192.

27 Sanz, G., Garmendia, J., Andres, M. A., & Mondragon, I. (1995). Dependence of dynamic mechanical behavior of DGEBA/DDM stoichiometric epoxy systems on the conditions of curing process. *Journal of applied polymer science*, *55*(1), 75-87.

28 Morgan, R. J., Kong, F. M., & Walkup, C. M. (1984). Structure-property relations of polyethertriamine-cured bisphenol-A-diglycidyl ether epoxies. *Polymer*, *25*(3), 375-386

29 Heravi, M. M., Ghavidel, M., & Mohammadkhani, L. (2018). Beyond a solvent: triple roles of dimethylformamide in organic chemistry. *RSC advances*, *8*(49), 27832-27862.

30 Canadell, J., Goossens, H., & Klumperman, B. (2011). Self-healing materials based on disulfide links. *Macromolecules*, *44*(8), 2536-2541.

31 Mathieu Capelot. Chimie de Polycondensation, Polymères Supramoléculaires et Vitrimères. Polymères. Université Pierre et Marie Curie - Paris VI, 2013. Français.

32 Denissen, W., De Baere, I., Van Paepegem, W., Leibler, L., Winne, J., & Du Prez, F. E. (2018). Vinylogous urea vitrimers and their application in fiber reinforced composites. *Macromolecules*, *51*(5), 2054-2064.

33 Taplan, C., Guerre, M., Winne, J. M., & Du Prez, F. E. (2020). Fast processing of highly crosslinked, low-viscosity vitrimers. *Materials Horizons*, *7*(1), 104-110.

34 Morrison, F. A. (2001). *Understanding rheology*. Oxford University Press, USA.

35 Dyre, J. C. (2006). Colloquium: The glass transition and elastic models of glass-forming liquids. *Reviews of modern physics*, *78*(3), 953.

36 Yang, Y., Zhang, S. Zhang, X., Gao, L., Wei, Y., & Ji, Y. (2019). Detecting topology freezing transition temperature of vitrimers by AIE luminogens. *Nature communications*, 10 (1), 1-8.

37 Ricarte, R. G., Tournilhac, F., Cloître, M., & Leibler, L. (2020). Linear viscoelasticity and flow of self-assembled vitrimers: The case of a polyethylene/dioxaborolane system. *Macromolecules*, *53*(5), 1852-1866.

38 Luo, C., Shi, X., Lei, Z., Zhu, C., Zhang, W., & Yu, K. (2018). Effects of bond exchange reactions and relaxation of polymer chains on the thermomechanical behaviors of covalent adaptable network polymers. *Polymer*, *153*, 43-51.

39 Hayashi, M., Yano, R., & Takasu, A. (2019). Synthesis of amorphous low T g polyesters with multiple COOH side groups and their utilization for elastomeric vitrimers based on post-polymerization cross-linking. *Polymer Chemistry*, *10*(16), 2047-2056.

40 Snijkers, F., Pasquino, R., & Maffezzoli, A. (2017). Curing and viscoelasticity of vitrimers. *Soft Matter*, *13*(1), 258-268.

41 Li, L., Chen, X., Jin, K., & Torkelson, J. M. (2018). Vitrimers designed both to strongly suppress creep and to recover original cross-link density after reprocessing: quantitative theory and experiments. *Macromolecules*, *51*(15), 5537-5546.

42 Luo, C., Shi, X., Lei, Z., Zhu, C., Zhang, W., & Yu, K. (2018). Effects of bond exchange reactions and relaxation of polymer chains on the thermomechanical behaviors of covalent adaptable network polymers. *Polymer*, *153*, 43-51.

43 Hayashi, M., Yano, R., & Takasu, A. (2019). Synthesis of amorphous low T g polyesters with multiple COOH side groups and their utilization for elastomeric vitrimers based on post-polymerization cross-linking. *Polymer Chemistry*, *10*(16), 2047-2056.

44 Matxain, J. M., Asua, J. M., & Ruipérez, F. (2016). Design of new disulfide-based organic compounds for the improvement of self-healing materials. *Physical Chemistry Chemical Physics*, *18*(3), 1758-1770.

45 J. D. Ferry, *Viscoelastic Properties of Polymers* (JohnWiley&Sons, NewYork, 1980).

46 Vinson, J. R., & Sierakowski, R. L. (2006). *The behavior of structures composed of composite materials* (Vol. 105). Springer.

47 Parbin, S., Waghmare, N. K., Singh, S. K., & Khan, S. (2019). Mechanical properties of natural fiber reinforced epoxy composites: A review. *Procedia Computer Science*, *152*, 375-379.

48 Siró, I., & Plackett, D. (2010). Microfibrillated cellulose and new nanocomposite materials: a review. *Cellulose*, *17*(3), 459-494.

49 Azizi Samir, M. A. S., Alloin, F., & Dufresne, A. (2005). Review of recent research into cellulosic whiskers, their properties and their application in nanocomposite field. *Biomacromolecules*, *6*(2), 612-626.

50 Lee, K. Y., Aitomäki, Y., Berglund, L. A., Oksman, K., & Bismarck, A. (2014). On the use of nanocellulose as reinforcement in polymer matrix composites. *Composites Science and Technology*, *105*, 15-27.

51 Nissilä, T., Hietala, M., & Oksman, K. (2019). A method for preparing epoxy-cellulose nanofiber composites with an oriented structure. *Composites Part A: Applied Science and Manufacturing*, *125*, 105515.

52 Lu, J., Askeland, P., & Drzal, L. T. (2008). Surface modification of microfibrillated cellulose for epoxy composite applications. *Polymer*, *49*(5), 1285-1296.

53 Saba, N., Safwan, A., Sanyang, M. L., Mohammad, F., Pervaiz, M., Jawaid, M., ... & Sain, M. (2017). Thermal and dynamic mechanical properties of cellulose nanofibers reinforced epoxy composites. *International journal of biological macromolecules*, *102*, 822-828.

54 Ansari, F., Galland, S., Johansson, M., Plummer, C. J., & Berglund, L. A. (2014). Cellulose nanofiber network for moisture stable, strong and ductile biocomposites and increased epoxy curing rate. *Composites Part A: Applied Science and Manufacturing*, *63*, 35-44.

55 Yang, Y., Pei, Z., Zhang, X., Tao, L., Wei, Y., & Ji, Y. (2014). Carbon nanotube–vitrimer composite for facile and efficient photo-welding of epoxy. *Chemical Science*, *5*(9), 3486-3492.

56 Zhao, W., Feng, Z., Liang, Z., Lv, Y., Xiang, F., Xiong, C., ... & Ni, Y. (2019). Vitrimer-Cellulose Paper Composites: A New Class of Strong, Smart, Green, and Sustainable Materials. *ACS applied materials & interfaces*, *11*(39), 36090-36099.

57 Lossada, F., Guo, J., Jiao, D., Groeer, S., Bourgeat-Lami, E., Montarnal, D., & Walther, A. (2018). Vitrimer chemistry meets cellulose nanofibrils: bioinspired nanopapers with high water resistance and strong adhesion. *Biomacromolecules*, *20*(2), 1045-1055.

58 Xu, C., Zheng, Z., Wu, W., Fu, L., & Lin, B. (2019). Design of healable epoxy composite based on β-hydroxyl esters crosslinked networks by using carboxylated cellulose nanocrystals as crosslinker. *Composites Science and Technology*, *181*, 107677.

59 Nair, S. S., Chen, H., Peng, Y., Huang, Y., & Yan, N. (2018). Polylactic acid biocomposites reinforced with nanocellulose fibrils with high lignin content for improved mechanical, thermal, and barrier properties. *ACS Sustainable Chemistry & Engineering*, *6*(8), 10058-10068.

60 Tingaut, P., Zimmermann, T., & Lopez-Suevos, F. (2010). Synthesis and characterization of bionanocomposites with tunable properties from poly (lactic acid) and acetylated microfibrillated cellulose. *Biomacromolecules*, *11*(2), 454-464.

61 Abdelmouleh, M., Boufi, S., Belgacem, M. N., Dufresne, A., & Gandini, A. (2005). Modification of cellulose fibers with functionalized silanes: effect of the fiber treatment on the mechanical performances of cellulose–thermoset composites. *Journal of applied polymer science*, *98*(3), 974-984.

62 Herrera-Franco, P., & Valadez-Gonzalez, A. (2005). A study of the mechanical properties of short natural-fiber reinforced composites. *Composites Part B: Engineering*, *36*(8), 597-608.

63 Yang, Y., Zhang, S., Zhang, X., Gao, L., Wei, Y., & Ji, Y. (2019). Detecting topology freezing transition temperature of vitrimers by AIE luminogens. *Nature communications*, *10*(1), 1-8.

64 Valadez-Gonzalez, A., Cervantes-Uc, J. M., Olayo, R., & Herrera-Franco, P. J. (1999). Chemical modification of henequen fibers with an organosilane coupling agent. *Composites Part B: Engineering*, *30*(3), 321-331.

65 Castellano, M., Gandini, A., Fabbri, P., & Belgacem, M. N. (2004). Modification of cellulose fibres with organosilanes: Under what conditions does coupling occur? *Journal of Colloid and Interface science*, *273*(2), 505-511.

66 Abdelmouleh, M., Boufi, S., ben Salah, A., Belgacem, M. N., & Gandini, A. (2002). Interaction of silane coupling agents with cellulose. *Langmuir*, *18*(8), 3203-3208

67 Khanjanzadeh, H., Behrooz, R., Bahramifar, N., Gindl-Altmutter, W., Bacher, M., Edler, M., & Griesser, T. (2018). Surface chemical functionalization of cellulose nanocrystals by 3-aminopropyltriethoxysilane. *International journal of biological macromolecules*, *106*, 1288-1296.

68 Robles, E., Csóka, L., & Labidi, J. (2018). Effect of reaction conditions on the surface modification of cellulose nanofibrils with aminopropyl triethoxysilane. *coatings*, *8*(4), 139.

69 Yeo, J. S., Kim, O. Y., & Hwang, S. H. (2017). The effect of chemical surface treatment on the fracture toughness of microfibrillated cellulose reinforced epoxy composites. *Journal of Industrial and Engineering Chemistry*, *45*, 301-306.

70 Salon, M. C. B., Abdelmouleh, M., Boufi, S., Belgacem, M. N., & Gandini, A. (2005). Silane adsorption onto cellulose fibers: Hydrolysis and condensation reactions. *Journal of colloid and interface science*, *289*(1), 249-261.

71 Salon, M. C. B., Gerbaud, G., Abdelmouleh, M., Bruzzese, C., Boufi, S., & Belgacem, M. N. (2007). Studies of interactions between silane coupling agents and cellulose fibers with liquid and solid-state NMR. *Magnetic Resonance in Chemistry*, *45*(6), 473-483.

72 Maréchal, Y., & Chanzy, H. (2000). The hydrogen bond network in Iβ cellulose as observed by infrared spectrometry. *Journal of molecular structure*, *523*(1-3), 183-196.

73 Šapić, I. M., Bistričić, L., Volovšek, V., Dananić, V., & Furić, K. (2009). DFT study of molecular structure and vibrations of 3-glycidoxypropyltrimethoxysilane. *Spectrochimica Acta Part A: Molecular and Biomolecular Spectroscopy*, *72*(4), 833-840.

74 Bistričić, L., Volovšek, V., Dananić, V., & Šapić, I. M. (2006). Conformational stability and vibrations of aminopropylsilanol molecule. *Spectrochimica Acta Part A: Molecular and Biomolecular Spectroscopy*, *64*(2), 327-337.

75 Plueddemann, E. P. (1991). Nature of adhesion through silane coupling agents. In *Silane coupling agents* (pp. 115-152). Springer, Boston, MA.

Epoxy vitrimer materials based on disulfide exchange chemistry: experimental study and modeling of the stress relaxation - application to composites reinforced by nanofibrillated cellulose.

Epoxy thermoset resins have drawn the attention of many industries due to their versatility, from adhesives to polymer composites. Yet, the ***re-processability, sustainability, and durability*** of resins limit their use. The covalent adaptable networks (CANs) like vitrimers can afford a solution to overcome these issues. The ***epoxy resin***, DGEBA–4-APDS, based on the disulfide exchange chemistry, has shown ***re-processability*** properties, but its vitrimer properties have not been fully verified. In the present work, all the vitrimer properties are reviewed ***to classify it as a vitrimer material***. Interestingly, the vitrimer exchange operating temperature (*T*v) is close to its glass transition (*T*g). So, its relaxation behavior, slightly above *T*g, is influenced by the bond exchange reactions and the segmental relaxations of the network. Thus, an ***adapted stress relaxation mode*l** that considers both relaxation phenomena is proposed. This developed rheological model leads to evaluate the ***epoxy vitrimer matrix reinforced by nano fibrillated cellulose*** **(NFC).** The vitrimer composite made with NFC performs a ***sustainable*** lightweight material and exhibits mechanical properties similar to non-covalent adaptable networks. A preliminary study to increase material ***durability*** has consisted in the ***NFC surface modification*** by glycidoxy silane coupling agent. A ***simple NFC grafting method*** is proposed, and the surface characterization of the silane network surrounding the NFC is well-explored.

Keywords: vitrimer-epoxy, relaxation behavior, bond exchange reaction, nano fibrillated cellulose, surface modification.

Matériaux époxy vitrimères basés sur la chimie des échanges de disulfures : étude expérimentale et modélisation de la relaxation de contrainte - application aux composites renforcés par des nano fibrilles de cellulose.

Les résines époxy thermodurcissables ont attiré l'attention de nombreuses industries en raison de leur polyvalence, des adhésifs aux matériaux composites. Malgré leur versatilité, ***le recyclage, la durabilité et développement durable*** de ces thermodurs majoritairement pétrosourcés limitent leur utilisation. Des réseaux adaptables covalents (CAN) comme les vitrimères peuvent offrir une solution pour faire face à ces problèmes. Le système ***époxy*** DGEBA–4-APDS, basé sur la chimie d'échange de disulfures, ***a montré des*** propriétés de recyclabilité, mais son comportement ***vitrimère n'a pas été encore complètement vérifié***. Dans le présent travail, toutes les propriétés propres aux vitrimères sont étudiées ***afin de s'assurer du caractère vitrimère de ce matériau***. De façon intéressante, la température d'échange des liaisons réversibles propre aux vitrimères (*T*v) est proche de la transition vitreuse du matériau (*T*g). Il en découle que sa relaxation, qui s'opère légèrement au-dessus de sa *T*g, est influencée à la fois par les réactions d'échange des liaisons réversibles et par la relaxation du polymère en lui-même. De ce fait, il est proposé un ***modèle adapté de relaxation des contraintes*** qui prend en compte ces deux phénomènes. Ce modèle rhéologique a permis également d'évaluer la relaxation de cette ***matrice époxy-vitrimère renforcée*** par des nanofibrilles de cellulose (NFC). Ce composite vitrimère à base de NFC est un matériau léger ***durable*** et présentant des propriétés mécaniques similaires à celles des réseaux covalents non-adaptables. Une étude initiale pour augmenter la ***durabilité*** de ce vitrimère époxy a consisté à ***modifier la surface de la NFC*** par un agent de couplage glycidoxy silane. Une ***méthode simple de greffage des NFC*** est proposée, et la caractérisation du réseau silane entourant les NFC a été réalisée.

Mots clés : époxy-vitrimère, relaxation de contrainte, réaction d'échange de liaisons réversibles, nano cellulose fibrillée, modification de la surface.